SP-611

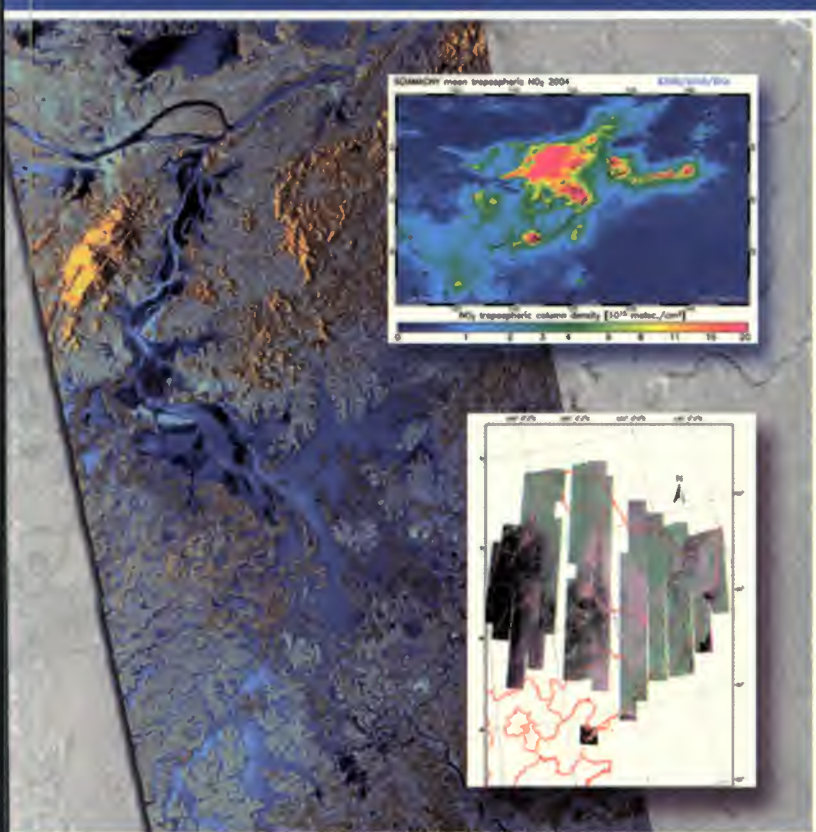

Proceedings of

Dragon Programme Mid-Term Results

27 June - 1 July 2005
Santorini, Greece

esa

NRSCC

SP-611
January 2006

Proceedings of the
2005 Dragon Symposium

Dragon Programme Mid-Term Results

27 June – 1 July 2005
Santorini, Greece

NRSCC

European Space Agency
Agence spatiale européenne

DRAGON Programme Coordinators

Yves-Louis Desnos
Head of R&D Section,
EO Science and Applications Department
Directorate of EO Programmes
ESA/ESRIN, via Galileo Galilei, I-00044, Frascati, Italy

Li Zengyuan
Deputy Director of Institute of Forest Resources Information Techniques
The Chinese Academy of Forestry
Wan Shou Shan Hou, Haidan District,
100091 Beijing, P.R. China

Cover Images:

- Mean annual concentration of atmospheric NO2 over P.R. China in 2004 measured using SCIAMACHY;
- ASAR HH/VV AP image of Poyang Lake, P.R.China acquired during the NRT test for ASAR data acquisition and delivery, Feb. 2005;
- ENVISAT ASAR Cycle35 Data Mosaic of N-E China.

Publication (Short Title)	Proc. 2005 Dragon Symposium "Mid-Term Results", Santorini, Greece 27 June – 1 July 2005 (ESA SP-611, January 2006)
Edited by:	H. Lacoste
Compiled by:	L. Ouwehand
Published and distributed by:	ESA Publications Division ESTEC Postbus 299 2200 AG Noordwijk, The Netherlands Tel: +31 71 565 3400 Fax: +31 71 565 5433
Printed in:	The Netherlands
Price:	60 €
ISBN No:	92-9092-922-7
ISSN No:	0379-6566 (Book) & 1609-042X (CD-ROM)
Copyright:	© 2006 European Space Agency

Contents

Internal Waves

Ocean Colour and Constituents

Bottom Topography

<u>Others</u>

Atmosphere

Air Quality Monitoring and Forecasting (id. 2580)

Chemistry of Climate Change in the Atmosphere (id. 2579)

Flooding and Hydrology

Drought Monitoring in China (id. 2608)

Flood Plain Disaster Rapid Mapping and Monitoring (id. 2551)

Agricultural Monitoring in Fujian Province (id. 2563)

Elevation Models and Terrain Motion

Landslides (id. 2558)

Monitoring Seismic Activity (id. 2577)

Terrain Measurement (id. 2567)

New project

EO and Sport Events (id 3362)

EO SCIENCE AND APPLICATIONS DEVELOPMENT IN P.R. CHINA

Yves-Louis Desnos[(1)] & Li Zengyuan[(2)]

[(1)] *Science and Applications Department, ESA Directorate of Earth Observation, ESRIN, Frascati, Italy*
[(2)] *Chinese Academy of Forestry and on behalf of National Remote Sensing Centre (NRSCC), Beijing, P.R. China*

ABSTRACT

ESA together with the National Remote Sensing Centre of China (NRSCC), an entity under the Ministry of Science and Technology, have cooperated in the field of Earth observation applications development for the last 10 years. Following initial high-level meetings between Chinese and ESA officials, it was decided to reinforce the cooperation in the field of Earth observation. The cooperation has taken a new momentum with the creation of a dedicated three years Earth Observation exploitation programme called Dragon. This programme focuses on science and applications development in China using mainly data from the ERS and Envisat missions. This preface will present the background to the cooperation and highlight some of the mid term results.

1. INTRODUCTION

Given the size of China, the total surface covers 9.6 million Square Kilometres, satellite Earth observation is a fundamental tool for the overall management of the country. Another important factor is that today China accounts for 1/5 of the world population with 1.45 billion inhabitants and it is currently the world's fastest growing economy. With this rapid growth and the stress it implies on the natural resources and on the environment, remote sensing can provide precise data for decision makers at all levels. (Fig. 1 illustrates Envisat MERIS capability to observe the Beijing area development).

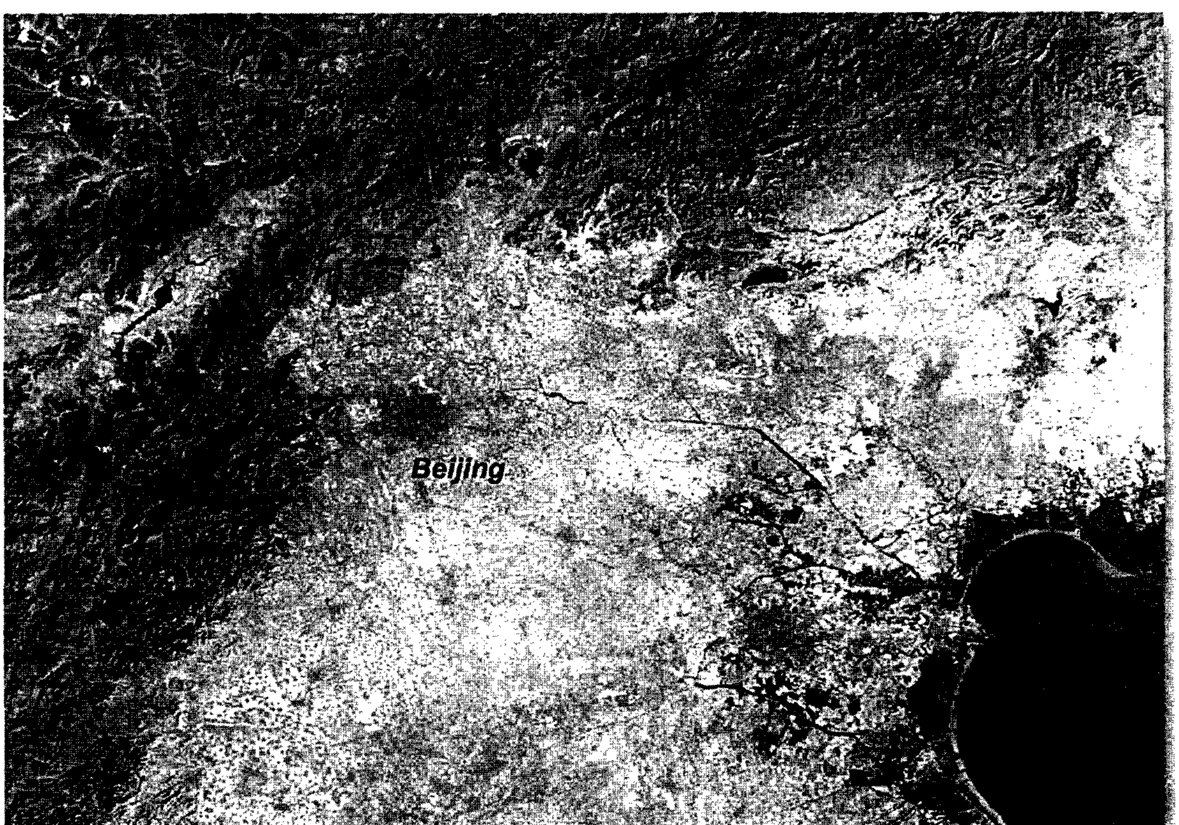

Fig. 1. MERIS Full Resolution image of Beijing and surrounding area, Oct. 2003

Proc. 2005 Dragon Symposium "Mid-Term Results", Santorini, Greece
27 June – 1 July 2005 (ESA SP-611, January 2006)

Satellite data can be used to assist land resource mapping applications such as forest inventory and management, rice production monitoring and water resources assessment and management. An important new element in the Dragon Programme is the extension of techniques and methods for monitoring oceans and atmosphere as well as land using the full complement of Envisat's EO instruments.

Satellite data can contribute to disaster mitigation with its capability to monitor natural disasters and thus providing timely information to local and national authorities. The natural disasters that affect China are on a gigantic scale and include flooding of the Yangtze River, earthquakes on the Tibetan plateau and droughts, which are particularly acute in China. For these calamities Earth Observation is a key tool for understanding and managing such crises and hopefully in the near future to be able to predict and to forecast events through the use of assimilation models and historical long time series data establishing trends and providing alert conditions when changes in those trends are first observed.

2. EARLY COOPERATION

ESA's first contacts with China in the field of Earth observation were established when the Chinese authorities expressed an interest to cooperate on ERS data applications. Subsequently the China Remote Sensing Ground Station in Beijing was upgraded to receive ERS data in 1994 and the two sides signed an agreement to that effect.

In May 1997 China and ESA decided to begin a cooperation project for the increased operational use of ERS data in China. In order to stimulate exploitation of ERS data five pilot projects were created, addressing:

- Rice Mapping in Southern China
- Land-use Mapping for the Beijing Area
- Flood Monitoring
- An Oceanographic Study
- Mapping China Forest with ERS 1 and 2 SAR Tandem Data.

The following year when China experienced its worst floods of the Century, ERS SAR imagery was used in operational mapping of the flood events. The Beijing ground station was able to process and deliver ERS SAR images to end users 24 hours after acquisition. This first cooperation was considered a success by ESA and NRSCC and led to discussions on how to consolidate and increase the cooperation. The Chinese Minister of Science and Technology, Mr Xu Guanhua, during a meeting with ESA Director General also highlighted China's interest in Earth observation applications development. Mr Xu stated that space applications were recognised in China as a key instrument for the development of the Chinese economy and living conditions for its people.

In light of the above progress, ESA's Earth Observation Directorate and their Chinese counterparts at NRSCC began a consultation process on how to reinforce and improve the cooperation to also include joint research. The result is the "The Dragon Programme", which was officially launched in Xiamen, China in April 2004.

3. DRAGON PROGRAMME

3.1 Objectives

The overall objectives of the Dragon Programme are:

- To promote the use of ESA data from the ERS and Envisat satellites
- To stimulate scientific exchange in EO science and technology by the formation of joint Sino-European teams
- To publish co-authored results of the research and applications development
- To provide training in processing, algorithm and product development from ESA EO data in land, ocean and atmospheric applications

These objectives were defined during the first joint ESA/NRSCC meeting held in Beijing in October 2003, Fig. 2.

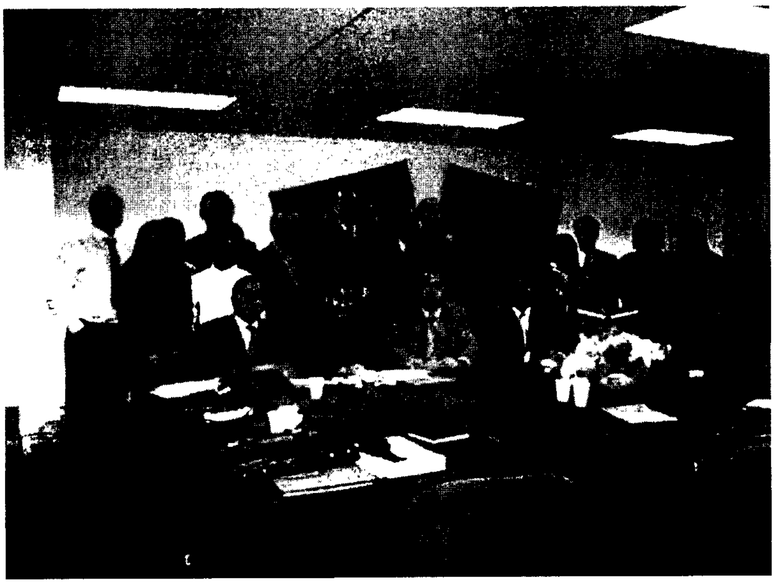

Fig. 2. ESA and NRSCC scientists and officials at Dragon Programme meeting no. 1, Beijing Oct. 2003

3.2 Update on the Dragon Programme

Programme preparation began with dedicated briefings organised respectively for European scientists in September 2003 in Rome and Chinese scientists in October 2003 in Beijing. The response from both European and Chinese scientists was very positive at these briefings. The Dragon call for Proposals was then jointly prepared by ESA-NRSCC and issued in November 2003. Some 25 proposals were received, peer reviewed from the scientific and technical feasibility viewpoints resulting in a final selection of 15 integrated projects covering the priority themes as defined by ESA and NRSCC. The projects address the following identified priority areas:

- Agricultural Monitoring
- Flood Monitoring
- Forest Mapping
- Rice Monitoring
- Forest Fire Monitoring
- Oceanography
- Terrain Measurement
- Seismic Activity
- Landslide Monitoring
- Air Quality Monitoring and Forecasting
- Chemistry/Climate Change in the Atmosphere
- Deriving Forest Information from POLInSAR Data
- Drought Monitoring
- Water Resources and Hydrology
- Climate and Ocean Systems.

On 11 October 2005 a new Dragon project was initiated on EO and sport events that seeks to demonstrate the application of EO data and technology in the organisation of major sport events with case studies focusing on the Athens, Beijing and London Olympic games. The project has partners from Greece, China and the United Kingdom. Fig. 3 shows the study areas in P.R. China requesting Envisat ASAR, MERIS and (A)ATSR data over land and sea. Fig. 4 shows the breakdown on the Dragon projects by thematic application.

Fig. 3. Dragon study areas in P.R. China requesting Envisat ASAR, MERIS and (A)ATSR data
N.B. ESA atmospheric instrument data coverage is for the whole of China

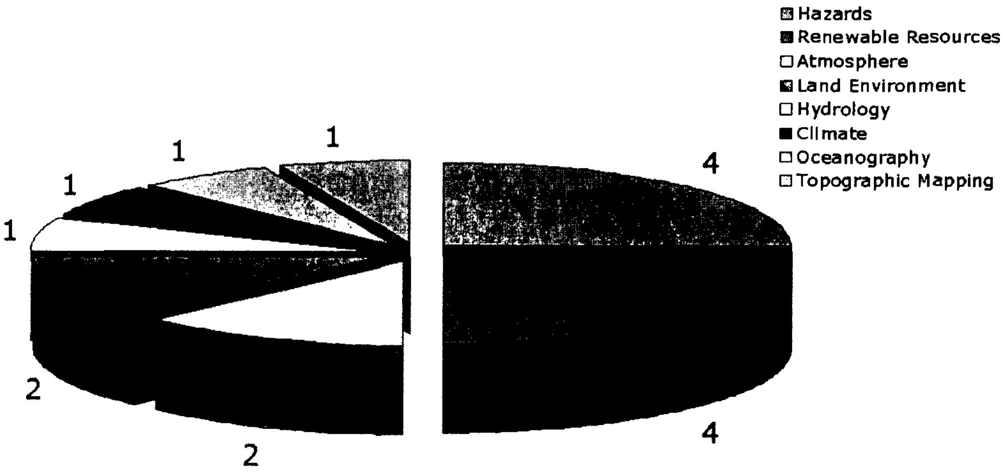

Fig. 4. Application domains for the 16 Dragon projects

In order to facilitate preparations an ESA-NRSCC Dragon web site (Fig. 5) was officially launched in March 2004 (http://earth.esa.int/dragon). The web site contains technical documentation on the programme and projects and it serves as an information and reporting portal. Information about the 2004 and 2005 Symposiums, project teaming, technical presentations, training courses and news items can be found on the web site.

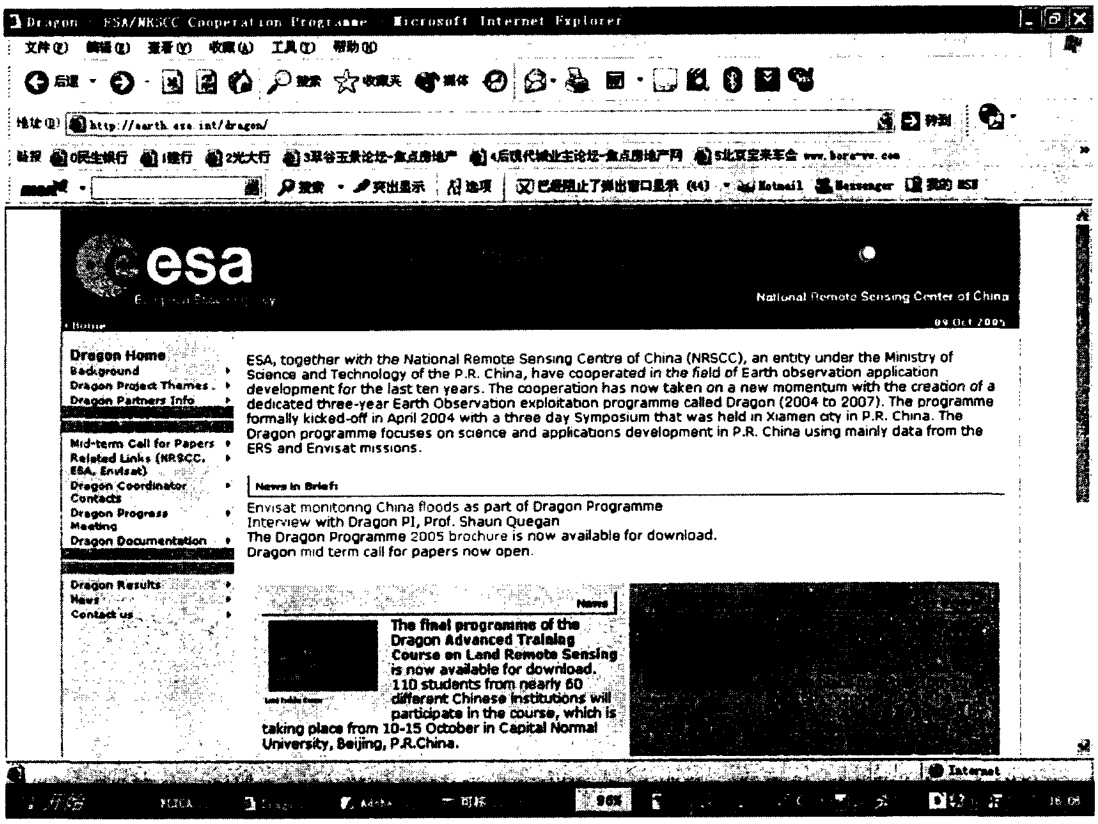

Fig. 5. The ESA-NRSCC Dragon web site [3]

A programme brochure (Fig. 6), has also been prepared by ESA-NRSCC and then widely distributed in Europe and China and provides further information as well as up-to-date scientific results from the project teams [2]. NRSCC have also provided a translation of the Santorini Symposium abstracts. Digital versions of these documents can be downloaded in .pdf from the Dragon web site (see http://uranus.esrin.esa.it/dragon/Dragon_documentation.htm)

Fig. 6. Front covers of the 2004 Dragon brochure (left), 2005 Dragon brochure (middle) and Santorini Symposium abstracts in Chinese (right)

In terms of programme management, ESA and NRSCC have had regular 6 monthly meetings with Chinese Dragon investigators. At these meetings the progress and status of ESA EO data delivery to the projects has been reviewed and further planning for EO data acquisitions made. Fig. 7a and b are from the progress meeting 8 held in Oct. 05 in Beijing. Visits have also been made to individual project teams to review progress and include:

- 28 and 29 April 2005, Dragon project meeting at Ocean University of China and First Institute of Oceanography, Qingdao
- 17 and 18 Oct. 2005, Dragon project meeting at Fuzhou University and Dept. of Science and Technology of Quanzhou

Fig. 7a. ESA and NRSCC officials with Dragon PIs and visiting young European scientists at Dragon progress meeting no. 8, 14 Oct. 2005, CAF, Beijing.

Fig. 7b. Dr. Iphigenia Keramitsoglou of University of Athens, Greece briefing Chinese Dragon PIs on the new project "EO and Sport Events"

3.3 Dragon Symposia

3.3.1 Xiamen Symposium

The 2004 Dragon Symposium was the formal KO for all of the Dragon teams. It was attended by 130 participants from 60 institutes in Europe and China, Fig. 8. The teams made presentations on their projects over 3 days. The programme included presentations on the monitoring of land natural resources, on supporting natural disasters management, on studying the atmosphere and oceanography in China (There are 50 presentations that can be viewed on line: http://uranus.esrin.esa.it/dragon/Dragon_symposium.htm)

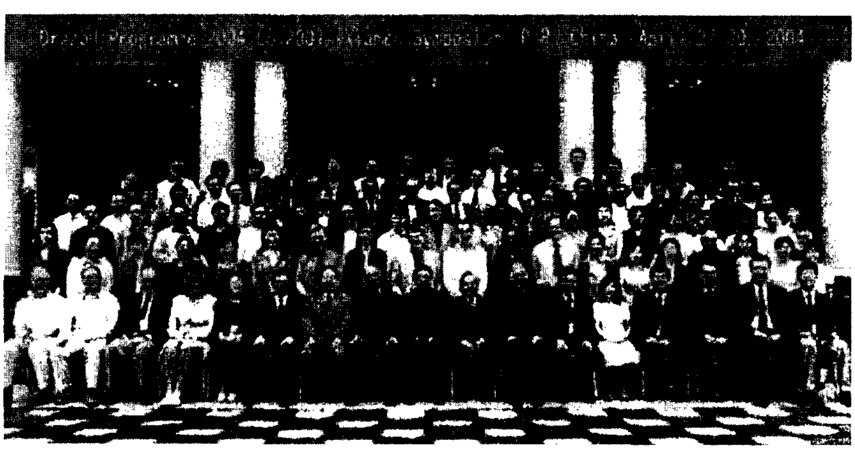

Fig. 8. Chinese and European participants to the Dragan Xiamen Symposium, April 27-30 April 2004

3.3.2 Santorini Symposium

The second Dragon Symposium was held successfully from 27th June to 1st July 2005 in Santorini, Greece organised in close cooperation with GSRT (Greece) and NRSCC (China). This event is of particular significance being the first ESA international symposium hosted by Greece as a full ESA member state.

120 participants, including 50 Chinese PIs and officials, attended the 2 days working meetings and 3 days symposium, Fig. 9. The symposium has allowed the 15 Sino European project teams to report on achievements after one year of cooperation via 65 detailed presentations. Highlights of the symposium the demonstration of NRT flood monitoring in China with data delivery post processing during the symposium and a special session where young European scientists working on the projects reported on their excellent achievements (see next section for an overview).

Fig. 9. Chinese and European participants to the Dragon Symposium, Santorini Island, Greece, 27 June to 1 July 2005

3.4 Young Scientists in Dragon

3.4.1 Training of European Scientists

In 2004, ESA has allocated resources for the training of young scientists on the Dragon projects. The applicable period is Sept. 2004 to May 2007. ESA issued a call to all 15 lead European Dragon investigators and in this call, European lead investigators were asked to:

- Select research topics and the appropriate degree level for the topic
- Identify candidates against a prioritised list of criteria
- Provide a proposal detailing:
  - the research work to be undertaken
  - the working visits required in China
  - an estimate of the travel budget required to support working visits and attendance of sessions dedicated to training at future Dragon Symposia

ESA has now place contracts with 13 institutions. There are now 21 supported trainees working on the Dragon projects and several trainees have undertaken field visits with host institutions in China during 2005. They reported for the first time at a special dedicated session at the 2005 Santorini Symposium, Fig. 10. See also
http://earth.esa.int/dragon/symp2005/photo_gallery/Symposium/Young_Scientist_Sessions

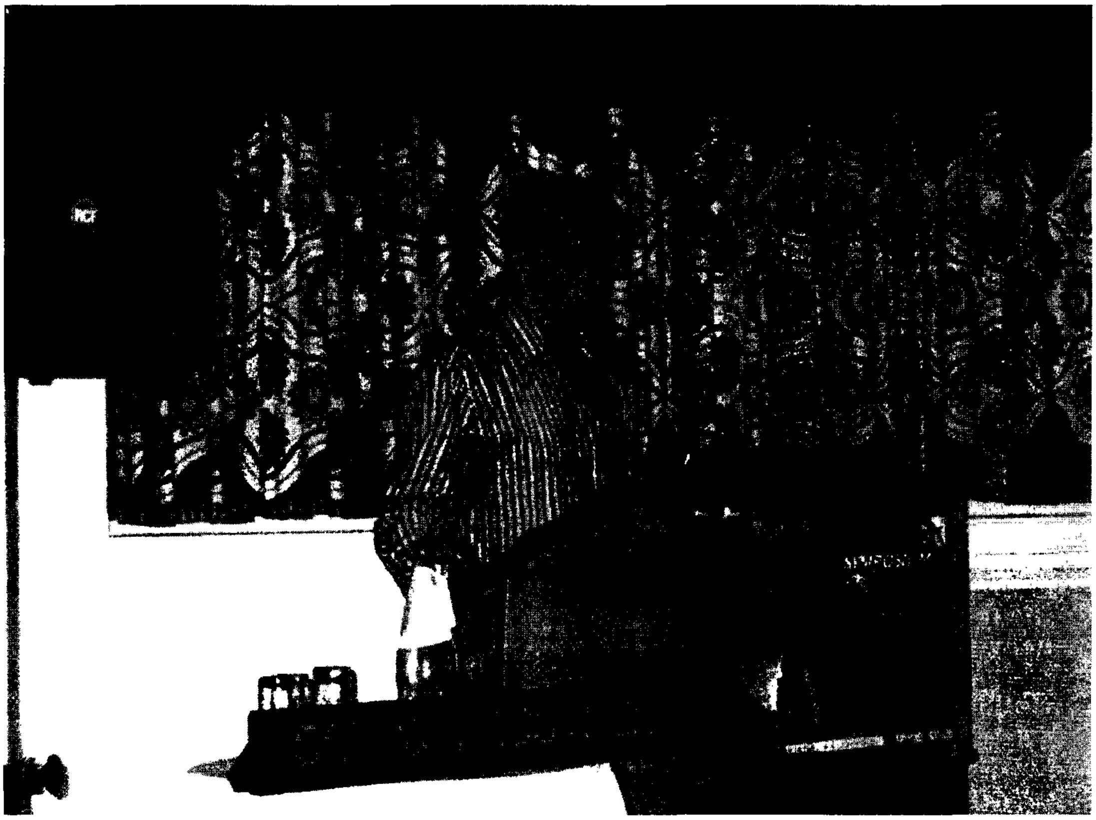

Fig. 10. Seppo Hassinen from the Finish Meteorogical Institute presents the results of his work on the session dedicated to presentations by Young Scientists at the 2005 Santorini Symposium

3.4.2 Training of Chinese Scientists

Within the framework of the Dragon Programme, ESA is hosting young Chinese scientists to undertake advanced training in Europe. From 17 Feb to 16 May 2004, Mr Chen Erxue and Mr Pang Yong from the Chinese Academy of Forestry, Beijing were hosted as trainees by ESA. Chen Erxue learned about and performed processing using experimental satellite and airborne fully polarimetric data sets for forest parameter retrieval, Fig. 11. Pang Yong studied ERS SAR Tandem data and Envisat ASAR AP IMS data processing and ILU generation with a view to mapping forest areas in China.

From 26 Sept. to 26 Dec. 2005 Mr Feilong Ling from Fuzhou University is being hosted as a trainee at ESRIN. His training is in the synergistic use of ERS SAR, ASAR and MERIS_FR data for land use mapping and decadal land use change detection with the focus on Fujian Province.

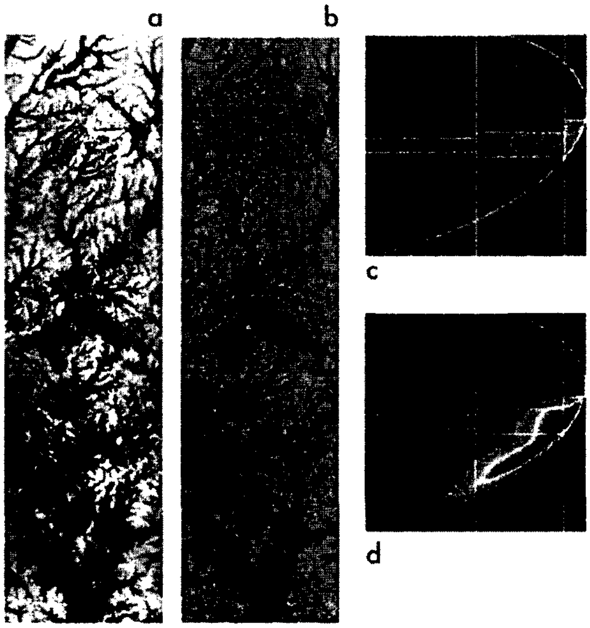

(a) L band Quad-polarization SIR-C/X SAR data, April 16, 1994, in NE of P.R. China, (b) H-Alpha unsupervised classification result, colours stand for terrain types defined in H-Alpha plane shown in (c). (d) 2-D representation of terrain types frequency occurrence in H-Alpha plane for different terrain types defined in (c).

Fig. 11. Results of polarimetric decomposition classification of forest non-forest from SIR-C/X data by Chen Erxue, Chinese Academy of Forestry, Beijing

3.5 Dragon Advanced Training

3.5.1 Advanced Training Course in Ocean Remote Sensing

This course was held from 25 to 30 Oct. 2005 and was hosted by the Ocean University of China, Qingdao. The goals were to provide understanding of ESA ERS and Envisat with respect to ocean remote sensing; to provide hands-on experience with tools and methods for the data exploitation and to provide participants with the theoretical and practical framework for further studies. The course was attended 78 participants ranging from associate professors to Ph.D. students, Fig. 12. There were 6 lecturers who gave lectures on:

- Current and future European and Chinese EO satellite missions
- Principles of SAR, MERIS, (A)ATSR, and RA measurements
- Products and applications in operational oceanography
- Practical exercises with BEAM and Bilko software tools

Fig. 12. Participants to the Advanced Training Course in Ocean Remote Sensing, 25 to 30 Oct. 2005

The lecturers were:

- Dr. Roland Doerffer GKSS Research Centre, Germany
- Prof. David Llewellyn Jones University of Leicester, UK
- Dr. Pierre-Yves Le Traon CLS, France
- Prof. Johnny Johannessen NERC, Norway
- Prof. Werner Alpers University of Hamburg, Germany
- Prof. Ming Xia-He Ocean University of China

3.5.2 Advanced Training Course in Land Remote Sensing

This training course was hosted by Capital Normal University in Beijing and took place from 10 to 15 Oct. 2005. The aims were to: enhance the academic exchange and cooperation between Chinese and European remote sensing scientists; to provide hands-on experience with ESA software tools (BEST and BEAM) and methods for data exploitation; and to contribute to the development of land remote sensing research and applications in China. There were 103 Chinese participants (from 167 applicants) with approx. 1/3 coming from outside Beijing. Over 50 institutions were represented with associate Professors, senior scientists, Master and PhD students in attendance, Fig. 13.

Fig. 13. Students and lectures with ESA, NRSCC and MOST officials at the photo-call for the land training course held from 10 to 15 Oct. 2005, Capital Normal University in Beijing.

The 7 European lecturers were awarded visiting professorships by CNU following the training course. The lecturers were:

- Dr. Thuy Le Toan, CESBIO France / SAR expert
- Prof. Christiane Schmullius, University of Jena, Germany / SAR expert
- Prof. Fabbio Rocca, Politecnico di Milano, Italy /SAR and InSAR expert
- Prof. Eric Pottier, University of Rennes, France / SAR and POLInSAR expert
- Prof. Bob Su, International Training Centre, The Netherlands / Optical-Thermal expert
- Dr. Wout Verhoef, National Aerospace Laboratory NLR - The Netherlands / Optical-Thermal expert
- Prof. Jose Cassanova, University of Vallodolid, Spain / Optical-Thermal expert

3.6 Mid Term Examples of Research Results

3.6.1 Flood Monitoring

Flooding is classed as the world's most costly type of natural disaster. As part of the of Dragon, Envisat ASAR image, wide swath and global monitoring mode and MERIS imagery have been acquired and processed in near-real time for mapping of flood events and as inputs for flood risk management. China experienced severe flooding during the 2005 season, including a more than once-in-a-hundred-year flood that occurred in the middle and upper reaches of the Xijiang River of the Pearl River Basin. The Hanjiang and Weihe Rivers experienced autumn flooding and flood-induced landslides took place in Hunan and Heilongjiang Provinces.

Some 1247 people were killed and another 331 left missing following these floods and landslides. At least 15 million hectares of cropland has been destroyed and 1.17 million houses ruined, with direct economic losses estimated to be as high as 136 billion Yuan (14.2 billion Euro).

However throughout the flood season, Envisat ASAR imagery was rapidly made available in near-real time to Dragon Rapid Mapping Principal Investigator Professor Li Jiren, of the Remote Sensing Technology Application Centre of China's Ministry of Water Resources, as a means for the authorities to identify floodwater extent and coordinate mitigation efforts, Table 1.

Table 1. Envisat ASAR data used in flood monitoring during the 2005 wet season, P.R. China

Date	Location	Province	Data acquisition	Date type	Type of event
Jul. 17	Dazhou	Sichuan	NRT	Envisat ASAR	Flood
Aug. 22	Fushun	Liaoning	NRT	Envisat ASAR	Flood
Oct. 3	Fuzhou	Fujian	Rolling archive	Envisat ASAR	Typhoon
Oct. 6	Fuzhou	Fujian	Rolling archive	Envisat ASAR	Typhoon
Jul. 15	Huaihe river	Anhui	NRT	Envisat ASAR	Flood
Aug. 30	Huaihe river	Anhui	Rolling archive	Envisat ASAR	Flood
Sep. 7	Huaihe river	Jiangsu	Rolling archive	Envisat ASAR	Flood
Sep. 9	Huaihe river	Anhui	Rolling archive	Envisat ASAR	Flood
Sep. 10	Huaihe river	Anhui	NRT	Envisat ASAR	Flood
Aug. 31	Jinjiang	Hubei	Rolling archive	Envisat ASAR	Flood
Jun. 25	Wuzhou	Guangxi	NRT	Envisat ASAR	Flood
Jul. 3	Wuzhou	Guangxi	NRT	Envisat ASAR	Flood

Sep. 27	Yangjiang	Guandong	NRT	Envisat ASAR	Typhoon
Aug. 14	Zhangzhou	Fujian	Rolling archive	Envisat ASAR	Typhoon

Fig. 14 shows the flood areas extracted from ASAR imagery acquired on 25 June 2005 that occurred around Wuzhou city, P.R. China. The flood areas were classified and then have been superimposed back on top of the ASAR image.

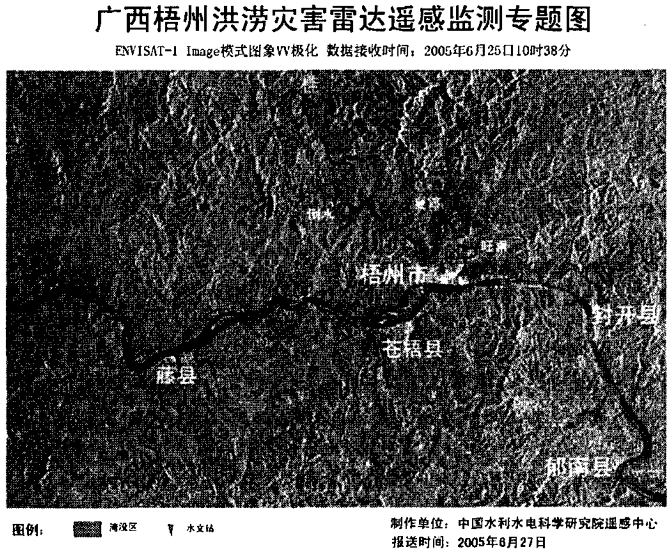

Fig. 14. Wuzhou city and surrounding area, flooded areas (in red) extracted from Envisat ASAR imagery acquired on 25 June 2005 (right) and the Xijiang flood overflowing the embankment of Hedong district, Wuzhou city on 22 June, 2005 (left). Courtesy of Prof. Li Jiren, Institute of water and hydropower research, Beijing.

3.6.2 Air quality

China's spectacular economic growth during the last decade has brought many benefits – and some challenges. Global atmospheric mapping of nitrogen dioxide pollution performed by ERS-2's GOME and Envisat's SCIAMACHY reveals the world's largest amount of NO2 hanging above Beijing and northeast China, as reported in Nature and shown in Fig. 15.

As part of ESA's Dragon Programme, European and Chinese researchers are using results returned from the Global Ozone Mapping Experiment (GOME) on ERS-2 and the Scanning Imaging Absorption Spectrometer for Atmospheric Chartography (SCIAMACHY) on Envisat to monitor and forecast Chinese air quality.

In this context, researchers at the University of Bremen, the Max-Planck Institute of Meteorology in Hamburg and France's Centre National de la Recherche Scientifique (CNRS) have been studying the retrieval of nitrogen dioxide variability from space and modelling its global behaviour.

The team have published an article in the 1 September 2005 edition of the science journal Nature [4] about the global changes in nitrogen dioxide observed in the last decade from space and highlighted the dramatic changes over China.

Nitrogen dioxide (NO_2) is associated with nitrogen oxide (NO) in the atmosphere and the sum of the two is called NOX. This is released into the troposphere from power plants, heavy industry and road transport, along with biomass burning, lightning in the atmosphere and microbial activity in the soil. The emission of nitrogen oxides has increased about six-fold since pre-industrial times and in cities above a thousand times more NOX is present.

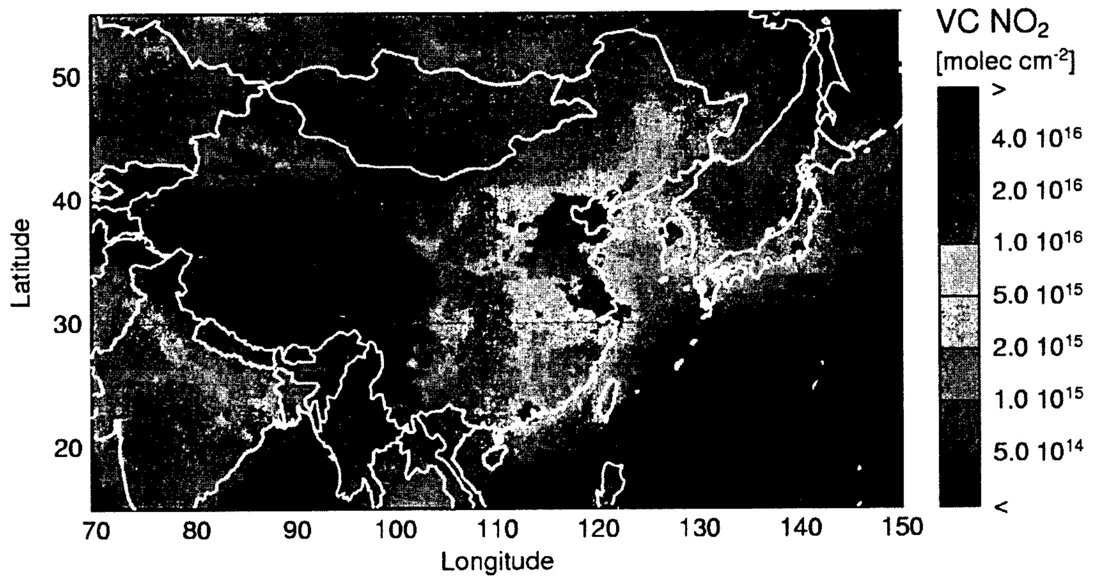

Fig. 15. Average annual NO2 changes 1996-2002 (Nature, Vol. 437, 1 Sept. 2005) Courtesy of Andreas Richter et al. Uni. Of Bremen, Germany

3.6.3 Oceanography

The Ocean, Environment and Climate project is a multi-disciplinary project that aims to study ocean and internal waves, currents, ocean colour and bottom sea topography with a combination of SAR and optical remote sensing. Fig. 16 shows an example of an ASAR image acquired for the East China sea. Several features can be interpreted.

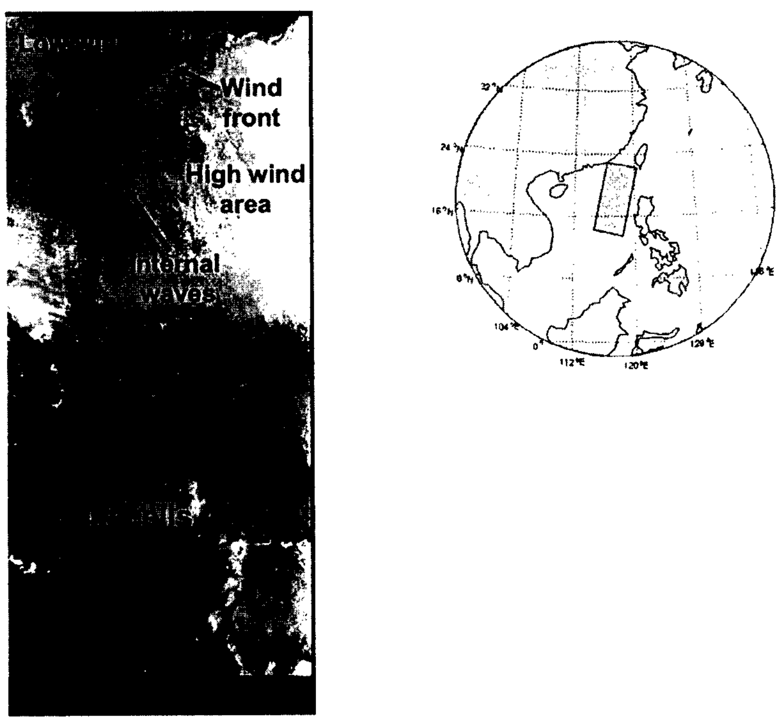

Fig. 16. ASAR image acquired in 7 June 2005 in the East China Sea. Courtesy of Dr. Knut. Frode Dagestad, NERSC

In the image, large internal waves can be seen propagating in an east to west direction. The length, frequency, distribution, and magnitude of such waves are the subject of the Dragon study. SAR backscatter also shows sensitivity to sea surface roughness depending on the wind field at the time of image acquisition. In Fig 16, the front between the high and low winds is also evident as there is a decrease in the backscatter from low wind to high wind regions. The presence of oil on the ocean surface affects surface roughness and backscatter under certain conditions. Therefore the dark strip shown top right (Fig. 16) is likely to be an oil slick. In the bottom part of the image some SAR backscatter variations due to heavy rain can be observed.

The East China Sea has complicated optical characteristics and contains a great amount of suspended matter, especially suspended sediment. The MERIS image shown in Fig. 17 is of the East China coast and shows the sediment loading of the ocean which is particularly heavy around the mouth the Yangtze river.

Fig. 17. MERIS reduced resolution image of the East coast of China acquired on 15 Feb. 2004 (R7, G5, B2)

During April 25 to May 25, 2005, the Ocean University of China organised a cruise to collect in-situ-spectral data and to measure suspended matter with their research vessel shown in Fig. 18. Several long track observations were deployed by OUC for a MERIS validation campaign organised within the framework of the Dragon Programme. In-situ spectral measurements were made using the high-spectral radiometer (Hyper-TSRB), high-spectral absorption/attenuation meter (AC-X), high-spectral irradiometer and radiometer (SAM8185 and SAM817D (see Fig. 19). The ocean optical data acquired in the cruise area has since been analysed and the early results have been presented at the Santorini Symposium. The analysis is significant for bio-physical retrieval algorithms in the East China sea and updated algorithms are in preparation based on the results of this validation campaign.

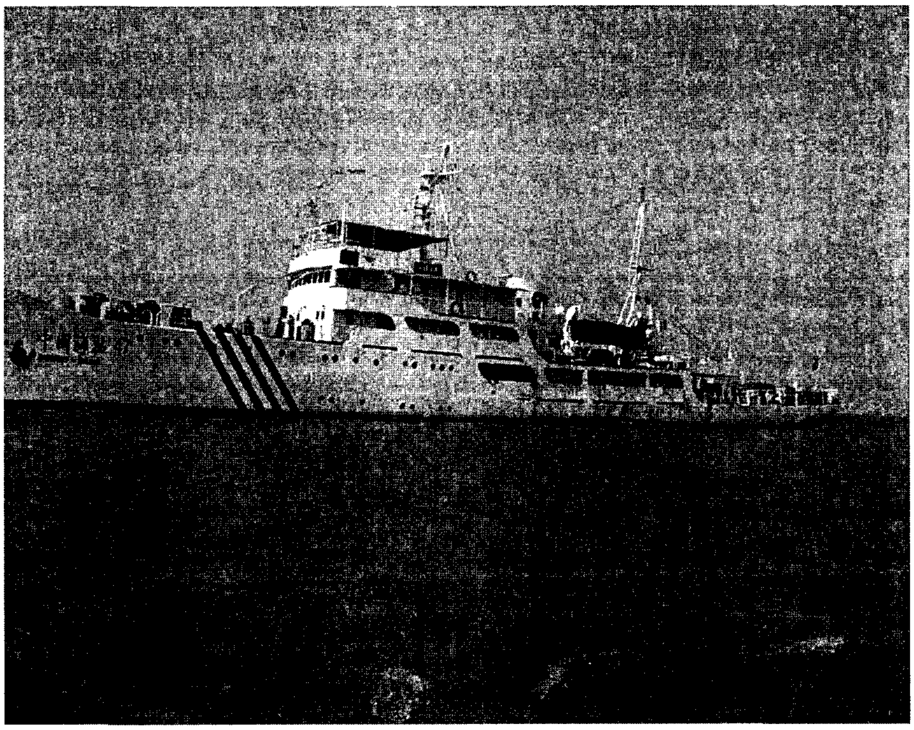

Fig. 18. Ocean research vessel of Ocean University of China. The vessel can accommodate 30 research staff and crew.

Fig. 19. HyperTSRB deployed in water (left), hyperspectral radiometer (AC-X), irradiometer and radiometer (SAM8185 and SAM817D) being prepared for deployment (right)

3.6.4 Forest map of China

One of the objectives of this project is to assess the potential of ENVISAT ASAR (Advanced Synthetic Aperture Radar) data to map forest over large areas and to update the forest map that was produced from ERS SAR images acquired in the 1990's. Envisat ASAR Alternating Polarisation (AP) data are used for the production of a forest/non-forest map in order to provide an update to the forest base map from ERS SAR data. Several cycles' ASAR AP mode data have been ordered since August 2004 (cycle 35). The HH/HV polarization was selected. A data processing chain, which includes ASAR data import, calibration, geo-reference and mosaic production has been implemented to process these ASAR data automatically. As the ASAR data are provided, they are geo-referenced using the orbit vector in the produce header according to the ENVISAT ASAR observation geometry. Then the data of each orbit is joined seamlessly. Fig. 20 shows the mosaic produced from one complete cycle of ASAR acquisitions in 2005.

The preliminary results show the potential use of HH/HV ASAR AP data for forest map update. The forest/non-forest types can be discriminated from both ERS-1/2 Interferometric Land Use (ILU) composites and from single date ASAR AP imagery. The base-line forest map from ERS SAR ILU can be updated from recent ASAR AP data to the current situation allowing forest change to be monitored from the two periods of data collection, i.e. from ERS SAR acquired in the 1990's to the current situation in 2005 using ASAR AP data.

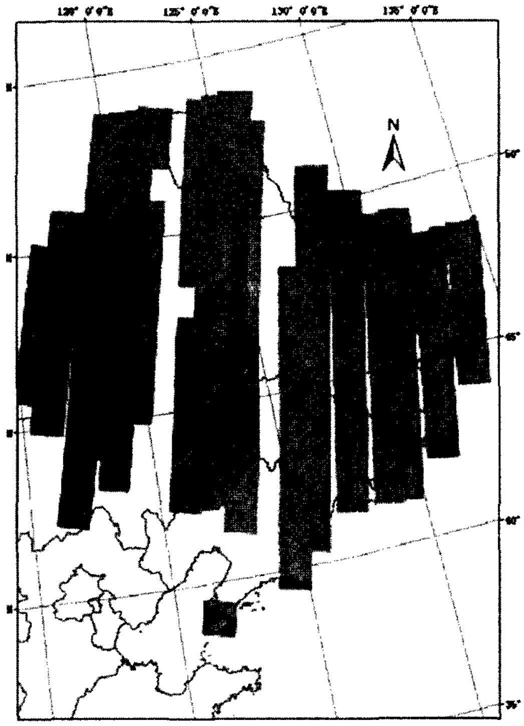

Fig. 20 ENVISAT ASAR AP Image Mosaic of NE China, All of the AP Imagery has been acquired in Cycle 35

ACKNOWLEDGEMENTS

NRSCC –Department of International Cooperation and Department of High and New Technology Development and Industrialization, MOST, for their funding support. Liao Xiaohan, Cao Xuejun, Yin Jun and Chen Linhao from MOST, Zhang Guocheng and Li Jiahong From NRSCC for their concern and support. The Dragon team in China for technical contribution, Gao Zhihai and Tian Xin for Programme management.

ESA – Karl Bergquist, Stephen Briggs and Mark Doherty for their continuous support. The Dragon team in Europe, Andy Zmuda (Programme secretariat and web site management), Rita Malosti (EO data planning and conflicts resolution), Irene Renis (Symposia secretariat) and Muriel Simon (training courses). Special thanks are due to ESA mission management for ERS and Envisat missions headed respectively by Wolfgang Lengert, Henri Laur, Pierre Potin and the EO help desk team for handling data orders and responding to Dragon PIs.

REFERENCES

1. ESA Bulletin 119 August 2004, The Dragon Programme, ESA and China cooperate in Earth Observation, pp 22 – 28.

2. Dragon Brochure, 2005 edition available for download (http://earth.esa.int/dragon/Dragon_documentation.htm)

3. Dragon Programme web site (http://earth.esa.int/dragon/)

4. Increase in tropospheric nitrogen dioxide over China observed from space, Andreas Richter, John P. Burrows, Hendrik Nu¨ß, Claire Granier & Ulrike Niemeier, Nature Vol. 437, 1 Sept. 2005, pp 129 to 132.

5. 2005 Dragon Programme mid term results (SP-611)

THE MEDIUM TERM PROGRESS OF MOST-ESA "DARGON PROGRAMME" IN CHINESE SIDE

Jiahong Li[(1)(2)], Zengyuan Li[(3)], Zhihai Gao[(3)], Xin Tian[(3)], Erxue Chen[(3)]

[(1)]Ocean University of China, No. 5 Yushan Road, Qingdao, 266003, Shandong, China, Email: lijiahong@nrscc.gov.cn
[(2)]National Remote Sensing Center of China, Fuxing Road B15, Haidian district, Beijing, 100862, China, Email: lijiahong@nrscc.gov.cn
[(3)]Research Institute of Forest Resources and Information Techniques, Chinese Academy of Forestry, 10009, Beijing, China, Email: zengyuan.li@forestry.ac.cn, zhgao@forestry.ac.cn, tianxin@forestry.ac.cn, chenerx@forestry.ac.cn

ABSTRACT

Following the successful Dragon Programme Kick-off Symposium held in Xiamen, P.R. China at the end of April 2004, the 2005 Dragon Symposium brought together the joint Sino-European teams again after one year's activity. As the consequence of great efforts made by the Chinese scientists and the European, all of the 15 Dragon Projects have achieved a lot, which develop the Earth Observation (EO) exploitation and application in China by using ERS and Envisat data. This paper is aimed at the outline of the medium-term progress in Chinese side including the data acquisition, data processing and the early results in the projects of the Programme. To make the next research go well in next 2 years, this paper advanced some proposals for the Chinese partners also.

1. INTRODUCTION

Since 1997, National Remote Sensing Center of China (NRSCC), Ministry of Science and Technology (MOST), has collaborated with European Space Agency (ESA) in the filed of remote sensing. On basis of the fruitful collaboration in the first phase (from 1997 to 2001), following a September 2003 meeting in Paris between Prof. Xu Guanhua, Minister of MOST, and Mr. Jean Jacques Dordain, Director General of ESA, it was agreed that the joint research programme in the field of remote sensing in the next phase be initiated. As the official departments responsible for the programme, NRSCC and ESA Directorate of Earth Observation have been stressed the creation of joint Sino-European teams as a means to stimulate scientific exchange in EO science and technology. As a consequence, a formal programme of co-operation, "The Dragon Programme", was initiated.

After the April 2004 Dragon Symposium, served as the formal kick off for joint EO exploitation and application development using ESA ERS and Envisat data in China, the 15 application projects investigated on the land, ocean and atmosphere have been undertaken[1].

The 2nd annual Dragon Symposium was taken place in Santorini, Greece, from 27th June to 1st July 2005. On a project-by-project basis, the joint Sino-European teams made the presentation on the progress of each project to date; including early results, details of EO data acquired and investigated, details of the in-situ data requirements and measurements, and status of cooperation within the project after one year's activities. This paper focuses on the progress gotten by the Chinese partners in cooperation with the European. It shows them in the applications and exploitations investigated on the land, ocean and atmosphere in the medium-term of the Programme. Furthermore, the proposal for the next 2 years is offered in the end.

Proc. 2005 Dragon Symposium "Mid-Term Results", Santorini, Greece
27 June – 1 July 2005 (ESA SP-611, January 2006)

2. THE LAND THEME

This thematic area under investigation includes 11 projects in the Dragon Programme. It covers the fields of Forest Mapping, Forest Fire Monitoring, Forest Information Deriving from POLInSAR, Agriculture Application, Rice Monitoring, Flood Monitoring, Water Resource Assessment, Drought Monitoring, Terrain Measurement, Seismic Activity Monitoring and Landslide Monitoring.

2.1. Data Acquisition

Provided freely by ESA, more than 2000 scenes ERS and Envisat data have been acquired by the Chinese teams in this thematic areas. Especially, the near real-time data delivered by ESA have been the basis of the disaster management projects in the Programme.

2.2. Data Processing

After the Chinese teams had received the ordered data from ESA, they started to process them by the common procedures, such as auto-registration, orth-rectification, speckle suppression, ground true data collection, reference data collection (TM, ETM+, DEM...) and database updating for test sites, etc.

2.3. Early Results

2.3.1 Projects on Forest

Both ERS-1/2 SAR data (undertaken by the European partners) and Envisat ASAR data are used successfully for forest mapping in Northeast China at regional scale. Forest/nonforest map and forest volume density map can be generated from ERS-1/2 tandem SAR data[2]. Envisat ASAR data was used to generate forest/nonforest map and update the base map from ERS SAR data. After image enhancement, the interferometric land use (ILU) image from ERS-1/2 Tandem SAR of Jan-1996 and Envisat ASAR image (HH/HV) of Mar-2005 shows good accordance of forest distribution in most areas and some changes in some clear-cut areas. The preliminary results show that there have big potentials to use HH/HV ASAR AP data for forest map update.

For the research on forest fire monitoring, in order to get the fire detection methodology in the northeast of China by using AATSR_TOA data, the analysis was carried out during the months of April, May, June and July corresponding to the year 2002, 2003 and 2004, although no fire was located in them. The parameters of fire, vegetation, land, cloud, water and burnt scar have been sampled from the AATSR-TOA production image. The statistic analysis includes their average, maximum, minimum and standard deviation. The results of fire identification and MODIS data have been validated everyday. To study on the fire danger index map by using MERIS and ASAR, the Chinese partners mapped by MODIS data.

The inversion of tree height is much important for understanding forest characteristics. To evaluate and study polarimetric SAR interferometry tree height inversion algorithm, three passes of SIR-C/X SAR L band full polarization SLC data were used for the same test site located in the western region of Hetian district, Xinjiang Autonomous Region of China. The Chinese partners adopted the general INSAR data processing routes to carry out the data pre-processing procedures. On basis of the polarimetric and interferometric data processing, the results of following three methods for tree height inversion were compared:

1) Maximum DEM Difference inversion (MDD);
2) Vegetation Bias Removal inversion (VBR);
3) Full Model inversion (FMI).

None-volumetric decorrelation in the smooth surface scatter region of the test site is observed and maybe caused by Signal Noise Ration (SNR) decorrelation. These regions should be masked out before applying full model inversion. In addition, temporal decorrelation, box filter[3] and vertical canopy structure are some possible error resources.

2.3.2 Agriculture Application and Rice Monitoring

The temporal behavior and polarization difference of varied land covers make it possible to classify agriculture and forest land from other land covers by ASAR data.

The agriculture application has been carried out in rice, banana and coastal shelter-forest. Especially, the principle component analysis was applied for the classification of rice and banana. Based on field survey and referred to optical remote sensing images, accuracy assessment was made in the Tab.1.

Table.1. Comparison of the accuracy among the three methods

Methods	Overall Accuracy (%)	Kappa
Supervised Classifier	32.5	0.295
Expert Classifier	60.8	0.584
Object-Oriented Classifier	81.2	0.786

In comparison with the supervised classifier and the expert classifier from Tab.1, the object-oriented classifier was found to be more efficient for classification.

For the application on coastal shelter-forest monitoring, VV and VH combination is more suitable for information extraction than single VV or VH.

The same filter method used in agriculture application project, developed by Shaun Quegan[4] and called as mutitemporal filter, played the key role for data pre-processing in the rice monitoring project. For the early result on this project, the Chinese team made an exploration of new techniques using single date of Envisat dual polarization data to map rice at local scale. As the consequence, a better understanding of SAR data's potential capability for rice mapping and practical system for operational use at local level, even if the rice mapping and monitoring at regional level have been carried out.

2.3.3 Flood Monitoring, Water Resource Assessment and Drought Monitoring

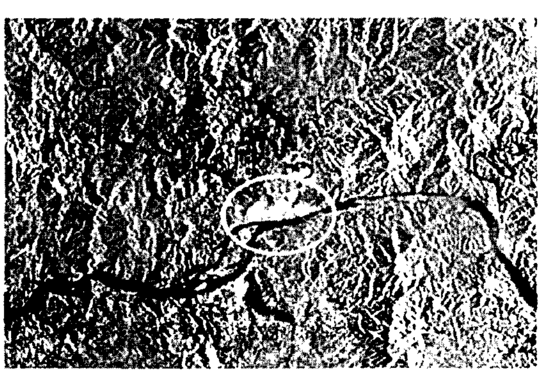

(a)

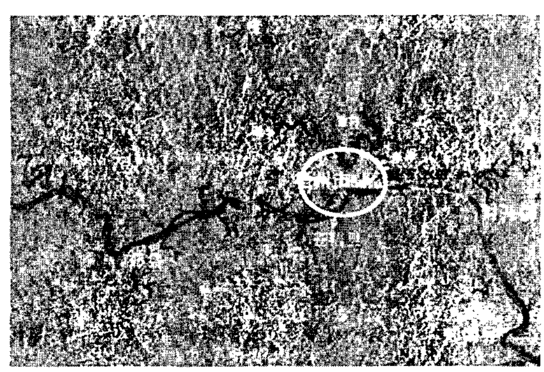

(b)

Fig.1. The near real-time Envisat data and the flood monitoring map

(a)The near real-time data; (b) The flood monitoring map, the red is the submerged area

Flood is one of the most important issues in China. As the state statistic, it loses (directly and indirectly) more than several hundreds billion yuan per year.

The near real-time Envisat data like ASAR and MERIS data have been delivered by ESA to Chinese team during the flood period. The near real-time operation for flood monitoring and assessment have been started to set up from this year. By using Envisat data, the flood monitoring map has made by Chinese partners by 13 times in this year. As shown in the Fig.1, since the near real-time Envisat data (a) for the Wuzhou flood had been received, the flood monitoring map (b) was made by Chinese team within 10 hours after data delivered.

For flood monitoring, the background database is very important for supporting decision-making. Since early time in this year, basin by basin, the database has been building.

The use of hydrological model, like Xin'anjiang Watershed Model that was developed by Chinese team, can contribute a lot for water resource assessment in China. In the model, some parameters can be determined directly or indirectly by RS and GIS. With comparison between predicted and observed hydrographs at Wangjiaba station, Huaihe River in China, the model shows the potentiality for remote sensing application in the field of water resources management.

In China, drought disaster occurs more frequently and widely. The project of drought monitoring has been dedicated to develop an operational system for nationwide drought monitoring and assessment. The study results shows that Envisat ASAR data are more available than normal optical data that are affected from cloudy weather for drought operational monitoring in the south-western China. The correlation model between drought index and soil moisture has been developed by Chinese partners.

2.3.4 Terrain Measurement, Seismic Activity Monitoring And Landslide Monitoring

SAR Interferometry gives researchers a new set of tools to measure topography, tiny shifts and deformations on Earth's surface, valuable in the study of landslides, urban subsidence, earthquakes and other geological disasters in China.
In the Dragon project of terrain measurement, the Chinese team has gotten some current-progress in topographic mapping and earth deformation monitoring.

A software for DEM generation from INSAR data has been developed by Chinese partners. The new modified strategy and algorithm were applied to derive DEM from ERS-1/2+ SRTM. As the result, the INSAR derived and aerial photograph derived (1:50000) DEMs are compared in the Fig.2.

The investigation on deformation phenomena in Shanghai was conducted by using the ERS-1/2 data, the preliminary validation shows the high accuracy of Persistent Scatters (PS) INSAR technique and the suitability of ASAR data for monitoring urban subsidence was evaluated in Shanghai test site.

By ASAR interferometry, the Chinese team in the project of seismic activity monitoring has mapped the co-seismic deformation and inversed the Zhongba (in Tibet of China) earthquake. Four pairs of ASAR data were used to extract the Zhongba earthquake deformation and the 5cm-cycle rewrapped phase for the earthquake deformation.

On basis of the Angular Dislocation Model, a new solution was sought to improve it. As the result, the result of inversion of the Zhongba earthquake is similar to the result of INSAR detection.

In this project, besides the progress mentioned above, the research on modeling co-seismic deformation of the Mani (Nov 8, 1997) earthquake (in Tibet of China) by combining INSAR data and tectonic observations has gone into deep.

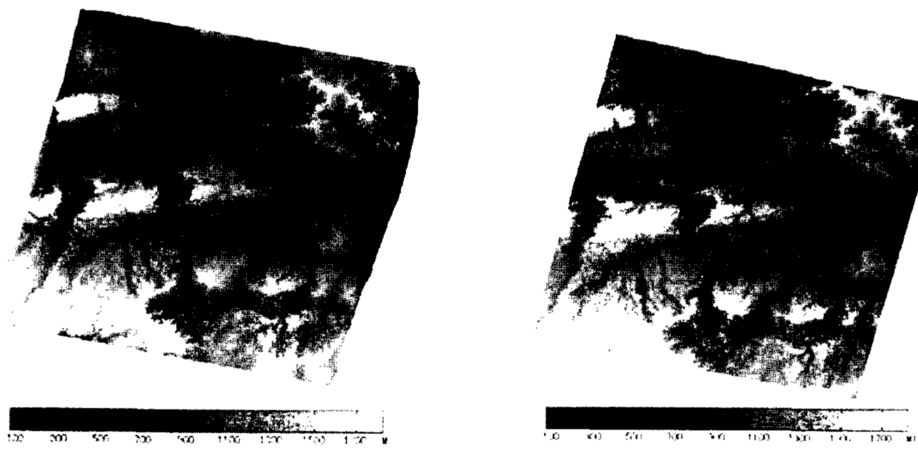

(a) (b)

Fig.2. Comparison between INSAR derived DEM and aerial photograph derived DEM(1:50000)
(a) INSAR Derived DEM(ERS-1/2 + SRTM) (b) Aerial photograph derived DEM

The Three Gorges Area was selected as the test site for the Dragon project of landslide monitoring. The DEMs, SAR interferometry, corner reflectors, GPS and in-situ measurements have been combined to develop a landslide monitoring system. In addition to the application of DEM for landslide susceptibility risk, the Chinese partners have set up GPS and corner reflector network in Wanzhou and Yichang. In cooperation with European partners, the Chinese have started to automate the corner reflector detection and retrieval of different interferometric phase related to stable reference point exploring natural stable scatters in these areas. On basis of these pre-research, the PS from ERS data in Wanzhou was processed.

3. THE OCEAN THEME

3.1 Data Acquisition

The Ocean thematic area covers the applications on the ocean environment and climate. In this project, the topics include research on internal waves, shallow water topography, ocean surface wave, ocean color and Kuroshio Current. More than 300 scenes ERS and Envisat data was provided for free by the ESA to Chinese team.

3.2 Data Processing and Early Results

For the satellite remote sensing of the internal waves in the China seas, comprehensive researches are made, which include the spatial-temporal distribution of internal waves in the China seas, the retrieval of internal wave parameters, in particular the amplitude of internal waves, from SAR imagery, the validation experiment of internal waves conducted simultaneously by Envisat/ASAR and field measurements in the East China Sea, the numerical simulation of internal waves in the northern South China Sea, the simulation of SAR image with internal wave signatures, and the extraction of internal wave signatures from SAR imagery.

By introducing a modification factor and adopting a parameterized continuously stratified buoyancy frequency, a new method based on the solitary wave solution of KdV equation has been proposed. Theoretically, the conditions in the shallow waters of the China Seas may not meet the requirement of KdV equation. By inducing the modification factor which is related to the local bathymetry and the width of internal waves, the original retrieval method is improved. The accuracy of retrieved amplitude of internal wave becomes acceptable, see table 2. Technically, a parameterized buoyancy frequency profile is adopted to simplify the description of the continuous stratification model. The parameters can be simply determined according to the climatology depth and thickness of pycnocline. By this way, non-linear factor can be tabulated on those parameters as a look-up table. User friendly application software for retrieving amplitude of internal solitary waves from SAR imagery based on this new method has been developed. Validation and comparison of the results with those data from simultaneous field experiment in Zhoushan, Asian Seas International Acoustics Experiment (ASIAEX), internal wave experiment in the South China Sea.

Table 2. The amplitudes of internal wave retrieved using the data acquired during the Zhoushan field experiment.

γ	λ	Measured Amplitude	Retrieved Amplitude (old method)	Relative Error	Retrieved Amplitude (new Method)	Relative Error
46	360 m	5.5 m	0.67 m	88%	4.4 m	20%

The studies of spatial-temporal distribution of internal waves in the China Seas have been made new progress. About 800 images with internal wave signatures are found out from approximately 15 thousand satellite images acquired between 1994 and 2004. Fig.3 gives the distribution of internal waves in the China seas based on the decadal timescale internal wave images. According to the generation mechanism of internal waves, the China seas are roughly divided into 5 areas, i.e., Yellow Sea, East Sea, Taiwan waters, DongSha Island waters and Hainan Island waters.

Fig. 3. Distribution of internal wave signatures in the China Seas obtained from analyzing the available satellite images.

For the ocean color remote sensing, the milestone is that Ocean Remote Sensing Institute, ocean university of China, purchased a set of international standardized instruments for ocean optical field measurements. The in-situ ocean optical data and Envisat/MERIS data in the coast of China have been collected for comparison and validation. For the retrieval algorithm of MERIS data, a semi-analytical model suitable to the China seas and the neural network method are studied. The results are compared with the results by BEAM of ESA and by SeaDAS 4.8 of NASA.

Basic researches on the underwater bottom topography detection using SAR images and Kuroshio by multi-sensor data are carried out. The researches on the retrieval of ocean wave directional spectrum from SAR wave mode data using cross spectrum method and Hasselmann's method and its validation in China Seas are ongoing.

4. THE ATMOSPHERE THEME

The atmospheric theme includes 3 research projects of chemistry/climate change in the atmosphere, air quality monitoring and forecasting, coupling climate and ocean system.

4.1 Data Acquisition

Chinese teams have acquired some 2500 orbits of atmosphere high resolution spectral data for atmospheric chemistry study.

4.2 Data Processing

On basis of the several decades of data accumulation of the broadband solar radiation measurement, the AERONET instrument and Broadband radiometers, the Chinese partners used the Broadband Extinction Method (BEM) to deriving AOT from the broadband data. The other two methods of the dense dark vegetation method and contrast reduction method have been used to retrieve AOT from satellite data. For the related ground data, the distributed observation stations and network (including Xianghe Station and Dust storm Observing Network) have been built in China. Subsequently, the Sunphotometers, Dust storm Observing Network and other data could be used to validate the AOT with AATSR.

4.3 Early Results

The following work has been done by the Chinese teams:

4.3.1 Interpreting and Understanding the Content of Satellite Data

With the help of Beat software, MIPAS (level 1, level 2), GOMOS (level 1) and SCIAMACHY(level 1, level 2), data were interpreted and mapped in order to understand its physical meanings and prepare for next retrieving work.

4.3.2 The initial Simulation to GOMOS, MIPAS and SCIAMACHY

With the radiative transfer code MODTRAN version 4 and SCIATRAN, the observation by GOMOS, MIPAS and SCIAMACHY was simulated as shown in Fig.4, Fig.5 and Fig.6.

5. OTHER ACTIVITIES

From 17 February to 16 May 2004, Dr. Erxue Chen and Dr. Yong Pang from the Chinese Academy Of Forestry got the chance to be the Dragon 3 month trainee. Both of them stayed in ESRIN to learn the related knowledge for their projects.

From September 2005 to February 2006, Mr. Feilong Lin and Mr. Xin Tian will go to the ESRIN and stay there one after the other to act as the trainees hosted by ESA under the frame of the Programme.

As one key component of the Programme, an advanced training course on Ocean remote sensing was successfully held at Ocean University of China, Qingdao. Besides 69 Chinese participants, another nine scientists came from Korea, Japan and India were acted as the trainees also.

An advanced training course on land remote sensing was held at Capital Normal University in Beijing in October of this year, more than 110 people registered to be the trainees.

A new research project on the application of spatial techniques on the Beijing 2008 Olympic Game will be joined into the Programme.

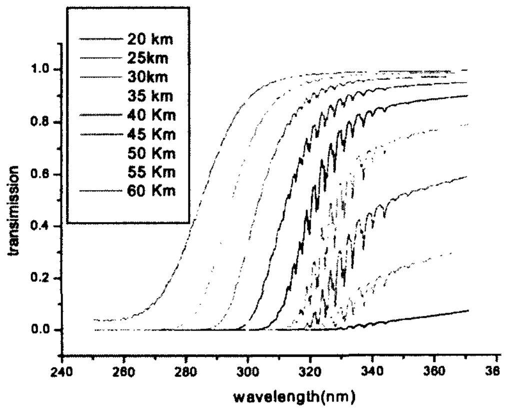

Fig. 4. GOMOS observed transmission with sun occultation between 20-60 Km

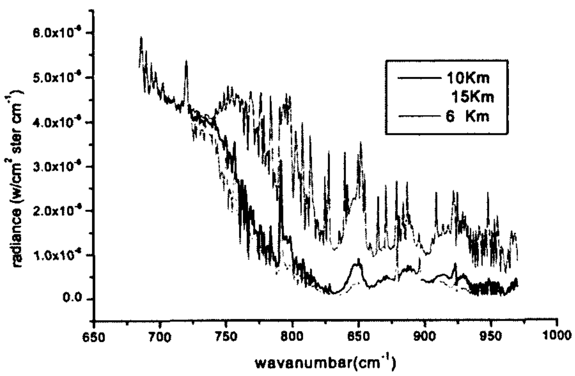

Fig.5. MIPAS observation at different

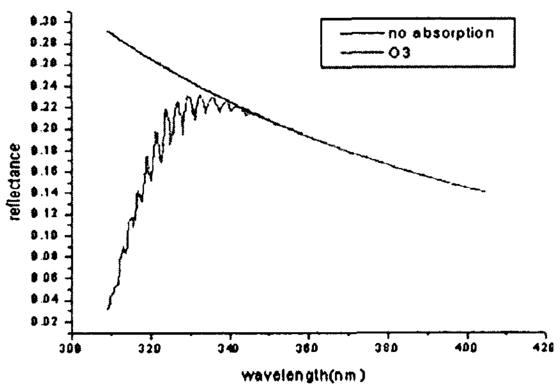

Fig.6. Retrieval by using SCIAMACHY

6. PROPOSAL

The Dragon Programme is the largest collaborated project in the filed of remote sensing between China and Europe. Particularly, for the Chinese investigators, it is uncommon chance to get so much free and valuable data from ESA to Dragon Programme. To develop the early results, the models, methodologies, algorithms and etc should be validated in the test sites further and precisely. The technical development for application of ERS and Envisat data in the subjects should be further enhanced. For disaster monitoring system, it is expected that everything related to operation would be in routine way in this year or next year. Furthermore, it will come into reality that the development of National Civil Economy can indeed get the contributions from the research results.

As the official organizer of the Programme in China, NRSCC would make great efforts to urge the fruitful outcome for this Programme in the next 2 years.

7. ACKONLEDGEMENTS

Thanks to Dr. Yves-Louis Desnos and Dr. Andy Zmuda for their great contribution to the implementation of Dragon Programme. Thanks a lot to all Chinese investigators of 15 projects for providing the information in details on the progress of each project.

REFERENCE

1. ESA, http://earth.esa.int/dragon.
2. Rosich B. and Li Z. Y., Forest Mapping in China with ERS SAR: Evaluation of Project feasibility and Future Perspectives, *Rev.* 1.1, July 1998.
3. Lee, J. S., Cloud S. R., et al., Speckle filtering of POLINSAR data, *Proceeding of IGRASS 2002*, Toronto, Canada, pp.892-831, 2002.
4. Quegan S. and Yu J. J., Filtering of Multichannel SAR Images, *IEEE transaction on geoscience and remote sensing*, Vol.39, No.11, 2373-2379, 2001.

Bilateral Sino-European Collaboration Projects

THE PROGRESS IN DETECTING OF COAL FIRE ON REMOTE SENSING* THE FIRST RESULT OF THE JOINT SINO-GERMAN RESEARCH PROJECT ON INNOVATIVE TECHNOLOGIES FOR EXPLORATION, EXTINCTION AND MONITORING OF COAL FIRES IN NORTH CHINA

Li Jing[1,4], Stefan Voight[2], Claudia Kunzer[2], Yang Bo[1], Zhang Jianzhong[2], Zhang Yianmin[3], Kong Bing[3], Zhang Songmeil[4]

[1] Beijing Normal University (BNU), Beijing 100875, China
[2] German Aerospace Center (DLR), Oberpfaffenhofen 82234 Wessling, Germany
[3] Beijing Remote Sensing Corporation, Beijing 100085, China
[4] Key Lab of 3D Information Acquisition and Application of MOE, CNU, Beijing 100037, China,
*Corresponding author: frances.zhang@163.com

Abstract--China is one of the countries with a vast coal resource in the world. However, many coalmines in China are seriously endangered by coal fire. These fires occur within a region that stretches over 5000 km east to west and 750 km north to south. About 100-200 million tons of coal is being lost because of coal fires each year. In this paper, we summarized the first result of Joint Sino-German Coal fire Research Project. Mostly focus on the progress we achieved in recent years especially in the field of Remote Sensing, and an outline of how to explore, extinct and monitoring coal fires by use of remote sensing imagery also summarized.

Keywords: Joint Sino-German, First result, Coal fire, Progress, Remote Sensing, North China.

1. PROBLEM OF COAL FIRES

Coal fires are known from different coalfields worldwide. China, India, USA, Australia, Indonesia and South Africa are the main countries affected by coal fires. Normally, the mineworkers and the people living in the surrounding area are affected by large amounts of aerosols and toxic gases, like carbon monoxide or sulphur oxides. But also greenhouse relevant gasses are being released in large amounts and affect the environment. Additional hazards include land-subsidence, contamination of drinking water and damage of flora and fauna around the fires. Protecting the economically valuable coal resources and the environment is of great relevance on a national and international level.

Fig. 1 Location of the study area—Wuda coalfield

2. Wuda coalfield--Study area

The Wuda coalfield is located NE of the Helan Mountain range in a desert-like environment with elevations ranging between 1100 and 1300m asl. This study area is easy to access, include different geological and morphological settings and are strongly affected by coal fires.

It's latitude range from 39°28' to 39°34' and longitude from106°36' to 106°40'. (Source: internal field report, 2002, unpublished)

The coal layers of the Wuda coalfield belong to the Upper Carboniferous and Lower Permian Taiyuan and Shanxi Formation. The coal bearing strata was deposited in marine

* Supported by the Sino-German ERSEC Research Project "Innovative Technologies for the Exploration, Extinction and Monitoring of Coal Fires in North China", under contract No.2002DFG00032, and also supported by "Hi-Tech research and development program of China", contract No.2003AA131100 and 2002AA130020.

near coastal swamps. 24 coal seams with a thickness of 0.2m to 6m are exposed in a 10km long and 4km wide N-S striking syncline. The coal quality is in the range of medium volatile bituminous coal. The surface of the Wuda coalfield is strongly mined and mainly covered by sandstone's or loose sand. Coal fires affect an area of 280000 m^2. Most Coal fires occur underground and can be related to small-scale mining operations.

3. Remote sensing activity

3.1 Detection of new Fires in 2003 and 2004

In September 2003 a new underground coal fire previously unknown to the regional mining authorities could be confirmed in the field. The coal fire was detected based on multi-spectral coal fire demarcation and thermal anomaly detection. It was the first fire, which was detected based on remote sensing data exclusively. The two valleys of Hulusitai and Shitanjing were once a prospering coal-mining region but are abandoned today. Many mines are improperly sealed and many coal waste piles are smoldering as well.

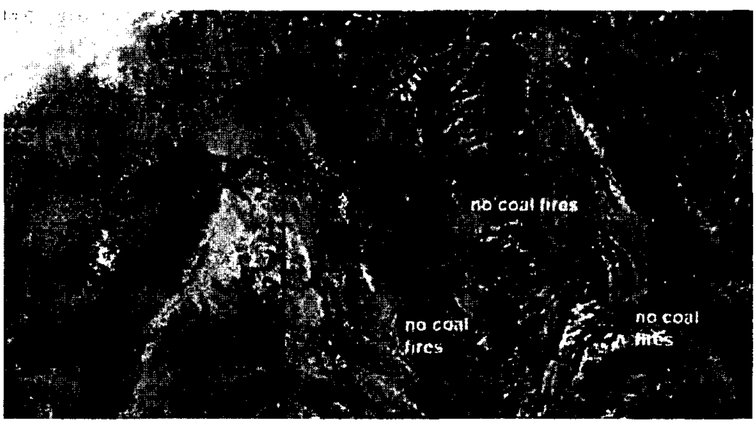

Left: Overview of fires and coal fire demarcation areas in the Helan Shan Mountains. Right: Detailed view of the Hulusitai and Shitanjing valleys - Legend - yellow dots: fire anomalies, cyan polygons: coal occurrences, red areas: coal demarcation area.

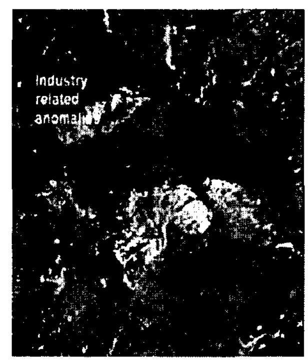

Detailed view of the coal fire area on the right of the Yellow River. Legend - yellow dots: fire anomalies, cyan polygons: coal occurrences, red areas: coal demarcation area.

In June 2004 a second previously unknown coal fire in a completely different region, which had been detected in remote sensing data could be verified during a field validation. The fire is located east of the Yellow River in an area, where private wild mining is commonplace.

3.2 Algorithm for the automated extraction of thermal anomalies

An algorithm for the automated extraction of regional thermal anomalies was developed. It works very well on nighttime data such as thermal data from ETM+, ASTER or MODIS. Its application is currently tested on ASTSR data. The algorithm is based on a moving window concept comparing the temperatures of the central pixel against their background. The histogram of a subset window is investigated for a background part and a coal fire related part.

It has been shown that the first turning point after the main histogram maximum can be employed to separate background pixels from warmer pixels. Depending on how often a pixel is counted as a fire pixel it is declared as a thermal anomaly. Such thermal anomalies are not all coal fire related but may originate from industry, biomass fires, limestone processing, solar effects in nighttime data and other sources.

However thermal anomaly detection in combination with coal fire area demarcation clearly helps to constrain the focus of coal fire monitoring to the right places.

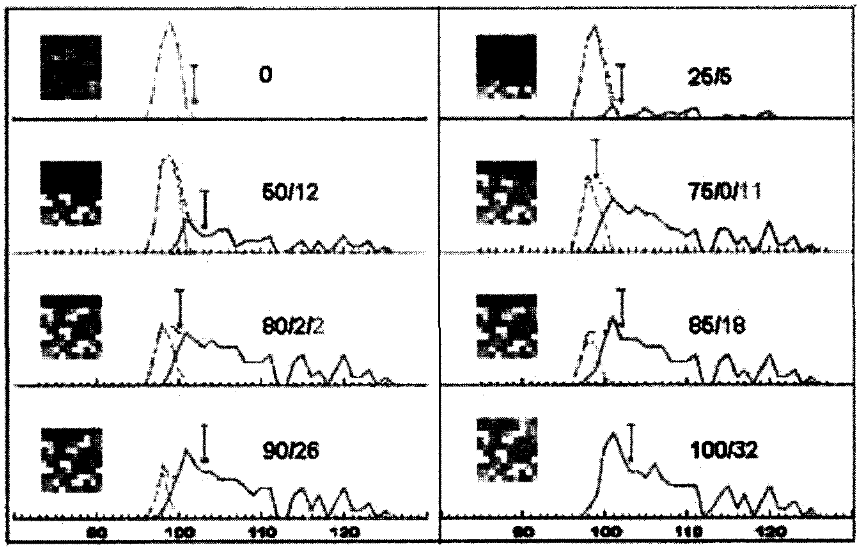

Fig. 3 Distribution of fire and background pixels in different subsets of a satellite image

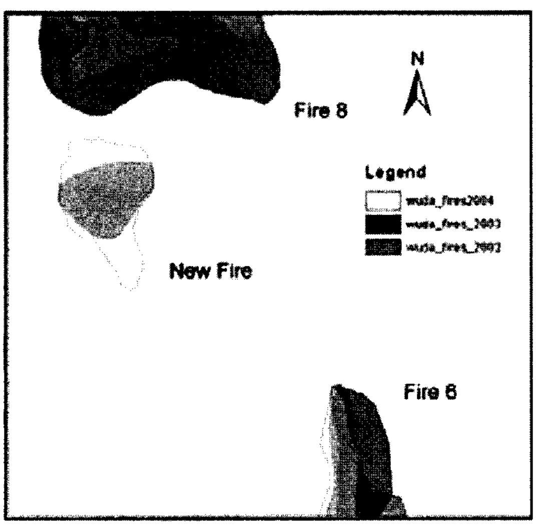

Left: Development of a new coal fire in Wuda between fire 6 and fire 8

Right: Development of coal fires in Wuda from 2000 to 2004

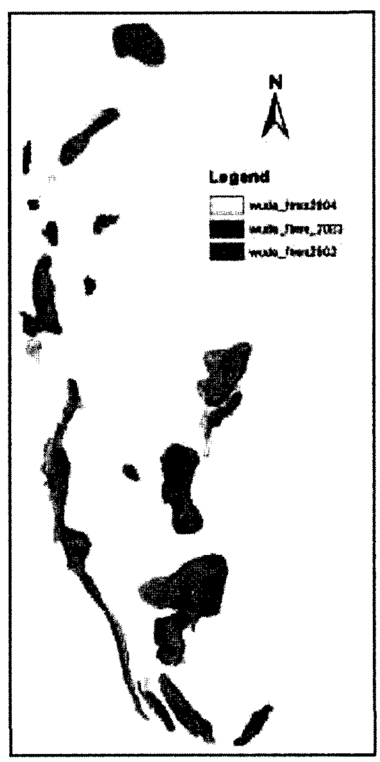

Fig. 4 Development of coal fires in Wuda

3.3 Fire development and dynamics in Wuda mine from 2002 to 2004

The coal fires in the Wuda syncline were mapped in the years of 2002-2004. Many of the fires are very dynamic. A report on the development of the individual fires and the spreading of new fires currently is in preparation at DFD. It will be supplied to the Wuda mine by the end of this year. The most important observation made during the recent years is the development of a new fire between fire6 South and fire8 North. This fire is thermally intensive and caused numerous sinkholes and large-scale subsidence.

3.4 High resolution imagery

Remote sensing data with a very high spatial resolution (4m-60 cm cell size) can support detailed analysis of the ground conditions in a spatially limited area. In this project, data from the sensors Ikonos and Quickbird is available for multi-temporal observations. The figure shows how infrastructure develops over time and how mining operations expand.

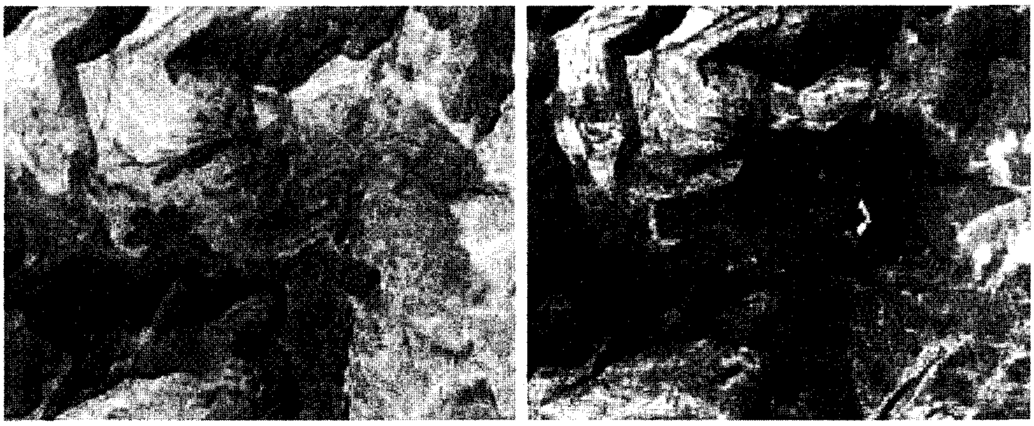

Fig. 5a Increasing size of an open pit in Rujiguo from 2000 to 2003

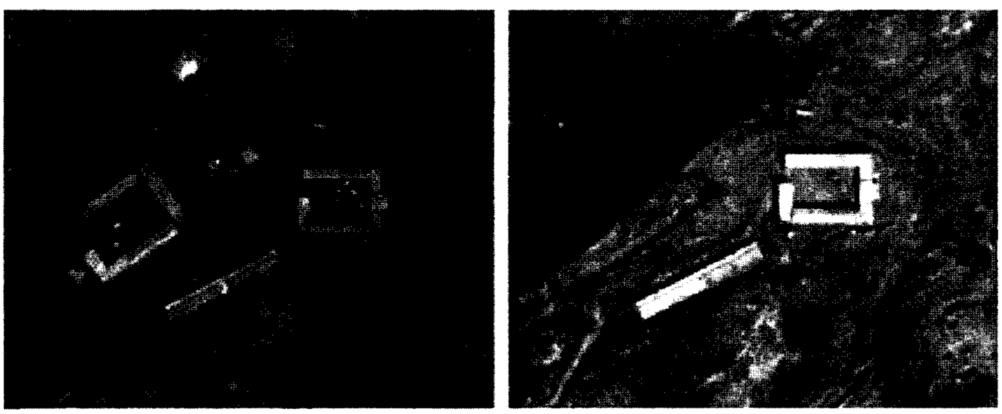

Fig. 5b Reduction of buildings due to expanding mining areas

3.5 DEM - digital elevation model

With the satellite data from ERS, digital elevation models are generated for the provinces Ningxia and Xinjiang as well as for areas where our project partners TU Dresden, TU Munich and University of Hohenheim are working. The DEM has a resolution of 25 m and is basis for satellite data calibration and rectification.

The ERS data will also be used for land subsidence assessment by means of differential interferometry.

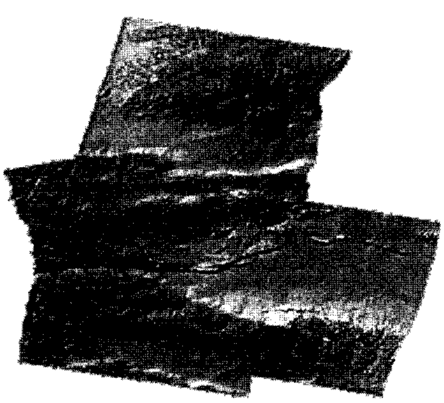

Fig. 6 In our study areas the relief differences from -200m to >5000 m.

3.6 Preprocessing

To make raw satellite data spatially and spectrally comparable and thus useful for quantitative and multi-temporal coal fires studies a thorough preprocessing of the imagery is necessary.

First, systematic errors (earth curvature, panorama distortions etc.)

have to be corrected. Secondly geometric/topographic corrections and atmospheric rectification need to be applied. The later only applies for optical/thermal data. For radar imagery usually no atmospheric correction is required.

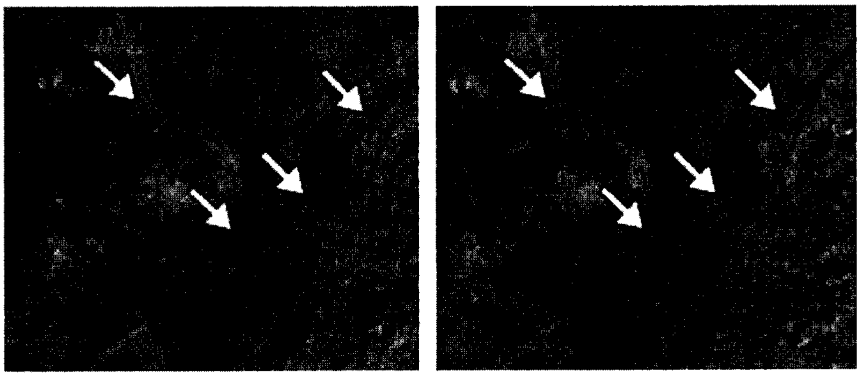

Fig. 7 The geometric correction results in the vicinity of the Yellow River.
Left: before correction, right: after correction.

Within this project all satellite images are corrected to the well-known Projection Universal Transverse Mercator (UTM), no matter whether it is Landsat ETM, BIRD, ASTER or ERS data. We use the digital elevation model (DEM) derived from ERS radar interferometric processing to correct the terrain induced geometric distortions.

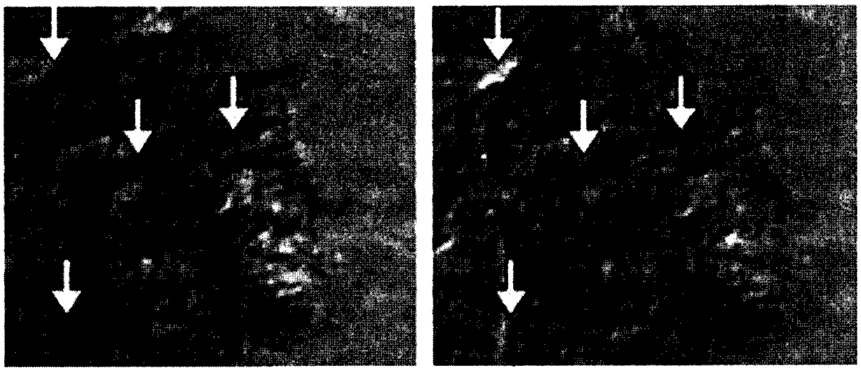

Fig. 8 The results of illumination correction of Helan Shan. Left: before correction; right: after correction.

Fig.9 The result map after mosaic treatment in XinJiang Uigur Autonomous Region.

Sensor calibration, atmospheric correction and topographic illumination correction are conducted using the DLR ATCOR-3 model (R.Richter, 1998) based on the MODTRAN-4 radiative transfer code. By doing this, the satellite data are corrected for the influence of the following parameters: air molecules (path radiance resulting from Raighley scattering), water vapor, ozone and aerosols (absorption and/or scattering).

3.7 Landsat 7 satellite mosaic

One goal of the Remote Sensing Project is to generate a Landsat 7 mosaic covering the coal fire areas in the province of Ningxia and adjacent regions as well as most parts of the province of Xinjiang. This satellite mosaic provides a general overview of two studied Chinese provinces affected by coal fires.

The false color infrared mosaic is generated from Landsat 7 data down linked during two acquisition campaigns with the DLR mobile receiving station at Ulan Bator (Mongolia). Some additional data sets are acquired from the EDC data archives. It is envisaged to cover an area of about 800.000 km? For the targeted test areas the satellite map will be generated at a scale of 1:100.000 and will be will include topographic contour lines.

3.8 Land cover classification

Land cover maps are being derived at two different scales.

1) On regional scale (1:100.000) land cover and land use classifications will be created for our coal fire areas of interest (Ke-erjian, Tielieke, Wuda, and Rujigou/Gulaben). These classifications show much more details than the products mentioned under (2) and include appr. 15 land cover classes including different geologic units, different types of vegetation, water and man-made features. This classification system is related to the official land cover assessment system of the Academic Sinica (CAS).

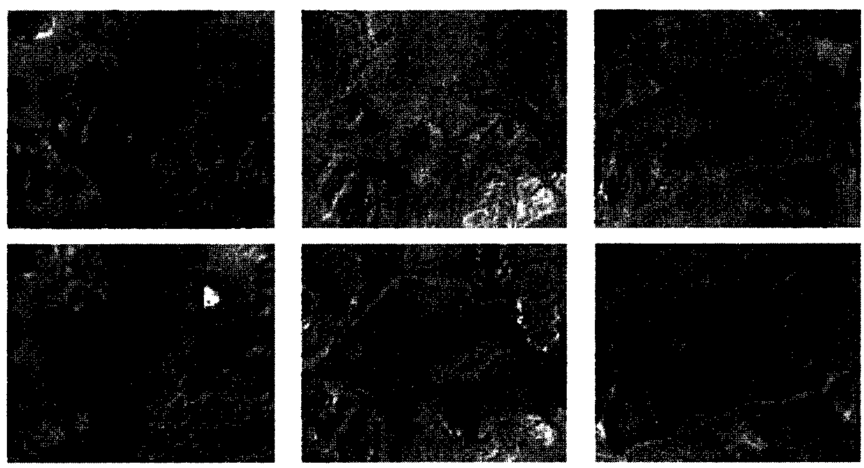

Fig.10 Changes in land cover at the Yellow River (left), in mining areas (center) and settlements (right). Top row: 1987; bottom row: 2002

2.) Land cover classifications are also generated at a broader scale (1:500.000) including the regions around the dedicated study areas. These classifications differentiate fewer classes and will provide a basis of ecosystem analysis and planning of coal fire fighting activities.

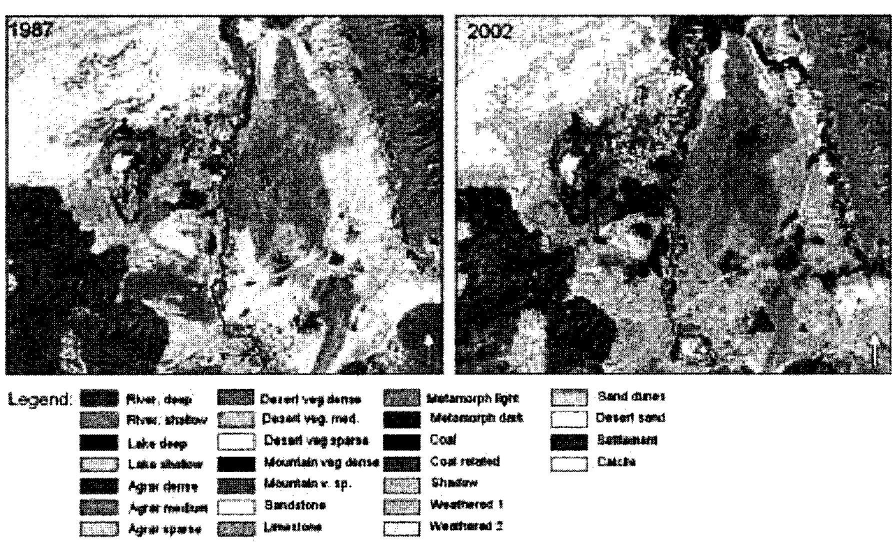

Fig.11 Multi-temporal Land Cover Change Detection, Wuda, 15 Years.
W-E: 42 km, N-S: 35 km, Elevation: 700 – 2000m

For the broader studa area of Wuda 25 land cover classes could be derived from Landsat 7 ETM+ satellite data. The data were orthorectified, sensor calibrated atmospherically and illumination corrected. As classification methods standard max likelihood classification was combined with knowledge based decision rules and NDVI and SAVI thresholding. It can clearly be observed that private and industrial coal mining spread substantially. Furthermore the city of Wuda has expanded, as have industrial settlements east of the yellow River.

These detailed land use classifications will serve as a cartographic base for various project activities such as field campaigns, extinction operation etc.

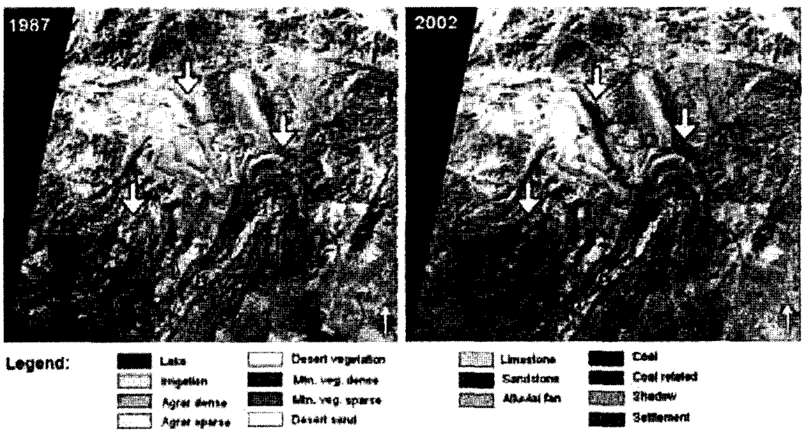

Fig.12 Multi-temporal Land Cover Change Detection in Ruqigou / Gulaben, 15 Years.

W-E: 42 km, N-S: 35 km

For the broader study are of Rujiguoi/Gulaben 15 Land cover classes were derived from the satellite data. As for wuda a strong increase in coal covered surfaces can be observed. Settlements spread less strongly since space for construction in this mountainous terrain is limited.

3.9 Thermal Analysis in the field

The figure shows a photograph taken with a thermal camera. The underground coal fire that can only be indirectly observed by cracks and fissures in the bedrock can clearly be recognized in the thermal image. Several hot cracks and vents were closely monitored and are thus comparable on a multi-temporal basis. Thermal cameras are a good tool to determine if extinguished coal fires stay extinct, and how the thermal intensity of a fire develops over time.

Fig.13 Thermal image over ordinary photograph. Note: The geometry of anomalies is related to the crack pattern

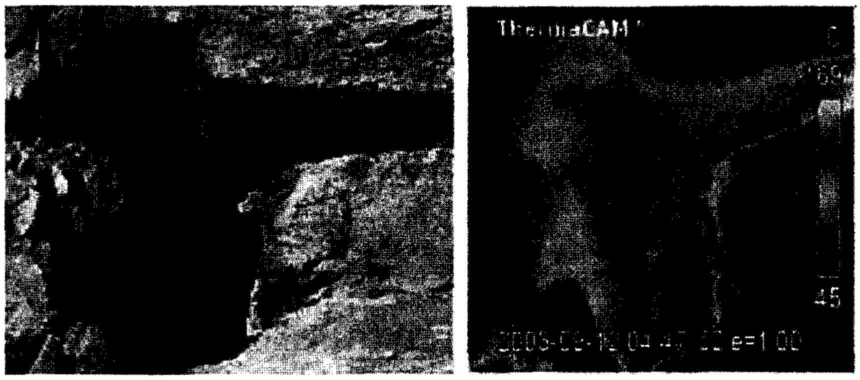

Fig.14 Close up of photograph and thermal image of a crack above a coal fire.

All 17-coal fires in the Wuda syncline were mapped during field campaigns in 2003, 2003 and 2004. These field-mapping campaigns act as ground truth for thermal satellite data analysis.

In the course of the project methods were developed to retrieve coal fire temperatures and coal fire related energy releases from thermal anomaly clusters. Hopefully in the future these methods can estimate the amount of coal burnt with in a subsurface fire.

3.10 Thermal Analysis Using Spaceborne Data

Thermal infrared satellite data are used for detection and quantitative analysis of the surface and near-surface coal fires. Such fires usually show enhanced brightness temperatures in the thermal part of the electromagnetic spectrum. Depending on the observing system there are usually one, two or more spectral bands available to detect coal fires.

Within this project we use imagery of the following satellite sensors: ETM, BIRD, ASTER and MODIS. The operational MODIS sensor has several thermal infrared channels at a pixel spacing of 1km, the DLR experimental satellite BIRD has one band in the mid-infrared and one band in the thermal infrared channel and has a pixel spacing of 185m. ASTER spans the 8-12 micron region with five contiguous bands at 90m-pixel spacing. ETM has only one thermal band between 10.4 and 12.5 microns at a spatial sampling interval of 60m.

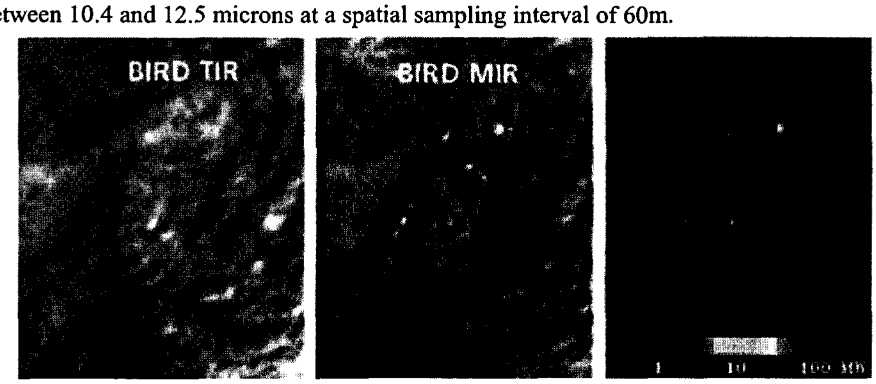

Fig.15 Quantitative analysis of coal fires in the Wuda coal field.

There are different methods to thermally assess the coal fires. In order to detect the thermal anomalies a simple threshold at a certain brightness temperature can be used to delineate the fires, however this often lead to over or underestimation of the fire area and it can not be applied over large areas. Therefore new statistical methods are being developed within this project, which are suitable for large area thermal anomaly detection.

If two thermal channels, picking up the coal fire signals are available, a quantitative assessment of the effective energy released from a coal fire can be estimated (Dozier, 1981). However, with ETM having only one thermal channel, this method is not applicable, other techniques are being developed.

Results show that BIRD, ASTER and ETM imagery have strong potential for coal fire detection and analysis. While

BIRD data allow the detection and analysis of hot surface coal fires, ASTER and ETM imagery can be used to also map large area subsurface coal fires. For all these sensors it can be said that nighttime data is more applicable for coal fire mapping due to smaller influence of the uneven solar heating effects.

3.11 Land surface subsidence mapping

As mentioned above coal fires can lead to severe land subsidence resulting form the underground loss of volume. Some of these subsidence processes can be observed by differential radar interferometry. For this purpose we use ERS tandem data over the test area of KeErJian in the Xinjiang province of China.

The method makes use of very subtle phase differences between the two tandem pairs acquired at a long time interval (several months or years). In order to derive the phase differences the data sets have to be co registered with very high precision. Later on two interferograms are being subtracted from each other to compute the differential phase. Depending on the observation baseline (distance between the two radar antennas) the phase differences can be converted to estimations of ground movement.

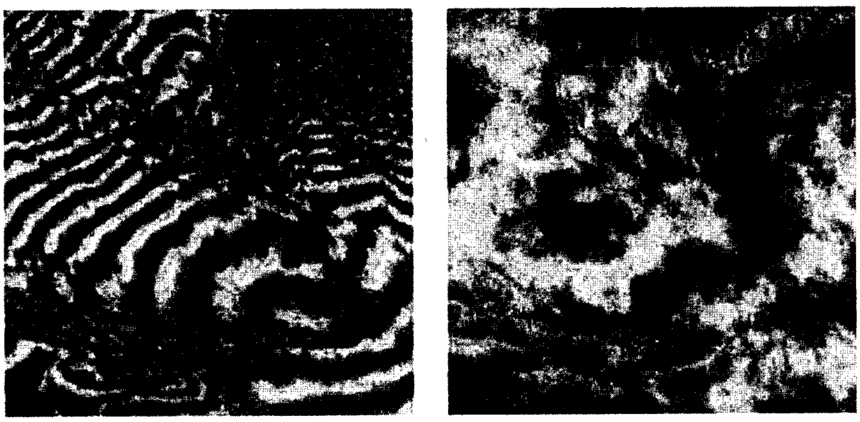

Fig.16 Interferogram (left) and differential interferogram (right).

Visible crack systems of the three test areas in Ningxia (Rujigou) and Inner Mongolia (Wuda, Gulaben) have been analyzed using high-resolution (60 cm) satellite images (QUICKBIRD). For all test areas the visible cracks and crack systems, which developed through subsidence of the surface after a coal fire, have been mapped and documented.

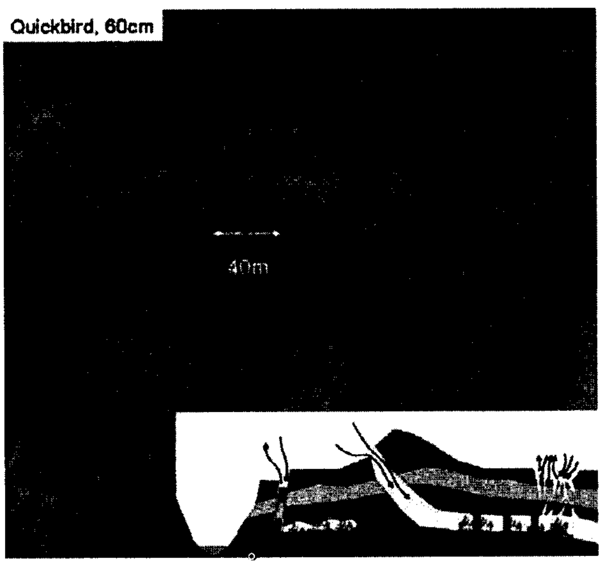

Fig.17 Quickbird image showing effects of land subsidence in mining area of the Wuda coal field.

4. Conclusion and discussion

This article chiefly introduced coal fires' exploration, extinction and monitoring methods based on remote sensing images and other new methods and technologies. Made a summarization of first results achieved by experts from Sino-Germany both sides since the kick off conference held in Beijing in Sep, 2003.

Quick identification of coal fires and dynamic monitoring are of utmost importance. It also can make sure of whether a coal fire is a new one or not and provide a necessary reasons for decision-making and fire fighting.

This paper summarized how to utilize multi-temporal, multi-sensors, multi-resolution and multi-spectral remote sensing images, and some auxiliary measures as well. Some attempts are proved to be effective and also easy and simple to handle.

We also encountered some difficulties that need our experts from both sides to overcome. For example: how to find a more efficient method to exchange our information and research fruits? Which is very important in prevention monitoring and early warning in the future.

5. Acknowledgments

This paper was summarized from publishes of the Sino-German ERSEC Research Project “Innovative Technologies for the Exploration, Extinction and Monitoring of Coal Fires in North China”, under contract No.2002DFG00032, and also supported by “Hi-Tech research and development program of China”, under contract No.2003AA131100 and 2002AA130020. We thank for German Remote Sensing Data Center (DFD), German Aerospace Center (DLR) and National Remote Sensing Centre of China (NRSCC) as well.

Reference

Jianzhong Zhang, 2004. Spatial and statistical analysis of thermal satellite imagery. Ph.D. dissertation. Vienna University of Technology.

Claudia Kuenzer, 2005. Demarcating coal fire risk areas based on spectral test sequences and partial unmixing using multi sensor remote sensing data. Ph.D. dissertation. Vienna University of Technology.

Anke Tetzlaff, 2004. Coal fire quantification using ASTER, ETM and BIRD satellite instrument data. Ph.D. dissertation. Ludwig Maximilian University of Munich.

Songmei Zhang, 2005. Monitoring subsurface coal fires in North China. Postdoctoral report.

http://www.coalfire.caf.dlr.de

http://www.itc.nl/personal/coalfire/index.html

ftp.dlr.de

SOIL MOISTURE ESTIMATION USING ASAR DATA

Nicolas Baghdadi[1], Mahmoud El Hajj[1], Noha Holah[1], Olivier Cerdan[1]
Jean Philippe Denux[2], Christine King[1], Michel Gay[2]

[1] French Geological Survey (BRGM), BP 6009, 45060 Orléans, France
Tel.: (33) 2 38 64 32 02, E-mail: n.baghdadi@brgm.fr

[2] E.S.A. PURPAN - 75, voie du TOEC, BP 57611
31076 TOULOUSE cedex, France
Tel.: (33) 6 83 64 36 39, E-mail: michel.gay@esa-purpan.fr

ABSTRACT

The potential of Advanced Synthetic Aperture Radar (ASAR) for the retrieval of surface soil moisture over bare soils was evaluated for several ASAR acquisition configurations: (1) one incidence and one polarization, (2) one incidence and two polarizations (one date), (3) two incidences and one polarization (two dates) and (4) two incidences and two polarizations (two dates). The retrieval of soil moisture from backscattering measurements is discussed using empirical inversion approaches. When compared with the results obtained with a single polarization, the use of two polarizations does not provide a significant improvement in estimating soil moisture (improvement <1%). For the best estimates of soil moisture, ASAR data should be acquired at both low and high incidence angles (RMSE=3.5%). Next, the soil moisture mapping was carried out for ASAR images acquired in 2005 over the Touch basin using empirical relationship between radar signal and soil moisture obtained from data collected between 1998 and 2004 on several study sites and in using ERS and ASAR sensors. The use of mono-date ASAR images with one incidence and one polarization enables a soil moisture mapping with accuracy better than 6%.

1. INTRODUCTION

Soil surface moisture and roughness are significant indicators for hydrologic studies and the monitoring of agricultural environments. These parameters play an important role in the distribution of precipitation between runoff and infiltration. Soil surface moisture is a key indicator for constraining the initial conditions of infiltration/runoff rates when modelling flood events. The possibility of retrieving these soil parameters has been investigated by using scatterometers, satellites, space shuttles, and airborne synthetic aperture radars [1,2,3,5,6,7,8,9,10,13]. The launch of the new European Environmental Satellite (ENVISAT) in March 2002, carrying the C-band Advanced Synthetic Aperture Radar (ASAR), should enable the scientific community to improve and increase its ability to retrieve physical parameters, based on ENVISAT's capability of providing images in HH, HV, and VV polarizations (two polarizations are possible simultaneously) and at various incidence angles between 15° and 45°. The objective of the present study is to analyze the accuracy of estimates of soil moisture for bare soils in using empirical inversion approaches from ASAR images acquired at various incidence angles and polarizations. This work,

Proc. 2005 Dragon Symposium "Mid-Term Results", Santorini, Greece
27 June – 1 July 2005 (ESA SP-611, January 2006)

involved into the Dragon project for flood risks management and prevention, will enable us to evaluate the potential of the new ASAR sensor for extracting surface soil moisture.

2. DATA SET

The image data used in this study were acquired by the ASAR SAR between 9 February 2003 and 16 May 2005 over two study sites (20 images, HH, HV and VV polarizations, incidence angle between 20° to 43°). The first lies to the west of Paris, near Villamblain, France (latitude 48° 00` N, longitude 01° 34` E). The second is located near Toulouse in the Touch catchment basin (latitude 43° 27` N, longitude 01° 02` E). The sites are composed mainly of agricultural fields intended for growing wheat and corn. The Villamblain site was chosen because it is composed of large and relatively flat fields whereas the Touch basin was selected because it is a site representative of Mediterranean type flash floods. The Touch basin is now selected as reference basin for several official authorities of flood forecasting and prevention, such as DIREN and SCHAPI.

Simultaneously with the radar acquisition, ground truth measurements including soil moisture, surface roughness, and bulk density were performed on several test fields. Soil moisture content was measured using gravimetric and TDR methods (upper 0-5 cm soil layer, 10 to 20 locations within each test field). The volumetric soil moistures range from 5.4% to 47.3% with a standard deviation of about ±1.7%. The soil bulk density ranges from 0.86 to 1.66 with a standard deviation of about 0.06. Most of the *in situ* ground measurements of soil moisture were made within ± 2 h of the ASAR overpasses. Soil roughness measurements were also carried out, using a 2 meter-long needle profilometer with a 1-cm sampling interval (10 roughness profiles for each test field : 5 parallel and 5 perpendicular to the row direction). On the basis of these measurements the roughness parameters, such as the root mean square (*rms*) surface height and the correlation length (*L*) were calculated using the mean of all experimental auto-correlation functions, both parallel and perpendicular. The *rms* values fluctuate between 0.5 cm and 3.56 cm; the lowest ones correspond mainly to wheat-sown fields and the highest ones to recently ploughed fields. The data set available for this study consists of about 400 triplets of backscattering coefficient, soil moisture, and surface roughness.

3. ACCURACY IN THE SOIL MOISTURE ESTIMATE USING ASAR DATA

The retrieval of volumetric soil moisture by means of an empirical inversion procedure requires the establishment of experimental calibration relationships between the backscattering coefficient and the soil moisture. ASAR data acquired in various configurations of polarization and incidence angle were used, together with ground measurements conducted over bare soil. In VV polarization, owing to the lower range of moisture content (only 10%) for each group of incidence angles, no relationship could be established between the radar signal and the soil moisture. The sensitivity of the radar signal to volumetric soil moisture is greatest in HH polarization and for low and middle incidence angles (0.18 dB/% for 20°-24° and 0.22 dB/% for 34°-37°, Fig.1) [6]. The objective of this study was to use empirical approaches to investigate the accuracy of estimates of soil moisture (*mv*). The contributions of polarization (only HH and HV) and incidence angle (θ) were studied, as well as the combination of multi-incidence and multi-polarization data. Four cases are considered in this study:

- ASAR images acquired with one incidence angle (20°-24°, 34°-37°, 40°-43°) and one polarization (HH, HV): one date.
- ASAR images acquired with one incidence (20°-24°, 34°-37°, 40°-43°) and two polarizations (HH, HV): one date.
- ASAR images acquired with two incidences (20°-24°, 34°-37°, 40°-43°) and one polarization (HH, HV): two dates.
- ASAR images acquired with two incidences (20°-24°, 40°-43°) and two polarizations (HH, HV): two dates.

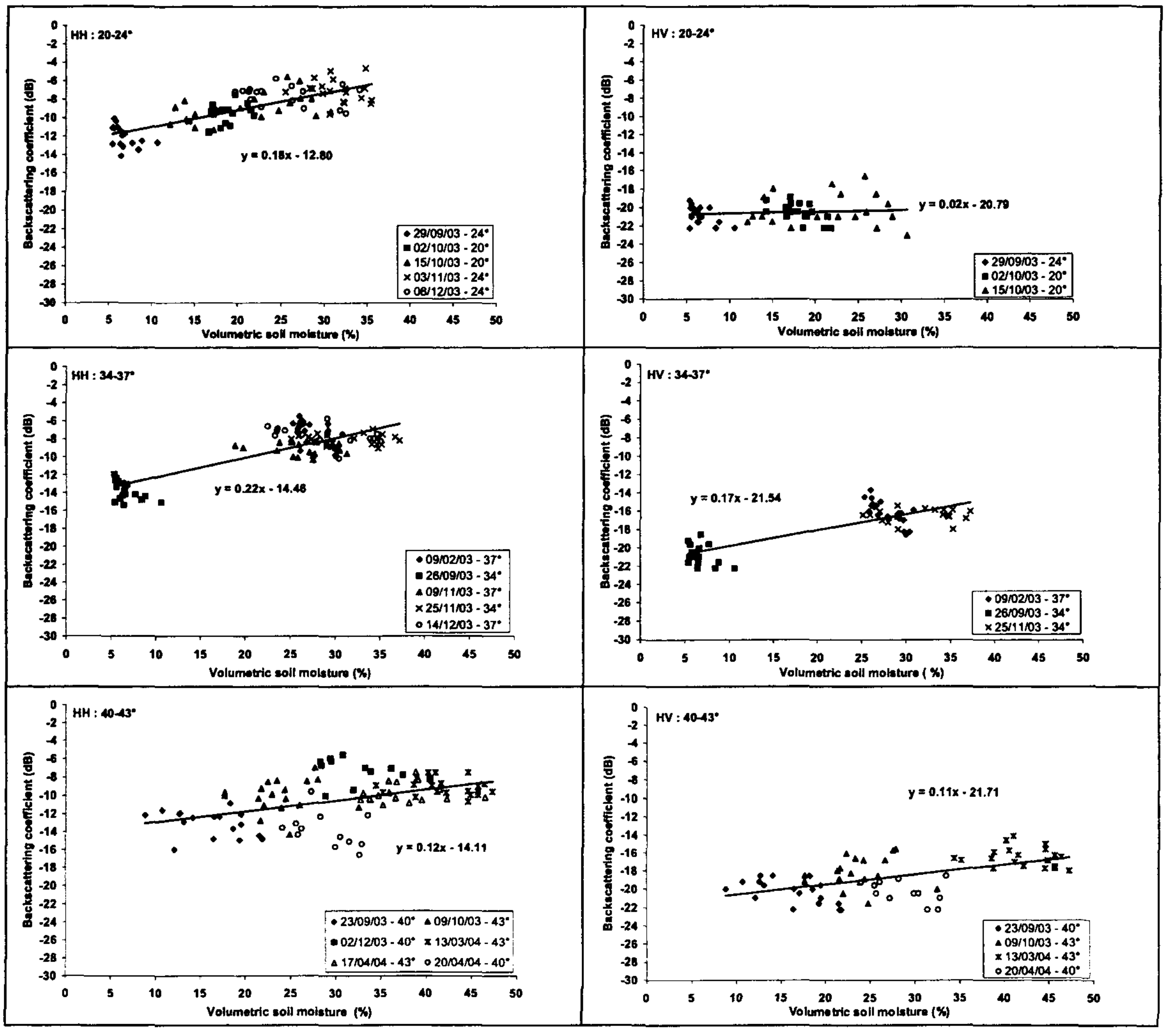

Fig. 1. ASAR signal versus volumetric soil moisture measured in the uppermost 5 cm. Each point corresponds to the average backscattering coefficient in decibels for one test field. Only Villamblain data were used in these plots.

To retrieve volumetric soil surface moisture (*mv*) from a single radar configuration, it is necessary to establish a relationship between the radar backscattering coefficient (σ^0) and *mv* alone, without having any knowledge of the *rms* surface height. Many studies have found a linear relationship between the radar signal acquired over bare soil surfaces and the soil moisture, up to values of *mv* of around 35% [6]. As a first approximation, the radar backscattering coefficient (in decibels, dB) may be expressed as follows:

$$\sigma^0_{dB} = \delta\, mv + \xi \qquad (1)$$

This simplified relationship ignores the surface roughness. For a given radar frequency, the coefficient δ was observed to be dependent on both radar incidence angle and polarization [6]. The coefficient ξ is primarily controlled by incidence angle, polarization, and surface roughness. The coefficients δ and ξ are often found to be dependent on the catchment basin, and thus different from one basin to another. However, for the same catchment, the slope of the observed linear relationship between radar signal and soil moisture is consistent [7].

To take the surface roughness into account, the radar backscattering coefficient σ^o (in decibels) of a bare soil can be expressed as the sum of two functions: the first one, *f* (linear), describes its dependence on volumetric surface soil moisture, while the second, *g* (exponential), illustrates the dependence of σ° on *rms* surface height [12,13]:

$$\sigma^0_{dB} = f(mv,\theta,mn,\lambda)_{dB} + g(rms,\theta,mn,\lambda)_{dB} = \delta\, mv + \mu\, e^{-krms} + \tau \qquad (2)$$

where *mn* is the polarization, and k the wave number ($\approx$1.11 cm^{-1} for ASAR).

The data set was divided equally into a calibration set and a validation set. First, empirical relationships between the backscattering coefficients and the ground truth volumetric soil moisture were established for the calibration set. Then the inversion procedure was applied to the validation set to estimate the soil moisture. The validity of this procedure was verified by comparing the output from the inversion procedure with the experimental data. The various cases that were studied for the purpose of estimating *mv* were:

- One date characterized by one incidence and one polarization:

$$mv = \alpha\sigma^0_{mn}(\theta) + \beta \qquad (3)$$

- One date characterized by one incidence and two polarizations (HH and HV). This case allows the benefits of the multi-polarization ASAR configuration to be tested. Solving equation (2) for two polarizations gives:

$$mv = \alpha\sigma^0_{HH}(\theta) + \beta\sigma^0_{HV}(\theta) + \gamma \qquad (4)$$

- Two dates characterized by one low incidence and one high incidence, and a single polarization (HH or HV). Solving equation (2) for two incidences leads to:

$$< mv > = \alpha\sigma^0_{mn}(\theta_{low}) + \beta\sigma^0_{mn}(\theta_{high}) + \gamma \qquad (5)$$

Several studies have used the ratio $\sigma^0_{HH}(20°)/\sigma^0_{HH}(40°)$ in formulating the inversion procedure, because of the extreme sensitivity of this ratio to surface roughness [11,13]:

$$< mv > = \alpha\sigma^0_{mn}\left(\theta_{low}\ or\ \theta_{high}\right) + \beta\left(\frac{\sigma^0_{mn}\left(\theta_{low}\right)}{\sigma^0_{mn}\left(\theta_{high}\right)}\right)_{dB} + \gamma \qquad (6)$$

This last equation is obtained by combining the σ° described by equation (2) and the ratio of σ° at low and high incidence angles, which follows an exponential function of the *rms* surface height.

where <*mv*> is the mean moisture for two different dates, *mn* = HH or HV, θ is the radar incidence = 20°-24° (θ_{low}), 34°-37°, or 40°-43° (θ_{high}).

- Two dates characterized by two incidence angles (20° and 40°), and two polarizations (HH and HV). In this case, we solve the set of equations based on equation (2):

$$\begin{cases} \sigma^0_{HH}(20°) = \alpha_1\, mv + \beta_1 e^{-krms} + \gamma_1 \\ \sigma^0_{HV}(20°) = \alpha_2\, mv + \beta_2 e^{-krms} + \gamma_2 \\ \sigma^0_{HH}(40°) = \alpha_3\, mv + \beta_3 e^{-krms} + \gamma_3 \\ \sigma^0_{HV}(40°) = \alpha_4\, mv + \beta_4 e^{-krms} + \gamma_4 \end{cases} \qquad (7)$$

The various calibration relationships defined by equations (3) to (7) are fitted to the calibration database by using the least squares method.

4. RESULTS

The results obtained in the validation phase with one incidence and one polarization show inversion errors in the estimation of *mv* of about 6% for HH polarization and incidence angles of 20°-24° and 34°-37°. The use of HV polarization for incidence angles of 34°-37° gives slightly poorer results (RMSE about 7%). In contrast, large errors in the retrieved soil moisture are observed for incidences of 40°-43° (RMSE of 9.6% and 9.1% for HH and HV polarizations respectively). This is due to the fact that the radar signal is much more sensitive to surface roughness at high incidence angles. It is therefore preferable to use radar observations at the lowest available incidence angle to estimate the soil moisture of a bare soil surface. The use of both HH and HV polarizations does not improve on the inversion results obtained from a single polarization. Indeed, the RMSE is reduced by about 1% at most for incidence angles of 20°-24°, and remains relatively unchanged for 34°-37° and 40°-43°.

The accuracy of estimates of soil moisture can be improved by about 2% by using ASAR multi-incidence data. In fact, the use of ASAR images at low and high incidence angles allows *mv* estimates with RMSEs of 3.5% to be obtained. Since the data set containing two incidences angles is small (between 17 and 21 points), we used all the points for the calibration phase. Fig.2 shows scatter plots for the estimated and measured *mv* values.

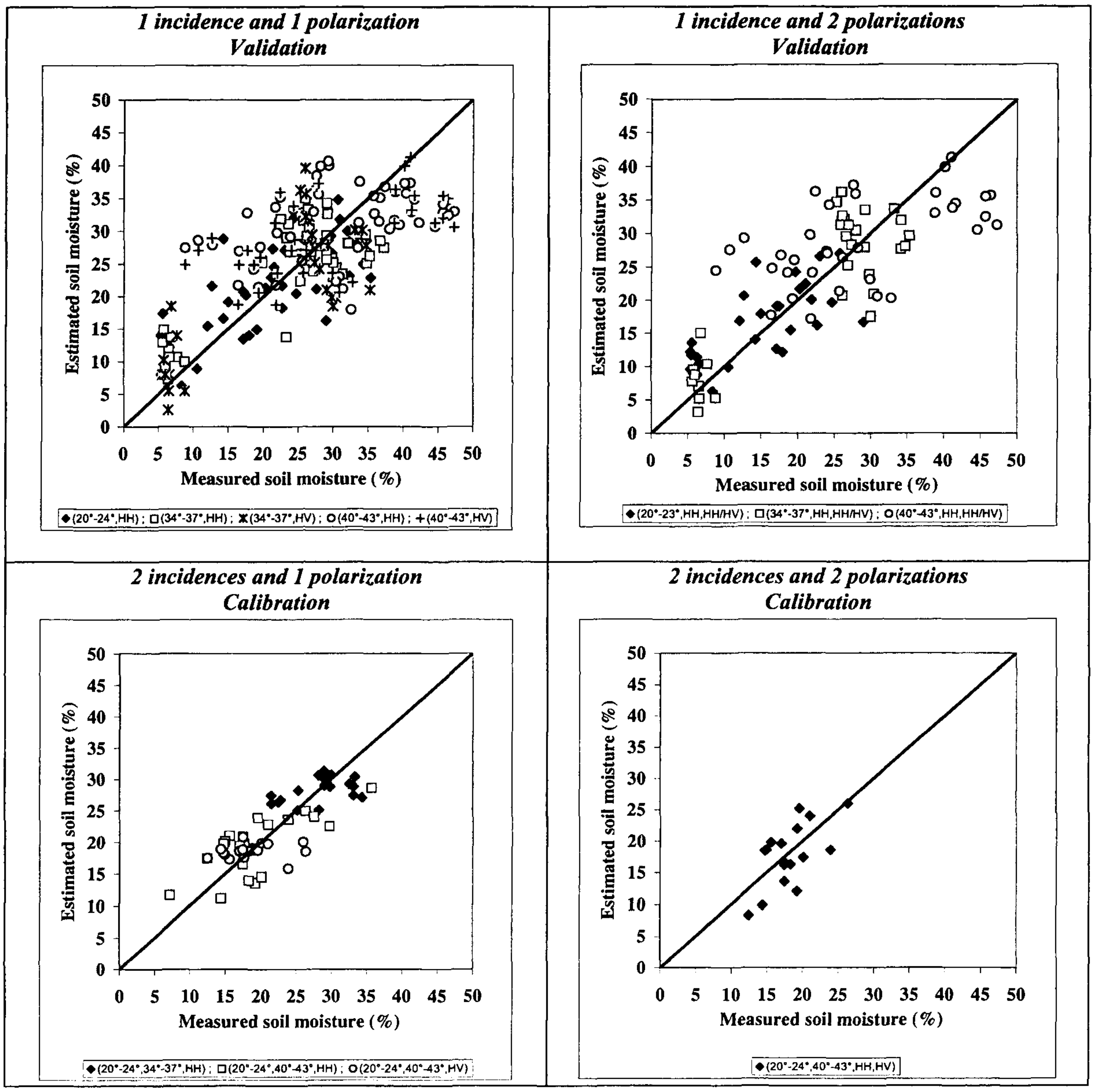

Fig. 2. Comparison between the estimated mv values and those measured in situ (from ASAR images).

5. SOIL MOISTURE MAPPING FROM ASAR DATA

Soil surface moisture is a key indicator for constraining the initial conditions of infiltration/runoff rate in case of catastrophic events, and its measurement is vital when modelling the risk of excess runoff. In the framework of Dragon flood project, we proposed to estimate the surface soil moisture from ASAR images as additional key indicator in the phase of vigilance over a catchment basin.

The use of SAR images acquired at two incidences, a low one of about 20° and a high one around 40°, produced a distinct improvement in the soil moisture estimate, in comparison with results obtained using a single incidence [2,11]. However, with the ASAR sensor, it is not possible to obtain images with two incidence angles simultaneously. The time elapsed between ASAR images acquired at two selected incidence angles (20° and 40°) is about 7 days over the Touch basin. Thus, the retrieving of soil moisture by this process is difficult because the soil moisture between the two acquisitions could change rapidly. Using only ASAR sensor, only the case of one incidence is thus possible.

Based on a single ASAR image, a simple procedure was used to map surface soil moisture over bare soils. Fig.3 shows the procedure applied on the ASAR image of 07 March 2005 (polarization: VV; incidence angle: 23°). The map of bare soils was recognized by SPOT 5 image acquired the 02 March 2005. A linear relationship between the backscattering coefficient (dB) and the soil moisture (%), established from data collected between 1998 and 2004 on several study sites (Villamblain, Pays de Caux, Touch, ...) and in using ERS and ASAR sensors, was used for retrieving soil moisture over Touch basin. The soil moisture mapping was realized by pedological zones. The pedological map, based on the analysis of soil texture and composed of four pedological zones [4], was divided randomly into 15 sub-zones in respecting the limit of pedological zones. For each sub-zone, the mean soil moisture is calculated from the mean backscattering coefficient corresponding to the sub-zone.

The soil moisture estimated was next compared to in situ soil moisture measurements. Results show a good agreement between estimated and measured soil moisture (Tabl.1).

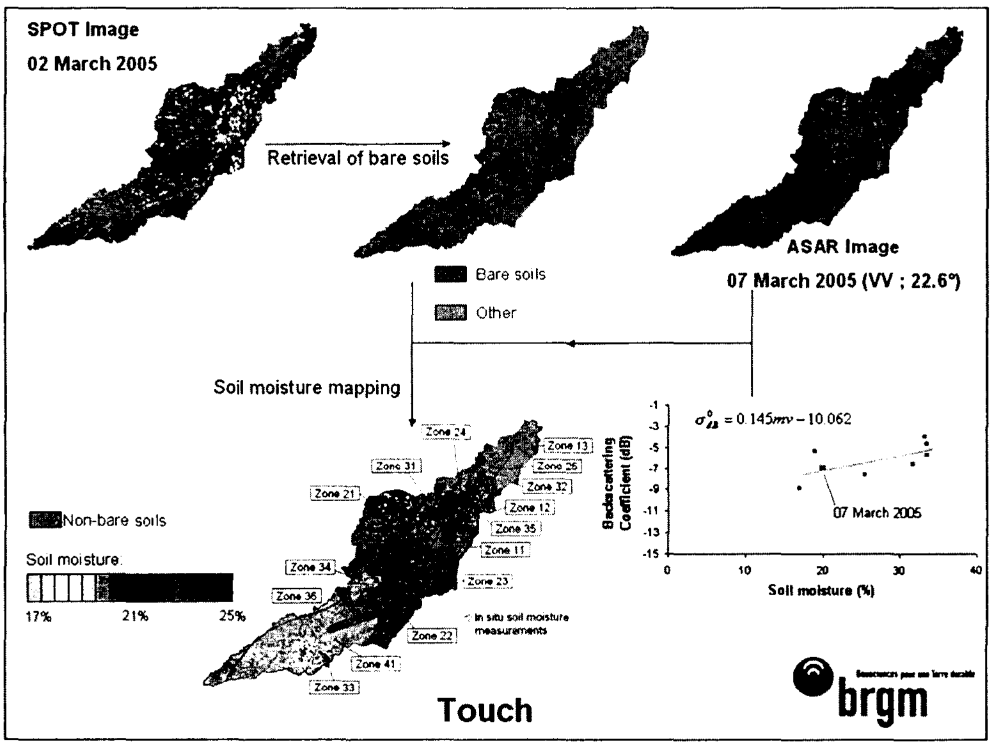

Fig. 3. Results of the soil moisture mapping over the Touch basin. The SPOT-5 image was used to map bare soils and the ASAR image at 23° (07 March 2005) for mapping soil moisture over bare soils. The class denominated "other" includes forests, soils covered with vegetation, etc.

Pedological sub-zone	Estimated soil moisture mv^{est}	Measured soil moisture mv^{mea}	mv^{est}-mv^{mea} (%)
11	23.71	-	-
12	18.70	-	-
13	22.88	-	-
21	22.36	24.72	-2.36
22	20.94	-	-
23	22.96	-	-
24	22.74	-	-
25	20.81	-	-
31	22.73	16.75	+5.98
32	24.51	-	-
33	17.11	-	-
34	20.71	-	-
35	22.82	16.85	+6.01
36	18.72	-	-
41	19.11	-	-

Tabl.1. Comparison between estimated soil moisture and in situ soil moisture measurements for three sub-zones (between 60 and 100 soil moisture measurements per sub-zones).

6. CONCLUSIONS

This study examined the potential of ASAR data for estimating volumetric soil moisture (*mv*) over bare soils. ASAR images collected between 9 February 2003 and 16 May 2005 over Villamblain and Touch basin (France) were used. The ASAR images were acquired mainly at HH and HV polarizations and for incidence angles between 20° and 43° (few data at VV polarization). The goal of this work was to compare estimates of *mv* obtained from various ASAR acquisition configurations, and to find the best sensor parameters (incidence angle and polarization) for measuring the bare soil moisture.

The study tested empirical approaches for soil moisture inversion from one channel ASAR data (one incidence and one polarization) and multi-channel ASAR data (multi-polarization and multi-incidence). The results of the study may be summarized as follows:

- For ASAR data with a single polarization and a single incidence, the retrieval algorithm performed very well for low incidence angles (20°-24° and 34°-37°). The RMSE for the soil moisture estimate is about 6% for HH and 20°-24°.
- The results are poor for high incidence angles (40°-43°) because of the low sensitivity to soil moisture and the high sensitivity of the backscattering coefficient ($\sigma°$) to surface roughness, which produces strong variations in the relationship between $\sigma°$ and *mv*. The RMSE between measured and estimated *mv* is of the order of 9%.
- Good agreement was obtained between observed and estimated *mv* when two incidence angles (one low and one high) were used. The RMSE of the comparison was found to be about 3.5%.

The accuracy of the soil moisture estimate does not improve when two polarizations (HH and HV) are used instead of one only (improvement <1%). Consequently, the improvement gained by the multi-polarization aspect of the ASAR sensor is minor. In the light of this study, the ASAR sensor does not seem to offer any advantage compared to the mono-polarization and multi-incidence RADARSAT-1 sensor.

An empirical relationship obtained between the backscattering coefficient and the soil moisture from data collected between 1998 and 2004 was applied with success to ASAR image acquired in March 2005 over the Touch basin. Results demonstrates the potential of simple operational processing of ASAR radar images for retrieving a geophysical variable such as soil moisture that could serve as a runoff indicator. These results appear promising for the development of simplified algorithms for retrieving soil moisture from ASAR data, and for monitoring multi-temporal moisture changes.

ACKNOWLEDGEMENTS

This contribution to Dragon project was possible thanks to the support of funding of WARM P2R (MAE-MENRT), of APIBAR project (CNES - BRGM and ESAP), and SCHAPI-BRGM agreement. The authors wish to thank ESA (European Space Agency) for kindly providing the ASAR images under Dragon project n° 2551. The SPOT images were obtained at special rates through the ISIS program of the CNES (French Space Agency). The authors also thank Hervé Yesou, Rita Malosti, and Mehrez Zribi for ASAR ordering (SERTIT, ESA, and CETP respectively), and INRA-Orléans for providing the soil texture data.

REFERENCES

1. Baghdadi N., Gaultier S., and King C., 2002. Retrieving surface roughness and soil moisture from SAR data using neural networks. *Canadian Journal of Remote Sensing*, vol. 28, no. 5, pp. 701-711.
2. Baghdadi N., Holah N., and Zribi M., 2005. Soil moisture estimation using multi-incidence and multi-polarization ASAR SAR data. *International Jounal of Remote Sensing, in press.*
3. Dubois P.C., Van Zyl J., and Engman E.T., 1995. Measuring soil moisture with imaging radar. *IEEE Transactions on Geosciences and Remote Sensing*, vol. 33, no. 4, pp.915-926.
4. French geographic soil database, scale 1:1,000 000 of INRA.
5. Fung A.K., Li Z., and Chen K. S., 1992. Backscattering from a randomly rough dielectric surface. *IEEE Transactions on Geoscience and Remote Sensing*, vol. 30, no. 2, pp. 356-369.
6. Holah N., Baghdadi N., Zribi M., Bruand A., and King C., 2005. Potential of ASAR/ENVISAT for the characterisation of soil surface parameters over bare agricultural fields. *Remote Sensing of Environment, vol. 96, no. 1, pp. 78-86.*
7. Le Hégarat-Mascle S., Zribi M., Alem F., Weisse A., and Loumagne C., 2002. Soil moisture estimation from ERS/SAR data: toward an operational methodology. *IEEE Transactions on Geoscience and Remote Sensing*, vol. 40, no. 12, pp. 2647-2658.
8. Oh Y., 2004. Quantitative retrieval of soil moisture content and surface roughness from multipolarized radar observations of bare soil surfaces. *IEEE Transactions on Geoscience and Remote Sensing,* vol. 42 , no. 3 , pp. 596 – 601.
9. Satalino G., Mattia F., Davidson M., Le Toan T., Pasquariello G., and Borgeaud M., 2002. On current limits of soil moisture retrieval from ERS-SAR data. *IEEE Transactions on Geoscience and Remote Sensing,* vol. 40 , no. 11 , pp. 2438 – 2447.
10. Shi J., Wang J., Hsu A.Y., O'Neill P.E., and Engman E.T., 1997. Estimation of bare surface soil moisture and surface roughness parameter using L-band SAR image data. *IEEE Transactions on Geoscience and Remote Sensing,* vol. 35, no. 5, pp. 1254 – 1266.
11. Srivastava H.S., Patel P., Manchanda M.L., and Adiga S., 2003. Use of multi-incidence angle RADARSAT-1 SAR data to incorporate the effect of surface roughness in soil moisture estimation. *IEEE Transactions on Geosciences and Remote Sensing*, vol. 41, no. 7, pp. 1638-1640.
12. Weimann A., Von Schönermark M., Schumann A., Jörn P., and Günther R., 1998. Soil moisture estimation with ERS-1 SAR data in the East-German loess soil area. *International Journal of Remote Sensing*, vol. 19, no. 2, pp. 237-243.
13. Zribi M., and Dechambre M., 2002. A new empirical model to retrieve soil moisture and roughness from C-band radar data. *Remote Sensing of Environment*, vol. 84, pp. 42-52.

Oceanography

Coupling Climate and Ocean Systems
(id. 2615)

MARINE MONITORING OF THE SOUTH- AND EAST CHINA SEAS BASED ON ENVISAT ASAR

Knut-Frode Dagestad[1], Johnny Johannessen[1], Vincent Kerbaol[2], Fabrice Collard[2], Vladimir Kudryavtsev[3, 4], Dmitry Akimov[4], Bertrand Chapron[5], Hui-Jun Wang[6], Zifa Wang[6], Ming-Xia He[7]

[1] Nansen Environmental and Remote Sensing Center, Thormøhlensgt. 47, N-5006 Bergen, Norway,
E-mail: knutfd@nersc.no; johnny.johannessen@nersc.no
[2] BOOST Technologies, 135, rue Claude CHAPPE, Technopole Brest Iroise, 29280 PLOUZANE, France,
E-mail: vincent.kerbaol@boost-technologies.com; fabrice.collard@boost-technologies.com
[3] Marine Hydrophysical Institute, National Academy of Science, Sebastopol, Ukraine
[4] Nansen International Environmental and Remote Sensing Center, St. Petersburg, Russia,
E-mail: Vladimir.Kudryavtsev@niersc.spb.ru; Dmitry.Akimov@niersc.spb.ru
[5] Institute Francais de Recherche pour l'Exploitation de la Mer, Plouzane, France, E-mail: bertrand.chapron@ifremer.fr
[6] Institute of Atmospheric Physics, Chinese Academy of Sciences, Beijing, China
E-mail: wanghj@mail.iap.ac.cn; zifawang@mail.iap.ac.cn
[7] Ocean Remote Sensing Institute, Ocean University of China, Qingdao, China,
E-mail: mxhe@orsi.ouc.edu.cn

ABSTRACT

Monitoring of the South- and East China Seas has been carried out for the period January to September 2005 with Envisat ASAR as the primary source of data. More than 130 Wide Swath scenes have been collected, showing a wide spectrum of oceanic features, such as current fronts, internal waves and wind generated surface waves, as well as rain cells, oil slicks, natural films and ships. Two software tools are here used to analyse the ASAR scenes: SARTool is a software developed for the analysis of SAR data for marine applications, and can be used to get quantitative estimates of wind and waves and to detect oil slicks and ships. The other tool used is the Radar Imaging Model (RIM), which couples a hydrodynamical model and a radar transfer model to calculate the radar backscatter that a SAR would measure for given wind speed and direction, surface current, surface film and, boundary layer stability, and radar geometry and wavelength. This paper shows some examples of applications of these two models to a selection of interesting ASAR scenes.

1 INTRODUCTION

Monitoring of the marine environment is important for many reasons: shipping and offshore industry need observations and forecasts of wind, currents and waves to improve safety and planning of operation; monitoring of oil spills can help the clean-up operation after major accidents and also quantify the amount of smaller spills from ships and oil-platforms for various regions, and mapping of offshore wind is of high interest as wind energy is the fastest growing source of renewable energy and since windmills are frequently placed offshore. In addition to such practical benefits, it is also important to observe the ocean to improve the understanding of the role of the ocean as a major component of the climate system. The Synthetic Aperture Radar (SAR) is a special type of microwave radar instrument which utilises the Doppler shift due to the movement of the satellite to get much finer resolution than would otherwise be possible: The "Advanced SAR" instrument (ASAR) onboard Envisat gives a pixel size of typically 10-150 metres, depending on mode of operation of the sensor and preprocessing of the signals. By comparison, pixel sizes are typically 1 kilometre for infrared and visible sensors onboard environmental satellites, and 5-50 kilometres for passive microwave instruments. Thus the (A)SAR gives the unique opportunity to get high resolution observations of several oceanic parameters, even at night and in the case of cloud cover. In this work, the Envisat ASAR is used to monitor the South- and East China Seas. This region is one of the busiest international sea lanes in the world, and more than half of the world's supertanker traffic passes through the waters of the region. In addition, the South China Sea region contains oil and gas resources strategically located near large energy-consuming countries. The fast economic growth of China and the other countries in the region is putting additional stress on the environment, and thus this area should be a natural focus area for marine monitoring.

2 STUDY AREA AND ACQUIRED ENVISAT ASAR DATA

The study area of this work are the South- and East China Seas (Fig. 1)

Proc. 2005 Dragon Symposium "Mid-Term Results", Santorini, Greece
27 June – 1 July 2005 (ESA SP-611, January 2006)

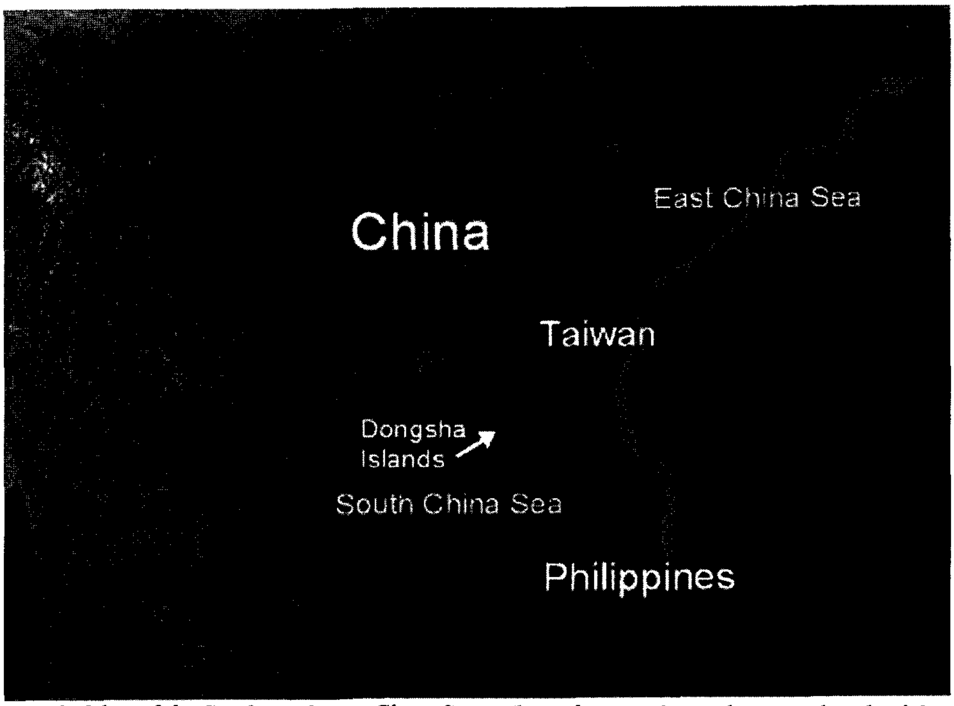

Fig. 1: Map of the South- and East China Seas. The red curve shows the typical path of the Kuroshio current.

A database system has been developed to automatically download, process and generate quicklooks of ASAR Wide Swath scenes for the area of interest from the Rolling Archive of ESA. This system permits spending more time on analysis of interesting scenes than on doing technical processing "by hand". For the period January to September 2005 more than 130 scenes have been downloaded and processed.

3 SOFTWARE TOOLS FOR ANALYSIS OF SAR DATA

ESA provides several free software tools for basic and general processing and plotting of Envisat satellite products (e.g. Beam, Best and Enviview). However, to derive secondary products for marine applications from SAR imagery, specialised tools are needed. Two such tools have emerged over the last years: SARTool and Radar Imaging Model ([1], [2], [3]). The following subsections describe briefly these two models, and Section 4 shows some examples of their applications.

3.1 SARTool

SARTool is developed by the French company "Boost Technologies" with the non-expert user in mind, and has an intuitive graphical user interface. It can read and process SAR images from the ERS, Radarsat and Envisat satellites. The program calibrates the scenes, and can do various image processing and geo-referencing for improved display. Additionally, it has modules to retrieve several scientific products: atmospheric wind speed and direction are calculated based on the influence on the ocean surface; wavelength, propagation direction and significant wave height can be calculated from Single Look Complex (SLC) images. It can detect ships and report the position, size, route and speed, and it can detect and report the position and size of oil spills. For more advanced users, SARTool can do multi-looks extraction from SLC images; estimate azimuth cut-off, and calculate moments and plot Pearson diagrams.

3.2 Radar Imaging Model

The mathematical model by Vladimir Kudryavtsev and others, described in [1], [2] and [3], combines a hydrodynamic module with a radar transfer module to calculate the radar signature (Normalised Radar Cross Section, NRCS) of the sea surface if the following parameters are known: wind speed and direction; stability of the atmospheric boundary layer (parameterised with the air-sea temperature difference), ocean surface current, surface films and radar-parameters such as incidence and azimuth angles and radar wavelength. The model calculates the radar return (for both VV and HH polarisations) due to quasi-specular reflection, Bragg scattering and impact from breaking waves (foam/whitecaps), and also takes into account the feedback of breaking waves on shorter waves causing Bragg scattering. This model is developed into a computer code, here referred to as the "Radar Imaging Model" (RIM). Although this model is not easily inverted, it is useful to get a qualitative description of e.g. ocean currents, which are otherwise not easily detected from satellites, at least not in case of clouds.

4 EXAMPLES OF OBSERVED OCEANIC PHENOMENA

More than 130 ASAR WSM scenes from the South- and East China Seas have been collected and visually inspected, and many marine features have been identified. No systematic overview of all features will be given here, but rather some examples of features for which SAR-instruments are particularly useful. In the next subsections three ASAR-scenes are discussed: one showing the wind field related to a typhoon, one showing the signature of the Kuroshio current, and one showing the signature of internal waves.

4.1 The Typhoon "Khanun"

On 12 September 2005 the typhoon "Khanun" struck Shanghai and East China, and killed at least 14 people. This typhoon was observed with ASAR over the East China Sea the day before, 11 September at 01:47 UTC. The bright spiral seen on the ASAR Wide Swath Image in Fig.2 is not clouds, but increased radar backscatter due to wind generated roughness of the sea surface. With SARTool it is possible to apply the CMOD-algorithm to estimate the wind speed that generated the surface waves. One can choose between two versions of the algorithm; CMOD-IFREMER [4] which is the operational module for low to moderately high winds, and CMOD-5 [5] which is tailored to perform accurately for high wind speeds, and is expected to become operational. Fig.3 shows the wind speed of "Khanun" estimated with the CMOD5-algorithm. It is seen that ASAR reveals a high resolution variable wind field, with maxima of ~100 knots (~50 m/s). The direction of the wind speed is estimated from the ASAR scene by detecting wind streaks signatures in the FFT-transform of small subsets of the image.

Fig. 2: Envisat ASAR Wide Swath image of the typhoon "Khanun" on 11 September 2005 01:47 UTC. The northern tip of Taiwan is seen at the bottom.

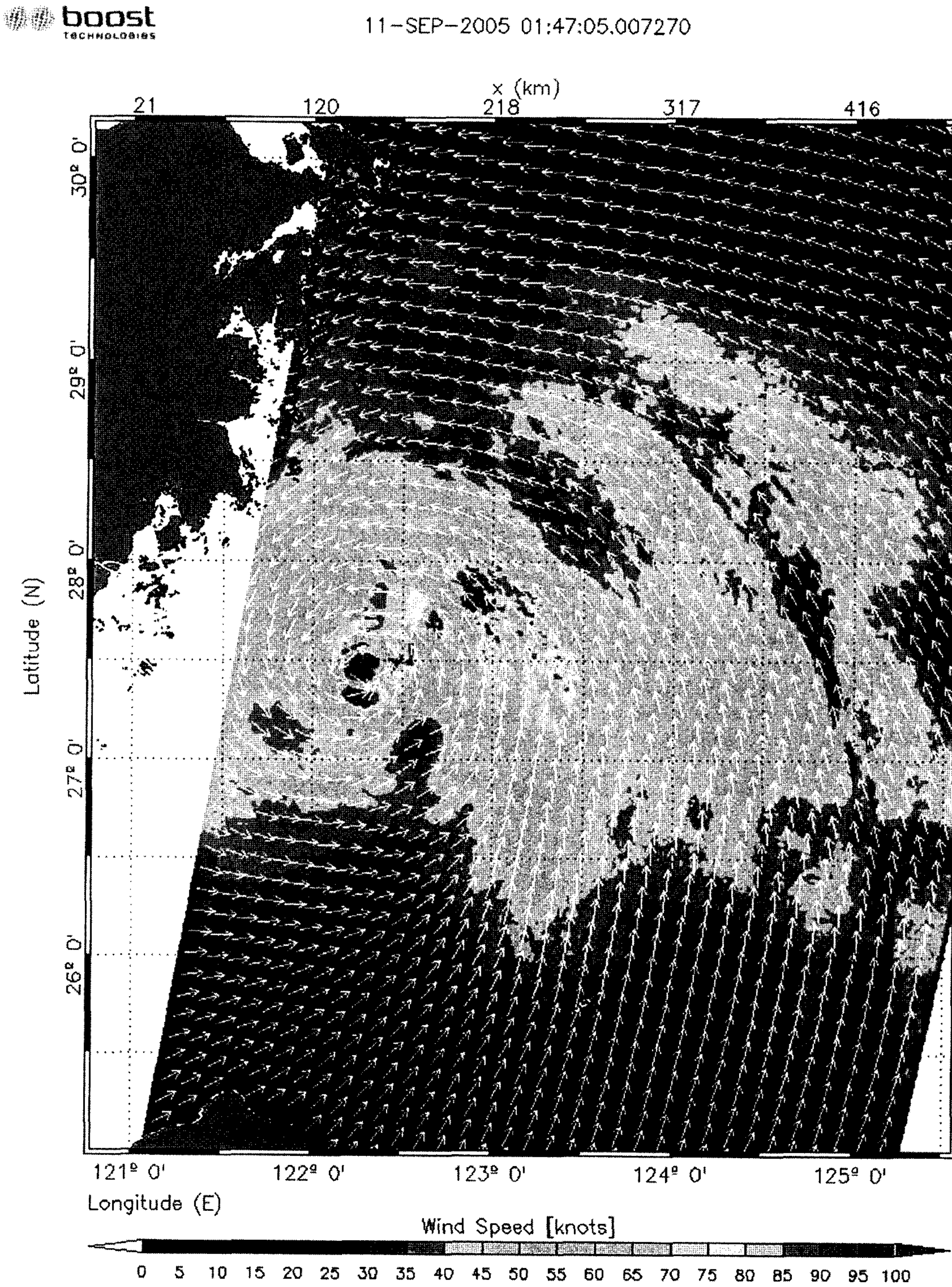

Fig.3: Wind speed for the typhoon "Khanun" calculated from the Envisat ASAR Wide Swath image in Fig. 2 using SARTool and the CMOD-5 algorithm. The arrows show the wind direction, calculated by detecting wind streaks signatures in the FFT-transform of small subsets of the image.

4.2 The Kuroshio current

Fig.4 shows an Envisat ASAR Wide Swath scene from the East China Sea on 13 July 2005 at 01:31 UTC. The location of the scene is indicated by the red box in Fig.5.

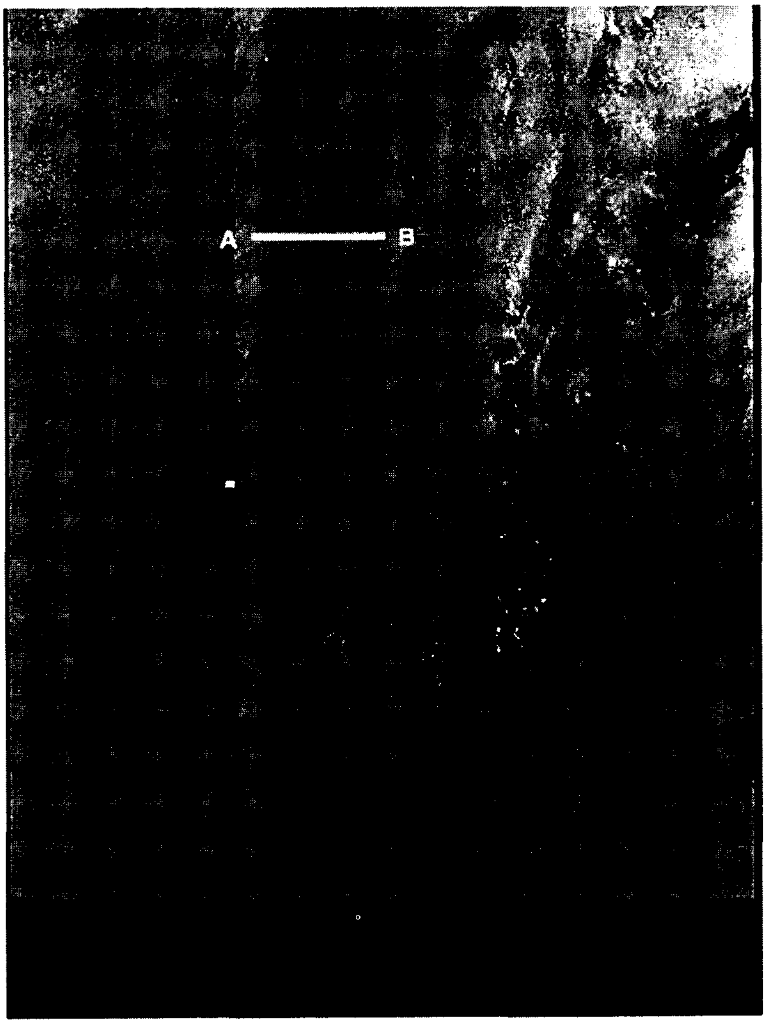

Fig. 4: Envisat ASAR WSM image over the East China Sea on 13 July 2005 at 01:31 UTC. The location of the scene is indicated with the red box on Fig. 5. The southernmost of the larger islands is Okinawa (Japan). Land is masked with black. The polarisation is VV, and the radar look direction is from the right (descending pass).

In the western part of the ASAR image one can see a structure stretching from the South-West to the North-East. Fig.5 shows the surface current field 1.5 hours prior to the ASAR acquisition for the East China Sea, assimilated into the Naval Coastal Ocean Model (NCOM) of the US Naval Research Laboratory. The structure on the ASAR image corresponds well with the strong surface current, exceeding 1 m/s, seen in the NCOM field. While there is little doubt that this is the Kuroshio current, the SAR imaging mechanism in this case is not evident. Fig. 4 shows that the current induces a decrease of the radar backscatter intensity, as seen e.g. over the transect from A to B. There are several mechanisms that can explain this feature.

One possibility is that convergence related to the current collects surface slicks, thus damping short surface waves and leading to a decrease of backscatter intensity. As the scene is from mid-summer (13 July), the primary production in the sea should be quite high, and surfactant films are probably abundant.

A second possible explanation is that the speed of the wind relative to the sea surface is lower across the current because the wind and current have the same direction. This explanation is supported by Fig.6, which shows that the wind direction derived from QuikSCAT is mainly along the Kuroshio current in this region the actual day. This figure also shows the speed of the wind, estimated by SARTool using the CMOD-IFREMER algorithm. The wind speed in the region around Kuroshio is about 8 m/s. Thus, since the model field of Fig.5 shows a maximum current speed of more than 1 m/s, the wind speed relative to the sea surface is about 13 percent lower than for the surrounding region where the speed of the current (according to the assimilated model field) is much smaller, and where the current is less directed along the main pathway of the Kuroshio current (Fig. 5).

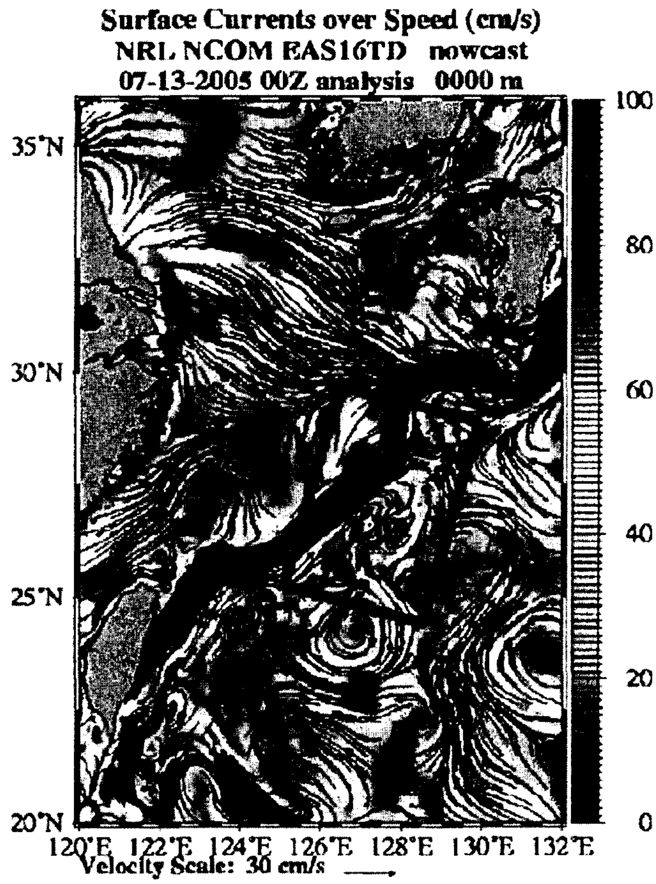

Fig. 5: The assimilated surface current field for the Naval Coastal Ocean Model of the US Naval Research Laboratory. The time corresponds to 1.5 hours prior to the acquisition of the Envisat ASAR scene of Fig.4 (position indicated by the red box).

A third explanation is due to hydrodynamic modulation of the ocean surface waves, caused by complex interaction between the current and waves at different scales, and further affected by breaking waves. Such complex interaction can be difficult to explain (and intuitively understand), but the Radar Imaging Model (Section 3.2) can assist the interpretation. For example, the model can be used to calculate the radar signature corresponding to divergent, convergent, or shear currents, which can then be compared to the SAR image. Here the model will be used to simulate the NRCS corresponding to the transect A-B of Fig.4. Similarly to [6], a hyperbolic tangent function will here be used to simulate such currents to be input to the RIM model:

$$F(x) = \frac{(1 + tanh(x / L))}{2} \tag{1}$$

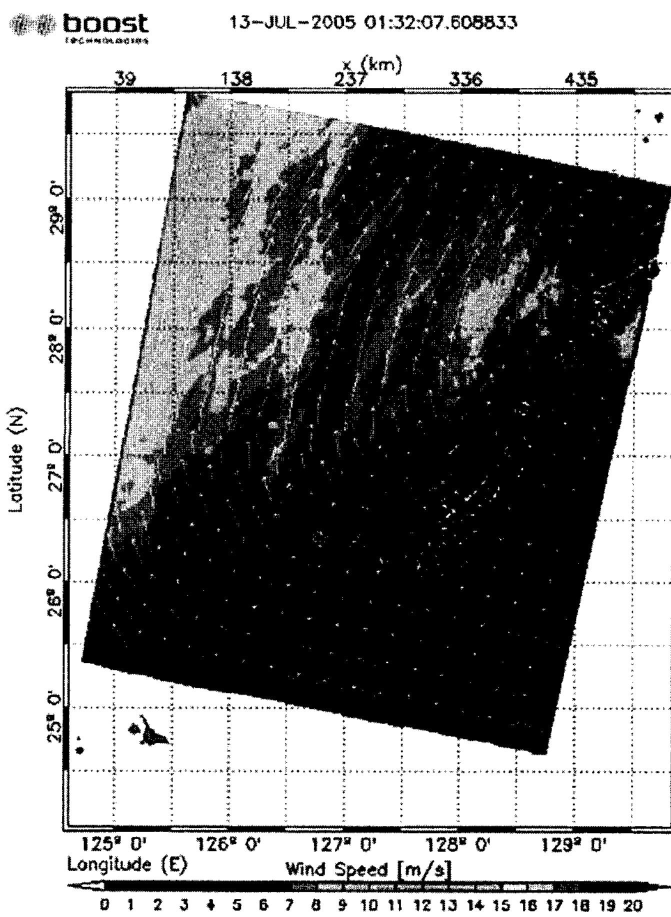

Fig. 6.: High resolution wind speed field (colours) for the ASAR image of Fig.4. This is estimated with SARTool using the CMOD-IFREMER algorithm. Also input to the algorithm is the wind direction field from QuikSCAT (white arrows). The QuikSCAT wind direction field is from a daily gridded dataset (12-13 July 2005), freely available from ftp://ftp.ifremer.fr/ifremer/cersat/products/gridded/mwf-quikscat/data/daily/

Here x is the distance perpendicular to the current, e.g. increasing from A to B in Fig.4, and the scale parameter L is taken as 250 metres. The three different current types are defined by:

$$\begin{aligned} U = F(x)\,,\ V = 0 \quad & \text{for a divergent current} \\ U = -F(x)\,,\ V = 0 \quad & \text{for a convergent current} \\ U = 0,\ V = F(x) \quad & \text{for a shear current} \end{aligned} \tag{2}$$

Other parameters input to RIM can be estimated from Figs. 4 and 6: Corresponding to the cross section A-B indicated on Fig.4, the incidence angle is taken as 35 degrees, and the radar look angle is in the negative x-direction. A constant wind speed of 8 m/s is used, in the direction of the V-component of the current (perpendicular to the x-axis and radar look direction). The simulated Normalised Radar Cross Section (NRCS) for the three different current properties is plotted in Fig.7. For the divergent current there is a decrease of the NRCS in the convergence zone, qualitatively similar to what is seen in the ASAR scene in Fig.4. The shear current creates contrast on the same order of magnitude as the divergent current, but there is not an overall decrease of the NRCS in the shear zone, and thus the shear current does not explain the dark band seen on Fig. 4. A convergent current, however, induces a brightness peak, thus opposite of what is observed.

Different stability of the atmospheric boundary layer can also cause signatures on the ocean surface because of variations in the transfer of momentum across the air-sea boundary. Variations in the sea surface temperature (SST), often the case over current zones, can cause such variations of the atmospheric stability. For this particular case, however, the assimilated (from AVHRR) SST for the NCOM model showed (not shown here) rather uniform temperatures across the Kuroshio current.

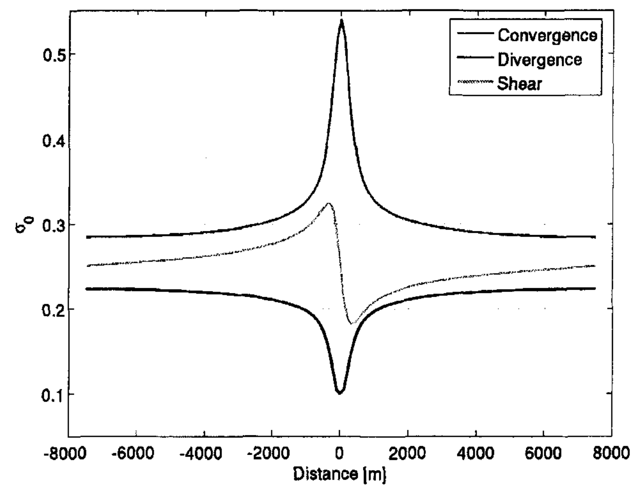

Fig. 7: Normalised Radar Cross Section (σ_0) (C-band, VV polarisation) simulated with the RIM model (Section 3.2) for convergent, divergent and shear currents defined by Eqs. 1 and 2. The radar look direction is perpendicular to the current fronts (from the right); the incidence angle is 35 degrees and the wind speed is 8 m/s along the front (positive y-direction).

4.3 Internal waves

Fig.8 shows an Envisat ASAR WSM scene from the South China Sea, around the Dongsha Islands (Fig. 1), acquired 27 March 2005. This is a typical scene from the South China Sea, where there is an abundance of expressions of internal waves. The internal waves are generated in the Luzon Strait (between Taiwan and the Philippines (Luzon Island)) by the tidal wave as it propagates westwards and interacts with the bathymetry (Werner Alpers, personal communication). The distance between the waves 'A' and 'B' in Fig.8 is measured with SARTool to be 75 kilometres. Thus, if they are generated from the semi-diurnal tidal component, the distance travelled corresponds to a speed of 1.7 metres per second, which is reasonable. If the depth of the mixed layer is small compared to the total depth and the wavelength, the speed of the internal waves can be approximated by:

$$c = \sqrt{(gH \frac{\delta \rho}{\rho})} \tag{3}$$

where g is the gravity acceleration, and $\delta \rho / \rho$ is the relative difference in density between the mixed layer and the lower layer. Taking $\delta \rho / \rho$ to be 0.002, Eq. 3 gives a mixed layer depth H of 147 metres.

The Radar Imaging Model nicely reproduces the increased radar brightness caused by such internal waves, see e.g. Fig.13 of [3]

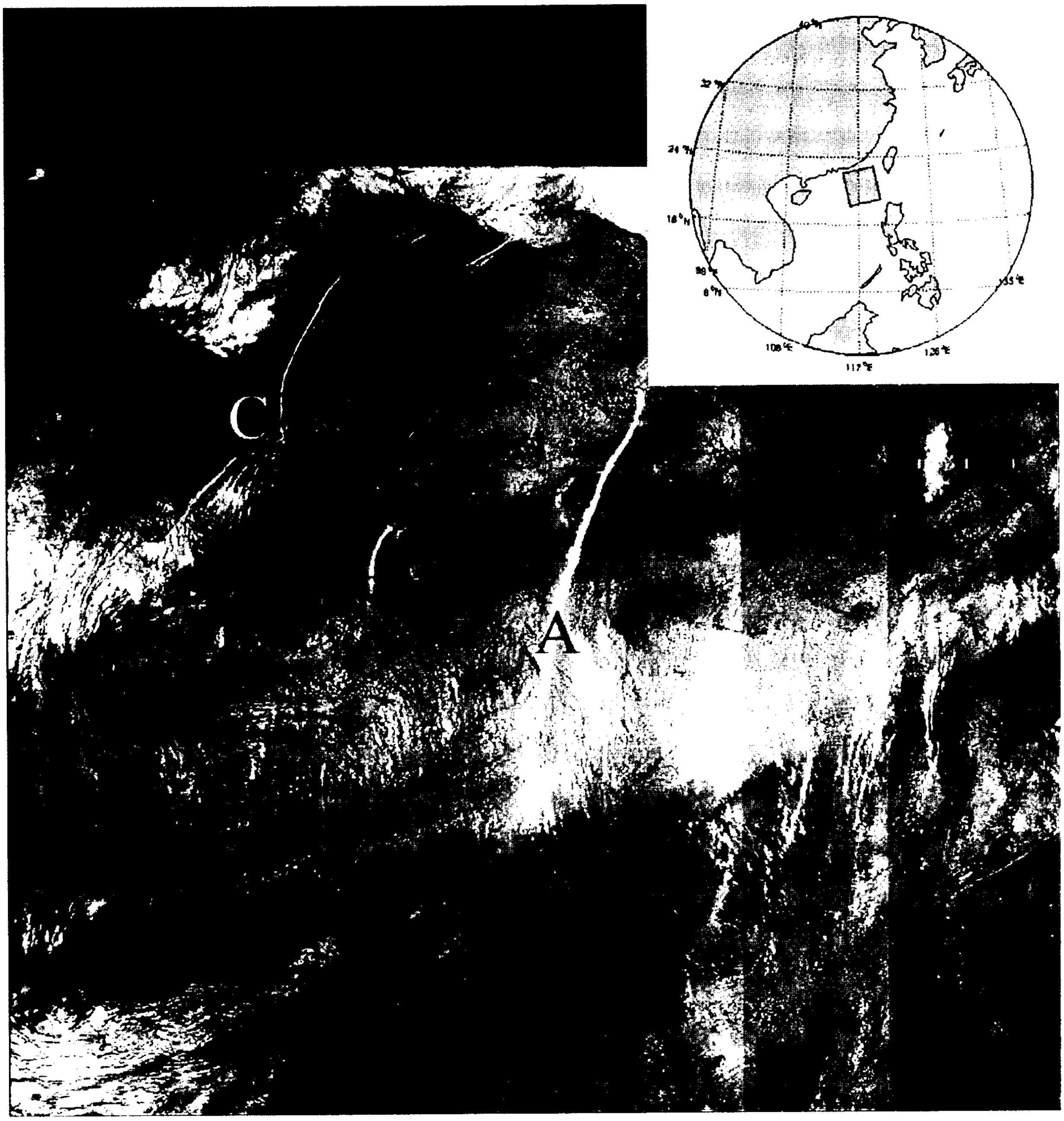

Fig.8: An Envisat ASAR WSM scene from the South China Sea acquired on 27 March 2005 at 14:13 UTC. The letter 'A' marks the signature of an internal wave travelling to the west. 'B' shows an internal wave interacting with and being diffracted at the Dongsha (Pratas) Islands. 'C' shows a diffraction pattern of internal waves refracted at an earlier time. The distance from 'A' to 'B' is 75 kilometres.

5 CONCLUSIONS AND FUTURE PROSPECTS

More than 130 ASAR Wide Swath scenes over the East- and South China Seas have been collected for marine monitoring. Here three interesting scenes are discussed:

The first image shows the typhoon "Khanun" which struck China on 12 September 2005. Using the software SARTool and the CMOD-5 algorithm [5], a high resolution wind field with maxima exceeding 50 m/s is found around the eye of the typhoon.

The second image shows a band of lower radar backscatter which corresponds well in time and space with a region of strong (> 1m/s) ocean surface current from the Naval Coastal Ocean Model (NCOM) of the US Naval Research Laboratory. Using the Radar Imaging Model ([1], [2] and [3]), hydrodynamic modulation of ocean waves due to divergent current is suggested as a reason for the signature on the ASAR scene, rather than convergent or shear currents. Other possible (additional) mechanisms suggested are collection of surfactant slicks due to convergent currents (thus an opposite effect of the hydrodynamic modulation due to divergent currents) or less impact of the wind on the sea surface due to coincident current and wind direction.

The third ASAR scene shows a train of internal waves travelling westwards in the South China Sea, and being refracted at the Dongsha Islands. The propagation speed of the waves is estimated to 1.7 m/s and the depth of the mixed layer is estimated to be 147 metres.

Synergy with other satellite sensors, model data or *in situ* data is seen to be very useful in assisting the interpretation of ASAR images. In the near future efforts will be spent on creating an efficient system for collecting and collocating imagery from other sensors (e.g. MERIS and AATSR) with ASAR scenes. In this work, an ASAR scene has been qualitatively compared with output of the NCOM ocean model. In the future more quantitative comparisons will be made, by e.g. calculating the surface velocity deformation field which is more suitable for comparison with SAR features [6].

The software tools used here are quickly evolving, and an idea is launched to include the Radar Imaging Model into the more easy-to-use SARTool. This idea will also consider to adopt the new algorithm developed to measure ocean surface velocity directly from space from the Doppler signal recorded by ASAR [7].

REFERENCES

1. Kudryavtsev, V., D. Hauser, G. Caudal, and B. Chapron, A semi-empirical model of the normalized radar cross-section of the sea surface. Part 1: The background model, J. Geophys. Res., 108, C3, doi:10.1029/2001JC001003, 2003.
2. Kudryavtsev, V., D. Hauser, G. Caudal, and B. Chapron, A semi-empirical model of the normalized radar cross-section of the sea surface. Part 2: Radar modulation transfer function, J. Geophys. Res., 108, C3, doi:10.1029/2001JC001004, 2003.
3. Kudryavtsev V., D.Akimov, J.A.Johannessen, and B. Chapron, On radar imaging of current features. Part 1: Model and comparison with observations, J.Geoph.Res., 110, C07016, doi:10.1029/2004JC002505, 2005.
4. Quilfen, Y., Chapron, B., Elfouhaily, T., Katsaros, K., Tournadre, J., and Chapron, B., Observation of Tropical Cyclones by High-Resolution Scatterometry, J. Geophys. Res., 103, 7767-7786, 1998.
5. Hersbach H, CMOD5 an improved geophysicalmodel function for ERS C-band scatterometry, Internal report, European Centre for Medium-Range Weather Forecast, 2003.
6. Johannessen, J. A., V. Kudryavtsev, D. Akimov, T. Eldevik, N. Winther, and B. Chapron, On radar imaging of current features. Part 2: Mesoscale eddy and current front detection, J.Geoph.Res., 110, C07017, doi:10.1029/2004JC002802, 2005.
7. Chapron, B., F. Collard, and F. Ardhuin, Direct measurements of ocean surface velocity from space: Interpretation and validation, J. Geophys. Res., 110, doi:10.1029/2004JC002809, 2005.

- *SARTool web page: http://www.boost-technologies.com/web/en/sartool.html*
- *NCOM EAS16 model web page: http://www7320.nrlssc.navy.mil/EAS16_NFS/TIDES/EAS16NFS.html*

Ocean Environment and Climate
(id. 2566)

Sea Surface Temperature

Internal Waves

Ocean Colour and Constituents

Bottom Topography

Others

REVIEW OF DRAGON OCEAN PROJECT ID2566

Ming-Xia He [(1)], Werner Alpers [(2, 1)], Roland Doerffer[(3)]

[(1)] *Key Laboratory of Ocean Remote Sensing, Ministry of Education, China, Ocean Remote Sensing Institute, Ocean University of China, China, E-mail: mxhe@orsi.ouc.edu.cn*

[(2)] *Institute of Oceanography, University of Hamburg, Germany, E-mail: alpers@ifm.uni-hamburg.de*

[(3)] *GKSS Forschungszentrum, Institute for Coastal Research, D-21502 Geesthacht, Germany E-mail: doerffer@gkss.de*

ABSTRACT

The dragon ocean project ID2566, titled "oceanography from space – internal wave, ocean wave, shallow water topography, ocean color, Kuroshio current", is the unique project focused on the oceanic study in the frame work of ESA -MOST Dragon Programme. The summary and review are focused on the mid-term progress of satellite remote sensing about internal waves and ocean color in this paper. The progress about the researches on the shallow water topography and Kuroshio current are also briefly introduced.

1. INTRODUCTION

ERS and ENVISAT provide 15 year continuous multi-sensor satellite measurements of the ocean with optical, infrared and microwave sensors. Undoubtedly, it provides a basic condition as never before for the development of the satellite oceanography and remote sensing physics.

The dragon ocean project ID2566, titled "oceanography from space – internal wave, ocean wave, shallow water topography, ocean color, Kuroshio current", is the unique project focused on the oceanic study in the frame work of ESA (European Space Agency)-MOST (Ministry of Science and Technology, China) Dragon Programme. Each item of it includes the retrieval of ocean environmental parameters from satellite data and its validation as well as the application research in the China seas and the north-west Pacific with the time series of multi-sensor data.

During the Dragon Symposium held in Santorini, Greece in 2005, there were eleven presentations for the ocean project, which included one for review, three for internal waves, three for ocean color, three for data merging and Kuroshio related data assimilation, and one for analysis of ASAR dual polarization data. The titles and corresponding authors are as following.

(1) Overview of Dragon Project ID 2566: Oceanography from Space - Internal Waves, Ocean Surface Waves, Shallow Water Topography, Ocean Color, and Kuroshio Current. Ming-Xia He, Werner Alpers, and Roland Doerffer.

(2) The Distribution of Internal Waves in the China Seas Studied by Multi-sensor Satellite Images. Werner Alpers, Ming-Xia He,Kan Zeng, Ling-Fei Guo, and Xiao-Ming Li.

(3) The Retrieval of Internal Waves Amplitude from SAR Images. Ming-Xia He, Kan Zeng , Chao-Fang Zhao, and Xiao-Ming Li.

(4) Automatic Internal Wave Extraction for Satellite SAR Imagery Based on Stationary Wavelet Transform. Ming-Xia He, Haihua Chen, Lingfei Guo, Xiaodong Zhuang, and Hongping Li.

(5) Assimilating SST and SSHA into an Ocean Model in the Kuroshio Regions. Mingqiang Fang.

(6) Sea Surface Temperature Merged from Multi-Sensor Data. Lei Guan, Hui Zhang, and Liqin Qu.

(7) Analysis of JEBAR on the East-Chinese Shelf. Xueen Chen and Thomas Pohlmann.

(8) A Novel Data Processing Method for the Satlantic Hyper-TSRB in Coastal Waters. Keping Du, Zhongping Lee, and Ming-Xia He.

(9) Retrieval of Oceanic Constituents from MERIS Data in Coastal Waters. Tinglu Zhang, Jürgen Fischer, Ming-Xia He.

Proc. 2005 Dragon Symposium "Mid-Term Results", Santorini, Greece 27 June – 1 July 2005 (ESA SP-611, January 2006)

(10) The Ocean Optics Data Analysis of Cruise the East China Sea. Zhi-Shen Liu, Ming-Xia He, and Lian-Bo Hu.

(11) Analysis on the Dual Polarization Data of ENVISAT ASAR. Jinsong Chong and Minhui Zhu.

The summary and review are focused on satellite remote sensing about internal waves and ocean color in this paper.

For the satellite remote sensing of the internal waves in the China seas, comprehensive researches are made, which include the spatial-temporal distribution of internal waves in the China seas, the retrieval of internal wave parameters, in particular the amplitude of internal waves, from SAR imagery, the validation experiment of internal waves conducted simultaneously by Envisat/ASAR and field measurements in the East China Sea, the numerical simulation of internal waves in the northern South China Sea, the simulation of SAR image with internal wave signatures, and the extraction of internal wave signatures from SAR imagery.

For the ocean color remote sensing, the milestone is that Ocean Remote Sensing Institute, ocean university of China, purchased a set of international standardized instruments for ocean optical field measurements. The in-situ ocean optical data and Envisat/MERIS data in the coast of China have been collected for comparison and validation. For the retrieval algorithm of MERIS data, a semi-analytical model suitable to the China seas and the neural network method are studied. The results are compared with the results by BEAM of ESA and by SeaDAS 4.8 of NASA.

2. SATELLITE REMOTE SENSING OF THE INTERNAL WAVES IN THE CHINA SEAS

2.1. Spatial-temporal distribution of internal waves in the China Seas

Historically, the in-situ data of internal waves in the China seas are sparse. While, many internal solitary waves are observed in the South China Sea, East China Sea and Yellow Sea after the lunch of ERS-1 and ERS-2. Hsu et.al. [4] published the paper about the distribution of internal waves in the China seas for the first time using hundreds ERS-1 and ERS-2 SAR images, which was cited in the website of image collections about the global distribution of internal waves opened by Jackson in 2004 [6].

Fig. 1. Distribution of internal wave signatures in the China Seas obtained from analyzing the available satellite images.

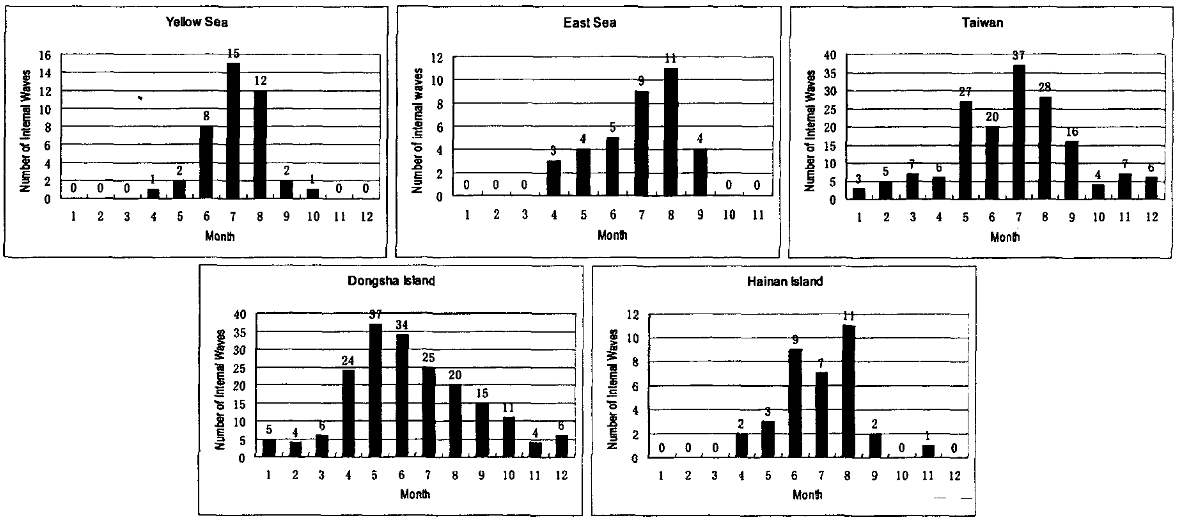

Fig.2. Internal wave signature as a function of season (month) for the different ocean areas

In this study, about 800 images with internal wave signatures are found out from approximately 15 thousand satellite images acquired between 1994 and 2004, which SAR and optical images occupy half and half respectively. The large number of internal wave images ensures the rationality of the statistics. Fig.1 gives the distribution of internal waves in the China seas based on the decadal timescale internal wave images. According to the generation mechanism of internal waves, the China seas are roughly divided into 5 areas, i.e., Yellow Sea, East Sea, Taiwan waters, DongSha Island waters and Hainan Island waters. Fig.2 shows the monthly and seasonal distribution of internal waves in the 5 areas. There are no internal waves observed in the areas of Yellow Sea, East Sea and Hainan Island in winter. However, internal waves can be observed in the areas of Dongsha Island and Taiwan for the whole year. In all the areas, summer has the highest occurrence of internal waves. Those results are roughly consistent to the bathymetry, pycnocline properties and spring tide time of the China seas [3].

2.2 Retrieval of the amplitude and other parameters of internal waves from SAR imagery

By image processing methods, the propagation direction of internal waves, distance between the internal wave packets, number of internal waves in one packet, the length of internal wave crest, and group velocity of internal waves can be extracted from the SAR images with internal wave signatures.

For the extraction of λ, the width of internal solitary waves, from SAR images, the method of measuring D, the distance, between the maximum and minimum values of the SAR signatures modulated by internal solitary waves is often utilized because of the relation $\lambda = 1.52D$ [8][10]. However, there is a difficult to accurately determine D. In this project, two methods are used to extract λ.

- Direct regression [10]

The relation $\Delta\sigma_0 = A_2 \operatorname{sec}h^2(2\theta/\lambda)\tanh(2\theta/\lambda)$ is used to regression the modulation signatures of internal solitary wave along the propagation direction.

- Regression combined with EMD filter

If the signal-to-noise ratio of SAR image with internal wave signatures is relative low, the Empirical Mode Decomposition (EMD) [5] is used as a filter to extract the modulation signatures of internal waves. Then the regression stated above is applied on the filtered modulations to obtain λ.

Retrieving amplitude of internal waves from SAR imagery is regarded as a difficult task. Very few papers about it had been published in last 25 years [1][2][8][10]. There are two kinds of methods documented. One is the variation-of-wavelength method based on the cnoidal or dnoidal solution of KdV equation for nonlinear internal wave [1][2]. The other one is characteristic width method based on the solitary wave solution of KdV equation [8][10]. The latter has been applied on both continuous stratification model [8] and two-layer model [10]. In fact, the methods mentioned above cannot be developed to application software.

By introducing a modification factor and adopting a parameterized continuously stratified buoyancy frequency, a new method based on the solitary wave solution of KdV equation has been proposed.

$$a_0 = n\frac{24H^3}{\lambda^2\gamma}$$

where a_0 is the amplitude of internal solitary wave, λ is the characteristic width of internal solitary wave, H is water depth, γ is a nonlinear parameter, and n is a modification factor.

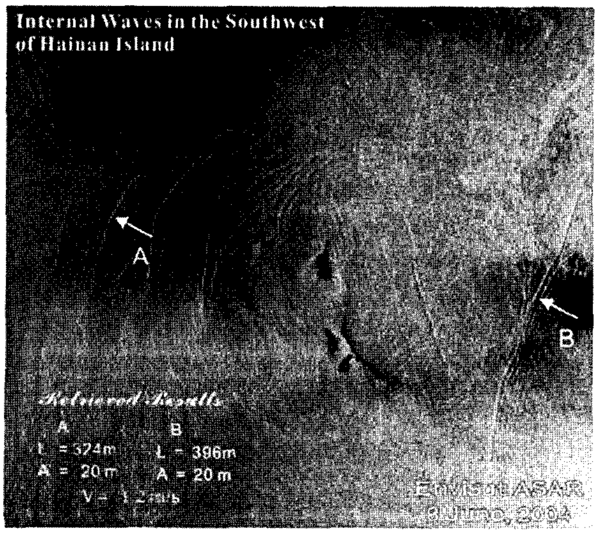

*Fig.3. **Amplitudes retrieved** from an Envisat ASAR images acquired in the **east of** South China Sea near Hainan Island on 8 June, 2004.*

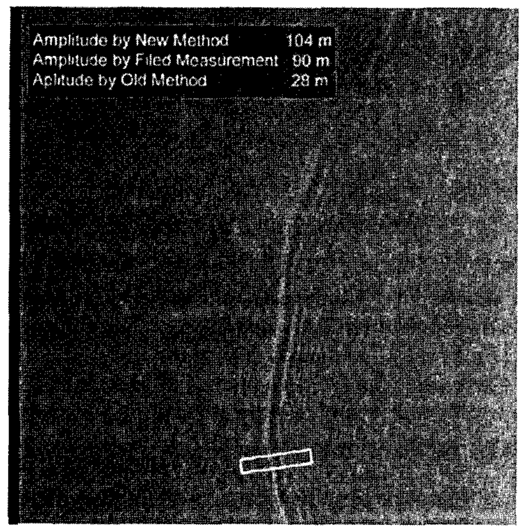

Fig.4. Amplitude retrieved from an ERS-2 SAR image acquired in the South China Sea north east off Dongsha atoll 26 April, 2000 during ASIAEX (Asia International Acoustic Experiment) 2000.

The relation above is obtained from the solitary solution of the nonlinear internal wave equation for continuously stratified fluids with the assumption of weak nonlinearity and weak dispersion. Theoretically, the conditions in the shallow waters of the China Seas may not meet the requirement of KdV equation. By inducing the modification factor, n, which is related to the local bathymetry and the width of internal waves, the original relation between a_0 and λ is improved. The accuracy of retrieved amplitude of internal wave becomes acceptable.

Technically, a parameterized buoyancy frequency profile is adopted to simplify the description of the continuous stratification model. The parameters can be simply determined according to the climatology depth and thickness of pycnocline. By this way, γ can be tabulated on those parameters as a look-up table. User friendly application software for retrieving amplitude of internal solitary waves from SAR imagery based on this new method has been developed.

Validation and comparison of the results with those data from simultaneous field experiment in Zhoushan, Asian Seas International Acoustics Experiment (ASIAEX) [9], internal wave experiment in the South China Sea and 10 published papers show the new method has potentials of application.

2.3. First validation experiment of internal waves conducted simultaneously by ENVISAT/ASAR and field measurements in the East China Sea

- Time: from 25 April 2003 to 7 May 2003. (the period when Severe Acute Respiratory Syndrome (SARS) was highly prevalent in China)

- Position: the sea area east off Zhoushan Island in the East China Sea
- Research Vessel: Environment Monitor Vessel of ZheJiang Province (rented)
- Satellite data: Envisat/ASAR
- Field instrument: TR7 thermistor string (rented) + 7 Starmon mini thermistors, CTD, ADCP, S4 wave recorder, wind meter, three-cup anemometer, electro-magnetic current meter, Secchi Disc.
- Results: Table 1 shows the results of validation experiment. The amplitude of leading internal soliton is 5.5 m from the measurements by thermistor string. The amplitude retrieved from ASAR image by the original method is 0.67 m. The relative error is up to 88%. The amplitude retrieved from ASAR image by the new method with modification factor is 4.4 m. The relative error is only 20%. The left image in fig. 5 is the internal wave packet observed by the thermistor string in the East China Sea on 4 May 2003. The right image is the same internal wave packet observed by the Envisat ASAR 6.5 hours later.

Table 1. The amplitudes of internal wave retrieved using the data acquired during the Zhoushan field experiment.

γ	λ	Measured Amplitude	Retrieved Amplitude (old method)	Relative Error	Retrieved Amplitude (new Method)	Relative Error
46	360 m	5.5 m	0.67 m	88%	4.4 m	20%

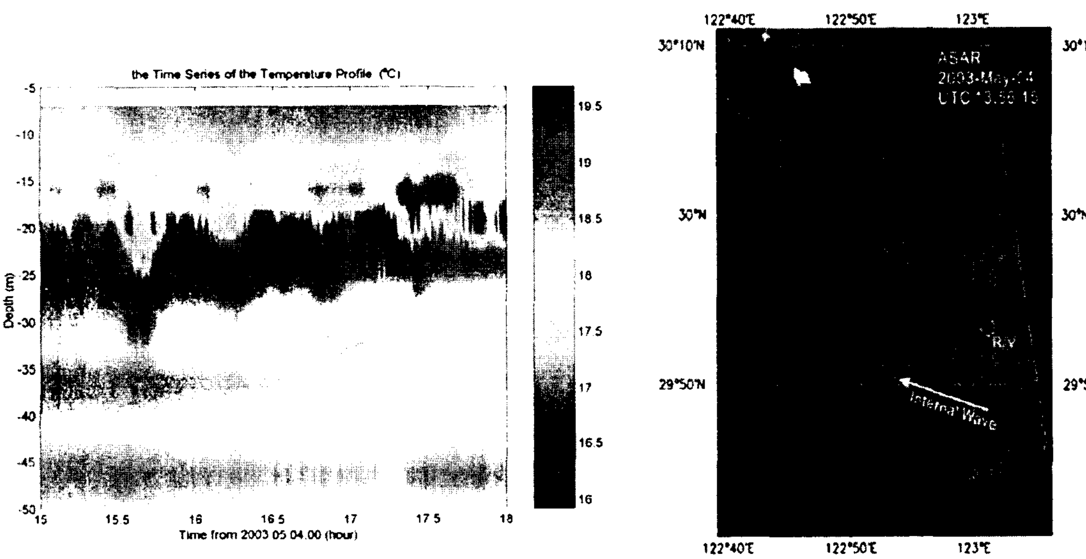

Fig.5. (left) The internal wave packet observed by the thermistor string in the East China Sea on 4 May 2003; (right) The same internal wave packet observed by the Envisat ASAR 6.5 hours later.

2.4. Extraction of internal wave signatures from SAR imagery

The initiative purpose of the investigation of the method of automatically extracting internal wave signatures from SAR images is to meet the requirements of the research on the distribution of internal waves in the China seas. Otherwise, it's time consuming work to produce Fig.1. Automatic extraction of internal wave signatures from SAR images is very useful for automatic classification of SAR images in a ground receiving station of SAR, and for the SAR users in the filed of ocean engineering, ocean navigation and underwater acoustic communication who care about the distribution of oceanic internal waves. However, very few papers have been published about it.[7]

Two algorithms are investigated for extracting the internal wave signatures from SAR images. One is based on the image segmentation with threshold and directional edge detection. It is effective in extracting internal wave signatures from local SAR image. The other one is based on the stationary wavelet transform. It is applicable for a SAR image of large area, e.g., 8000 x 8000, and it has better performance than discrete wavelet transform (DWT) [7]. Fig. 6 shows the results using the method of stationary wavelet transform. Fig. 6a and 6b show ERS-2 (21.35N, 117.767E) SAR image and the internal wave extracted from the image, respectively.

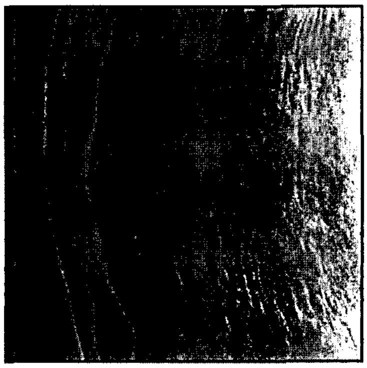

(a)

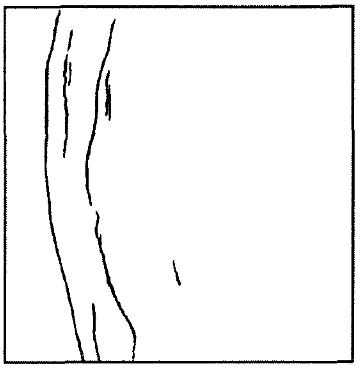

(b)

Fig.6. (a) ERS-2 (21.35N, 117.767E) SAR internal wave image; (b)The internal wave finally extracted from the SAR image.

3. SATELLITE REMOTE SENSING OF OCEAN COLOR IN THE CHINA SEAS

3.1 The ocean optics experiment and comparison with MERIS data in the China coastal waters

An ocean optics field observation was carried out in the East China Sea from Aprl.28 to May 18, 2005. The route of the cruise is shown in Fig. 7. Fig. 8 shows typical remote-sensing reflectance spectrum in the China coastal waters. Fig. 9 shows vertical distribution of absorption coefficients and attenuation coefficients. The figures indicate the interesting characteristics in the China Coastal waters. Fig. 10 and 11 show the comparison of in situ measurement and MERIS remote sensing reflectance spectrum in Zhoushan coastal area. The results suggest remote sensing reflectance retrieved from MERIS using BEAM software is relatively high at blue band.

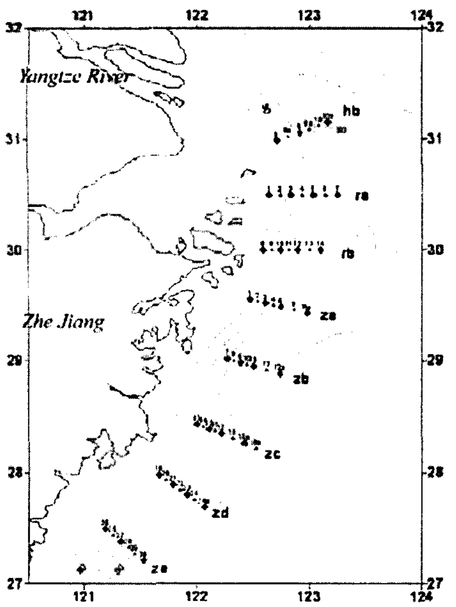

⇦ *Fig.7. The Validation cruise of MERIS data in the East China Sea*

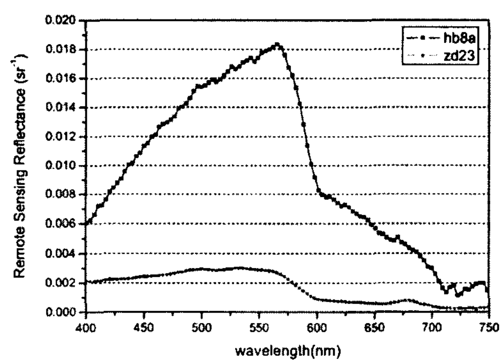

Fig.8. Comparison of remote-sensing reflectance spectrum at hb8a and zd23stations

3.2 Statistical inversion model for chlorophyll a concentration in the Bohai

Bio-optical observations of about 50 stations were carried out in June, 2005 in Bohai. The experiment acquired apparent optical properties, inherent optical properties, biological, chemical and water quality data. Using these data, a statistical inversion model of chlorophyll a concentration (chl-a) of Bohai was developed based on MERIS bands configuration. Fig.12 gives the layout of experimental stations in Bohai and the validation of the results retrieved from the model.

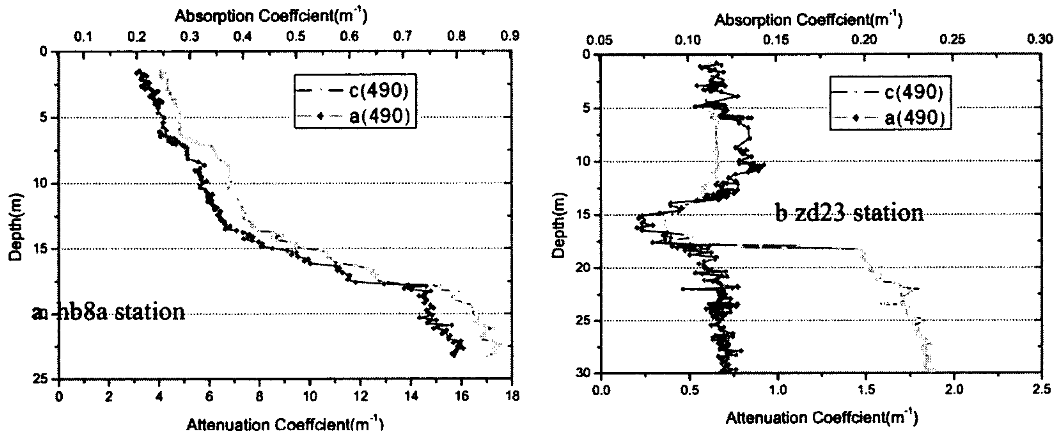

Fig.9. Vertical distribution of absorption coefficients (a-a_w) *and attenuation coefficients (c-c_w) at 490nm at hb8a and zd23 station*

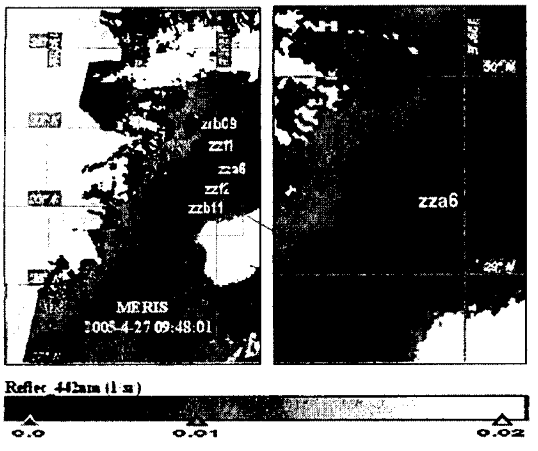

Fig 10. (left) April 27 2005 (09:48) MERIS image in East China Sea, zza6 station (13:30). (right) 3×3 MERIS pixel box for comparison centered at zza6 station.

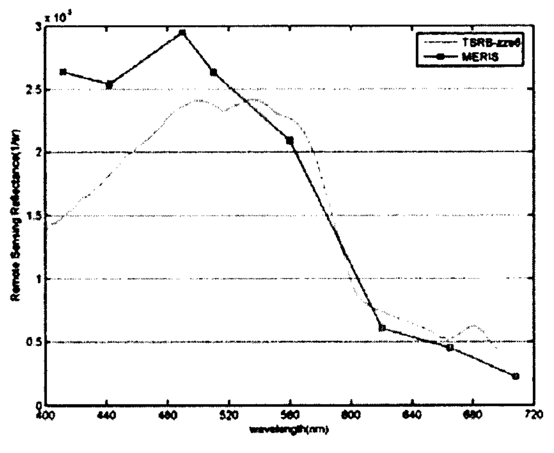

Fig.11.Comparison of situ measurement and MERIS remote sensing reflectance spectrum, R_{rs}, in Zhoushan costal.

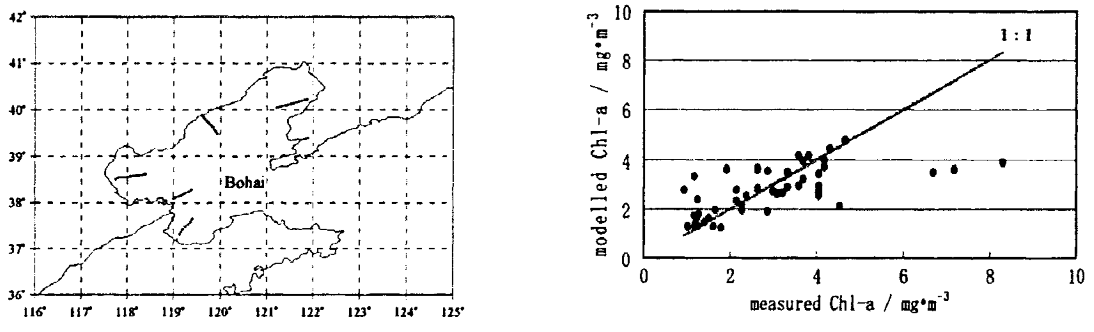

Fig.12. (left) Layout of experimental stations in Bohai; (right) statistic model results for Bohai chl-a

Fig.13. Suspended matter concentration in the Yellow Sea, May 25, 2005

3.3 Analysis of MERIS data of Yangtse Coastal Waters

TSM (total suspended matter) plays a major role in the cycle of matter in the sea: transport of matter, carrier of many trace substances, cleans the water by scavenging contaminants into the sediment, substrate for microbial life and metabolism, source of minerals and nutrients. TSM determines light climate and thus primary production in coastal waters and indicates coastal erosion. Fig. 13 shows the suspended matter concentration on May 25, 2005.

4. UNDERWATER BOTTOM TOPOGRAPHY DETECTION WITH ENVISAT ASAR IMAGES

The underwater bottom topography detection model with SAR image is developed. Underwater bottom topography of Shuangzi Reefs in Nansha islands is detected by this model with three scenes of ENVISAT ASAR images acquired in different time as shown in Fig.14. The results are affected by ocean conditions and initial water depth.

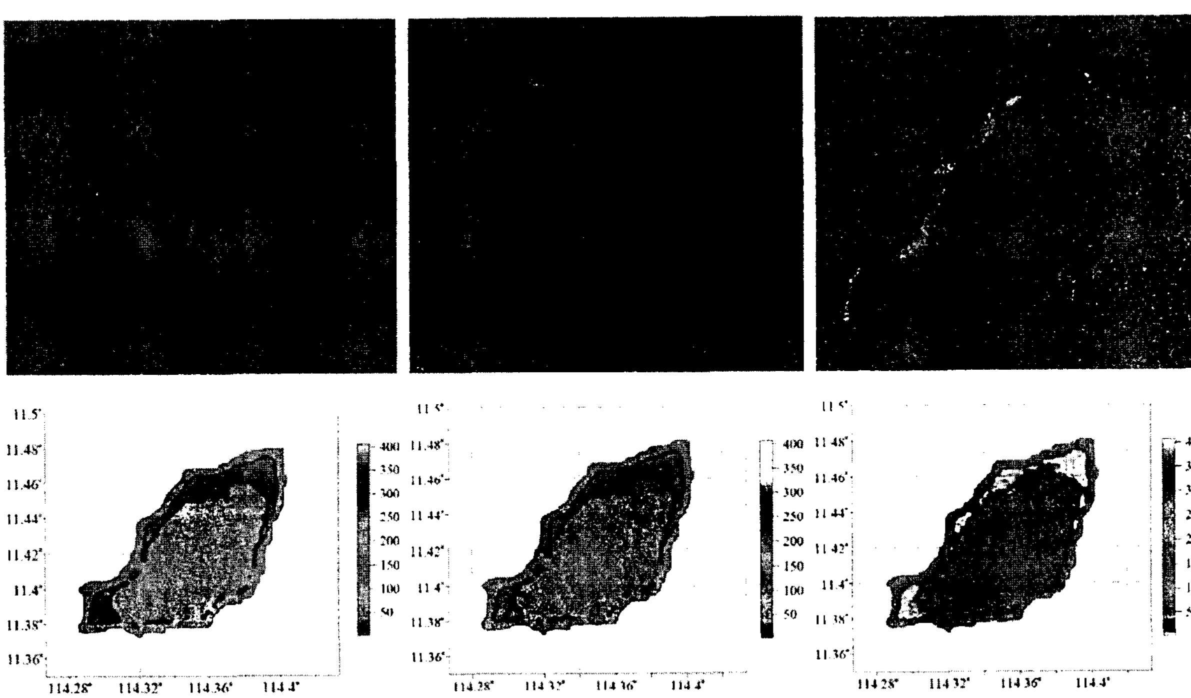

Fig. 14. (upper) Three Envisat ASAR sub-images acquired over Shuangzi Reefs in the South China Sea on August 21, 19 and 18, 2004, respectively from left to right; (lower) The retrieved bottom topography from the corresponding three images.

5. THE APPLICATIONS OF ERS AND ENVISAT DATA IN THE STUDY OF KUROSHIO

5.1. Sea surface temperature merged from multi-sensor data

The polar-orbit satellite products have high spatial resolution about 1 km. However, the applications of satellite infrared SST have been limited by the presence of the clouds. The accurate satellite microwave measurements of SST have been available. The advantage of microwave SST is the penetration of cloud. But the spatial resolution is relatively low, about 50 km. The cloud-free high-resolution SST is promising by the merging of microwave and infrared SST data. Currently SST data from AVHRR, AATSR, and AMSR-E are merged to produce could-free high-resolution SST for the observation and modeling of the Kuroshio.

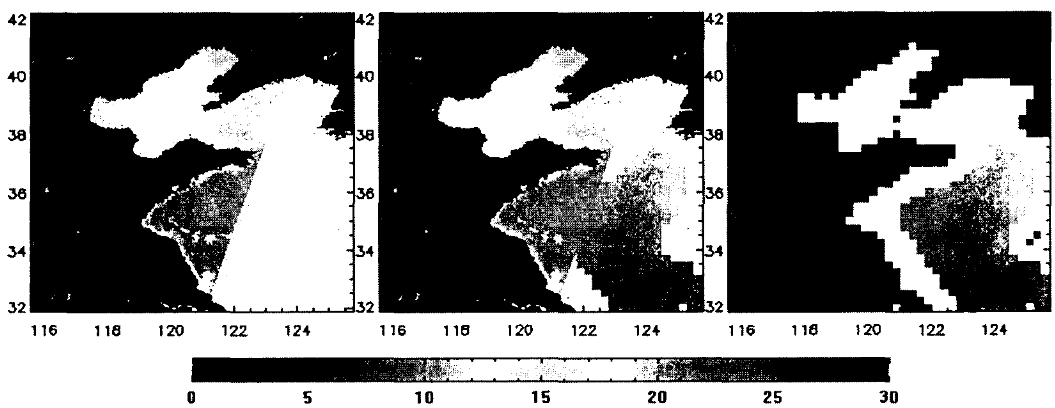

Fig. 15. AATSR SST (left), merged SST (middle) and AMSRE SST (right) on 17 October 2003

5.2. Assimilating satellite sea surface temperature and sea surface height anomaly data into an East China Sea model

The satellite sea surface temperature (SST) data are assimilated into the Princeton Ocean Model (POM) for the East China Seas. Our results, after being compared with the in-situ data and other model outputs, suggest that the satellite SST assimilation can help produce a realistic heat flux for the model surface forcing. At the same time, the sea surface height anomaly (SSHA) assimilation is also done in the deep Kuroshio area and it seems to be able to significantly improve the deep ocean temperature and velocity fields of the model. These preliminary results have grounded future studies in a further look into the Kuroshio.

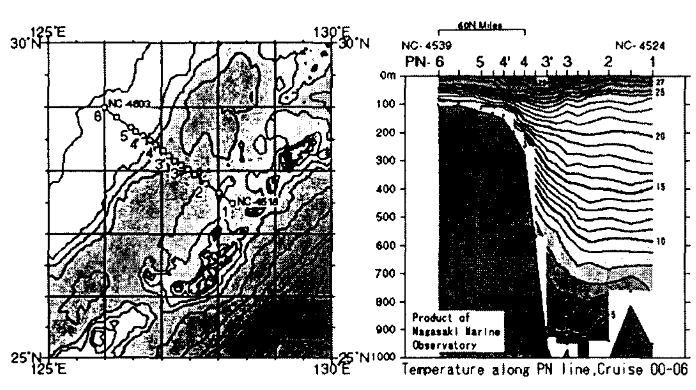

Fig. 16. PN section temperature profile observations for 2000/7/15 - 2000/7/16 from Nagasaki Marine Observatory (Near-goos, 2000)

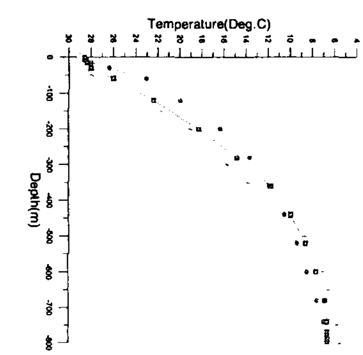

Fig.17 .Temperature profile at 3'along the PN section on 2000/7/16. Red plot indicates the in-situ measurement, Green the model outputs only with SST assimilation and Blue the model outputs with both SST and SSHA assimilations

6. SUMMARY

The mid-term progresses of Dragon Project 2566 are summarized and reviewed. The studies of internal wave by SAR imagery are comprehensive. Some good results are presented. The preliminary results of ocean color studies using MERIS data are obtained. Basic researches on the underwater bottom topography detection using SAR images and Kuroshio by multi-sensor data are carried out. Three topics of ocean waves are being carried out, i.e., comparison and validation of the results from cross spectrum method and Hasselmann's method in the China seas, spatial-temporal variability of the directional ocean wave spectra in the China seas as well as applications of directional ocean waves spectra for the observation of the typhoon.

ACKNOWLEDGMENT

This research has been supported by the ESA-MOST Dragon Programme, Satellite Oceanography Project 2566 and China 863 Program (Project ID 2005AA132030XZ09).

REFERENCES

1. Apel, J. R., and F. I., Gonzalez, 1983, "Nonlinear Features of Internal Waves off Baja California as Observed From the SEASAT Imaging Radar", *J. Geophys. Res.*, Vol.88, C7, pp4459-4446.
2. Apel, J.P. 2003, "A new analytical model for internal solitions in the ocean", *J. Phys. Oceanogr.*, Vol.33, pp.2247-2269
3. Editorial Board For Marine Atlas, 1992, "Marine atlas of Bohai Sea, Yellow Sea, East China Sea (Hydrology)", *China Ocean Press*, Beijing, China, 524pp.
4. Hsu, M.K., A.K. Liu and C. Liu, 2000, "A study of internal waves in the China Seas and Yellow Sea using SAR", *Continental Shelf Research*, Vol.20, pp.389-410
5. Huang, N.E. ,Z. Shen, S.R. Long, M.L. Wu, H.H. Shih, Q. Zhen, N.C. Yen, C.C. Tung, and H.H. Liu, 1998, "The empirical mode decomposition and Hilbert spectrum for nonlinear and nonstationary time series analysis" *Porc. Roy. Soc. London A*, vol. 454, pp. 903-995
6. Jackson,C.R., and J. Apel, "An atlas of internal solitary-like waves and their properties", second edition, *http://www.internalwaveatlas.com/Atlas_index.html*, 2004
7. Rodenas, J.A., and Garello, R., 1998, "Internal wave detection and location in SAR images using wavelet transform", *IEEE Trans. on Geoscience and Remote Sensing*, Vol.36, No.5, 1494 ~ 1507
8. Small, J., Z. Hallock, G. Pavey and J. Scott, 1999, "Observations of Large Amplitude Internal Waves at the Malin Shelf Edge during SESAME 1995", *Continental Shelf Res.*, Vol., 19, pp1389-1436.
9. Yang, Y.J., T.Y. Tang, M.H. Chang, A.K. Liu, M.K. Hsu, and S.R. Ramp, 2004, "Soltions Northeast of Tung-Sha Island During the ASIAEX Pilot Studies", *IEEE Journal of Oceanic Engineering*, Vol.29, No.4, pp.1182-1199.
10. Zheng, Q., Y. Yuan, V. Klemas and X.-H. Yan, 2001, "Theoretical Expression for an Ocean Internal Soliton Synthetic Aperture Radar Image and Determination of the Soliton Characteristic Half Width", *J. Geophys. Res.*, Vol.106, No.C11, pp.31,415-31,423.

STUDY OF ASSIMILATING THE SATELLITE SEA SURFACE TEMPERATURE AND SEA SURFACE HEIGHT ANOMALY INTO AN EAST CHINA SEA MODEL - A PROGRESS REPORT

Mingqiang Fang[1,2]
[(1)]*Ocean Remote Sensing Institute, Ocean University of China.*
[(2)]*Key Laboratory of Ocean Remote Sensing, Ministry of Education, China.*
Yushan Rd5,Qingdao,266003,China,E-mail: Fmq@orsi.ouc.edu.cn

ABSTRACT

The Kuroshio plays a very important role in both local and global climate changes. Temperature and velocity profiles and their variations are key aspects in understanding the Kuroshio. In this study, the satellite sea surface temperature (SST) data are assimilated into the Princeton Ocean Model (POM) for the East China Seas in which the Kuroshio offers the largest water transport. Compared with the in-situ data and other model outputs, results of this study show that the satellite SST assimilation can help produce a realistic heat flux for the model surface forcing. The sea surface height anomaly (SSHA) assimilation is also tested in the deep Kuroshio area and the results show that the SSHA assimilation can significantly improve the deep ocean temperature and velocity fields. This study has grounded future studies of the Kuroshio under the framework of MOST-ESA Dragon Programme.

1. INTRODCUTION

The Kuroshio, a strong western boundary current in the Pacific Ocean, like Gulf Stream in the Atlantic, plays a very important role in both local and global climate changes. Kuroshio brings the largest water transport from the tropical areas to the higher latitudes. It is a warm (average sea surface temperature about 24°C) current and about 100 kilometers wide. It usually has an average speed of ~1m/s. Fig.1 is the schematic current system of the Kuroshio regions and the sea bottom topography.

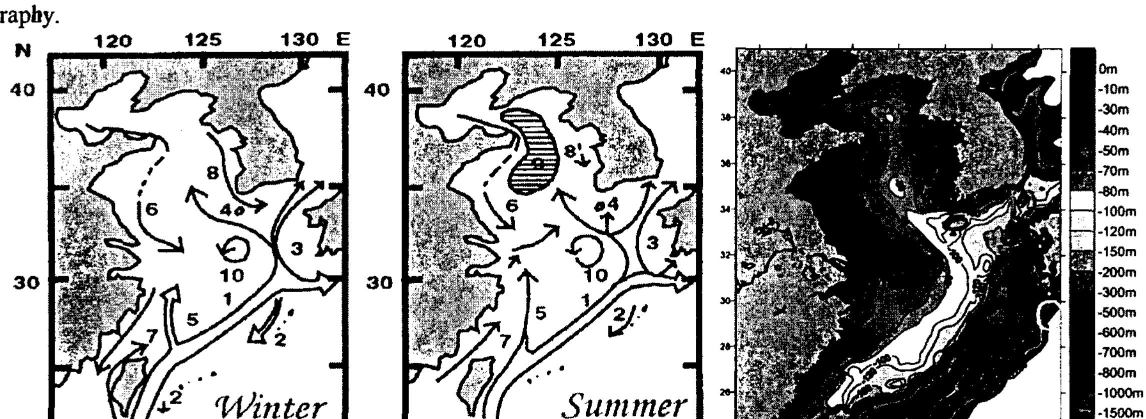

Current System Topography

Fig.1. The schematic current system of the Kuroshio region (Left 2), redrawn from [1] and the sea bottom topography (Right).

It can be seen that the main part of the Kuroshio current is just along the deep trough from the north-east tip of Taiwan province of China to the south tip of Japan. There are several branches from Kuroshio which flow into the continental slope of East China Seas. The temperature and velocity profiles and their variations of Kuroshio may have great effects on these branched currents which bring warm and salty water mass into high latitudes into the slope. It will be very important and necessary to understand the mechanisms of Kuroshio variations.

Proc. 2005 Dragon Symposium "Mid-Term Results", Santorini, Greece
27 June – 1 July 2005 (ESA SP-611, January 2006)

The in-situ experiments to measure in the Kuroshio are usually very costly and thus the measurements are very sparse. However, the ocean modeling techniques and the satellite sensors are developing so fast that it becomes possible to simulate the Kuroshio by some of the ocean models with forcings from the retrieved sea surface parameters from the satellite missions such as ERS-1/2, Envisat and so on. Among those ocean models, the Princeton Ocean Model (POM) has been frequently used [2].

2. CONFIGURATION OF POM

The principal attributes of POM are: **A.**) It contains an imbedded second moment turbulence closure sub-model to provide vertical mixing coefficients; **B.**) It is a sigma coordinate model in that the vertical coordinate is scaled on the water column depth. **C.**) The horizontal grid uses curvilinear orthogonal coordinates and an "Arakawa C" differencing scheme. **D.**) The horizontal time differencing is explicit whereas the vertical differencing is implicit. The latter eliminates time constraints for the vertical coordinate and permits the use of fine vertical resolution in the surface and bottom boundary layers. **E.**) The model has a free surface and a split time step. The external mode portion of the model is two-dimensional and uses a short time step based on the CFL condition and the external wave speed. The internal mode is three-dimensional and uses a long time step based on the CFL condition and the internal wave speed. **F.**) Complete thermodynamics have been implemented. Fig.2 is an experimental simulation of the Kuroshio region by POM. As can been seen, POM is capable of Kuroshio simulation in the north-west Pacific area.

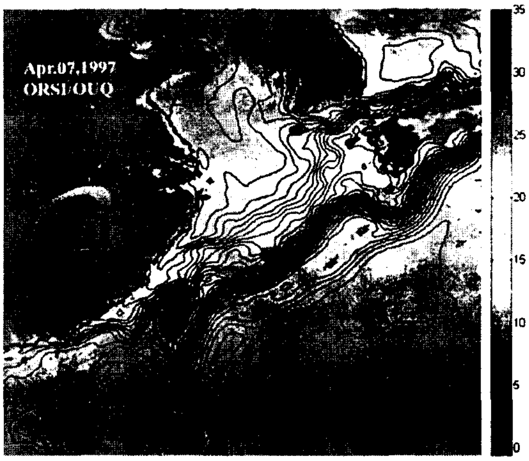

Fig.2. Experimental Simulation result by POM: Model Output Sea Surface Height over Satellite Sea Surface Temperature (NOAA/AVHRR). This model was forced by ERS scatterometer wind fields. It can be seen that the SST feature and the SSH feature are quite similar.

The simulation domain is shown as the sea bottom topography in Fig.1. The spatial resolution is 1/6° • 1/6° • 21σ levels. There are four open boundaries (as shown in Fig.1 indicated by A, B, C and D). Two are on both sides of Taiwan at the latitude of 24°N, one is below Japan at the longitude of 131°E and one is for the Tsushima strait outflow. The temperature and salinity profiles are provided by climatological values. The water transports through the open boundaries are described as monthly averaged transports from historical measurements in numerous literatures (mostly in Chinese). In this experimental study, the model surface is mainly forced by the operational QuikScat wind fields and heat flux by means of SST assimilation (after the forcing parameters are interpolated in to the model grids) for the year 2000.

3. RESULTS OF SIMULATION WITH SST ASSIMILATION

One of the most important forcings to the ocean model is the surface heat flux, which has been a hot issue in current researches. A realistic heat flux through the ocean surface is not easy to acquire, especially in the shallow coastal area [3]. Although heat flux data can be obtained through some atmosphere/ocean coupled model, when the model configurations are different, the heat flux can still cause unrealistic results. It seems better to use directly the SST from some validated operational model results or satellite (infrared or microwave) sensors as the surface forcing by some certain schemes. In this study, because of lack of continuous heat flux data for present time, the SST is tried to be assimilated into POM. When the coverage of the satellite infrared SST is limited, the SST from other sensors and operational model outputs are used instead of infrared SSTs. The scheme for the SST assimilation is like that of [3]. Specifically, the SST data are assimilated in to POM by Eq.1 below:

$$Q_M = Q_C + \left(\frac{\partial Q}{\partial T}\right)_C \cdot \left(T_S^0 - T_M^0\right) \tag{1}$$

where Q_M is for the heat flux into POM, Q_C is the climatological heat flux, $\left(\frac{\partial Q}{\partial T}\right)_C$ is the climatological relation between the heat flux and surface temperature, T_S^0 is the satellite SST and T_M^0 is the SST from POM outputs. The climatological Q_C and $\left(\frac{\partial Q}{\partial T}\right)_C$ are from COADS and the boundary temperature and salinity are from GDEM [4]. Eq.1 limits the model output temperatures close to the satellite SST. Figs.3 and 4 show the effects of Eq.1.

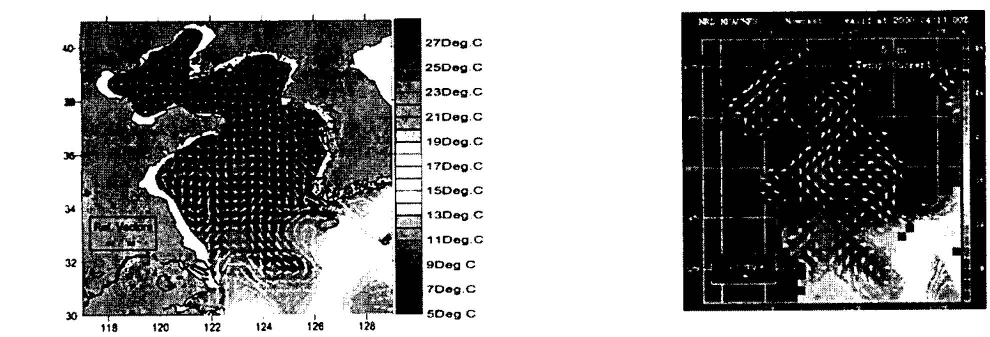

A. APR. 13,2000, 5m

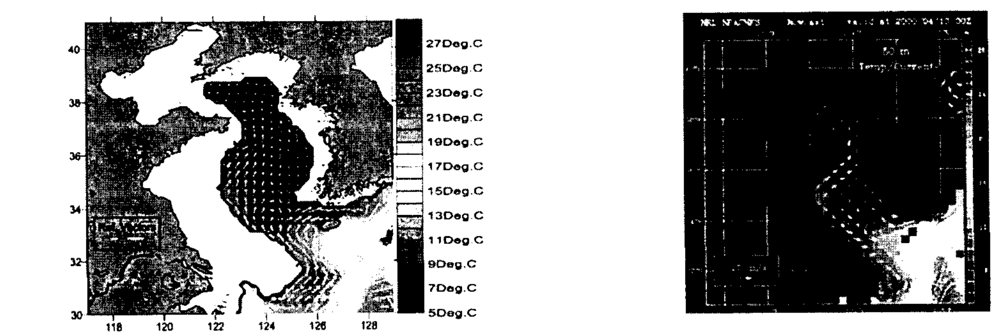

B. APR. 13,2000, 50m

Fig.3. Comparison of model outputs of this study (Left) with NRL model outputs (Right) for the day of Apr.13, 2000.

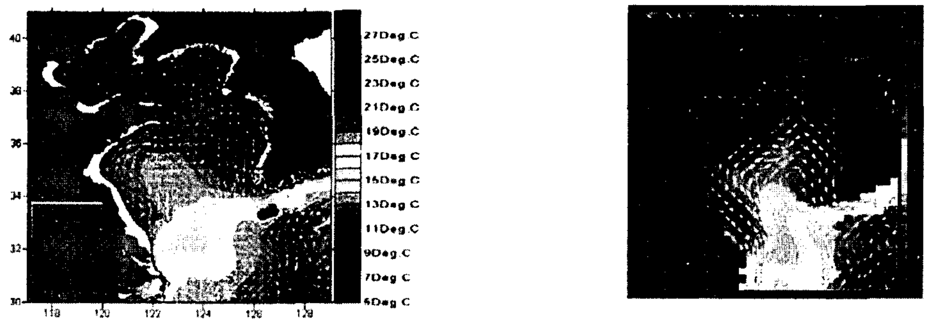

A. DEC.15,2000, 5m

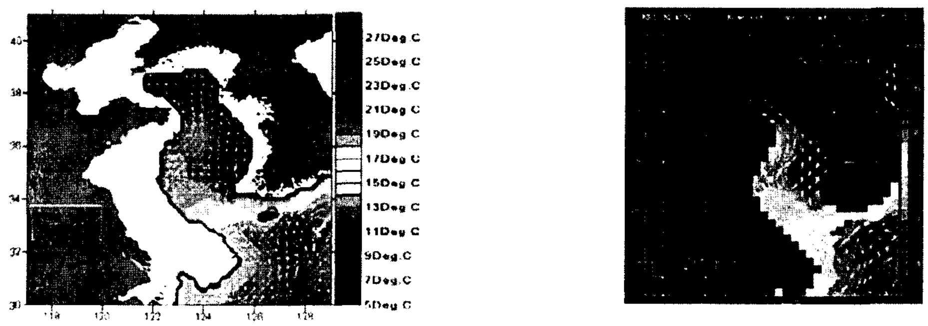

B. DEC.15,2000, 50m

Fig.4. Comparison of model outputs of this study (Left) with NRL model outputs (Right) for the day of Dec.15, 2000.

Figs.3 and 4 show that after the satellite SST data are assimilated in to POM, the model output temperature fields are quite similar to other operational model outputs such as from that of NRL. Not only the near surface (5m depth) temperature fields but also the deep level (50m depth) temperature fields are close to those of operational model outputs. The scheme described in Eq.1 seems to have practically resolved the heat flux to POM.

4. RESULTS OF SIMULATION WITH SST AND SSHA ASSIMULATION

Experimental results show that, the SST assimilation alone may not be enough. Fig.5 shows that with the SST assimilation alone, the temperature profile in the Kuroshio pathway from model outputs differs significantly from the in-situ measurements, especially in the deep level. The discrepancies may come from the unrealistic open boundary inflow configurations. One way to correct this problem is to assimilate the SSHA from altimeter data into the ocean model. The similar scheme as in [5] is used for SSHA assimilation in this study. The physical background for this scheme is to keep the water pressure at the sea bottom unchanged when the SSHA corrects the model surface elevation by raising (or lowing) the water column with fixed temperature and salinity structure. The SSHA assimilation is applied in the Kuroshio pathway where the water depth is more than 800m. For page limits, the scheme will not be detailed here.

The SSHA data (T/P) are interpolated into each model time step and the difference between the SSHA variations and the model output sea surface dynamic height variations are taken account into the correction of the model sea surface elevations. Thus the sea surface elevation trends are limited in a reasonable range set by the satellite SSHA trends. After a long period of run of the model, the model elevation will oscillate coherently with the SSHA, which is closer to the "true" state of the real oceans. Because the model adjusts vertical structures to balance the elevation differences set by the SSHA, it can significantly improve the deep level parameter outputs of the simulations.

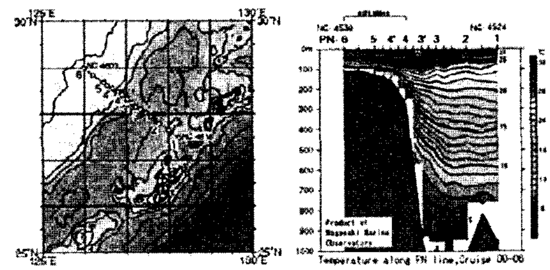

PN section temperature profile observations for 2000/7/15 - 2000/7/16 from Nagasaki Marine Observatory (Near-goos, 2000)

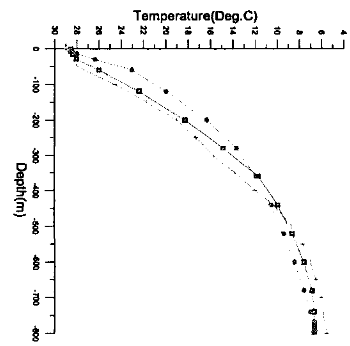

Fig.5 .Temperature profile at 3'along the PN section on 2000/7/16. Red plot indicates the in-situ measurement, Green the model outputs only with SST assimilation and Blue the model outputs with both SST and SSHA assimilations

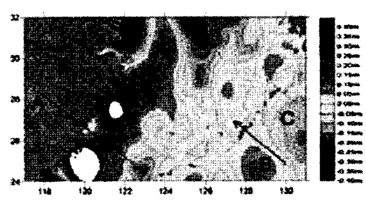

SSHA on 2000/2/13

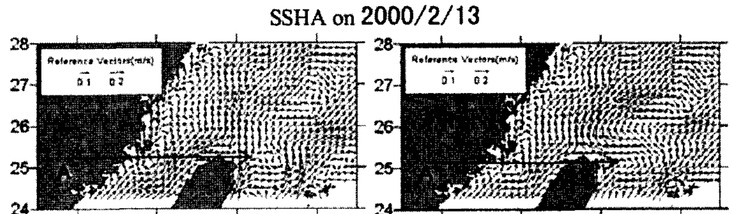

Before SSHA assimilation After SSHA assimilation

Fig.6.Depth averaged velocity fields change after the SSHA on 2000/2/13 is assimilated into POM

Fig.5. suggests that the SSHA assimilation significantly improves the model output temperature profile. Fig.6. further shows that the SSHA scheme can also change the velocity fields to get in more accordance with the surface height conditions. The SSHA assimilation scheme seems effective in the Kuroshio regions.

5. CONCLUSIONS

The preliminary results of this study show that both the SST and SSHA assimilations into the ocean model are necessary and effective in driving the ocean model correctly. The SST assimilation can help produce a realistic surface heat forcing and, to a certain extent, to maintain a reasonable temperature structure of the ocean model, especially for the upper level. However, the SST assimilation alone seems not enough for a correct simulation of the deeper levels. The SSHA assimilation is helpful in correcting the deeper level of the ocean model. It might be necessary to combine the SST and SSHA assimilation together to get a better model output. The SST and SSHA in present study are from NOAA/AVHRR and TOPEX/Poseidon respectively. In the near future, merged SST from Envisat/AATSR and NOAA/AVHRR and merged SSHA from T/P and Envisat altimeter will be used in further study.

ACKNOWLEDGEMENTS

This study is supported by the MOST-ESA Dragon Programme within the project ID2566 and also partly supported by the Natural Science Foundation of China (Grant No.40506035).

REFERENCES

1. Andrea C. Mask, James J. O'Brien, and Ruth Preller. Wind driven effects on the yellow sea warm current, *Journal of Geophysical Research*, Vol. 103, No. C13, 30,713-30,729,1998.
2. Mellor, G. L. Users guide for a three-dimensional, primitive equation, numerical ocean model. *Program in Atmospheric and Oceanic Sciences*, Princeton University.2004.
3. Ezer, T. and Mellor, G. L., Sensitivity studies with the North Atlantic sigma coordinate Princeton Ocean Model, *Dyn. Atmos. & Oceans*, **32**, 185-208, 2000.
4. Teague, W.J., M.J. Carron, and P.J. Hogan. A comparision between the Generalized Digital Environmental Model and Levitus climatologies, *J. Geophys. Res.*, 95 C5, 7167-7183, 1990.
5. Wu, C.-R., P.-T. Shaw and S.-Y. Chao. Assimilating altimetric data into a South China Sea model. *J. Geophys. Res.*, 104, 29987-30006, 1999.

SEA SURFACE TEMPERATURE MERGED FROM MULTI-SENSOR DATA

Lei Guan, Hui Zhang, Liqin Qu

Key Laboratory of Ocean Remote Sensing, Ministry of Education, China
Ocean Remote Sensing Institute, Ocean University of China, China
Yushan Road 5, 266003, Qingdao, China
Email: leiguan@orsi.ouc.edu.cn

ABSTRACT

Sea surface temperature (SST) from satellite infrared measurements has long history. The polar-orbit satellite products have high spatial resolution about 1 km. However, the applications of satellite infrared SST have been limited by the presence of the clouds. The accurate satellite microwave measurements of SST are available. The advantage of microwave SST is the penetration of cloud. But the spatial resolution is relatively low, about 50 km. The cloud-free high-resolution SST is promising by the merging of microwave SST with infrared SST. Regional high-resolution data from NOAA AVHRR have been received by a ground station at Ocean University of China. With the Dragon Program, the ENVISAT/AATSR SST data are provided. The could-free high-resolution SST are obtained by merging of infrared and microwave SSTs from AVHRR, AATSR, and AMSR-E, which are being used for oceanic studies such as the observation and modeling of the Kuroshio.

1. INTRODCUTION

Sea surface temperature (SST) from satellite infrared measurements has long history. The polar-orbit satellite SST data have been used for oceanic studies. The Advanced Very High Resolution Radiometers (AVHRR) on board National Oceanic and Atmospheric Administration (NOAA) polar-orbiting operational environmental satellites have provided operational SST observations for more than two decades [1][2]. The rms error of AVHRR-derived SST for the global coverage is about 0.6-0.7K [3] [4]. The Advanced Along Track Scanning Radiometer (AATSR) onboard ENVISAT is the third in a series of instruments, continuing from ATSR-1 and ATSR-2, which aim to provide 10 year near-continuous precise SST data set at the levels of accuracy required (0.3K or better) for climate research [http://envisat.esa.int/instruments/aatsr/]. However, the availability of SST from infrared sensors is very low due to frequent cloud presence [5]. With the advent of well-calibrated microwave sensors with low frequency channels, such as Tropical Rainfall Measuring Mission (TRMM) Microwave Imager, AMSR-E (Advanced Microwave Scanning Radiometer for EOS) on board Aqua, the accurate measurements under cloud have been available [6]. But the spatial resolution of microwave SST is about 50 km, much lower than that of AVHRR and AATSR SST, i.e., 1km. The cloud-free high-resolution SST is promising by the merging of microwave and infrared SST data [7][8].

In this paper, firstly, the SST data used are introduced. Secondly the methods and results of cloud-free high resolution SST by the merging of infrared and microwave data are presented. The summary is given finally.

Proc. 2005 Dragon Symposium "Mid-Term Results", Santorini, Greece
27 June – 1 July 2005 (ESA SP-611, January 2006)

2. DATA

The NOAAAVHRR, ENVISAT AATSR and Aqua AMSR-E SST products are used in this study. NOAA satellite data have been received and processed by the TeraScan system of the Ground Station at Ocean University of China. The default retrieval algorithm for SST is MCSST (Multi-Channel SST) algorithm with NOAA global coefficients [9]. The SST products are equal-angle maps with spatial resolution of 0.01° from 10° N to 50°N and 105° E to 145°E. The ENVISAT AATSR SST products have been provided by European Space Agency (ESA) with the oceanography project ID 2566 of the NRSCC (National Remote Sensing Center of China) -ESA Dragon program. AATSR level 2 products (ATS_NR__2P) are used. The spatial resolution of the mapped SST is 1 km. There are 512x512 pixels in each frame. The global AMSR-E SST data are produced and provided by Remote Sensing Systems [www.ssmi.com]. The grid size is 0.25 °.

3. METHODS AND RESULTS

Two methods, objective analysis and discrete wavelet transform, were applied to merge the infrared and microwave SST data. Firstly, the AVHRR and AMSR-E SST data were merged by objective analysis. The details of the merging procedure were described by Guan & Kawamura [8]. The AVHRR and AMSR-E daily averaged SST images were generated first. Fig. 1 shows 3-day AVHRR SST images. Fig. 2 shows 3-day AMSR-E images.

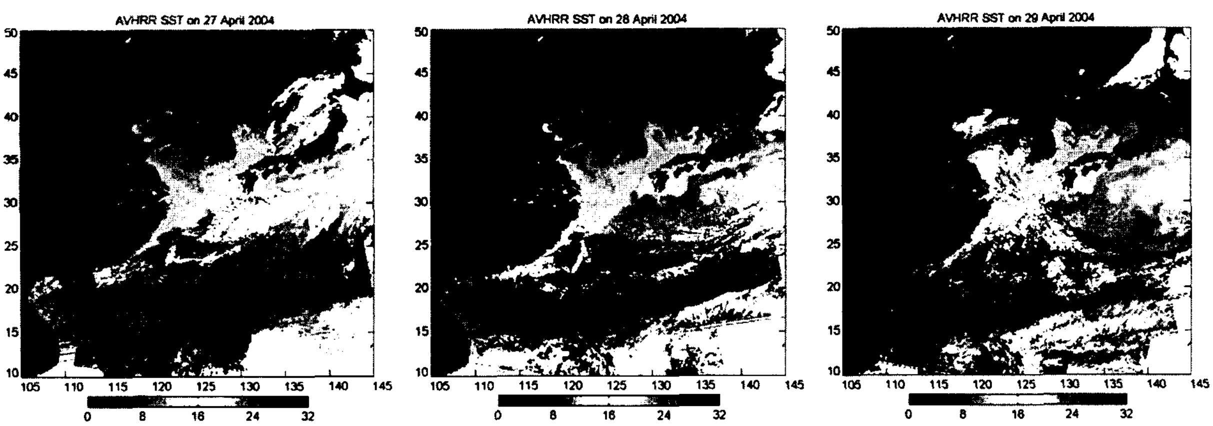

Fig. 1. NOAA AVHRR SST on 27, 28 and 29 April 2004

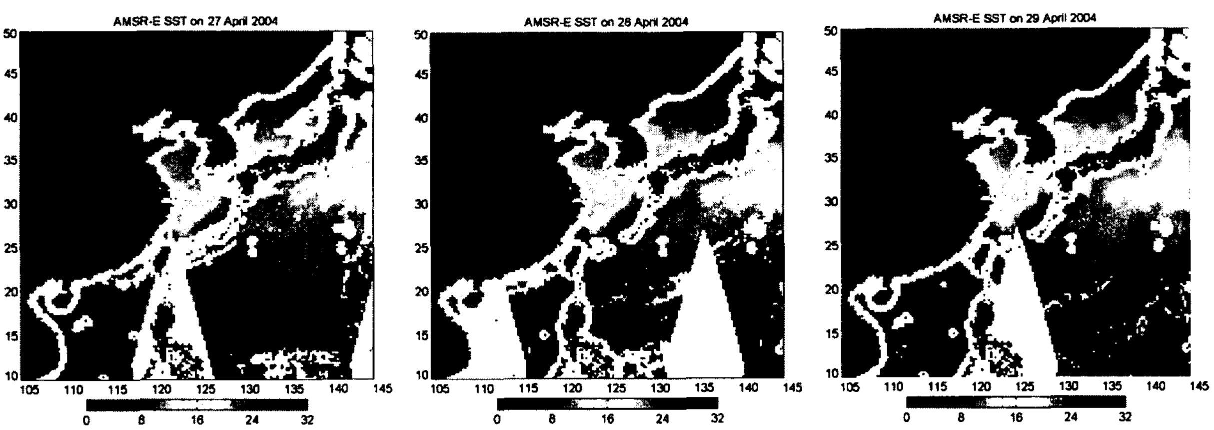

Fig. 2. Aqua AMSR-E SST on 27, 28 and 29 April 2004

The spatial decorrelation scale was set to 1°. The temporal decorrelation scale was set to 5 days. The merged daily SST with spatial resolution of 0.05° is shown in fig. 3.

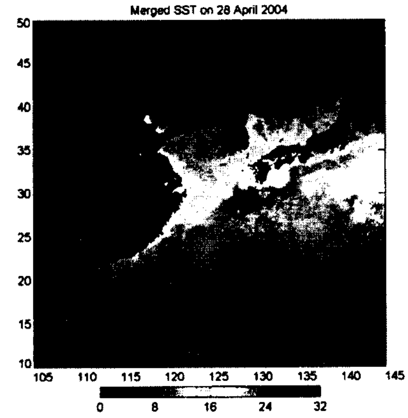

Fig. 3. Merged SST on 28 April 2004

Secondly, discrete wavelet transform was applied to merge AATSR and AMSR-E SST data. Wavelet transform has been widely used for image fusion. It decomposes an image into a set of multi-resolution images with wavelet coefficients for each resolution level. The two-dimensional wavelets transform defined as [10]:

$$W_j^\lambda f(x,y) = f \times \Psi_j^\lambda(x,y) = \iint_{R^2} f(u,v)\Psi_j^\lambda(x-u, y-v)dudv \tag{1}$$

Where $f(x,y)$ is an image, λ represents different frequency components. Assuming that H and G represent the matrix of scaling function $\varphi(x)$ and wavelet function $\psi(x)$ respectively, the original image $f(x,y)$ is denoted by C_0, two-dimensional decomposition function is defined as,

$$\begin{cases} C_{j+1} = HC_jH' \\ D_{j+1}^h = GC_jH' \\ D_{j+1}^v = HC_jG' \\ D_{j+1}^d = GC_jG' \ \left(j = 0,1,\ldots,J-1\right) \end{cases} \tag{2}$$

Where h, v, d represent the horizontal, vertical and diagonal details, respectively. The matrix C_{j+1} represent the smoothing part of the image, i. e., approximation coefficients. Matrices D^h_{j+1}, D^v_{j+1}, D^d_{j+1} represent the horizontal, vertical and diagonal details, respectively. H' and G' represent associate matrices of H and G. The wavelet reconstruction function is defined as,

$$C_jH + G'D_j^hH + H'D_j^vG + G'D_j^dG$$

$$\left(j = J, J-1, \ldots, 1\right) \tag{3}$$

Where J is the number of decomposition level.

A single-level wavelet decomposition of AATSR and AMSR-E SST images with rbio1.1 wavelet was performed respectively. The approximation coefficients matrix and details coefficients matrices were obtained. The corresponding component of two kinds of data was merged respectively. Concerning horizontal, vertical and diagonal details, the maximum of the high frequency coefficients of AATSR and AMSR-E image at the same location was selected. Concerning the approximation coefficients, weighted average of the coefficients of two images was used. The image was reconstructed by inverse discrete wavelet transform after merging each component. Specific treatment for the border was conducted in the merging procedure. Fig. 4 is an example. The left and right images are AATSR and AMSR-E SST acquired 17 October 2003. The middle image is merged image using discrete wavelet transform.

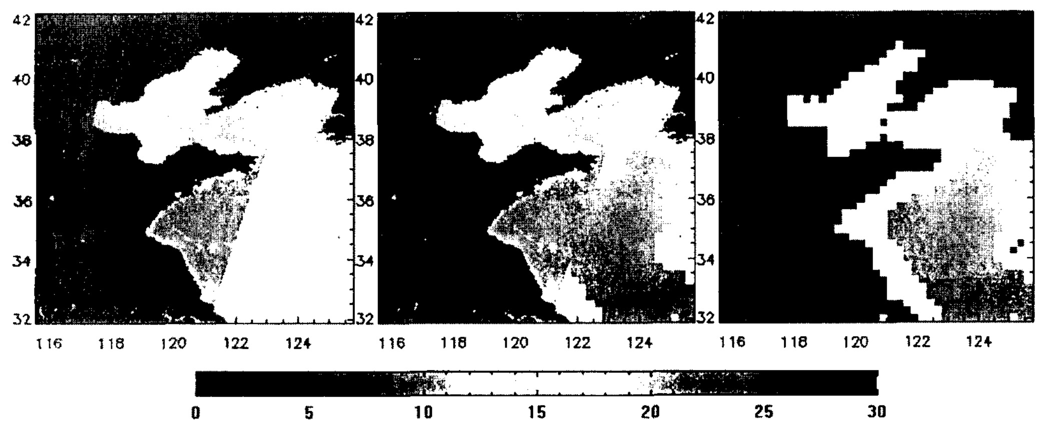

Fig. 4. AATSR SST (left), merged SST (middle) and AMSRE SST (right) on 17 October 2003

4. SUMMARY

The infrared and microwave SST data obtained from AVHRR, AATSR, AMSR-E were merged by objective analysis and discrete wavelet transform for demonstration. The intercomparison of the SST data sets as well as further investigation of the methods will be conducted in the next stage. The final goal is to provide accurate cloud-free high resolution SST data for the oceanic studies especially the observation and modeling of the Kurosio.

ACKNOWLEDGEMENTS

The study was supported by NRSCC-ESA Dragon program – Oceanography Project ID 2566 and the National Natural Science Foundation of China (Grant No. 40306029). The AVHRR data were provided by the Satellite Ground Station of Ocean University of China. The AATSR data were provided by ESA. The AMSR-E data were produced by Remote Sensing Systems and sponsored by the NASA Earth Science REASoN DISCOVER Project and the AMSR-E Science Team.

REFERENCES

1. Kiddwell, K. B., *NOAA Polar Orbiter Data User's Guide (TIROS-N, NOAA-6, NOAA-7, NOAA-8, NOAA-9, NOAA-10, NOAA-11, NOAA-12, NOAA-13 AND NOAA-14)* November 1998 Revision. NOAA/NESDIS/NCDC, 1998.

2. Goodrum, G., K. B. Kidwell and W. Winston, *NOAA KLM User's Guide September* 2000 Revision. NOAA/NESDIS/NCDC, 2000.

3. Strong, A., and E. P. McClain, Improved ocean surface temperautres from space – Comparisons with drifting buoys. *Bull. Amer. Meteor. Soc.*, 65, 138-142, 1984

4. McClain, E. P., Global sea surface temperautres and cloud clearing for aerosol optical depth estimates. *Int. J. Remote Sens.*, 10, 763-769, 1989.

5. Guan, L. and H. Kawamura, SST availabilities of satellite infrared and microwave measurements. *J. Oceanogr.*, Vol. 59, No. 2, 201-209, 2003.

6. Wentz, F. J., C. Gentemann, D. Smith and D. Chelton, Satellite measurements of sea surface temperature through clouds. *Science*, 288, 847-850, 2000.

7. Kawamura, H., New Generation Sea Surface Temperature for Ocean Weather Forecasts, *Techno-Ocean 02*, Kobe Port Island, CD-ROM, 2002.

8. Guan, L. and H. Kawamura, Merging satellite infrared and microwave SSTs— Methodology and Evaluation of the new SST. *J. Oceanogr.*, Vol. 60, No. 5, 905-912, 2004.

9. SeaSpace Corporation, *TeraScan Reference Manual*, 2000.

10. Tan, Z, F. Bao, A. Li, B. Yang and Y. Gong, *Digital Image Fusion.* Xi'an Jiaotong University Press, Xi'an , China, 2004

THE OCEAN OPTICS EXPERIMENT AND COMPARISON WITH MERIS DATA IN THE CHINA COASTAL WATERS

Ming-Xia He, Zhi-Shen Liu, Lian-Bo Hu, Qian Yang, Yun-Fei Wang, Ting-Lu Zhang
Key Laboratory of Ocean Remote Sensing, Ministry of Education, China,
Ocean Remote Sensing Institute, Ocean University of China, China,
E-mail: mxhe@orsi.ouc.edu.cn; Hulb@orsi.ouc.edu.cn

ABSTRACT

An ocean optics field observation was carried out in the East China Sea from Aprl.28 to May 18, 2005. Firstly, the paper gives main results of this field observation and the results are analyzed with data processing methods. Then the empirical algorithm and semi-analytical method are used to retrieve ocean optics parameters from remote-sensing reflectance. The primary results indicate that semi-analytical method has an advantage in East China Sea. Finally, these results are compared with MERIS data. The preliminary results indicate that remote-sensing reflectance derived from MERIS data using BEAM software is higher in blue region.

1. INTRUDUCTION

The East China Sea is a typical case 2 water or turbid water because of discharging from the Yangtze River and the Yellow River and land runoff of cities and industries on the coast [1]. The current operational algorithms for various ocean color satellites, including atmospheric corrections and bio-optical algorithms, produce large error in the west of 125oE in East China Sea. For example, simultaneous validation experiment of Sea-viewing Wide Field-of-view Sensor (SeaWiFS) data in the East China Sea in July 1998, indicated a high error of 1000% for the retrieved chlorophyll concentration between current operational chlorophyll algorithm and the field observation. The location and result of this experiment are illustrated in Fig.1 and Fig2 respectively. Therefore, in-situ ocean optics measurements and an ocean optics database in these areas are important and urgent fundamental research.

Aimed to validate Medium Resolution Imaging Spectrometer Instrument (MERIS) data with the field observation in East China Seas, an observation was carried out at eight transects from April 27 to May 18, 2005. As shown in Fig.3, the cruise and location of the stations are located in the estuary of Yangtze River, outside of Qiantang River, among zhoushan Archipelago. Zhoushan Archipelago is the biggest fishery in china and becomes one of the most serious areas of red tide bloom occurrence in recent years.

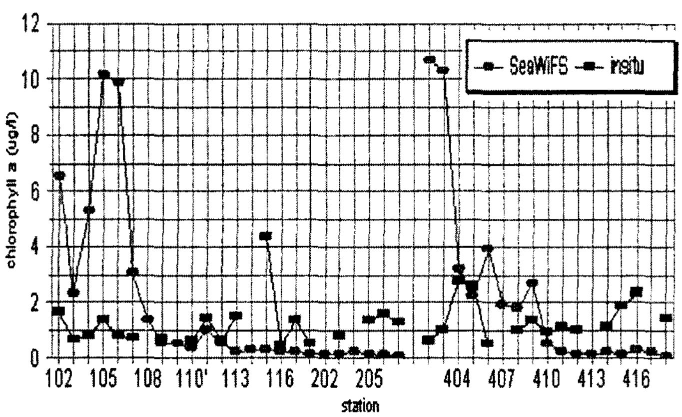

Fig.1.Validation of chlorophyll concentration derived from OC4 algorithm for SeaWiFS and field observation in East China Sea in 1998

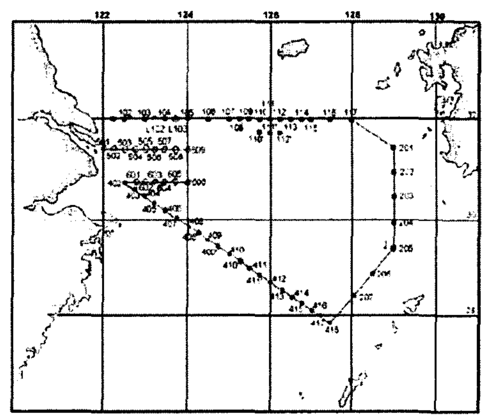

Fig.2.The validation cruise of SeaWiFS data in East China Sea in 1998

Proc. 2005 Dragon Symposium "Mid-Term Results", Santorini, Greece
27 June – 1 July 2005 (ESA SP-611, January 2006)

The cruise was deployed with hyper-spectral tethered spectral radiometer (Satlantic, Inc.), hyper-spectral absorption / attenuation meters (WETLabs, Inc.), underwater hyper-spectral radiometer (TriOS, Inc.). The paper gives some of the results of field observation including absorption coefficient a, beam attenuation coefficient c, remote-sensing reflectance Rrs, downwelling irradiance profile Ed(z), upwelling radiance profile Lu(z) and diffuse attenuation coefficient K. The results are analyzed with data processing methods. Finally, these results are compared with MERIS data.

2. FIELD EXPERIMENT

The field experiments joined with MC2005-3 red tide cruise of 973 Program (National Basic Research Program) in East China Sea from April 27 to May 18, 2005, with the Research Vessel No.47 of China Marine Surveillance. In addition to ocean optics parameters, ocean biological, ocean chemical, hydrological and meteorological parameters were measured at the same time. Unfortunately, it was overcast and rainy in most days, which was a great disadvantage to ocean optics measurement. It was sunny only on May 7 and May 8, whereas Envisat satellite didn't pass through the experiments area.

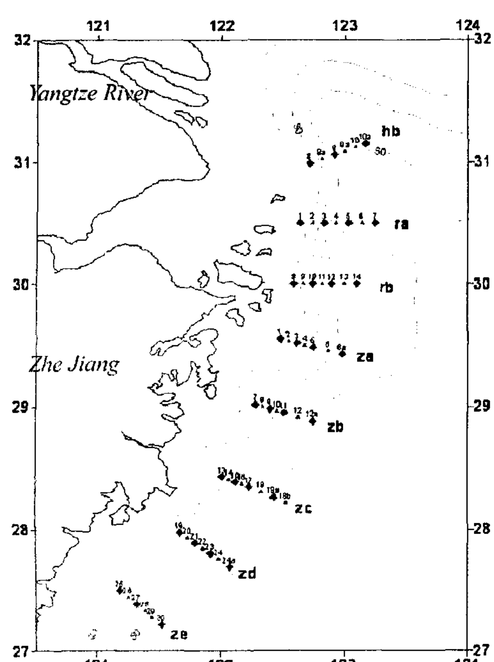

Fig.3. The Validation cruise of MERIS data in the East China Sea

Lower hyper-spectral tethered spectral radiometer (HTSRB) by power/telemetry cable into water on windward side of vessel and allow instrument to drift away (at least 50 m) from vessel in order to avoid vessel shallow and runoff of vessel. Downwelling spectral irradiance above surface, upwelling near surface spectral radiance and water leaving spectral radiance were measured by HTSRB with 128 bands from 400nm to 800nm and 1 HZ frame rate. Underwater hyper-spectral radiometer (RAMSES) and hyper-spectral absorption / attenuation meters (AC-S) were mounted together on an optical instrument package at the fore part of the vessel. RAMSES consists of radiance sensor (SAM8185) and irradiance sensor (SAM5018) with 190 bands from 320nm to 950nm, measuring upwelling radiance profile Lu(z) and downwelling irradiance profile Ed(z) respectively. Diffuse attenuation coefficients were derived from Lu(z) profile and Ed(z) profile. The stability of the SAM8181 and SAM5018 were confirmed by periodic checking with a stander lamp FidCal 201F (TriOS Inc.), which generated new calibration files. AC-S has 83 output bands between 400nm and 750nm with 0.01m-1 measurement accuracy. The optics and flow tubes were cleaned per day while at sea according to standard criterion [3]. Sea water bottle samples were taken at depths representative of the main hydrographic layers. These samples passed through a 0.7μm Whatman GF/F filters, then the unfolded filters were immediately placed into flat tissue containers designed for liquid nitrogen storage. In the laboratory, the absorption spectrum of each sample filter was measured using U/V spectrophotometer (Carry100, Varian Inc.). After measurement the sample filters were soaked into methanol to dissolve phytoplankton pigments and then inorganic suspended material absorption spectrums were obtained using U/V spectrophotometer again. [4].

HTSRB data was processed by ProSoft, a data analysis package recommended by Satlantic Inc. The final data products include upwelling radiance Lu, water leaving radiance Lw, downwelling irradiance Ed(0+), remote-sensing reflectance Rrs, photosynthetically available radiation PAR, solar energy flux and pigments concentration C etc. Since the sensor to measure Lu is not just beneath the sea surface (below surface 0.65m), Lu (0.65) is needed to propagate to just beneath the sea surface. ProSoft use Austin and Pezold 's models [5] to estimate the K(490) value and then use K (490) in Morel's model inverted to get K(λ).

Immersion factor corrections are applied to RAMSES. TriOS company only provides absolute radiance and irradiance calibrations for use in air. For absolute calibration radiance and irradiance measurement in water, immersion coefficients are important. Immersion factors of radiance sensor were derived by Austin empirical method [6] and material of the optical window of the radiance sensor by T Ohde [7].Recently, TriOS Company provides irradiance calibration file in water. Fig.4 shows comparisons of irradiance and radiance values with and without immersion factor correction. Obviously, both irradiance and radiance values increase considerably after applying immersion factor correction.

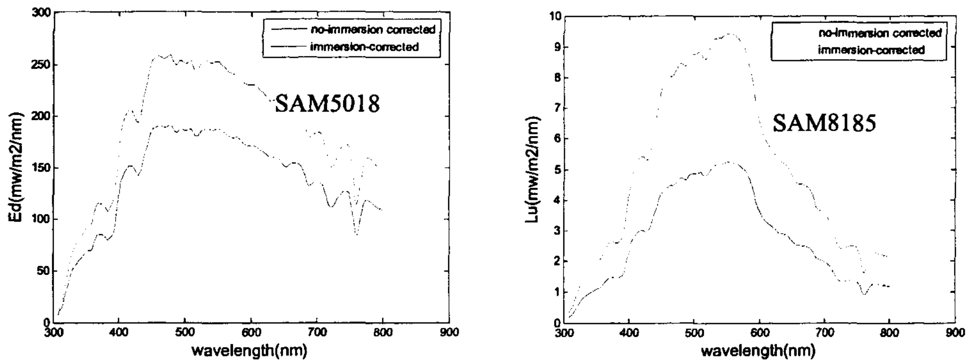

Fig .4. Comparisons of irradiance and radiance values with and without immersion factor correction.

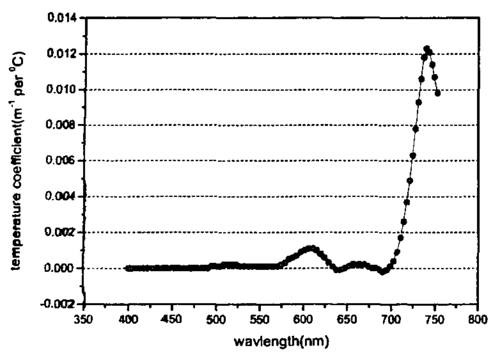

Fig.5. Temperature dependent absorption coefficients of pure water

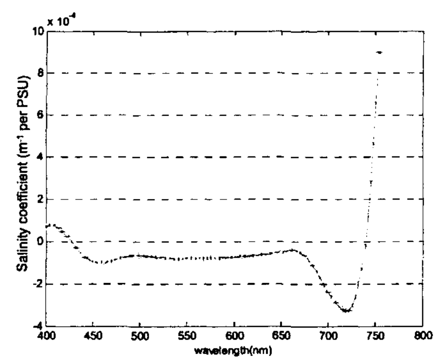

Fig.6.Salnity dependent absorption coefficients of sea water

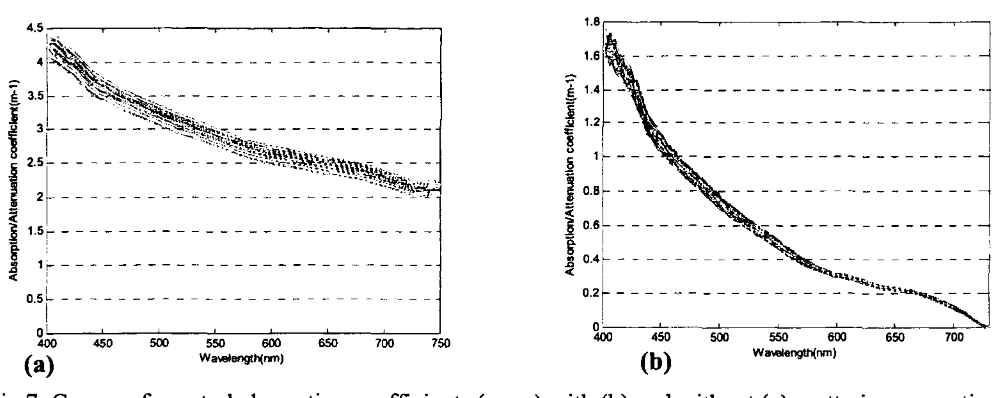

Fig.7. Curves of spectral absorption coefficients (a-aw) with (b) and without (a) scattering corrections

The absorption of pure water is dependent on water temperature and the absorption coefficient of seawater is also dependent on its salinity [8]. Temperature and salinity corrections need to be applied to data measured by AC-S. The temperature and salinity dependent absorption coefficients of water are from Pegau's data [8]. Those coefficients cover only several discrete bands, so interpolation is needed. The results are illustrated in Fig.5 and Fig.6. As reflecting tube absorption meters do not collect all of the light scattered from the beam, the uncollected scattered light causes the instrumentation to overestimate the absorption coefficient. For this reason the third method recommended by Zeneveld

[3] is applied to correct scattering errors. Fig.7 shows the changes of absorption coefficient (a-aw) with and without scattering correction at zd23 station.

3. MAIN RESULTS OF THE EXPERIMENT

3.1 Remote-sensing reflectance R_{rs}

The magnitude and spectral variation of remote-sensing reflectance (Rrs) depend on the absorption and backscattering properties of seawater itself, phytoplankton, colored dissolved organic matter (CDOM), and detritus. There were 31 stations remote-sensing reflectance data measured by HTSRB. Fig.8 is remote-sensing reflectance spectrum of two typical stations hb8a and zd23. The sea water is turbid at hb8a station where Secchi disc depth is 1.5m, whereas sea water is clearer at zd23 station where Secchi disc depth is 7m. The spectral curve of Rrs of station hb8a reaches maximum at 570nm with 0.02sr-1 and is about 0.002sr-1 near NIR region, which are typical spectral characters of turbid sea water. The spectral curve of Rrs of station zd23 reaches maximum at 540nm with 0.003sr-1 and is only about 0.0003sr-1 near NIR region, which are typical spectral characters of coastal sea water. The slope of Rrs(hb8a) in blue region is much bigger than Rrs(zd23) because hb8a station is located in estuary of Yangtze River with high CDOM concentration. Fluorescence peak occurs at 680nm at zd23 station but is not obvious at hb8a station. The chlorophyll concentrations of field measurements of station hb8a and station zd23 are 0.50mg/m3 and 0.84mg/m3 respectively.

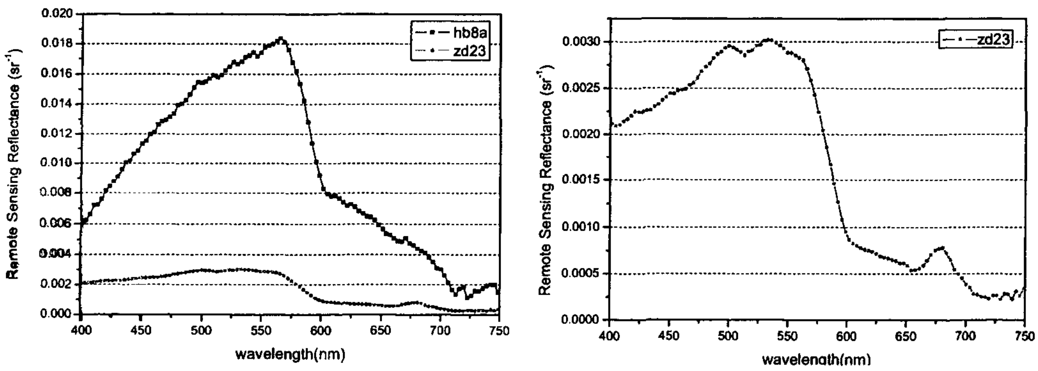

Fig.8. Comparison of remote-sensing reflectance spectrum at hb8a and zd23stations

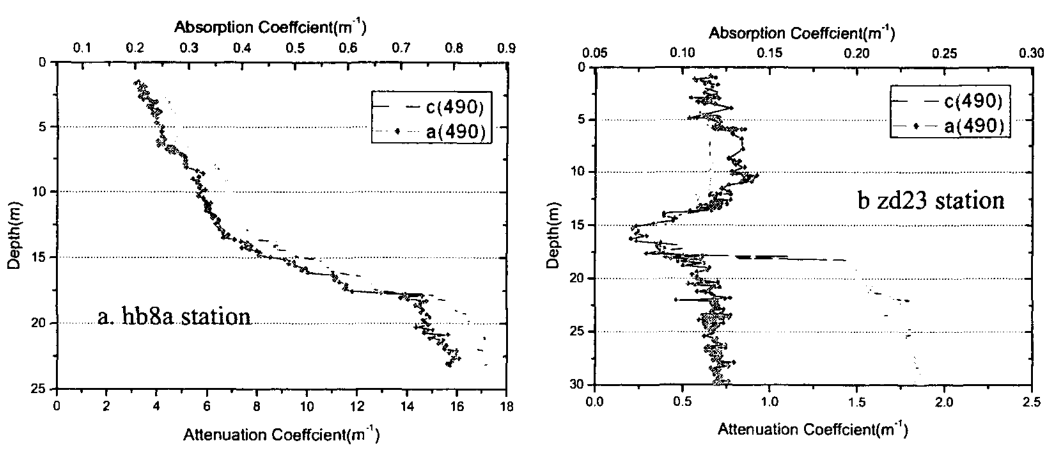

Fig.9. Vertical distribution of absorption coefficients ($a-a_w$) and attenuation coefficients ($c-c_w$) at 490nm at hb8a and zd23 station

3.2 Absorption / attenuation coefficient a, c

There were 30 stations volume absorption and beam attenuation coefficients data measured by AC-S. As is illustrated in Fig.9 (a), absorption coefficients (a-aw) and attenuation coefficients (c-cw) of each component in sea water expect for pure water increase with depth, indicating that phytoplankton, CDOM and inorganic suspended matter concentrations increase vertically downwards at the estuary of the Yangtze River. The curves of absorption and attenuation coefficients at hb and ra transect are similar to Fig.9(a), which seem to represent one of characters of inherent optical properties (IOP) at the estuary of river. Fig.9 (b) shows absorption coefficients (a-aw) and attenuation coefficients (c-cw) vertical distribution with depth at zd23 station. There is a saltation layer and inverse layer from 10m to 20m, indicating there is a clear water layer available. The absorption coefficients a-aw change a little above and below the saltation layer, whereas attenuation coefficient c-cw increase from 0.75m-1 to 1.8m-1 , which shows the increase of inorganic suspended matter concentration. The curves of absorption and attenuation coefficients at zb, zc and zd transects have the similar character, which is one of characters of IOP in coastal waters.

Fig.10 shows spectral distribution of absorption coefficients a-aw in three main hydrographic layers at these two stations. As is illustrated in Fig.10 (a), absorption coefficients a-aw are mainly determined by CDOM concentration increase with depth at the estuary of the Yangtze River. In Fig. 10 (b), there is an absorption peak at 665nm at 5m and 25m depth, indicating high chlorophyll concentration there. There is only weak absorption peak of chlorophyll at 440nm that is caused of CDOM strong absorption in blue region. It is also shown from Fig. 10 (b) that there is no absorption peak at 25m depth. The spectral distribution of absorption coefficients a-aw at 5m and 25m depth are very close and bigger than at 15m depth, which agree with results of Fig.9 (b).

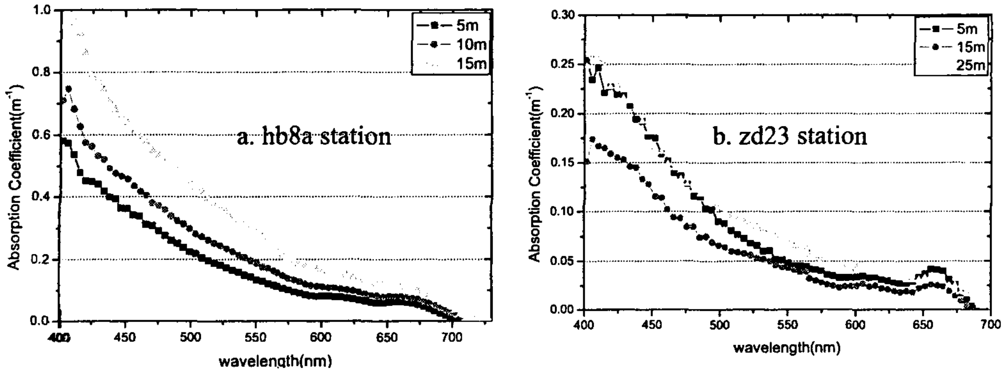

Fig. 10 Depth dependence of spectral absorption coefficients ($a\text{-}a_w$*) at three different depths at hb8a station and zd23 station*

3.3 Diffuse attenuation coefficient K

Profile measurements of irradiance or radiance can be used to calculate diffuse attenuation coefficient K (λ), and can also be extrapolated to just beneath sea surface for calculating remote-sensing reflectance. There were 31 stations downwelling irradiance profile Ed (z) and upwelling radiance profile Lu(z) measured by the underwater hyper-spectral radiometer. The values of K (z) were determined as cubic polynomials between Ed(z) and z in order to reduce random errors. Fig.11 shows the spectral distribution of downward irradiance at different depths at zd23 station: blue light is attenuated extremely rapidly by CDOM and red light mainly by water. In Fig.12 the depth profile for downward irradiance at 412nm, 490nm and 550nm, are plotted (log scale). The slope of ln[Ed(z)]is different along the depths. For example, the slope centered at 5m, 15m, 25m are 0.198m-1, 0.104m-1 and 0.375m-1, respectively. It is agreement with the changes of absorption and attenuation coefficients with depth shown in Fig.9 (b).

4. RETRIEVAL OPTICAL PROPERTIES of SEA WATER from REMOTER-SENSING REFLECTANCE

4.1 Retrieval absorption coefficient from remote-sensing reflectance

In 1998, Lee et al. [10] developed an empirical algorithm for absorption coefficient a (440) and the spectral ratio of remote-sensing reflectance using a variety of oceanic and costal environment data sets. In 2002, Lee et al [11] developed a multi-band quasi-analytical algorithm (QAA) to retrieve absorption and backscattering coefficients, as well as absorption coefficient of phytoplankton pigments and CDOM. QAA method had been adopted by SeaWiFS Data Processing System (SeaDAS) 4.8 version. The main idea of QAA is to calculate optical properties in a level-by-level scheme. Firstly, the values of total absorption and backscattering coefficients are analytically calculated from values of remote-sensing reflectance. Then, phytoplankton and CDOM coefficients are decomposed from the total absorption

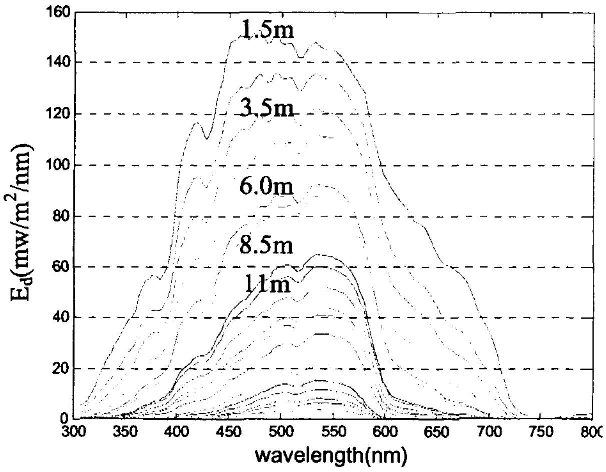

Fig.11 Spectral distribution of downward irradiance at zd23 station

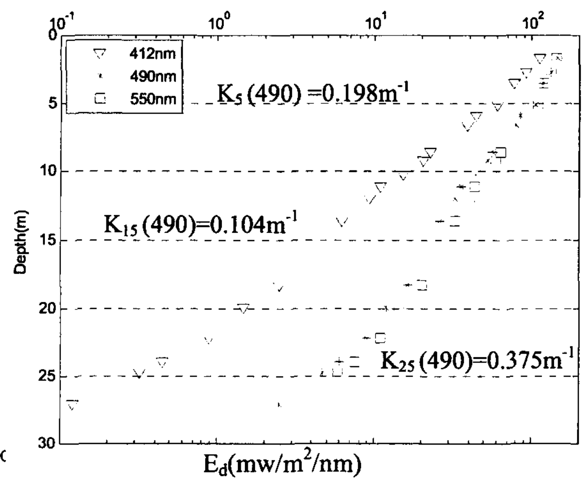

Fig.12. Depth dependence of downward irradiance at 412nm, 490nm, 550nm at zd23 station

coefficients. Only the first step is involved in this paper. Considering high turbid water of East China seas, we choose 640nm as reference wavelength. go of 0.077 and gl of 0.219 are selected for QAA method according to Keping Du's numerical simulation of China sea[12]. Fig.13 compares the QAA-derived a(440) versus AC-S-measured a(440), along with the empirical algorithm-derived a(440). The relative errors of a(440) derived from empirical algorithm and QAA method are 17.3% and 13.7% respectively. Fig.14 compares a (λ) from QAA-method and from AC-S measurement at 410nm, 440nm, 490nm, 530nm, and the error is 16.4%. It is found that absorption coefficient at 490nm derived from QAA method is generally smaller than a (490) measured by AC-S.

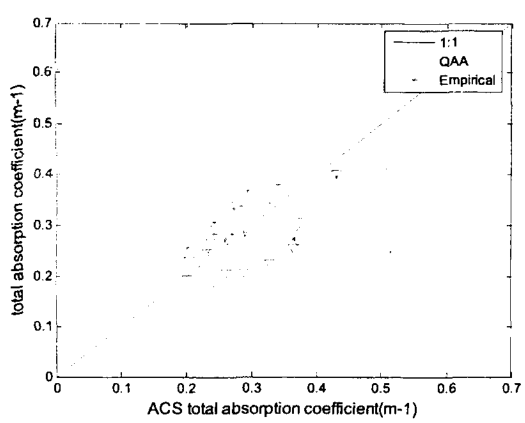

Fig.13.Comparison of QAA-derived a (440) versus AC-S measured a(440), along with empirical algorithm-derived a(440)

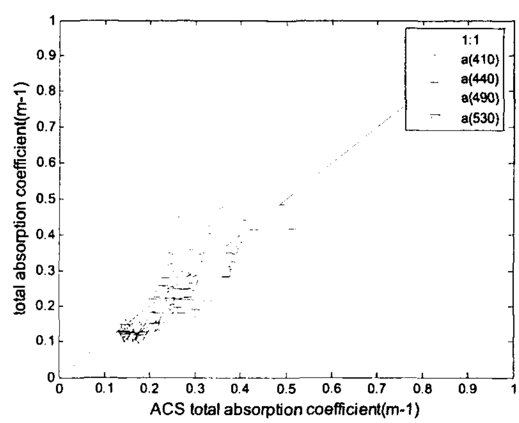

Fig.14 Comparison of QAA-derived a versus AC-S-measured a at four wavelengths

4.2 Retrieval diffuse attenuation coefficients $K_d(490)$from remote-sensing reflectance

For estimating Kd (490) from SeaWiFS, Mueller and Trees [13] developed the following algorithm in 2000:

$$K_d(490) = K_w(490) + 0.15465(1.03\frac{R_{rs}(490)}{R_{rs}(555)})^{-1.5401} \qquad (1)$$

where, Kw (490) is diffuse attenuation coefficient of pure water at 490nm.

Lee et al. [14] developed a semi-analytical model based on radiative transfer equation to estimate Kd (λ) from absorption and backscattering coefficient and boundary conditions. The equation shows as follows:

$$K_d = m_0 a + m_1(1 - m_2 e^{-m_3 a}) b_b \tag{2}$$

Where, $m_0 = 1 + 0.005\theta$, θ is the solar zenith angle in air. The values for model constants ml, m2 and m3 are constant. Combined equation (2) with QAA method, Kd(λ) can be easily calculated from remote-sensing reflectance and solar angle. To demonstrate the performance of the two methods, we present the results in Fig.15 .The Kd(λ) values are determined from the measured profiles of Ed(λ). The errors of two methods are 32.5% and 13.9%. The correlation coefficients are 61%and 94%, respectively. Obviously, Semi-analytical method has much better results than the empirical method, especially in turbid waters where Kd(490)>0.3 m-1. If a(490) is measured by AC-S in the equation (2) and bb (490) is still derived from QAA method, the error is reduced to 1.9% as shown in Fig.16.

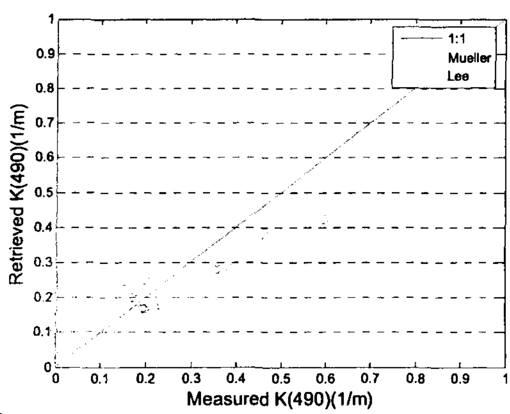

Fig.15.Comparison of K_d (490) derived from empirical algorithm versus derived from semi-analytical method

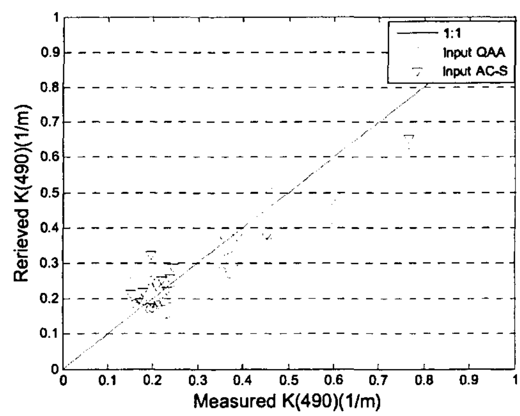

Fig.16. Comparison of semi-analytical method-derived K_d(490) between using a(490) measured by ACS and a(490) derived form QAA method as input

5. COMPARISONS OF IN SITU OCEAN OPTICS EXPERIMETNTS WITH MERIS DATA

As mentioned above, in the field experiments in East China Sea in 2005, it was overcast and rainy in most days and sunny only on May 7 and May 8. Unfortunately, Envisat satellite didn't pass the area at this time. So MERIS and in situ data were not matched well in time and space. The time and route selections depend on the red tide cruise with which this field experiment joined. However, red tide bloom occurrence in Zhoushan Archipelago was one month later than former years.

In order to compare with in-situ ocean optical data and chlorophyll concentration at zd23, zd24 and zd24a station, 3×3 pixel box without cloud are selected from May 3, 2005 MERIS image (31°08'N 125°22'E, 1.2km), which is heavily covered with clouds. Figure 17 shows the MERIS image and sub image for comparison. zd23, zd24, zd24a station and 3×3 MERIS pixel box are also shown in sub image.

Remote sensing reflectance of eight bands (412, 442, 490, 510, 560, 620, 665, and 708nm) are obtained from atmospheric correction of MERIS Level-1 TOA radiance using BEAM software, compared with remote sensing reflectance got from HTSRB. Figure 18 provides the comparison of in situ and MERIS remote-sensing reflectance spectrum in Zhejiang coastal area, which shows good agreement at wavelength larger than 560nm. The relative error is 27%. MERIS Rrs data are abnormally higher at wavelength smaller than 500nm, which is also found at ZZ cruise on April 27, 2005. Figure 19 and 20 show corresponding MERIS and station image and comparison of remote sensing reflectance spectrum, Rrs, respectively. The two examples above suggest Rrs data retrieved from MERIS using BEAM software are higher at blue band.

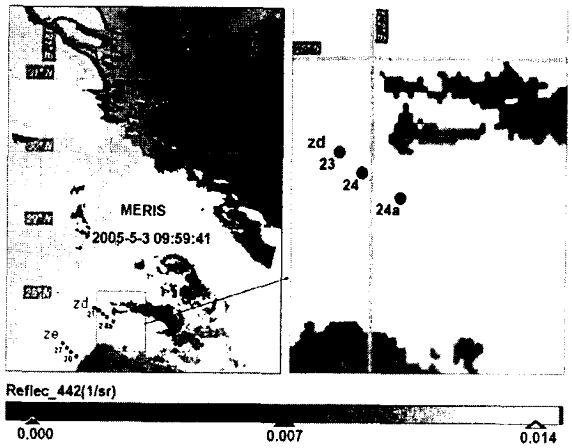

Fig 17. (left) May 3 2005 (09:59) MERIS image in East China Sea, zd23 (15:06), zd24 (14:18), zd24a (13:20) station of zd cruise. (right) Three stations for comparison and 3×3 MERIS pixel box

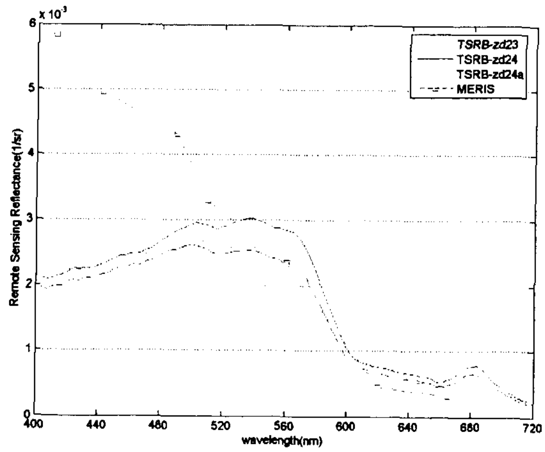

Fig 18. Comparison of in situ and MERIS remote sensing reflectance, R_{rs}, in Zhejiang coastal area.

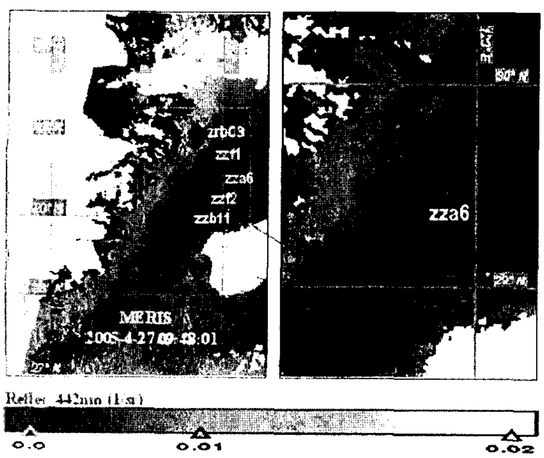

Fig 19. (left) April 27 2005 (09:48) MERIS image in East China Sea, zza6 station (13:30). (right) 3×3 MERIS pixel box for comparison centered at zza6 station.

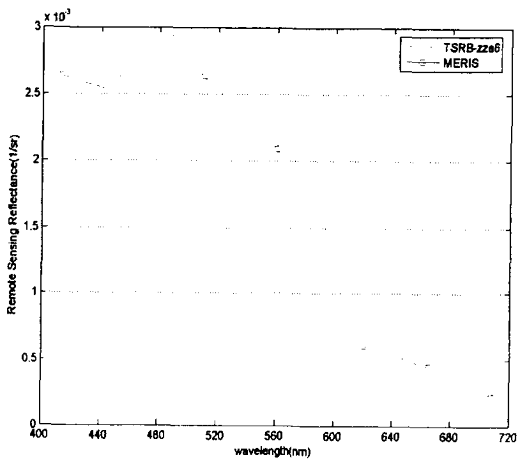

Fig.20. Comparison of situ measurement and MERIS remote sensing reflectance spectrum, R_{rs}, in Zhoushan coastal area.

Total absorption coefficient, a, and backscattering coefficient, bb, are retrieved from remote sensing reflectance, Rrs, after atmospheric correction using Semi-analytical (SA) and QAA algorithm respectively. Total scattering coefficients, b, are estimated based on Petzold's backscattering ratio [15] and then the attenuation coefficient, c, can also be obtained. The retrieved a and c are compared with AC-S measurements. Once the retrieved a, bb are obtained, Kd can be got from eq. (2), which is compared with RAMSES measurement.

Figure 20(1)(2)(3) shows absorption coefficient, a, attenuation coefficient, c and diffuse attenuation coefficient, K retrieved from MERIS remote sensing reflectance, Rrs, using BEAM respectively. As is shown, all results of two methods are smaller than in situ measurements. Figure 21(1)(2)(3) are results corresponding to figure 20(1)(2)(3), which only in situ measurement of Rrs replaces the retrieved Rrs using BEAM. The comparison shows good agreement. By combining SeaDAS V.4.8 QAA and BEAM algorithm, ocean optical parameters, a, b, c and K can be retrieved from MERIS data.

Table 1 shows the comparison of retrieved and in situ chlorophyll concentration, where the retrieved methods are BEAM and SA algorithm. The in situ data is from zd23 station surface layer (1m). It shows relative error is large.

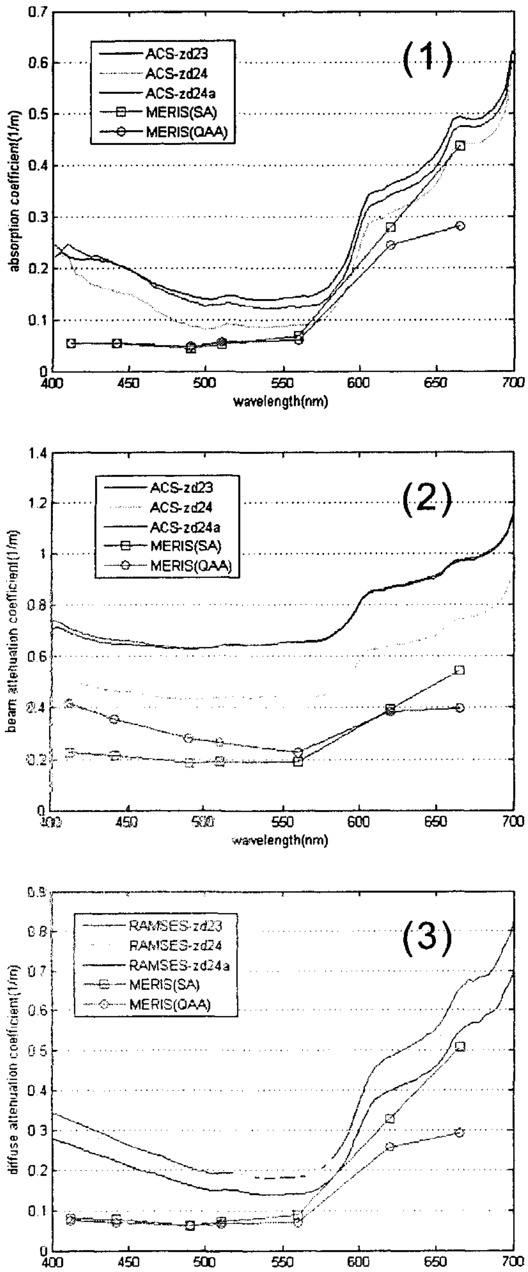

Fig.21 Comparison of retrieved ocean optics parameters (a, c, K) using SA and QAA algorithm with field observation (MERIS Rrs)

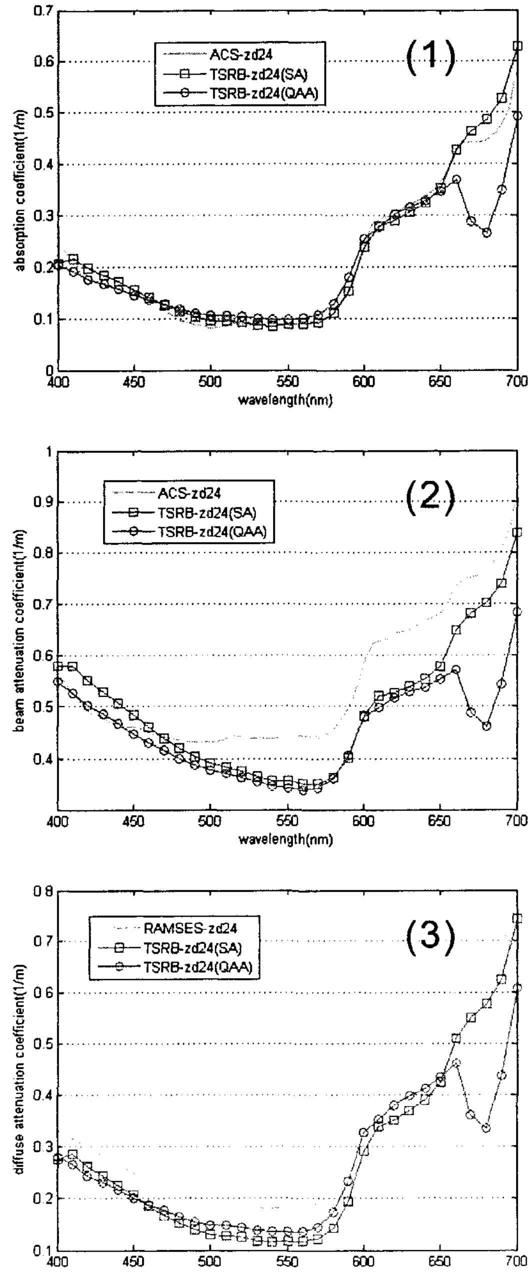

Fig.22 Comparison of retrieved ocean optics parameters (a, c, K) using SA and QAA algorithm with field observation (field observation Rrs)

Table 1 Comparison of retrieved and in situ chlorophyll concentration

Method	Chlorophyll concentration	Relative error
BEAM	$0.09mg/m^3$	89%
SA	$0.39mg/m^3$	53%
In situ (zd23)	$0.84mg/m^3$	

References:

1. Ming Xia HE, Zhi-Shen Liu, Ke-Ping Du et al., Retrial Chlorophyll from Remote-Sensing reflectance in the China seas, *Applied Optics,* Vol.39, No.15 2467-2474,2000
2. Ming Xia HE et al., Validation and merging of Ocean Color Multisensor Data in the Eastern China Sea, NASA SIMBIOS PI Report. Cited in *SIMBIOS Project 1998 Annual Report* edited by Charles R. McClain.
3. J.L. Mueller et al., Ocean Optics for Satellite Ocean Color Sensor Validation, Revision4m, Vol.4, 27-38
4. J.L. Mueller et al., Ocean Optics for Satellite Ocean Color Sensor Validation, Revision4m, Vol.4, 39-46
5. Austin, R.J. and T.J. Petzold, Spectral dependance of the diffuse attenuation coefficient of light in ocean waters. Ocean Optics VII, 1984, 168~178.
6. Austin R W, Air-water radiance calibration Factor Technical Memorandum Ml-76-004 8, 1976
7. T Ohde and H Siegel, Derivation of immersion factors for the hyperspectral TriOS radiance sensor, Journal of Optics A: Pure and *Applied Optics,* L12-L14, 2003
8. W. Scott Pegau, Deric Gray, and J. Ronald V. Zaneveld, Absroption and attenuation of visible and near-infrared light in water: dependence on temperature and salinity, *Applied Optics,* Vol.36 No.24 6035-6045,1997
9. Pinder,G.F., and W.G. Gray, Finite Element Simulation in Surface and Subsurface Hydrology, Academic Press, 29,1977.
10. Z.P. Lee, K.L Carder, R.G. Steward, and T. G. Peacok, An empirical algorithm for light absorption by ocean water based on color. *Journal of Geophysical Research* 103,12,27,967-27,978,1998
11. ZhongPing Lee, Kendall L. Carder, Deriving inherent optical properties from water color a mutiband quasi-analytical algorithm for optically deep waters. *Applied Optics* Vol.41, No.27, 5755-5772, 2002
12. Ke-Ping Du Ph.D. Dissertation, Research on the computing platform of bio-optics in China Seas and its applications, 73-83,2003
13. Mueller,J. L., SeaWIFS algorithm for the diffuse attenuation coefficient, K(490), using water-leaving radiance at 490 and 555nm, SeaWiFS Postlaunch Calibration and Validation Analyses, part3
14. Zhong-Ping Lee, Ke-Ping Du, and Robert Arnone, A model for the diffuse attenuation coefficient of downwelling irradiance, *Journal of Geophysical Research,* 110, C02016,2005
15. Pezold,T.J., 1972. Volume scattering functions for selected ocean waters, SIO Ref.72-78

THE DISTRIBUTION OF INTERNAL WAVES IN THE CHINA SEAS STUDIED BY MULTI-SENSOR SATELLITE IMAGES

Werner Alpers [1, 2], Ming-Xia He [2], Kan Zeng [2], Ling-Fei Guo [2], and Xiao-Ming Li [2]

[1] *Institute of Oceanography, University of Hamburg, Germany, E-mail: alpers@ifm.uni-hamburg.de*
[2] *Key Laboratory of Ocean Remote Sensing, Ministry of Education, China,*
Ocean Remote Sensing Institute, Ocean University of China, China,
E-mail: mxhe@orsi.ouc.edu.cn; zengkan@orsi.ouc.edu.cn

ABSTRACT

The distribution of internal waves in the China Seas has been studied by screening a large number of images of the sea surface acquired by the ERS, Radarsat, Envisat, and SPOT satellites and by the Spaceshuttle for sea surface signatures of internal waves. The occurrence of internal wave signatures is shown as a function of 1) position in the China Seas, 2) season, and 3) phase of the spring-neap tidal cycle.

1. INTRODUCTION

The East China Sea and the Yellow Sea are sea areas where little information exists on the generation, propagation and distribution of internal waves, see [1] – [8]. The first systematic study of the distribution of internal waves in these sea areas was carried out by Hsu et al. in 2000 [1], who analysed radar images for internal wave signatures which were acquired by the synthetic aperture radar (SAR) onboard the satellites ERS-1 and ERS-2 between 1993 and 1997. In the present study we have extended their investigation by including SAR images which were acquired by the ERS satellites after 1997, by the Radarsat and the Envisat satellites, and by the Spaceshuttle during the SIR C/X-SAR mission, and optical images that were acquired in the visible bands by the French SPOT satellites. This has increased the data base considerably and made it possible not only to generate much more detailed maps of the distribution of internal waves in the China Seas, but also to study how the occurrence of internal waves depends on the time of the year and on the phase of spring-neap tidal cycle. The occurrence of internal waves is an indicator for the stratification of the ocean column, i. e., for the existence of a pycnocline. In winter the water columns in the East China Sea and the Yellow Sea are usually well mixed due to the prevailing cold winds from the north and thus no internal wave signatures are observed.

2. EXAMPLES OF IMAGES

2.1. Yellow Sea and East China Sea

Examples of images showing sea surface signatures of internal waves in the Yellow Sea and East China Sea are depicted in Fig.1 and Fig. 2. The two images in Fig.1 were acquired by the C-band, VV polarization SAR onboard the European Remote Sensing satellite ERS-2 and Fig.2 by the optical sensor onboard the French SPOT 2 satellite. All these images show packets of internal waves which have been tidally generated. This generation mechanism can be inferred from the periodicity of the internal wave packets. The distance between successive internal wave packets is related to the semi-diurnal tidal period. The separation of the solitary internal waves within these packets is of the order of 100–1000 m, which is relatively small when compared with the internal wave packets observed in the South China Sea, Andaman Sea, and Sulu Sea.

The ERS-2 SAR image depicted in Fig. 1a shows a large number of internal wave signatures propagating away from the shallow areas southwest of the Korean peninsula. The island visible in the upper section is the Korean island Sokuksan. The ERS-2 SAR image depicted in Fig. 1b shows internal waves farther south in the East China Sea. The irregular dark-white patches visible in this image are sea surface signatures of rain cells.

The SPOT image depicted in Fig.2 shows also signatures of a large number of internal wave packets propagating in different directions. This is due to the complex tidal flow regime in the shallow waters between the islands. Sea surface signatures of internal waves are particularly well visible in SPOT images when the imaged area lies in the sunglint area. However, close to the center of the sunglint area, the reflection from the sun is too strong and no modulation of the sea surface roughness induced by the internal waves is detectable anymore. This can be seen in the upper part of the image.

Proc. 2005 Dragon Symposium "Mid-Term Results", Santorini, Greece
27 June – 1 July 2005 (ESA SP-611, January 2006)

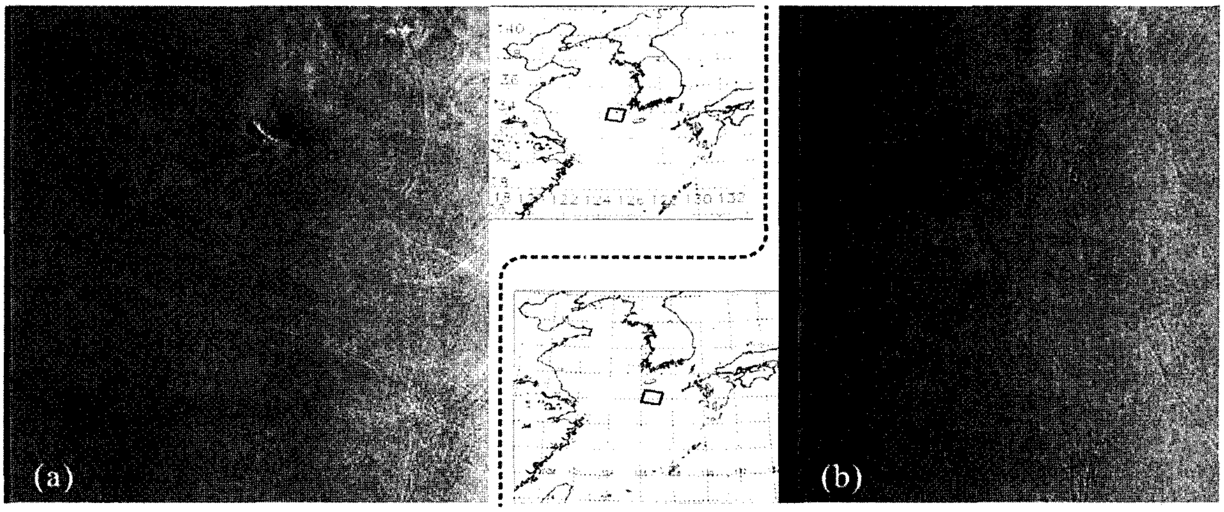

Fig.1. (a)ERS-2 SAR image acquired over the Yellow Sea off the southwest coast of Korea on 8 July 1998 at 02:20 UTC (orbit: 16805, frame: 2925). Imaged area: 110 km x 100 km. © ESA; (b) ERS-2 SAR image acquired over the East China Sea off the east coast of Korea on 5 August 1997 at 02:12 UTC (orbit: 11981, frame: 2961). Imaged area: 140 km x 100 km. © ESA

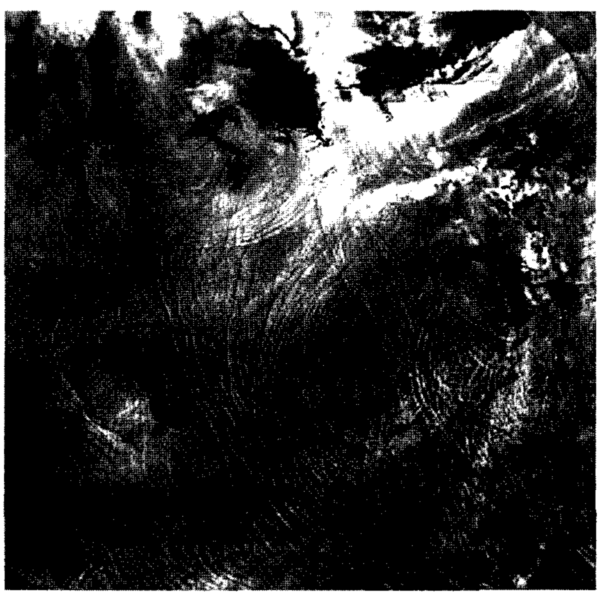

Fig. 2. SPOT 2 image acquired over the East China Sea off the south coast of Korea on 1 June 2004 at 02:37 UTC (center coordinates: 33.909 N, 126.037 E). Imaged area: 63 km x 64 km. © Spot Image

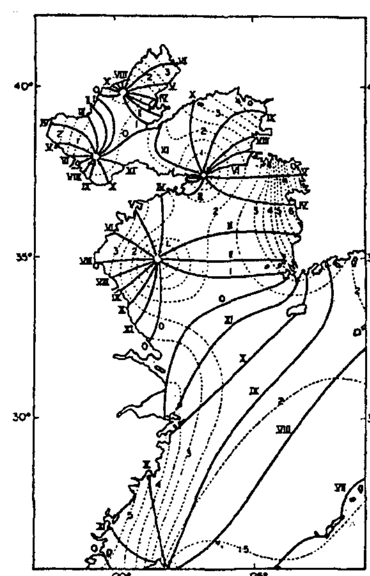

Fig. 3. Map of the phase (solid lines) and the tidal range (dotted lines) of the semi-diurnal tide in the Yellow Sea and the East China Sea (after Ogura; from Defant, 1961).

In some sea areas off the west and southwest coast of Korea the tidal range is quite large as shown in Fig.3. These areas are hot spots for internal wave generation.

2.2. South China Sea

Examples of images showing sea surface signatures of internal waves in the South China Sea are depicted in Figs. 4–9. The first 5 images were acquired by the C-band Advanced Synthetic Aperture Radar (ASAR) onboard the Envisat satellite in the Wide Swath Mode. They are quick-look images with reduced resolution. The last image depicted in

Fig. 4. Envisat ASAR image acquired over the South China Sea around Dongsha Island on 21 June 2005 at 14:09 UTC. Dongsha atoll is the ring-shaped feature in the lower left-hand section of the image. Imaged area: 305 km x 280 km. © ESA

Fig.5. Envisat ASAR image acquired over the South China Sea around Dongsha Island on 11 March 2005 at 14:15 UTC (orbit: 111981, frame: 2961). Imaged area: 250 km x 200 km. © ESA

Fig.6. Envisat ASAR image acquired over the South China Sea around Dongsha Island on 1 May 2005 at 14:13 UTC. Imaged area: 235 km x 200 km. © ESA

Fig. 7. Envisat ASAR image acquired over the South China Sea around Dongsha Island (located in the lower central section of the image) on 4 May 2005 at 14:18 UTC. Note the semi-circular wave pattern in the lower left-hand section of the image which is very likely the sea surface signature of a locally generated internal wave packet. Imaged area: 190 km x 125 km. © ESA

Fig.9 is a SPOT-1 image. All images with the exception of the image depicted in Fig.8 show sea surface signatures of nonlinear packets around the Dongsha Island. The large amplitude internal solitary waves generated in the Luzon Strait interact with the atoll around this island. They are refracted and even reflected by the atoll(see Fig.5). Also the shallow bathymetry west of Dongsha island effects the propagation of the internal waves. It seems that also secondary internal waves are generated here (see Fig.5). In Fig.8 an Envisat ASAR image of the sea area west of the Luzon Strait is depicted. It reveals that there are at least two areas in the Luzon Strait where strong internal solitary waves are generated. Very likely the internal solitary generated at the two location finally merge when propagating westward . This would explain the often observed bended shape of the solitary waves when they reach Dongsha Island. A map of the bottom topography of this area is depicted in Fig. 10.

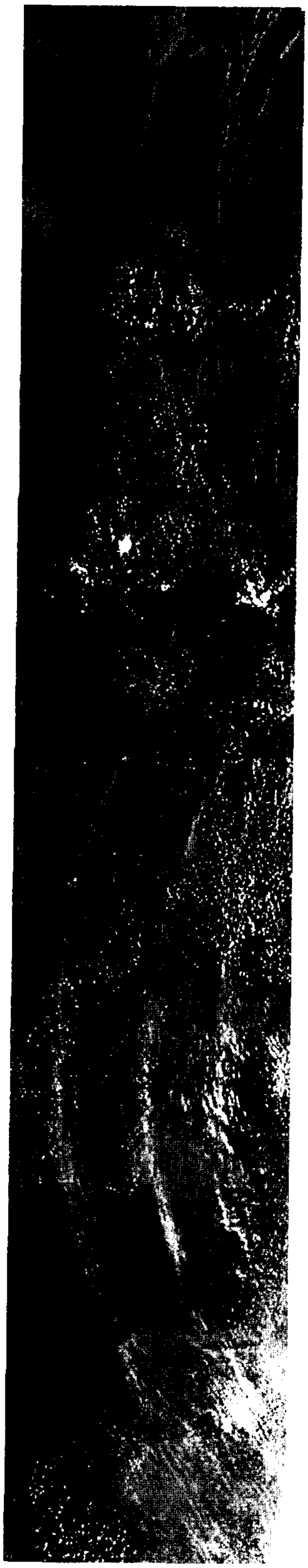

Fig. 8. Envisat ASAR image acquired over the South China Sea west of Luzon Strait on 9 July 2005 at 01:59 UTC. Visible is in the upper right-hand corner the southern tip of Taiwan and in the lower right-hand corner the northern tip of Luzon (Philippines). This image reveals that there are two mayor locations for internal wave generation in the Luzon Strait. Imaged area: 440 km x 400 km. © ESA

⇦ *Fig. 9. Spot 1 image acquired over the South China Sea around Dongsha Island on 31 August 1999 at 02:57 UTC. It shows the interaction of an internal wave packet with the Dongsha atoll (blue ring in the center). © SPOTIMAGE*

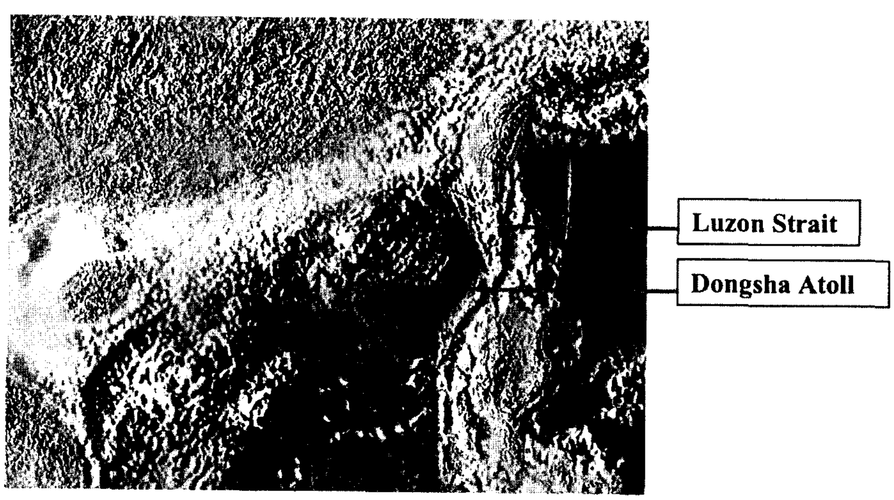

Fig. 10. Map of the bottom topography of the South China Sea.

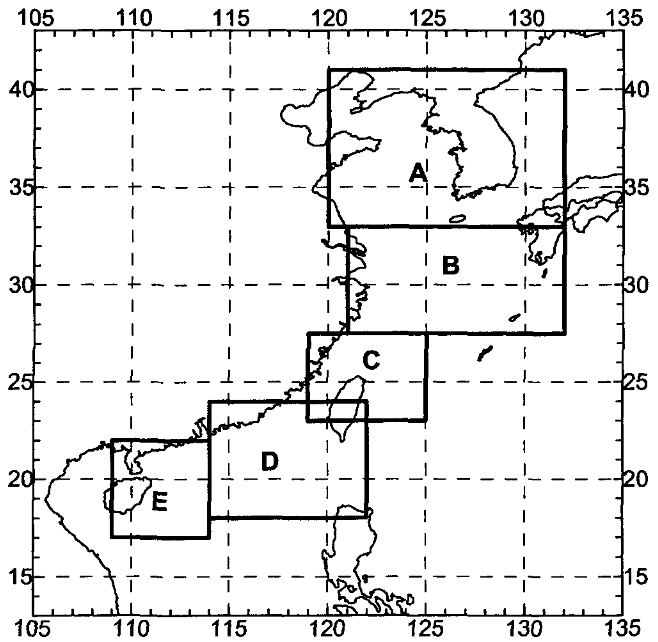

A (Yellow Sea, sea area around Korea)

$117^\circ E - 130^\circ E$, $33^\circ N - 41^\circ N$

B (East Sea)

$121^\circ E - 132^\circ E$, $27.5^\circ N - 33^\circ N$

C (Sea area around Taiwan)

$119^\circ E - 124^\circ E$, $23^\circ N - 27.5^\circ N$

D (Sea area around Dongsha Island)

$114^\circ E - 122^\circ E$, $18^\circ N - 24^\circ N$

E (Sea area around Hainan Island)

$105^\circ E - 114^\circ E$, $17^\circ N - 22^\circ N$

Fig. 11. Sections of the China Seas for which the analyses were carried out separately.

3. Statistical Analysis of internal wave signatures

In this study we have separated the study area in five sections, called sections A, B, C, D, and E, which are shown in Fig.11. For brevity we have called them here Yellow Sea, East Sea, and Taiwan, Dongsha Island, and Hainan Isand, respectively.

As stated in the introduction, we have used images acquired from the satellites ERS, Radarsat, Envisat and SPOT and from the SIR-C/X-SAR Spaceshuttle mission. Table 1 shows the number of images with internal wave signatures identified from approximately 15 thousand satellite images mentioned above. The second column of Table 2 shows their distribution over the areas A, B, C, D, and E. However the internal waves often covered by several continuous images, counting the number of images with internal wave signatures is actually counting one internal wave repeatedly several times. Besides, the same internal waves may be observed by more than one sensors, which may induce the repeated counting too. In order to avoid the indefinitness caused by the repeated counting, we count only once when either of the two cases is encountered. In that way, the distribution of internal waves are generated and shown in the third column of Table 2.

3.1. Maps of the spatial distribution of internal wave signature

The map depicted in Fig.12 shows that areas of high internal wave activities are sea areas 1) off the southwest and south coast of Korea, 2) north of Taiwan, and 3) in the South China Sea between the Luzon Strait and the island of Hainan. The high internal wave activity in the sea area off the southwest and south coast of Korea is due to the shallow bathymetry between the islands and due to the strong tidal currents encountered in the channels between them. The tidal range along the Korean coast is 4 to 8 m, while along the China coast it is only 1 to 2 m as shown in Fig.3. The tidal currents reach peak values of 4.4 m/s in the passages off the southwest tip of the Korean Peninsula. In the central basin, the tidal speed is only of order 0.5 m/s. North of Taiwan internal waves are generated by upwelling water produced by the interaction of the Kuroshio with the continental shelf. In the South China Sea the area around Dongsha Island is an area of very high internal wave activity. Here internal solitary waves generated in the Luzon Strait interact with shallow bottom topography. The internal waves are refracted and secondary internal wave packets are generated

Table 1. Number of images from satellites and from Spaceshuttle (SIR-C/X-SAR) used in the statistical analysis.

Image type	Number of images
RADARSAT/SAR	16
ENVISAT/ASAR	5
ERS-1,2/SAR	352
SIR-C/SAR(L)	16
SIR-C/SAR(C)	16
SIR-C/SAR(X)	16
SPOT	363

Table 2. Distribution of the images over the areas A, B,C,D and E and the spatial distribution of sea surface signatures of internal wave packets identified on the images.

Area	Number of images	Number of internal wave
A (Yellow Sea)	71	41
B (East Sea)	58	36
C (Taiwan)	243	166
D (Dongsha Island)	325	191
E (Hainan Island)	55	35

Fig. 12. Distribution of internal wave signatures in the China Seas obtained from analyzing the available satellite images.

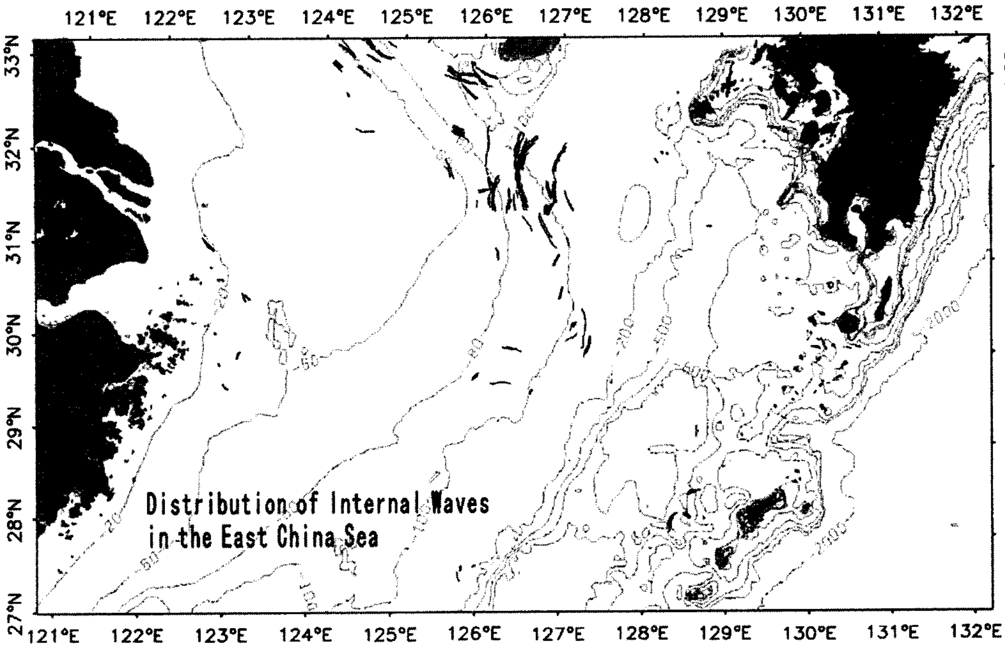

Fig.13. Distribution of internal wave signatures in the East Sea.

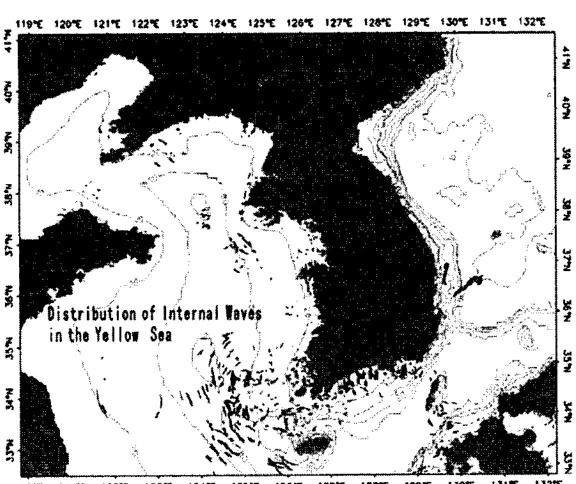

Fig 14. Distribution of internal wave signatures in the Yellow Sea

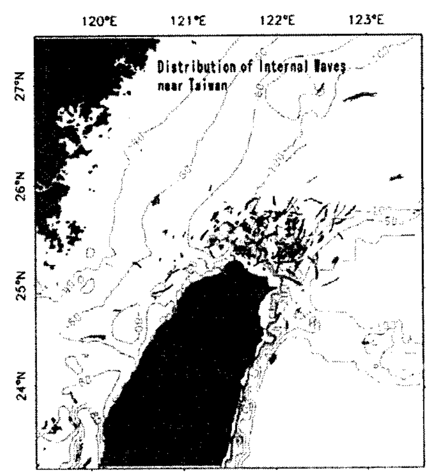

Fig. 15. Distribution of internal wave signatures in the Taiwan area.

3.2. Internal wave signature as a function of season (month)

The dependence of the occurrence of internal wave signatures on the time of the year for the five ocean areas is depicted in Fig. 18. These plots clearly show that no internal waves are encountered in the Yellow Sea and the East Sea in late

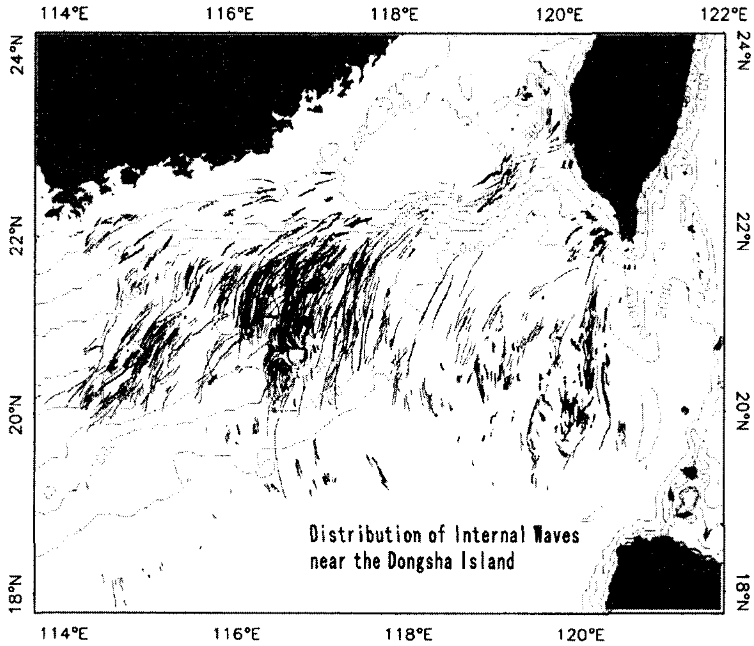

Fig. 16. Distribution of internal wave signatures in the Dongsha area.

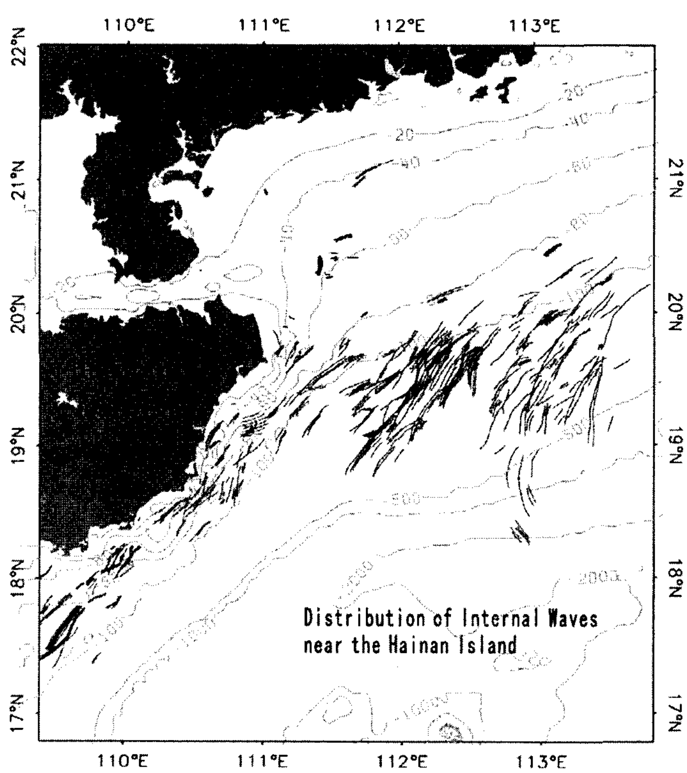

Fig. 17. Distribution of internal wave signatures in the Hainan area.

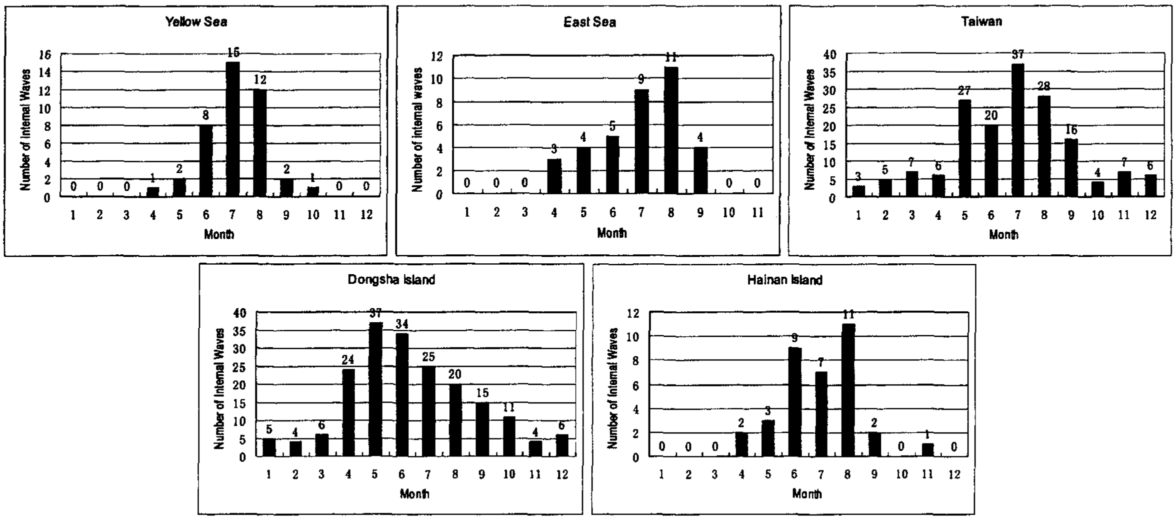

Fig.18. Internal wave signature as a function of season (month) for the different ocean areas.

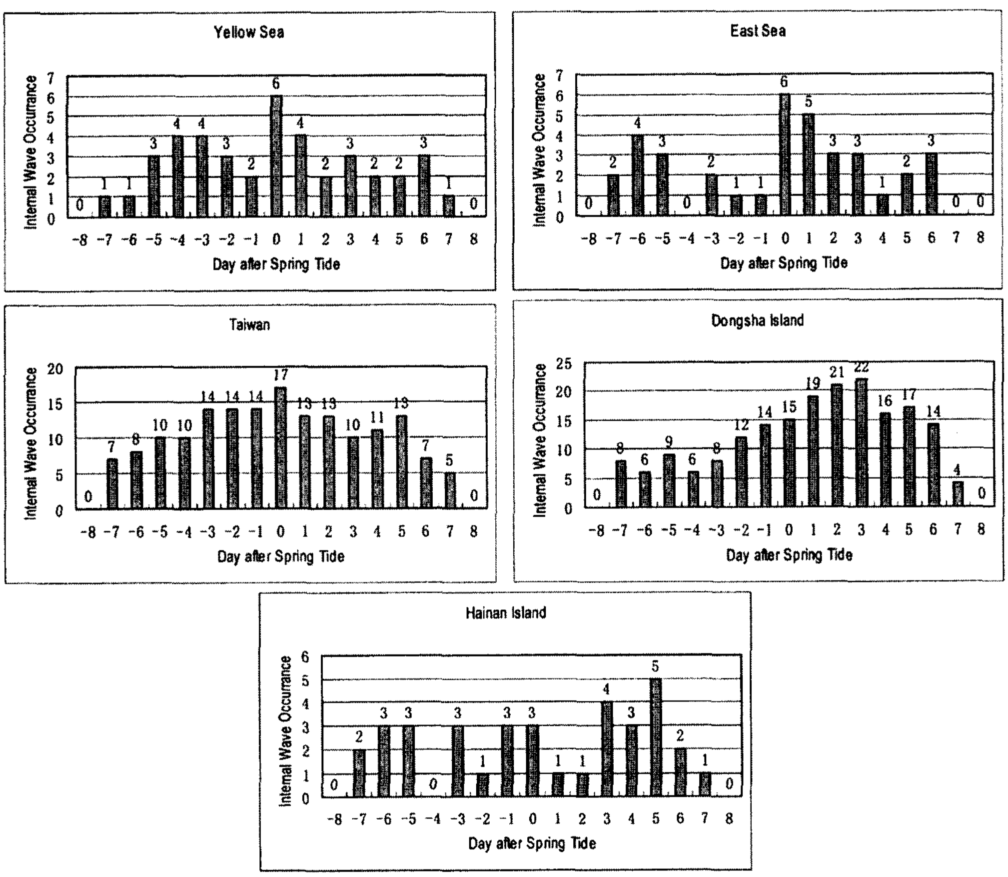

Fig. 19. Internal wave signature as a function of time after spring tide for the different ocean areas.

autumn, winter, and early spring. This is due to the absence of a pycnocline during this time of the year. Cold winds which often blow from the Chinese Continent over the Yellow Sea and the East China Sea cause mixing of the water. Also in the Hainan area there seems to no pycnocline because in this coastal area the sea is quite shallow. In the upwelling area north of Taiwan and in the South China Sea near Dongsha Island internal wave signatures are encountered the whole year, but much less frequently in autumn, winter, and spring.

3.3. Internal wave signature as a function of time after spring tide

The dependence of the occurrence of internal wave signatures on the time after spring tide for the five ocean areas is depicted in Fig.19. These plots clearly show that no internal wave signatures are strongest close to spring tide as expected. Around this time the tidal currents are strongest.

4. SUMMARY AND DISCUSSION

In contrast to the South China Sea, the Yellow Sea and the East China Sea are shallow seas with depths seldom larger than 100 m. The pycnocline is in general much shallower (typical depth is 20 m) and is less strong than in the South China Sea. This gives rise to weaker internal waves which seldom have peak-to-trough amplitudes larger than 10 m and wavelengths longer than 1000 m. There are two hot spots of internal wave generation: one is located in the shallow waters off the southwest coast of Korea where tidal currents are extremely strong, and the other one in the upwelling area north of Taiwan.

In late autumn, in winter and early spring, the stratification of the water column in the Yellow Sea and the East China Sea becomes very weak or disappears completely such that no internal waves can exist. Our results are in good agreement with information on water stratification contained in the maps of the pycnocline distribution published in the Marine Atlas of the Bohai Sea, Yellow Sea and East China Sea (China Ocean Press, Beijing, 1992). On the other hand, in the deep areas of the South China Sea, there is always a pycnocline such that internal waves can be present all year round.

ACKNOWLEDGMENT

This research has been partially funded by the project CHN 02/001 of the German-Chinese Bilateral Cooperation in Science and Technology and has also been supported by the ESA-MOST Dragon Programme, Satellite Oceanography Project 2566.

References

1. Hsu, M. K, Liu, A. K., and. Liu, C. A study of internal waves in the China Seas and Yellow Sea using SAR, *Continental Shelf Research*, Vol. 20, 389–410, 2000.
2. Liang, N. K., Liu, A. K., and Peng, C. Y. ,A preliminary study of SAR imagery on Taiwan coastal waters, *Acta Oceanography Taiwanica*, Vol. 34, 17–28, 1995.
3. A. K. Liu, Chang Y. S., Hsu, M. K., and Liang, N. K., Evolution of nonlinear internal waves in the East and South China Seas". *J. Geophys. Res.*, Vol.103, 7995–8008, 1998.
4. Ogura, S., The tides in the seas adjacent to Japan". Hydrog. Bull. Dep. Imp. Jap. Navy, vol. 7, 1-189, 1933.
5. Hsu, M.-K., and. Liu, A. K ,2000: Nonlinear internal waves in the South China Sea. *Canadian J..Rem. Sens.*, Vol. 26, 72-81, 2000.
6. Orr, M. H., and. Mignerey , P. C, Nonlinear internal waves in the South China Sea:Observation of the conversion of depression internal waves to elevation internal waves," *J.Geophys. Res.*, Vol. 108, 2003
7. Ramp, S. R., Tang, T.Y., Duda T. F., Lynch, J. F., Liu, A. K., Chiu, C.-S., Bahr F. L., Kim H.-R., and Yang Y. -J., Internal solitons in the northeastern South China Sea Part I: Sources and deep water propagation, *IEEE J. Oceanic Engineering (ASIAEX Special Issue)*, Vol. 29, 1157-1181, 2004
8. Duda, T. F., Lynch, J. F., Irish, J. D., Beardsley, R. C., Ramp, S. R. Chiu, C.-S., Tang, T. Y., and Yang, Y.-J., Internal tide and nonlinear internal wave behavior at the continental slope in the Northern South China Sea, *IEEE J. Oceanic Engineering (ASIAEX Special Issue)*, Vol. 29, 1105-1130, 2004

INTERNAL WAVE EXTRACTION IN SAR OCEANIC SURFACE IMAGE BASED ON STATIONARY WAVELET TRANSFORM

Ming-Xia He, Haihua Chen, Lingfei Guo, Xiaodong Zhuang, Hongping Li
Key Laboratory of Ocean Remote Sensing, Ministry of Education, China,
Ocean Remote Sensing Institute, Ocean University of China, China,
E-mail: mxhe@orsi.ouc.edu.cn, chenhh@orsi.ouc.edu.cn

ABSTRACT

An Internal Wave Feature Extraction (IWFE) algorithm based on Stationary Wavelet Transform (SWT) in SAR oceanic surface images is proposed. In this algorithm, SWT is applied to process SAR images and its coefficients are used to calculate the Wavelet Gradient Information (WGI). And the IWFE is obtained as edges by searching the calcaulated WGI's maximum module value.. The morphological thinning algorithm and threshold technique are also used for edge refinement to suppress the other oceanic features, isolate Speckle noise. The results obtained from ERS-1 and ERS-2 SAR images show that the proposed method is more efficient than the traditional down sampling discrete wavelet transform in IWFE. The algorithm can be easily implemented and give an accurate and complete location of internal waves in SAR images.

1. INTRODUCTION

Oceanic internal wave is a general oceanic phenomenon. It is a very important research topic of oceanic dynamics and is close related to the ocean bionomics, ocean sedimentology and ocean physics. The observation of internal waves is very essential in ocean engineering, ocean navigation and undersea sound communication, etc. Internal wave travels within the interior of the sea, its space–time distribution is widely and diversified, hence, in-situ observation of internal waves is time consuming and expensive.

Satellite remote sensing as an effective tool to observe oceanic internal waves is well recognized by both oceanographers and remote sensing scientists. Oceanic internal wave remote sensing starts with visible light. In 1978, American Seasat-A satellite first testified that Synthetic Aperture Radar (SAR) had a potential ability to observe oceanic internal waves [1]. Satellite SAR can provide all-weather, all time imagery ability to the ocean, and its imaging mechanism and spatial resolution bring it to be a sophisticated tool to observe internal waves.[2]. SAR internal wave images can be used for researchers to study its generation and propagation mechanisms [3] [4] [5], analyze its space-time distribution, extract and retrieve its parameters including wavelength, amplitude, propagation direction and speed [6] [7] [8] [9]. After Seasat-A, SAR observation of internal waves is recognized as one main task in many satellite missions including the European Space Agency ERS-1/2 satellite, Russian ALMAZ-1 satellite, Japan JERS-1 satellite, SIR-C aircraft by United States and Germany, Canadian Radarsat satellite, ESA Envisat and the China radar satellite (will launch in 2006). With the rapid development of SAR technology and commercial operational SAR availible, the exponential growing mount of SAR data and the increasing demands from end users urge us to find a faster and automatic method to screen SAR internal wave images and extract internal wave features automatically in SAR image. Many research efforts have been put in IWFE, and a few results have been published. Rodenas [10] applied the binary discrete wavelet transform (DWT) to extract the edge of the internal waves. In the DWT, SAR image data should be enlarged or intercepted due to the down sampling. At mean time, the information searching between the scales is complicate which affects the internal waves detection accuracy and integrity. The algorithm is in relative complex and SAR image size need to be modified to be power of 2.

Proc. 2005 Dragon Symposium "Mid-Term Results", Santorini, Greece
27 June – 1 July 2005 (ESA SP-611, January 2006)

In SAR image, the internal wave appears as long, bright and dark strips with a certain radian. The internal wave is one strip and the internal soliton is a group strips with decrescendo contrast and space in SAR image. The gray intensity of every strip of internal waves and the contrast to background are always asymmetrical. In addition, internal wave often intersects together. In this paper, we first use the most obvious bright and dark strip feature which reflects the discontinuous gray intensity. The strips' edge depicts the discontinuity so locating the edge accurately is very important in the internal wave feature extraction. The traditional edge operators such as Robert, Sobel and Laplacian are widely used in the image processing but they are sensitive to the noise.

Wavelet transform (WT) is a relatively fine analysis tool for analyzing the time-varying non-stationary signals. Its main advantage remains in the ability to describe the signal local time and frequency contents. Grossman and Morlet [13] first introduce the wavelet concept to engineering application. After that the wavelet analysis develops quickly and is applied in non-stationary signal processing. Mallat [14] [15] applied the wavelet transform in the image processing, and have testified that it is a good edge extraction tool. The Mallat algorithm based on MRA makes the wavelet analysis application become reality. The position of the Mallat algorithm in wavelet domain corresponds to the FFT in the classic Fourier transform. In 1995, Nason and Silverman [16] presented the stationary wavelet transform (SWT), which can be implemented for any size of image. It has better denoising quality and edge extracting capacity than the DWT.

In this paper, based on the SWT an automatic internal wave feature extraction method in SAR images is presented. The internal wave Extraction System is described in Fig. 1. In the system, the Lee filter [11] [12] is used to alleviate the effect of speckle noise and use 8*8 sizes window to compress the SAR image. After that, the SWT is applied in the SAR image and the Sobel gradient operator is used to produce the Wavelet Gradient Information (WGI). According to the WGI, the module maximum is searched along the gradient direction as the internal wave edge feature. Further, the morphological transform, threshold technique and local contrast adjustment methods are applied to refine the edge extraction results. Experimental results by ERS-1, ERS-2 SAR internal wave oceanic surface images show that the algorithm keeps the internal wave information and suppress the noise effectively. It can process the 8000*8000 SAR image quickly for the method is easy to carry out. The algorithm avoids the complicate researching course in the adjacent scales and the internal wave feature detection is accuracy and integrity.

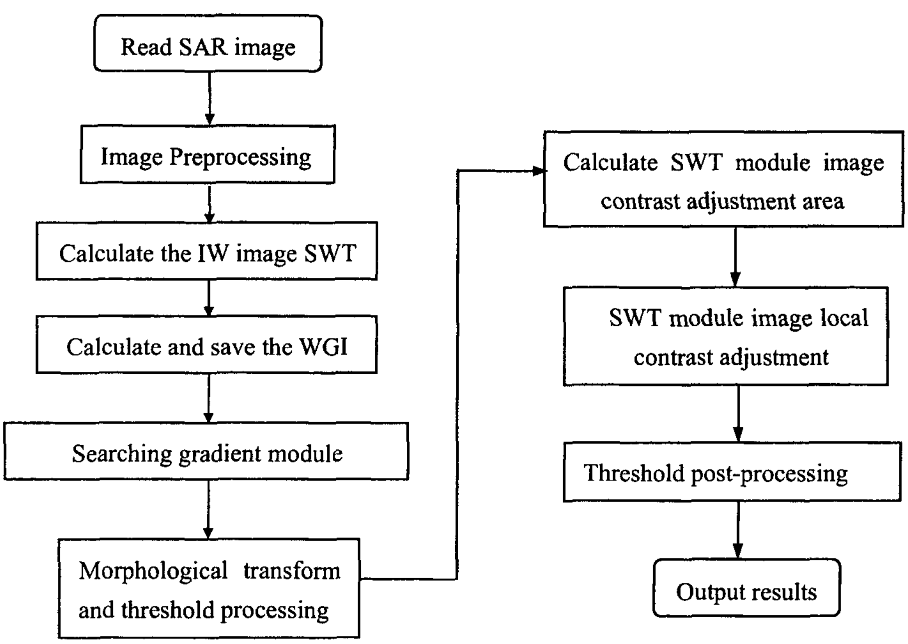

Fig.1. Chart of the internal wave feature extraction system

2. STATIONARY WAVELET TRANSFORM AND EDGE EXTRACTION PRINCIPLE

SWT presented by Nason and Silverman [16], which is widely used in the image processing. Nason and Silverman [12] gave the decomposition and reconstruction algorithm of the SWT in 1995. They apply appropriate high and low pass filters HFD and LFD to the signal data at each level to produce two sequences at the next level. The output of the filter does not down-sampling so as to the two new sequences each has the same length as the original sequence. Instead, the filters are modified at each level by padding them out with zeroes. Thus the representation is accordingly non-redundant and the total number of sample in the representation is equal to the total number of the image pixels. The decomposition frame is shown in Fig.2.

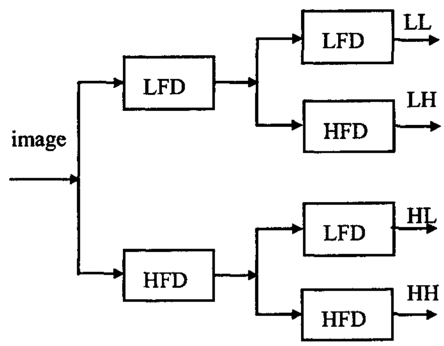

Fig.2. Decomposition frame of the SWT

According to the two dimensions separable discrete SWT the original image can be transformed into four pieces that are labeled as LL, LH, HL, and HH where LL denotes that horizontal and vertical directions have low frequencies, LH is the horizontal direction has low frequencies and the vertical one has high frequencies, HL is the horizontal direction has high frequencies and the vertical one has low frequencies and HH is both horizontal and vertical directions have high frequencies. The SWT has better denoising quality and better edge extracting capacity. In the image processing, it can process any arbitrary size of images, which is very important in the SAR internal wave detection.

Wavelet transform can detect local singular point so it is an excellent edge detection tool. The edge extraction principle based on the wavelet transform is as follows.

Supposing that there is a smooth function $\theta(x_1,x_2)$ and considering that the partial derivatives along x_1, x_2 directions of $\theta(x_1,x_2)$ as the basic wavelet functions which are shown in Eq.1.

$$\psi^{(1)}(x_1,x_2) = \partial\theta(x_1,x_2)/\partial x_1 \;,\; \psi^{(2)}(x_1,x_2) = \partial\theta(x_1,x_2)/\partial x_2 \tag{1}$$

$$\psi_a^{(1)}(x_1,x_2) = \frac{1}{a^2}\psi^{(1)}(\frac{x_1}{a},\frac{x_2}{a}) = \frac{\partial\theta_a(x_1,x_2)}{\partial x_1} \;,\; \psi_a^{(2)}(x_1,x_2) = \frac{1}{a^2}\psi^{(2)}(\frac{x_1}{a},\frac{x_2}{a}) = \frac{\partial\theta_a(x_1,x_2)}{\partial x_2} \tag{2}$$

Where, $\theta_a(x_1,x_2) = \theta(\frac{x_1}{a},\frac{x_2}{a})$ and a is the dilation of the wavelet transform.

For $\forall f(x_1,x_2) \in L^2(R^2)$, wavelet transform along x_1, x_2 direction are expressed in Eq.3.

$$WT^{(1)}f = f(x_1,x_2) ** \psi_a^{(1)}(x_1,x_2),\ \ WT^{(2)}f = f(x_1,x_2) ** \psi_a^{(2)}(x_1,x_2). \tag{3}$$

Wavelet Transform can be rewritten as Eq.4.

$$WT^{(i)}f = \frac{1}{a^2}\iint f(u_1,u_2)\psi^{(i)}(\frac{x_1-u_1}{a},\frac{x_2-u_2}{a})du_1du_2. \tag{4}$$

Thus the vector form of WT is defined as Eq.5.

$$\begin{aligned}\begin{bmatrix} WT^{(1)}f(a,x_1,x_2) \\ WT^{(2)}f(a,x_1,x_2)\end{bmatrix} &= a\begin{bmatrix}\frac{\partial}{\partial x_1}(f**\theta_a)(x_1,x_2) \\ \frac{\partial}{\partial x_2}(f**\theta_a)(x_1,x_2)\end{bmatrix} \\ &= a*grad[f(x_1,x_2)**\theta_a(x_1,x_2)] \\ &= a*grad[f^s(x_1,x_2)] = WTf(a,x_1,x_2)\end{aligned} \tag{5}$$

If $f(x_1,x_2)$ is the original image signal, $f^s(x_1,x_2)$ is the result after smoothing by $\theta_a(x_1,x_2)$. The wavelet transform coefficient $WT^{(1)}$ and $WT^{(2)}$ are the gradient messages of the gray image along the (x_1,x_2) direction. In our research, we adopt dyadic SWT so a is equal to $2^j\ (j \in Z)$. The gradient module and magnitude-angle pairs are expressed in Eqs.6-8.

$$\{Mod[WTf(2^j,x_1,x_2)], Arg[WTf(2^j,x_1,x_2)]\} \tag{6}$$

$$Mod\ [WTf\ (2^j,x_1,x_2)] = [|WT_{2^j}^{(1)}f|^2 + |WT_{2^j}^{(2)}f|^2]^{1/2} \tag{7}$$

$$Arg\,[WTf\ (2^j,x_1,x_2)] = tg^{-1}[\frac{WT_{2^j}^{(1)}f(2^j,x_1,x_2)}{WT_{2^j}^{(2)}f(2^j,x_1,x_2)}] \tag{8}$$

Mallat [14][15] has testified that the maximum of $Mod[WTf]$ is the edge of the image and the direction is vertical to the magnitude-angle $Arg[WTf(2^j,x_1,x_2)]$. The SAR image internal wave feature extraction algorithm is based on the principle.

3. EDGE EXTRACTION BASED ON THE WAVELET GRADIENT INFORMATION (WGI)

After preprocessing, we use the SWT to process the SAR internal wave image and get four pieces LL, LH, HL, and HH that have the same size as the original SAR image. In order to suppress the noise signal and at the same time maintain the feature of the internal wave, we decompose the SWT coefficient sub-band LL in certain level. Extract the sub-band LL, LH, HL in every lever transform to produce the wavelet Gradient Information (WGI) and search the internal wave edge message based on the WGI. Instead of the traditional gradient transform we use the Sobel gradient operator to get the WGI. The Soble gradient operators are defined as

$$H = \begin{bmatrix} 1 & 2 & 1 \\ 0 & 0 & 0 \\ -1 & -2 & -1 \end{bmatrix} \qquad V = \begin{bmatrix} -1 & 0 & 1 \\ -2 & 0 & 1 \\ -1 & 0 & 1 \end{bmatrix}.$$

The gradient direction is divided 8 fan-shaped averagely, which is shown in the Fig.3. According to the gradient module and the direction we defined we search the module maximum as the edge of the SAR internal wave image.

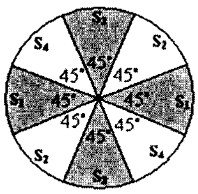

(i-1,j-1)	(i-1,j)	(i-1,j+1)
(i,j-1)	(i,j)	(i,j+1)
(i+1,j-1)	(i+1,j)	(i+1,j+1)

Fig.3. Sketch map of gradient direction segmentation and image pixel coordinate

Supposing that SWT_{LL} is the SWT LL sub-band coefficient, $SWGI_H$ and $SWGI_V$ are the horizontal and vertical directions gradient information respectively. The relations among them are expressed as Eq.9.

$$SWGI_H = SWT_{LL} * H, SWGI_V = SWT_{LL} * V \tag{9}$$

Where the "*" denotes the convolution operation. The gradient module matrix M and the magnitude-angle matrix θ are depicted in Eq.10.

$$M = \left[|SWGI_H|^2 + |SWGI_V|^2 \right]^{1/2}, \theta = arctg\left[SWGI_H / SWGI_V \right] \tag{10}$$

According to the magnitude-angle direction finding the module maximum, the searching strategy is expounded as follows.

(1) If $\theta(i,j) \in s_1$, $M(i,j) > M(i,j+1) \& M(i,j) > M(i,j-1)$;

(2) If $\theta(i,j) \in s_2$, $M(i,j) > M(i-1,j+1) \& M(i,j) > M(i+1,j-1)$;

(3) If $\theta(i,j) \in s_3$, $M(i,j) > M(i-1,j) \& M(i,j) > M(i+1,j)$;

(4) If $\theta(i,j) \in s_4$, $M(i,j) > M(i-1,j-1) \& M(i,j) > M(i+1,j+1)$.

From the above estimation, we take the module maximum $M(i,j)$ as primary election edge of the image. In order to reduce wrong maximum we set two threshold values Th and Tl. The estimate approach is as follows.

(1) If the $M(i,j) > Th$, $M(i,j) = 255$;

(2) If the $M(i,j) < Tl$, $M(i,j) = 0$;

(3) If $Tl < M(i,j) < Th$, we look for the neighboring area of 8 connection of the point (i,j). If there exist one or more than one point larger than Th the $M(i,j) = 255$ else $M(i,j) = 0$.

From the above analysis, we get the maximum points that manifest the image edges. In order to suppress the noise and effect of other oceanic feature in SAR image, we apply the morphological transform and threshold technique in post-processing.

4. THE POST-PROCESSING OF THE INTERNAL WAVE EXTRACTION

Mathematical Morphology is a powerful tool for image processing it has been used in a wide range of applications [17-20]. In binary morphology transform, there are two basic operations: dilation and erosion. The combination of dilation and erosion produces another morphological operation: opening and closing. They can be used in the image thinning by Hit-Miss operation.

There is non-internal wave information in the edge image after SWT and gradient module maximum searching. In order to extract the main internal wave feature, the morphological thinning algorithm is applied to the edge image and then estimate the non-internal wave line based on the internal wave length and shape information.

The thinning algorithm is as following. For each edge point, label the points in the 3×3 neighboring area as Fig.4. Each of the 9 points takes the value 1 if it is an edge point otherwise it takes the value 0. If all the four conditions listed in the paper are satisfied, then P1 is deleted [21]. The program flow chart is depicted in Fig 5.

Condition1: $2 \le NZ(P1) \le 6$;

Condition2: $Z0(P1) = 1$;

Condition3: $P2 \times P4 \times P8 = 0$ or $Z0(P1) \ne 1$;

Condition4: $P2 \times P4 \times P6 = 0$ or $Z0(P4) \ne 1$.

P3	P2	P9
P4	P1	P8
P5	P6	P7

Fig. 4. Labels of the points in the 8 neighboring area

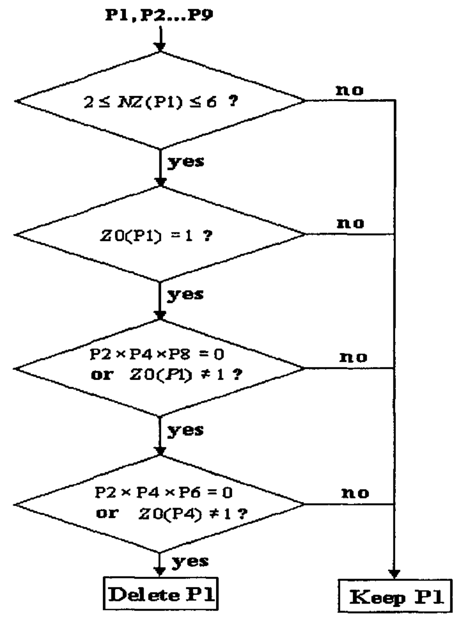

Fig. 5. Program flow chart of morphological algorithm

Where $NZ(P)$ is the number of edge points in the 8 neighboring points of P. $Z0(P)$ is the number of adjacent $< 0,1 >$ point pairs along the anticlockwise direction in the 8 neighboring points of P. The thinning processing will end when there is no edge points that satisfy the above four conditions.

Because the lines of the internal waves are the main lines in the edge image after thinning, the line whose length is smaller than a pre-defined threshold T is deleted. At the same time, determining the internal wave area according the internal wave edge and enhance the SWT module image locally so that the main internal wave features can be extracted more accuracy and integrity. In the image process because of some reasons it may be exist continue black strip area, which has not imaging successfully. It appears as straight-line edge in the image and we delete them based on this feature in the post processing.

5. EXPERIMENTS AND ANYLYSIS

Experiments have been done to show the performance of our algorithm.Fig.6 (a) and Fig.7 (a) are the ERS-2, ERS-1 SAR image (8000*8000 pixels), which reflect the large amplitude internal wave and internal soliton near the east of Dongsha island ocean area.

Fig.6 (a) is the image mode ERS-2 SAR internal wave image with 100km swath width observed on June 12, 1998. There exists very sharp westward propagating internal wave striation. Fig.6 (b) is the Fig.6 (a) SWT module image after preprocessing, Fig.6 (c) is the module maximum image searched by global threshold value, Fig.6 (d) is the result by morphological thinning and threshold technique, Fig.6 (e) is the local module value contrast adjusting result by the area of Fig.6 (d), Fig.6(f)is the Fig.6(e) segment result by threshold value, Fig.6(g)is the internal wave extraction result after deleting the isolate point and short non-internal wave line.

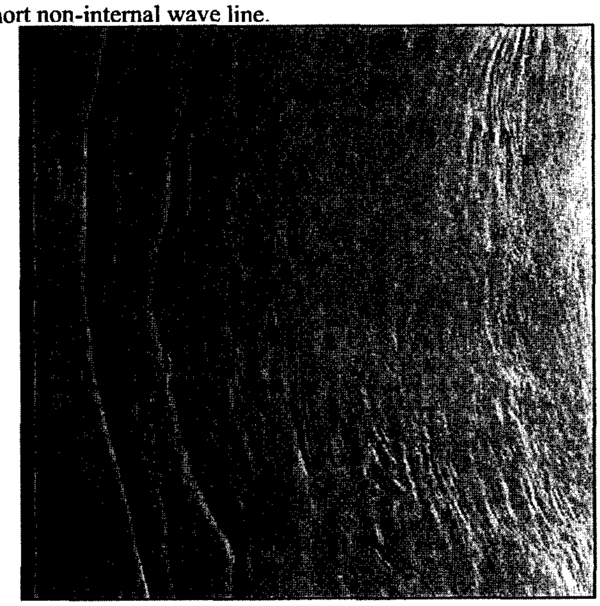

Fig.6 (a) ERS-2 (21.35N, 117.767E) SAR internal wave image

Fig.6 (b) SWT module image

Fig.6 (c) Module maximum result based on SWT

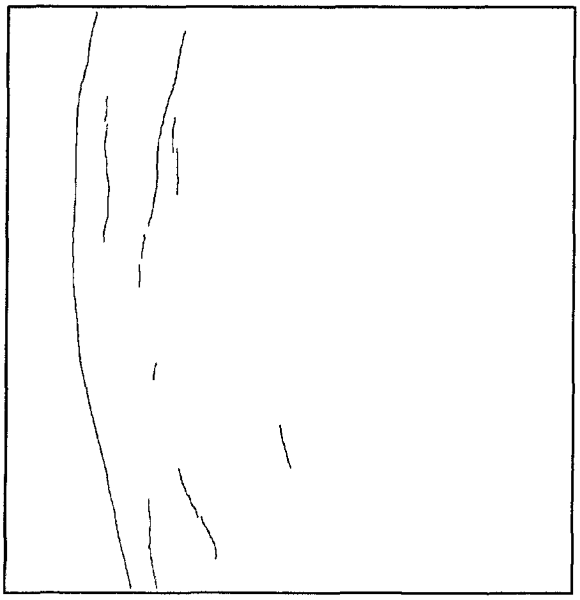

Fig.6 (d) Result by morphological thinning and threshold

Fig.6 (e) Module local contrast enhanced image

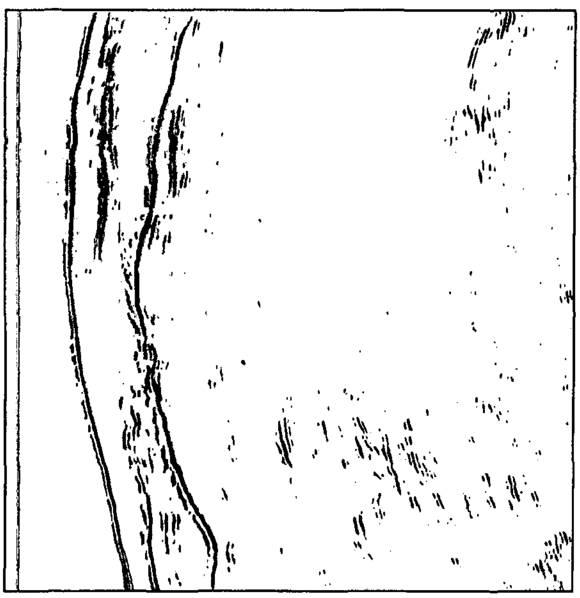

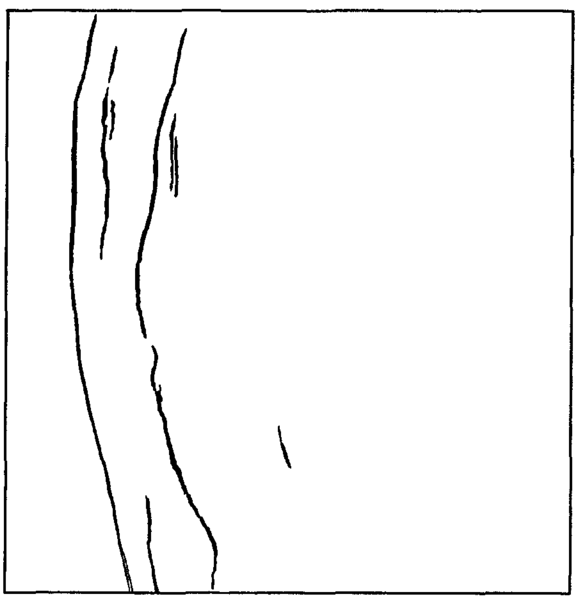

Fig.6 (f) Result of Fig.6 (e) processed by threshold result

Fig.6 (g) SAR internal wave extraction

Fig.7 (a) is the ERS-1 image with the same mode as ERS-2 observed on June 25, 1995. From the SAR image we can see internal wave, internal soliton, swallow sea terrain and ocean wave. According to the method of Fig.6, the internal wave extraction result is shown in Fig.7 (b).

From the experimental results, it can be seen that the internal wave feature are well extracted by the proposed SWT algorithm and the computer detection method. The running time is only 15s to the 8000*8000 pixels SAR internal wave image

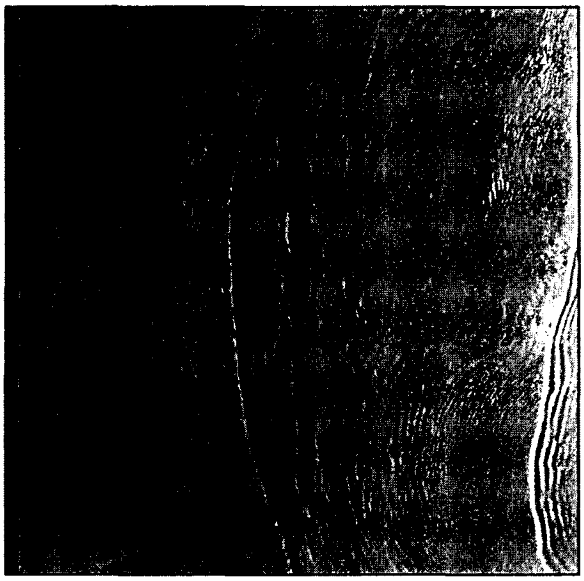

Fig.7 (a) ERS-1 (N 21.35, E 116.33) SAR internal wave image

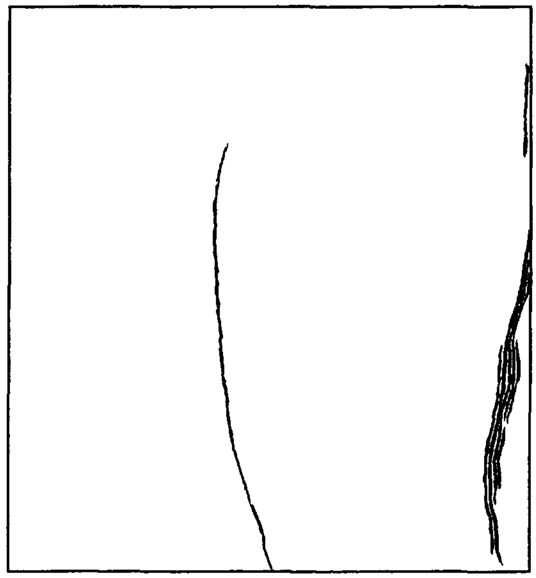

Fig.7 (b) SAR internal wave extraction result

6. DISCUSSION

In this paper, an IWFE algorithm is proposed based on the SWT and the process steps are descried in detail . The results show that IWFE algorithm can give us a better result for the internal wave extraction. In the algorithm we process the SWT's low frequency coefficients so that its robust to noise is better than traditional edge operators. The input image size is not limited which is very important to the information integrality and the accuracy in the SAR IWFE. Morphological transform, threshold technique and gray contrast adjustment were used and shown efficient in the SAR internal wave feature refinement. The algorithm can be implemented easily and has a better performance speed which is more practical.

In SAR image, discontinuous gray intensity could be caused by different oceanic wind field, temperature and current, hence this can be used to detect front edges. However, firstly, in IWFE algorithm, the internal wave edge is extracted as double line, the front edge only appears as single line though. Moreover, their processing threshold values will be different due to the weak gray intensity contrast changing of those fronts in SAR images .

Oceanic internal wave features in SAR image are complicated and diversiform. Next, lots of different SAR images will be used to test this algorithm, especially those intersecting and weak bright and dark contrast internal wave SAR images in the near future.

7. REFERENCE

1. Jordan, R. L., The Seasat-A Synthetic-Aperture Radar System. IEEE J. of Oceanic Eng., Vol. OE-5, 154~164, 1980.
2. Alpers, W., Theory of Radar Imaging of Internal Waves, Nature, Vol.314, 245~247,1985.
3. Liu A. K, Apel J. R, Holbrook J. R, Nonlinear internal wave evolution in the Sulu Sea Journal of Physical Oceanography, Vol, 15, 1613~1624,1985.

4. Du Tao, G.H.Fang and X.H.Fang, A Layered Numerical Model for the Generation and Propagation of Internal Tides over Continental Slope, China. J. Oceanol. Limnol. (English), I. Model Design Vol. 17(2), 125~131,1999.

5. Zeng, K., Alpers, W, Generation of internal solitary waves in the Sulu Sea and their refraction by bottom topography studied by ERS SAR imagery and a numerical model, International Journal of Remote Sensing Vol.25, No.7-8, 1277~1281, 2004.

6. Ming-Xia He, Werner Alpers, and Roland Doerffer, Overview of Dragon Project ID 2566: Oceanography from Space - Internal Waves, Ocean Surface Waves, Shallow Water Topography, Ocean Color, and Kuroshio Current, 2005 Santorini Symposium, Greece.

7. Ming-Xia He, Kan Zeng, Alpers, W., et al., The Distribution of Internal Wave in the East China Sea and Yellow Sea Studied by Multi-sensor Satellite Image, IGARSS 2005.

8. M. K. Hsu, A. K. Liu, and C. Liu, A study of internal waves in the China Seas and Yellow Sea using SAR, Continental Shelf Research, Vol. 20, 389-410, 2000.

9. A. K. Liu, Y. S. Chang. , M. K. Hsu, et al., Evolution of nonlinear internal waves in the East and South China Seas, J. Geophys. Res., Vol.103, 7995-8008, 1998.

10. Rodenas, J.A., Garello, R., Internal wave detection and location in SAR images using wavelet transform, IEEE Trans. on Geoscience and Remote Sensing, Vol.36, No.5, 1494 ~ 1507, 1998.

11. Lee J.S., Speckle suppression and Analysis for Synthetic Aperture Radar Images, Optical Engineering, Vol.25, No.5, 636-645, 1986.

12. Lee J.S., Refined filtering of image noise using local statistics, Comput. Graph. Image Process, Vol.15 No.14, 380-389, 1996.

13. Grossman A., Morlet J., Decomposition of Hardy functions into square integrable wavelets of constant shape, SIAM J. Math., Vol.15, 723~736, 1984.

14. Mallat S., A theory for multiresolution signal decomposition: The wavelet Represention, IEEE Trans.On Patter Analysis and Machine Intelligence, Vol.11, No. 7, 674~693, 1989.

15. Mallat S., Zhong S., Characterization of signals from Multiscale Edges, IEEE Trans. On Patter Analysis and Machine Intelligence, Vol. 14, No.7, 710-732, 1992.

16. Nason G. P., Silverman B. W., The stationary wavelet transform and some statistical applications in wavelet and statistics, Lecture notes in statistics. A. Antoniadis Ed. Berlin: Spinger Verlag, 281-299, 1995.

17. Henk J. A., Heijmans M., Theoretical aspects of Gray-Level morphology, IEEE Trans. on Pattern Analysis and Machine Intelligence, Vol.13, No.6, 568~582, 1991.

18. Jones R., Svalbe I., Morphological filtering as template matching, IEEE Trans. on Pattern Analysis and Machine Intelligence, Vol. 16, No. 4, 438~443, 1994.

19. Jones R., Svalbe I., Algorithms for the decomposition of Gray-Scale morphological operations, IEEE Trans. on Pattern Analysis and Machine Intelligence, Vol.16, No.6, 581-588,1994.

20. Schonfeld D., Goutsias J., Optimal morphological pattern restoration from noisy binary images, IEEE Trans. on Pattern Analysis and Machine Intelligence, Vol.13, No.1, 14~29,1991.

21. He B., Ma T., et al., Digital Image Processing with Visual C++, Posts & Telecommunications Press of China, 386~393, 2002.

OCEAN INFORMATION ANALYSIS AND COMPARISON OF MERIS WITH COCTS DATA —TAKING LIAODONG BAY AS AN EXAMPLE

FU Jun[1, 2], ZHANG Jie [2, 3], CUI Ting-wei [2], MA Yi [2, 3]

[1]Ocean University of China, Yu-Shan road, Qingdao, Shandong, P.R.C., 266003, fujun@fio.org.cn
[2]First Institute of Oceanography, S.O.A., Xianxialing Road, High-Tech Park, Qingdao, Shandong, P.R.C., 266061, cokkiecui@sohu.com
[3]Key Laboratory of Marine Science and Numerical Modeling, S.O.A., Xianxialing Road, High-Tech Park, Qingdao, Shandong, P.R.C., 266061, mayimail@fio.org.cn

ABSTRACT

MERIS data are compared with COCTS data by the methods of Histogram analysis, principal component analysis, correlation analysis and image visual interpretation in Liaodong Bay of China. These data were acquired on October 17th, 2003. The application potential of qualitative analysis about ocean color is discussed. It is shown that both of MERIS and COCTS data can be used for large scale information extract of ocean color. In addition, the result also indicates that the inversion potential by using MERIS data is better than that of COCTS data.
Key words: Liaodong Bay, MERIS, COCTS, spectral characteristics, ocean color

1. INTRODUCTION

Remote sensing can provide different data of electromagnetic wave spectrum bands in form of different spatio-temporal, wave spectral and radiated resolution. Due to variety of imaging mechanism and restriction of technique, any single remote sensing image cannot reflect the whole feature of the object. Moreover, the applied range is limited to almost all single images.

Numerous works have been devoted to spectroscopic analysis of remote sensing images in many countries. The image information characters of different sensors were extracted and optimal combinations of wave band were researched in different regions based on different applied fields.

MERIS and COCTS were loaded by America launched SEASAT and Chinese HY-1 satellites respectively. MERIS-RR is a reduce resolution product, and its resolution is 1.2 km. The resolution of COCTS data is 1.1 km. Though the spatial resolution of MERIS-RR and HY-1 COCTS data is finite, it behaves obvious superiority in investigation of large scale ocean color.

Based on the experiences of color remote sensing application, the color composed image which includes three wave bands and its central wave lengths are 650nm, 550nm and 440nm respectively can fully express the information of ocean color. By comparing MERIS-RR data of wave band 7, 5, 2 and COCTS data of wave 6, 5, 2 in this article, we discussed the feasibility of the application of two kinds of data to ocean color by qualitative analysis.

2. DATA AND RESEARCH REGION

In this article, we selected the synchronized data of MERIS and COCTS in Liaodong Bay of Bohai. MERIS data were acquired by reduced resolution.

Proc. 2005 Dragon Symposium "Mid-Term Results", Santorini, Greece
27 June – 1 July 2005 (ESA SP-611, January 2006)

2.1. MERIS-RR

MERIS (Medium Resolution Imaging Spectrometer) is one of the payload components of ESA's Envisat-1, which was launched in March 2002. MERIS is a 15-band, programmable imaging spectrometer, which allows for changes in band position and bandwidths throughout its lifetime [2]. It is designed to acquire data at variable bandwidth of 1.25 to 30 nm over the spectral range of 390-1,040 nm [3]. Data will be acquired at 300 m or 1,200 m spatial resolution over land, thus vegetation can be monitored at regional to global scales.
A reduce resolution MERIS level 1b data set for the Liaodong Bay was obtained on 17 October 2003. Specifications of the spectral bands are given in Table 1.

2.2. HY-1 COCTS

The China first Ocean satellite (HY-1) is an experimental and operational satellite for detecting ocean color and sea surface temperature. It was successfully launched on 15 May, 2002. The payloads on satellite include a 10-band Chinese Ocean Color and Temperature Scanner (COCTS) and a 4-band CCD imager.
COCTS has a function to detect the amount of chlorophyll and dissolved substances in the water, and temperature distribution. The data of COCTS will be used to get the information of ocean conditions for fishery and environment monitoring. There are 8-channel visible and near-infrared band and 2-channel thermal infrared band with the spatial resolution of 1.1km.
The COCTS used in this paper was acquired on the same time with MERIS data of Liaodong Bay. Specifications of the spectral bands are still given in Table 1.

Table 1. Main specifications of MERIS-RR and COCTS

	MERIS-RR			COCTS		
Band number	Band centre /nm	Bandwidth /nm	Resolution /km	Band centre /nm	Bandwidth /nm	Resolution /km
1	412.5	9.9		412	20	
2	442.4	10.0		443	20	
3	489.7	10.0		490	20	
4	509.7	10.0		520	20	
5	559.6	10.0		565	20	
6	619.6	10.0	1.2	670	20	1.1
7	664.6	10.0		755	20	
8	680.9	7.5		855	20	
9	708.4	10.0		1085	55	
10	753.5	7.5		1195	55	
11	761.6	3.7				
12	778.5	15.0				
13	864.8	20.0				
14	884.8	10.0				
15	899.8	10.0				

2.3. Research region

The Bohai Sea is a semi-enclosed sea situated in the northwest part of the Yellow Sea, and Liaodong Bay lies in the north of Bohai Sea. Liaodong Bay has high biological productivity and behaves bio-diversity. In the coastal area of Bohai Sea, there are many industrial cities, such as Dalian and Jinzhou, etc. This area is a part of large scale economically developing zone in China.

The water quality in majority areas of Liaodong Bay belongs to typical Case II water. It is difficult to inverse the components in ocean color research field.

3. COMPARE OF MERES DATA WITH THOSE OF COCTS

3.1. Histogram analysis

Histogram analysis describes statistical distribution of pixel numbers with certain radiance. Histograms of MERIS and COCTS image in the same bands are given in Fig.1.

From Fig. 1, we can see that MERIS and COCTS images have similar histogram shape: histograms of the first two bands have only one peak and histogram of the last band has two peaks. Also COCTS data have a wider radiance distribution range compared with that of MERIS. Thus, it can be concluded that COCTS data have much more information than that of MERIS data, the reason is that band width of COCTS data is 2 times of MERIS.

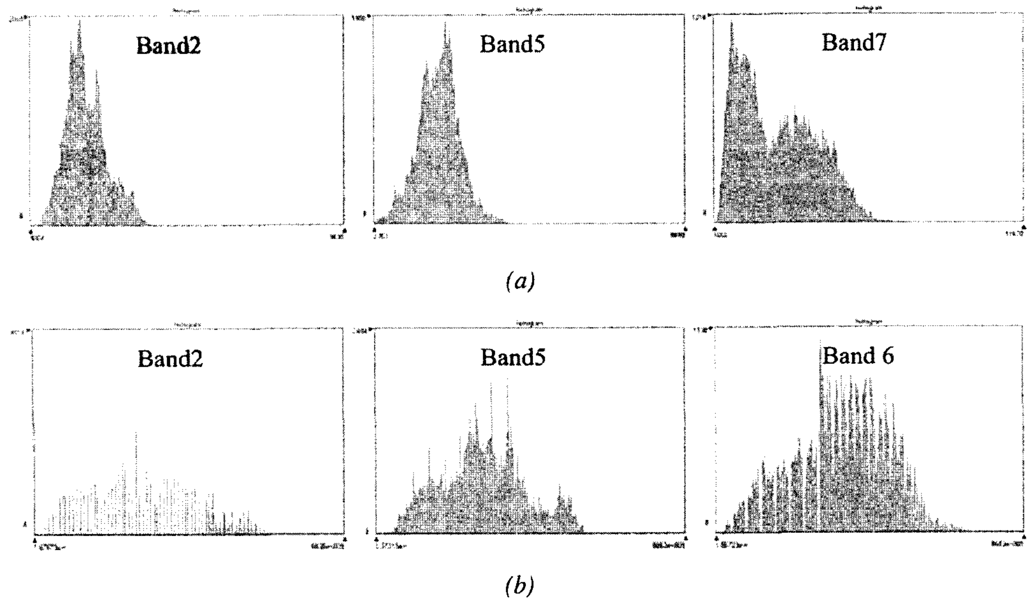

Fig. 1. Histogram of MERIS (a) and COCTS (b)

3.2. Statistical analysis

Mean vector characterizes the mean reflectance density of image pixels and standard deviation describes the dispersion degree of radiance for different pixels in the image, i.e. the radiant difference among the different objects. Statistical analysis results of MERIS and COCTS data after being normalized are shown in Table 2.

Table 2. Statistical information of the MERIS and COCTS data

	MERIS			COCTS		
	665nm	560nm	442nm	670nm	565nm	443nm
Mean value	106.45	132.00	119.06	138.04	122.64	118.85
Standard deviation	71.15	55.22	60.37	64.11	64.56	67.96

From Table 2, we can see that MERIS data of 665nm has the highest value of Standard deviation, which means that in this band the radiance dispersion degree of different objects is highest. This is probably due to the largest information amount and the most significant objects differences. COCTS data of 565nm band has the richest information.

Standard deviations of COCTS data associated with 443nm, 565nm and 670nm are similar in absolute value. However, Standard deviations of MERIS data have relative significant difference. We can infer that MERIS bands combination for false color composite would have better ability to characterize image details.

3.3. Correlation analysis

Image information quantity of single band can be expressed by its histogram, mean value and standard deviation, and that of RGB composite image not only depends on radiance scope of single band image, but also relates to three band images' correlation degree. Correlation coefficient is a statistical quantity denoted redundant information quantity between two band images. Table 3 and 4 are the correlation coefficients of three MERIS bands and three COCTS bands data respectively in Liaodong Bay.

Table 3. Correlation analysis results for the MERIS bands

Band	Band 7	Band 5	Band 2
Band 7	1.00		
Band 5	0.66	1.00	
Band 2	0.01	0.60	1.00

Table 4. Correlation analysis results for the COCTS bands

Band	Band6	Band 5	Band2
Band6	1.00		
Band 5	0.37	1.00	
Band 2	0.05	0.84	1.00

Correlation analysis results show that: correlation coefficient of MERIS 7th and 5th band of MERIS is greater 0.39 than that of COCTS 6th and 2nd band; correlation coefficient of MERIS 7th and 2nd band close to that of COCTS 6th and 2nd band with difference 0.04; correlation coefficient of MERIS 5th and 2nd band is less 0.24 than that of COCTS 5th and 2nd band. As a whole, superposition information quantity of MERIS bands is less than that of COCTS.

According to histogram, statistical and correlation analysis, we find that information quantity of MERIS composite image is close to that of COCTS on the whole.

3.4. Comparison analysis of images

In Fig. 2, there are two false color composite images of MERIS and COCTS respectively, here the red band is selected 665nm, the green one is 560nm and the blue one is 442nm. By visual interpretation of two images, we can find that

(1) The spectral characteristics of 7th, 5th and 2nd bands of MERIS is similar to that of 6th, 5th and 2nd bands of COCTS. For ground objects (such as ocean color and vegetation) recognized by MERIS, it can be distinguished by COCTS.

(2) Although the spatial resolution of COCTS image is higher than the one of MERIS reduced image, the definition of COCTS image is lower than the one of MERIS reduced image. In COCTS image, color lever is not enough, and there are some mosaic areas. However in MERIS image, the texture of ground objects is fine and smooth.

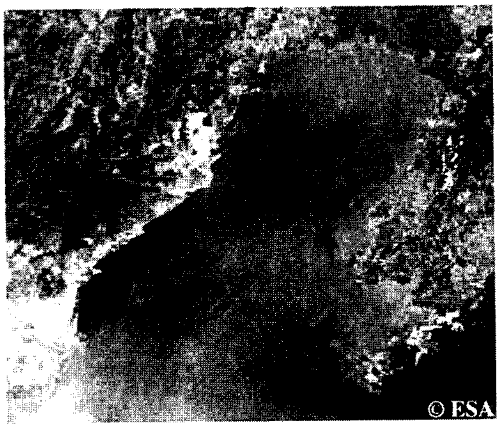

(a) MERIS image with R7,G5 and B2

(b) COCTS image with R6,G5 and B2

Fig. 2. False color composite image of Liaodong Bay

4. CONCLUSION AND DISCUSSION

According to histogram, statistical and correlation analysis, it can be seen that information quantity of MERIS composite image is close to that of COCTS on the whole. The resolution and definition of COCTS data are affected by their instability and striping, even if COCTS data has higher resolution than MERES data.

The result of visual interpretation indicated that both MERIS and COCTS data can be used in the information extract at large scale, and application potential of MERIS data is better than that of COCTS.

From the two aspects of spectral characteristics and visual interpretation effect, this paper discussed the application capability of MERIS data in ocean color inversion. In future study, MERIS data with full resolution should be applied, and a contrastive analysis should be carried out. Only by this means, can the capability of MERIS data in measuring ocean color be exerted.

5. ACKNOWLEDGEMENTS

This research was supported by the Dragon Project through id 2566 and by the High-tech Research and Development Program of China through grant 2002AA634020.

6. REFERENCES

1. Zou Y. R., Wang Q. M. et al. Information Contents and Correlation Analysis for HY-1/COCTS Bands, *Advances in Marine Science*, vol. 23, 70-77, 2005.
2. Clevers J. and Bartholomeus H., Land Cover Classification With the Medium Resolution Imaging Spectrometer (MERIS), *EARSeL Proceedings*, vol.3, 354-362, 2004.
3. Rast M. and J. L. Bezy, ESA's Medium Resolution Imaging Spectrometer (MERIS): Mission, System and Applications. *SPIE*, vol.1298: 114-126, 1999.

RETRIEVAL OF OCEANIC CONSTITUENTS FROM MERIS IMAGERY OVER CASE II WATERS WITH ARTIFICIAL NEURAL NETWORK

Tinglu Zhang[(1)], **Jürgen Fischer**[(2)], **Mingxia He**[(1)]

[(1)] *Ocean Remote Sensing Laboratory of Ministry of Education of China*
Ocean Remote Sensing Institute
Ocean University of Qingdao, 5 Yushan Road, Qingdao 266003, China
zhangtl@orsi.ouc.edu.cn

[(2)] *Institut für Weltraumwissenschaften*
Freie Universität Berlin
Carl-Heinrich-Becker-Weg 6-10, 12165 Berlin, Germany

ABSTRACT: In this study, an ANN-based algorithm is developed for the retrieval of oceanic constituent concentrations (CHL, SPM and CDOM) from MERIS imagery over Case II waters. The algorithm is derived from radiative transfer simulations and subsequent application of Artificial Neural Network (ANN) techniques. In the simulations of data set, the aerosol models characterized by Asian aerosols are considered. The performance of this algorithm is assessed by applying it to the synthetic data sets containing the different aerosols mixtures in the atmosphere. The results show that this algorithm has the capability to deal with various atmospheres from weakly to strongly absorbing aerosols. The algorithm is applied to MERIS images taken over the China Seas, the results need to be further validated with the simultaneous *in-situ* measurements.

1. INTRODUCTION

There are two strategies to derive oceanic constituents from the signal of ocean colour sensor at top of atmosphere (TOA), a one-step method and a two-step method. For the traditionally used two-step method, the water leaving radiance (or reflectance) is firstly derived from the signal at TOA (this procedure is called 'atmospheric correction'), and then oceanic constituents are retrieved from water leaving radiance (or reflectance). For the one-step method, oceanic constituents are directly derived from the signal at TOA. The one-step method assumes that radiative transfer in the ocean and atmosphere is coupled. The oceanic constituents and aerosol properties are simultaneously derived from satellite measurements at TOA by using the entire spectrum available to ocean colour instruments. It has been recognised that the one-step method has good performance for dealing with strongly absorbing aerosols [1][2].

The atmospheric correction algorithms which are commonly used are based on 'the black pixel assumption' *[3][4][5]*. These algorithms were primarily designed for clear deep ocean areas. Unfortunately, the algorithms developed for applications to clear ocean waters cannot be easily modified to retrieve water leaving radiance from remote sensing data acquired over the coastal environments.

Besides, even in the open ocean, the commonly used algorithms for atmospheric correction fail in the presence of strongly-absorbing aerosols [6][2][7]. If the aerosol is strongly absorbing, due to soot or dust component, the visible reflectance can not be derived from the NIR reflectance [6]. Furthermore, the strongly absorbing aerosols (soot or dust) are coloured, i.e., their absorption is a function of wavelength [8]. Even if it was possible to estimate the absorption characteristics of these strongly absorbing aerosols in the NIR, the absorption in the visible could not be obtained by extent. *Gordon et al.* [7] proposed a one-step algorithm to simultaneously determine aerosol properties and pigment concentration in Case I waters, which uses all the spectral bands of the sensor and can be applied to deal with weakly or strongly absorbing aerosols. *Chomko and Gordon* [9] and *Chomko et al.* [10] further extended this method. The look-up table or optimisation procedure was employed to retrieve the desired parameters in these studies. The limit of these processing methods is slowly computing, and not well suited to be used as an operation algorithm.

In recent years, Artificial Neural Networks (ANN) have been increasingly applied to remote sensing data from ocean observing instruments, among those scatterometers and ocean colour sensors [11][12][13][14][15]. ANN techniques are well suited for solving non-linear problems [11]. They may be used to approximate the non-linear relationship between observations and target parameter(s) without explicitly knowing their direct functional dependence. Neural networks have the ability to generalize in the face of noisy data [14][15]. Furthermore, although the training of the ANN requires considerable computational effort, its application is very fast. Therefore, ANN techniques are a promising method to derive oceanic constituents from ocean colour measurements.

Proc. 2005 Dragon Symposium "Mid-Term Results", Santorini, Greece
27 June – 1 July 2005 (ESA SP-611, January 2006)

The objective of this study is to develop a scheme for the retrieval of oceanic constituents from ocean colour measurements at top of atmosphere with the one-step method. The scheme employed in this study is derived from Radiative transfer calculations (RTC) in atmosphere-ocean system and subsequent application of Artificial Neural Network (ANN) techniques.

2. SYNTHETIC DATA

The synthetic data set used for the training of ANN was created using the radiative transfer model *MOMO* [16]. The inputs required for radiative transfer simulations: Inherent Optical Properties (IOPs) and vertical distributions of the constituents in ocean and atmosphere, are described in the following subsections.

2.1. Atmosphere

The following atmospheric constituents are considered: air (molecular scattering) and aerosols (scattering and absorption). Other atmospheric constituents (clouds, absorbing gases, rain) are neglected.

The vertical profile of molecular scattering is taken from *Elterman* [17]. The total optical thickness at a specific pressure p is computed from the approximation given by *Hansen and Travis* [18].

Six basic constituents of aerosols are used in this study. Based on the above basic constituents, five aerosol models have been defined (listed in Table 1). The vertical distribution of the aerosols is assumed as depicted in Table 1.

Table 1 Aerosol models used in this study

Aerosol model	Constituent	Vertical distribution	Reference
Maritime	Rural aerosol mixtures (70% water soluble, and 30% dust-like particles) Oceanic	0-2 km	[19]
Continental	Water soluble Dust-like Soot	2-12 km	[20]
Dust	Asian dust	2-12 km	[21]
Soot	Soot	0-2 km	[20]
H_2SO_4	75% solution of sulphuric acid in water	12-50 km	[20]

2.2. Water

In this study, three optically significant constituents CHL, SPM and CDOM are considered. Their IOPs models are listed in Table 2. The IOPs of sea water as required for the RTC can be obtained for given the concentrations of oceanic constituents. The following assumptions for the radiative transfer simulations in ocean are made: (1) no vertical stratification of the ocean; (2) the ocean is of infinite depth, (3) no inelastic scattering inside the water body (*i.e.* no Raman scattering, no chlorophyll-a fluorescence, no CDOM fluorescence).

2.3. Sea Surface State

The rough sea surface is considered. The effects of the air-sea interface on the light field are introduced in the radiative transfer simulations by applying the statistic model of the wave surface distribution by *Cox & Munk* [22], assuming a gaussian distribution of waves and a variable wind speed. The wind direction is not considered.

2.4. Range of wavelength

The wavelengths used in this study are the same as MERIS's wavelengths, but the following wavelengths are not included: 681.25 nm (chlorophyll fluorescence peak), 753.75 nm (cloud), 760.6 nm (O_2 absorption), 865 nm (water vapour reference), and 900 nm (water vapour absorption).

2.5. RT Simulations

The concentrations of the oceanic constituents for the RT simulations were selected according to the procedures described by Zhang [23]. The optical thickness of the aerosols, the pressure at sea level, as well as the wind speed was selected randomly within the defined ranges.

Based on the above strategies, simulations of the remote sensing reflectance at the top of atmosphere were made.

2.6. Creation of ANN Training Data Set

Following the simulation strategy described in section 2.5, the spectra which correspond to different combinations of oceanic and atmospheric constituents and different observation geometries are simulated. These spectra are used for ANN training.

Through adding noise to synthetic training data, the robustness of the trained ANN with respect to noisy input data is increased. In the present study, measurement errors exist more or less in all input parameters, e.g., radiometric calibration errors [4]. Thus, it is necessary to add the appropriate noise to the data set used for the training of the ANNs to resist these measurement errors.

Table 2 Parameterisation of inherent optical properties of pure sea water and constituents of Case II waters.

Constituents	IOP	Model / Measurement	Reference
Pure sea water	Absorption	Directly measured	[24]
	Scattering	$b_w(\lambda) = 0.00288(\frac{\lambda}{500})^{-4.32}$	[25]
	Phase function	$p_w(\lambda) = 0.06225(1+0.835\cos^2\theta)$	[25]
Particulate matter	Absorption	$a_{p1}(\lambda) = A_{ap}(\lambda)[Chl]^{B_{ap}(\lambda)}$	[26]
		$a_{p2}(\lambda) = a_{p2}(443)e^{-Sp(\lambda-443)}$, $a_{p2}(443) = A_{p2} < SPM >^{B_{p2}}$, S_p=0.0122, A_{p2}=0.0216, B_{p2}=1.0247	[27]
	Scattering	$b_p(\lambda) = A < SPM >$, A=0.5	[27]
	Back scattering probability	$\tilde{b}_b = f(r,\lambda)$	[23]
CDOM	Absorption	$a_y(\lambda) = a_y(443)e^{-S_y(\lambda-443)}$, S_y=0.0176	[27]

In order to reduce the complexity, a Rayleigh scattering correction was applied to the reflectance at the top of atmosphere. Here, no interaction between aerosol scattering and Rayleigh scattering was assumed. The algorithm for the Rayleigh scattering correction uses an ANN trained with radiative transfer calculations.

3. ANN-BASED ALGORITHM FOR RETRIEVAL OF THE CONSTITUENTS

3.1. Architecture of the ANN for Retrieval of the Constituents

In the present study, Multi-Layer Perceptrons (MLPs) ANN are used for the retrieval of the oceanic constituents from TOA data. The MLP used within this study consists of three layers: input layer, one hidden layer and output layer. A bias parameter is added both to the input layer and to the hidden layer.

The retrieval of the oceanic constituents is based on the information contained in 15 parameters: Rayleigh-corrected remote sensing reflectances in 10 spectral channels at TOA: Rrs (412), Rrs(443), Rrsp(490), Rrs(510), Rrs(560), Rrs(620), Rrs(665), Rrs(709), Rrs(779), Rrs(885), wind speed, as well as four geometric parameters.

A principal component analysis (PCA) was used to decorrelate all input parameters.

The output layer consists of 4 neurons which correspond to three oceanic constituents concentrations (CHL, SPM and CDOM) and total aerosol optical thickness at 550 nm. The hidden layer consists of 50 neurons.

3.2. Performance of the ANN-based Algorithm with Simulated Data

3.2.1. Performance with respect to the training data

40000 samples which have been generated according to the procedure described in Section 2.6 were used to train the ANN. The ANN-derived parameters were compared to the corresponding parameters used as input for the radiative transfer simulations. The calculated RMSE and Pearson's correlation coefficient are depicted in Fig. 1. As shown in the figure, the inversion for the four parameters is successful with regard to the simulated training data.

3.2.2 Performance with respect to the test data

In order to examine the performance of ANN-based algorithms for various atmospheric studies which may occur in the real environment, seven test data sets which correspond to different aerosol mixtures in the atmosphere were simulated (listed in Table 3). The inherent optical properties of the oceanic constituents used for simulations of test data sets are the same as used for the simulations of the training data set. Each test data set consists of 500 combinations of concentrations of three oceanic constituents, optical thickness of aerosols, air pressures, as well as wind speeds. The trained ANN was applied to these seven test data sets. The desired parameters:

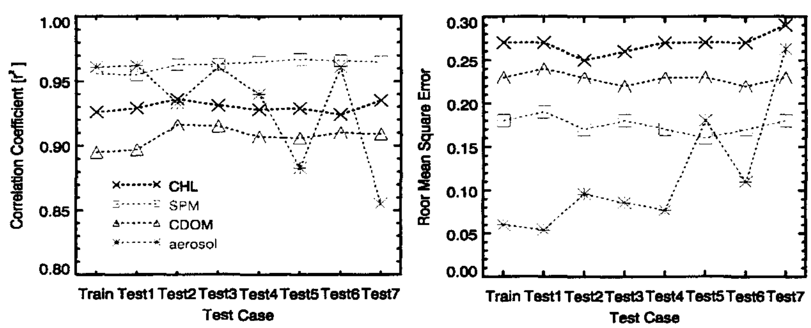

Fig. 1 Comparison of the performance of the ANN-based algorithm for different test data

CHL, SPM, CDOM and $\tau_a(550)$ are derived. The calculated RMSE and Pearson's correlation coefficient are also depicted in Fig. 1. Based on these results, the following conclusions can be drawn:

(1). With the trained ANN, the three oceanic constituents concentrations can be successfully derived from simulated reflectances at TOA for atmospheres ranging from weakly to strongly absorbing aerosols.

(2). With the trained ANN, the total optical thickness can be successfully derived for most cases except for TEST5 and TEST7. For both TEST5 and TEST7, the derived $\tau_a(550)$ is underestimated. TEST5 represents the most strongly absorbing aerosols, and TEST7 (Urban aerosol) is not included in the simulations of training data set. Although the retrieval of the total optical thickness for these two cases has a large error, it does not significantly impact the retrieval of oceanic constituent concentrations.

4. APPLICATION TO THE MERIS IMAGERY OVER THE CHINA SEAS

MERIS (Medium Resolution Imaging Spectrometer) has been launched on board the earth observation satellite ENVISAT on March 1, 2002. It has the following main specifications: spatial resolution of 300 m in full resolution mode, revisit period of 2-3 days, 15 programmable spectral bands with high radiometric sensitivity. These specifications are very suitable for monitoring water properties in coastal waters.

The MERIS images over the China Seas were selected to test the ANN-based algorithm. The China Seas belong to Case II waters. The China Seas are greatly influenced by the discharge of Yellow River and Yangzi River. These two rivers are famous for their high SPM concentration: SPM values can exceed 100 mg/m^3 at the estuary of the two rivers [28][29][30]. Besides, aerosols over the China Seas are characterised by their high variability in type and concentrations because of the presence of Asian dust particles as well as soot which originates from the main land of China [21][5].

Two MERIS scenes were selected: One scene of the Bohai Sea and Yellow Sea for May 5, 2004 (Fig. 2a), and one scene of the eastern China Sea for Feb. 15, 2004(Fig. 2b). The ANN-based algorithm described in Section 3 was applied to these two selected images. The pigment concentration, SPM concentration, CDOM absorption coefficient at 443 nm, and total optical thickness of aerosols at 550 nm have been calculated. The results are shown in Fig. 3 and 4 for the yellow Sea and the Eastern China Sea, respectively.

Table 3: Aerosol mixtures for testing the performance of the trained ANN

Test Data	Aerosol	Vertical Profile	Test Data	Aerosol	Vertical Profile
Test1	Maritime Soot Continental Asian dust H2SO4	0~2 km 0~2 km 2~12 km 2~12km 12~50 km	Test5	Maritime Soot H2SO4	0~2 km 0~2 km 12~50 km
Test2	Maritime H2SO4	0~2 km 12~50 km	Test6	Maritime Asian dust H2SO4	0~2 km 2~12km 12~50 km
Test3	Maritime Continental H2SO4	0~2 km 2~12 km 12~50 km	Test7	Urban H2SO4	0~2 km 12~50 km
Test4	Maritime Soot Asian dust H2SO4	0~2 km 0~2 km 2~12km 12~50 km			

Since simultaneous *in-situ* measurements in these areas for the four selected images are not available, the derived results from the algorithm developed in this study can not directly be validated. Here, the following criteria to assess whether the derived results are reasonable.

(1). A low covariance between the distributions of SPM and aerosols.

By visual inspection, it becomes clear that the structures of the SPM distribution are different from the structures of the aerosol distribution (Fig. 3b and 3d, Fig. 4b and 4d), except for the area of Subei shoal and the mouth of Yellow River in the China Seas, where the concentrations of SPM are very high.

(2). The agreement of the distributions of the derived parameters with known distributions.

In the China Seas, SPM distribution shows the expected pattern in the mouth of Yellow River, in the Subei shoal, in the centre of Yellow Sea, in the Bohai Strait, as well as along the coast of Eastern China Sea. In the mouth of Yellow River, SPM concentration is very high due to the discharge of inorganic particles. In the Subei shoal, SPM concentration is also very high due to the re-suspended sediments. The centre of Yellow Sea is very clear and SPM concentrations are frequently found to be less than 0.5 g/m^3 [31]. In the strait of the Bohai Sea, SPM concentration is relatively low due to the influence of Yellow Sea, from which a band of low SPM concentration stretches into the Bohai Sea [29]. CDOM distributions in the Bohai Sea and around the mouth of Yangzi River are also within the expected pattern. In the Bohai Sea, CDOM is always high due to the discharge of Yellow River and waste water from factories. Around the mouth of Yangzi River, input of riverine waters causes high CDOM concentrations. The CHL concentrations in the Bohai Sea and around the outer path of Yangzi River plume are typically higher than that in Yellow Sea. The range of derived SPM concentration is within the range known for the China Seas. The range of derived CHL concentration is also within the known range, except for the highly turbid waters. In the highly turbid waters, the derived CHL concentration is unreasonably high: around the Subei shoal and the mouth of Yangzi River, the derived CHL concentration exceeds 30 mg m^{-3}. In fact, although there is a rich nutrient supply in these areas, the availability of light is reduced due to the high SPM concentration. As a result, photosynthesis is reduced and the CHL concentration should be comparably low. The observed values in these areas are between 0.1 ~ 10 mg m^{-3} [28].

Judging from the above two criteria, the derived results seem to be reasonable except for the CHL retrieval in highly turbid waters of the China Seas.

5. DISCUSSION

In this study, a methodology for the retrieval of three oceanic constituents from ocean colour at TOA above Case II waters has been derived. The retrieval method is derived by applying ANN techniques to a set of remote sensing reflectance spectra at TOA typical of Case II waters, which have been obtained from RT simulations.

The ANN employed in this study is a MLP with three layers: one input, one hidden and one output layer. A bias parameter is added both to the input layer and to the hidden layer. The input layer consists of 15 neurons which correspond to Rayleigh-corrected remote sensing reflectances of 10 wavelengths at TOA and other 5 auxiliary parameters. The hidden layer consists of 50 neurons. The output layer consists of four neurons which correspond to the concentrations of CHL, SPM and CDOM, as well as the total optical thickness of aerosols.

The ANN-based algorithm developed in this study seems to be a promising technique for the retrieval of oceanic constituents in Case II waters from ocean colour measurements at TOA. The examination of the performance of the ANN-based algorithm shows that it can deal with various atmospheres from weakly to strongly absorbing aerosols. Up to now, the algorithm has been tested for only a few images, and the validation is preliminary.

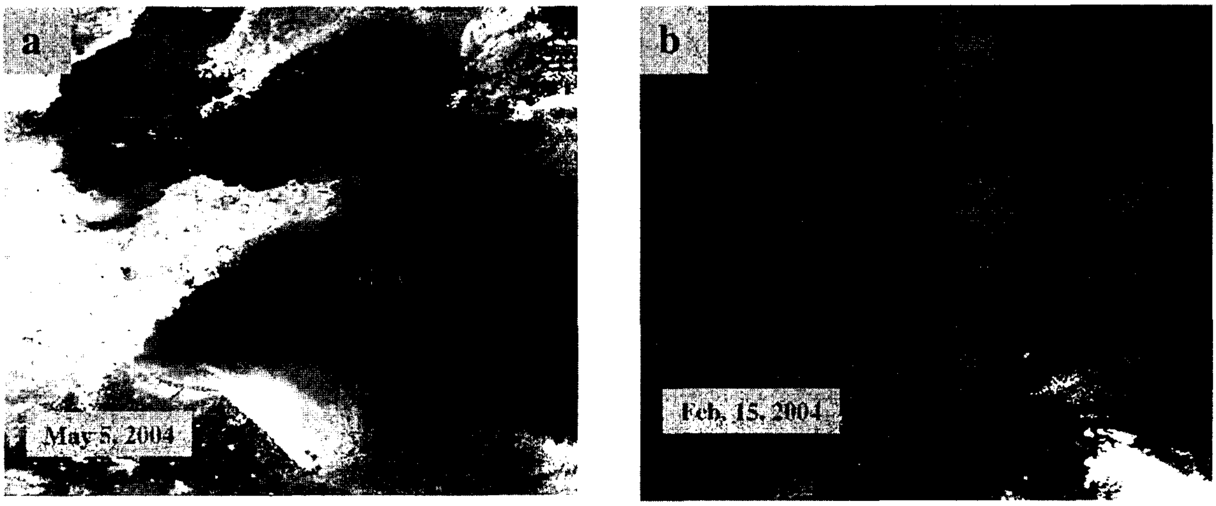

Fig. 2. RGB images of MERIS in the Bohai Sea and Yellow Sea (a), and in the Eastern China Sea (b)

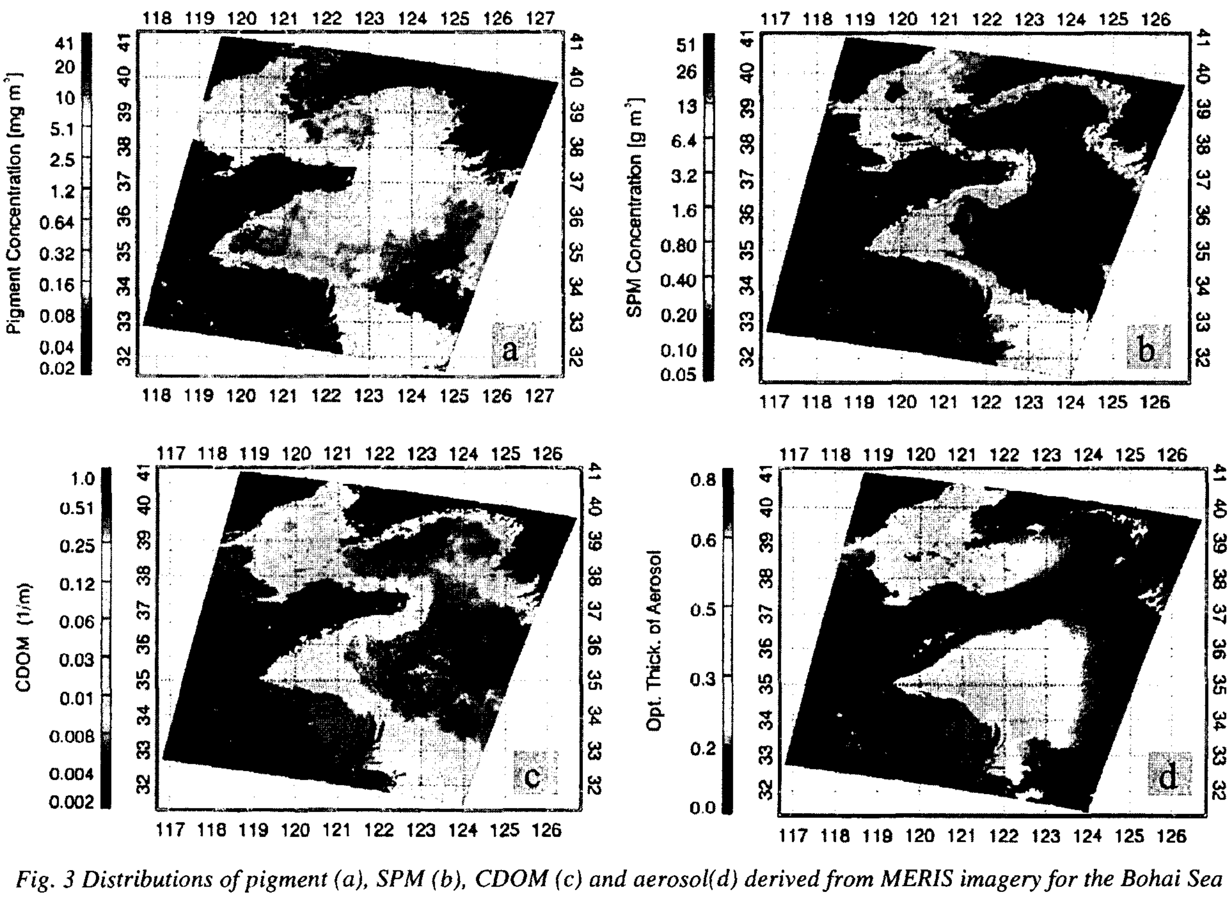

Fig. 3 Distributions of pigment (a), SPM (b), CDOM (c) and aerosol(d) derived from MERIS imagery for the Bohai Sea and the Yellow Sea

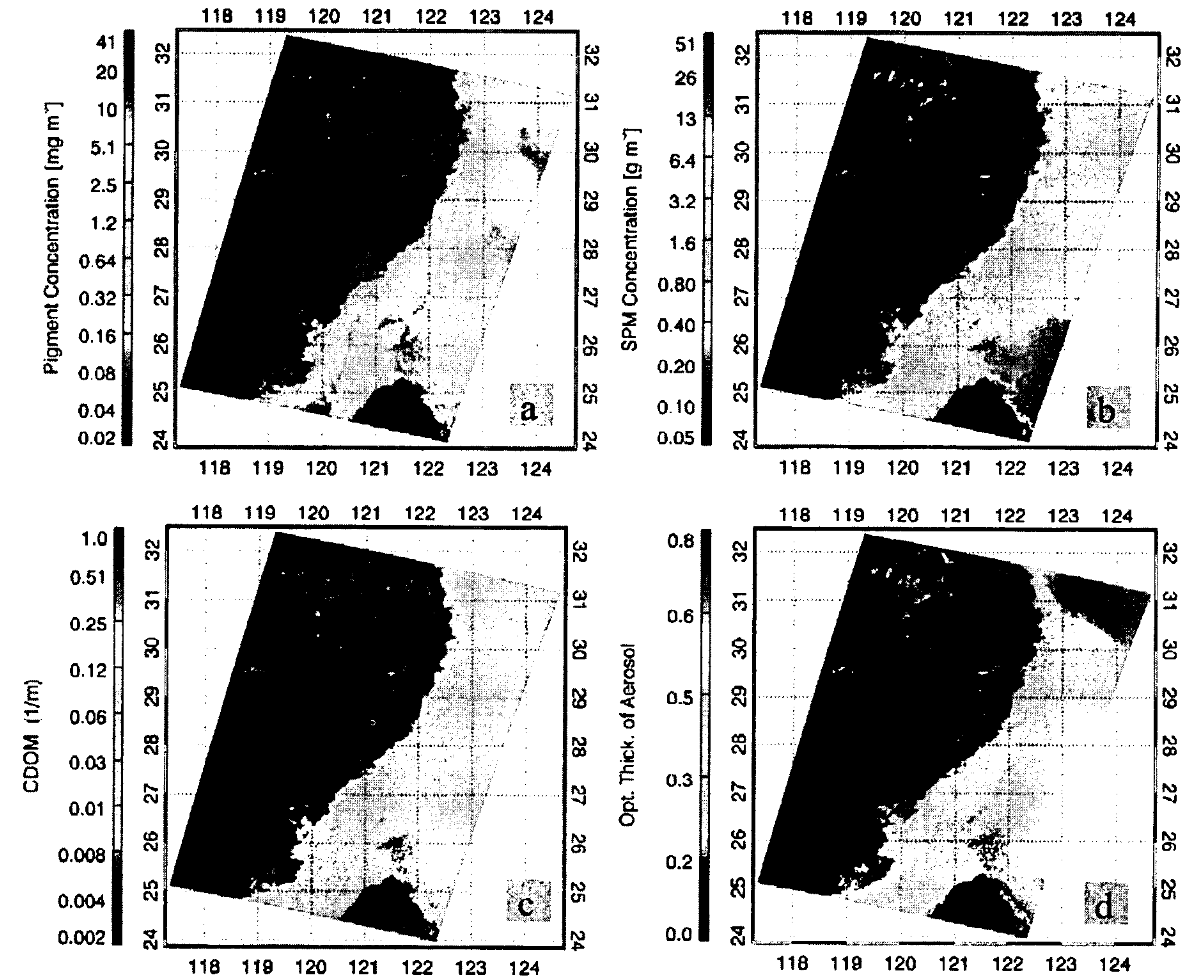

Fig. 4 Distributions of pigment (a), SPM (b), CDOM (c) and aerosol (d) derived from MERIS imagery for the Eastern China Sea

REFERENCES

1. Gordon, H. R., Atmospheric correction of ocean colour imagery in the Earth Observing System era, *J. Geophys. Res.*, 102, 17,081-17,106, 1997.
2. Chomko, R. M., and H. R. Gordon, Atmospheric correction of ocean colour imagery: use of the Junge power-law aerosol size distribution with variable refractive index to handle aerosol absorption, *Appl. Opt.*, 37, 5560-5572, 1998.
3. Gordon, H. R., and D. K. Clark, Clear water radiances for atmospheric correction of coastal zone color scanner imagery, *Appl. Opt.*, 20, 4175-4180, 1981.
4. Gordon. H. R., In-orbit calibration strategy for ocean colour sensors, *Remote Sensing of Environment*, 63, 265-278, 1998.
5. Siegel, D. A., M. Wang, S. Maritorena, and W. Robinson, Atmospheric correction of satellite ocean colour imagery: the black pixel assumption, *Appl. Opt.*, 39, 3582-3591, 2000.
6. Gordon, H. R., T. Du, and T. Zhang, Remote sensing of ocean colour and aerosol properties: resolving the issue of aerosol absorption, *Appl. Opt.*, 36, 8670-8684, 1997.
7. Li, L. P., H. Fukushima, R. Frouin, B. G. Mitchell, M. X. He, I. Uno, T. Takamura, and S. Ohta, Influence of sub-micron absorptive aerosol on SeaWiFS-derived marine reflectance during ACE-Asia, *J. Geophys. Res.*, 108, 4472, 2003.

8. Nakajima, T., M. Tanaka, M. Yamano, M. Shiobara, K. Arao, and Y. Nakanishi, Aerosol optical characteristics in the yellow sand events observed in May 1982 at Nagasaki Part II: models, *J. Meteorol. Soc. Jpn.* 67, 279-291, 1989.

9. Chomko, R. M., and H. R. Gordon, Atmospheric correction of ocean colour imagery: test of the spectral optimisation algorithm with SeaWiFS, *Appl. Opt.*, 40, 2973-2984, 2001.

10. Chomko, R. M., H. R. Gordon, S. Maritorena, and D. A. Siegel, Simultaneous retrieval of oceanic and atmospheric parameters from ocean colour imagery by spectral optimisation: a validation, *Remote Sensing of Environment*, 84, 208-220, 2003.

11. Thiria, S., C. Meija, F. Badran, and M. Crepon, A neural network approach for modelling non-linear transfer functions: Application for wind retrieval from space borne scatterometer data, *J. Geophys. Res.*, 98, 22827-22841, 1993.

12. Keiner, L. E., and C. W. Brown, Estimating oceanic chlorophyll concentrations with neural networks, *Int. J. Remote Sens.*, 20, 189-194, 1999.

13. Schiller, H., and R. Doerffer, Neural network for emulation of an inverse model - operational derivation of Case II water properties from MERIS data, *Int. J. Remote Sens.*, 20, 1735-1746, 1999.

14. Gross, L., S. Thiria, R. Frouin, and B. G. Mitchell, Artificial neural networks for modelling the transfer function between marine reflectance and phytoplankton pigment concentration, *J. Geophys. Res.*, 105, 3483-3495, 2000.

15. Zhang, T., F. Fell, Z. S. Liu, R. Preusker, J. Fischer, and M. X. He, Evaluating the performance of artificial neural network techniques for pigment retrieval from ocean colour in Case I waters, *J. Geophys. Res.* (in press, 2003).

16. Fell, F., and J. Fischer, Numerical simulation of the light field in the atmosphere-ocean system using the Matrix-Operator method, *J. Quant. Spectrosc. Radiat. Transfer*, 69, 351-388, 2001.

17. Elterman L., UV, visible, and IR attenuation for altitudes to 50 km, Air Force Cambridge Research Laboratories, *Environmental Research papers, N° 285, AFCRL-68-0153*, 49pp, 1968.

18. Hansen, J. E., and L. D. Travis, Light scattering in planetary atmospheres, *Space Science Reviews,* 16, 527-610, 1974.

19. Shettle, E. P., and R. W. Fenn, Models for the aerosols of the lower atmosphere and the effects of humidity variations on their optical properties. *Environmental Research Papers, AFGL-TR-79-0214, 20 September 1979, AFGL*, Hanscom, MA, 1979.

20. WCRP, A preliminary cloudless standard atmosphere for radiation computation. *Int. Ass. for Meteor. and Atm. Phys.*, Radiation Commission, March 1986, WCP-112, WMO/TD-N° 24, 1986.

21. Fukushima, H., and M. Toratani, Asian dust aerosol: Optical effect on satellite ocean colour signal and a scheme of its correction, *J. Geophys. Res.*, 102, 17119-17130, 1997.

22. Cox, C., and W. Munk, Some problems in optical oceanography, *J. Mar. Res.*, 14, 63-78, 1954.

23. Zhang, T., Retrieval of oceanic constituents with Artificial neural network based on radaitive transfer simulation techniques, PhD thesis, *Institut für Weltraumwissenschaften*, Freie Universität Berlin, Germany, 2003.

24. Pope, R. M., and E. S. Fry, Absorption spectrum (380-700) of pure water. II. Integrating cavity measurements, *Appl. Opt.*, 36, 8710-8722, 1997.

25. Morel, A, Optical properties of pure water and pure sea water, in *Optical Aspects of Oceanography*, edited by N. G. Jerlov and E. S. Nielsen, pp. 1-24, Academic Press, New York, USA, 1974.

26. Bricaud A., A. Morel, M. Babin, K. Allali, and H. Claustre, Variations of light absorption by suspended particles with chlorophyll-a concentration in oceanic (case 1) waters: Analysis and implications for bio-optical models, *J. Geophys. Res.*, 103, 31033-31044, 1998.

27. Babin ,M., D. Stramski, G. M. Ferrari, H. Claustre, A. Bricaud, G. Obolensky, and N. Hoepffner, Variation in the light absorption coefficient of phytoplankton, nonalgal particles, and dissolved organic matter in coastal waters around Europe, *J. Geophys. Res.*, 108, 3211-3230, 2003.

28. Hu, D.X., *Cruise Report of JGOFS-China Project (1990-2000)*, Oceanology Institute, Chinese Academy of Sciences, China, 2000.

29. Jiang, W., J. Su, H. Yang, Y. Zhang, H. Jiang, Q. Wang, K. Zhang, and T. Tian, The relationship between SPM concentration and hydrodynamic condition in the Bohai Sea, *Acta Oceanologica Sinica*, 24, 212-217, 2002.

30. Wu, D., Z. S. Liu, K. L. Zhang, B. Zhang, and Y. He, Lidar measurement of ocean suspended matter, *Acta Optica Sinica*, 23, 245-248, 2003.

31. Ahn, Y. H., J. E. Moon, and S. Gallegos, Development of Suspended Particulate Matter Algorithms for Ocean colour Remote Sensing, *Korean Journal of Remote Sensing*, 17, 285-295, 2001.

MERIS OCEAN COLOR REMOTE SENSING MODEL OF CHINA BOHAI SEA BASED ON OPTIMIZATION METHOD

MA Yi [1,2], ZHANG Jie [1,2], CUI Ting-wei [1]

[1] *First Institute of Oceanography, SOA., Xianxialing Road, High-Tech Park, Qingdao, Shandong, P.R.C., 266061, mayimail@fio.org.cn*

[2] *Key Laboratory of Marine Science and Numerical Modeling, SOA., Xianxialing Road, High-Tech Park, Qingdao, Shandong, P.R.C., 266061, zhangjie@public.qd.sd.cn*

ABSTRACT

Based on the known research results of inherent optical quality of ocean color constituents, this paper uses optimized parameters to put forward a remote sensing reflectance model of seawater, which is applicable in Bohai, China. A MERIS ocean color inverse model is constructed by introducing a functional extreme problem. The evaluation of this model by the in situ data shows that the model is feasible, but its practicability needs to be verified.

1. INTRODUCTION

Bohai, surrounded by the land in the north, the west and the south, is connected with Yellow Sea via Bohai Strait only in the east. Its major area belongs to typical Case II water, and the quantitative inversion of its constituent concentration is difficult in the ocean color research field. So up till now, there hasn't been operational remote sensing inversion model and the corresponding algorithm.

ENVISAT-1 was launched on 1st, March, 2002, and Medium Resolution Imaging Spectrometer (MERIS) is its ocean color sensor. MERIS, designed mainly for ocean color detection, sets 15 channels (in Tab. 1), with ground resolution of its image being 300m. Its can revisit for 2-3 days, and its swath is 1450km. Compared with other ocean color sensors, MERIS has spatial and spectral advantages, and is more suitable to Case II water ocean color remote sensing.

Tab. 1. MERIS spectral channels

No.	Band center(nm)	Application
1	412.5	Yellow substance and detrital pigments
2	442.5	Chlorophyll absorption maximum
3	490	Chlorophyll and other pigments
4	510	Suspended sediment, red tides
5	560	Chlorophyll absorption minimum
6	620	Suspended sediment
7	665	Chlorophyll absorption & fluo. reference
8	681.25	Chlorophyll fluorescence peak
9	708.75	Fluo. Reference, atmosphere corrections
10	753.75	Vegetation, cloud
11	760.625	O_2R-branch absorption band
12	778.75	Atmosphere corrections
13	865	Vegetation, water vapour reference
14	885	Atmosphere corrections
15	900	Water vapour, land

Proc. 2005 Dragon Symposium "Mid-Term Results", Santorini, Greece
27 June – 1 July 2005 (ESA SP-611, January 2006)

This paper explores ocean color constituent concentration retrieval by MERIS data by developing a multi-constituent seawater reflectance model and putting forward two new models: a simulation remote sensing reflectance model with ocean color constituent concentration and an ocean color constituent concentration inversion model with seawater remote sensing reflectance by optimization method.

2. METHODS

2.1 Seawater remote sensing reflectance model

Remote sensing reflectance $R(\lambda)$ can be approximately represented as a function of inherent optical properties[1]:

$$R(\lambda)=\frac{f}{Q}\frac{t}{n^2}\frac{b_b(\lambda)}{a(\lambda)+b_b(\lambda)} \tag{1}$$

where $b_b(\lambda)$ is total backscatter coefficient of seawater, $a(\lambda)$ is total absorption coefficient, $Q\approx 5$ is distribution function of optical field, n is refraction index of seawater, $t/n^2=0.54$ is transmissibility of sea-atmosphere interface, f is a function of solar zenith angle. f/Q ($f/Q=0.0095$) is independent of solar zenith angle changes[2, 3]. Then

$$R(\lambda)=0.051\frac{b_b(\lambda)}{a(\lambda)+b_b(\lambda)} \tag{2}$$

Without considering absorption coefficient of suspended particle matter, seawater absorption coefficient $a(\lambda)$ can be expressed as a sum of pure seawater, phytoplankton pigments and yellow substance absorption coefficients, that is

$$a(\lambda)=a_w(\lambda)+a_p(\lambda)+a_y(\lambda) \tag{3}$$

Here, $a_w(\lambda)$, $a_p(\lambda)$ and $a_y(\lambda)$ represent absorption coefficients of pure seawater, phytoplankton pigments and yellow substance.

With the empirical model, phytoplankton pigments absorption coefficient $a_p(\lambda)$ can be expressed as [4]

$$a_p(\lambda)=[a_0(\lambda)+a_1(\lambda)\ln(a_p(440))]a_p(440) \tag{4}$$

where $a_0(\lambda)$ and $a_1(\lambda)$ are empirical parameters. For phytoplankton pigments absorption coefficient $a_p(440)$ at $440nm$ [5], there is

$$a_p(440)=0.06P^{0.65} \tag{5}$$

where P is chlorophyll-a concentration.

Yellow substance absorption coefficient $a_y(\lambda)$ can be expressed as[6]

$$a_y(\lambda)=Y\exp(-0.014(\lambda-440)) \tag{6}$$

where $Y = a_y(440)$ is yellow substance absorption coefficient at $440nm$.
Without considering backscattering coefficient of yellow substance, seawater backscattering coefficient $b_b(\lambda)$ can be expressed as a sum of pure seawater and suspended particle matter backscattering coefficients

$$b_b(\lambda) = b_{bw}(\lambda) + b_{bs}(\lambda) \tag{7}$$

where $b_{bw}(\lambda)$ and $b_{bs}(\lambda)$ are the backscattering coefficients of pure seawater and suspended particle matter.
For pure seawater backscattering coefficient, there is

$$b_{bw}(\lambda) = 0.5b_w(\lambda) \tag{8}$$

where $b_w(\lambda)$ is scattering coefficient of pure seawater, and by Smith[7]

$$b_w(\lambda) = 0.005862\left(\frac{400}{\lambda}\right)^{4.322} \tag{9}$$

For the backscattering coefficient of suspended particle matter, there is[8]

$$b_{bs}(\lambda) = B_1 b_1(\lambda) C_1 + B_2 b_2(\lambda) C_2 \tag{10}$$

where $B_1 = 0.039$ is backscattering probability of small-diameter suspended particles, $B_2 = 0.00064$ is backscattering probability of large-diameter suspended particles, $b_1(\lambda)$ and $b_2(\lambda)$ are specific scattering coefficients of small-diameter and large-diameter suspended particles, and C_1 and C_2 are concentrations of small-diameter and large-diameter suspended particles. The specific scattering coefficient is given by the following two equations[9]

$$\begin{aligned} b_1(\lambda) &= 0.0011513\left(\frac{400}{\lambda}\right)^{1.7} \\ b_2(\lambda) &= 0.0003411\left(\frac{400}{\lambda}\right)^{0.3} \end{aligned} \tag{11}$$

Hydrosol scattering is linear superposition of scattering from detritus caused by terrigenous deposit and plankton activity. The terrigenous deposit detritus are small-diameter suspended particles, and plankton activity-induced detritus are large-diameter suspended particles[10].
In the above expressions, the unit of absorption and scattering coefficients is m^{-1}, that of chlorophyll-a concentration P is mg/m^3, that of suspended particle concentrations C_1 and C_2 is mg/m^3, that of band length is nm. To sum up, the seawater remote sensing reflectance can be worked out when P, Y, C_1 and C_2 are known.

2.2 Optimization of the seawater remote sensing reflectance model

Although the above model can calculate seawater remote sensing reflectance, its applicability is restricted by the empirical parameters in the research area--Bohai Sea. Usually, these parameters are fixed in a local area.

In Fig.1, the dashed line is in situ remote sensing reflectance spectrum from optical experiment cruise in Bohai in June, 2005, and the solid line is the simulated spectrum of the model. The trend of the simulated result agrees with that of the in situ spectrum, but there is a big difference in quantity, with an average relative error of 21.49%. Obviously, a remote sensing reflectance model with fixed parameters lacks universality.

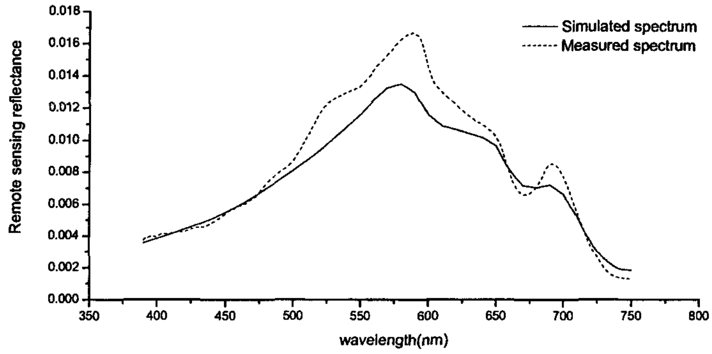

Fig.1. Measured remote sensing reflectance spectrum and modeled remote sensing reflectance spectrum

In order to obtain the remote sensing reflectance model parameters applicable to the research area, we introduce a departure function between in situ and simulated spectra to calculate the parameters by use of iteration numerical method.

The parameters to be optimized consist of x_1, x_2, x_3, x_4, x_5, x_6, x_7, x_8, x_9 and x_{10}, all of which can be found in the following expressions

$$R(\lambda)=x_1\frac{b_b(\lambda)}{a(\lambda)+b_b(\lambda)} \tag{12}$$

$$a_p(440)=x_2P^{x_3} \tag{13}$$

$$a_y(\lambda)=x_4\exp(-0.014(\lambda-440)) \tag{14}$$

$$b_{bs}(\lambda)=x_5b_1(\lambda)C_1+x_6b_2(\lambda)C_2 \tag{15}$$

$$\begin{aligned} b_1(\lambda)&=x_7\left(\frac{400}{\lambda}\right)^{x_8} \\ b_2(\lambda)&=x_9\left(\frac{400}{\lambda}\right)^{x_{10}} \end{aligned} \tag{16}$$

Then the simulated remote sensing reflectance spectrum R_c is a function with ten arguments.

We introduce a departure function

$$E(x_1,x_2,x_3,x_4,x_5,x_6,x_7,x_8,x_9,x_{10})=\sqrt{\sum_{i=1}^{n}[R_m(\lambda_i)-R_c(\lambda_i)]^2} \tag{17}$$

where R_m is in situ remote sensing reflectance spectrum, R_c is simulated remote sensing reflectance spectrum and n is band number. Then the ten parameters can be obtained through the following optimization problem

$$\min E(x_1,x_2,x_3,x_4,x_5,x_6,x_7,x_8,x_9,x_{10})=\sqrt{\sum_{i=1}^{n}[R_m(\lambda_i)-R_c(\lambda_i)]^2} \tag{18}$$

The Fig.2 shows the in situ and best-fitted spectra. We can see that the two spectra exhibit similar trend, and more important, their difference is largely narrowed. The optimization of the parameters is obvious because the average relative error between two spectra is 8.32%, much less than 21.49%.

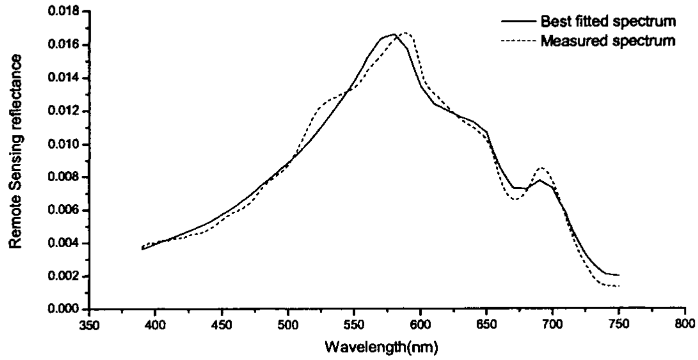

Fig. 2. In situ remote sensing reflectance spectrum and best fitted remote sensing reflectance spectrum

2.3 Ocean color constituent concentration inversion model

The numerical simulation of seawater remote sensing reflectance is a forward problem, i.e., to calculate remote sensing reflectance by ocean color constituent concentration, and to retrieve ocean color constituent concentration by remote sensing reflectance is an inverse problem. Just as we did with parameters optimization, here we introduce a cost function

$$E(P,C)=\sqrt{\sum_{i=1}^{n}[R_m(\lambda_i)-R_c(\lambda_i,P)]^2} \tag{19}$$

where P is seawater chlorophyll concentration, C is suspended particle concentration R_m is in situ remote sensing reflectance spectrum, R_c is remote sensing reflectance spectrum calculated by the forward problem, $n=10$ is the number of MERIS channels used for inversion calculation, and central wavelength of the channels are 412.5nm, 442.5nm, 490nm, 510nm, 560nm, 620nm, 665nm, 681.25nm, 708.75nm and 753.75nm respectively. Then seawater chlorophyll concentration can be retrieved by the following optimization problem

$$\min E(P,C)=\sqrt{\sum_{i=1}^{n}[R_m(\lambda_i)-R_c(\lambda_i,P,C)]^2} \tag{20}$$

where the parameters x_1, x_2, x_3, x_4, x_5, x_6, x_7, x_8, x_9 and x_{10} in R_c adopt the optimized results of the forward problem.

3. RESULTS

To optimize seawater remote sensing reflectance, we use the ocean color constituent concentration data obtained from 16 stations of the optical experiment cruise in Bohai in June, 2005. The optimization results are in Tab. 2. We take average value of the results in each station as parameters of inversion model.

Tab. 2. Optimization results of the model parameters

Station	x_1	x_2	x_3	x_4	x_5	x_6	x_7	x_8	x_9	x_{10}
LDW-01	0.0243	0.0374	0.4083	0.1000	0.0095	0.1299	0.2933	0.4076	0.3414	0.3000
LDW-02	0.0108	0.0580	0.7776	0.2308	0.1866	0.0006	0.2448	2.4750	0.3411	0.3000
LDW-03	0.0120	0.0714	0.5861	0.1000	0.0278	0.0018	0.9086	1.0742	0.3411	0.3000
LDW-04	0.0145	0.0662	0.7113	1.0932	0.2478	0.0001	0.2640	3.0000	0.3411	0.3000
LDW-05	0.0194	0.0580	0.3159	0.1000	0.0163	0.0000	0.8143	0.8194	0.3411	0.3000
LDW-06	0.0227	0.0464	0.3000	0.1613	0.0177	0.0046	0.6197	1.4831	0.3411	0.3000
LDW-07	0.0153	0.0785	0.6040	0.1936	0.0338	0.0058	0.8881	1.9969	0.3411	0.3000
LDW-08	0.1347	0.0900	0.8562	0.4957	0.0283	0.0011	0.0994	3.0000	0.3411	0.3000
QHD-01	0.0412	0.0850	0.5953	0.3064	0.0271	0.0012	0.1364	1.6439	0.3411	0.3000
QHD-02	0.0217	0.0900	0.6160	0.1000	0.0073	0.0003	0.5058	0.2018	0.3411	0.3000
QHD-03	0.0461	0.0570	0.4329	0.1237	0.0097	0.0059	0.5052	0.0000	0.3411	0.3000
QHD-04	0.0140	0.0877	0.7101	2.0668	0.0483	0.0005	0.4061	2.0183	0.3411	0.3000
QHD-05	0.0471	0.0300	0.3365	0.4596	0.0151	0.0018	0.1108	1.0648	0.3411	0.3000
QHD-06	0.0624	0.0300	0.5424	0.7481	0.0253	0.0006	0.6104	2.1062	0.3411	0.3000
QHD-07	0.0853	0.0544	0.3000	0.7483	0.0184	0.0066	0.4817	0.0000	0.3411	0.3000
QHD-08	0.0859	0.0799	0.6869	2.2228	0.0098	0.0012	0.5564	0.0000	0.3411	0.3000

To verify the inversion modal effectiveness, the paper chooses the seawater reflectancel data and ocean color constituent concentration data obtained in June, 2005 in Liaodong Bay of Bohai Sea. According to the central potision of 10 MERIS channels, we simulate R_m in Eq. 20 by the measured seawater optical spectra. The inversion results are in Tab. 3. The average relative error Chlorophyll-a concentration is 24.82%, and that of inorganic suspended matter concentration is 28.92%.

Tab. 3. Measured and inversed Chlorophyll-a and inorganic suspended matter concentration

Station	Chl-a concentration		Inorganic suspended matter concentration	
	Inversion value	Measured value	Inversion value	Measured value
LDW-09	2.25	2.99	4.76	7.60
LDW-10	4.04	3.11	7.33	9.20
LDW-11	5.01	3.59	4.80	3.0
LDW-12	3.02	3.35	13.35	16.20
QHD-09	2.50	1.91	5.97	8.40
QHD-10	2.43	3.59	2.68	3.80
QHD-11	10.47	9.83	5.11	5.60

4. CONCLUSION AND DISCUSSION

This paper introduces an optimized seawater remote sensing reflectance model according to the departure function between in situ and stimulated spectral curves. The error analysis shows that the parameter-optimized model is more applicable to Bohai Sea.

Based on the seawater remote sensing reflectance model used in Bohai Sea, this paper presents a MERIS ocean color constituent inversion model through functional optimization. The verifying case shows that the inversion model is feasible. But its practicability needs validation by MERIS image data.

Because the data for optimization calculation in this paper is obtained from Liaodong Bay of Bohai alone, the application of this model may be restricted.

5. ACKNOWLEDGEMENT

The work associated with this paper was funded under the Dragon Project (ID: 2566), the High-tech Research and Development Program of China S863-2005AA604150.

6. REFERENCES

1. Tang Junwu and Tian Guoliang, Ocean Color Analysis and an Algorithm for the Retrieval of Multiconstituents Based on Remote Sensing Reflectance. *Journal of Remote Sensing*, Vol. 4, 252-256, 1997.
2. Morel. A. and Gentili. B., Diffuse reflectance of oceanic waters. II. Bidirectional aspects. *Applied Optics*, Vol. 33, 6864-6879, 1993.
3. Gordon, H. R, et al. A semianalytic Radiance Model of Ocean Color. *Journal of Geophysics Research*, Vol. 93, 90909-90924, 1988.
4. Lee Zhongping., Visible-infrared remote-sensing model and applications for ocean waters. Ph.D. dissertation, University of South Florida, St. Petersburg, 1994.
5. Prieur. L. and Sathyendranath. S., An optical classification of coastal and oceanic waters based on the specific spectral absorption curves of phytoplankton pigment, dissolved organic matter and other materials. *Limnology and Oceanography*, Vol. 26, 671-689, 1981.
6. Bricaud. A., Morel, A. et al. Absorption by dissolved organic matter of the sea (yellow substance) in the UV and visible domains. *Limnology and Oceanography*, Vol. 26, 43-53, 1981.
7. Smith, R. C., Optical properties of the clearest waters (200-800nm). *Applied Optics*, Vol. 20, 177-184, 1981.
8. Vladimir I. Haltrin., An algorithm to restore spectral signatures of all inherent optical properties of seawater using a value of one property at one wavelength. Proceeding of the 4th International Airborne Remote Sensing Conference and Exhibition, Ottawa, Ontario, (I), 680-687, 1999.
9. Vladimir I. Haltrin., Propagation of Light in the Sea Depth. In Optical Remote Sensing of the Sea and the Influence of the Atmosphere, 20-62, 1985.
10. O. V. Kopelevich., Small–Parametric Model of the Optical Properties of Seawater. In *Ocean Optics*, I: Physical Ocean Optics, Moscow: Nauka Publishing, 1983.

STATISTICAL INVERSION MODEL FOR CHLOROPHYLL A CONCENTRATION IN THE BOHAI

CUI Ting-wei (1), ZHANG Jie (1, 2), MA Yi (1, 2)

(1) First Institute of Oceanography, S. O. A., Xianxialing Road, High-Tech Park, Qingdao, Shandong, P.R.C., 266061, cokkiecui@sohu.com

(2) Key Laboratory of Marine Science and Numerical Modeling, S. O. A., Xianxialing Road, High-Tech Park, Qingdao, Shandong, P.R.C., 266061, zhangjie@public.qd.sd.cn, mayimail@263.net

ABSTRACT

Bio-optical observations of about 50 stations were carried out in June, 2005 in Bohai, the major area of which belongs to Optical Case II water. The experiment acquired apparent optical properties, inherent optical properties, biological, chemical and water quality data, in accordance with NASA Ocean Optics Protocols. Using these data, a statistical inversion model of chlorophyll a concentration (chl-a) of Bohai was developed based on MERIS bands configuration. The inversion model has the performance of 29.83% average relative error (ARE) and 16.45% root mean square error (RMSE) between the measured and inversed data.

Key words: Bohai, Ocean color, statistical algorithm, Inversion, Chlorophyll a, Case II water

1. INTRODUCTION

Bohai is the inland water of China and surrounded by the land from 3 sides. Several rivers such as the Yellow River, the Haihe River and the Liao River run into Bohai, carrying a large amount of organic and inorganic suspended matter. As a result, optical properties of Bohai are relatively complex and the major area of Bohai belongs to typical Case II water. Compared with bio-optical observations and researches for the Yellow Sea, East China Sea [1-3] and South China Sea [4], the work in Bohai is not sufficient. Due to the lack of high quality bio-optical dataset, there were few reports on the inversion model of ocean color constituents such as chlorophyll a concentration (chl-a).

In 2005, 3 cruises of bio-optical experiment were carried out in Bohai. Comprehensive investigation content and elements, normative observation technique and top-ranking optical instruments such as ASD, HyperPro, AC-9, HS-6, provide foundation for ocean color inversion model development. This paper studies the chl-a inversion by statistical regression method, utilizing the *in situ* data of first cruise.

2. DATA AND METHOD

2.1. General introduction of Bohai experiment

In June, 2005, bio-optical data of 50 stations in Bohai were acquired. Fig. 1 gives the experiment area and stations distribution. In Bohai experiment, main observation content includes:

(1) Apparent optical properties: water-leaving radiance L_w, normalized water-leaving radiance L_{wn} and remote sensing reflectance R_{rs}.

(2) Inherent optical properties: seawater beam attenuation coefficient, seawater beam absorption coefficient, absorption coefficient spectra of phytoplankton, total suspended matter and colored dissolved organic material.

Proc. 2005 Dragon Symposium "Mid-Term Results", Santorini, Greece
27 June – 1 July 2005 (ESA SP-611, January 2006)

(3) Ocean color constituents: concentration of chlorophyll a, b, c and carotenoid, concentration of total suspended material and inorganic suspended material, phytoplankton dominant species,.

(4) Atmospheric parameters: total column ozone, vapor and aerosol optical thickness.

(5) Routine parameters: ocean color, transparency, sea surface temperature (SST), air temperature, air pressure, wind speed and wind direction.

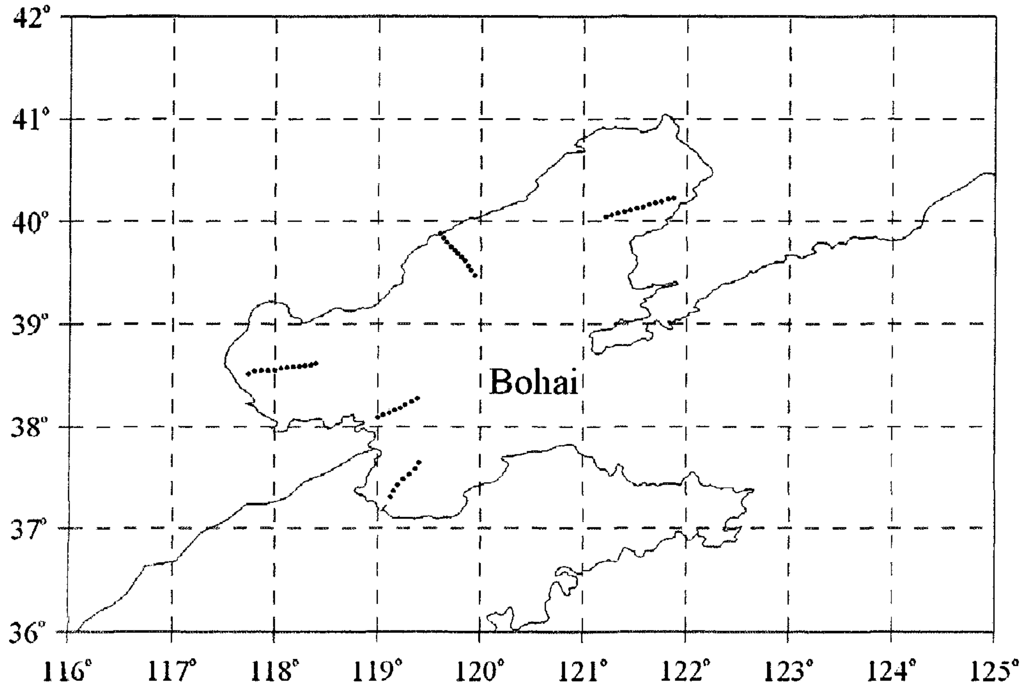

Fig. 1 Layout of experimental stations in Bohai

2.2. Apparent optical properties

The experiment adopted the above-water method and used FieldSpec® Pro Dual VNIR spectroradiometer of the ASD (Analytic Spectral Device). Data acquisition and processing are done according to Ocean Optics Protocols of NASA [5]. Typical remote sensing reflectance spectra in Bohai are given in Fig. 2.

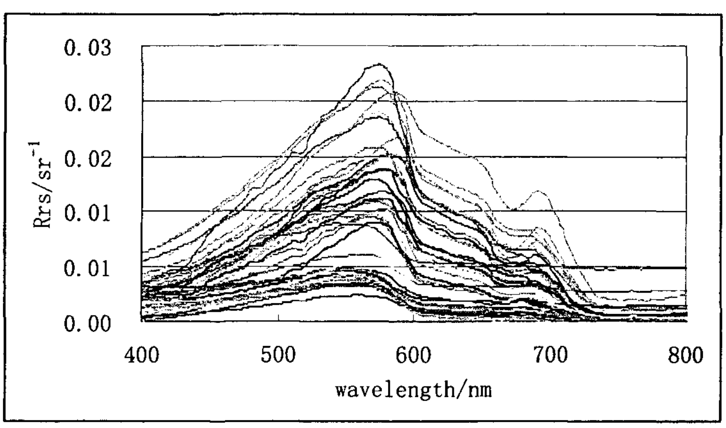

Fig. 2 Typical remote sensing reflectance spectra of Bohai

2.3. Chl-a

In Bohai experiment, chl-a data were measured by three different methods and instruments: fluorometry, spectrophotometer and High Performance Liquid Chromatogram (HPLC). This research prefers chl-a data from fluorescence method. The chl-a range is 0.95-9.83 mg·m^{-3}.

3. STATISTICAL INVERSION MODEL

Two parameters are used to evaluate the statistical inversion model performance: average relative error (ARE) and root mean square error (RMSE), as shown in Eq.1-2.

$$ARE = \frac{1}{N}\sum_{i=1}^{N}\left|C_i^m - C_i^n\right| / C_i^n \tag{1}$$

$$RMSE = \sqrt{\frac{\sum_{i=1}^{N}(\log_{10}(C_i^m) - \log_{10}(C_i^n))^2}{N}} \tag{2}$$

in which, C_i^m is inversion value, C_i^n is measured value and N is number of data points.

MERIS has several ocean color bands, such as 412nm, 442nm, 490nm, 510nm, 560nm, 665nm, 681nm etc. By comparing the correlations between chl-a and remote sensing reflectance of these bands and their combination of *in situ* spectra, we finally choose $R_{rs}(490)/R_{rs}(560)$ as the input parameter of the inversion model. The model performance is given in Fig. 3: R^2=72.32%, ARE=29.83%, RMSE=16.54%.

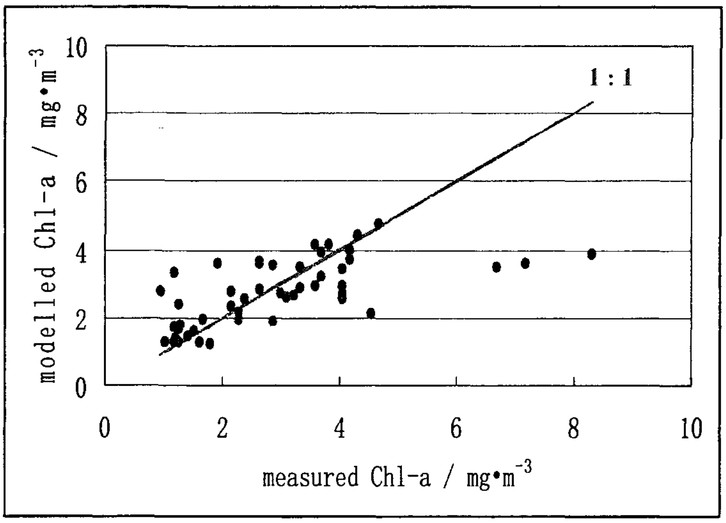

lg Chl-a=ax^2+bx+c
x=lg(R_{rs}(490)/R_{rs}(560))
a=-5.5872, b=-4.3751, c=-0.1808

N=49(deleting 1 abnormal data)
R^2=72.32%
ARE=29.83%
RMSE=16.45%

Fig. 3 Inversion model results for Bohai chl-a

4. DISCUSSION

4.1. Comparison with chl-a model for the Yellow Sea and East China Sea

The statistical inversion model for Bohai is Comparable to that for the Yellow Sea and East China Sea developed by Tang et al. (2004), which is shown in Table 1.

Table 1 Comparison between statistical inversion model for Bohai (this paper) and the Yellow Sea and East China Sea(Tang et al., 2004)

	R^2	ARE	RMSE	Expression
TANG(2004)	74%	36%	/	lg Chl-a=ax^2+bx+c $x=lg(R_{rs}(443)/R_{rs}(555)\ R_{rs}(412)/R_{rs}(510)^a)$
This paper	72.32%	29.83%	16.45%	lg Chl-a=ax^2+bx+c $x=lg(R_{rs}(490)/R_{rs}(560))$

4.2. Model application foreground

Our research aims at MERIS bands configuration and the model developed here can be easily used in chl-a inversion by MERIS data.

As mentioned above, chl-a used for developing the model is 0.95-9.83 $mg{\cdot}m^{-3}$, most of which is less than 5 $mg{\cdot}m^{-3}$. And for about 70 percent of all the stations, concentration of total suspended matter (TSM) is less than 10mg/L. So, for water with high TSM and chlorophyll concentration, this model should be used much more cautiously.

5. CONCLUDING REMARK

Utilizing bio-optical dataset acquired in Bohai in 2005, we developed a preliminary statistical inversion model for chlorophyll a concentration based on MERIS ocean color bands. After further validation and modification with much more *in situ* bio-optical data, the statistical inversion model developed here would be more applicable and helpful to the future use of MERIS data in Bohai.

6. ACKNOWLEDGEMENTS

This research was supported by the Dragon Project through id 2566 and by the High-tech Research and Development Program of China through grants 2005AA604150. The authors thank Mrs. H. Zhang for her helpful comments.

7. REFERENCES

1. Tang J. W., Wang X. M., Song Q. J., et al. Statistical Inversion Models for Case II Water Color Elements in the Yellow Sea and East China Sea, *Advances in Marine Science*, Vol. 22 (Suppl.):1-7, 2004.
2. Zhu J. H. and Li T. J. Spectral Mode Research about Absorption Coefficient of the De-pigment Particles and Yellow Substance in Yellow Sea and East China Sea, *Ocean Technology*, 23(2), 7-13, 2004.
3. Zhu J. H. and Li T. J. Relationship Research of Phytoplankton Pigments Absorption and Chlorophyll A Concentration in the East China Sea and Yellow Sea. *Ocean Technology*, 23(4), 117-122, 2004.
4. Zhang Q. L., Chen C. Q. and Shi P. Characteristics of $K_d(490)$ around Nansha Islands in South China Sea. *Journal of Tropical Oceanography*, 22(1), 9-16, 2003.
5. Mueller L. J., Fargion S. G. and McClain C. R., *Ocean Optics Protocols for Satellite Ocean Color Sensor Validation*, Revision 5. USA: NASA, 2004.

OCEAN COLOR ANALYSIS OF BOHAI BASED ON MERIS IMAGES

XIN Hong-mei (1, 2), ZHANG Jie (2, 3), MA Yi (2, 3), CUI Ting-wei (2)

(1)*Ocean University of China, Yu-Shan road, Qingdao, Shandong, P.R.C., 266003, zhangjie@public.qd.sd.cn*
(2)*First Institute of Oceanography, S.O.A., Xianxialing Road, High-Tech Park, Qingdao, Shandong, P.R.C., 266061, cokkiecui@sohu.com*
(3)*Key Laboratory of Marine Science and Numerical Modeling, S.O.A., Xianxialing Road, High-Tech Park, Qingdao, Shandong, P.R.C., 266061, mayimail@fio.org.cn*

ABSTRACT

Utilizing reduced resolution MERIS images of April, 2005, October, 2003 and December, 2003, this paper calculates statistical quantities such as maximum, minimum, mean and standard deviation and makes a comparison of MERIS ocean color information obtained from three bays of Bohai: Liaodong Bay, Bohai Bay and Laizhou Bay. Also, by comparing MERIS ocean color interpretation results with *in situ* observations, we found: (1) Liaodong Bay is the clearest one among the three bays of Bohai. Bohai Bay is more turbid than Liaodong Bay, but its optical property seems much more homogeneous. Laizhou Bay has higher reflectance, or because the Yellow River carries a large amount of inorganic suspended matter into Bohai. (2) From the consistency between the MERIS image interpretation and *in situ* data, it can be concluded that MERIS data has the potential to extract ocean color information quantitatively.

Key words: Bohai, Ocean color, Statistic, MERIS

1. INTRODUCTION

Bohai is an inland sea, surrounded by the land in the north, west and south, only connecting to the Yellow Sea through the Bohai Strait in the east. It is roughly triangular and the three angles form three bays: Bohai Bay in the west, Laizhou Bay in the south and Liaodong Bay in the north. The first two Bays are separated by the Yellow River Delta (Fig. 1). Bohai, covering an area of $7.7\times10^4 km^2$, is 18 meters deep on the average and 83 meters deep at the maximum. Because of the large amount of suspended sand brought by Yellow River, Haihe River, Liaohe River and Luanhe River, appropriate temperature, rich plankton, the transparency of Bohai is the lowest in the near-sea area in China. The water along the coast, yellow and unclear, has the transparency of less than 5 meters. The case is more serious near the mouth of Yellow River, with the transparency being as low as 1-2 meters, and even less than 0.5 meters in some area. Only the center of Bohai, featuring green and clear water, has the transparency of around 10 meters [1].

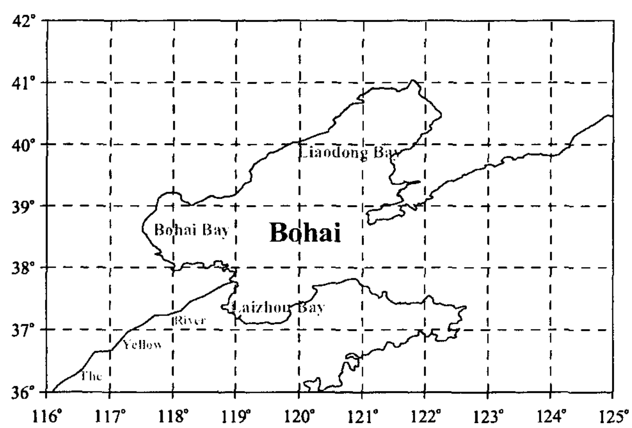

Fig. 1. Bohai and its three bays

MERIS is a 68.5° field-of-view pushbroom imaging spectrometer that measures the solar radiation reflected by the Earth, at a ground spatial resolution of 300m (1200m of reduced resolution), in 15 spectral bands in the visible and near infra-red (Table 1). The primary mission of MERIS is the measurement of sea colour in the oceans and in coastal areas. Knowledge of the sea colour can be converted into a measurement of chlorophyll pigment concentration, suspended sediment concentration and of aerosol loads over the marine domain [2].

Proc. 2005 Dragon Symposium "Mid-Term Results", Santorini, Greece
27 June – 1 July 2005 (ESA SP-611, January 2006)

Table 1. MERIS spectral channels

No.	Band center(nm)	Application
1	412.5	Yellow substance and detrital pigments
2	442.5	Chlorophyll absorption maximum
3	490	Chlorophyll and other pigments
4	510	Suspended sediment, red tides
5	560	Chlorophyll absorption minimum
6	620	Suspended sediment
7	665	Chlorophyll absorption & fluo. reference
8	681.25	Chlorophyll fluorescence peak
9	708.75	Fluo. Reference, atmosphere corrections
10	753.75	Vegetation, cloud
11	760.625	O_2R-branch absorption band
12	778.75	Atmosphere corrections
13	865	Vegetation, water vapour reference
14	885	Atmosphere corrections
15	900	Water vapour, land

Utilizing reduced resolution MERIS images of April, 2005, October, 2003 and December, 2003, firstly, we calculated statistical quantities such as maximum, minimum, mean and standard deviation to compare MERIS ocean color information of the three bays of Bohai and explained the results in terms of oceanography. Secondly, we compared MERIS ocean color interpretation results with *in situ* observations.

2. MERIS IMAGES INFORMATION COMPARISON OF THREE BAYS

Among the 26 MERIS image data, this paper chooses three clearer MERIS Level 1B ones (spatial resolution is 1200 m), obtained on Oct 17th, 2003, Dec 20th, 2003 and Apr 13th, 2005 and uses 665nm, 560nm and 442nm for false color composite (Fig. 2).

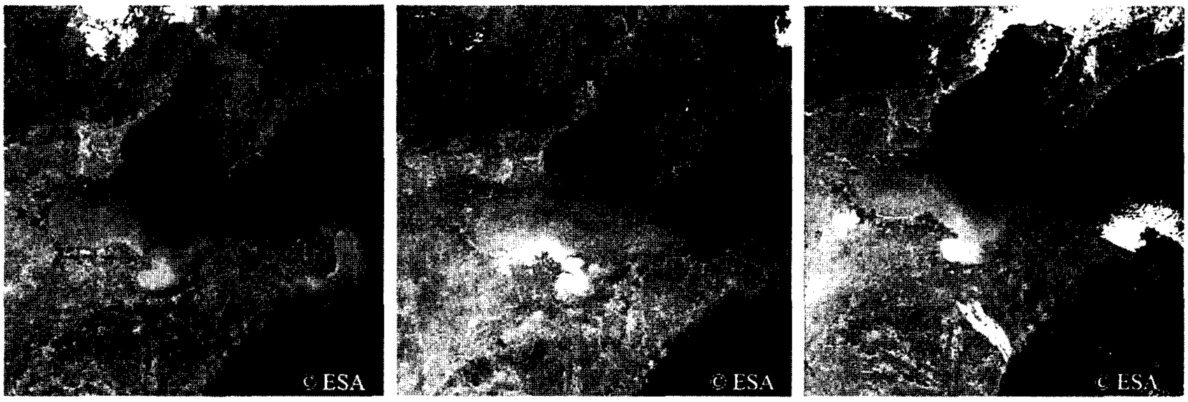

(a) *(b)* *(c)*

Fig. 2. Three MERIS images, obtained on (a) Oct 17th, 2003, (b) Dec 20th, 2003 and (c) Apr 13th, 2005, respectively

2.1. MERIS Image in April, 2005

Statistical quantities of Liaodong Bay, Bohai Bay and Laizhou Bay in MERIS images of 665nm, 560nm and 442nm are given in Table 2 and Fig. 3, including mean, maximum, minimum and standard deviation.

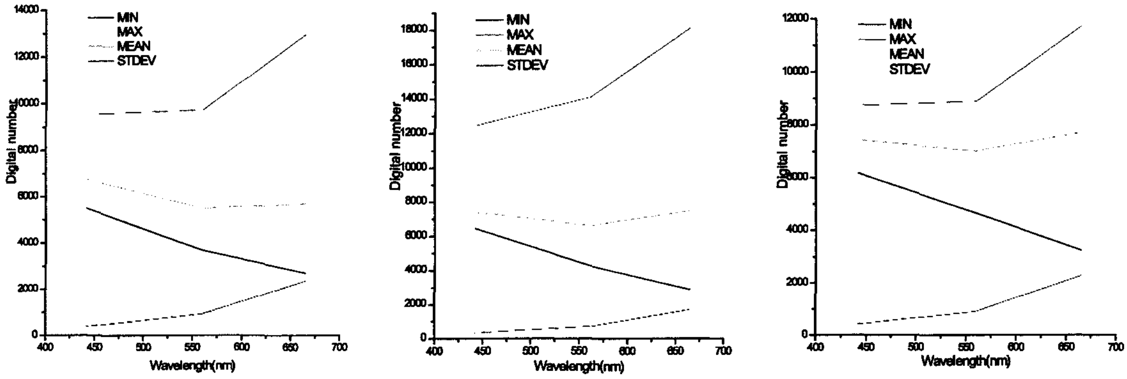

Fig. 3. Statistical results of Liaodong, Bohai and Laizhou Bay MERIS images obtained in April

Table 2. Statistical information of the MERIS image in April, 2005

Location	Channel	Statistical information			
		Minimum value	Maximum value	Mean value	Standard deviation
Liaodong Bay	Blue	5496	9559	6763.47	384.89
	Green	3686	9738	5501.24	922.65
	Red	2704	12976	5677.64	2358.32
Bohai Bay	Blue	6434	12448	7399.00	326.33
	Green	4293	14076	6608.55	694.48
	Red	2865	18121	7489.40	1694.80
Laizhou Bay	Blue	6170	8735	7434.38	413.17
	Green	4635	8883	7013.15	906.30
	Red	3217	11719	7698.35	2265.58

2.2. MERIS Image in October, 2003

Statistical quantities of Liaodong Bay, Bohai Bay and Laizhou Bay in MERIS images of 665nm, 560nm and 442nm are given in Table 3 and Fig. 4, including mean, maximum, minimum and standard deviation.

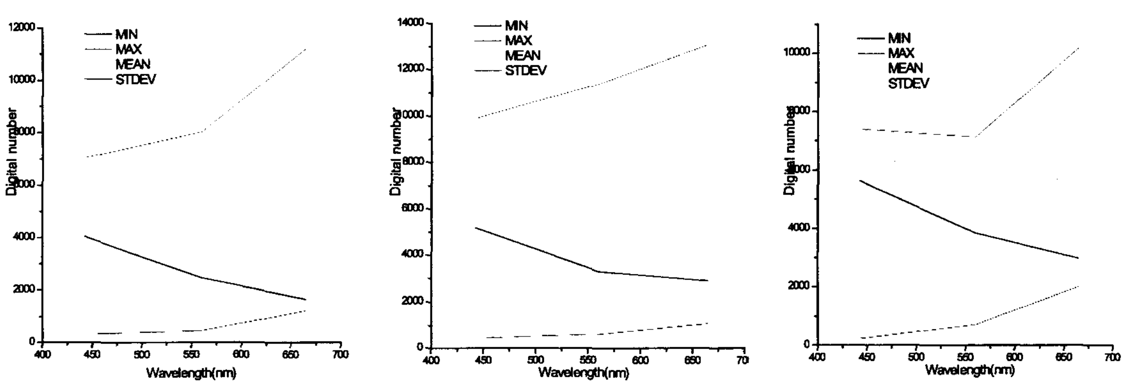

Fig. 4. Statistical results of Liaodong, Bohai and Laizhou Bay MERIS images obtained in October

Table 3. Statistical information of the MERIS image in October, 2003

Location	Channel	Statistical information			
		Minimum value	Maximum value	Mean value	Standard deviation
Liaodong Bay	Blue	4040	7056	5040.47	347.10
	Green	2453	8020	3836.16	445.80
	Red	1636	11210	3368.65	1213.00
Bohai Bay	Blue	5192	9885	6292.04	430.90
	Green	3295	11380	5358.07	614.53
	Red	2889	13088	5442.73	1080.64
Laizhou Bay	Blue	5630	7400	6548.07	230.32
	Green	3840	7130	5706.28	717.41
	Red	2969	10172	5651.21	1996.35

2.3. MERIS Image in December, 2003

Statistical quantities of Liaodong Bay, Bohai Bay and Laizhou Bay in MERIS images of 665nm, 560nm and 442nm are given in Table 4 and Fig. 5, including mean, maximum, minimum and standard deviation.

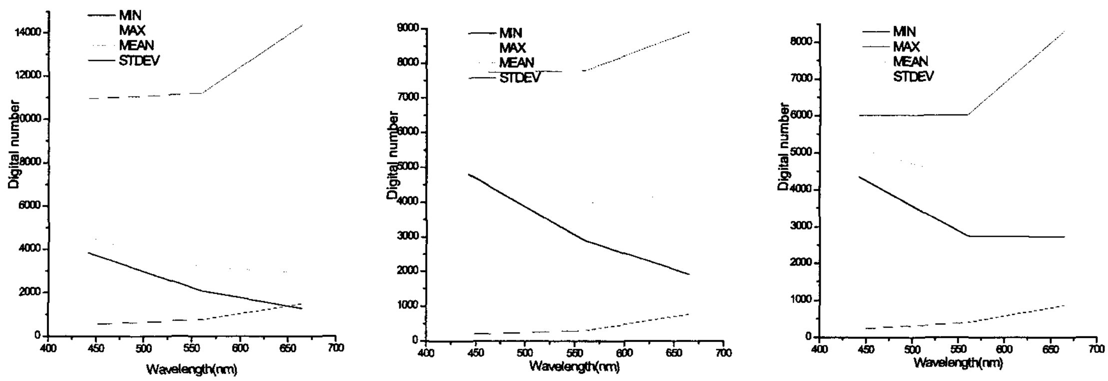

Fig. 5. Statistical results of Liaodong, Bohai and Laizhou Bay MERIS images obtained in December

Table 4. Statistical information of the MERIS image in December, 2003

Location	Channel	Statistical information			
		Minimum value	Maximum value	Mean value	Standard deviation
Liaodong Bay	Blue	3835	10948	4548.87	547.41
	Green	2059	11198	3163.42	742.29
	Red	1257	14365	2916.03	1472.65
Bohai Bay	Blue	4803	7710	5317.86	188.59
	Green	2889	7782	3963.54	299.57
	Red	1901	8901	4250.28	758.39
Laizhou Bay	Blue	4359	6011	5117.45	230.78
	Green	2737	6021	4289.33	395.65
	Red	2719	8303	5079.83	853.64

2.4. RECIPROCALCOMPARISON

The statistical quantity calculations of MERIS image on April, 2005 produce the following results: STDEV in Bohai Bay is the lowest due to the even distribution of water optical properties, MIN in Liaodong Bay is the lowest due to a large area of clear water, MEAN in Bohai Bay is the highest due to high reflectance brought about by extensive suspended matter and Max in Bohai Bay is the highest. There is a gap between the last result and what can be seen from the images. The difference may be caused by pixels of high brightness.

The statistical quantity calculations of MERIS on Oct, 2005 produce the following results: Bohai Bay has the highest radiance because a smog belt floats from the border between Hebei province and Shandong province to the center of Bohai via Bohai Bay and smog sends strong Mie scattering signals. Liaodong Bay has the lowest radiance because the water around Qinghuadao, west of the Bay, is very clean. Qinghuangdao, well-known for its bathing beaches across the China, has higher transparency. Besides, the mean is the smallest in Liaodong Bay, because the water there is clearer than that in Bohai Bay and Laizhou Bay, and STDEV has no such obvious characteristics.

The statistical quantity calculations of MERIS in Dec, 2003 produce the following results: for the maximum value of radiance, the highest is in Liaodong Bay because the reflectance of sea ice is noticeably higher than that of water; for the minimum value of radiance, the lowest is also in Liaodong Bay, which can be explained by the clear water area southwest of the bay; for the mean value of radiance, the highest is in Laizhou Bay because the suspended sand brought by the Yellow River has higher reflectance; for standard deviation of radiance, the highest is in Liaodong Bay, where there is sea ice with high reflectance and clear water with low reflectance. Besides, the seawater radiance there is uneven .

3. COMPARISON WITH IN SITU OCEAN COLOR DATA

Fig. 6 is monthly averaged Bohai transparency chart with the scale of 1:7000000 (i.e. in April, October and December). Their original data comes from years of in situ observation.

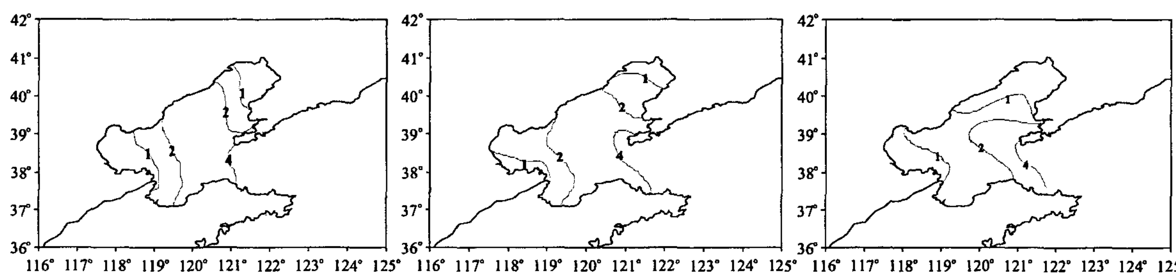

Fig. 6. Transparency of Bohai in (a) April,(b)October and (c) December [3]

In Fig. 1(a), the turbid area is located at the bottom of and east of Liaodong Bay, the major part of Bohai Bay and near the mouth of Yellow River. This basically corresponds to the area with the transparency of less than 1m. The clear area in Fig. 1(a) is in the west of Liaodong Bay and the center of Bohai. It corresponds to the area with the transparency of more than 1m. In Fig. 1(b), the turbidity in the three bays is not entirely consistent with that in the Fig. 6(b), and its transparency is generally lower than that in Fig. 6(b). In Fig. 1(c) the turbidity in the three bays finds agreement with the transparency distribution in Fig. 6(c). But in the sea area near Qinghuangdao, Fig 6 (c) is lower than the interpretation from the MERIS image. This is consistent with the in situ data.

It should be pointed out that the transparency of the Yellow River mouth sea area in Fig. 6 is higher than that of MERIS images interpretation results, because the data used in Fig. 6 were acquired before the course of the Yellow River was changed by human force.

4. CONCLUSION AND DISCUSSION

The statistical analysis and the comparison between monthly average transparency distributions demonstrate that among the three bays, Liaodong Bay is the clearest; Bohai Bay is less clear than Liaodong Bay but even in the spatial distribution of optical properties; Laizhou Bay has higher reflectance due to the large amount of inorganic suspended matter brought by Yellow River.

The interpretation of Bohai ocean color in the MERIS images is consistent with the in situ data. This suggests the potential of MERIS in ocean color information extraction.

This paper uses the Reduced MERIS data with a spatial resolution of 1200m. This restricts the interpretation and analysis to some extent. The MERIS data with a spatial resolution of 300m will produce better results.

5. ACKNOWLEDGEMENTS

This research was supported by the Dragon Project through id 2566, by the High-tech Research and Development Program of China through grant 2002AA634020, by Marine Science and Technology Research Program of State Oceanic Administration of China through "Research on Quantitative Inversion Technology for Inorganic Suspended Matter Concentration by Airborne Hyperspectral Data ".

6. REFERENCES

1. Feng S. Z, Li F Q, and Li S. Q., *Introduction to Oceanography*, China: Higher Education Press, 1999.
2. http://envisat.esa.int/instruments/meris/
3. Editorial Board for Marine Atlas, *Marine Atlas of Bohai Sea, Yellow Sea and East China Sea: Hydrology*. China: Ocean Press, 1992.

IMAGING ABILITY RESEARCH OF SHALLOW UNDERWATER BOTTOM TOPOGRAPHY BY SAR IN CHINESE COASTAL SEA

Huang Jianbo [(1), (2)], Zhang Jie [(2), (3)], Yang Jungang [(2)], Meng Junmin [(2)]

[(1)] *Ocean University of China, Yu-Shan Road, Qingdao, Shandong, China, 266003, E-mail:huangjianbo_qd@sohu.com*

[(2)] *First Institute of Oceanography, S. O. A., Xianxialing Road, High-Tech Park, Qingdao, Shandong, China, 266061*
E-mail:yangjg@fio.org.cn, mengjm@fio.org.cn

[(3)] *Key Laboratory of Marine Science and Numerical Modeling, S. O. A., Xianxialing Road, High-Tech Park, Qingdao, Shandong, China, 266061, E-mail: zhangjie@public.qd.sd.cn*

ABSTRACT

Based on the SAR imaging mechanism of shallow underwater bottom topography, this paper analyzes the status of tide and tidal current and the distribution of shallow underwater bottom topography in Chinese coastal sea. About 100 scenes of ENVISAT ASAR quick look images and ERS SAR quick look images are analyzed combined with the analyses of the status of tide and tidal current and the distribution of shallow underwater bottom topography. Four main areas where underwater bottom topography can be imaged by SAR are obtained. They are area around Bohai Sea, area around Subei Shoal, area around Taiwan Shoal and area of Nansha Islands. Four examples of SAR images included information of underwater bottom topography are presented. It can be shown through above analyses that fluctuation of underwater bottom topography and the status of tide and tidal current are the crucial factors for SAR being imaged in shallow underwater bottom topography.

1. INTRODUCTION

Synthetic Aperture Radar (SAR) is one advanced sensor of environment and resource in the microwave remote sensing. SAR has many virtues such as high resolution, all-weather, all day and all night, multi-band, multi-polarization etc. Since SEASAT-1 equipped SAR was launched in 1978 by America, SAR was used in many research areas of oceanography. For example internal waves, ocean waves, marine and submarine, sea ice, oil spill and underwater bottom topography. Since find of underwater bottom topography in one airborne SAR image firstly by De Loor[1], the SAR imaging mechanism of underwater bottom topography and detection model became the research hotspot in the ocean. Alpers and Hennings[2] presented a simple theoretical model of SAR imaging mechanism of underwater bottom topography, in which topography-tidal current interaction was described by a one-dimensional continuity equation, and current-wave interaction was described by weak hydrodynamic interaction theory. Yuan Yeli[3] put forward an analytical representation of the high frequency spectra of ocean waves which derived from wave number spectrum balance equation, and constructed the theoretical basis of shallow underwater topography detection with SAR image.
China locates in the northwest of the Pacific Ocean and has vast sea areas. There are Bohai Sea, Yellow Sea, East China Sea and South China Sea from the north to the south and the total area of sea is about 4,700,000 square kilometers. Over 5400 islands distribute in Chinese sea area. Coastline of main land is about 1.8 million kilometers. There are many coastal sea areas or areas of islands where water depth changes from several meters to several decade meters. Some underwater bottom topography of these areas is unchangeable, but others change with the action of strong ocean current, typhoon and storm tide. Area monitoring is important work to the management of coastal zones and islands. Thus the research of underwater bottom topography and their changes has very important meanings.

Proc. 2005 Dragon Symposium "Mid-Term Results", Santorini, Greece
27 June – 1 July 2005 (ESA SP-611, January 2006)

The basic research of the theory of SAR detection of underwater bottom topography began from 1990s in China. The application researches of SAR detection of underwater bottom topography were seldom done and only few examples of SAR detection of underwater bottom topography were carried out. In order to realize the practical application of SAR detection of underwater bottom topography, and to know imaging ability of SAR in shallow underwater bottom topography in Chinese coastal sea area, it is necessary to find out appropriate area where underwater bottom topography can be imaged by SAR in Chinese coastal sea. It is helpful to find out the area of practical application of SAR detection of underwater bottom topography.

2. SAR IMAGING MECHANISM OF SHALLOW UNDERWATER BOTTOM TOPOGRAPHY

SAR works in microwave band and can only penetrate into sea water several centimeters, so SAR cannot detect underwater bottom topography directly. The reason of SAR detecting underwater bottom topography is that underwater bottom topography changes backscattering of sea surface indirectly. By many experiments and theoretical researches, it is found that the main mechanism of SAR imaging of underwater bottom topography is hydrodynamic modulation of tidal current flowing over underwater bottom topography to micro-scale wave in the sea surface. This mechanism includes three physical processes (see fig.1):

(1) Interactions of underwater bottom topography and tidal current change tidal current in the sea surface.
(2) Tidal current in the sea surface modulates micro-scale wave in the sea surface.
(3) Micro-scale wave in the sea surface changes backscattering section of SAR.

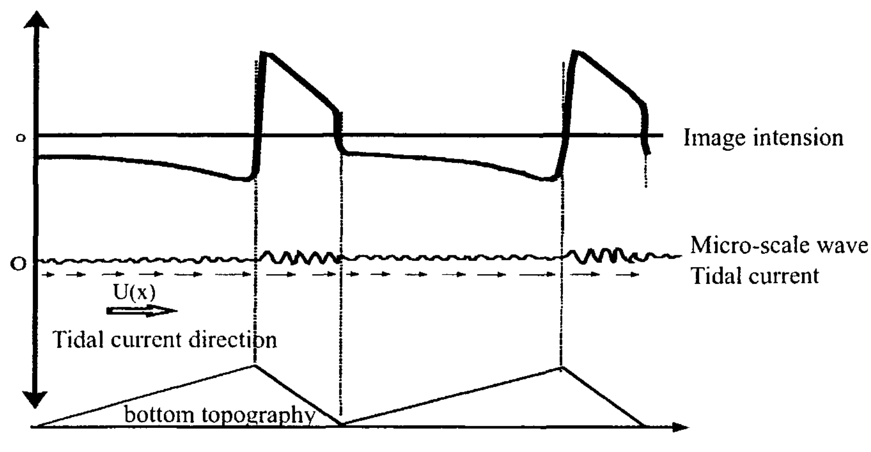

Fig.1 the sketch map of the mechanism of SAR imaging of underwater bottom topography

3. ANALYSIS OF THE STATUS OF TIDE AND TIDAL CURRENT IN CHINESE COASTAL SEA

It is known that tidal current is an important influence factor of SAR imaging of underwater bottom topography from the mechanism of SAR imaging of underwater bottom topography. If there are appropriate tidal current fields, shallow underwater bottom topography can be seen in SAR image. So we should know the status of tide and tidal current in Chinese coastal sea before studying SAR imaging ability of underwater bottom topography in Chinese coastal sea.

3.1 Statuses of tide and tidal current in Bohai Sea, Yellow Sea and East China Sea

From 1950s, many experiments of in situ measure of tide and tidal current have been done in China. In the end of 1980s, numerical simulation of tide and tidal current in Bohai Sea, Yellow Sea and East China Sea were carried out with the development of computer technology, and more detailed understanding of the status of tide and tidal current is obtained. Fig.2 is the distribution map of tide type in China coastal sea. Tides in Bohai Sea, Yellow Sea and East China Sea are mainly regular semidiurnal tide, and less is irregular semidiurnal tide. Tide in very small area is diurnal tide.

Fig.3 is the ellipse map of M_2 component tidal current in Bohai Sea, Yellow Sea and East China Sea. We can see that M_2 tidal currents in the northwest of Yellow Sea, which is area of Subei shoal, become complicated. M_2 tidal currents in Bohai Sea also behave varieties due to the action of coastline and underwater bottom topography in coastal sea.

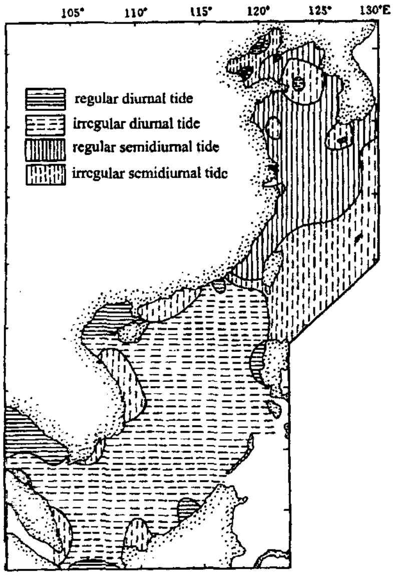

Fig.2 Distribution map of tide type in Chinese coastal sea[5]

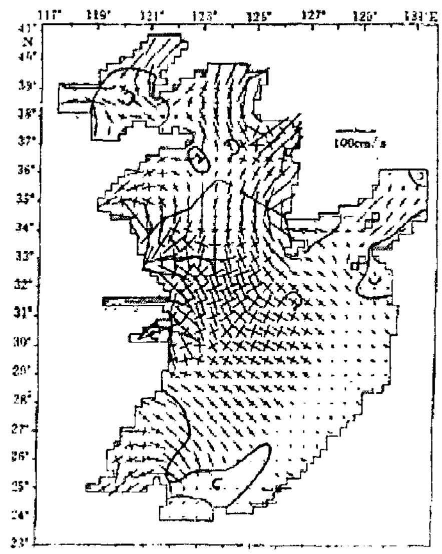

Fig.3 Ellipse map of M_2 component tidal current in Bohai Sea, Yellow Sea and East China Sea[6]

3.2 Status of tide and tidal current in South China Sea

South China Sea is a deep margin sea. Its area is vast and its tide and tidal current are complex. In situ measure data are absent in South China Sea. Since 1980s many Chinese scientists simulated numerically tide and tidal current in South China Sea and obtained some uniform conclusion. They think tides in South China Sea are mainly diurnal tide and tides in several small areas are semidiurnal tide (see fig.2). Tidal current in South China Sea is mainly diurnal current.

Fig.4 gives tidal current distribution in South China Sea. Tidal currents in most areas of South China Sea distribute equably except in the areas near the coast and the area of Nansha Islands. Varieties of tidal currents in coastal areas are caused by the action of coastline. Varieties of tidal currents in Nansha Islands are caused by varieties of water depth of islands area. In addition, tidal current in Taiwan Strait is complex and changes frequently for its special geophysical location.

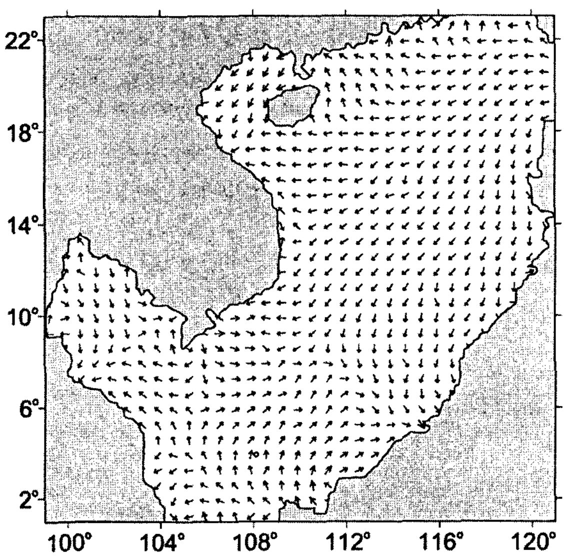

Fig.4 tidal current field of South China Sea

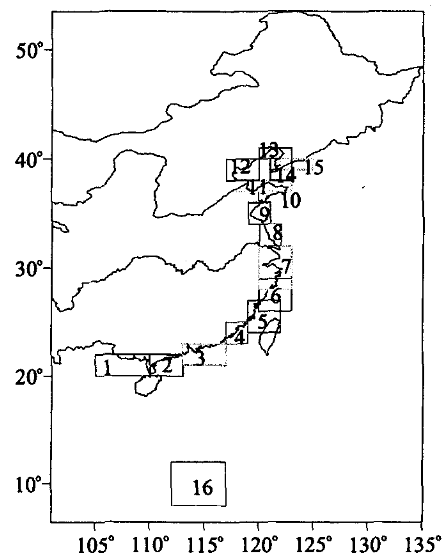

Fig.5 Sketch map of analysis area of underwater bottom topography

4. ANALYSIS OF UNDERWATER BOTTOM TOPOGRAPHY IN CHINESE COASTAL SEA

In order to understand SAR imaging ability of underwater bottom topography in Chinese coastal sea, it is very necessary to analyze underwater bottom topography in Chinese coastal sea with the actual water depth. Chinese coastal sea area is divided into 16 areas, see in fig.5. Table.1 is the range of area of these 16 areas.

Table.1 Range of 16 areas of underwater bottom topography

serial number	range	serial number	range	serial number	range	Serial number	Range
1	105°~110°E 20°~22°N	5	119°~122°E 24°~27°N	9	119°~121°E 34°~36°N	13	120°~123°E 40°~41°N
2	110°~113°E 20°~22°N	6	120°~123°E 26°~29°N	10	120°~123°E 36°~37°N	14	121°~123°E 38°~40°N
3	113°~117°E 21°~23°N	7	120°~123°E 28°~32°N	11	118°~123°E 37°~38°N	15	122°~125°E 39°~40°N
4	117°~119°E 23°~25°N	8	120°~122°E 32°~34°N	12	117°~120°E 38°~40°N	16	122°~117°E 8°~12°N

Drawing isoline map and 3-D frame map of water depth of these 16 areas with data of ETOP2 and sea charts, and analyzing these maps of every area, we can select areas where underwater bottom topography can potentially be imaged by SAR. Fig.6 is isoline map of No.5 area and fig.7 is its 3-D frame map. Water depth of this area (southwest of Taiwan Strait) is in range of several decade meters and water depth outside of this area is more than hundreds. So there are the areas where underwater bottom topography can be imaged by SAR in No.5 area, and Taiwan Shoal is in this area.

The areas selected through analyses of these 16 areas where underwater bottom topography can potentially be imaged by SAR in Chinese coastal sea are area around Bohai Sea, area around Subei Shoal, area near mouth of Changjiang River, western area of Taiwan Strait, area near coast of Guangdong and area of Nansha islands.

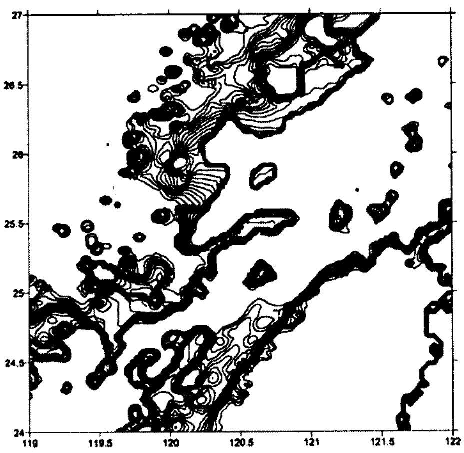

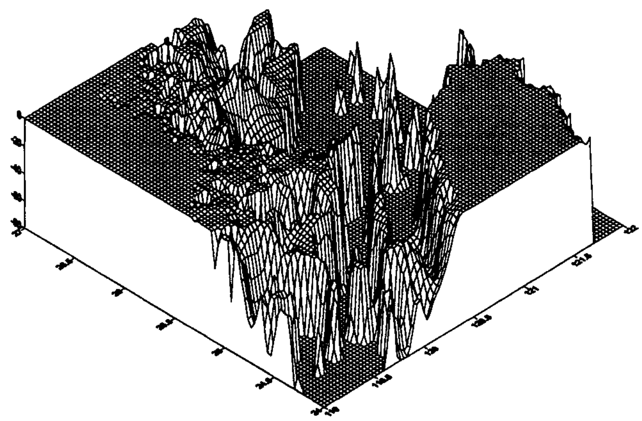

Fig.6 Isoline map of water depth of No.5 area *Fig.7 3-D frame map of water depth of No.5 area*

5. DIVISION OF AREAS WHERE UNDERWATER BOTTOM TOPOGRAPHY CAN BE IMAGED BY SAR

Tide and tidal current and underwater bottom topography are the main factors which decide whether underwater bottom topography can be imaged by SAR. After analyses of the status of tide and tidal current and distribution of underwater bottom topography in Chinese coastal sea, we collected about 100 scenes of quick look SAR images with DESCW software of European Space Agency and online catalogue system of ENVISAT ASAR images and ERS SAR images in the website of China Remote Sensing Satellite Ground Station. Fig.8 is the sketch map of covering area of these quick look SAR images.

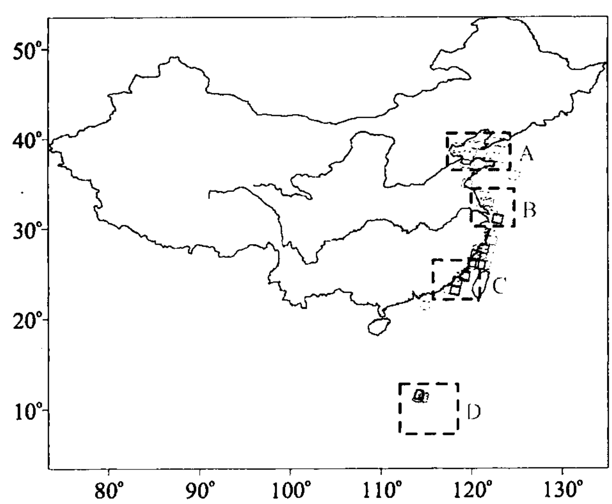

Fig.8 Sketch map of covering area of quick look SAR images in Chinese coastal sea area

After analyses, it is known that four main areas where underwater bottom topography can be imaged by SAR are obtained through analyzing these quick look SAR images associated with ENVISAT ASAR images provided by Dragon Project and analyses of the status of tide and tidal current and underwater bottom topography in Chinese coastal sea.

5.1 Area around Bohai Sea

Underwater bottom topography in this area can be imaged by SAR is because that tidal currents are complex and fluctuation of underwater bottom topography is evident near the coast of Bohai Sea. Fig.9 is the sea area of Tanggu. Left map of fig.9 is the whole ENVISAT ASAR image acquired in August 8th 2004. Upper right map is ENVISAT ASAR image of the white pane in the left map. Lower right map is the gray map of water depth of sea chart.

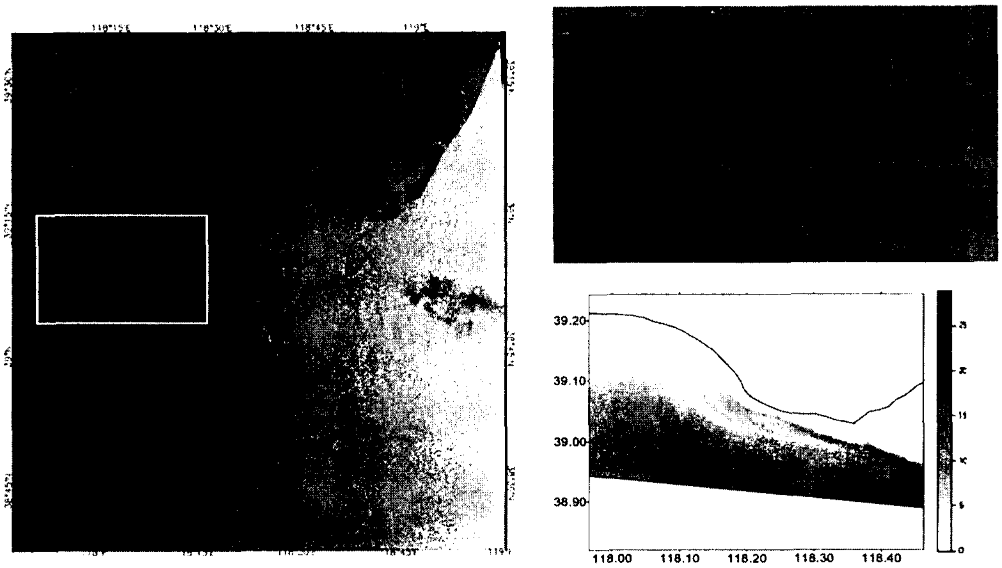

Fig.9 ENVISAT ASAR image of Tanggu area and gray map of water depth of sea chart

5.2 Area around Subei Shoal

This area locates in the west of Yellow Sea, and Subei Shoal is in this area. There are many sandbanks in this area and water depth is between 0~30m in the sandbank area. Fig.10 is ENVISAT ASAR image of Subei Shoal which is obtained by put two scenes of SAR images acquired in August 30th 2004 together and sea chart of this area.

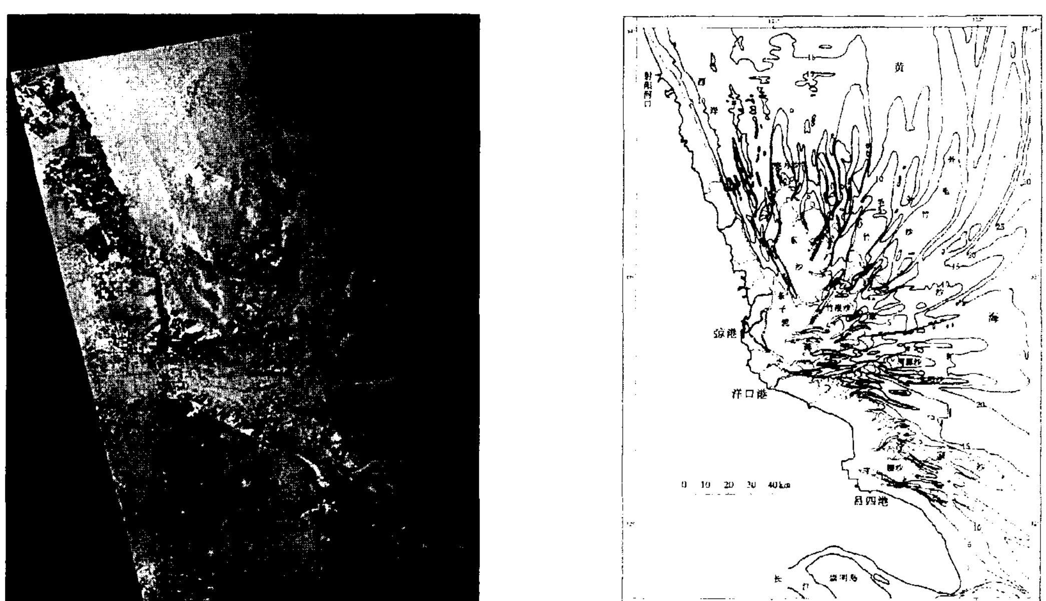

Fig.10 ENVISAT ASAR image of Subei Shoal (left map) and sea chart (right map)

5.3 Area around Taiwan Shoal

This area locates in the south of Taiwan Strait and Taiwan Shoal is in this area. Taiwan Shoal is the shallowest shoal in the Taiwan Strait. It is a mesa where fluctuation of water depth is small and is surrounded by steep slopes. Water depth in the steep slopes changed from 50m to 100m quickly. Width of Taiwan Shoal from South to North is about 60~80km and length from west to east is about 150km. Taiwan shoal is composed by over 150 pieces of sandbanks. Fig.11 is ERS-2 SAR image of Taiwan Shoal acquired in October 31st 1999. Left map of fig.15 is the whole SAR image covering Taiwan Shoal. Upper right map is SAR image of small area in Taiwan Shoal. Lower right map is the isoline map of water depth obtained by SAR detection.

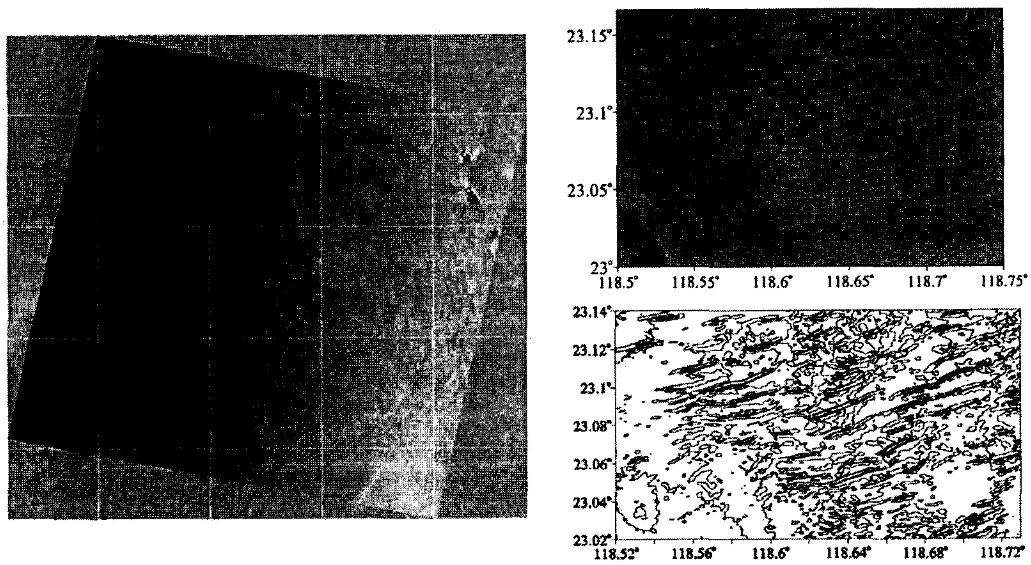

Fig.11 ERS-2 SAR image of Taiwan Shoal and isoline map of water depth obtained by SAR deteciton

5.4 Area of Nansha Islands

Nansha Islands locate in south of South China Sea. It is the archipelago where distribute about 200 islands and reefs. The width from north to south is about 550km and the length from east to west is about 650km. underwater bottom topography of Nansha Islands is trapezoid. The area of islands and reefs is about several decade meters, and water depth outside of islands and reefs changes from several decade meters to over thousands meters quickly. Nansha Islands can be imaged by SAR for tidal currents flowing over islands and reefs changes when they fall across raised underwater bottom topography. Fig.12 is ENVISAT ASAR image covering Shuangzi Reefs in Nansha Islands acquired in August 18th 2004 and sea chart of Shuangzi Reefs. Left map of fig.12 is the whole scene SAR image and upper right map is SAR image of area of Shuangzi Reefs. Lower right map is isoline map of water depth of sea chart.

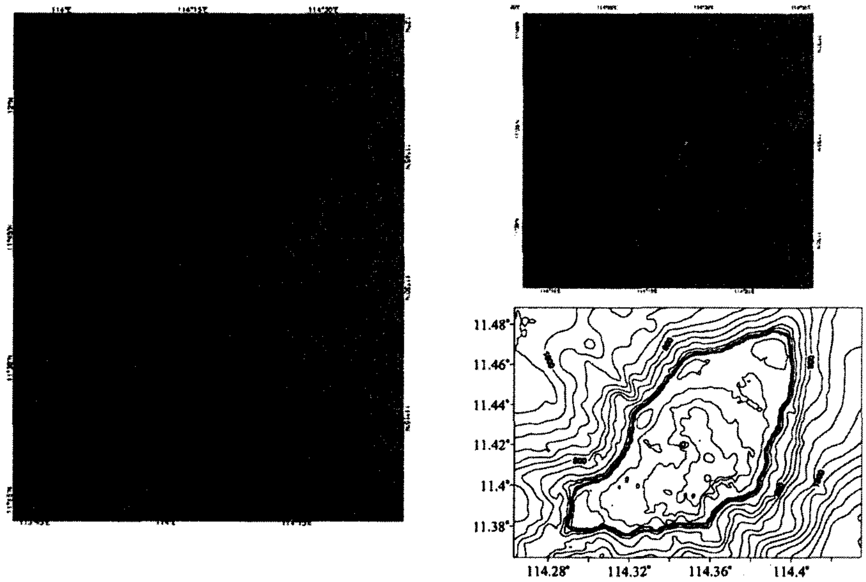

Fig.12 ENVISAT ASAR image of Shuangzi Reefs in Nansha Islands and isoline map of water depth of sea chart

6. CONCLUSION AND DISCUSSION

When water depth is in several decade meters and appropriate tidal current field exists, underwater bottom topography can be imaged by SAR. According to SAR imaging mechanism and analyses above, it can be found that tidal current and underwater bottom topography is necessary condition of being imaged by SAR for underwater bottom topography, and tidal current takes a key role. Thus analyses of status of tidal current and underwater bottom topography are necessary to analyze whether underwater bottom topography can be imaged by SAR in some areas.

From this paper, there are four main areas in Chinese coastal sea where underwater bottom topography can be imaged by SAR. They are the area around Bohai Sea, the area around Subei Shoal, the area around Taiwan Shoal and the area around Nansha Islands. Four examples of SAR images in these four areas were presented and compared with sea water depth of sea chart and detection results by SAR. This paper analyzes generally the area where underwater bottom topography can be imaged by SAR. The further work is to develop detailed research of underwater bottom topography detection by SAR image in these four areas.

7. ACKNOWLEDGEMENTS

This research was supported by the Dragon Programme through id 2566 and by National Natural Science Foundation of China through grants 40176040. Some ENVISAT ASAR image data were provided by ESA as part of the AO project AOE.382.

8. REFERENCES

1. De Loor, G. P., The observation of tidal patterns, currents and bathymetry with SLAR imagery of the sea, *IEEE. Journal of Oceanic Engineering*, Vol.6, 124-129, 1981.

2. Alpers W, Hennings I, A theory of the imaging mechanism of underwater bottom topography by real and synthetic

aperture radar, *Journal of Geophysical Research,* Vol.8, 10 529-10 546,1984.
3. Yuan Y L, Representation of high frequency spectra of ocean waves and the basis for analyzing SAR images (in Chinese), *OCEANOLOGIA ET LIMNOLOGIA SINICA*, Vol.**28,** 1-5, 1997.
5. Feng Shizuo, Li Fengqi and Li Shaoqing, *An* introduction *to Marine Science* (in Chinese), Higher education press, China, Beijing, 1999.
6. Zhao Baoren, Fang Guohong and Cao Deming, Numerical simulation of tide and tidal current in Bohai Sea, Yellow Sea and East China Sea (in Chinese), *ACTA OCEANOLOGICA SINICA*, Vol.16, 1-10, 1994.

UNDERWATER BOTTOM TOPOGRAPHY DETECTION OF SHUANGZI REEFS WITH ENVISAT ASAR IMAGES ACQUIRED IN DIFFERENT TIME

Yang Jungang(1), (2), (3) **Zhang Jie**(3), (4) **Meng Junmin** (3)

(1) *Institute of Oceanology, Chinese Academy of Sciences, Nanhai Road, Qingdao, China, 266071*

(2) *Graduate School, Chinese Academy of Sciences, Yuquan Road, Beijing, China, 100039*
E-mail: yangjg@fio.org.cn

(3) *First Institute of Oceanography, S. O. A., Xianxialing Road, High-Tech Park, Qingdao, Shandong, China, 266061,*
E-mail: mengjg@fio.org.cn

(4) *Key Laboratory of Marine Science and Numerical Modeling, S. O. A., Xianxialing Road, High-Tech Park, Qingdao, Shandong, China, 266061, E-mail: zhangjie@public.qd.sd.cn*

ABSTRACT

Imaging mechanism of underwater bottom topography by SAR and underwater bottom topography detection model with SAR image is introduced. Underwater bottom topography of Shuangzi Reefs in Nansha islands is detected by this model with three scenes of ENVISAT ASAR images acquired in different time. Detection results are compared and errors are analyzed. Underwater bottom topography detection experiments of Shuangzi Reefs show that the detection model used in this paper is practicable. Detection results indicate that SAR images acquired in different time also can be used to detect underwater bottom topography, and detection results are affected by the ocean conditions in SAR acquiring time.

1. INTRODUCTION

Synthetic Aperture Radar (SAR) is one of the advanced microwave remote sensors of environment and resource. It can observe targets all weather and all day and night in multi-band, multi-polarization and multi-look angle mode. Since American Seasat-1 equipped SAR was launched in 1978, SAR has been used in many observations and researches of ocean, such as internal waves, ocean waves, marines and submarines, ocean ices, oil spill and underwater bottom topography etc. Underwater bottom topography detection with SAR image is one of important applications of SAR in ocean research. Since De Loor[1] firstly found shallow underwater bottom topography on X-band airborne real aperture radar imagery, many scientists began to research SAR imaging mechanism and detection model of shallow underwater bottom topography with SAR image. Alpers and Hennings[2] presented a simple theoretical model of SAR imaging mechanism of underwater bottom topography, in which topography-tidal current interaction was described by a one-dimensional continuity equation and current-wave interaction was described by weak hydrodynamic interaction theory. Yuan Yeli[3] presented an analytical representation of the high frequency spectra of ocean waves which derived from wave number spectrum balance equation, and constructed the theoretical basis of shallow underwater bottom topography detection with SAR image. Ma Yi and Zhang Jie[4] simulated SAR image of underwater bottom topography, and analyzed the differences of simulation SAR images in different water depth and in different gradient of underwater bottom topography.

In this paper we detect underwater bottom topography of Shuangzi Reefs in Nansha islands with three scenes of ENVISAT ASAR images acquired in different time. In this process, we use underwater bottom topography simulation

Proc. 2005 Dragon Symposium "Mid-Term Results", Santorini, Greece
27 June – 1 July 2005 (ESA SP-611, January 2006)

and detection models, which are constructed on SAR imaging mechanism of underwater bottom topography, and damped Newton-row action method. Furthermore, we compare detection results and analyze errors. Detection results show that detection model and algorithm of underwater bottom topography are feasible. Detection experiments realize underwater topography detection of the same area with SAR images acquired in different time, and establish the foundation on practical detection of underwater bottom topography of Nansha islands with SAR images.

2. DETECTION MECHANISM OF UNDERWATER BOTTOM TOPOGRAPHY WITH SAR IMAGE

2.1 SAR imaging mechanism of underwater bottom topography

SAR can penetrate into sea water only to a depth on the order of centimeter, so SAR can not observe underwater bottom topography directly. The reason underwater bottom topography can be observed by SAR is that underwater bottom topography modulates radar backscattering of sea surface indirectly, and SAR measures radar backscattering of sea surface. It is well known that the main SAR imaging mechanism of underwater bottom topography is hydrodynamic modulation of the short-scale ocean waves by tidal current which flows over underwater bottom topography. This mechanism includes three physical processes. Firstly, Interaction of the tidal current with underwater bottom topography induces varieties of sea surface current. Secondly, short-scale ocean waves are modified by sea surface current. In the end, varieties of short-scale ocean waves induce varieties of radar backscattering.

Yuan Yeli presented an analytical representation of the high frequency spectra of ocean waves which derived from wave number spectrum balance equation. Furthermore, he used the expression of backscattering cross section introduced by Valenzuela[5] to analyze every component of SAR images in detail. SAR image related to large-scale background field can be written by:

$$\sigma_{0c} = \frac{\pi}{8} ctg^4(\theta) F_1(\theta) m_3^{-1} \omega^{-1} \left(l_m l_n + \frac{1}{2} l_\alpha l_\beta \zeta_{\alpha\beta} L_m L_n \right) \frac{\partial u_m}{\partial x_\alpha} \tag{1}$$

Here θ is incidence angle of microwave. $F_1(\theta)$ is polarization function of emitting and receiving signals. $\{l_\alpha\}$ is direction component of short-scale waves on the sea surface. m_3 is a dimensionless constant to be determined. $\{L_m\}$ is direction component of tidal waves. ω is a function of radar wave number and incidence angle. $\{u_m\}$ is flowing speed of the large-scale sea water. $\zeta_{\alpha\beta} = \frac{\partial}{\partial \zeta} \left(\frac{\partial U_{\omega\beta}}{\partial x_\alpha} \right) \Big|_{\zeta=0}$. $\{U_{w\alpha}\}$ is flowing speed of water particle of ocean wave.

2.2 Model and algorithm of SAR image simulation of underwater bottom topography

Model of SAR image simulation of underwater bottom topography includes two parts. One is calculating tidal current field with hydrodynamic model, and the other is calculating gray value of simulate SAR image with tidal current field. Hydrodynamic model used to calculate tidal current is Princeton Ocean Model (POM).

From Eq.1, the relation of radar backscattering σ_{0c} and modulating function G of short wave field and large-scale ocean current is:

$$\sigma_{0c} = M(\theta,\kappa)G(u,v,\theta_1) \tag{2}$$

Here $M(\theta, \kappa)$ is a function having nothing to do with radar parameters and underwater bottom topography. Its value is invariable. Physics magnitude related to bright-dark stripes in SAR image is the function $G(u, v, \theta_1)$, so gray image of G is used to represent simulate SAR image. The expression of $G(u, v, \theta_1)$ is:

$$G(u,v,\theta_1) = (l_m l_n + \frac{1}{2} l_\alpha l_\beta \zeta_{\alpha\beta} L_m L_n)\frac{\partial u_m}{\partial x_n} \tag{3}$$

Algorithm of SAR image simulation of underwater bottom topography is calculating tidal current field with program of POM which introduces σ-coordinate and Arakawa-C gridding, and then calculating gray value of simulate SAR image by Eq.3 with tidal current field.

2.3 *Model and algorithm of detection of underwater bottom topography with SAR image*

Model of detection of underwater bottom topography with SAR image is composed of shallow water hydrodynamic equations (Eqs.4-6) and the function expression of radar gray value Eq.3.

$$\frac{\partial U}{\partial t} + U\frac{\partial U}{\partial x} + V\frac{\partial U}{\partial y} - fV = -g\frac{\partial \zeta}{\partial x} + \frac{C_b U}{H} \tag{4}$$

$$\frac{\partial V}{\partial t} + U\frac{\partial V}{\partial x} + V\frac{\partial V}{\partial y} + fU = -g\frac{\partial \zeta}{\partial y} + \frac{C_b V}{H} \tag{5}$$

$$\frac{\partial \zeta}{\partial t} + \frac{\partial (HU)}{\partial x} + \frac{\partial (HV)}{\partial y} = 0 \tag{6}$$

Initial condition: $u|_{t=t_0} = U_0$, $v|_{t=t_0} = V_0$, $\zeta|_{t=0} = 0$ (given forced water level in open boundary), $H = H_0$, where U_0、V_0 are u、v components of tidal current field in SAR imaging time. H_0 is initial water depth.

Solid boundary condition: $\partial u/\partial n = 0$, $\partial v/\partial n = 0$, $\partial\zeta/\partial n = 0$ and $\partial h/\partial n = 0$, here n is normal direction in the boundary.

Algorithm of detection of underwater bottom topography with SAR image is damped Newton-row action method. This method has been testified to be highly efficient, reliable and steady with simulate data by Cui[6].

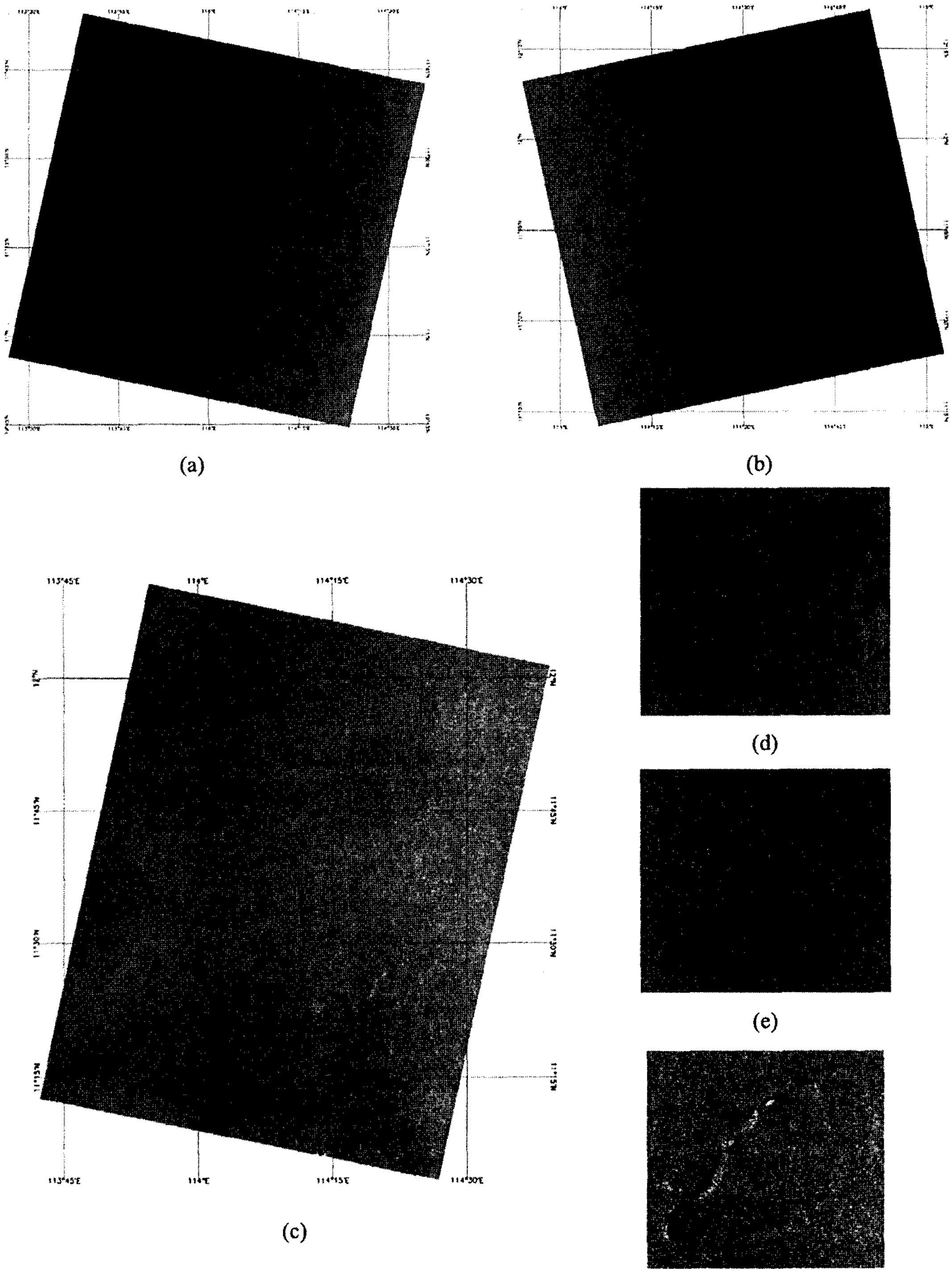

Fig.1 Three scenes of ENVISAT ASAR images of Shuangzi Reefs (Copyright European Space Agency)

3. UNDERWATER BOTTOM TOPOGRAPHY DETECTION OF SHUANGZI REEFS WITH ENVISAT ASAR IMAGES

3.1 Data of underwater bottom topography detection experiments

Three scenes of ENVISAT ASAR images are used in underwater bottom topography detection experiments with SAR image. They are respectively acquired in August 21st 2004 (call the first SAR image), in August 19th 2004 (call the second SAR image) and in August 18th 2004 (call the third SAR image). All these images show in fig.1. Fig.1 (a), (b), (c) are the first, second and third SAR image and (d), (e) and (f) are Shuangzi Reefs corresponding to (a), (b) and (c).

3.2 Underwater bottom topography detection of Shuangzi Reefs with SAR image

Model and algorithm of underwater bottom topography detection with SAR image presented above are introduced into underwater bottom topography detection experiment of Shuangzi Reefs with SAR image. Range of the experiment area is 114°16′~114°26′E, 11°21′~11°30′N. Gridding introduced into detection experiment is 0.02′×0.02′ (about 30.74m×30.74m) and number of gridding is 501×451. Initial speed of tidal current inputted into calculation is the speed of tidal current in SAR imaging time, which is obtained by the calculation of POM program. Open boundary condition is to input water level in SAR imaging time. Initial water depth is obtained by interpolation with coarse-gridding actual water depth. Wind direction of sea surface in SAR imaging time is obtained by the maximum correlation coefficient of SAR image and simulated SAR image. Underwater bottom topography detection results of three scenes of SAR images are shown in fig.2.

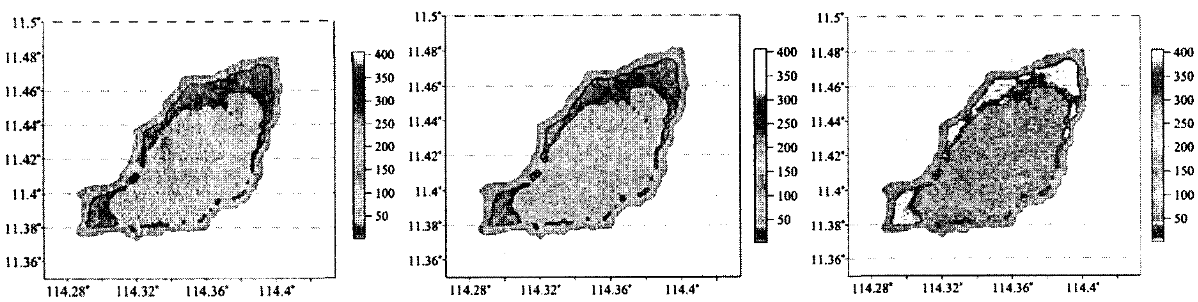

Fig.2 Pseudo-color map of detection results of water depth with the first (left), second (middle) and third (right) SAR image

4. ANALYSIS OF DETECTION RESULTS

Detection results of underwater bottom topography by three scenes of SAR images are analyzed by Comparisons of water depth obtained by SAR image detection and real water depth. Average absolute errors and average relative errors are calculated. Errors in the gridding points whose water depths are in the range of 2~60m, which is detectable range of SAR, are analyzed. Analyses of detection results of three SAR image list as follows.

4.1 Analysis of detection result of the first SAR image

Detection result of the first SAR image is shown in the left of figure.2. Contour of the whole area of islands and reefs is clear and four islands and reefs are visible. Varieties of water depth in the middle area of islands and reefs are small. By comparing detection result and real water depth, we can obtain that average absolute error is 4.19m and average relative error is 35.6%. Comparison of some detection result of water depth with real water depth is shown in Figure.3 (a).

4.2 Analysis of detection result of the second SAR image

Detection result of the second SAR image is shown in the middle of figure.2. The islands and reefs are visible and the trend of varieties of water depths from islands and reefs to the middle area is also visible. By comparing detection result of water depth with real water depth, we can obtain that average absolute error is 4.10m and average relative error is 34.8%. The comparison of some detection result of water depth with real water depth is shown in Figure.3 (b). The detection results of the second SAR image are better than the first SAR image. The reason is that ocean conditions in imaging time of the second SAR image are better than that of the first SAR image. It can be seen from fig.2 (d) and (e).

4.3 Analysis of detection result of the third SAR image

Detection result of the third SAR image is shown in the right of figure.2. By comparing detection result of water depth and real water depth, we can obtain that average absolute error is 8.06m and average relative error is 44.5%. The comparison of some detected water depth with real water depth is shown in Figure.3(c).

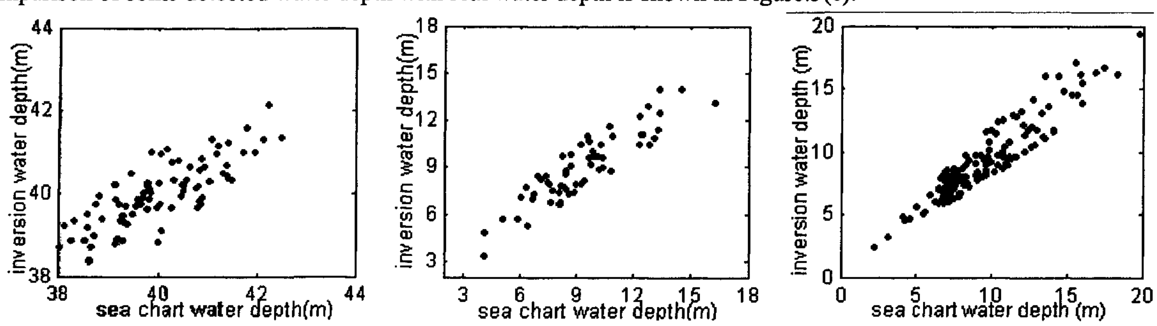

(a) (b) (c)

Figure.3 comparison of real water depth with detection results of water depth of three scenes of SAR images

In fig.4, we compare real water depth and detection results of these three SAR images in some one section paralleling to longitude. All detection results are closed to real water depth except very few points. The fluctuation of underwater bottom topography obtained by three SAR images is similar, except the difference of amplitude of fluctuation and the phase excursion of waves of topography.

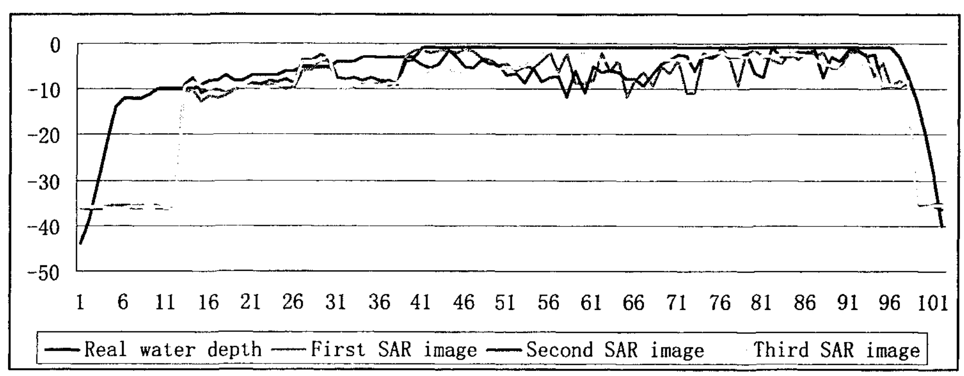

Fig.4 Comparison of real water depth and detection results of water depth of three SAR image

Fluctuation of underwater topography is presented as bright-dark stripes in SAR image. From error analyses of detection results of three scenes of SAR images, we can see that detection results of the third SAR image are best than other two SAR images. The main reason why errors of detection result are large is that detection results of underwater bottom topography with SAR image much rely on initial water depth of detection calculation. In addition, ocean condition in SAR imaging time also affects detection result.

5. CONCLUSION

In this paper, underwater bottom topography detection experiments of Shuangzi Reefs in Nansha islands with three scenes of ENVISAT ASAR images, which are acquired in different time, testifies practicability of model and algorithm of underwater bottom topography detection with SAR image. This paper shows that it is feasible to detect underwater bottom topography with SAR images of the same area acquired in different time. This establishes the foundation on practical detection of underwater bottom topography with SAR images. From this paper we can draw the following conclusions:

(1) Model and algorithm of underwater bottom topography detection with SAR image are feasible and effective.
(2) All SAR images of the same area including information of underwater bottom topography can be used to detect underwater topography, and they need not be limited by SAR imaging time.
(3) Detection result of underwater bottom topography with SAR image is affected by ocean condition in SAR imaging time.
(4) The choice of initial water depth of detection calculation affects final detection result of water depth in *inversion calculation of underwater bottom topography.*

Works of this paper establish foundation on which practical detection of underwater topography with SAR image will be realized in the final.

6. ACKNOWLEDGEMENTS

This research was supported by the Dragon Programme through id 2566 and by National Natural Science Foundation of China through grants 40176040. Some ENVISAT ASAR image data were provided by ESA as part of the AO project AOE.382.

7. REFERENCES

1. De Loor, G. P., The observation of tidal patterns, currents and bathymetry with SLAR imagery of the sea, *IEEE Journal of Oceanic Engineering*, Vol.6, 124-129, 1981.

2. Alpers W. and Hennings I., A theory of the imaging mechanism of underwater bottom topography by real and synthetic aperture radar, *Journal of Geophysical Research*, Vol.89, 10,529-10,546, 1984.

3. Yuan Y L, Representation of high frequency spectra of ocean waves and the basis for analyzing SAR images (in Chinese), OCEANOLOGIA ET LIMNOLOGIA SINICA, Vol.28(supplement), 1-5, 1997.

4. Ma Y and Zhang J, Simulation study of imaging of underwater bottom topography by synthetic aperture radar, *Journal of Hydrodynamics* (Ser.B), Vol.13, 57-64, 2001.

5. Valenzuela, G.R., Theories for the interaction of electromagnetic and oceanic waves-A review, *Boundary-Layer meteorology*, Vol.13, 61-85, 1978.

6. Cui J H, Chen G Q and Zhang J, Damped Newton-Row Action Method for SAR Image Simulation and Underwater Topography Inversion (in Chinese), *Advances in Marine Science*, Vol.21, 68-77, 2003.

INTERPRETATION AND COMPARISON RADIAL SAND RIDGES FEATURES RETRIEVED FROM SAR AND TM IMAGES

Meng Junmin (1) **Zhang Jie**(1), (2) **Yang Jungang**(1)

(1) *First Institute of Oceanography, S. O. A., Xianxialing Road, High-Tech Park, Qingdao, Shandong, China, 266061, E-mail: mengjm@fio.org.cn*

(2) *Key Laboratory of Marine Science and Numerical Modeling, S. O. A., Xianxialing Road, High-Tech Park, Qingdao, Shandong, China, 266061, E-mail: zhangjie@public.qd.sd.cn*

ABSTRACT

In this study, it has collected several scenes of ENVISAT ASAR and LANDSAT TM images covering radial sand ridges off the coast of Jiangsu. Radial sand ridges features retrieved from SAR and TM images are interpreted and compared. SAR and TM have different virtues in the sand ridges dynamic monitoring, so combination these two means can get better results. Several factors affected submarine sand ridges imaging in SAR are discussed.

1. INTRODUCTION

The radial sand ridges in the coast off the Jiangsu Province are one of the unique topographic features of the continental shelf of the East China Sea. It consists of more than 70 submarine sand ridges and covers an area of 200 km long from the north to the south and 90 km wide from the west to the east. All of the ridges array in a radial pattern with a center at Jianggang[1,2]. Area of ridges over sea level is about 2100 square kilometers. These ridges are the important components of coastal zones of Jiangsu. Radial sand ridges belong to a special system of physiognomy, and it is famous by their special conformation and varieties of complicated topography. Study of their formation and evolution has crucial theoretical and practical meanings.

The range of water depth of radial sand ridges in the beach of Jiangsu is about 0~25 m. The tidal current is strong in this area. Xiyang in the north and Huangshayang and Lanshayang in the south are the main tidal channels (see fig.1). Average speeds of flooding and ebbing of tidal current in this area are over 1.4 m/s. Average tide range in this area is about 2.5~4.0 m, and the largest tide range of Huangsha tidal channel is up to 9.28 m. The topography of this area is very complicated, and topography of sand ridges change ceaselessly by the action of tidal current. The average moving speed of northern sand ridges is about 580 m/a. The average moving speed of southern sand ridges is about 280m/a. So monitoring of dynamic movement with routine investigation technology is very difficult. Remote sensing has virtues such as large area, multi-temporal, high resolution etc, and it can make up deficiency of routine investigation. It is a very effective means of monitor. In recent years, some investigators have obtained plenty of fruits by monitor of varieties of radial ridges and tidal channels of this area using LANDSAT TM images. SAR is one advanced imaging sensor of remote sensing. It has been proved by a lot of practice that SAR can be used in detecting shallow underwater bottom topography. SAR has an advantage in observing the large area of radial sand ridges, and it not only can monitor the varieties of sand ridges, but also inverse quantitatively water depth. In this paper, ENVISAT ASAR image and TM

Proc. 2005 Dragon Symposium "Mid-Term Results", Santorini, Greece
27 June – 1 July 2005 (ESA SP-611, January 2006)

image are interpreted and features of sand ridges in these two images are compared and analyzed by superposition of interpretation results. Furthermore, we study movement of sand ridges using multi-temporal SAR images and TM images and discuss virtues and deficiencies of SAR images and TM images in the monitor of dynamic movement of sand ridges respectively.

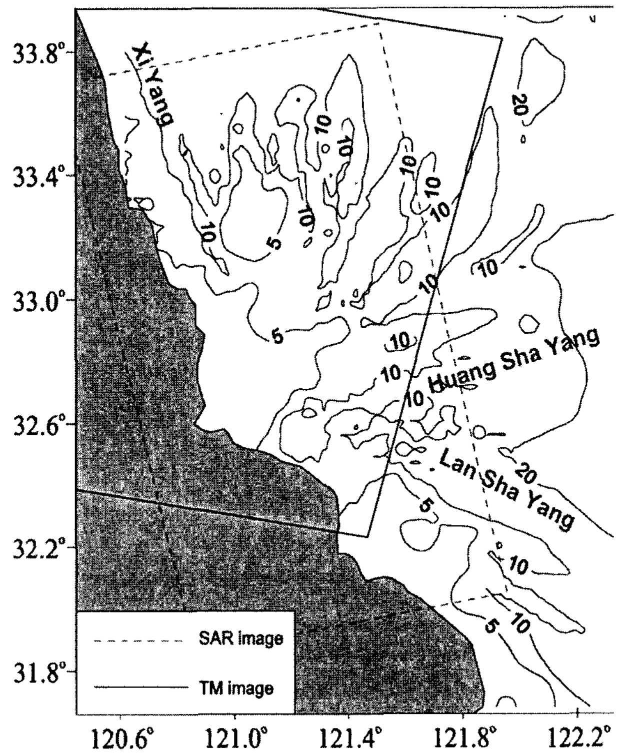

Fig. 1 water depth contour map along North Jiangsu and remote sensing images coverage

2. RADIATIVE SAND BANKS INTERPRETATION BY USING SAR AND TM IMAGES

SAR maps the sea surface roughness through Bragg scattering from the capillary waves and short gravity waves. Sand ridges in shallow sea change sea currents of sea surface and sea currents modulate further distribution of micro-scale waves of sea surface, so sand ridges can be imaged in SAR scenes. Optical sensors of remote sensing such as TM have the ability to penetrate through water in some range of water depth, so TM can observe distribution of sand ridges in shallow sea areas. Two sensors base on different imaging mechanism, so not all the method of interpretation is uniform. In this paper, we interpret respectively ENVISAT ASAR (fig.3) images acquired in August 30th 2004 and Landsat ETM+ images (fig.2) acquired in May 26th 2002.

By comparison of interpretation results of SAR images and TM images, it can be known that sand ridges are easy to identify in SAR images. Because of tidal flow's converging and diverging over sand ridge, it shows bright-dark stripes in SAR images. Although tidal channels can also modulate SAR image intensity, it is much weaker than sand ridges. Tidal channels can be observed clearly in TM images, but it is difficult to distinguish exactly with sand ridges near coast. This is because that water of tidal channels is deep and gradient of water depth is large but alongshore water depth gradient is small and concentration of suspended sediments is high.

Fig. 2 LANDSAT ETM+ image acquired on May 26, 2002 with interpretation of sand ridges, where a: Liangyue sand ridge, b: Dong sand ridge, c: Tiaozi sand ridge, d: Zhugen sand ridge, e: Jiangjia sand ridge, f: Waimaozhu sand ridge, g: Maozhu sand ridge, ①: Huangsha tidal channel, ②: Kushui tidal channel, ③: Caomishu tidal channel, ④: Chenjiawu tidal channel.

Table 1 **Comparison** of interpretation results between SAR and TM images

Sands ridge / Tidal channels	SAR	TM	**Sands ridge / Tidal channels**	SAR	TM
Xiaoyin sand ridge	√	-	Hetun sand ridge	√	-
Liangyue sand ridge	√	√	Taiyang sand ridge	√	-
Dong sand ridge	√	√	Yao sand ridge	√	-*
Tiaozi sand ridge	√	√	Chenjiawu tidal channel	-	√
Zhugen sand ridge	√	√	Caomishu tidal channel	-	√
Maozhu sand ridge	√	√	Kushui tidal channel	-	√
Waimaozhu sand ridge	√	√	Huangsha tidal channel	-	√
Jiangjia sand ridge	√	√	Lansha tidal channel	-	√

*out of the TM image coverage

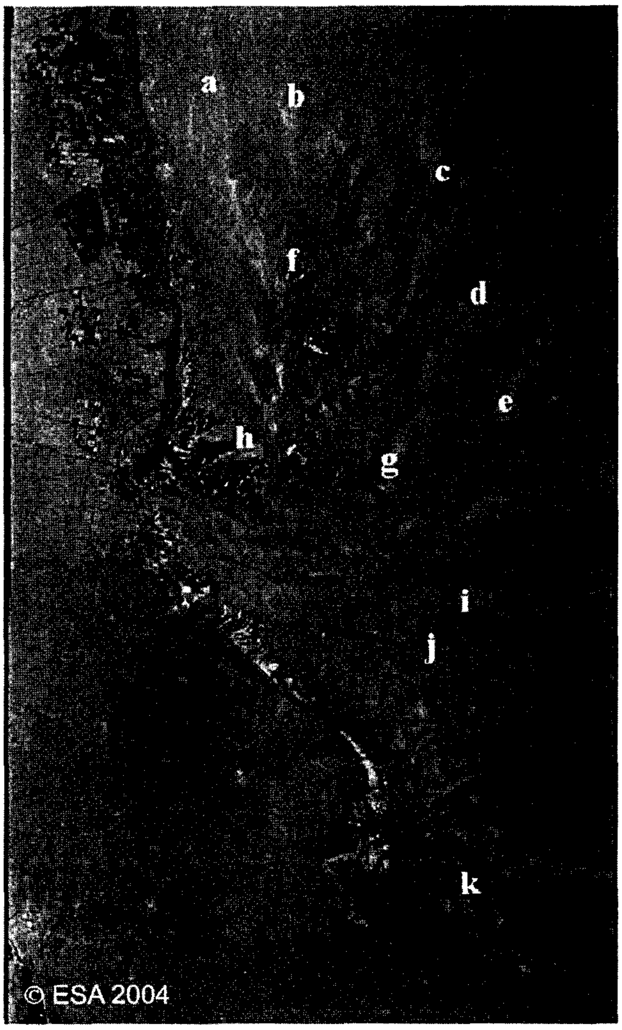

Fig. 3 ENVISAT ASAR image (IS2, VV) acquired on Aug 30, 2004 of Subei Shoal with interpretation results where a: Xiaoyin sand ridge, b: Liangyue sand ridge, c: Maozhu sand ridge, d: Waimaozhu sand ridge, e: Jiangjia sand ridge, f: Dong sand ridge, g: Zhugen sand ridge, h: Tiaozi sand ridge, i: Hetun sand ridge, j: Taiyang sand ridge, k: Yao sand ridge

3. INTERPRETED RESULTS COMPARISON BETWEEN SAR AND TM IMAGES

In this paper, features of three kinds of typical sand ridges in SAR images and TM images are compared. We can see that the outline obtained by TM image is different completely from the one obtained by SAR images. In fig.4, West Taiyang sand ridge is easy to identify in TM image and its shape likes a triangle. A bright triangle also can be identified in the same position of SAR image to TM image. But the triangle in SAR image is horizontal flip of that in TM image. Is this variety of West Taiyang sand ridge in two years? Analyzing acquired time of SAR image and looking for tide table [3], we know tide is flooding after up to ebb tide in SAR image acquired time. The direction of tidal current is demonstrated by arrow from the result of Wang [2]. So we can obtain the exact location of West Taiyang sand ridge, which is shown by dashed, according to SAR imaging mechanism of underwater bottom topography. Both TM and

SAR are difficult to demarcate the range of sand ridges alongshore, but SAR can give the location of ridges. It is easily to distinguish the range and shape of sand ridges that come out water by SAR and TM.

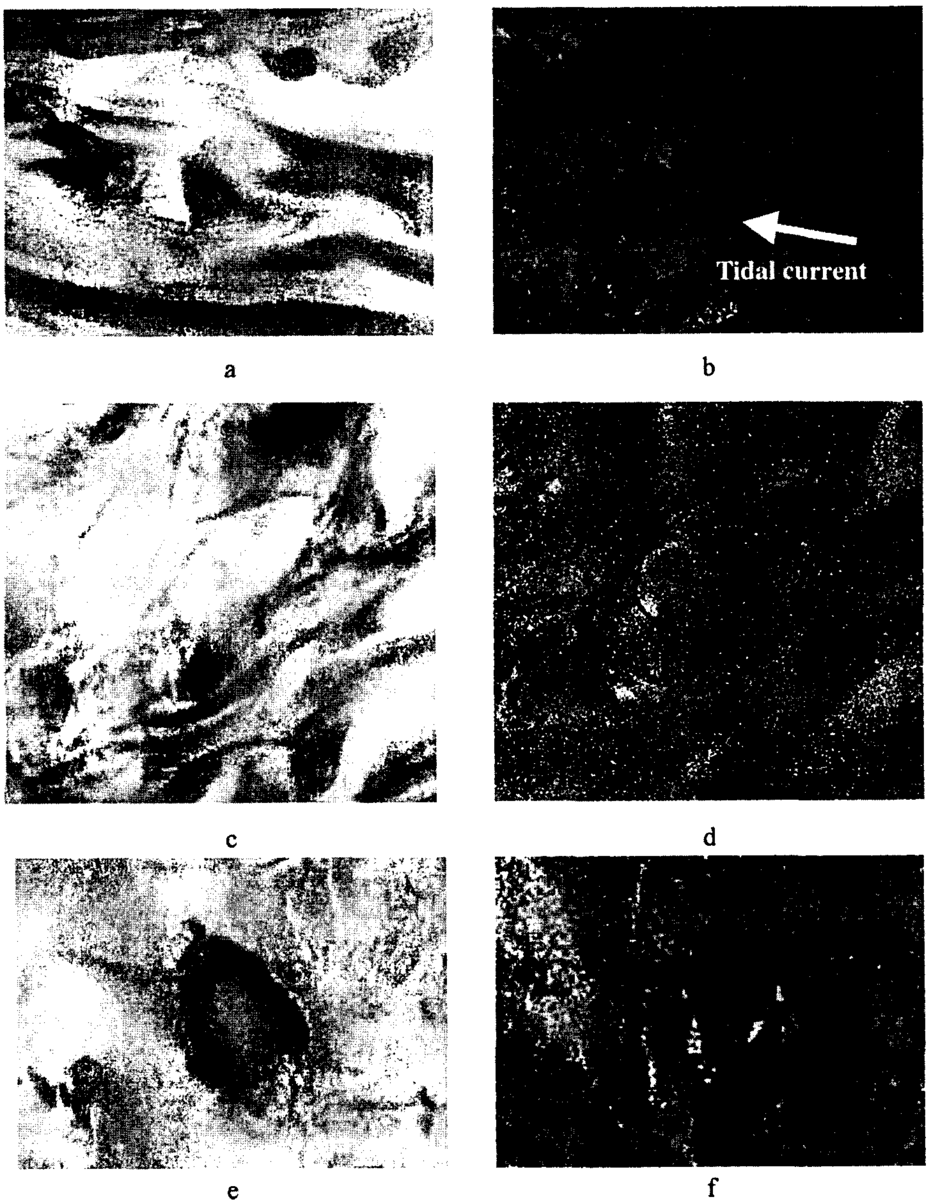

Fig. 4 Interpretation results comparison between SAR and TM

4. EVOLUTION OF RADIAL SAND RIDGE

In this paper features of sand ridges are compared using two scenes SAR images and two scenes TM images acquired in different time respectively. TM images are used to analyze evolution of tidal channels and SAR images are used to analyze evolution of sand ridges based on their virtues in observing tidal channels and sand ridges. LANDSAT7 ETM+

image acquired in 2002, LANDSAT5 TM image acquired in 1992, ENVISAT ASAR image acquired in 2004 and ERS-2 SAR acquired in 1997 are used in this study. Varieties of tidal channels during ten years are distinct from fig.5, and this is because that the action of aggrading and eroding of tidal current makes tidal channel become narrow and steep. We select the sub-image in the same place of two SAR images to compare. Over 6 pieces of sand ridges can be found in fig.6a. There are many changes about these sand ridges after seven years' evolution. 1 and 2 is growing and gradual amalgamating. A part split from 3 is amalgamating with 4, 5 and 6 is unchanged. Location of these sand ridges changed through turning and moving.

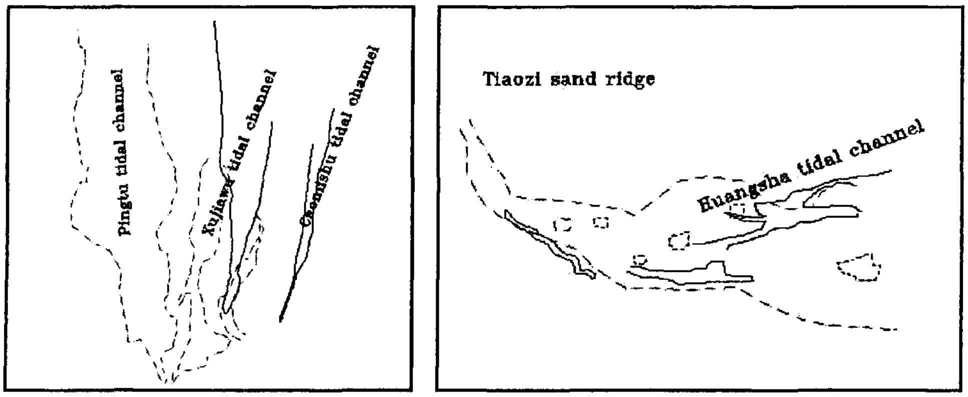

Fig. 5 Tidal channel interpretation map from Landsat TM images on May 26, 2002 (solid) and June 7, 1992 (dash)

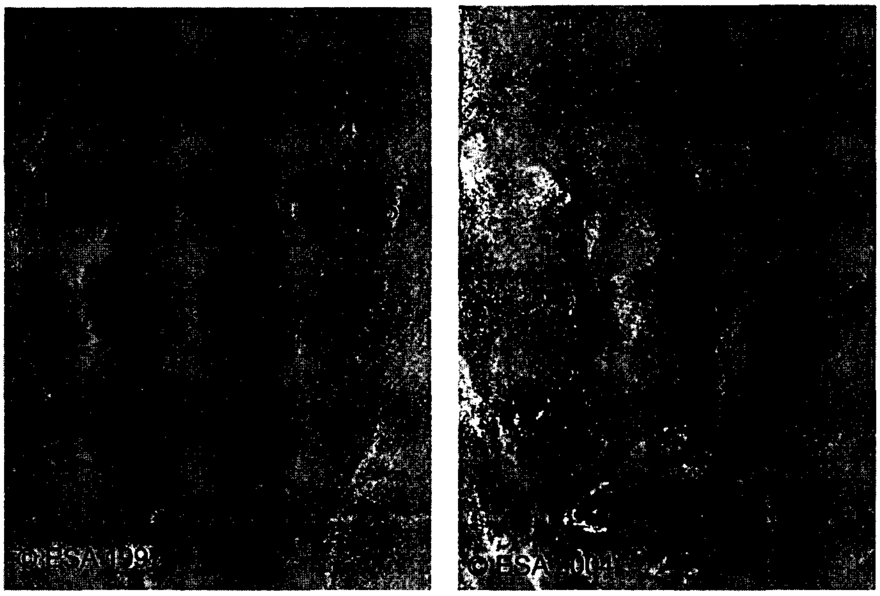

Fig. 6 ERS-2 SAR and ENVISAT ASAR images of Subei shoal off the coast of Jiangsu Province on Aug 17, 1997 and Aug 30, 2004 showing several sand ridges

5. SEA LEVEL AND SAR BEAM MODE'S EFFECT

In this paper we collected 7 scenes ENVISAT ASAR images of four days with different incidence angles and polarizations. By comparison fig 3, 7, 8, 9, the image of Aug 11, 2004 with less information is not fit to our research.

The image of Aug 30 with clear sand ridge features fits our needs. We find the image of Aug 11 acquired near high tide time and the others acquired on ebb tide time by looking up tide table. So there are many sand ridges above water in these three images and clear topographic features. But it can be find few small tidal flat in the image of Aug 11. Although with different incidence angle and polarization, there is not obvious difference between fig 3, 8 and 9. The fig 7 (IS1) has low incidence angle less than 20 degree in some area so mirror reflection maybe play an important role. So the radar incidence angle has more obvious effect on submarine sand ridge imaging than polarization.

Fig. 7 ENVISAT ASAR (IS1, VV) image acquired 11 August 2004 showing the Subei Shoal off the coast of Jiangsu

Fig. 8 ENVISAT ASAR (IS4, VV) image acquired 17 August 2004 showing the radial sand ridge off the coast of Jiangsu

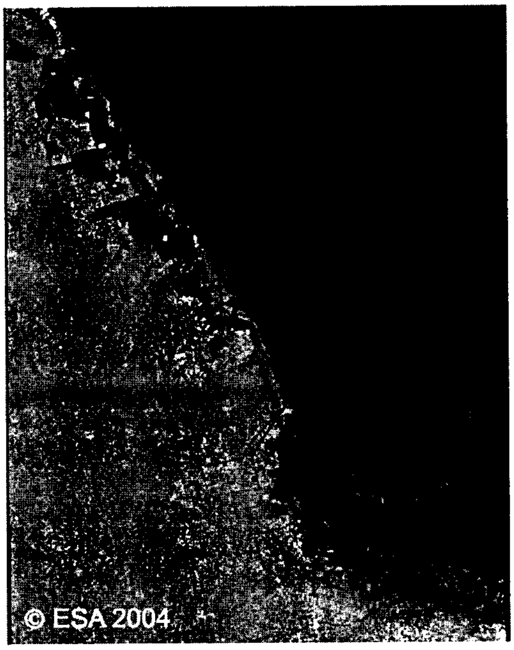

Fig. 9 ENVISAT ASAR (IS4, HH) image acquired 16 September 2004 showing the radial sand ridge off the coast of Jiangsu

Table 2 Jianggang tidal hour vs. SAR acquire time

Date	Tidal Hour (UTC)	Height of Tide (cm)	SAR image acquired time (UTC)	Pol.	Swath
Aug-11-2004	08:18 14:26	154 415	13:42	VV	IS1
Aug-17-2004	13:47 17:52	112 620	13:54	VV	IS4
Aug-30-2004	13:05 17:04	78 639	13:45	VV	IS2
Sep-16-2004	01:33 05:38	116 667	01:59	HH	IS4

6. CONCLUSION

SAR and TM both are effective means monitoring submarine radial sand ridges. SAR can work all weather and TM with 7 bands can get clearly results. By comparison with SAR and TM images, we can get:

(1) SAR and TM both can be used to monitoring sand ridges dynamic;

(2) SAR and TM are appropriated to observing sand ridge and tidal channel respectively;

(3) TM cannot well distinguish sand ridge with tidal channel near coast and SAR cannot get exact outline of sand ridge;

(4) Tidal direction is necessary for sand ridges interpretation from SAR image;

(5) Tidal current and sea level are two dominant factors affected sand ridge imaging in SAR

7. ACKNOWLEDGE

This research was supported by the Dragon Programme through id 2566 and by Chinese offshore marine complete survey and assessment project under grants 908-01-WY-02. ENVISAT ASAR image data were provided by ESA as part of the AO project AOE.382. The authors would like to thank Ms. Wang and Ms. Liu for their assistance processing data.

8. REFERENCE

1. Huang Hai-jun, Li Cheng-zhi, A study on the present evolution of submarine radial sand ridges in the southern Yellow Sea using remote sensing images, *Oceanologia et Limnologia Sinica*, Vol29(6), 640-645, 1998.

2. Wang Yin, *Radiative Sandy Ridge Field on Continental Shelf of the Yellow Sea*, China environmental science press, Beijing, 2002

3. National marine data and information service, *Tide Tables 2004*, Vol.1 from the Yalu River Mouth to the Changjiang River Mouth, Shandong Cartographic Publishing House, Jinan, 2003

4. Alpers W. and Hennings I., A theory of the imaging mechanism of underwater bottom topography by real and synthetic aperture radar, *Journal of Geophysical Research*, Vol.89, 10,529-10,546, 1984.

AN AUTOMATIC DETECTING METHOD OF SAR V-IMAGE SHIP WAKE

Wang Ruifu[1, 2] ZhangJie[2,3] Bi Zhe[4]

[1] *Ocean University of China, Yu-Shan road, Qingdao, Shandong, P.R.C., 266003, wangruifu@263.net*
[2] *First Institute of Oceanography, S. O. A., Xianxialing Road, High-Tech Park, Qingdao, Shandong, P.R.C., 266061, zhangjie@public.qd.sd.cn*
[3] *Key Laboratory of Marine Science and Numerical Modeling, S. O. A., Xianxialing Road, High-Tech Park, Qingdao, Shandong, P.R.C., 266061*
[4] *DaLian Maritime University,Linghai Road,Dalian,P.R.C,116026, bzjimmy@hotmail.com*

ABSTRACT:

Due to intense reflect signal of ship wake in the SAR image, Radon transform or Hough transform is often used in getting the line information in a SAR image. Then we judge whether these lines intersect each other. Based on the feature of ship wake, this article gives a new method of V-image ship wake detection, which includes the information of the geometry shape, angle and the intense ship reflection of ship wake. Result shows that this method can detect Kelvin V-image wake and narrow V-image wake automatically by three experiments.

Keyword: SAR Ship Wake V-image

1. INTRODUCTION

Synthetic Aperture Radar (SAR) has many virtues, such as high resolution, all-weather, all day and all night, etc., and has been used in many research fields. Ship wake detection is one of the important applications for SAR. Ship wakes can be divided into Kelvin-wake parts and non-Kelvin–wake parts. The Kelvin wake is the far-field wave pattern resulting from the fluid mechanical flow around the ship hull. Non-Kelvin–wake includes dark trailing centerline region, bright V-images aligned at some angle to the ship's path[1]. V-shaped images have rich geometry texture characters, and attract many research interests. There is controversy as to whether these narrow V-images come from the steady Kelvin wakes or from related unsteady motions.

Until now, arithmetic of ship wake detection is mainly focused on Radon transform[2]. Radon transform is to distinguish line information by integral of all possible lines in the image, and thus the information used in the image is insufficient[3].

The method of detecting ship wakes with Radon transform cannot distinguish the categories of the ship wake[4]. This article put forward a new method to detect the V-image ship wake. V-image can be divided to Kelvin V-image ship wake and narrow V-image ship wake. Kelvin V-image ship wake is ordinary ship wake, and its angle is about 39.5 degrees. However, the angle of narrow V-image is less than 10 degrees. Generally, it can be obtained one type of V-image ship wake for the same ship.

Due to the high resolution of SAR image, so the margins of V-image ship wake always behave band shape[5]. The arithmetic in this article is based on two symmetrical boundary bands, the angle of V-image and the intense reflectance of ship to detect the ship wake.

Proc. 2005 Dragon Symposium "Mid-Term Results", Santorini, Greece
27 June – 1 July 2005 (ESA SP-611, January 2006)

2. V-IMAGE SHIP WAKE AUTOMATIC DETECTION

It is difficult to extract accurate ship wake from the SAR image directly[6-7]. So this article applies the idea of Radon transform in detecting line information by integral to get the maximum[8-10], and put forward a V-image searching method within the whole image base on target shape feature[11].

This method mainly includes following steps: (1) Take the SAR image as a matrix, construct a V-image object based on the geometry characters of V-image ship wake, which includes the vertex coordinates pairs of the V-image, two boundary band equations and V-image angle. (2) Rotate the V-image object from the low left corner of the matrix clockwise or anti-clockwise, compute the average value and variance of pixels within the range of the boundary bands. (3) Set the thresholds of the average value and variance, extract the V-image object whose average value and variance are bigger than the set two thresholds, get the discrepancy between two average values of boundary bands and then judge whether the discrepancy locates in some range or not. (4) Set each point in the SAR image as the vertex of the V-image, and compute repeatedly according to the above method.

Considering the intense reflection of the ship, namely the vertex during the computing, we need make sure that the vertex coordinate pairs fall in some range. Fig. 1 is the sketch of the V-image ship wake detection. Region ABEDCF is the V-image object, regions ADCF and ABED are two boundary bands of ship wake respectively, d is the width of the boundary band, and L is the length of boundary band. The detail arithmetic is as followings:

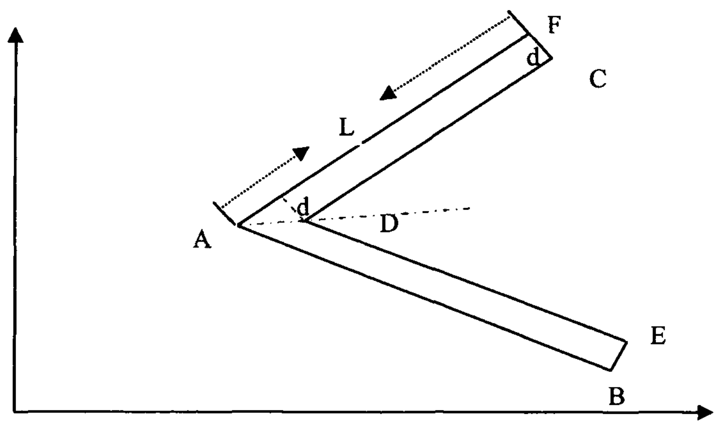

Fig.1. Sketch of V-image ship wake detection

Setting the low left corner coordinate pairs of the matrix as (0, 0), $A\ (i, j)$ as the vertex of the V-image object, where i and j are subscripts of the coordinate. The equation of line AB can be expressed as $y = k\,x + b$, where k is slope and $k = tg\alpha$ (α is angle between line AB and axis X, and increases by defined interval from 0). Let the V-image angle is θ and falls in some range, and its interval is defined by user. Equation of line AF can be obtained by rotating line AB to an angle θ, so its slope $k=tg\ (\alpha + \theta)$. According geometry relation, the length of AD is $Lad = d / \sin(\theta/2)$. Since α and θ are known, so the slope of line AD is $tg\ (\alpha+\theta/2)$. Using the length of AD and coordinates of point A, we can get the coordinates of point D.

Based on the value of angle θ, we can obtain unique solution of coordinate point, which satisfies following conditions

$$\begin{cases} -\theta/2 \le \alpha < 180^0-\theta/2, & \text{if } \ y_d > y_a, \\ 180^0-\theta/2 \le \alpha < 360^0-\theta/2, & \text{if } \ y_d < y_a, \end{cases} \qquad (1)$$

where y_d and y_a are Y coordinate values of point D and point A respectively.

Based on the values of θ and d, we can get the lengths of DC and DE, and then get coordinates of point C and point E. In the same way, we can get coordinates of point F and point B. After getting the equations of AB, AF, DC and DE, we can obtain the range of boundary bands of the ship wake. Based on the four margin coordinates of the boundary bands, we can get the minimum boundary rectangle of the belt, and judge whether all the pixel points within the minimum boundary rectangle locate in the belt.

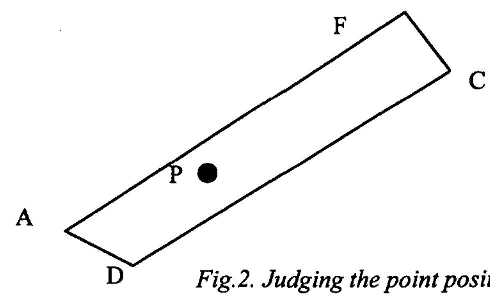

Fig.2. Judging the point position

Judging criterion is that the pixel point must locate in different sides of the two lines, as shown in Fig 2. Because AF parallels to DC, according the location relation between point and line, if the relation between point P and AF differ from that of point P and DC, then point P falls in the belt range.

3. EXPERIMENTS RESULT

Three experiments were carried out in this article, which based on the simulated image, standard Kelvin V-image ship wake SAR image and narrow V-image ship wake SAR image (show as Fig4~6). SAR image used here are base on ENVISAT SAR IMAGE, and our experiments were finished on Dell workstation.

We apply two parameters to analyze the accuracy of detecting results. One of them is the accuracy of vertex, the other is ship wake boundary band accuracy. Vertex accuracy is judged by the pixel distance between the vertex position of source image and that of detected image, while boundary band accuracy is judged by the product of two ratios. Two ratios are defined as side slope of original image to detected side slope respectively.

3.1. Detection in the Simulated image

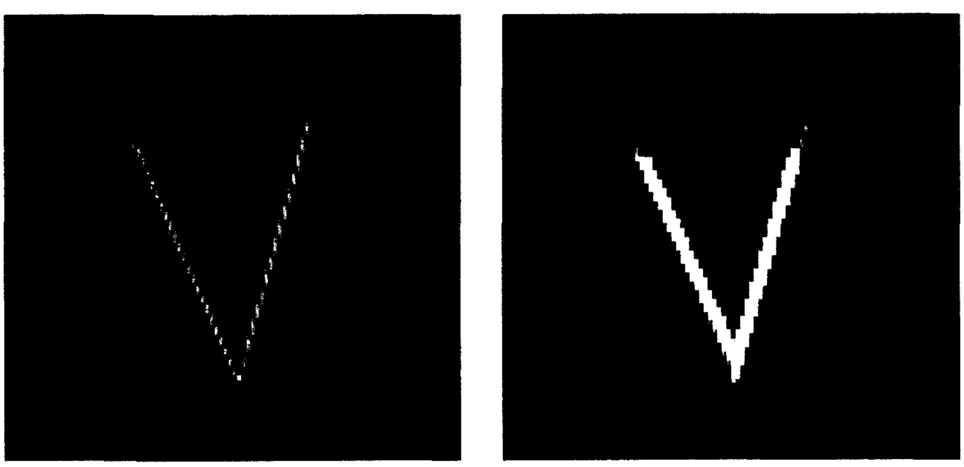

Fig.3. Simulated image and detecting result

The angle of V-image in the simulated image is 39.5 degree, the same as Kelvin wake angle. There is no noise in the image. The result of detection is shown as Fig. 3, and it agrees well with simulated image. In this experiment, there is no wrong detected result. Error analysis can be found in table 1.

Table.1 Experiment 1 error estimated result

Source vertex	Result vertex	Ratio of Left side slop	Ratio of Left side slop
(52,84)	(52,84)	3.66/3.66=1	-2.77/-2.77=1

3.2. Kelvin V-image ship wake detection experiment

SAR image with obvious Kelvin V-image ship wake was detected in Fig. 4. The detected result is also good. However, the detected boundary band length is less than the one in original image. The reason is that the original ship wake is too long, so the wake in the end of boundary band runs away from the original position and became asymmetrical due to the effect of ocean current. Error analysis can be found in table 2.

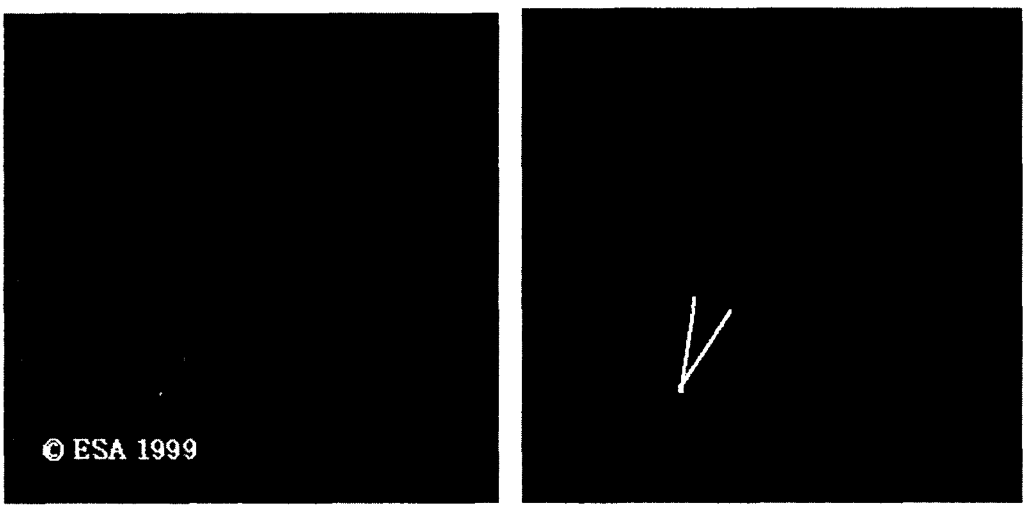

Fig.4. Kelvin V-image ship wake SAR image and result

Table.2 Experiment 2 error estimated result

Source vertex	Result vertex	Ratio of Left side slop	Ratio of Left side slop
(126,316)	(126,315)	6.75/6.75=1	1.74/1.80=0.97

3.3. Narrow V-image ship wake detection experiment

In this experiment, the SAR image has been disturbed by internal wave, as shown in Fig. 5. The angle of V-image ship wake is less than 10 degree, and belongs to narrow V-image ship wake. It also shows that the detect result accords with original image wake. However, several wrong ship wakes are detected due to image noises and obvious belt character in the region of internal wave. Our arithmetic can remove wrong information from detected results by taking the variable of the side belt and the intense of reflect vertex into account. Error analysis can be found in table 3.

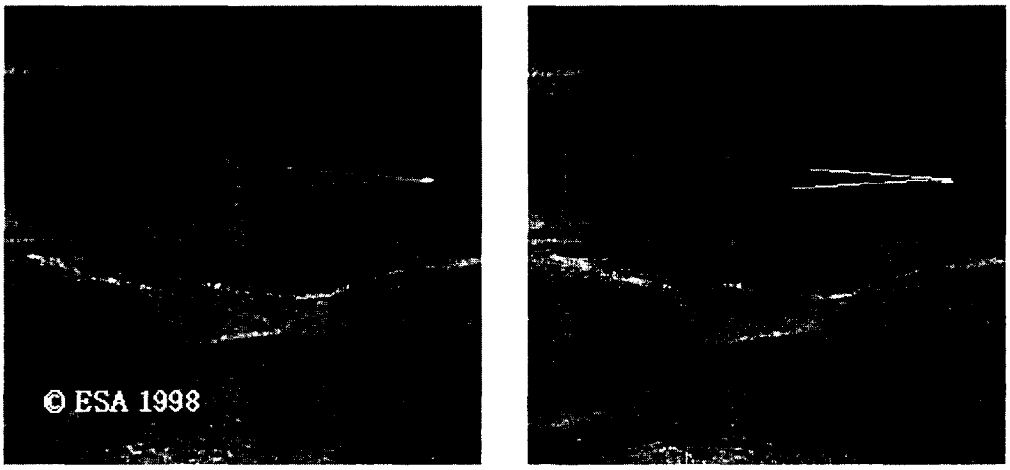

Fig.5. Narrow V-image ship wake SAR image and result

Table.3 Experiment 3 error estimated result

Source vertex	Result vertex	Ratio of Left side slop	Ratio of Left side slop
(226,115)	(226,115)	0.0349/0.0.349=1	0.077/0.078=0.987

4. CONCLUSION

Ship wake automatic detection is an important technique to SAR image application. The dynamical feature of ocean environment determines the complexity of ocean phenomena. The V-image ship wake detecting arithmetic in this article can take fully advantage of the geometry shape character, angle and reflection intense of the ship wake. Detected result is satisfactory. Compared to other ship wake detecting method, this method is faster and more accurate. By error analysis, we can find that the detecting result of the two SAR image is very accurate.

ACKNOWLEDGEMENTS

This research was supported by the Dragon Project through id 2566.

REFERRENCE

1. Arthur M. Reed and Jerome H. Milgram,Shipwakes and their radar images,*Annu. Rev. Fluid* Mech.Vol 34:469–502 ,2002.

2. Lin, L.K. Kwoh , Y.-C. Lin, and V. Khoo, “Ship and ship wake detection in the ERS SAR imagery using computer based algorithm”. *Proc. International Geoscience and Remote Sensing Symposium*,151-153, 1997

3. A. C. Copeland, G. Ravichandran , and M. M. Trivedi, ``Localized Radon Transform-Based Detection of Ship Wakes in SAR Images," *IEEE Trans. Geoscience and Remote Sensing, 33, No. 1, January 1995*, pp. 35-45

4. Tupin F,Mattre H,Mangin J F, et al. “Detection of Linear Features in SAR Images: Application to Road Network Extraction”.*IEEE Transform on Geoscience and Remote Sensing*.36(2):434-453,1998

5. Wang Ruifua, Zhang Jie, Belt-Oriented Radon Transform And Its Application To Extracting Features From High-Resolution Remote Sense Images. *b, Huang Jianboa, Chen Miaoa, Leng Xiuhuaa .Proceedings of SPIE* Vol. 4892 (2003) © 2003 SPIE . 0277-786X/03 .p 354~362

6. Trinder J C,Li H. "Semi-automatic Feature Extraction by Snakes [A].Automatic Extraction of Manmade Objects from Aerial and Space Images " *.Basel:Birkhaeuser Verlag*, 95-104, 1995

7. Nevatian, Babu K R. "Linear Feature Extraction and Description". *Computer Graphics and Image Processing*,1980 ,13(2):257-269

8. Barzohar M,Cooper D.B. "Automatic Finding of Main Roads in Aerial Images by Using Geometric-stochastic Models and Estimation",*IEEE Transform on Pattern Analysis and Machine Intelligence*,18(7):707-71,1996

9. Shi Wenzhong, "Brief and Expectation of Method about Extracting Road Feature from Remote Sensing Image", *Acta Geodaetica Of Cartographica Sinaica*, 30(3),257~262,2001

10. Wang F G,Newkikr."A Knowledge-based system for Highway Network Extraction" *.IEEE Transform Geoscience and Remote Sensnig*,1988,26(5):525—531.

11. Gruen A,Li H. "Road Extraction from Aerial and Satellite Images by Dynamic Programming".*ISPRS Journal of photogrammetry and Remote Sensing*,50(4):11-20 I-I,1995

Atmosphere

Air Quality Monitoring and Forecasting
(id. 2580)

CARBON MONOXIDE, METHANE AND CARBON DIOXIDE OVER CHINA RETRIEVED FROM SCIAMACHY/ENVISAT BY WFM-DOAS

M. Buchwitz, R. de Beek, S. Noël, J. P. Burrows, and H. Bovensmann

Institute of Environmental Physics (iup) / Institute of Remote Sensing (ife), University of Bremen FB1, Otto Hahn Allee 1, 28334 Bremen, Germany, E-mail: Michael.Buchwitz@iup.physik.uni-bremen.de

ABSTRACT

The three "carbon gases" carbon monoxide (CO), methane (CH_4) and carbon dioxide (CO_2) are important atmospheric constituents affecting air quality and climate. We present maps of time averaged (yearly, tri-monthly) CO, CH_4 and CO_2 over China for the year 2003. They are derived from the near-infrared nadir observations of the SCIAMACHY spectrometer aboard the European environmental satellite ENVISAT using the scientific WFM-DOAS retrieval algorithm (version 0.4 for CO_2; version 0.5 for CO and CH_4). The maps show vertical columns of carbon monoxide and dry-air column averaged mixing ratios of methane (denoted XCH_4) and CO_2 (XCO_2). The SCIAMACHY near-infrared nadir observations are nearly equally sensitive to concentration changes at all altitude levels including the boundary layer and therefore enable the detection of surface source regions of carbon monoxide, methane, and CO_2. The measurement errors for CO and methane are small enough to clearly identify at least moderate to strong source regions. The XCO_2 measurements are more difficult to interpret because the measurement error due to, e.g., aerosol and albedo variability, is currently on the order of the weak source/sink signal to be detected. Our future work will aim at reducing the sensitivity to these and other error sources.

1. INTRODUCTION

Air pollution resulting from large-scale biomass burning, fossil fuel combustion, and other fossil fuel related activities has become a problem with increasing importance, especially for countries with an increasing energy demand and fuel consumption such as China. The quantification of concentrations near the sources and the subsequent transport of pollutants is important, for example, for monitoring and forecasting of air pollution. Increasing concentrations of radiatively active so-called greenhouse gases are expected to result in a warmer climate with possible adverse consequences such as rising sea levels and an increase of extreme weather conditions. China emits the greenhouse gas methane in large quantities, e.g., due rice cultivation, ruminants and waste handling (see, e.g., [15] and references given therein). Also large amounts of the air pollutant CO are emitted due to, e.g., fossil fuel combustion and biomass burning.

Carbon monoxide contributes to air pollution because it is toxic in large concentrations, acts as a pre-curser to tropospheric ozone and - because CO is the leading sink of the hydroxyl radical (OH) - largely determines the self-cleansing efficiency of the troposphere (see, e.g., [2] and references given therein). CO is highly variable in time and space and detailed monitoring of its spatial pattern and time evolution is therefore important.

Carbon dioxide and methane are the two most important anthropogenic greenhouse gases and contribute to global climate change. A prerequisite to predict future climate change resulting from emissions of carbon dioxide and methane is a good understanding of their (surface) sources and sinks. Information on CO_2 and methane sources and sinks on the global scale are currently derived from a highly precise but rather sparse (~100) network of ground stations (e.g., NOAA/CMDL). Satellite measurements have the potential to overcome the limitations of the surface network and help to obtain a better understanding of the methane and CO_2 sources and sinks (see, e.g., [10,11,15] and references given therein). For the near future dedicated satellite missions are planned to globally measure carbon dioxide and methane accurate and precise enough to obtain information on their surface sources and sinks, e.g., OCO (USA) and GOSAT (Japan), both being primarily passive near-infrared nadir missions. SCIAMACHY [3] is not a dedicated carbon mission but due to its near-infrared nadir observation capability is the first satellite instrument that is very sensitive to methane, CO_2, and CO boundary layer concentration changes as demonstrated by its averaging kernels for CO [9], methane [10] and CO_2 [10]. Therefore, SCIAMACHY plays a pioneering role in this new area of satellite remote sensing.

Here we present new results for CO and methane obtained with version 0.5 of the WFM-DOAS retrieval method. The CO_2 results have been obtained with WFM-DOAS version 0.4 described in detail in previous papers [10,11]. This paper is organized as follows: first, a short overview about the SCIAMACHY instrument is given followed by a description of the retrieval algorithm and, finally, a discussion of the trace gas results focusing on China.

Proc. 2005 Dragon Symposium "Mid-Term Results", Santorini, Greece
27 June – 1 July 2005 (ESA SP-611, January 2006)

2. SCIAMACHY INSTRUMENT

SCIAMACHY is a spectrometer that measures reflected, scattered and transmitted solar radiation in the spectral region 214-2380 nm at moderate spectral resolution (0.2-1.6 nm). On the Earth's day side SCIAMACHY mainly performs a sequence of alternating nadir and limb observations. The horizontal resolution of the nadir measurements depends on orbital position and spectral interval but is typically 60 km (e.g., for methane) or 120 km (e.g., for CO) across track times 30 km along track. These measurements can be inverted to obtain a large number of (primarily) atmospheric data products [3].

Overall, the in-flight optical performance of SCIAMACHY is as expected from the on-ground calibration and characterization activities [4]. One exception is a time dependent optical throughput variation in the SCIAMACHY near-infrared (NIR) channels 7 (the main CO_2 channel) and 8 (the only CO channel and main CH_4 channel) due to ice build-up on the detectors [4] which adversely affects the trace gas retrieval [11,16,19]. This effect is minimized by regular heating of the instrument. The methane results presented in this paper have been derived from channel 6 not affected by an ice layer. CO is retrieved from channel 8 using a correction procedure for ice induced errors (see next section for details).

3. RETRIEVAL ALGORITHM AND ITS VALIDATION

The retrieval of a long-lived and therefore relatively well-mixed gas such as methane is extremely challenging as only small variations on top of a large background are of relevance in order to obtain information on its surface sources. Therefore, the retrieval algorithm has to be very accurate. In addition, the algorithm also has to be very fast to process huge amounts of data. We have developed the Weighting Function Modified Differential Optical Absorption Spectroscopy (WFM-DOAS) retrieval algorithm to accomplish this task. Basically the same algorithm is also used to retrieve CO and CO_2. Because accuracy and speed are typically contradicting requirements a good compromise has to be found. In this context it is relevant to point out that other groups are also work on this challenging retrieval task using somewhat different approaches (see, e.g., [14,15,16,17]).

WFM-DOAS [5,7-11] is an unconstrained linear-least squares method based on scaling (or shifting) pre-selected vertical profiles. The fit parameters for the trace gases are directly the desired vertical columns. The logarithm of a linearised radiative transfer model plus a low-order polynomial is fitted to the logarithm of the ratio of a measured nadir radiance and solar irradiance spectrum, i.e., observed sun-normalized radiance. The WFM-DOAS reference spectra are the logarithm of the sun-normalized radiance and its derivatives computed with a radiative transfer model [6]. In order to avoid time-consuming on-line radiative transfer simulations, a fast look-up table scheme has been implemented.

The validation of our data products with independent ground based (FTS) vertical column measurements is an ongoing activity. Available studies [13,18,19,20] report on the validation of previous versions of our data products (e.g., methane v0.4/0.41 and CO v0.4) and/or on a comparison of a small sub-set of the data as for CO_2 [13,20]. A detailed comparison of our new version 0.5 data products has not yet been performed but will be available in the near future.

3.1 CO specific aspects

Carbon monoxide is retrieved from a small spectral fitting window located in channel 8 covering several absorption lines of CO. Compared to our initial version 0.4 CO [9,11] the version 0.5 data product presented here has been significantly improved. The v0.5 CO column product is retrieved from an optimised spectral fitting window and generated without the application of a scaling factor (the v0.4 product was scaled with the factor 0.5). In addition, a correction has been applied to reduce time dependent biases caused by the ice-issue (e.g., slit function change), to improve the retrieval for partially cloud covered scenes and to make the retrieval less sensitive to aerosol and albedo variability. The correction is based on the retrieved methane column obtained from the same fitting window. A correction factor, defined as the ratio of an assumed (a-priori) methane column and the retrieved methane column, is applied to the retrieved CO column. The a-priori methane column is computed using a single (scene independent) profile of methane but taking into account the surface elevation of the corresponding ground pixel. This approach makes use of the fact that the variability of the methane column is small compared to the variability of the CO column. A quality flag is set for each pixel to indicate a (potentially) successful measurement. To decide if a measurement is successful, a number of criteria have been defined based on the value of the root-mean-square of the fit residuum, the CO fit error, and the methane correction factor. The methane correction factor, for example, has to be close to 1.0 (within 20%) for a measurement to be classified as successful. Otherwise the disturbances due to clouds, aerosols, surface reflectivity, calibration issues, etc., are considered too large to be corrected for.

A detailed validation by comparison with ground based FTS measurements has not yet been performed but is planned for the future. To assess the quality of this data product we have compared monthly mean v0.5 CO columns with the operational CO column product of MOPITT/EOS-Terra [12] (L2V3 data product obtained from NASA Langley DAAC). We found good to reasonable agreement. For example, both sensors show a similar seasonal dependence of CO originating from biomass burning in Africa and South America (not shown here). Our quantitative comparison revealed that the SCIAMACHY v0.5 CO columns (over land and water) are on average systematically higher compared to MOPITT by about 0.2 10^{18} molecules/cm^2 (northern hemisphere: ~16%). The inter-hemispheric difference is in good agreement (the mean difference (SCIA-MOPITT) is -3%, the correlation coefficient is 0.9). For a number or reasons (e.g., different altitude sensitivity, spatial resolution, and measurement time), perfect agreement is not to be expected.

3.2 Methane specific aspects

For methane we derive dry air column averaged mixing ratios (denoted XCH_4) by normalizing the retrieved methane column by the simultaneously observed airmass estimated by retrieving the column of a reference gas whose column is less variable than methane. Initially (for v0.4) we used oxygen (O_2) columns retrieved from the O_2 A band (760 nm) [10,11]. Unfortunately, the sensitivity of the retrieved O_2 column with respect to, e.g. aerosol, is quite different compared to methane mainly because of the large spectral distance between the two fitting windows. For v0.41 XCH_4 [11] we use CO_2 retrieved from the 1.6 μm region (channel 6). The new v0.5 XCH_4 data product is derived in a similar way as the v0.41 data product, except that methane is retrieved from channel 6 instead of channel 8. There are two reasons why methane retrieval from channel 6 should give better results compared to channel 8: (i) channel 6 is not affected by the ice issue, and (ii) the channel 6 methane absorption band is located close to the channel 6 CO_2 band thus improving the cancellation of errors when the ratio is computed (see also [15] where a similar approach has been used for the same reasons).

We have performed an initial comparison of v0.5 XCH_4 with TM5 model simulations [1] performed at the EC Joint Research Centre, Ispra, Italy (similar as described in [11] for XCH4 v0.4/v0.41) and found in general good agreement, typically within a few percent. Under certain conditions the observed XCH_4 is significantly lower than the model XCH_4: over Antarctica observations less than 1560 ppbv occur and north of 20 deg North values below 1670 ppbv are found, in particular during January to March and around October. More investigations are needed to find out what the reason for this potential underestimation is. Likely candidates are snow/ice covered surfaces due to their low albedo in the NIR. Excluding the low values from the comparison results in a mean difference of the global daily data of less than 2% for nearly all days of the year 2003 (nearly constant low bias of SCIAMACHY of about 1%). The standard deviation of the difference is in the range 1.5-2.5% and the correlation coefficient is typically higher than 0.6. For each ground pixel a quality flag is set using similar criteria as for CO.

3.3 Carbon dioxide specific aspects

Absorption bands of CO_2 are covered by the SCIAMACHY channels 7 (~2 μm) and 6 (~1.6 μm). Because channel 7 is affected by a changing ice-layer on the detectors we currently retrieve CO_2 from channel 6. The WFM-DOAS version 0.4 CO_2 data products are the absolute CO_2 column (in molecules/cm^2) and the dry air column averaged mixing ratio of carbon dioxide XCO_2 (in ppmv) obtained by normalizing the CO_2 column by the observed airmass obtained from the simultaneously retrieved O_2 column derived from the O_2-A-band. Details on our version 0.4 CO_2 retrievals are given in [10,11]. Two points should be mentioned here: (i) we have aimed at rejecting as good as possible all even slightly cloud contaminated ground pixels from the data shown here and (ii) that the WFM-DOAS version 0.4 XCO_2 product is scaled by a constant (i.e., time/space/scene independent) factor which has been applied to eliminate an obvious bias. Therefore, the interpretation of the XCO_2 results shown here should focus on space / time variability but not on the absolute XCO_2 level. The single measurement precision of the XCO_2 v0.4 data product is estimated to be on the order of a few percent [10,11,13,20].

4. TRACE GAS RESULTS

We have processed all available SCIAMACHY spectra of the year 2003 (details concerning the processed orbits are given in [11]). The results will be shown in the following focusing on China. Yearly averages will be presented as well as tri-monthly averages. Because for January 2003 only a few orbits were available and no data for November and December (for ground processing related reasons) the tri-monthly averaged data cover the time period February to October using an untypical grouping of the months not reflecting the standard definition of seasons. Because of the low reflectivity of water (oceans, great lakes) in the near-infrared the quality of the measurements over water is typically reduced and only measurements over land are discussed here.

4.1 Carbon monoxide (CO)

The left panel of Fig.1 shows yearly averaged vertical columns of CO over China (grid: 0.5x0.5 degrees). Clearly visible are large regions of elevated CO (shown in red) indicating CO source regions. Elevated CO is present over a large area south of Beijing, in the region around Chengdu/Chongqing (Red Valley), around Shenyang, and over Hainan Dao and Zhanjiang. The elevated CO detected with SCIAMACHY clearly correlates with major industrialized areas.

The three panels on the right hand side of Fig.1 show tri-monthly averaged CO columns for (from top to bottom) February-April, May-July, and August-October 2003. The largest CO columns are observed in the May to July 2003 average over large parts of eastern China and around Chongqing/Chengdu. High columns are also observed over these regions during other times of the year, especially around Beijing during February to April.

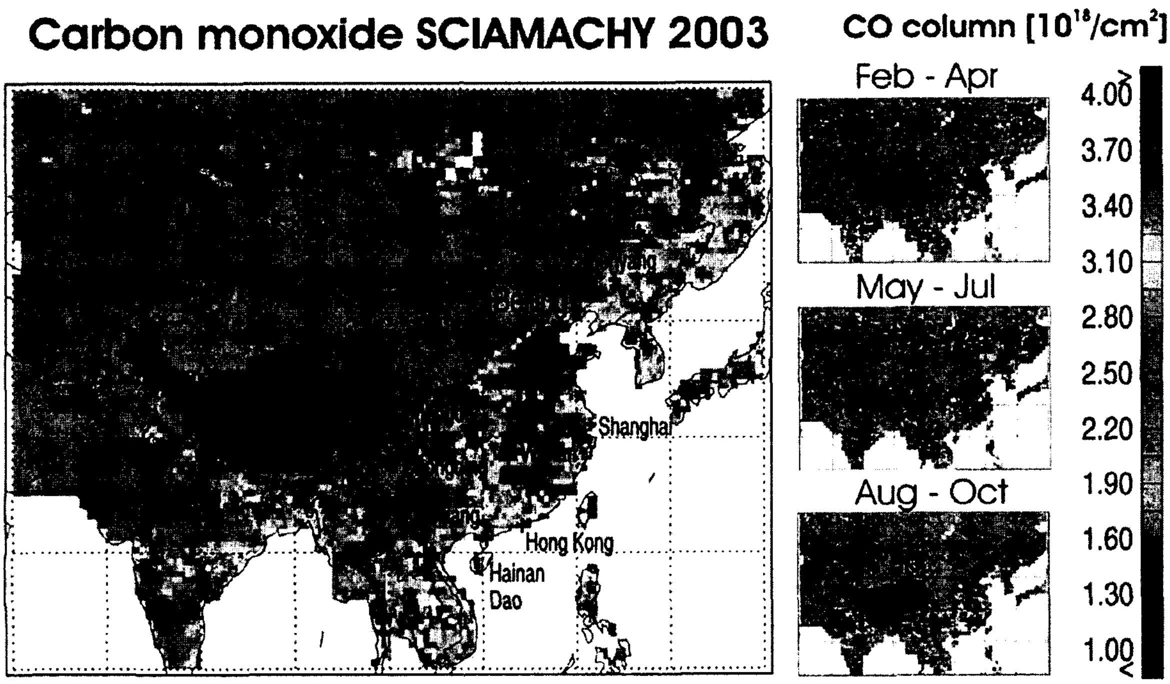

Fig. 1: Carbon monoxide vertical columns over China as measured by SCIAMACHY. The left panel shows the year 2003 average. The three panels on the right hand side show tri-monthly averages for the year 2003. The latitude range covered is 10 °N-60 °N and the longitude range is 60 °E-140 °E.

4.2 Methane (CH_4)

The left panel of Fig.2 shows the dry air column averaged mixing ratio of methane over China obtained by averaging all SCIAMACHY measurements available for the year 2003. Shown are only measurements over land for which the quality flag determined by the retrieval algorithm indicates a (potentially) successful measurement. Using this approach the measurements over the Himalaya region are filtered out. Clear visible are large regions of elevated methane (shown in red) indicating methane source regions over large parts of south-east China (as well as over India, south-east Asia, and Japan).

The panels on the right hand side of Fig.2 show tri-monthly averages of the year 2003 methane data set. During February to April 2003 (top panel) elevated concentrations are present around Chongqing/Chengdu (see annotation of Fig.1 left panel) and along the Pacific ocean coast line around and south of Shanghai, over Hainan Dao and north of Hainan Dao. During May to July (middle panel) the methane concentration is significantly higher compared to February-April over large parts of south-east China. The highest mixing ratios occur over the Chongqing/Chengdu area. Even larger methane concentrations are visible in the August to October average (bottom panel) were highly elevated mixing ratios are observed over large parts of eastern China (as well as over India and south-east Asia). The August to October 2003 measurements confirm the data shown in [15] also derived from SCIAMACHY but with an independent somewhat different retrieval algorithm. The main methane sources of China are rice cultivation, waste handling, ruminants, fossil-fuel related activities, and wetlands (see [15] and references given therein). The tri-monthly averaged concentrations are highest during August to October in-line with the seasonal dependence of the methane emission from rice-paddies.

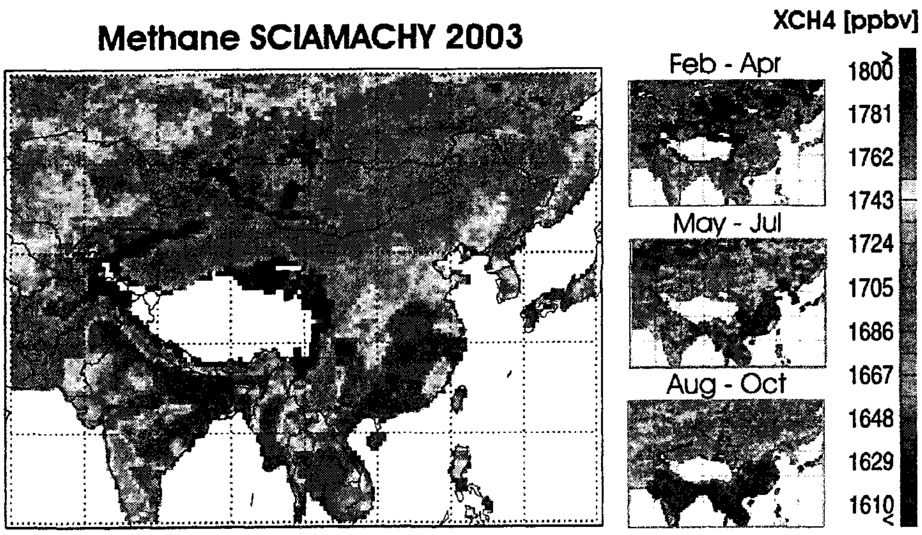

Fig. 2: Methane column averaged mixing ratios over China as measured by SCIAMACHY. The left panel shows the year 2003 average. The three panels on the right hand side show tri-monthly averages for the year 2003. The latitude range covered is 10 °N-60 °N and the longitude range is 60 °E-140 °E.

4.3 Carbon dioxide (CO_2)

The left panel of Fig. 3 shows the XCO_2 over and around China obtained by averaging all SCIAMACHY measurements available for the year 2003 [11]. Shown are only measurements over land for which a relatively good fit has been achieved (using this approach the measurements over the Himalaya region are filtered out). The largest mixing ratios are observed in the north-eastern part of China around and north of Harbin. The lowest mixing ratios are observed over the southern part of China along the Mekong river.

The panels on the right hand side of Fig. 3 shows tri-monthly XCO_2 averages of the year 2003 data set. On average the values are lowest in the May to July average. This minimum around the mid-of the year is consistent with the uptake of atmospheric CO_2 by vegetation which is in its main growing phase during this time of the year [11]. Superimposed on this large scale behaviour is a considerable regional fine structure. The interpretation of these measurements is difficult because the retrieval errors due to instrument and retrieval noise and biases are estimated to be on the same order as the weak source/sink signals to be detected [8,10,11]. More studies are needed including comparison with land cover maps and model simulations before a clear interpretation of these maps can be made.

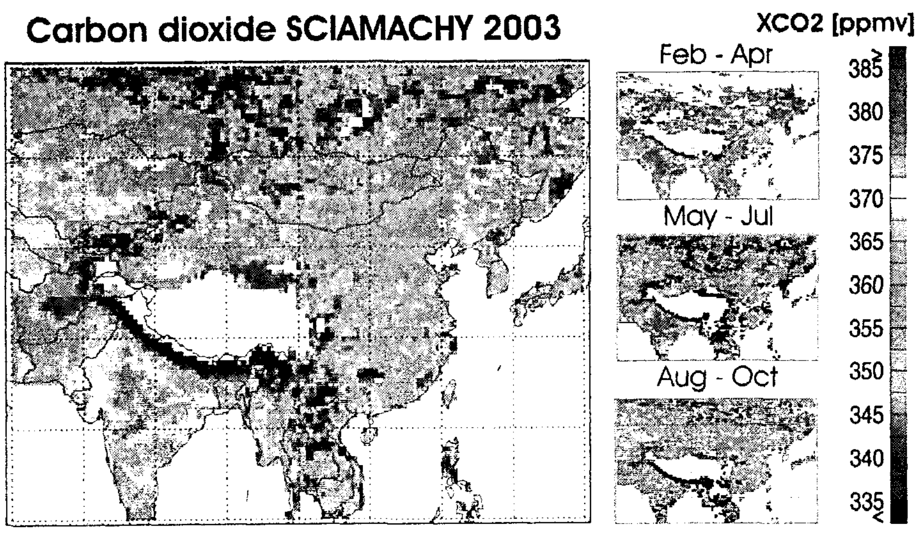

Fig. 3: Carbon dioxide column averaged mixing ratios over China as measured by SCIAMACHY. The left panel shows the year 2003 average. The three panels on the right hand side show tri-monthly averages for the year 2003. The latitude range covered is 10 °N-60 °N and the longitude range is 60 °E-140 °E.

5. CONCLUSIONS AND OUTLOOK

Satellite derived maps of carbon monoxide, methane and CO_2 over China have been presented. The maps enable the identification of surface source regions. Our future work will focus on further analysing the presented data by performing a detailed comparison with model simulations using the latest emission data bases. Our goal is to generate data products that can provide quantitative information on surface sources and sinks via inverse modelling. So far we have only processed the SCIAMACHY year 2003 spectra. More data will be processed in the near future. Information about the latest status is given on our SCIAMACHY/WFM-DOAS web page:
http://www.iup.physik.uni-bremen.de/sciamachy/NIR_NADIR_WFM_DOAS/index.html .

ACKNOWLEDGEMENTS

We thank ESA and DLR for providing us with the SCIAMACHY spectra (operational Level 1 data products). Funding for this study came from the German Ministry for Research and Education (BMBF) via DLR-Bonn (project SADOS), the EC 5th FP on Energy, Environment and Sustainable Development (EVERGREEN, see http://www.knmi.nl/evergreen), from ESA (GMES-PROMOTE, see http://www.gse-promote.org) and from the University and the State of Bremen. We acknowledged exchange of information within the EU 6th FP Network of Excellence ACCENT (http://www.accent-network.org).

REFERENCES

1. Bergamaschi, P., Krol, M., Dentener, F., Vermeulen, A., Meinhardt, F., Graul, R., Peters, W., and Dlugokencky, E. J., Inverse modelling of national and European CH_4 emissions using the atmospheric zoom model TM5, Atmos. Chem. Phys. Disc., 5, 1007-1066, 2005.
2. Bergamaschi, P., Hein, R., Heimann, M., and Crutzen, P. J.: Inverse modeling of the global CO cycle, 1. Inversion of CO mixing ratios, J. Geophys. Res., 105, 1909--1927, 2000.
3. Bovensmann, H., J. P. Burrows, M. Buchwitz, J. Frerick, S. Noël, V. V. Rozanov, K. V. Chance, and A. H. P. Goede, SCIAMACHY - Mission objectives and measurement modes, J. Atmos. Sci., 56, (2), 127-150, 1999.
4. Bovensmann, H., Buchwitz, M., Frerick, J., Hoogeveen, R., Kleipool, Q., Lichtenberg, G., Noël, S., Richter, A., Rozanov, A., Rozanov, V. V., Skupin, J., von Savigny, C., Wuttke, M., and Burrows, J. P.: SCIAMACHY on ENVISAT: In-flight optical performance and first results, in Remote Sensing of Clouds and the Atmosphere VIII, edited by Schäfer, K. P., Comeron, A., Carleer, M. R., and Picard, R. H., vol. 5235 of Proceedings of SPIE, 160-173, 2004.
5. Buchwitz, M., V.V. Rozanov, and J.P. Burrows, A near-infrared optimized DOAS method for the fast global retrieval of atmospheric CH_4, CO, CO_2, H_2O, and N_2O total column amounts from SCIAMACHY Envisat-1 nadir radiances, J. Geophys. Res. 105, 15,231-15,245, 2000.
6. Buchwitz, M., V.V. Rozanov, and J.P. Burrows, A correlated-*k* distribution scheme for overlapping gases suitable for retrieval of atmospheric constituents from moderate resolution radiance measurements in the visible/near-infrared spectral region, J. Geophys. Res. 105, 15,247-15,261, 2000.
7. Buchwitz, M., S. Noël, K. Bramstedt, V. V. Rozanov, H. Bovensmann, S. Tsvetkova, and J. P. Burrows, Retrieval of trace gas vertical columns from SCIAMACHY/ENVISAT near-infrared nadir spectra: First preliminary results, Adv. Space Res., 34, 809-814, doi:10.1016/j.asr.2003.05.054, 2004.
8. Buchwitz, M., and John P. Burrows, Retrieval of CH_4, CO, and CO_2 total column amounts from SCIAMACHY near-infrared nadir spectra: Retrieval algorithm and first results, SPIE 10th International Symposium "Remote Sensing", 8-12 September 2003, Barcelona, Spain, Conference 5235 "Remote Sensing of Clouds and the Atmosphere VIII", Editors K. P. Schäfer, A. Comèron, M. R. Carleer, R. H. Picard, Proceedings of SPIE Volume 5235, 375-388, 2004.
9. Buchwitz, M., R. de Beek, K. Bramstedt, S. Noël, H. Bovensmann, and J. P. Burrows, Global carbon monoxide as retrieved from SCIAMACHY by WFM-DOAS, Atmos. Chem. Phys., 4, 1945-1960, 2004.
10. Buchwitz, M., R. de Beek, J. P. Burrows, H. Bovensmann, T. Warneke, J. Notholt, J. F. Meirink, A. P. H. Goede, P. Bergamaschi, S. Körner, M. Heimann, and A. Schulz, Atmospheric methane and carbon dioxide from SCIAMACHY satellite data: Initial comparison with chemistry and transport models, Atmos. Chem. Phys., .5, 941-962, 2005.
11. Buchwitz, M., R. de Beek, S. Noël, J. P. Burrows, H. Bovensmann, H.. Bremer, P. Bergamaschi , S. Körner, and M. Heimann, Carbon monoxide, methane and carbon dioxide columns retrieved from SCIAMACHY by WFM-DOAS: year 2003 initial data set, Atmos. Chem. Phys. Discuss., 5, 1943-1971, 2005.
12. Deeter, M. N., Emmons, L. K., Francis, G. L., Edwards, D. P., Gille, J. C., Warner, J. X., Khattatov, B., Ziskin, D., Lamarque, J.-F., Ho, S.-P., Yuding, V., Attie, J.-L., Packman, D., Chen, J., Mao, D., and Drummond, J. R.:

Operational carbon monoxide retrieval algorithm and selected results for the MOPITT instrument, J. Geophys. Res., 108, 4399--4409, 2003.

13. Dils, B., M. de Mazière, T. Blumenstock, M. Buchwitz, R. de Beek, P. Demoulin, P. Duchatelet, H. Fast, C. Frankenberg, A. Gloudemans, D. Griffith, N. Jones, T. Kerzenmacher, E. Mahieu, J. Mellqvist, S. Mikuteit, R. L. Mittermeier, J. Notholt, H. Schrijver, D. Smale, A. Strandberg, W. Stremme, K. Strong, R. Sussmann, J. Taylor, M. van den Broek, T. Warneke, A. Wiacek, S. Wood, Comparisons between SCIAMACHY scientific products and ground-based FTIR data for total columns of CO, CH_4, CO_2 and N_2O, Atmos. Chem. Phys. Discuss., 5, 2677-2717, 2005.
14. Frankenberg, C., U. Platt, T. Wagner, Retrieval of CO from SCIAMACHY onboard ENVISAT: Detection of strongly polluted areas and seasonal patterns in global CO abundances, Atmos. Chem. Phys. Discuss., 4, 8425-8438, 2004.
15. Frankenberg, C., J. F. Meirink, M. van Weele, U. Platt, T. Wagner, Assessing methane emissions from global spaceborne observations, Science, 308, 1010-8438, 2005.
16. Gloudemans, A. M. S., H. Schrijver, Q. Kleipool, M. M. P. van den Broek, A. G. Staume, G. Lichtenberg, R. M. van Hess, I. Aben, J. F. Meirink, The impact of SCIAMACHY near-infrared instrument calibration on CH_4 and CO total columns, Atmos. Chem. Phys., 5, 2369-2383, 2005.
17. Houweling, S., W. Hartmann, I. Aben, H. Schrijver, J. Skidmore, G.-J. Roelofs, F.-M. Breon, Evidence of systematic errors in SCIAMACHY-observed CO_2 due to aerosols, Atmos. Chem. Phys. Discuss., 5, 3313-3340, 2005.
18. Sussmann, R., and Buchwitz, M., Initial validation of ENVISAT/SCIAMACHY columnar CO by FTIR profile retrievals at the ground truthing station Zugspitze, Atmos. Chem. Phys., 5, 1497-1503, 2005.
19. Sussmann, R., W. Stremme, M. Buchwitz, R. de Beek, Validation of ENVISAT/SCIAMACHY columnar methane by solar FTIR spectrometry at the ground-truthing station Zugspitze, Atmos. Chem. Phys., 5, 2419-2429, 2005.
20. Warneke, T., de Beek, R., Buchwitz, M., Notholt, J., Schulz, A., Velazco, V., and Schrems, O., Shipborne solar absorption measurements of CO_2, CH_4, N_2O, and CO and comparison the SCIAMACHY WFM-DOAS retrievals, Atmos. Chem. Phys., 5, 2029-2034, 2005.

TROPOSPHERIC NO_2 OVER CHINA

R.J. van der A[1], D.H.M.U. Peters[1,2], J.J.P. Kuenen[1,2], H.J. Eskes[1], K.F. Boersma[1], M. Van Roozendael[3], I. De Smedt[3], P.Zhang[4], H.M. Kelder[1,2]

[1] Royal Netherlands Meteorological Institute, The Netherlands
[2] Eindhoven University of Technology, The Netherlands
[3] Belgian Institute For Space Aeronomy, Belgium
[4] National Satellite Meteorological Center, Chinese Meteorological Administration, Beijing

ABSTRACT

The results are presented of a study to tropospheric NO_2 over China, based on measurements from the satellite instruments GOME and SCIAMACHY. A data set of 10 year tropospheric NO_2 has been processed from GOME and SCIAMACHY observations using a combined retrieval/assimilation approach. This approach allows the retrieval of global, accurate tropospheric concentrations and detailed error estimates. The resulting dataset has been analysed with statistical methods to derive trends in NO_2 and the seasonal variability on a grid of 1x1 degree for all regions of China. The variance and the autocorrelation of the noise are used to calculate the significance of the trend. The results show a large growth of tropospheric NO_2 over eastern China, especially above the industrial areas with a fast economical growth. The seasonal pattern of the NO_2 concentration shows a clear difference between East and West China. This spatial difference correlates with the dominating source of emissions.

1. INTRODUCTION

Nitrogen oxides (NO_x=NO + NO_2) play an important role in atmospheric chemistry. NO_x has significant natural sources (e.g. lighting and soil emissions) and anthropogenic (e.g. biomass burning, fossil fuel combustion) sources. Global tropospheric NO_2 distributions are measured by the satellite instruments GOME (from 1995-2003) aboard ERS-2, SCIAMACHY (from 2002) aboard Envisat platform and OMI aboard EOS-AURA (from 2004) [Leue et al., 2001, Richter et al., 2005; Martin et al., 2002; Boersma et al., 2004]. In Fig. 1. two examples are shown of NO_2 observations over China by both GOME and SCIAMACHY.

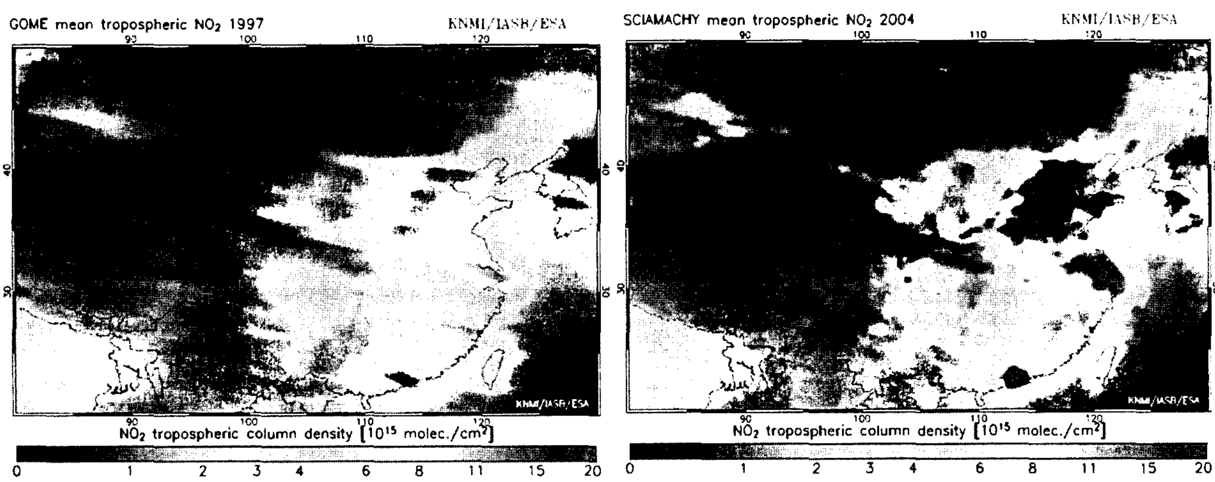

Fig. 1. Mean tropospheric NO_2 as measured by GOME in 1997 (left panel) and by SCIAMACHY in 2004 (right panel). Note the difference in resolution of both instruments but also the increase in measured NO_2 in only 7 years time.

Proc. 2005 Dragon Symposium "Mid-Term Results", Santorini, Greece
27 June – 1 July 2005 (ESA SP-611, January 2006)

Recent studies on the tropospheric NO_2 columns show that the satellite measurements are suitable for improving emission inventories and air quality studies. Jaeglé et al. [2004] used GOME measurements over the Sahel to map the spatial and seasonal variations of NO_x, mainly caused by biomass burning and soil emissions. Martin et al. [2003] used GOME measurements to derive a top-down emission inventory. The top-down inventory in combination with bottom-up emission inventory is used to achieve an optimised posterior estimate of the global NO_x emissions. Boersma et al. [2005] used GOME measurements to estimate the global NO_x production from lightning by comparing modelled and measured spatial and temporal patterns of NO_2 in the tropics. In Blond et al. [2005] SCIAMACHY measurements are compared with an air quality model and ground measurements. They showed that SCIAMACHY measurements are able to monitor the air pollution over Europe and its day-to-day changes.

In this study we focus on China for the period 1996 to 2004. China has one of today's fastest growing economies of the world. This increase in economical activity is accompanied by a strong increase of emissions of tropospheric pollutants and therefore leads to extra pressure on the environment. We will combine GOME and SCIAMACHY measurements to obtain a 9-year dataset that is suitable for a trend study. The strong increase in NO_x emissions in China is due to a increase in industry and traffic, see Wang et al. [2004]. These emissions are concentrated on the densely populated and industrialized eastern part of China, as can be seen in Fig. 2.

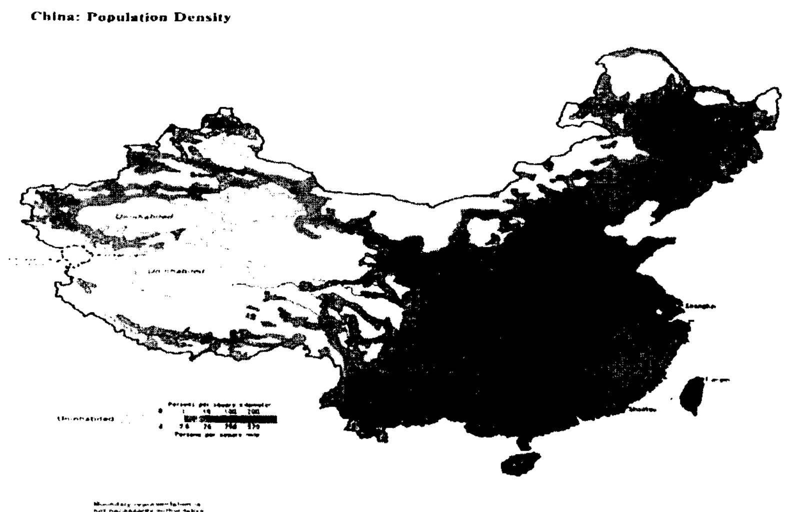

Fig. 2. The population density in China. The red areas in East China are the major industrial and urbanized regions of China. (Courtesy of the University of Texas Libraries, The University of Texas at Austin.)

The combination of the variability in both chemistry and emissions leads to a seasonally dependent NO_2 concentration with an expected maximum of NO_2 in wintertime. The NO_2 lifetime is in the order of one day depending on many factors like meteorological conditions, photolysis time scale and OH concentrations. A higher actinic flux results in a higher OH concentration (if the water vapor concentration is high enough), which reacts with NO_2 to form HNO_3, the principal sink for NO_x. The emissions also show variability.

2 Tropospheric NO_2 retrieval

The GOME and SCIAMACHY spectrometers measure backscattered light from the Earth in the UV and visible wavelength range. From the observed spectral features around 425-450 nm slant column densities (SCD) of NO_2 are derived with the Differential Optical Absorption Spectroscopy (DOAS) method [Platt, 1994]. The work presented here is based on slant columns retrieved from the satellite data by BIRA-IASB [Vandaele et al., 2005]. The NO_2 stratospheric column is deduced from a chemistry-transport model assimilation run of the NO_2 slant column data. Subsequently, the assimilated stratospheric slant column is subtracted from the retrieved DOAS total slant column, resulting in a tropospheric slant column. The tropospheric NO2 columns are derived from these slant columns [Boersma et al., 2004]. Height-dependent air mass factor (AMF) lookup tables are based on calculations with the Doubling-Adding KNMI (DAK) radiative transfer model. The tropospheric vertical column is retrieved using TM4 [Dentener et al., 2003] tropospheric model profiles (co-located for each GOME and SCIAMACHY pixel individually) and combined with albedo and cloud information. The latter consists of cloud fraction and cloud top height derived by the FRESCO algorithm [Koelemeijer et al., 2003]. Only observations with an estimated cloud radiance of less than 0.5 are used in this study. The retrieval includes surface albedo values constructed from a combination of the TOMS-Herman-Celarier-1997 and Koelemeijer-2003 surface reflectivity maps (available on a monthly basis). No aerosol correction is applied. This choice is based on the realization that the cloud retrieval will be influenced by aerosol as well, and is further motivated by the error analysis presented in the work of Boersma et al. [2004]. The final NO_2 column data product is publicly available on the TEMIS project website (www.temis.nl) with detailed error estimates and kernel information [Eskes and Boersma, 2003]. In Fig. 3 the year average tropospheric NO_2 column of 2004 is given. The Figure shows high concentration above the highly populated regions like Beijing, Shanghai, Hong Kong and South Korea. It can also be seen that the satellite is detecting the emissions around the Yellow river (Huang He). Over western China, low NO_2 columns are observed except over the large city Urumqi in the Northwest.

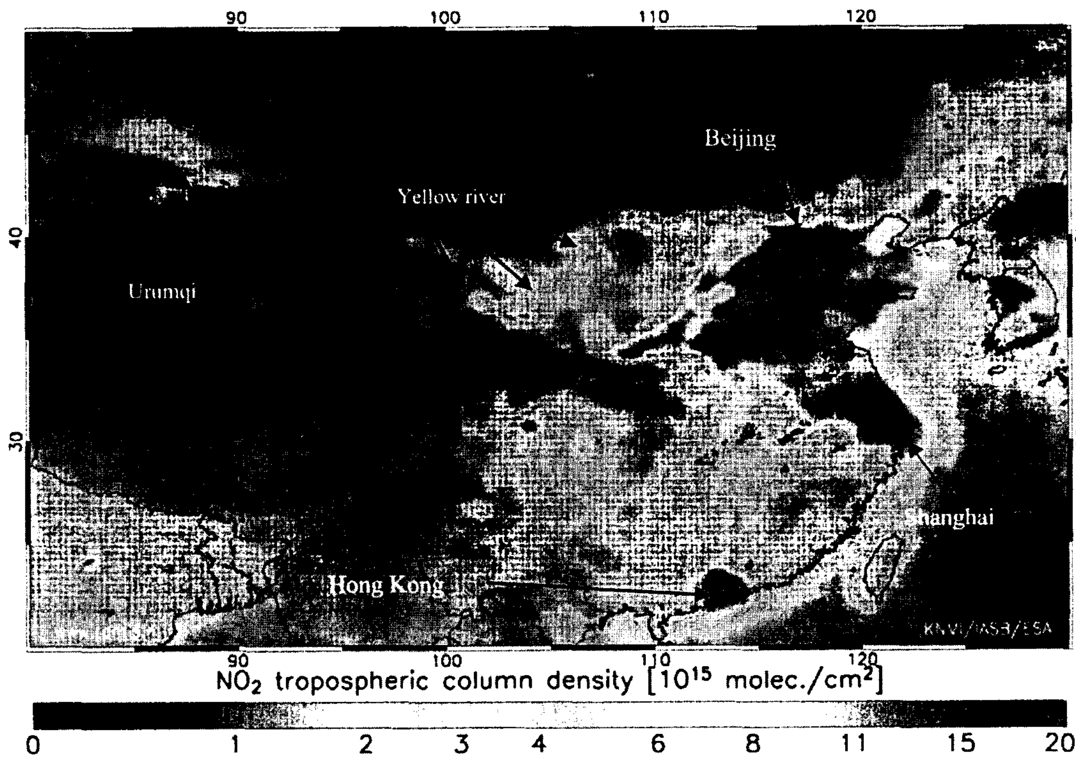

Fig. 3. The yearly averaged tropospheric NO_2 column measured by SCIAMACHY for 2004.

3 Data analysis

The GOME data from March 1996 till March 2003 and the SCIAMACHY data from April 2003 till December 2004 have been used to analyze the trends and variability in NO_2 over China. April 2003 is the first month where SCIAMACHY NO_2 columns are retrieved successfully. The retrieved tropospheric NO_2 columns are gridded on a 1° by 1° grid, using weighting factors for the overlap between satellite pixel and grid cell. The 1 by 1 grid is chosen to average out the effect of different satellite pixel sizes.

For each cell two time series are determined; a time series based on a two weeks average and one based on a monthly average. Both time series are tested for the best fit. Because of the larger sample the monthly average lead to a better and more consistent time series. The negligible weekly cycle of the NO_2 concentration above China makes it unnecessary to compensate for lower weekend measurements.

The temporal variability in the NO_2 columns is usually larger than the precision of the measurements. To account for both effects, the uncertainty of the monthly mean is determined by taking the sample standard deviation of the mean. The measurement error on the tropospheric NO_2 for individual pixels as calculated by [Boersma et al.,2004] shows a dependency on the absolute value of tropospheric NO_2, having a minimum error of about $1 \cdot 10^{15}$ molec/cm^2. This minimum error is used as lower limit for the error on the monthly average NO_2 concentration to avoid a non-realistic accuracy caused by a limited number of samples.

Two models have been used to fit the time series, a model with a linear trend and a seasonal component for the annual cycle of NO_2, and a model with an exponential trend. The model with the linear trend is described by the following function based on Wheaterhead et al. [1998],

$$Y_t = A + BX_t + C\sin(DX_t + E) + \delta U_t + N_t, \qquad (1)$$

where Y_t represents the monthly NO_2 column of month t and X_t is the number of months after January 1996, N_t is the remainder (residual unexplained by the fit function) and A,B,C,D,E,δ are the fit parameters. Parameter A represents the NO_2 column in January 1996, and B is the monthly trend in NO_2. The seasonal component contains amplitude C, a frequency D and a phase shift E. The fit of the frequency D leads to an expected period of one year, therefore this fit parameter was fixed for the final analyses. The data has also been fitted with a linear model, without a seasonal component. The analyses of this fit showed that the seasonal component was an essential part of the model. A linear growth was used to fit the time series since there is no large distinction between a linear and an exponential growth of the tropospheric NO_2 column over China in the period 1996 to 2004.

The term δU in Eq. 1 is used to fit the bias between the measurements of GOME and SCIAMACHY, where δ is the value of the bias and U_t is,

$$U_t = \begin{cases} 0 & t < T_0 \\ 1 & t \geq T_0 \end{cases}. \qquad (2)$$

In this Eq. 2 the time T_0 $(0 < T_0 < T)$ is the moment when the time series switches from using GOME to using SCIAMACHY data, which in this case is April 2003. The total number of months is denoted by T. The bias δ is fitted and checked for latitude dependence over China. We find that the bias is negligible, with values less than 0.01 10^{15} molec/cm^2. Based on this result the bias term is set to zero in analysis below.

The remainder, N_t in Eq. 1 is the difference between the model and the measured value. Weatherhead et al. [1998] suggest modeling the remainder by

$$N_t = \phi N_{t-1} + \varepsilon_t, \qquad (3)$$

where ε_t is the white noise and ϕ is the autocorrelation in the remainder. The autocorrelation in the remainder is a result from processes which are persistent with time and which are not described by the fit function, see Tiao et al. [1990]. We produced plots of the correlation between remainders as a function of the time difference. A typical autocorrelation of 0.1 is found, indicating that the remainders are only weakly correlated. The autocorrelation in the remainder affects the precision of the trend. In Wheaterhead et al. [1998] a derivation is given for the precision of the trend as function of the autocorrelation, the length T of the dataset in months and the variance in the remainder, σ_N.

The length of the dataset in years, n, is introduced to express the precision of the trend per year. For small autocorrelations the standard deviation σ_B of the trend per year is approximately given by

$$\sigma_B \approx \left[\frac{\sigma_N}{n^{3/2}} \sqrt{\frac{1+\phi}{1-\phi}} \right]. \qquad (4)$$

4 Trends in tropospheric NO2

For each grid cell in China the model following Eq. 1, is applied, leading to a spatial distribution of each of the fitting parameters of the model. In Fig. 5 the trend in NO_2 concentration is, shown as the yearly increase in tropospheric NO_2. The trend is the highest in the eastern part of China, corresponding to the regions with a fast industrial and economical development. The fastest growing economy is in the Shanghai region, which also shows the largest growth of tropospheric NO_2. It is interesting to note that the growth in the region around Hong Kong is less than for other regions with a high economical activity. This is probably due to the already high level of economic activity in 1996 when our trend study started and a package of measures against air pollution in Hong Kong over the last years.

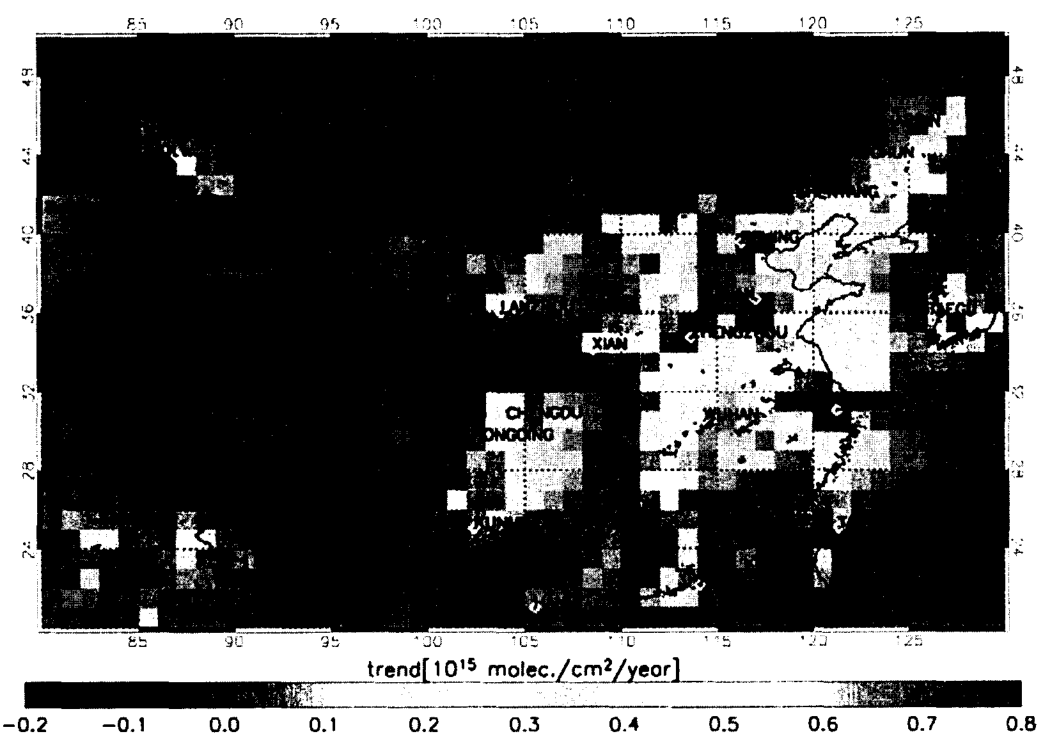

Fig. 4. The trend of the NO_2 concentration over China for the period 1996-2004.

The precision σ_B of the trend on NO_2 is calculated using Eq. 4. In Fig. 4 the trend divided by the precision is shown. It is a common decision rule for trend detection that a trend B is real with a 95% confidence level if $|B/\sigma_B| > 2$ [Wheaterhead et al., 1998]. Fig. 5 shows that a significant trend (white grid cells) is detected in the regions of East China with a high population and high industrial activity. From Eq. 4 can be seen that the standard deviation of the trend decreases if the length of the dataset increases. Therefore, it can be expected that for more grid cells a significant trend can be detected with a longer dataset.

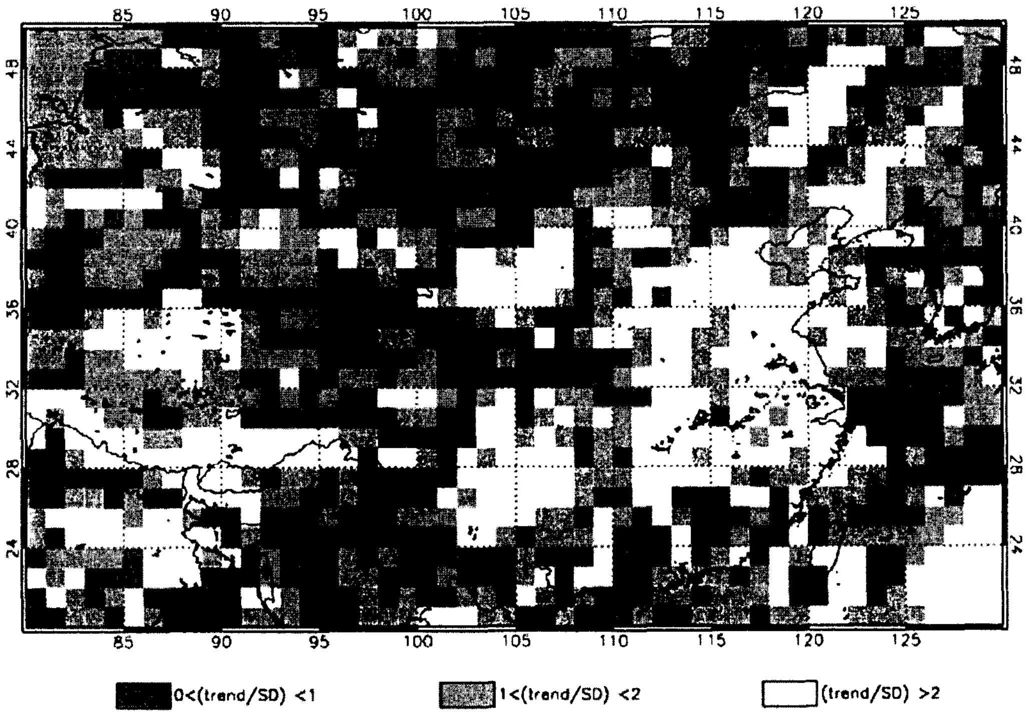

Fig. 5. The NO_2 trend per year divided by the standard deviation. If this value is higher than 2 (white areas) a real trend is indicated with a 95% confidence level.

In Table 1 the trend estimates and start values for some major cities are shown. A yearly growth is determined in terms of percentage with respect to the start value in 1996. Shanghai is one of the fastest growing industrial areas, which is reflected in a large growth in NO_2. The trend over Taipei is not significant in this period. This is probably due to the effect of measures by the government to improve the air quality in Taiwan (These measures included subsidies on environmental-friendly techniques in traffic, improved public transport, and imposing pollution penalties)

Table 1. The observed trends for some cities in East Asia. The percentage is calculated with respect to the year 1996.

	NO_2 concentration in January 1996 [10^{15} molec/cm^2]	Linear trend in NO_2 [10^{15} molec/cm^2/ year]	Error on trend [10^{15} molec/cm^2/year]	Growth (reference year 1996)
Hong Kong	7.63	0.72	0.48	8%
Beijing	10.92	1.20	0.48	11%
Shanghai	5.48	1.44	0.35	25%
Taipei	4.89	-0.02	0.06	0%
Chongqing	3.10	0.40	0.10	13%
Seoul	9.95	0.36	0.21	4%
Background (86°E x 40°N)	0.5	0	0.01	0%

5 The relation between tropospheric NO_2 columns and NO_x emissions

To see how a change in NO_x tropospheric column density is related to a change in NO_x emissions, the effect of doubling the anthropogenic emissions on the NO_x tropospheric column density has been studied. Using the chemistry-transport zoom model TM5 (Krol et al., 2005) with zooming on China, tropospheric NO_x columns can be determined on a 1x1 degree resolution for China. In Fig. 6 the ratio between two tropospheric columns is plotted; one with regular emissions and one where the anthropogenic emissions are doubled. This factor 2 has been chosen, because it is a typical increase in NO_2 tropospheric column over a 10-year period.

From this picture it can be concluded that in places where very little anthropogenic NO_x emissions are present (like in West China), the ratio is close to 1, as expected. In places with high anthropogenic NO_x emissions however, doubling the NO_x emissions means that the NO_x tropospheric column density becomes nearly twice as large. The highest values typically occur in the places with the highest tropospheric NO_2 column density, the anthropogenic NO_x emissions are predominant here.
The ratio between the tropospheric column densities does not exceed the factor 2, which means that the trend in tropospheric NO_x column is a minimum for the trend in NO_x emissions.

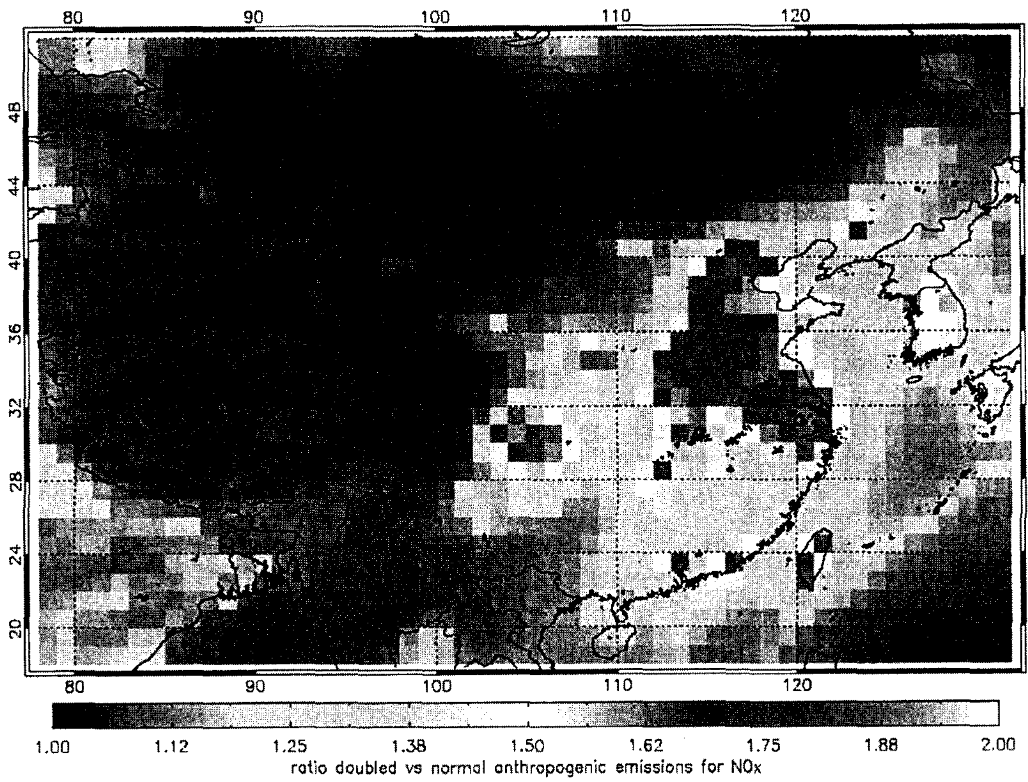

Fig. 6. Map of ratios between tropospheric NO_x columns modelled with standard emissions and modelled with doubled anthropogenic emissions. The model runs are performed for the annual average of 2001.

6 The NO_2 seasonal cycle

The time series of NO_2 usually show a strong seasonal cycle, which has also been fitted using Eq. 1 allowing us to study the seasonal cycle of the NO_2 concentration. Since the lifetime of NO_x is longer in wintertime, a NO_2 maximum is expected in the winter. Fig. 7 shows that the month with the largest NO_2 abundances in the East and South of China is according to the expected winter maximum, but in the West a NO_2 maximum during summertime is found. The black grid cells correspond to regions where a linear fit works just as well but without a clear seasonal cycle.

The western part of China has a low population density (see Fig. 2). As a consequence natural emissions are expected to dominate the tropospheric column. Fig. 6 shows that in the North West, above the large city Urumqi, a winter maximum is found, which strengthens the idea that the summer maximum in NO_2 over the rest of West China is caused by natural emissions.

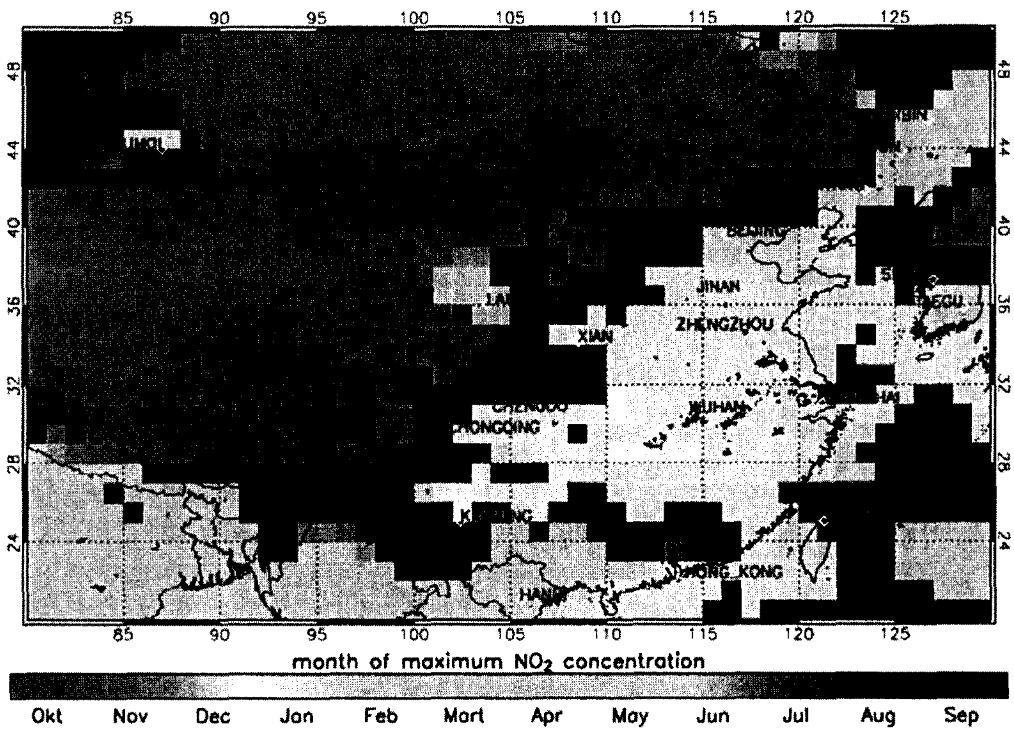

Fig. 7. Map of China showing the month where the yearly seasonal component has its maximum in NO_2 concentration. In East China a maximum is found during the winter and in the West of China a maximum is found during the summer. The black pixels are regions where a linear fit without a seasonal component is more accurate.

Lightning flash densities are measured by the Optical Transient Detector (http://thunder.msfc.nasa.gov/OTDsummaries). From a comparison between the summer and winter flash densities can be concluded that lightning above China especially occurs during summertime. The contribution of lightning to the tropospheric NO_2 column is strongest in the tropics, with an estimated maximum of 0.4 10^{15} molec/cm^2 [Edwards et al., 2003, Boersma et al., 2005]. Because the difference between summer and winter tropospheric columns is typical of the order 1.0 10^{15} molec/cm^2, lightning alone cannot account for all the natural emissions in West China. Bryan et al. [2003] show that there is no biomass burning in the western part of China.

In Yienger et al. [1995] it is suggested that in remote agriculture regions soil emissions contribute 50% to the total NO_x budget and that in July these percentages can rise to more than 75%. Yienger et al. [1995] also suggested that soil NO_x emissions are temperature dependent, soil dependent and precipitation dependent. A higher surface temperature leads to more NO_x emissions, which would explain higher NO_x concentrations in summer time. They also found higher NO_x emissions for grassland that together with desert and scrub land form the main soil composition in West China. Another effect that increases soil NO_x emissions in summertime is "pulsing", which is described in [Yienger et al., 1995] and [Jaeglé et al., 2004] as an increase in NO_x measured after a shower of rain. From the IRI/LDEO Climate Data library it can be seen that in the West part of China it is only raining in the summer season. This also contributes to enhanced NO_2 concentrations during summertime.

7 Conclusions

The tropospheric NO_2 columns measured by GOME and SCIAMACHY have been used for trend analysis over China. A linear model with a seasonal component is used to fit the time series of NO_2 concentrations. By applying this model to each grid cell a spatial distribution of the fit parameters is calculated. Furthermore the precision of the trend is calculated.

It can be concluded that the 9 years long NO_2 dataset from GOME and SCIAMACHY can be used for trend analysis in the eastern part of China. In this highly populated and industrialised area the trend is large enough to be significant. For instance Shanghai had a yearly increase of 25% in 1996. For other regions longer time series are needed to detect a significant signal.

The geographic distribution of the seasonal cycle of tropospheric NO_2 was studied. In the eastern part of China an expected winter maximum is found. In the western part of China this cycle shows a NO_2 maximum in summer time. As there is nearly no anthropogenic activity in Western China, this cycle is attributed to natural emissions, especially soil emissions and lightning.

The bias between the monthly GOME and SCIAMACHY tropospheric NO_2 series appears to be negligible and does not show any latitude dependence. This shows the consistency in the retrieval method of tropospheric NO_2 and allows the use of long time series by combining different instruments to detect a significant trend for regions without a large trend.

It is well known that emissions are increasing over China [Streets et al., 2003; Wang et al., 2004]; this study shows that the satellite measurements are able to measure the increase of atmospheric concentrations. Our first results from modelling studies indicate that the trends found in the satellite observations of NO_2 can be considered lower boundaries of the actual trends in emissions of NO_x.

References

Blond, N., K.F. Boersma, H.J. Eskes, R.J. van der A, M. Van Roozendael, I. De Smedt, G. Bergametti, and R. Vautard (2005), Intercomparison of SCIAMACHY nitrogen dioxide observations, in-situ measurements, and air quality modeling results over Western Europe, submitted to *J. Geophys. Res*

Boersma, K.F., H.J. Eskes and E.J. Brinksma (2004), Error analysis for troposheric NO2 retrieval from space, *J. Geophys. Res.*, *109*(D0) ,4311, doi: 10.1029/2003JD003961.

Boersma, K.F., H.J. Eskes, E.W. Meijer, and H.M. Kelder (2005), Estimates of lightning NO_x production from GOME satellite observations, *Atmos. Chem. Phys. Discuss,* 5, 3047-3104

Boersma, K.F.(2005), Satellite observations of tropospheric nitrogen dioxide; retrieval interpretation and modelling, Ph.D Thesis, Universiteitsdrukkerij Technische Universiteit Eindhoven, Eindhoven

Bryan N. D., R.V. Martin, A.C. Staaudt, R.Yevich, and J.A. Logan. (2003),Interannual and seasonal variability of biomass burning emissions constrained by satellite observations, J. *Geophys. Res.*, *108* (D2), 4100, doi:10.1029/2002/JD002378

Dentener, F.,M. van Weele, M. Krol, S Houweling, and P. van Velthoven (2003), Trends and inter-annual variability of methane emissions derived from 1979-1993 global ctm simulations, *Atmos. Chem. Phys., 3,* 73-88

Edwards, D. P., J.F. Lamarque, J.L, Attie, L. K. Emmons, A. Richter, J.P. Cammas, J. C. Gille, G. L. Francis, M. N. Deeter, J. Warner, D. C. Ziskin, L. V. Lyjak, J. R. Drummond, and J. P. Burrows (2003), Tropospheric Ozone Over the Tropical Atlantic: A Satellite Perspective, *J. Geophys. Res*, *108*(D8), 4237, doi:10.1029/2002JD002927,

Eskes, H. and F. Boersma (2003), Averaging Kernels for DOAS total-column satellite retrievals. *Atmos Chem. Phys.*, *3*, 1285 – 1291, 2003

Jaeglé, L., R.V.Martin, K.Chance, L.Steinberger, T.P. Kurosu, D.J. Jacob, A.I.Modi, V.Yoboué, L. Sigha-Nkamdjou, and C.Galy-lacaux (2004), Satellite mapping of rain-induced nitric oxide emissions from soils, *J. Geophysical. Res.* *109*(D2), 1310, doi:10.1029/2004JD004787

Koelemeijer, R.B.A., J.F. de Haan, and P. Stammes (2003), A database of spectral surface reflectivity in the range 335-772 nm derived from 5.5 years of GOME observations, *J. Geophys. Res.*,*108*(D2), doi: 10.1029/2002JD002429

Krol, M., S. Houweling, B. Bregman, M. van den Broek, A. Segers, P. van Velthoven, W. Peters, F. Dentener and P. Bergamaschi, The two-way nested global chemistry-transport zoom model TM5: algorithm and applications, *Atmos. Chem. Phys.*, *5*, 417-432, 2005.

Leue, C., M. Wenig, T. Wagner, O. Klimm, U. Platt, and B. Jähne (2001), Quantitative analysis of NO_x emissions from Global Ozone Moinitoring Experiment satellite image sequences, *J. Geophys. Res*,*106*, 5493-5505

Martin, R.V., K.V. Chance, D.J.Jacob, D.J., Kursou, T.P., Spurr, R.J.D., Bucsela, E., Gleason, J.F., Palmer, P.I., Bey, I., Fiori., A.M., Li, Q. and Koelemeijer, R.B.A.(2002), *An improved retrieval of tropospheric nitrogen dioxide from GOME, J. Geophys. Res*,*107*(D20)4437, doi:10.10129/2001JD001027

Martin, R.V., D.J. Jacob, K.V. Chance, T.P. Kurosu, P.I. Palmer, and M.J. Evans (2003), Global inventory of Nitrogen Dioxide Emissions Constrained by Space-based Observations of NO_2 Columns, *J. Geophys. Res.*, *108*(D17), 4537, doi:10.1029/2003/JD003453

Richter A., J.P. Burrows, H. Nüβ, C. Granier, U. Niemeier, Increase in tropospheric nitrogen dioxide over China observed from space, Nature, 437, 129-132, doi: 10.1038/nature04092, 2005.

Platt, U.(1994), Differential Optical Absorption Spectroscopy (DOAS), in *Air Monitoring by Spectroscopic Techniques, Chem. Anal., vol. 127, edited by M.W. Sigrist, pp. 27-76, Wiley-Interscience, Hoboken, N.J.*

Streets, D.G., T.C. Bond, G.R. Carmichael, S.D. Fernandes, Q. Fu, D. He, Z. Klimont, S.M. Nelson, N.Y. Tsai, M.Q. Wang, J.-H. Woo, and K.F. Yarber (2003), An inventory of gaseous and primary aerosol emissions in Asia in the year 2000 *J. Geophys. Res.*, *108*(D21), 8809, doi:10.1029/2002JD003093

Tiao, G.C. Reinsel, Daming XU, J.H. Pedrick, Xiaodong Zhu, A.J. Miller, J.J. DeLuisu, C.L. Mateer, and D.J. Wuebbles (1990), Effects of autocorrelation and temporal sampling schemes on estimates of trend and spatial correlation, *J. Geophys. Res.*, *95*,20.507-20.517

Vandaele, A.C., C. Fayt, F. Hendrick, C. Hermans, F. Humbled, M. Van Roozendael, M. Gil, M. Navarro, O. Puentedura, M. Yela, G. Braathen, K. Stebel, K. Tørnkvist, P. Johnston, K. Kreher, F. Goutail, A. Mieville, J.-P. Pommereau, S. Khaikine, A. Richter, H. Oetjen, F. Wittrock, S. Bugarski, U. Friess, K. Pfeilsticker, R. Sinreich, T. Wagner, G. Corlett, R. Leigh, (2005), An intercomparison campaign of ground-based UV-Visible measurements of NO_2, BrO, and OClO slant columns. I. Methods of analysis and results for NO_2, *J. Geophys. Res.*, 110, D08305, doi:10.1029/2004JD005423.

Wang, Y. X., and M.B. McElroy (2004), Asian emissions of CO and NO_x: Constraints from aircraft and Chinese station data, *J. Geophys. Res*, *109*,(D2),4304, doi:10.1029/2004JD005250.

Weatherhead, E.C., G.C. Reinsel, G.C. Tiao, X. Meng, D. Choi, W. Cheang, T. Keller, J. DeLuisi, D. J. Wuebbles, J.B. Kerr, A.J. Miller, S. J. Oltmans, and J.E. Frederick (1998), Factors affecting the detection of trends: Statistical considerations and applications to environmental data, *J. Geophys. Res.*, *103*, 17.149-17.161

Yienger J.J., and H. Levy II(1995), Empirical model of global soil-biogenic NO_x emissions, *J. Geophys. Res.*, *100*, 11.447-11.464

Chemistry of Climate Change in the Atmosphere (id. 2579)

DRAGON-STAR: VARIABILITY OF THE LOCAL MIDDLE ATMOSPHERE

E. Kyrölä, S. Hassinen, J. Tamminen
Finnish Meteorological Institute, P.O. Box 503, FIN-001010, Helsinki, Finland

ABSTRACT

The Dragon-Star project studies the middle atmosphere in global and local context using satellite and ground based measurements as well modelling results. In this work we show first results from the study of the variability of the local middle atmosphere over China. The data source is the GOMOS instrument on Envisat. We make use of nearly 2000 nighttime measurements in 2003 to study the distribution of ozone and nitrogen dioxide vertical profiles.

INTRODUCTION

The purpose of the Dragon-Star project is to study global and local aspects of the middle atmospheric phenomena using three atmospheric instruments, GOMOS, MIPAS and SCIAMACHY, on ESA's Envisat satellite. In future we will also exploit the OMI instrument on EOS-Aura and the OSIRIS instrument on the Odin satellite. In particularly we want to concentrate on investigations of middle atmosphere phenomena over China. The middle atmosphere defined in this work extends from the tropopause to the lower thermosphere (around 15-100 km). It is not obvious that there are good reasons to study any local area in studies of the middle atmosphere. The latitude variation of atmospheric properties is a well-known fact but variations in longitude direction are often ignored because zonal flows tend to smooth out these variations. We will discuss this question in this initial work.

The source of data for this work comes from GOMOS only. The MIPAS instrument started to experience strong difficulties in 2003 and SCIAMACHY data is exploited in other Dragon projects. The validation and comparison of GOMOS measurements with Chinese ground based measurements is still missing at this stage of the project.

GOMOS

The GOMOS (Global Ozone Monitoring by Occultation of Stars) instrument is a spectrometer on board the European Space Agency's Envisat satellite that was launched on March 1st 2002. GOMOS uses the stellar occultation measurement principle in monitoring ozone and other trace gases in the Earth's stratosphere (see Fig. 1). The main wavelength region is the ultraviolet-visible region and additional two channels are located in the near-infrared. The species covered by GOMOS are O_3, NO_2, NO_3, neutral density, aerosols, H_2O, O_2, and in favourable conditions also OClO. The two fast photometers in blue and red wavelengths allow investigations of atmospheric turbulence. Photometer data can also be used to derive high-resolution temperature profiles.

GOMOS was proposed in 1988 by Finnish Meteorological Institute (FMI) and Service d'Aeronomie du CNRS (Sd'A) as an AO-instrument for ESA's POEM-satellite [1]. POEM became later two satellites, Envisat and Metop. GOMOS was selected to fly and ESA gave GOMOS the EFI (ESA Funded Instrument) status. Matra (now Astrium) was selected to be the main contractor of the GOMOS instrument. The ACRI company in France was selected to develope the GOMOS processing prototype with the support from the scientific institutes FMI, Sd'A and BIRA-IASB from Belgium forming the GOMOS ESL (Expert Support Laboratories). The Space Systems Finland Ltd developed the GOMOS data processor for the actual processing. The operational GOMOS processing takes place at ESA facilities in Kiruna and Frascati and at FMI's Sodankylä Arctic Research Centre.

Proc. 2005 Dragon Symposium "Mid-Term Results", Santorini, Greece
27 June – 1 July 2005 (ESA SP-611, January 2006)

The telescope and the pointing system of GOMOS capture a star at a tangent height around 150 km, locks to the star and follows the star down to about 10 km. On the day side of the orbit the GOMOS telescope will also receive scattered solar light. In order to minimize the scattered solar light a slit is incorporated. The challenge of the pointing system is too keep the star image in the centre of the slit with a good stability in order to minimize wavelength shifts. The incoming light is forwarded to several detectors. The first detector is the star tracker operating in 650-950 nm and working with 100 Hz to guide the pointing system. The remaining light is divided between the spectrometers and the two photometers. The photometers work in the blue and red wavelength regions with 1 kHz frequency. The spectrometers work in the ultraviolet-visible wavelengths 250-690 nm

and two channels are in the near infrared at 750-776 nm and at 916-956 nm. The CCD detectors make it possible to estimate radiation coming from extended sources and extract it from the stellar signal. The integration time of the UVIS-spectrometer and IR-spectrometers is 0.5 sec (for more information, see [2-5]).

The important advantage of GOMOS is the self-calibration. The reference spectrum of a radiation source is first measured when the source can be seen above the atmosphere. During the occultation repeated observations through the atmosphere at descending altitudes provide spectra with absorption features. When these occulted spectra are divided by the reference spectrum, nearly calibration-free horizontal transmission spectra are obtained. Transmissions provide the basis for retrieval of atmospheric constituent densities. The self-calibration means that occultation measurements can be used to create long time series, which is necessary to monitor the predicted slow recovery of the depleted ozone layer. In the case of GOMOS the limb viewing geometry, the point source nature of stars and short enough measurement integration time mean a good vertical resolution. The vertical integration distance for GOMOS is 1.7 km in occultations taking place in the orbital plane of Envisat. When measuring occultations outside the orbital plane the integration distance gets even smaller. The good vertical resolution is important in resolving the altitude dependent chemical processes. Besides the self-calibration and the good vertical resolution the advantage of the stellar occultation method is the good global coverage provided by the multitude of suitable star targets. During 24 hours, the total number of occultations is 400-600. Measurements are obtained from both night and day side of the Earth.

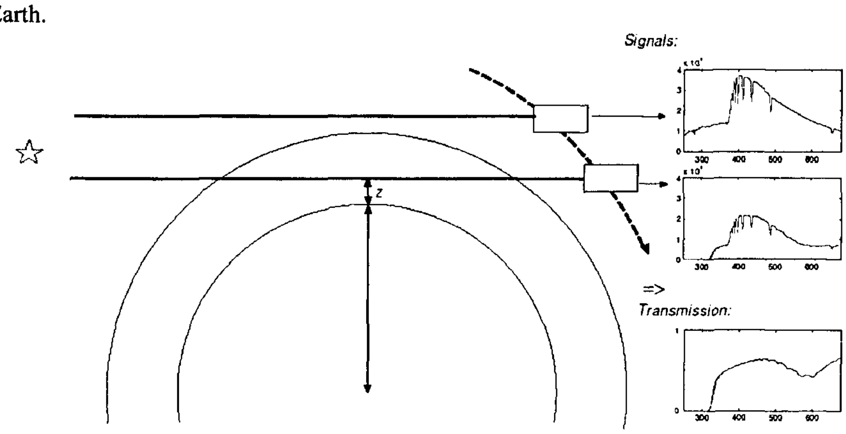

Fig. 1. The occultation principle.

GOMOS DATA

The basic GOMOS data processing levels are 1b and 2. The division between the Level 1b and the Level 2 is the transmission function. In Level 1b (see Fig. 2) data is geolocated using the ECMWF meteorological data (temperature, pressure) for the ray tracing calculations. All instrumental corrections are applied and the diffuse background from scattered solar light is removed from the stellar signal. The Level 1b products are transmission spectra, photometer fluxes and limb radiance spectra from dayside occultations. The level 2 processing use level 1b products but photometer measurements are used also in novel turbulence studies.

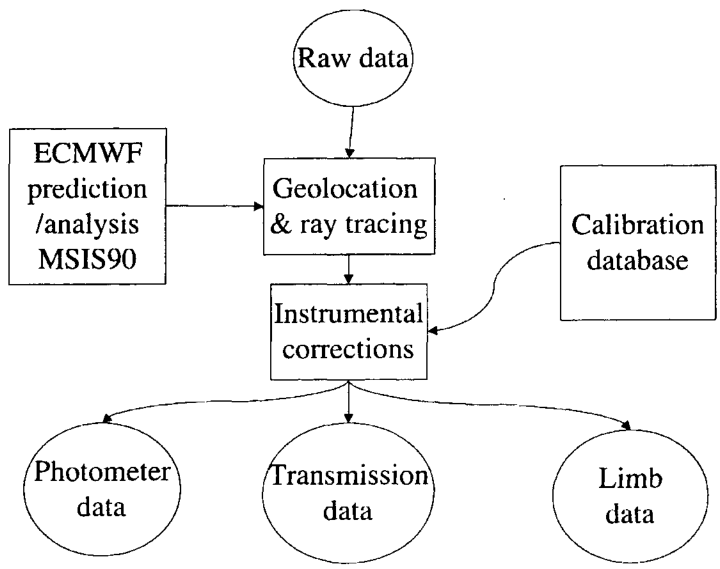

Fig. 2. GOMOS Level 1b processing.

of
and
The retrieval technique applied by the GOMOS Level 2 processing (see Fig. 2) splits the inversion problem into a spectral inversion and a vertical inversion using the effective cross section method [2] and making an approximation for the integration time averaging. The spectral inversion produces horizontal column densities for different constituents by fitting the modelled extinction transmission to the observed, refraction corrected transmission [2]. All constituents are retrieved simultaneously and all wavelengths are used. The more familiar vertical density profiles are the result of the vertical inversion horizontal column densities assuming local spherical symmetry. The inversion method is onion peel type inversion. Spectral vertical dependence of aerosol extinction will also be estimated from transmission data. From the analysis of fast photometers the high-resolution temperature and density profiles are calculated [2-5]. Level 2 products are geophysical data. The most important ones are

- Horizontal line densities
- Vertical profiles of constituents and temperature
- Aerosol extinction
- High-resolution temperature profile

is
The large number of measurements and the wealth of spectral data make it mandatory to have an effective data processing system for GOMOS. GOMOS is an ESA developed instrument, which means that ESA has not only developed the instrument but it has also developed the ground segment scheme. The ground processing is divided to the near-real time processing and the off-line processing. For GOMOS the difference between these two is that the off-line products can use the more accurate determination of the Envisat orbit and the ECMWF analysis instead of prediction. ESA will take charge of the near-real time processing of Levels 1b and 2 and the off-line processing of Level 1b. The off-line processing centre for Level 2 located at Finnish Meteorological Institute's Arctic Research Centre in Sodankylä (the FIN-CoPAC facility). The dissemination of off-line data will be through DLR's D-PAC in Oberpfaffenhofen. Some part of the Level 2 products will be delivered to various Meteo Offices and other users, as fast delivery products (available within 3 hours of the ground reception).

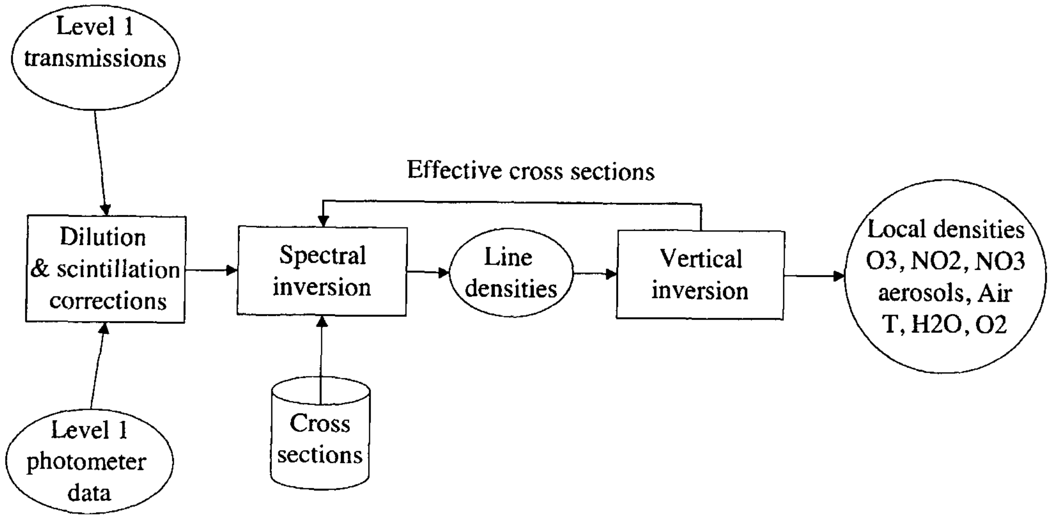

Fig. 3. Level 2 GOMOS data processing.

RESULTS FOR MIDDLE ATMOSPHERE OVER CHINA

In order to study the middle atmosphere behaviour over China we have selected a latitude-longitude rectangle to represent the geographical extent of China. In latitudes we have a range from 20N to 55N and in longitude from 75E to 135E. In this work we concentrate only on night occultations and we require the solar zenith angle to be larger than 108 deg during the occultation. In this way we find 1893 occultations in 2003. The distribution of measurements on a geographical map is shown in Fig. 4.

Fig. 4. GOMOS night occultations over China in 2003.

It is well known that concentrations of many trace gases exhibit strong variations in latitude. On the contrary, longitudinal variations are often neglected because winds tend to be approximately in zonal direction. In order to see how our object of study, China, shows in this respect we will show ozone and NO_2 vertical distributions as a function of latitude and longitude in the following figures. In the latitude variation figures we have fixed the longitudes to cover only China and in the latitude variation figures latitudes are restricted similarly. The figures show the situation as monthly median values in January.

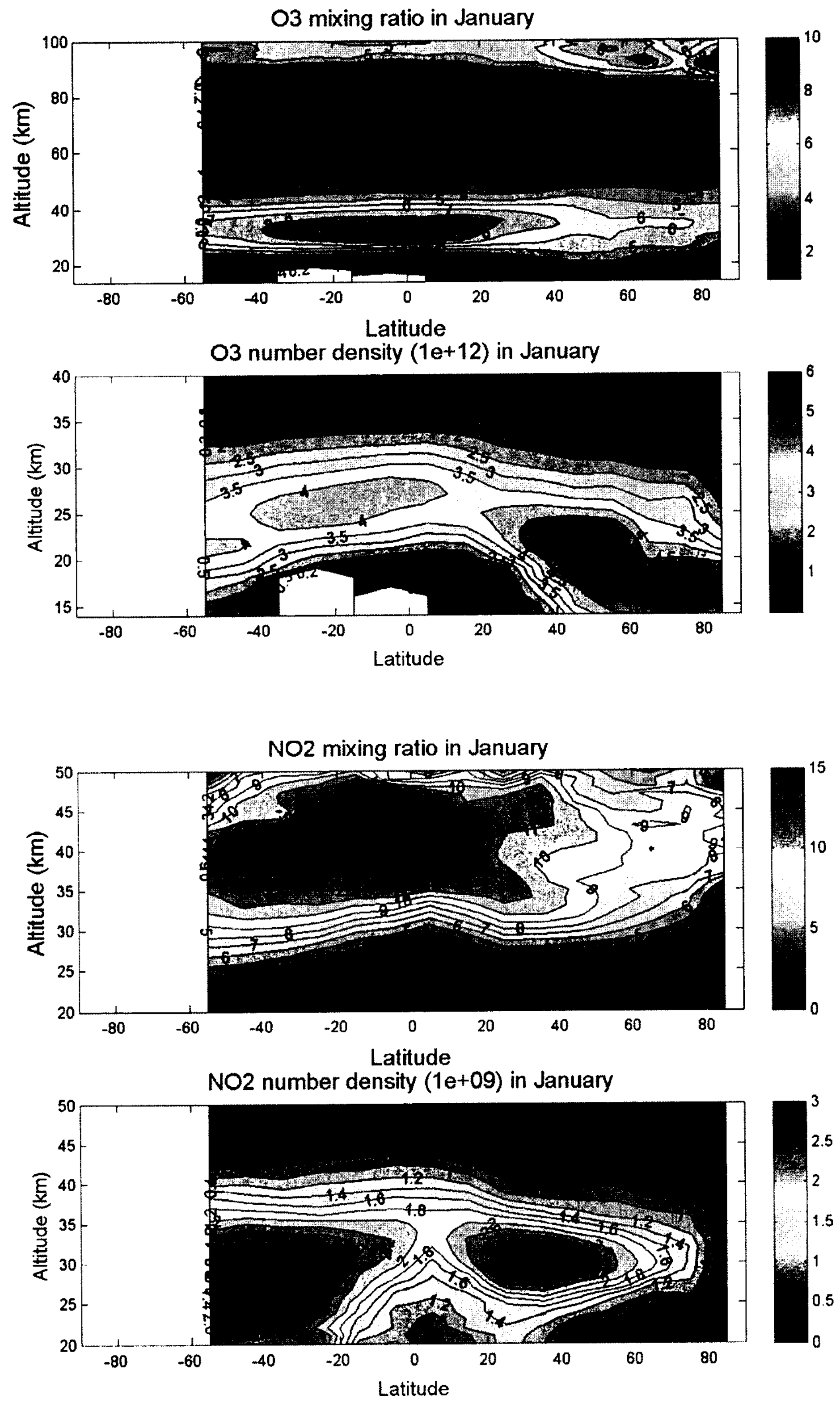

Fig. 5. The latitudinal distributions of ozone and NO_2 in the longitudinal strip 75E-135E. The latitudinal grid 10 deg. The values represent medians in the month of January. China is located inside the latitude band 20N-55N.

Figs. 5 show the latitudinal variations for ozone and NO_2. The first figure shows that China sees both the high ozone content near the polar region and the low ozone content area near Equator. The ozone maximum in the northern polar region is a seasonal feature. In the fall the maximum appears in high southern latitudes. The equatorial low ozone density region is a relatively stable region in the global ozone distribution. The ozone maximum altitude changes by several kilometers inside the latitudinal extent of China. In ozone mixing ratio changes are small. The maximum number density of NO_2 peaks at 30N around 30 km altitude whereas the mixing ratio peaks at Equator at 40 km. The seasonal variability of the NO_2 distribution is quite large. The latitudinal and seasonal variations of ozone and NO_2 zonally averaged distributions are discussed further in [6-7]. The following figures show lat longitudinal variations.

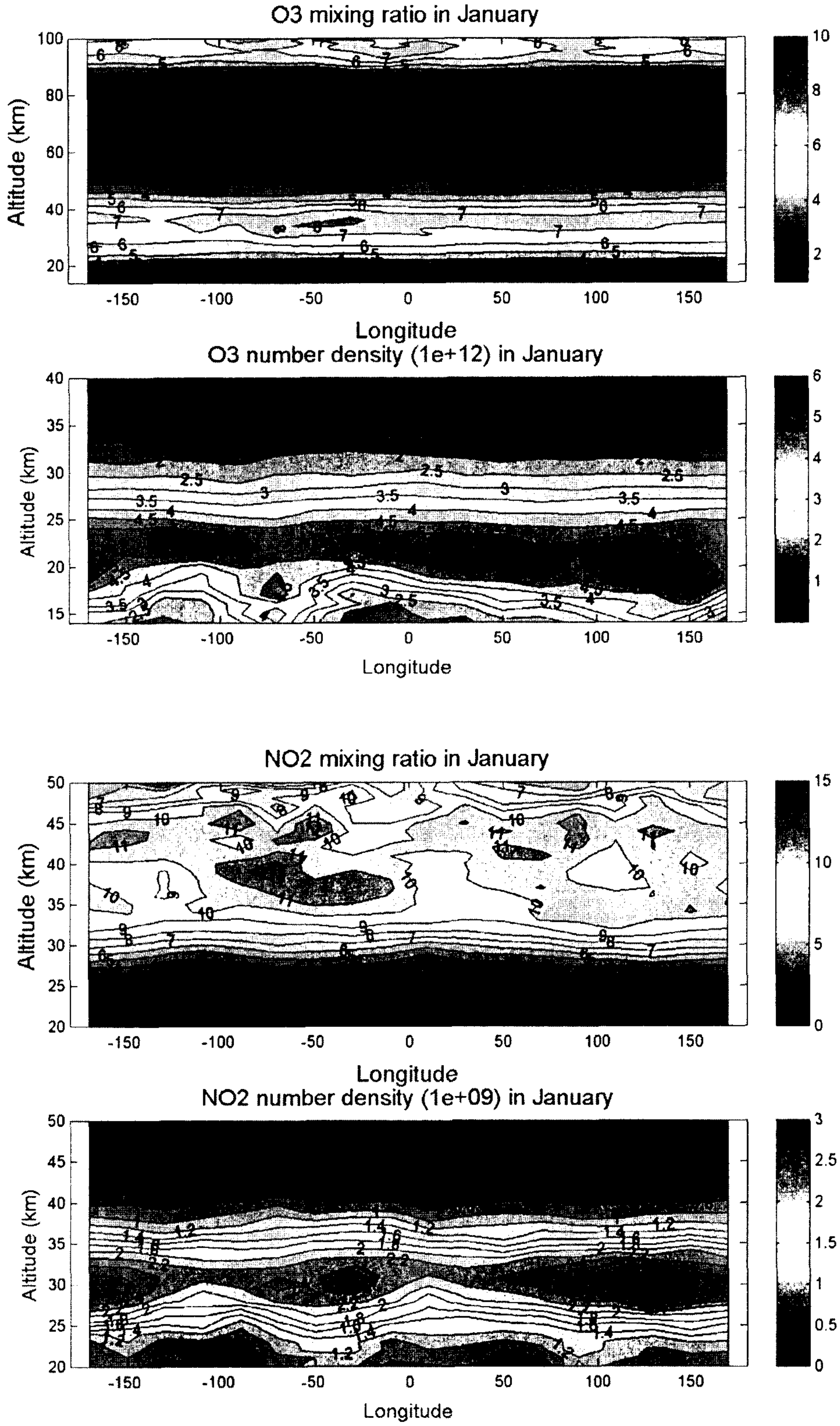

Fig. 6. The longitudinal distributions of ozone and NO_2 in the latitudinal belt 20N-55N.

Fig. 6 show that changes as a function of longitude are small in the ozone distribution whereas in the NO_2 distribution there are wavelike structure. Ozone keeps the smooth longitudinal variation through the seasons but shows enhanced values during the spring maximum. NO_2 shows undulating structures and in summer season the layer of maximum density extends down to 20 km (see Figs. 7 below). When looking the pictures above, it must be kept in mind that the time average is one month. It is certainly quit too long to capture the variation of trace gases induced by individual weather fronts.

Even if our results show large latitudinal variations, we will finally investigate the seasonal variation using data collected from the whole China box. In Figs. 7 we show the ozone and NO_2 number density as a function of altitude and month. Seasonal variations indicated by these figures are relatively large.

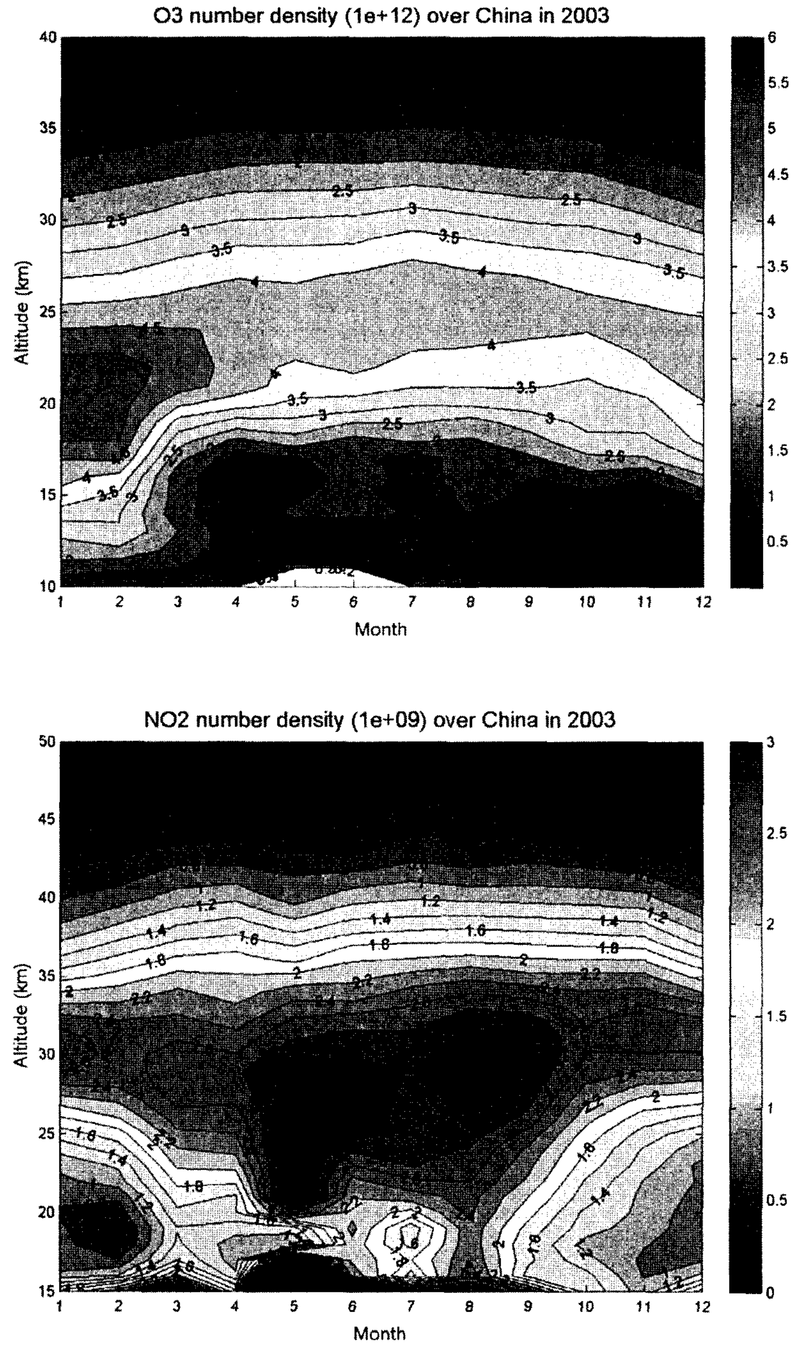

Fig. 7. Seasonal variation of ozone and NO2 number density from the China box.

SUMMARY

In this work we have shown first results from Dragon-Star project using GOMOS data from 2003. With almost 2000 measurements GOMOS makes a large additional contribution to the measurement activity by the ground-based networks. The results in this work show large latitudinal and seasonal variations in trace gas concentrations inside in the geographical location of China. In future studies we will try to get more detailed picture of the time and spatial development of the middle atmosphere. In order to create a complete picture GOMOS measurements are not, however, enough. We need other satellite and ground based instruments as well help from the data assimilation.

REFERENCES

1. Bertaux, J-L., G. Megie, T. Widemann, E. Chassefiere, R. Pellinen, E. Kyrölä, S. Korpela, and P. Simon, Monitoring of ozone trend by stellar occultations: The GOMOS instrument, *Adv. Space Res.*, 11(3):237-242, 1991.
2. Kyrölä, E., J. Tamminen, G.W. Leppelmeier, V. Sofieva, S. Hassinen, J.L. Bertaux, A. Hauchecorne, F. Dalaudier, C. Cot, O. Korablev, O. Fanton d'Andon, G. Barrot, A. Mangin, B. Théodore, M. Guirlet, F. Etanchaud. P. Snoeij, R. Koopman, L. Saavedra, R. Fraisse, D. Fussen, F. Vanhellemont, GOMOS on Envisat: An overview, Advances in Space Research, Volume 33, Issue 7, p. 1020-1028 (2004).
3. Bertaux, J. L., Hauchecorne, A., Dalaudier, F., Cot, C., Kyrölä, E., Fussen, D., Tamminen, J., Leppelmeier, G. W., Sofieva, V., Hassinen, S., Fanton D'Andon, O., Barrot, G., Mangin, A., Théodore, B., Guirlet, M., Korablev, O., Snoeij, P., Koopman, R., Fraisse, R., First results on GOMOS/ENVISAT, Advances in Space Research, Volume 33, Issue 7, p. 1029-1035 (2004).
4. Envisat-GOMOS, An Instrument for Global Atmospheric Ozone Monitoring, ESA SP-1244, 2001.
5. ESA-Envisat WWW: http://envisat.esa.int/dataproducts/gomos
6. Hauchecorne, A.; Bertaux, J.-L.; Dalaudier, F.; Cot, C.; Lebrun, J.-C.;Bekki, S.; Marchand, M.; Kyrölä, E.; Tamminen, J.; Sofieva, V.; Fussen,D.; Vanhellemont, F.; Fanton d'Andon, O.; Barrot, G.; Mangin, A.;Théodore, B.; Guirlet, M.; Snoeij, P.; Koopman, R.; Saavedra de Miguel,L.; Fraisse, R.; Renard, J.-B., First simultaneous global measurements of nighttime stratospheric NO2 and NO3 observed by Global Ozone Monitoring by Occultation of Stars (GOMOS)/Envisat in 2003 J. Geophys. Res., Vol. 110, No. D18, D18301 10.1029/2004JD005711, 2005.
7. Kyrölä, E. et al., Night-time ozone profiles in the stratosphere and mesosphere by GOMOS on Envisat, in preparation.

CONTRIBUTION TO DRAGON-STAR BY THE GREEK TEAMS

Dimitrios Balis[1], Kostas Kourtidis[2], and Christos Zerefos [3]

[1] Aristotle Univ. of Thessaloniki, Physics Dept., 54124 Thessaloniki, Greece, balis@auth.gr

[2] Demokritus University of Thrace, Dept. of Environmental Engineering, 67100 Xanthi, Greece, kourtidi@env.duth.gr

[3] University of Athens, Faculty of Geology, 15784 Athens, Greece, Zerefos@geol.uoa.gr

ABSTRACT

This paper aims at presenting the contribution of the Greek team to the project until June 2005 as well as providing an update on the foreseen activities during the next year of the project.

Satellite measurements of total ozone obtained with the GOME instrument onboard ESA's ERS-2 satellite and measurements obtained with EP-TOMS have been compared with ground-based Dobson and Brewer total ozone measurements at Long Fen Shan, Mt. Waliguan, Kunming and Shianger. The agreement between satellite and ground-based retrievals is within 1% for two of the stations, while the others exhibit larger differences. The validation exercise gives an insight for the differences between the different estimates of total ozone related to (a) certain characteristics of the ground-based and satellite algorithms and (b) to the quality of the ground-based measurements. Possibilities to tailor the approach described above for use with GOMOS data will be examined in cooperation with the GOMOS data provider. During the next year(s) of the project, this approach will be expanded to investigate:

(a) The influence of load and origin of aerosols to the ozone retrieval by satellite and ground-based instrumentation. This will be done by studying the ground and satellite ozone retrievals in environments with different aerosols (Mediterranean and China).

(b) The possibility of using combined satellite/ground based total ozone measurement instrumentation for aerosol studies.

INTRODUCTION

The teams from Greece that participate in DRAGON star have considerable experience in ozone product validation, summarized below:

- Quality control of archived Dobson, Brewer and M-124 total ozone measurements extracted from the World Ozone Data Centre of WMO at Toronto, Canada
- Validation of GOME total ozone data v2.7 and v3.0 processed by DLR for the period 1996-2003
- Validation of GOME v4.0 for the period 1996-2004
- Validation TOMS v7 and v8 overpasses from NASA/GSFC for the whole Earth Probe period (1996-2004)
- OMI total ozone preliminary validation
- Participation in Ozone SAF (Satellite Application Facility) of EUMETSAT (see http://lap.physics.auth.gr/eumetsat)

RESULTS AND DISCUSSION

We present here results from the GOME Data Product (GDP) v. 4.0 overpasses from 4 stations in China with ground-based instrumentation for total ozone retrieval. Two of the stations are equipped with Brewer (Longfenshan, Mt. Waliguan) and two with Dobson (Kunming, Shiangher) spectrophotometers (Fig. 1 to 4).

Proc. 2005 Dragon Symposium "Mid-Term Results", Santorini, Greece
27 June – 1 July 2005 (ESA SP-611, January 2006)

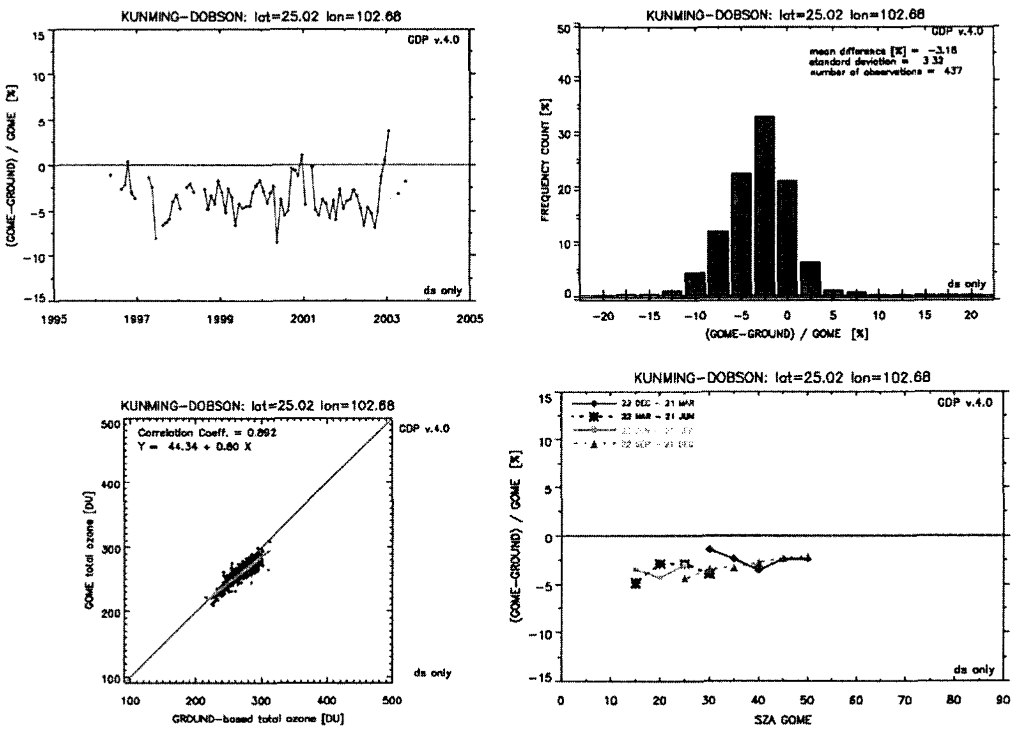

Fig. 1. Intercomparison results between GDP 4.0 overpass and ground-based Dobson instrumentation at Kunming.

The observed differences between the different estimates of total ozone relate to (a) certain characteristics of the ground-based and satellite algorithms and (b) to the quality of the ground-based measurements.

CONCLUSIONS

Summarising,

- The new GDP has almost no offset
- There is still a seasonal dependence in the middle and high latitudes, more evident in the Dobson comparisons.
- The different temperature dependence of the ozone absorption coefficients between the various algorithms may account for part of the observed seasonalities.
- Comparisons between GDP4.0 and ground data do not show any trend till mid 2003
- Comparisons between GDP4.0 and ground data showed some inconsistencies between nearby stations

Future work will focus on possibilities to tailor the approach for use with GOMOS data (in cooperation with the GOMOS data provider). Further, it is intended to study

- The influence of load and origin of aerosols to ozone retrieval by satellite and ground-based instrumentation
- The possibility of using combined satellite/ground based total ozone measurement instrumentation for aerosol studies
- Possible upper atmosphere teleconnections between China and Mediterranean
- Energetic events from the sun and their influence on upper atmosphere ozone (from the GOMOS data provider) and Schumann resonances (the latter from a station in Athens)

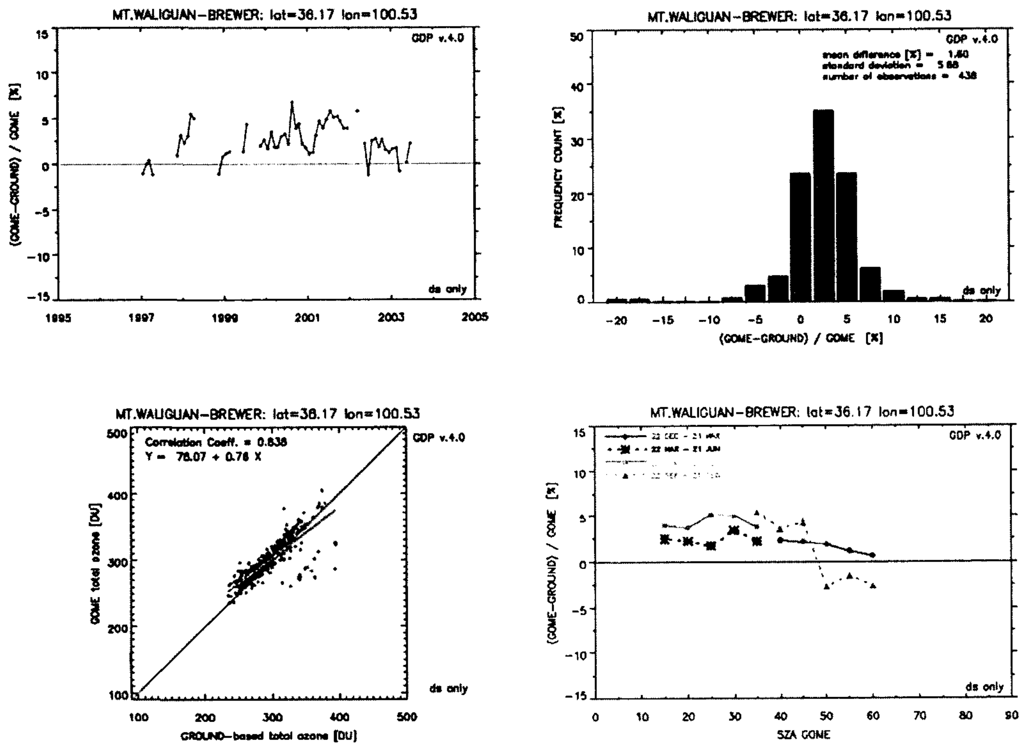

Fig. 2. Intercomparison results between GDP 4.0 overpass and ground-based Brewer instrumentation at Mt. Waliguan.

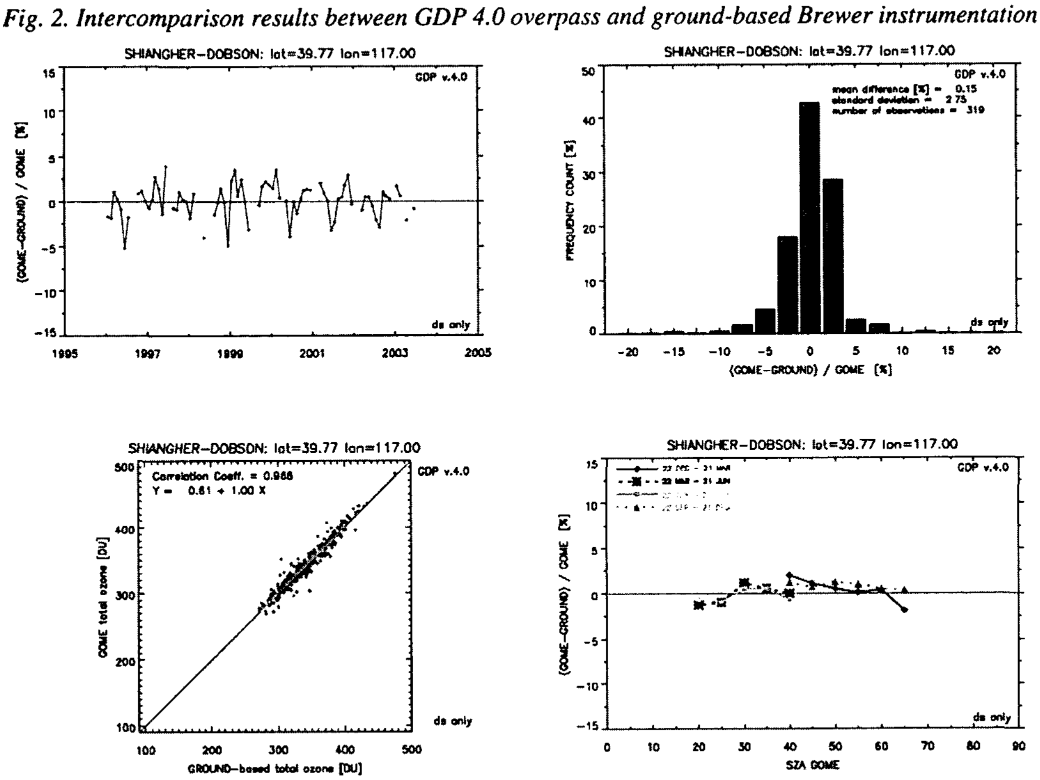

Fig. 3. Intercomparison results between GDP 4.0 overpass and ground-based Dobson instrumentation at Shiangher.

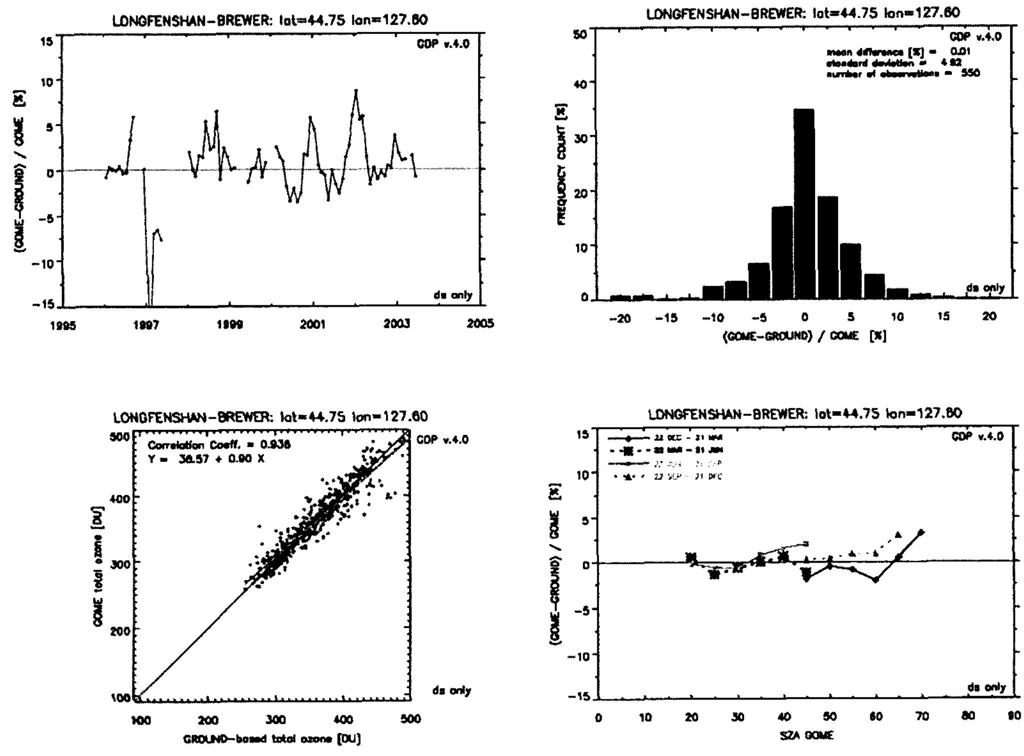

Fig. 4. Intercomparison results between GDP 4.0 overpass and ground-based Brewer instrumentation at Longfenshan.

Flooding and Hydrology

Drought Monitoring in China
(id. 2608)

A PRELIMINARY STUDY ON MONITORING THE SOIL MOISTURE OF WINTER WHEAT AREA IN NORTHERN CHINA BY USING ENVISAT-1/ASAR

Limin Wang[(1)], Youqi Chen[(1)]

[(1)] *Institute of Agricultural Resources & Regional Planning, Chinese Academy of Agricultural Sciences, Beijing 100081,China E-Mail: wlmbs@163.com*

ABSTRACT

In this paper, ENVISAT-1/ASAR VV polarization data and the measured soil moisture in Huabei plain(Northern China) are used to make a relationship between the backscattering coefficient and soil moisture. As the result, in three days—March 21, April 28 and July 7 in 2005, the correlation of soil moistures at depths of 10cm and 20cm is obvious, but not obvious while the proportion of soil moisture volume is lower than 50%, and the relationship of soil with higher crop coverage doesn't seem to be very sensitive than the bare soil. In the study, it has been found that ASAR data has extensive application prospects in monitoring soil moisture in large scale.

Key Words: ENVISAT-1/ASAR, backscatter coefficient, soil moisture.

Soil moisture, one of the important parameters in gas transmission in the agricultural ecological system, gives important information in the agricultural irrigation management, and serves as a major indicator in the evaluation of crops drought. However, it cannot be efficiently obtained by routine measurements over large areas or regions. The remote sensing technology of soil moisture that depends on the visible light and near infrared band cannot operate for all the days and nights, as constricted by parameters like the cloud cover, atmosphere and hydrology. Therefore, all the applications of these technologies are restricted to some extent.

Based on its solid theoretical foundation, microwave remote sensing adopts the dielectric constant (εr) between the two extremes of dry soil and water, which is around 3 to 80, and varying with the soil moisture. In real application, researches on empirical formula that combines ground survey soil moisture data with backscatter coefficient and the linear relationship in particular have been quite popular. Based on ground surveys of the soil moisture content in the North China Plain, this article undertakes to make some primary analysis on the possibilities of microwave remote sensing to monitor soil moisture in this region, by taking advantage of ENVISAT-1/ASAR data of the ESA (European Space Agency).

1. OVERVIEW OF THE STUDY AREA

Located at the 118 ~114 east longitude and 36 ~ 39 north latitude, the study area lies in the hinterland of the North China Plain (Figure 1). It falls into the piedmont alluvial plain area along the Taihang Mountain, and is 50 meters above sea level on average. Thanks to its flat grounds, it has been the production area of winter wheat, corns and cottons. Moreover, this region lies between the temperate zone and the warm temperate zone, and enjoys the semi-humid and semi-dry continental monsoon climate. Its average annual rainfall ranges from 400mm to 800mm, with great changes in different years. It is also unevenly distributed within a year as the rainfall in summer accounts for 70 percent of the yearly total. The area takes on a plain landform and the soil texture is almost the same as cinnamon and brown soil. Winter wheat starts to have joints in March and April every year, and harvest at the end of June and early July. From July to October, it is the growth period for spring sowing or autumn sowing crops such as corn and cotton.

Proc. 2005 Dragon Symposium "Mid-Term Results", Santorini, Greece
27 June – 1 July 2005 (ESA SP-611, January 2006)

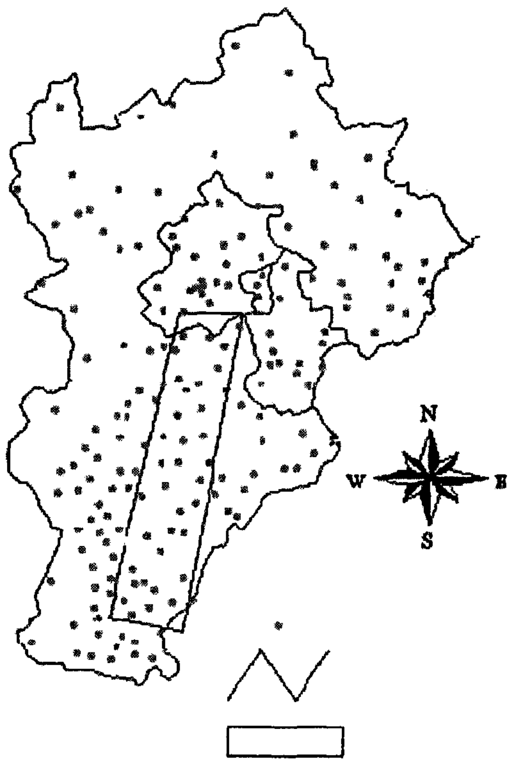

Fig 1. Position of the Study Area, Orbit Cover and Distribution of the Sample Spot

2. DATA SOURCE AND THEIR PROCESSION

2.1 Ground Soil Moisture Data

At the dates before or after March 21, May 1 and July 7, 2004, soil moisture at the spots on the study sample area were measured by the oven-drying method. At the same time, growth conditions of crops, geographical coordinates, irrigation and management conditions are recorded. In order to make sure the representation of the selected sample spots, the grounds selected, with the area of no smaller than 500×500m, should lie in places where crop distribution, soil texture and moisture conditions are relatively identical. The soil water content measured is then converted into the water content volume ratio by the local soil saturation moisture capacity, which maintains at the 30～40% level. The spots at the three periods are as indicated in Figure 1.

2.2 EnviSat-1/ASAR Data

EnviSat-ASAR falls into the C wave band (5.6cm), and it was the ASAR (Advanced Synthetic Aperture Radar, ASAR) Imaging System carried on the Envisat –1 environmental satellite launched by the ESA on March 1st, 2002. It is characterized by many kinds of operation models such as the dual polarization (HH, VV) and the alternating polarization (HH/HV, VV/VH). Table 1 lists the major data products that incorporate the ASAR data.

2.3 Data Processing

The data products made by the PRI (ASR_IMP_1P) technology is a kind of distance digital image with an entrance angle of 23.99° suitable for the backscatter coefficient and multi-temporal analysis. With a width of 100×100km, and a nominal resolving power (distance×direction) of 30×30m. It is also characterized by the W polarization mode.

Similar to the ground survey data, the four consecutive images at March 24th, 2004 and the four consecutive images at July 7th, 2004 on the same orbit Number 2218 covering an area of 100×400km (figure 1) are selected.

Tabel. Standard Data Products of ASAR

Product_ID	Resolution Azimuth and Slant	Polarization	Swath	Nlook
IMP	30×30	HH or VV	56~100×100	>3
IMS	9×6	HH or VV	56~100×100	1
IMM	150×150	HH or VV	56~100×100	40
IMP	450×450	HH or VV	56~100×100	80
APP	30×30	VV/HH	56~100×100	>1.8
APS	9×12	VV/HH	56~100×100	1
APM	150×150	VV/HH	56~100×100	50
APB	450×450	VV/HH	56~100×100	75
WSM	450×450	VV or HH	400×400	11. 5
WSB	1800×1800 (about)	VV or HH	400×400	30～48

Since there is relatively large geographical derivation of the PRI data from the real ground geographical coordinates, the national TM image base map of 1996 are chosen to make an accurate adjustments for these data, with the corrected derivation controlled within one picture element. The data processing procedure is shown on figure 2.

2.4 Sampling Method

The match of the ground survey area and ASAR data guarantees the correctness of this research result, since the separated point value chosen from the remote sensing images can lead to a great random error in the result. Therefore, the backscatter coefficient of the nine picture elements around the sampling point has been selected, and their average figure is calculated to be the backscatter coefficient related to that point by excluding the highest and the lowest.

3. RESULT

After statistics analysis on the three ASAR backscatter coefficients of three time phases and the soil moisture data of the 10cm and 20cm grounds, the result shows that at the three time phases, when the volume ratio of the water content at the two levels of ground is below 50% (equivalent to a volumetric moisture content at 5.0～8.0%), the backscatter coefficient has no obvious relationship with the soil moisture content.

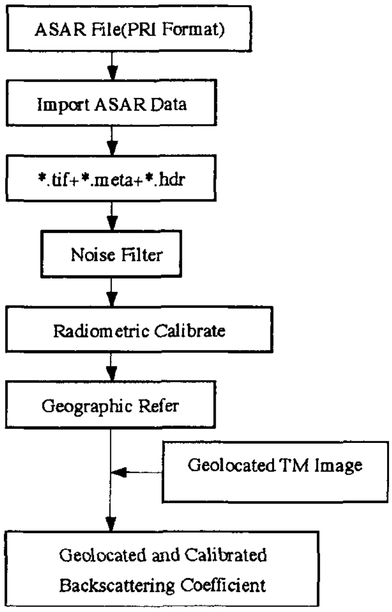

Fig. 2 . Technological Flow Chart

At the ranges of 50～100% (equivalent to a volumetric moisture content at 10.0～30.0%), there are more or less some linear relationships between the two levels at the three time phases. Table 2 lists some relevant coefficients and variance tests of the two levels at the time phases. Table 2 shows the relationship of the 10cm, 20cm soil moistures and the backscatter coefficients at the three phases, and figure 3 gives an outline of the distribution of 10cm soil water content on March 24 inversed with the above mentioned relationships. Figures of other research findings are omitted.

Table 2. Relationship Between Backscattering and Soil Moisture

Time	Sample number	Soil depth	Multiple (R)	F	Significance (F)	Coefficient	Constant	Relative errors (%)
2004/03/24	35	10	0.81	52.83	6.51E-08	0.23	-24.70	3.73
2004/03/24	37	20	0.67	26.79	1.1E-05	0.16	-20.12	4.42
2004/04/28	38	10	0.79	54.95	1.62E-08	0.15	-18.31	4.25
2004/04/28	32	20	0.68	25.47	2.04E-05	0.13	-16.49	5.29
2004/07/07	34	10	0.53	10.41	0.003376	0.07	-11.34	8.64
2004/07/07	28	20	0.30	2.49	0.126623	0.05	-10.16	8.23

From table 2, it can be noticed that the deviation of the relevant test on July 7 is higher than that of the previous two phases. Since it is the harvest time for winter-sowed crops and booming season of summer-sowed crops, the deviation may just be caused by the failure to take the vegetation coverage into account when making the regression analysis.

4. Discussion and Conclusion

The backscattering of the bare ground is mainly based on the dielectric constant and its surface roughness, which is then expressed in its autocorrelation formula and standard variances. As the theoretical foundation of the radar remote sensing inversion ground soil moisture, the theoretical model evaluates the impact on backscatter coefficients brought out by changes of ground parameters, and further builds the foundation for the application of remote sensing data into the soil moisture examination by objectively describing the real ground conditions. Common scattering theories on surface roughness include the variation model (SPM), physical optics model (POM), geometric optics model (GOM) and the latest integration model (IEM), which can be made to adjust to a larger surface roughness range. In addition, empirical models that can inverse the relationships of the dielectric constant and the surface roughness are Oh, [1] Dubois [2], Shi3]models and etc. In the real inversion process of the soil moisture, the statistical analysis of the backscatter coefficients and ground water content is the most frequently used method, which is also employed in this article. As reported in relevant literature, the traditional statistical method combing the two extreme ranges at the low-end and high-end of the soil water content does not apply anymore. When the volume ratio of water content is below 50%, this problem is also identified, but it does not turn up at the high-end, which might be related to the saturated threshold value. Though not as precise as the theoretical models, this method serves as n effective supplement for the theoretical model under some assumptions.

March 24, 2004
10cm Depth Soil Moisture (m_v)and Backscattering Coefficient(σ^0)

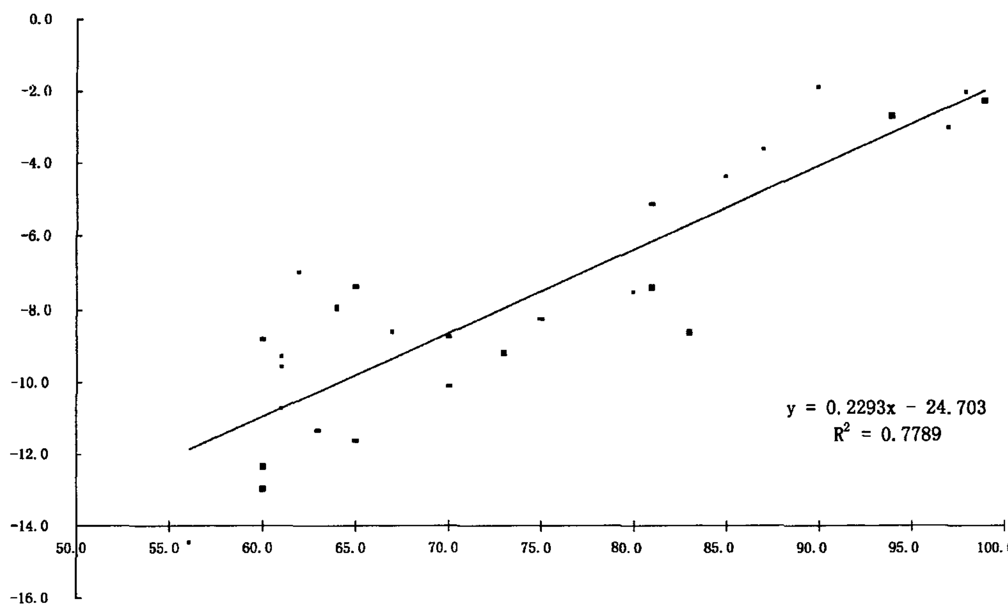

April 28, 2004
10cm Depth Soil Moisture (m_v)and Backscattering Coefficient(σ^0)

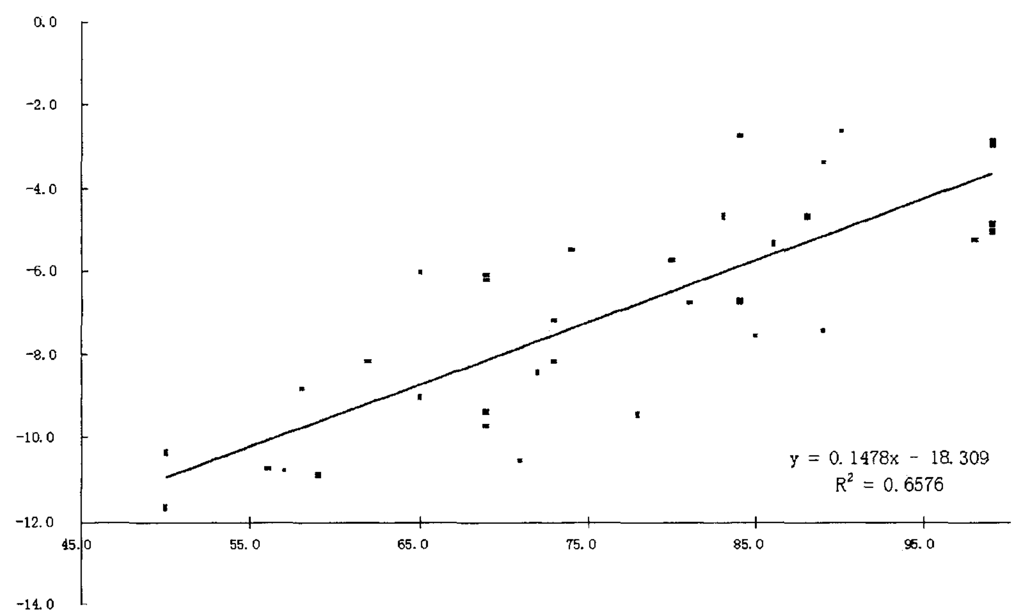

In fact, since it is exactly the seedling stage for winter wheat in March, the influence of the backscatter coefficient on crops can be neglected, while the soil conditions in the study area can be assumed as the same. Based on the assumption of the theoretical models, only the changes of soil moisture on the dielectric constant is considered, that is, only the moisture factor can have an impact on the backscatter coefficient, and a simple linear relationship between the two can be built up. In July, however, the crop vegetation is quite complicated, and a simple linear description is far more than sufficient to meet the assumed conditions. Vegetation factors have to be separated and our omission in this regard can be easily noticed in this article.

At present, only the VV polarization mode data have been employed, while HH or HV or VH polarization mode data have been unavailable. Meanwhile, we have assumed that the ground parameters (texture structure and roughness) are the same, and have not done any particular measurement. It is obvious that consideration of these factors will bring out a more objective inversion process and accurate soil moisture inversion result.

References

1. Zhang Junrong. et al. The microwave dielectric constant of canopy and soil. Remote sensing Technology and Application, 1995, 10 (3) : 40~50
2. Chanzy A. Basic soil surface characteristics derived from active microwave remote sensing[J]. Remote Sensing Review, 1993, 7: 303~320
3. Y.-L. Desnos, et al.. The ENVISAT advanced synthetic aperture radar system. Geoscience and Remote Sensing Symposiun[J], 2000. IEEE 2000 International. 2002, 2: 758~760
4. Chen Er-xue, Li Zengyuan. Study on ENVISAT ASAR image geolocation method. Journal of Image and Graphics. Vol. 9, No.8: 991~996
5. Li xingchao. A study on soil moisture monitoring by using microwave remote sensing. Remote sensing Technology and Application, 1995,10(4): 1~8
6. Fung A K, et al.. Backscattering from a randomly rough dielectric surface[J]. IEEE Trans. Geosci. Remote Sensing, 1992, 30 (5):1254~1266
7. Yang Hu, et al.. Plorimetric SAR surface parameters inversion based on neural network[J]. Journal of Remote Sensing, 2002, 6 (6): 451~455

DROUGHT MONITORING AND DROUGHT PREDICTION IN CHINA USING REMOTE SENSING, LAND SURFACE MODELS (LSM) AND DATA ASSIMILATION: PRELIMINARY RESULTS OF THE LOESS PLATEAU FIELD EXPERIMENT IN 2005 (LOPEX05)

Rogier van der Velde[1], Jun Wen[2], Tangtang Zhang[2], Tom Rientjes[1], Alicia T. Joseph[3], Bob (Z.) Su[1]

[1]Internationational Institute for Geo-Information Science and Earth Observation (ITC), Hengelsostraat 99, P.O. Box 6, 7500 AA Enschede, The Netherlands.

[2] Cold and Arid Region Environmental and Engineering Research Institute, Chinese Academy of Sciences, Lanzhou, Gansu 730000, China.

[3] Hydrological Sciences Branch/614.3, Laboratory for Hydrospheric Processes, NASA/Goddard Space Flight Center, Greenbelt, MD 20771, USA.

ABSTRACT

Drought disasters have often caused great hunger, social instability, large scale migration of the population and the distinction of civilizations in the history. The conflict between supply and demand of water resources constitutes the biggest problem for food security of a huge population in China and drought has become a key factor constraining China's economic development.

The Dragon project "drought monitoring and drought prediction" will be used to develop a system to monitor and generate predictions of the soil moisture conditions in the root zone. The methodology that will be employed is based on the direct assimilation of satellite observation in a land surface modeling framework. The advantage of this methodology is that physically based methods can be used as compared to (semi-) empirical direct-retrieval algorithms.

Within the framework of this project a field campaign was held in the summer of 2005 near the city of Pingliang in Gansu province, China. The ground truth data set collected during this experiment consists of continuous time series of land surface radiation, water and heat fluxes and an extensive set of land surface parameter observations, such as soil moisture, Vegetation Water Content (VWC) and Leaf Area Index (LAI). In conjunction with the ground observations a series of EnviSat AATSR[1], ASAR[2] and MERIS[3] scenes have been requested. This data set will be used to develop the drought monitoring and forecasting systems. In this paper, some of the preliminary results from the ASAR and MERIS data sets are presented.

[1]AATSR ~ Advanced Along Track Scanning Radiometer
[2]ASAR ~ Advanced Synthetic Aperture Radar
[3]MERIS ~ Medium Resolution Imaging Spectrometer

1. INTRODUCTION

Food security is one of the biggest social-economical problems in the world and often causes political conflicts within and among countries. Often crop water availability is a major concern of farmers in non-irrigated agriculture. In China, approximately once every two years severe droughts occur and in most cases the area affected is larger than 33.3 million hectares and the annual loss of grain amounts to more than 10 billion kilograms. Within the framework of the European Space Agency (ESA)-National Remote Sensing Center of China (NRSCC) Dragon "drought monitoring and drought prediction" project a system will be developed to monitor and predict droughts based on moisture changes in the upper part of the soil layer. The monitoring component of the project will be based on the retrieval of land surface parameters using near real-time satellite observations acquired by the ESA Environmental Satellite (EnviSat). The prediction part will be achieved by assimilation of satellite retrievals in a Land Surface model (LSm).

Proc. 2005 Dragon Symposium "Mid-Term Results", Santorini, Greece
27 June – 1 July 2005 (ESA SP-611, January 2006)

Remote sensing provides spatially distributed observations of the land surface. The remotely sensed reflectivity's are sensitive to states that relate to the vegetation and soil layer, such as vegetation water content (*VWC*), Leaf Area Index (*LAI*), surface temperature (T_s) and soil moisture. These characteristics have been used by various scientists to retrieve either these land surface variables [1-3] or to generate higher level products from the retrieval products [4-7]. For this study similar retrieval algorithms will be applied, and if necessary adjusted to develop a drought monitoring system for China. The Land Surface parameters that are of interest to this study are: root zone soil moisture, evaporation and vegetation parameters.

The root zone soil moisture content is an important state variable and is a good drought indicator. Under limiting soil moisture conditions the evaporation of crops is restricted and the yield is immediately reduced. However, under non-limiting conditions percolation to the groundwater occurs and river flow is generated. Remote sensing of soil moisture is being studied in several experiments [10] and by many investigators [11-13], but it has been very difficult to estimate the spatial and temporal variability of soil moisture using satellite observations [14].

Other drought indicators are, for example, the vegetation conditions and the actual evaporation. The state of the vegetation throughout a growing season is strongly influenced by the crop water availability. Satellite retrieved vegetation parameters contain information about the plant water availability. From remote sensing observations alone the actual state of the vegetation layer can be retrieved and assimilation techniques can be used to derive the root zone soil moisture content [8]. The uptake of soil moisture by crops is restricted by the soil water suction and constrains the portioning between latent and sensible heat fluxes. In this perspective, the remotely sensed latent heat flux is a measure for the crop water availability and can, thus, be used as a drought indicator [6]. Evaporation cannot be directly observed, but could be derived from satellite retrieved land surface parameters and meteorology data, such as surface temperature and vegetation parameters.

Within the framework of the Dragon drought project, a two-month field EXperiment was conducted in the Chinese LOess Plateau in the summer of 2005 (LOPEX05). The selected study area is located near the city of Pingliang in Gansu province, China. The objective of the LOPEX05 campaign was to collect ground truth observations for validation and development of land surface parameters and heat flux retrieval algorithms based on satellite observations. Soil moisture, temperature, Leaf Area Index (LAI) and Vegetation Water Content (VWC) measurements were made in conjunction with the satellite overpasses. In addition, meteorological flux towers were installed at three locations and provided continuous observation of the important energy balance components. This extensive set of ground and satellite observations will be used in this research. In this paper, the development of the drought monitoring methodology is discussed. Further, the data sets collected during the LOPEX05 experiment are described in detail and some preliminary results of the LOPEX05 fields experiment are presented.

2. DROUGHT MONITORING COMPONENT OF THE DRAGON PROJECT

In our research, a distinction is made between so-called states and process variables. State variables describe the dynamic properties of the land surface system and affect the magnitude of land surface processes, such as the partitioning of latent and sensible heat fluxes, and groundwater recharge. Satellite observations are capable of observing the states of the earth's surface and process variables have to be computed from the remotely sensed retrievals. As a result, the accuracy of modeled land surface processes is strongly related to the accuracy of satellite retrievals

More generalized methods are necessary to improve the accuracy of land surface modeling. Theoretical Radiative Transfer models (RTm), such as Scattering from Arbitrarily Inclined Leaves (SAIL) [16] and Michigan Microwave Canopy Scattering (MIMICS) [15] have been developed to simulate the satellite observations. These models have been successfully validated in small-scale experiments for a variety of surface conditions. A major drawback of most theoretical methods is the extensive parameterization required, which is typically not available on a global scale. Model inversion is inevitable, but a number of unknown parameters typically exceeds the available number of independent observations leading to ill-posed optimization schemes.

Space agencies acknowledge this problem and are continuously in the process of launching more advanced sensors, which are able to acquire more independent observations. In addition, advances in land surface modeling have demonstrated that the synergistic use of traditional LSm's, RTm, and satellite observations can improve hydrological and crop yield predictions [8]. The RTm's are used to simulate the canopy reflectance observed by satellite sensors based on a parameterization provided by the LSM's. Based on comparisons of the simulation results and satellite observed canopy reflectance in combination with statistical assimilation procedures, the state variables within the LSm are optimized. A schematic layout of this assimilation procedure is given in figure 1 and similar approaches have been frequently applied to optical and thermal observations [7, 9]. Incorporation of microwave data into the assimilation scheme has been limited to application of semi-empirical microwave scattering methods [8].

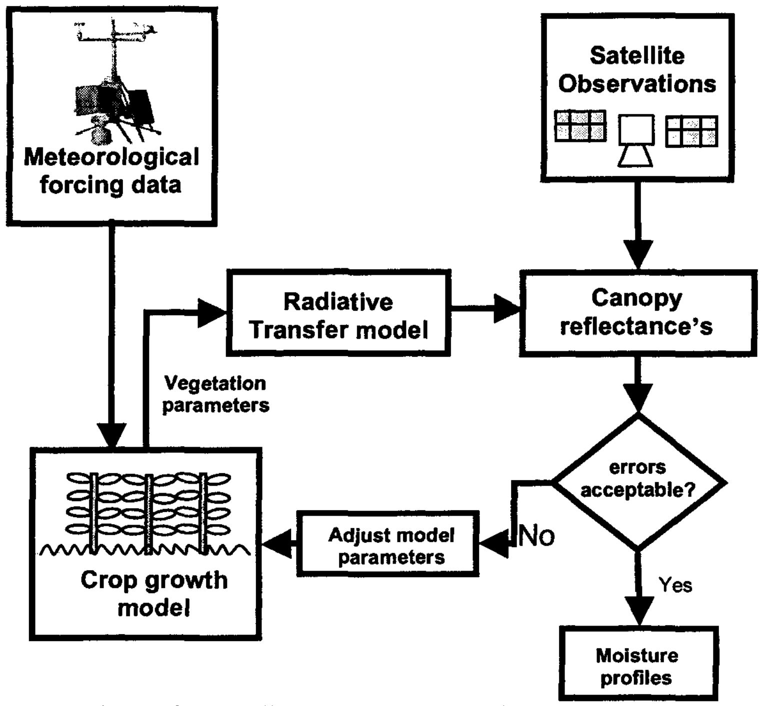

Figure 1: Schematic outline on the assimilation procedure that will be used for the retrieval of land surface parameters as a part of the drought monitoring system.

Drought monitoring in this research will be established through direct assimilation of the satellite observations into a modeling framework. A theoretical radiative transfer model will be used in a forward application for which a crop growth model will be employed to provide the vegetation parameterization required for RTm's. A combination of the Properties Spectra (PROSPECT) [17] leaf reflectance model and GeoSAIL [7] two layered canopy reflectance models will be used to simulate the satellite observations from the spectral range from 400 to 2400 nm. For the simulation of microwave observations, the coherent scattering model developed by Karam et al. (1992) [18] will be used. The data set collected in the LOPEX05 experiment will be used to validate this methodology in future studies.

3. LOPEX05 FIELD EXPERIMENT

The LOPEX05 experiment was conducted on the top of the loess plateau (mesa area) near the city of Pingliang in Gansu province, China. The selected area is characteristic for the Chinese Loess Plateau, which is a typical terrace landscape formed through fluvial erosion. The mesa area is located approximately 1500 meters above sea level and is primarily used for agricultural purposes. Corn, millet and winter wheat are the dominant crop types. The hill slopes consist of abandoned farmlands and are now covered by shrubs and grass. The valley is imbedded in the landscape about 300 to 400 meters below the peaks of the plateau, where corn and millet are the dominant crop types. Heat, water fluxes and land surface parameter measurements were collected on the plateau and in the valley.

During the two-month Intensive Observation Period (IOP), heat and water fluxes observations were collected continuously using three eddy correlation systems (ECS) and one automated weather station (AWS). Two ECS's and the AWS were installed on the mesa, and the third ECS was stationed in the valley. Each ECS was equipped with a 3D-sonic-amonemeter, a kip&zonen net radiometer, humidity equipment and four TDR probes installed at depths of 2.5, 10, 20 and 40 cm. The AWS consists of basic meteorological instrumentation such as humidity, wind speed and direction.

Intensive ground sampling strategy was conducted on clear days and included soil moisture, Leaf Area Index (LAI), Vegetation Water Content, temperature and some basic geometric measurements of the canopy layer (i.e. crop height, number of leaves). The sampling transect covered of eleven sites, of which five sites were located on the plateau and the other sites were situated in the valley. At each sampling location one set of measurement was acquired over a bare soil surface and another set over a vegetated area next to a bare soil field (millet or corn). In figure 2 an ASAR image acquired on 28th of July, 2005 over the LOPEX05 study area is shown and the approximate locations of the experimental sites are added.

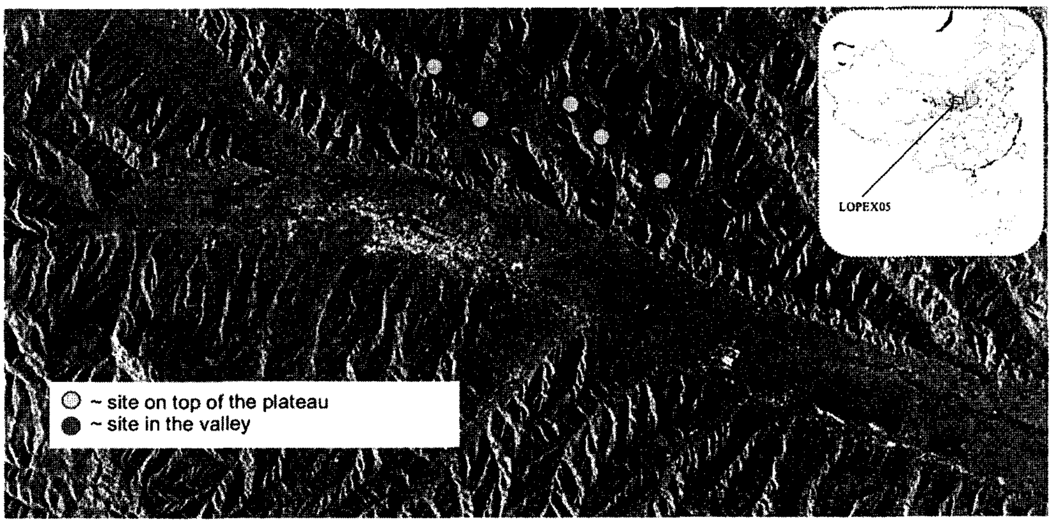

Figure 2: A HH/VV-polarized ASAR image (IS5, with central incidence angle of 38 degrees) of the LOPEX05 study area in which the sampling locations are indicated. The HH-polarized band is projected in the red and blue bands, and the VV-polarized channel is presented in the green band.

Soil moisture was measured using gravimetric and impedance probe techniques. The hand-held Stevens hydra-probe was used to collect capacitance observations over a soil depth of 6 cm. A scoop tool was used to extract soil samples of 6 cm depth, from which the gravimetric moisture content can be obtained using an oven-drying method. The gravimetrically derived soil moisture measurements are taken to calibrate the hydra-probe dielectric observations. However, due to time constraints, the hydra-probe observations have not been calibrated yet. Therefore, the soil moisture measurements presented in this paper are derived from the gravimetric samples.

A portable LICOR LAI-2000 Canopy Analyzer was used to collect spectral observations over the vegetated study sites, which are converted into Leaf Area Index (LAI) values. At each vegetated experimental field two sets of spectral measurements were made resulting in two LAI values. The average of these two values is used in the analysis.

4. SATELLITE OBSERVATIONS

In the framework of the LOPEX05 field campaign, a series of 10 ASAR Alternating Polarization (AP) and 15 MERIS full resolution images has been received. The ASAR instrument is the first dual-polarized C-band (5.3 GHz) radar instrument mounted on a satellite platform. Compared to the predecessors onboard the ERS-1/-2 platforms, two new features have been added to the high resolution mode. The viewing angle of the ASAR antenna can be set between 15 and 45 degrees and dual-polarized observations (HH/VV, HH/HV and VV/VH) can be acquired. For the LOPEX05 experiment, multiple HH/VV-polarized AP images in ascending and descending passes have been requested in the IS1, IS2, IS5 and IS7 image swath modes, which correspond to central incidence angles of 19, 23, 38 and 44 degrees, respectively.

The MERIS instrument is an imaging spectrometer designed to acquire data at a variable band width (1.25 – 30.0 nm) over a spectral range of 390-1040 nm [19]. The spectrometer has 15 bands that can all be programmed in width and centre wavelength. The standard band setting of the MERIS instrument and the potential application of each band is given in table 1. The MERIS instrument can operate in reduced resolution or in full resolution mode acquiring surface reflectance at resolutions of 1.2 km and 300 m, respectively.

Table 1: MERIS spectral bands in standard setting and their potential application [19].

Band	*Wavelength centre (nm)*	*Bandwidth (nm)*	*Potential application*
1	412.5	10	Yellow substance, turbidity
2	442.5	10	Chlorophyll, absorption maximum
3	490	10	Chlorophyll, other pigments
4	510	10	Turbidity, suspended Sediment, red tides
5	560	10	Chlorophyll reference, suspended sediment
6	620	10	Suspended Sediment
7	665	10	Chlorophyll absorption
8	681.25	7.5	Chlorophyll fluorescence
9	705	10	Atmospheric correction, red edge
10	753.75	7.5	Oxygen absorption reference
11	760	2.5	Oxygen absorption R-branch
12	775	15	Aerosols, vegetation
13	865	20	Aerosols corrections over ocean
14	890	10	Water vapor absorption reference
15	900	10	Water vapor absorption, vegetation

In this study, the sensitivity of the ASAR backscatter measurements to the gravimetrically derived soil moisture is explored using the data sets acquired during the ascending passes. The spectral surface reflectance computed from MERIS observations are compared to the ground based LAI measurements made during the experiments. For the development of the drought monitoring and drought prediction system, these results will be taken into consideration.

5. PRELIMINARY RESULTS

Simultaneous to the in-situ soil moisture measurements, multiple ASAR alternating polarization images with various image swaths have been acquired in descending as well as ascending satellite passes. Since the influence of the incidence angle on backscatter observations (σ^0) is only partly understood, the backscatter measurements can be compared with each other when they are acquired in the exact same configuration (i.e. incidence angle and pass). Unfortunately, at the time of this writing, not all requested images have been received. Therefore, the presented analysis is restricted to a simple comparison of the σ^0 sensitivity to soil moisture observed for the different Image Swath modes. The date of acquisition and incidence angle of the used scenes are listed in table 2. Further, due to calibration problems of the capacitance observations, the soil moisture measurements used for this study are derived from gravimetric samples, which have not been collected on every sampling day for each site.

Table 2: List of ASAR HH/VV polarized scenes acquired in an ascending satellite pass.

Date of acquisition	Image Swath (IS)	Incidence angle range (degrees)
2005/07/22	IS2	19.2 - 26.7
2005/07/28	IS5	35.8 - 39.4
2005/07/31	IS7	42.5 - 45.2
2005/08/07	IS1	15.0 - 22.9

The σ^0 observations are extracted from each of the scenes and averaged per sampling location. In figure 3, the averaged HH and VV-polarized radar responses are plotted against the ground observed soil moisture values. Despite the somewhat scattered distribution of data points, a positive relationship between σ^0 and soil moisture can be observed. The incidence angle, however, appears to have a strong influence on the σ^0 response to changes in soil moisture. At low viewing angles of nadir (IS1 and IS2), the range in σ^0 is wider than at higher viewing angles (IS5 and IS7).

Radar observations acquired at low viewing angles typically have a higher σ^0 response to changes in soil moisture, but the backscatter response is also sensitive to variations in other land surface parameters, such as surface roughness, vegetation geometry and vegetation density [20]. At higher viewing angles, the radar sensor observes a large vegetation volume, which often saturates C-band observations [21]. The soil moisture sensitivity of σ^0 observed at large viewing angles originates from vegetated-soil surface interactions, which is a first-order scattering term and is small compared to the zeroth order surface and vegetation scattering terms [22]. Consequently, the σ^0 sensitivity to changes in soil moisture is lower for observations made at high viewing angles [21].

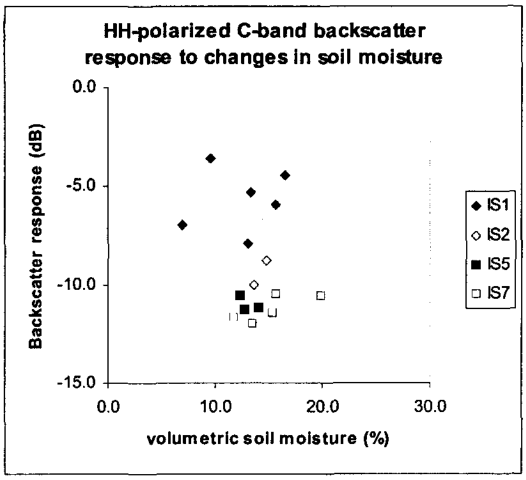

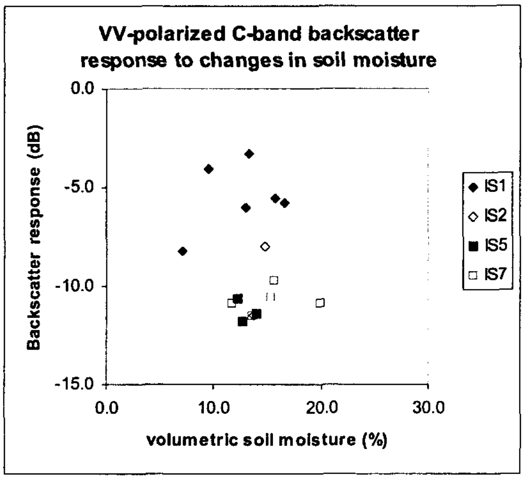

Figure 3: ASAR HH-and VV-polarized backscatter values acquired at different viewing angles plotted against volumetric soil moisture derived from gravimetric soil samples.

Within the IOP of the field campaign, all available MERIS full resolution scenes were requested. However, because optical satellite observations are obscured by clouds, only a limited of number scenes provided useful cloud free data. Figure 4 shows a selection of three cloud free false color MERIS images that have been geocoded and atmospherically corrected using the Basic ERS & Envisat (A)ATSR and Meris

(BEAM) Toolbox. The increasing density of red colors in the series MERIS images illustrate that further in the growing season the vegetation biomass increases.

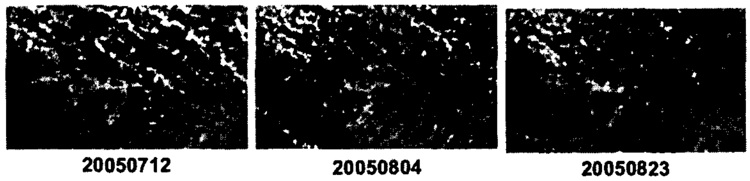

Figure 4: A series of MERIS false color image acquired over the LOPEX study area, in which the spectral bands 13, 8 and 5 are displayed in red, green and blue, respectively.

The sensitivity of the MERIS reflectance observations is further explored by comparing the reflectance observations with the LAI measurements. Figure 5, reflectance's observed in band 5, 12 and 15 are plotted against the LAI observed with the field spectrometer. The sensitivity of the reflectances to changes in vegetation biomass is very weak. However, it is difficult to draw conclusions from this figure because the resolution of the MERIS products is 300 meters, while agricultural fields in this area are approximately 10 meters wide and up to 100 meters long. Using a data assimilation system, such as employed by Verhoef and Bach [7], probably more information can be retrieved from the series MERIS images.

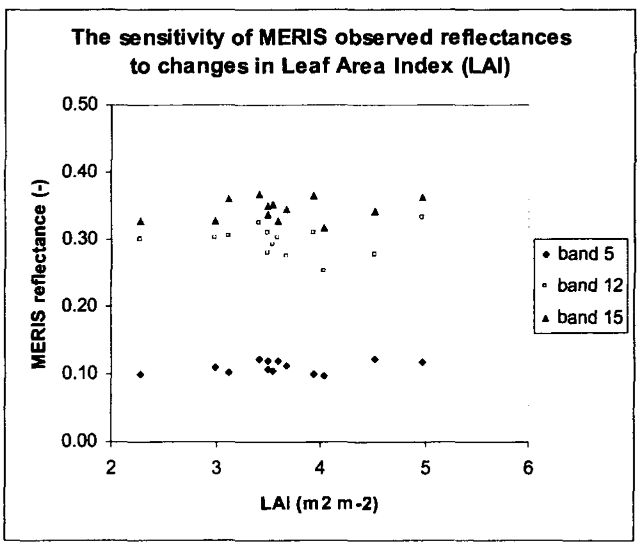

Figure 5: geocoded and atmospherically corrected MERIS reflectances plotted against ground measured LAI values.

6. SUMMARY

Within the dragon drought monitoring and drought prediction project, a system will be developed to monitor and generate predictions of the root zone soil moisture conditions. Direct assimilation of satellite observations into a Land Surface modeling system will be used to obtain estimates of the land surface state variables. The advantage of this methodology is that theoretically based models can be used over the semi-empirical satellite retrieval algorithms.

In this paper, some preliminary results of the ASAR and MERIS data sets have been presented. The ASAR backscatter observations show some response to changes in the soil moisture content measured in the top 5-cm soil layer. The interpretation of the MERIS reflectance measurements is more complicated because of the rather coarse resolution cells (300 m) within a rather heterogeneous study area. In the near future, more detailed investigations will be conducted to explore the full potential of the ground truth and satellite data sets within a data assimilation modeling framework.

7. REFERENCES

1. Jackson, T.J., 1993, Measuring surface soil moisture using passive microwave remote sensing, *Hydrological Processes*, **7**, 139 -152.

2. Wen, J. and Su, Z., 2003, A times series based method for estimating relative soil moisture with ERS wind scatterometer data, *Geophysical Research Letters*, **30 (7)**, 50-1 – 50-4.

3. Owe, M., De Jeu, R., and Walker, J., 2001, A methodology for surface soil moisture and vegetation optical depth retrieval using the microwave polarization differece index, *IEEE Transactions on Geoscience and Remote Sensing*, **39**, 1643-1654.

4. Jia, L., Su, Z., Van den Hurk, B., Menenti, M., Moene, A., De Bruin, H.A.R., Javier Baselga Yrisarry, J., Ibanez, M., Cuesta, A., 2003, Estimation of sensible heat flux using the Surface Energy Balance System (SEBS) and ATSR measurements, *Physics and Chemistry of the Earth*, **28**, 75-88.

5. Norman, J.M., Kustas, W.P., Humes, K.S., 1995, Source approach for estimating soil and vegetation energy fluxes in observations of directional radiometric surface temperature, *Agricultural and Forest Meteorology,* **77**, 263-293.

6. Su, Z., 2002, The Surface Energy Balance System for estimation of turbulent heat fluxes, *Hydrology and Earth System Sciences,* **6**, 85-99.

7. Verhoef, W., Bach, H., 2003, Simulation of hyperspectral and directional radiance image using coupled biophysical and atmospheric radiative transfer models, *Remote Sensing Environment,* **87**, 23-41.

8. Bach, H., Mauser, W., 2003, Methods and examples for remote sensing data assimilation in land surface process modeling, *IEEE Transactions on Geoscience and Remote Sensing*, **41**, 1629-1637.

9. Bicheron, P., Leroy, M., 1999, A method of biophysical parameter retrieval at global scale by inversion of a vegetation reflectance model, *Remote Sensing Environment*, **67**, 251-266.

10. Paloscia, S., Macelloni, G., Santi, E., and Toshio Koike, 2001, A multifrequency algorithm for the retrieval of soil moisture on a large scale using microwave data from SMMR and SSM/I satellites, *IEEE Transactions on Geoscience and Remote Sensing*, **39**, 1655-1661.

11. Engman, E.T., and Chauhan, N., 1995, Status of microwave soil moisture measurements with remote sensing, *Remote Sensing Environment*, **51**, 189-198.

12. Pampaloni, P., Sarabandi, K., 2004, Microwave remote sensing of land, *The radio science bulletin,* **308**, 30-48.

13. Ulaby, F.T., Dubois, P.C. and Van Zyl J., 1996, Radar mapping of surface soil moisture, *Journal of Hydrology*, **184**, 57-84.

14. Wagner, W., and Pathe, C., 2004, Has SAR failed in soil moisture retrieval?, in: "*Proceedings of the Envisat & ERS Symposium*".

15. Ulaby, F.T., Sarabandi, K., McDonald, K., Whitt, M., and Dobson, M.C., 1990, Michigan microwave canopy scattering model, *International Journal of Remote Sensing*, **11**, 1223-1253.

16. Verhoef, W., 1984, Light scattering by leaf layers with application to canopy reflectance modelling: The SAIL model, *Remote Sensing of Environment*, **16**, 125-141.

17. Jacquemond, S., and Baret, F., 1990, PROSPECT: A model of leaf optical properties spectra. *Remote Sensing of Environment*, **34,** 75-91.

18. Karam, M. A., Fung, A.K. Lang, R.H., and Chauhan, N.S., 1992, A microwave scattering model for layered vegetation, *IEEE Transactions on Geoscience and Remote Sensing,* **30**, 767-784.

19. Rast, M., Bezy, J.L., and Bruzzi, S., 1999, The ESA Medium Resolution Imaging Spectrometer MERIS- a review of the instrument and its mission, *International Journal of Remote Sensing.*, **20**, 1681-1702.

20. Ulaby, F.T., Moore R.K., and Fung, A.K., 1982, *Microwave remote sensing: active and passive. Vol. II Radar Remote Sensing and Surface Scattering and Emission Theory* (Norwood, MA: Artech House).

21. Ulaby, F.T., Moore R.K., and Fung, A.K., 1986, *Microwave remote sensing: active and passive. Vol. III From theory to application* (Norwood, MA: Artech House).

22. Van Oevelen P.J., 2000, Estimation of areal soil water content through microwave remote sensing, Ph.D thesis, Wageningen University.

Flood Plain Disaster Rapid Mapping and Monitoring (id. 2551)

ENVISAT ASAR MEDIUM AND HIGH RESOLUTION IMAGES FOR NEAR REAL TIME FLOOD MONITORING IN CHINA DURING THE 2005 FLOOD SEASON

LI Jiren[1], YESOU Hervé[2], HUANG Shifeng[1] LI Jing[3], LI Xiufen [4], XIN Jingfeng[1]
WANG Xingling [5] and ANDREOLI Rémi [2]

[1] *IWHR, Ministry Water Resource, Beijing, China lijiren@iwhr.com; xinjf@iwhr.com*
[2] *SERTIT, Université Louis Pasteur, Strasbourg, France, herve@sertit.u-strasbg.fr*
[3] *Geoinformation Centre, Beijing Normal University, Beijing, China, lijing@irs.bnu.edu.cn*
[4] *Institute of Meteorological Sciences, Harbin, China, china_licn@yahoo.com.cn*
[5] *Chinese National Center for Disaster Reduction, Beijing, China, wangxingling@ndrcc.gov.cn*

Abstract: The Flood Dragon project will enhance the ENVISAT objective to monitor natural disaster such as flooding. The project's first objective was to explore ENVISAT ASAR and MERIS spatial and temporal resolution potential for rapid flood mapping and monitoring. One of the major final goals is to provide data exploitation guidelines and system improvement's recommendations for a Real Near Time exploitation of ASAR data for flood monitoring. China flood prones more precisely the proposed test sites, Songhua watershed, Poyang and Dongting lakes, appear as a very adequate case of study in term of extent of the flooded area, and long period of flood in regard of High, Medium and low resolution ASAR products. During the 2005 flood period, fifteen NRT exploitations of ENVISAT ASAR have been tented. Ten were successful exploiting both Emergency programming procedure and Rolling archive ones based on Ordinary acquisition scheduling. The results obtained in four NRT cases carried over Chinese major flood prone, Dongting and Poyang lakes, Pearl, Nen and Songhua rivers are illustrated and lessons discussed in terms of programming, downloading and processing.

Keywords: Flood mapping, monitoring, ENVISAT, ASAR medium resolution, Rolling Archive, NRT

1. INTRODUCTION

China is one of the countries in which flood occurs most frequently in the world[1] and with economy increasing, flood disaster causes more and more economic loss. The application of radar remote sensing on flood monitoring and impact evaluation is very helpful to assist decision-making of flood control and protection and decreasing the loss of flood disaster. Radar remote sensing has capability of "all weather" monitoring and capability of penetration, and large coverage is an important tool for flood monitoring [1-6]. These capabilities have been well demonstrated during the 1998 and 1999 flood events in China, where Radar remote sensing played a very important role in flood disaster monitoring and evaluation [7-10]. The SAR potential for flood mapping and monitoring has also been evaluated during demonstration projects and tested in operational condition, including numerous Charter Space and major disaster actions [11]. Therefore, ENVISAT data assessment for flood mapping has not fully/systematically done; there are only few references, concerning mostly small flooded areas and a single image exploitation [12]. The first objective of the Flood DRAGON project is to explore ENVISAT ASAR and MERIS spatial and temporal resolution potential for rapid flood mapping and monitoring [13]. A second purpose of the flood DRAGON project consists to extend and improve methods and tools for flood and drought management in terms of prevention and forecast using space technologies. Space Earth observation coupled with physically based models should permit to access to some evolution indicators useful for land use or urban planning policies at the scale of catchments and hydrological balances [14].

As already mentioned, the rapid mapping part of the project is focussed on the assessment of the ENVISAT ASAR and MERIS, potential for flood mapping. ASAR spatial resolution ranging from Precision to Global modes in order to maximize

[1] The dramatic event affecting large territories in China in 1998 involved 4,150casualties, 14 millions homeless, for 250 millions of affected people. The induced economic losses were estimated at 24 billions $

Proc. 2005 Dragon Symposium "Mid-Term Results", Santorini, Greece
27 June – 1 July 2005 (ESA SP-611, January 2006)

the revisit and coverage, as well as polarization mode for thematic accuracy will be assessed during this three years project. One of the major final goals is to provide data exploitation guidelines and system improvement's recommendations for a Real Near Time exploitation of ASAR data for flood monitoring. China flood prones more precisely the proposed test sites, Songhua watershed, and the Poyang –Dongting lakes, appear as a very adequate case of study in term of extent of the flooded area, and long period of flood in regard of High, Medium and low ASAR products.

The aim of this paper is to present the improvement done in Near Real Time exploitation of ENVISAT ASAR images for flood mapping, in terms of programming, downloading and processing,. The results obtained in four successful NRT works over Chinese major flood prone are illustrated and lessons discussed.

2. METHODOLOGICAL PART

2.1. NRT data acquisition mode, ie rush mode programmation and rolling archive exploitation

Envisat has two acquisition's procedures: an Ordinary one corresponding to a scheduling by pair of cycles, twice periods of 35 days, prepared month in advances, and it is the standard Cat1 mode of programming. There is a special mode, an Emergency one, allowing faster programming and data producing ASAR Envisat data, in Near Real Time, NRT, a mode which is usually reserved to the International "Space and major disaster" actions as well for commercial purposes.

For the Flood Dragon team, a crucial key point was the possibility to access to NRT acquisition, an agreement was found in January establishing the rules and procedures for requesting a NRT mode and followed by a test. A first quota of five NRT acquisitions has been given to the Flood DRAGON project in case of major flood events occurring in China. For such rush mode of programming, a request signed by the Flood Dragon PI, Pr LI Jiren, has to be sent two and half full working days before the scheduled acquisition at ESA as for such Envisat rush programming has been reviewed internally at ESA, involving the satellite command and control centre. This time in programming need a minimum of anticipation, which is not so obvious in case of flood, as for a flood occurring a Monday, the request has to be sent on the previous Wednesday morning, five days before. The NRT mode acquired data are accessible for the Flood Dragon partners on the ESA Rolling archive WEB sites, either on the Esrin or Kiruna ones, the day after[2] the acquisition for medium resolution products (IMM APM, WSM formats) and one or two days later for the high resolution images (IMP, APP).

A test of procedures occurred in February 2005 and was successful, enabling procedures training of the teams and to test and verify the networks capabilities. It was pinpointing out the complexity of founding the wanted data within one or the two potential ESA rolling archive sites. Sometime, this search can look like a fishing party. This test also allowed evaluating downloading time towards a European laboratory or Chinese Institute. It was noticed that downloading time varies from a factor of 40 depending, if the downloading time within Europe or towards China, as in this case usual transfer speed is 1 Mega bite by second. After this training, participant Flood Dragon teams were ready to be operational for the coming flooding season. In some cases, Envisat data could also downloaded by the Beijing ground station, which can be a way of saving time.

2.2. Water extraction methods

Flood inundation mapping corresponds in fact to a surface water extraction exploiting the low backscattering characteristic of water, which appears usually in dark tone on SAR image. Therefore in case of windy condition, or partially submerged vegetation, the backscattered signal can be affected presenting higher backscattering values [1, 6]. Semi automatically classical water extraction techniques such crisis image binarization through thresholding, or change detection technique on reference –crisis pair of SAR image, including, differencing, rationing can fail. A part of the flood DRAGON project is the assessment of innovative image processing techniques such as target oriented approach. Object based approach applied during the presented NRT flood mapping action consists in creation of homogeneous objects in terms of radiometry and

---

[2] This is particularly interesting, as all Envisat ASAR acquired data, following the standard or NRT programming procedures, are firstly produced in a medium resolution format (IMM mode). So if the standard programming scheduling has integrated a monitoring aspect such as done for the Flood DRAGON project, it is possible to exploit the Rolling archive facilities to carry NRT mapping actions.

forms using eCognition v3.0 software. Two levels of object scale were created: the first one corresponds to the recognition of homogeneous macro-object and the second one to creation of fine homogeneous objects. The first level object was used to discriminate low radiometry areas corresponding to a large envelope of flooding areas and was obtained by thresholding the object mean radiometry in respect to the mean radiometry of the whole image. Whereas the second object level was used in order to refine flooded areas contours taking into account discrimination between water and moisture according to object radiometry.

3. NRT APPLICATIONS DURING THE 2005 FLOOD SEASON IN CHINA

The 2005 flood season in China was dramatic, beginning very early in the year with major events in early and end of June and has been more devastating than usual. 2005 summer floods have affected 90 million people in China, a minimum of 764 people have been killed with another 191 missing, more than 3.72 million people have been evacuated to safer places. About seven million hectares of crops were destroyed as well as 702,000 houses over 27 regions involving a 47.65 billion yuan (5.79 billion US dollars) in direct economic losses. The worst-hit regions have been in Southern and Eastern parts of China, including the provinces of Guangxi, Fujian, Hunan, Guangdong, Jiangxi, Sichuan, Anhui and Henan, and in the Northeast part of China the Heilongjiang province.

Table I: List of NRT actions exploiting EMERGENCY programming as well as systematic Rolling Archive exploitation carried by the Flood Dragon team over China during the 2005 flood period

	Location	Province	Type of action	Date of request	Type of event	Scheduled days of acquisition	Date type	Status
1	Dongting Poyang lake	Hunan Jiangxi	Rolling archive		Flood	01-05	IMM WSM	Success
2	Wuzhou	Guangxi	NRT	23-06-05	Flood	25 -06-05	APP	Conflict with Charter but access to data
3	Wuzhou	Guangxi	NRT	27-06-05	Flood	03 -07-05	APP	success
4	Huaihe river	Anhui,	NRT	11-07-05	Flood	17-07-05		Cancelled (time delay)
5	Dazhou	Sichuan	NRT	11-07-05	Floods	17-07-05	App	success
6	Nen and Songhua Rivers	Jilin, Heilongjiang	NRT + Rolling archive	25-07-05	Flood	21-07-05 25-07-05 28-07-05 31-05-07	APM, IMM	NRT failed, but rolling archive exploitation
7	Songhua tributary	Heilongjiang	NRT	4-08-05	Flood			Technical fail
8	Huaihe	Anhui	NRT	5-8-05	Flood	9-8-05	APP	Cancel (time delay)
9	Shanghai	Shanghai	NRT	5-8-05	Typhoon	10-8-05	APP	Cancel (time delay)
10	Zhangzhou	Fujian	Rolling archive		Typhon	14-08-05	APP, APM	Success
11	Fushun	Liaoning	NRT	16-08-05	Flood	22-08-05	APP	Success
12	Huaihe	Anhui	NRT	29-08-05	Floods	7-09-05		Technical fail
13	Huaihe River	Anhui,	Rolling archive		Floods	09-09-05	APP	Success
14	Huaihe River	Anhui,	NRT	05-09-2005	Flood	10 – 09 -05	APP	Conflict with commercial but successful
15	Yangjiang	Guangdu	NRT	23-9-05	Typhoon	27-9-05	APP	Success

Within this dramatic context[3], between June and September 2005, the flooding period as well as the typhoon period in China, fifteen flood rapid mapping actions in NRT have been carried out by Flood Dragon team. These NRT cases have exploited both the Emergency and the Rolling archives, facilities. Over the twelve request of EMERGENCY, indicated as NRT in the table I, seven were successful in term of acquisition, downloading, processing and dissemination, few were not taken in account due to delay in requesting the NRT activation, others where in conflict wit commercial and/or Charter order therefore the data were made accessible to the Flood DRAGON tem through the Rolling archive, and two failed due to technical constraint on the satellite management. Part of the NRT action were carried over Flood DRAGON tests sites, Poyang, Dongting lakes in Central Chain and Nen-Songhua rivers in Northeast China, but also on others major flood prone in China such as the Huaihe River and the Peal River watershed as well as after typhoon (Fig. 1).

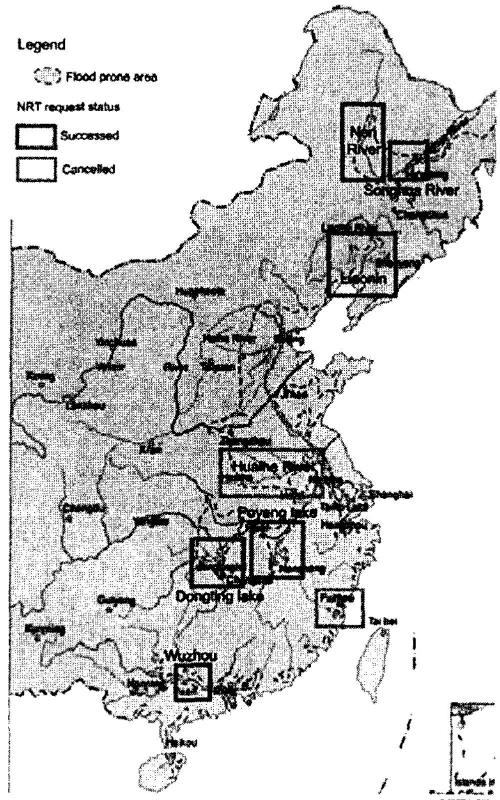

Figure 1: Major flood prone in China and Spring summer 2005 Flood DRAGON NRT actions.

3.1. The June floods events in Central Southern China

Late May, beginning of June, Central Southern Chinese was severely affected by flood events, inducing 200 people killed and 138,000 homes destroyed. After an image search within ESA database exploiting the EOLI tools, few suitable images have been downloaded and processed by SERTIT. The processing of the downloaded medium resolution image, WSM and IMM format, has allow to produced flooded area maps over the Poyang Dongting lakes areas as well, as the Jiulong River near Zhangzhou town, Fujian province Southern China. The generated documents have been disseminated to the Chinese Flood Dragon partners one day after the data acquisition (Fig. 2 and 3.).

[3] By September 20-2005, natural disasters across China had killed 1,630 people and caused economic losses of 163 billion yuan (US$19.9 billion) since the beginning of the 2005 year, according to the Ministry of Civil Affairs.(Xinhua News Agency, September 23, 2005)

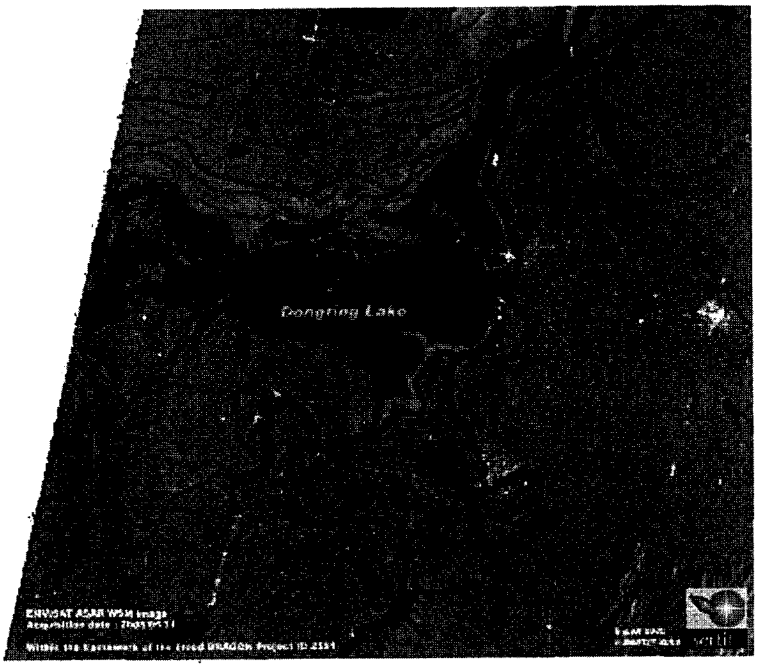

Figure 2: Flooded area map generated the 6th of June 2005 in NRT from WSM image acquired the 31st of may 2005 over the Dongting lake.

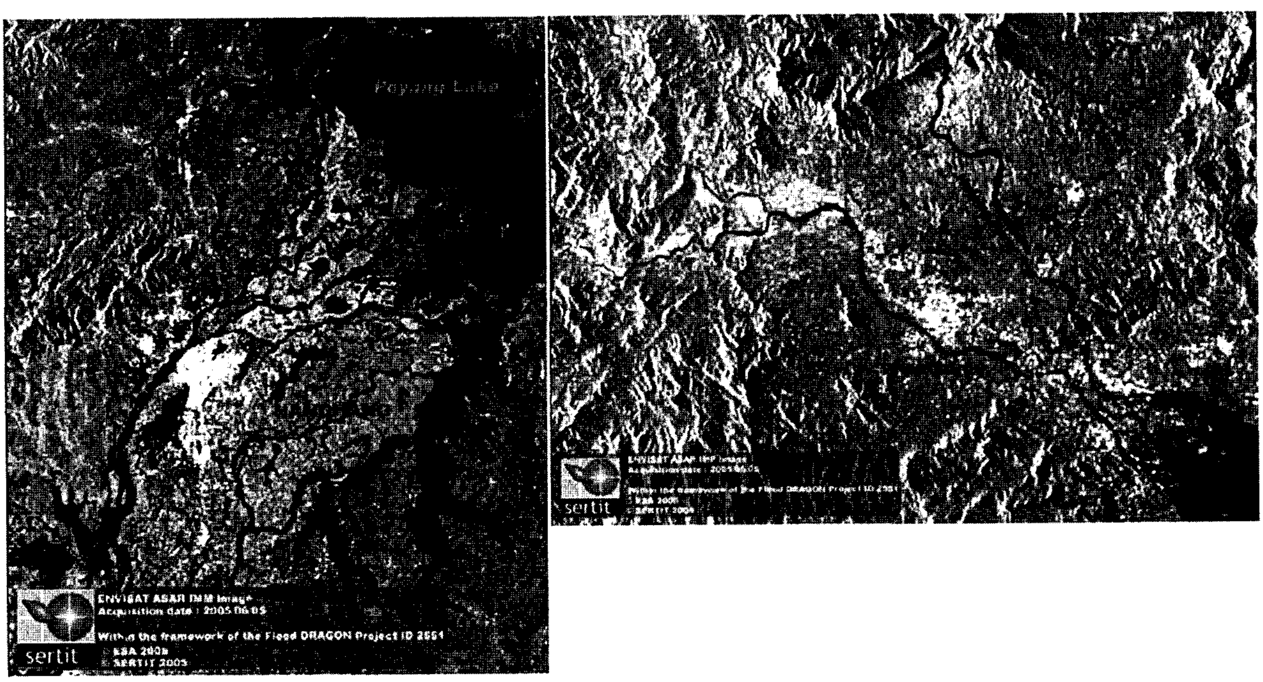

Figure 3: Flooded area map generated over the Nanchang town, on the vicinity of the Poyang lake and over the Jiulong River near Zhangzhou, **Fujian province**, based on the processing of ASAR IMM ENVISAT image acquired the 5th of June 2005 and downloaded, processed and disseminated the 6th of June.

Comparing the 5^{th} of June ENVISAT image with recent archive data, an IMM image acquired the 1^{rt} of May 2005, it was possible to characterize the infilling of the Poyang lake. This comparison shown that this annual phenomena is very impressive as at beginning of June, which normally correspond to the start of flooding period in medium, a large part of the lowland areas are already under water (Fig 4). Based on the highest flood level available in our database[4], derived from a Landsat image acquired in July 1989, it is noticeable that in June the water level was near the same level as it would be normally one and half month later (Fig .4).

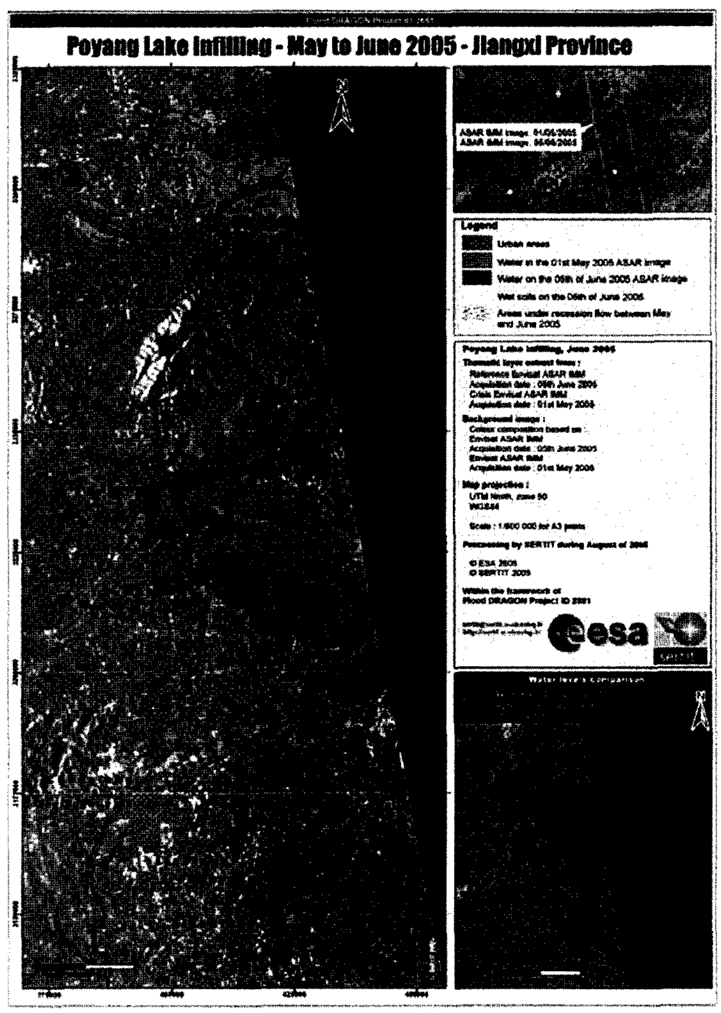

Figure 4: Flooding dynamic of the Poyang lake between May and June 2005 based on Envisat ASAR data

3.2. The June 2005 Wuzhou flood mapping action

Late June 2005, heavy rains affected the Guangxi Zhuang Autonomous Region in the Southwest of China. Floodwaters forced the mass evacuation overnight of residents in low-lying areas of the industrial city of Wuzhou where the Xijiang

[4] The July 1989 flood is considered in the literature as a standard event [15].

river had reached 25.74 meters by 21 of June, more than 8 m higher than the warning level over passing dikes (Fig.5). More than 330,000 people had been evacuated to higher ground in the region where the flooding has caused 1.67 billion yuan ($201 million) in economic losses, damaged 328,000 hectares of crops and toppled more than 20,000 houses.

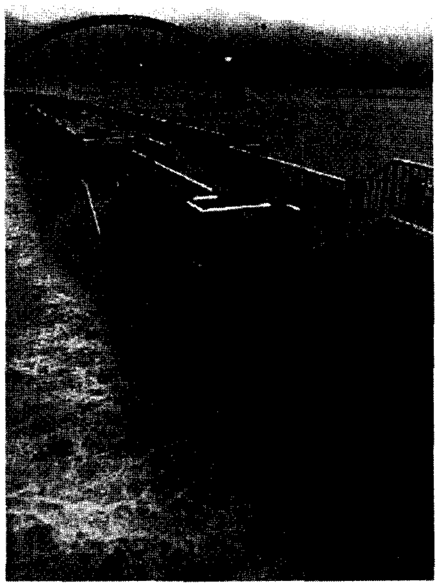

Figure 5:Xijiang water overpassing the dikes at Wuzhou

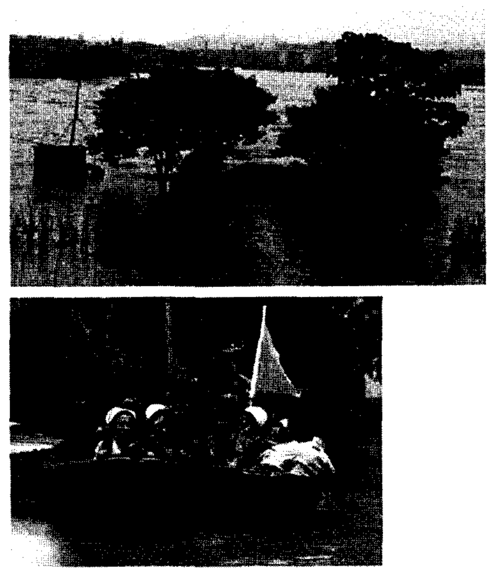

Flooded areas and people escaping water's rise in Wuzhou,

The 23rd of June, a NRT ENVISAT acquisition was requested in an APP mode, HH-HV polarization which appears to be most suitable for water mapping, and scheduled for the 25th of June, first potential revisit over the area of interest. Therefore due to an International Charter "Space and Major Disasters" ongoing action, the requested format was not acquired but a VV polarization mode which were made accessible to the Flood Dragon team. Wuzhou hydrological station gauges analysis shows that on the 23rd of June corresponding to the flood peak whereas on the 25th the water discharge has just begun to decrease (Fig 6).

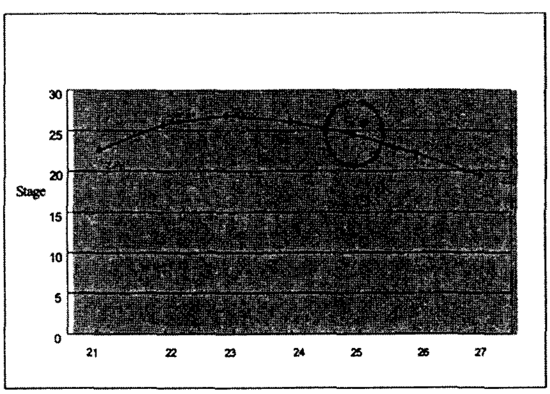

Figure 6: Water Level at Wuzhou Hydrological Station – June 2005. Red circle indicates the Envisat acquisition

The systematically produced medium resolution IMM image was put on the Rolling archive on the Saturday 25th of June, mid day. This IMM data were downloaded at the IWHR and processed both in China and Europe (Fig.7 to 9). The obtained results are very similar highlighting the flooded low valleys near the Xijiang River as well on the border of its tributaries. In addition, exploiting its socio-economic database, the IWHR was able to provide in time to the Ministry a first precise impact of the flood. The on request high resolution PRI images were made available on Monday 27th afternoon during the Second Dragon Symposium, which much of the Flood Dragon teams attempt in Santorini Island (Greece).

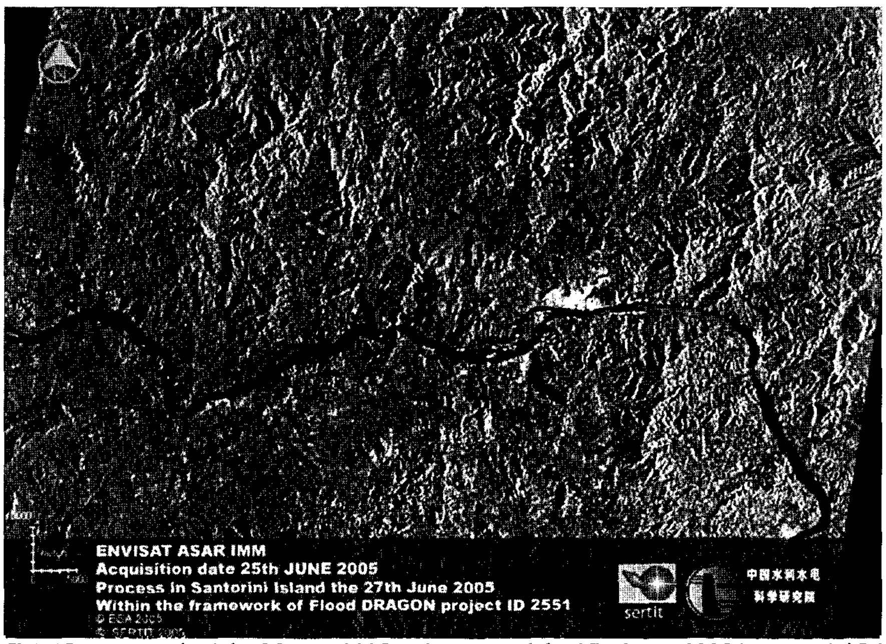

Figure 7: Envisat IMM Image acquired the 25 June 2005 and processed the 27 of June 2005 in Santorini Island during the Second Dragon Symposium

Figure 8 : Derived flood map over the Wuzhou city based on IMM image, processed in Santorini Island

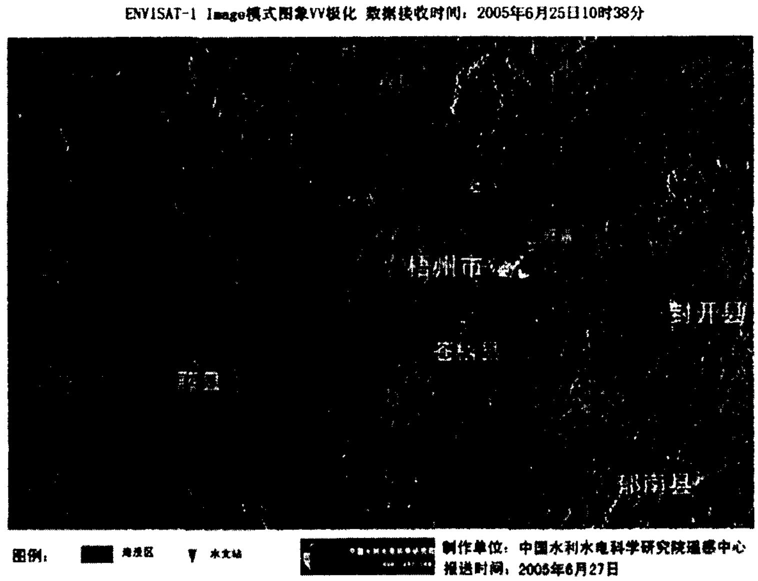

Figure 9: Derived flood map over the Wuzhou city based on IMM image acquired the 25 of June, processed in Beijing by IWHR team in NRT condition

Exploiting local low speed network, Esrin Rolling archive was reached from Santorini by ESA staff, taking hours to download the 290 mega corresponding to the IMP images. From these high resolution data it was then possible to precise the potential impact over the city of Wuzhou, identifying low districts of the town that might have been flooded (Fig.9°).

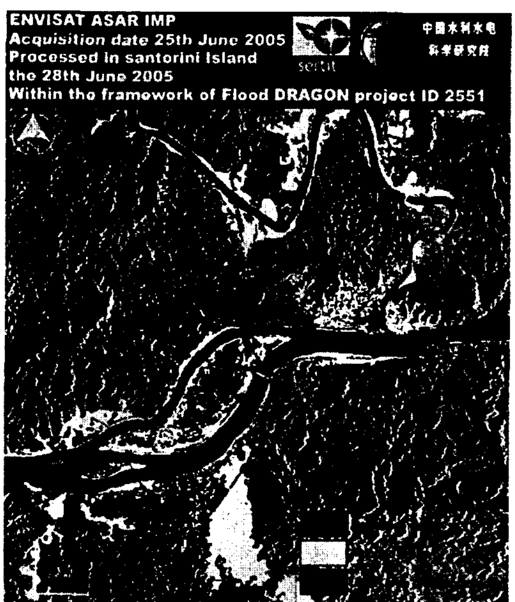

Figure 9: Detailed flooded impact map derived from ASAR IMP image dressed in Santorini Island (Greece).

3.3. Nen-Songhua flood events in July 2005

In July 2005, strong rains with an average rainfall up 67% from past years struck the North Eastern part of China, causing flooding in Jilin and Heilongjiang provinces. The Nen River and its continuation the Songhua River, as well as theirs Southern and Northen tributaries, the Di'er Songhua and Lalin rivers, were flooded menacing the Daqing, Qiqihar and Harbin areas. This event affected 1.27 million people in 252 towns in Jilin province; 5,287 houses and 354,900 hectares of crops have been destroyed. A rush mode acquisition and production was requested but it was an aborted tentative due to delays in information transmission. Therefore, as a "background" Flood Dragon acquisition request was on going, a set of images were acquired (Tab. 2°) and the middle resolution products were downloading from the ESA Rolling archive site.

All the involved Chinese partners were informed of the existence of this interesting data set containing two images acquired the same day, the 28 of July over the city of Harbin, an ascending and descending orbits, accessible through the Rolling Archive by SERTIT and ESA staff. Exploiting these crisis medium resolution images, acquired the 25 and 28 of July, as well as the already set up database, a set of flood extent maps products has been generated presenting flooding water, reference water, as well as very wet area covering 240 km from North to South over the Nen River enclosing the Qiqihar vicinity, the Zhalong natural reserve and 5600 square kilometres over Harbin area. (Fig. 10 and 11).

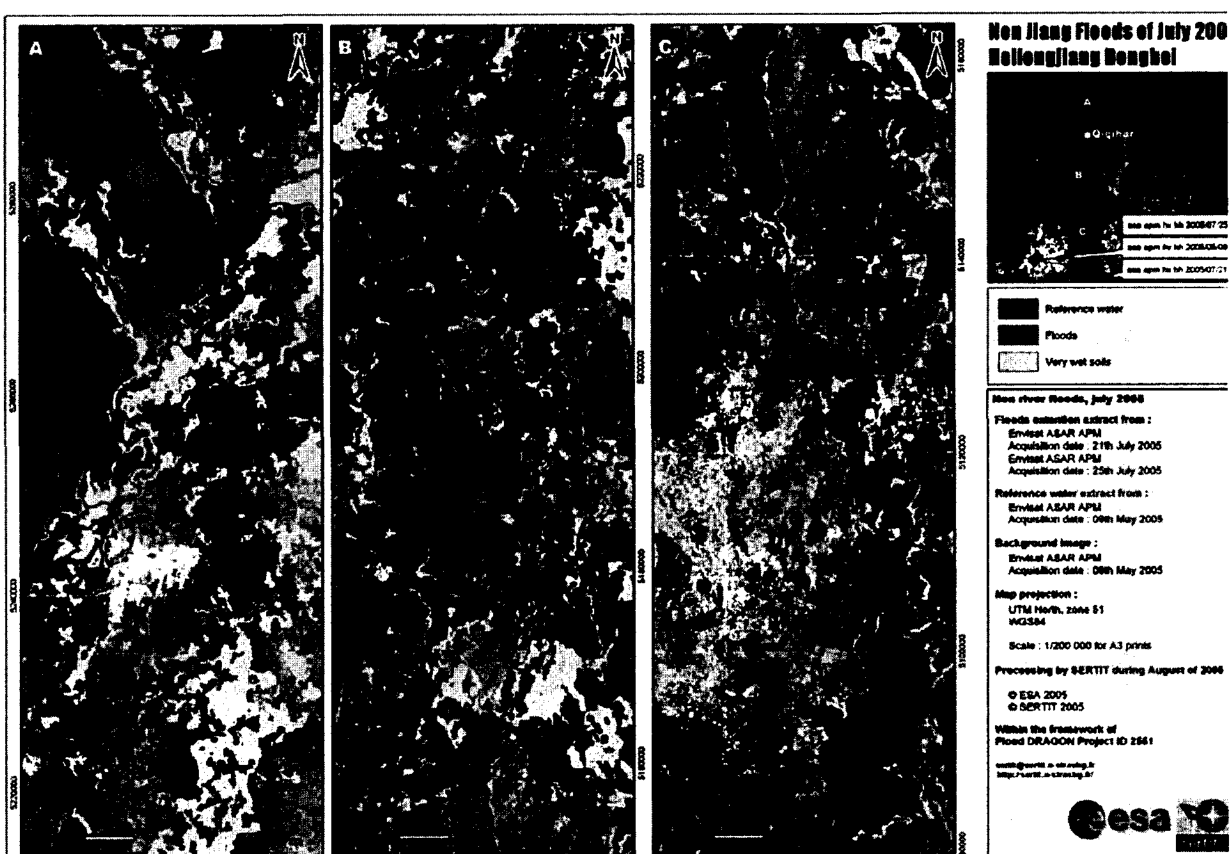

Figure 10: Flood map set up over the 240km of Nen river exploiting two medium resolution ASAR images acquired the 21[st] and 25[th] of July 2005 and reference data

Table 2: Exploited NRT data for the mapping of Nen and Songhua rivers flood.

type	resolution	incidence angle	date	mode	polarization	orbit	track
ASAR_APM	75	14	25/07/2005	D	HH	17778	11
ASAR_APM	75	15	21/07/2005	A	HH/HV	17728	8
ASAR_IMM	75	12	28/07/2005	D	VV	17821	771
ASAR_IMM	75	12	28/07/2005	A	VV	17828	443

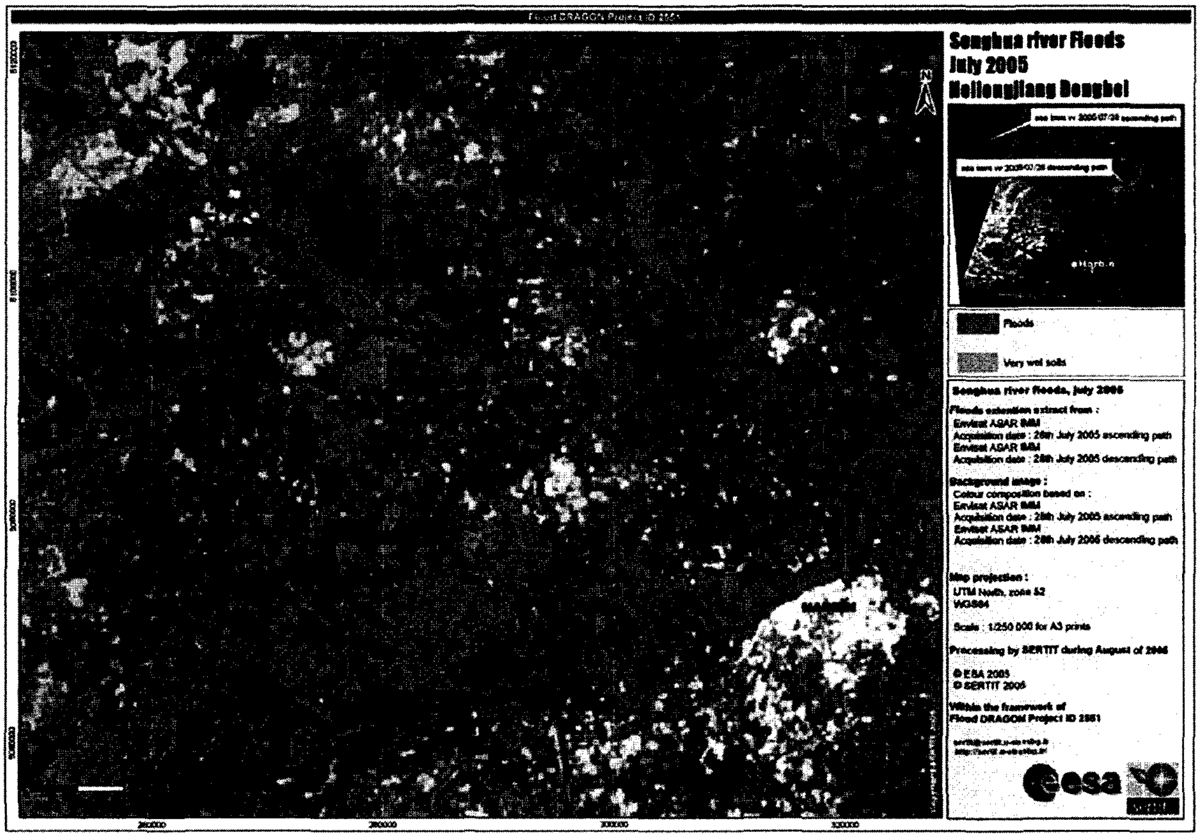

Figure 11: Flood map set up over the Harbin city neighbourhood, Heilongjiang province derived from ENVISAT medium resolution products combining ascending and descending data acquired the 28 of July 2005.

3.4. NRT mapping of the Sanyu typhoon impact over the Fujian province

Typhoon Sanvu-inflicted rainstorms hit central and southern parts of east China's Fujian Province over the 13 and 14 of August 2005, affecting 2.113 million people, 302,000 people were evacuated to safe places. Heavy rain damaged 61,500 hectares of crops and flattened 3,100 houses, causing an economic loss of 1.63 billion yuan (US$200 million), according to the provincial office for flood control. A strip of ENVISAT ASAR data, acquired 14 of August during the peak of crisis were downloaded the 16 August and processed by the IWHR rapid mapping team (Fig. 12).

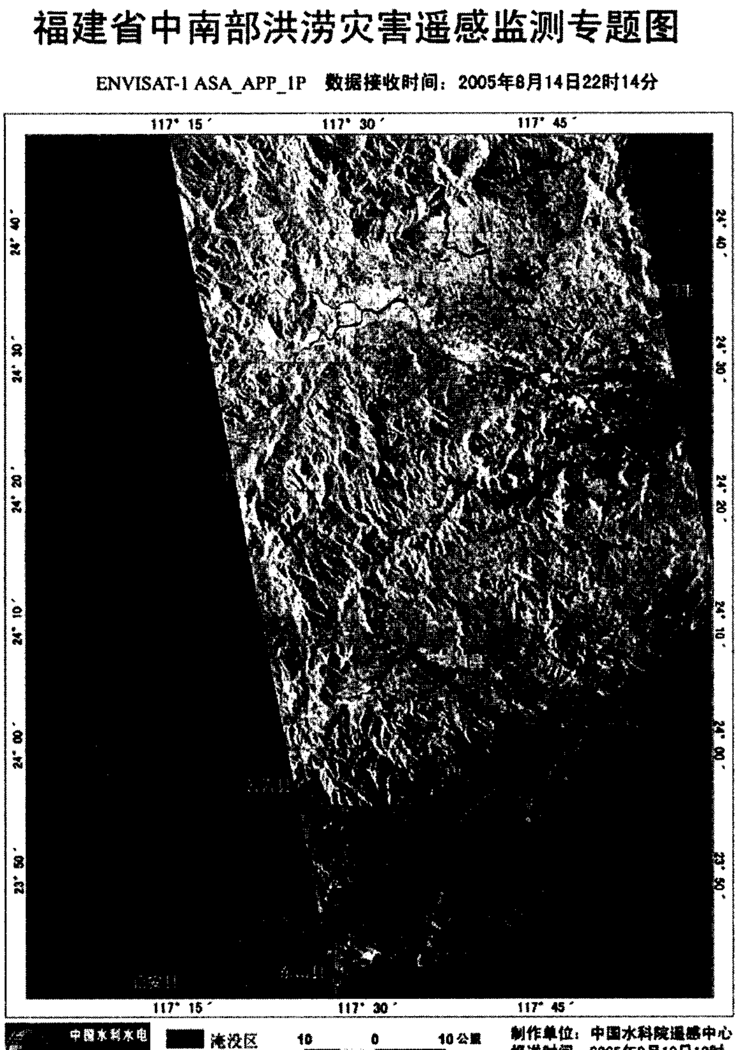

Figure 12: Extract of the ENVISAT ASAR APP stripe acquired over the Fujian province during the passage of the devastating Sanyu typhoon. Red indicates flooded area; orange, waterlogged areas.

4. CONCLUSION AND PERSPECTIVES

In spring and summer 2005, exploiting of Envisat ASAR data, a first test of NRT flood monitoring of the major Chinese flood prone as well as typhoon impact has been carried out. Over the fifteen attempts, ten were successful and five failed. Reasons of failing are mostly related to delays in information dissemination and technical fail. It is took time at the beginning to well apply the defined rules for Emergency request. While the flood season was on going, better was the knowledge exchange in procedures application, so increased the accepted requests. Plus, the two and half working days needful for programmation is also a source of request's reject as it is not always obvious to forecast up to five days in advance a flood event. For the 2006 flood season, the experience gained during this first year of monitoring will allow an higher rate of successful Emergency request. Another key issue could also be a more systematic long term acquisition plan scheduling over sensitive areas as in few cases, it were on going Ordinary acquisition scheme that have been exploited as ASAR Medium Resolution production which are systematically generated are accessible on he ESA rolling archive sites. Confirming previous studies [12], it has been shown that the medium resolution ASAR product with a pixel spacing of 75m, both Wide Swath Mode and Medium resolution strip, can provide valuable information covering in addition very large areas, up to thousands kilometres in case of IMM stripes. Therefore, if the medium resolution products provide information over natural and agricultural large area, in case of flood affecting a city, the high resolution mode is requested. For the 2006 flood season in China, a higher number of NRT requests would be allowed, and maybe the organisation of the Rolling archive could be discussed in order to provide project's dedicated directories allowing a faster recognition of data of interest. The 2005 season was focussed exclusively on the exploitation of ASAR data, for the 2006 flood period an assessment of the potential of MERIS data for NRT action should be carried over Chinese areas were dual acquisition, ie ASAR and MERIS are technically feasible in NRT in order to explore all the potential of the Envisat imaging sensors. This involve from a practical and administrative point of view to discuss the up dating of the NRT procedure defined for the Flood DRAGON project and from technical and thematic point of view to optimize the exploitation of full resolution MERIS data in a crisis context.

Acknowledgement: Flood DRAGON would like to thank ESA staff, H. LAUR, ENVISAT mission manager, and his team for allowing us access to Emergency mode, the helpdesk for his support. Special thanks also for the Chinese and ESA DRAGON staff, particularly to R. MALOSTI for her help and patience all along the year, for conflicts' resolution during the Ordinary scheduling as well as during Emergency actions. Authors would also like to associate at this paper the staff of IWHR involved in the NRT actions, Ms. Li Lin, Ms. Xu Mei, Dr. Sun Tao, Mr. Li Xiao-Tao.

5. REFERENCES

1. Tholey N., Clandillon S. and de Fraipont P, 1997: The contribution of spaceborne SAR and optical data in monitoring flood events: examples in Northern and Southern France. Hydrological Processes, .11, 1409-1413.
2. Chen Deqing, Huang Shifeng, Yang Cunjian, 1999: Construction of watershed flood disaster management information system and its application in great flooding of Yangzi River in 1998, Journal of Chinese Geography.
3. Mahmood A., Parashar S. and Giguère C., 1999: Radarsat 1 background mission data for flood monitoring. Proceedings IGARSS, Hamburg, Germany.
5. Sarti F., J.Inglada J., Landry R; and Pultz T, 2001: Risk management using Remote Sensing data moving from scientific to operational applications. Proceedings of X SBSR April 23-27, 2001 (Brasil);
6. Yésou H., Chastanet P., de Fraipont P., Dossmann P., Stock N, Béquignon J., 2001: Mapping Floods in France, Backscatter, 12, 3, 23-26.
7. Laugier O., Fellah K., Tholey N., Meyer C., de Fraipont P., 1997: High Temporal Detection and Monitoring of Flood Zone Dynamic using ERS Data around Catastrophic Natural Events: the 1993 and 1994 Camargue Flood Events, Proceedings of the third ERS Symposium, ESA SP-414, 1, 559-564.
8. Xu Mei, Li Jiren, Huang Shifeng,2003: Quickly Monitoring and Evaluation of Floodwater and Waterlogging Disaster in Huaihe River Remote Sensing and GIS Technology, Water Resource and Hydropower Engineering, 34(7).
9. Zhou C. and Luo J., 2000: Flood monitoring using multi-temporal AVHRR and RADARSAT imagery, Photogrammetric Engineering and Remote Sensing, 66 (5), 633-638.
10. Li Jiren and Huang Shifeng, 2003: *Guide for Application of ¡°3S¡± in Water Resources*, China WaterPower Press.
11. Allenbach B., Andreoli R., Battiston S., Bestault C., Clandillon S., Fellah K, Henry J-B., Meyer C., Scius H., Tholey N., Yésou H., de Fraipont P., 2005: Rapid EO Disaster Mapping Service: Added value feedback and perspectives after 4 Years of Charter Actions. IGARSS Proceedings, Seoul, Corea, 2005.
12. Henry J.-B., Chastanet P., Fellah K., Desnos Y.L., 2003: ENVISAT Multi-Polarised ASAR data for flood mapping, Proceedings of IGARSS'03, Toronto, Canada.
13. Yésou H., Li J., Li J., Wang X., Yida F., Wang Y., Huang S., Xin J., de Fraipont P., 2004: Assessment of the Synergistic Exploitation of ENVISAT ASAR and MERIS Data for Plain Flood Rapid Mapping: a Part of the Dragon Flood Project. ENVISAT Symposium Salzburg 6-10 September 2004.
14. King C, Li Jing, Costes M., Yésou H., Prinet V., 2004: WARM Water Risk. Management Research Network CEOS meeting Information, Products and Services for Disaster Management, Beijing China, 17-19 November 2004
15. Shankman D. and Qiaoli L.., 2003: Landscape Changes and Increasing Flood Frequency in China's Poyang Lake Region. The Professional Geographer, 55(4) 434-445.

MONITORING WATER LEVEL SEASONAL VARIATIONS OF LARGE NATURAL LAKE EXPLOITING ENVISAT ASAR LOW RESOLUTION TIME SERIES: APPLICATION TO THE POYANG LAKE (P.R. CHINA) DURING THE 2004 – 2005 HYDROLOGICAL PERIOD

Andreoli Rémi, Yésou Hervé

SERTIT, Université Louis Pasteur, Strasbourg Parc d'Innovation Bvd Sebastien Brant, BP10413, F-67412 Illkirch Graffenstaden, France, remi@sertit.u-strasbg.fr

ABSTRACT

Within the framework of the Flood DRAGON project, an assessment of ASAR Global Monitoring (GMM) data has been carried out over the Poyang Lake, Jiangxi province, P.R. China. This study consists of one of the first assessment of low resolution ASAR data, ENVISAT low rate mode, for land applications. Sixteen ASAR GMM images, which give a good overview of an on going situation over very large area with a high temporal revisit, was analysed, and GMM's potential for flood risk management has been assessed. A new processing chain was created including pre-processing steps (calibration, import and geo-referencing), radiometric enhancement and water bodies extraction. GMM analysis allowed the distinguishing over the very sensitive Poyang lake ecosystem, three major land cover types: permanent water bodies between February 2004 and April 2005, areas of seasonal water level variations, and wet lowlands mostly consisting of marshes. These are in very good concordance with results obtained from reference optical high resolution data. Water body extraction was performed on ASAR GMM images and a map of the annual dynamic of the Poyang Lake was elaborated. In the near future, more GMM data will be integrated within the database in order to improve the revisit frequency at critical period. Hence these first results will be compared with optical (MERIS) and radar (Envisat Wide Swath mode and Precision mode) data and, in parallel with hydrological and meteorological data over the Poyang Lake area and Changjiang catchment.

Key words: Poyang Lake, flood mapping, flood monitoring, Envisat, ASAR Global Monitoring Mode

1. INTRODUCTION

The evaluation of the ASAR modes for flood mapping is performed by synergistically using multi resolution SAR products, ranging from high resolution ASAR products to Global Monitoring Mode images. If flood monitoring capabilities exploiting High resolution SAR data has already been demonstrated [1, 2] nothing has been carried exploiting low resolution SAR data such as the ENVISAT ASAR *Global monitoring* mode which is actually mostly exploited for ice mapping and monitoring [3]. Within the framework of the Flood DRAGON project [4], an assessment of Global monitoring data which would allow a good overview of the on going situation over very large area with an high temporal revisit, has been carried over the Poyang Lake, Jiangxi province, P.R. China, a less sensitive areas, mostly agricultural and with a poor density of inhabitants Thus, a dataset of 16 ENVISAT ASAR Global Monitoring Mode covering one hydrologic year, ie January 2004 to April 2005, had been selected, pre-processed and exploited to monitor the water level seasonal variation over the Poyang Lake area. It's the first time that such a number of low resolution ASAR data was analysed and assessed for the hydrological risk management thematic.

The first step has consisted in database set up over the Poyang Lake area where high resolution DEM, optical high resolution time series have already be integrated. These optical times series are particularly interesting as covering two major hydrological stages of the lake corresponding to winter very low storage level and summer high water level. Then, ENVISAT ASAR integration and processing procedures have been developed succeeding in landscape characterisation and water level seasonal variations extraction.

2. REGIONAL OVERVIEW

Located in the Jiangxi Province, Poyang Lake is the largest freshwater lake in China and constitutes a major hydrological subsystem of the middle Changjiang basin in central China. Its extends in a flat depression at very low elevation, only a few ten meters above sea level, surrounded by mountains. The Jiangxi Province major rivers, Xiushui, Ganjiang, Fuhe, Raohe and Xinjinag, flow into Poyang Lake. The Poyang lake drainage is only a narrow outlet into the Changjiang which lies on the northern border of the province (Fig. 1). Poyang Lake is exposed to very significant seasonal variations of its water level: lake elevation varies between 13 and 18 m and his size fluctuate from less than 1,000 km² during the dry winter period to more than 4,000 km² during the summer wet season.

During normal hydrological year, Jiangxi rivers' discharge peak occurs between April and June during the rainy season, raising the water level of Poyang Lake. Jiangxi rivers'discharge decrease from July to September, but at the same time

Proc. 2005 Dragon Symposium "Mid-Term Results", Santorini, Greece
27 June – 1 July 2005 (ESA SP-611, January 2006)

the water level of the Changjiang increases. As a result, the drainage from the lake to Changjiang reverses and begins moving from the Changjiang into Poyang Lake about mid-July [5]. Thus, Poyang Lake and the lower section of the major rivers flood most years during the summer month. The major floods occur when high discharge from the Jiangxi rivers and Changjiang are concomitant. Seven major floods have occurred in the past fifty years and the most severe ever recorded was in 1998 [5].

Fig 1. Poyang Lake (PR China), localisation map

3. DATABASE AND METHODOLOGY

Database set up over Poyang Lake area include a set of optical high resolution reference data at different hydrological periods for a preliminary thematic validation, SRTM DEM and ENVISAT ASAR GMM images. Then, a processing chain for ENVISAT Global Monitoring Mode time series had been finalized with the aim of landscape analysis and water level monitoring.

3.1. Reference database set up

Reference database includes SRTM DEM and two sets of Landsat optical high resolution mosaics (fig. 2). The first set had been acquired the 10th December of 1989 during rainy season by Landsat 5 TM, and the second one the 15th July of 1999 by Landsat 7 ETM+ during low water period. According to reference [5], summer 1989 is known as a normal hydrologic year for the Poyang Lake: water level haven't exceed 20.5 m. Floods occurred in summer 1999 and water level came close to the record levels set in 1998 [6]. We suppose that low water level record in 1999 were highest than normal. These reference data have been used for hydrodynamic characterization of Poyang Lake's water level annual variations and land cover mapping (fig. 3). Water bodies and wet areas have been extracted by thresholding starting from the 2 sets of Landsat images. Lowlands, including lands below 20 m above mean sea level (msl) and overbank usually flooded, have been discriminated using SRTM DEM and medium scale landscape analysis. Finally it is 8 classes land cover map which has been dressed from EO reference multitemporal data set (Fig. 3).

These two classifications have been combined in the aim to enhanced water level annual dynamic while differentiating reference low water level, areas of water seasonal variations and wet soils associated with lowlands (Fig. 4). Water areas and water level derived from these classifications considering Poyang Lake *ss* are presented in table 1. The obtained water extents are just lower than 1000 km for the dry period, reaching more than 3500 km2 during the flood season. These values have been compared to ground truth found in literature[1]. In which it appears that water areas of the Poyang Lake vary between less than 1.000 km ^{2} to 3.583 km ^{2} according to reference [5] and Chinese Ministry of Water Resources but it can exceed 4.000 km ^{2} during severe flood [5]. Theses results tend to validate our reference database as characteristic of normal hydrologic years both for dry and rainy period.

---

[1] Others sources, but not validated ones, said that water extent could varies from 500 km ^{2} up to 4600 km ^{2}. What is certain, it is that in the middle of the XX century, the Poyang lake area covered 5200 km ^{2}, therefore land reclamation and siltation due to sediment deposit in relation with erosion in the upper part of the catchment have reduced considerably its size accentuating height of the floods and their duration. [6]

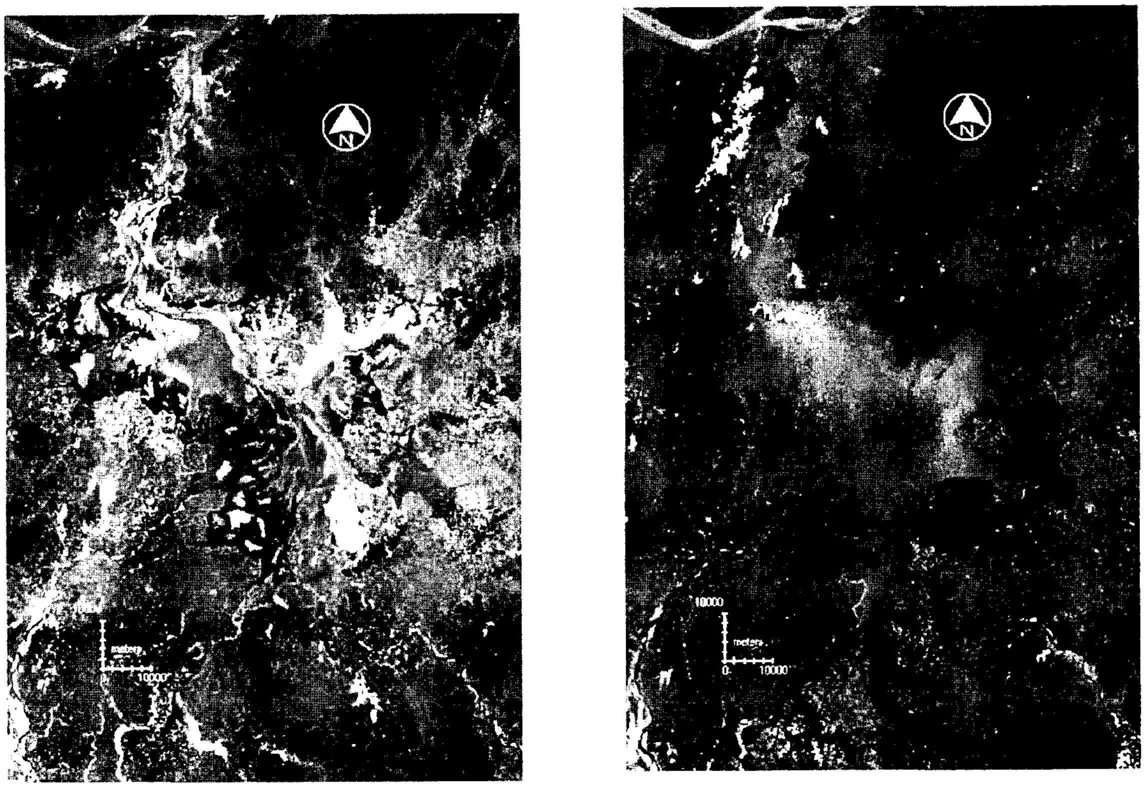

A **B**

Fig 2. A: Landsat 7 ETM + image of the Poyang Lake during dry season the 10th December 1999 ; B: Landsat 5 TM image of the Poyang Lake during summer rainy season the 15th July 1989

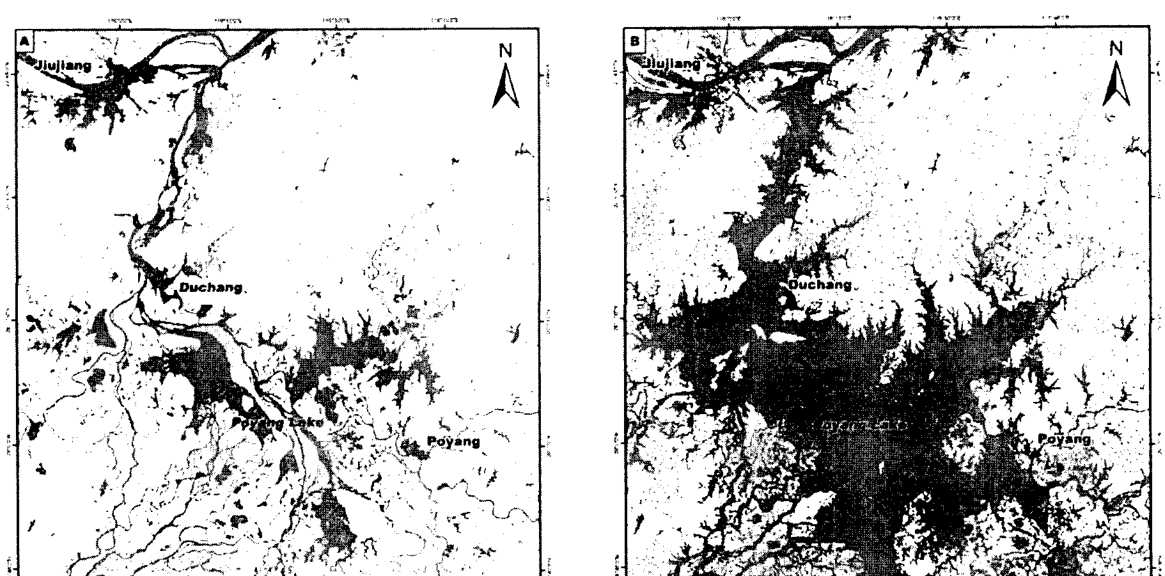

A **B**

Fig. 3 : Poyang Lake land cover during A. dry period (extracted from LANDSAT 7 ETM+ imagery of the 10th December 1999); B. Rainy season (extracted from LANDSAT 5 TM imagery of the 15th July 1989)

These two classifications have been combined in the aim to enhanced water level annual dynamic while differentiating reference low water level, areas of water seasonal variations and wet soils associated with lowlands (Fig. 4). Water areas and water level derived from these classifications considering Poyang Lake *ss* are presented in table 1. The obtained water extents are just lower than 1000 km for the dry period, reaching more than 3500 km2 during the flood season. These values have been compared to ground truth found in literature[2]. In which it appears that water areas of the Poyang Lake vary between less than 1.000 km ^{2} to 3.583 km ^{2} according to reference [5] and Chinese Ministry of Water Resources but it can exceed 4.000 km ^{2} during severe flood [5]. Theses results tend to validate our reference database as characteristic of normal hydrologic years both for dry and rainy period.

Table 1. Poyang Lake Characteristics calculated from EO reference dataset versus ground truth.

	Areas of water level during dry period	**Areas of water level during rainy season**	**Areas of water level seasonal variations**	**Water surface elevation during dry period**	**Water surface elevation during rainy season**
Calculated	995 km²	3446 km²	2451 km²	13.7 m above mean sea level (msl)	19.1 m (msl)
Ground truth	< 1.000 km²	3.583 km² (can exceed 4.000 km² during severe flood)	-	13.5 m (msl)	Between 19 and 21 m (msl)

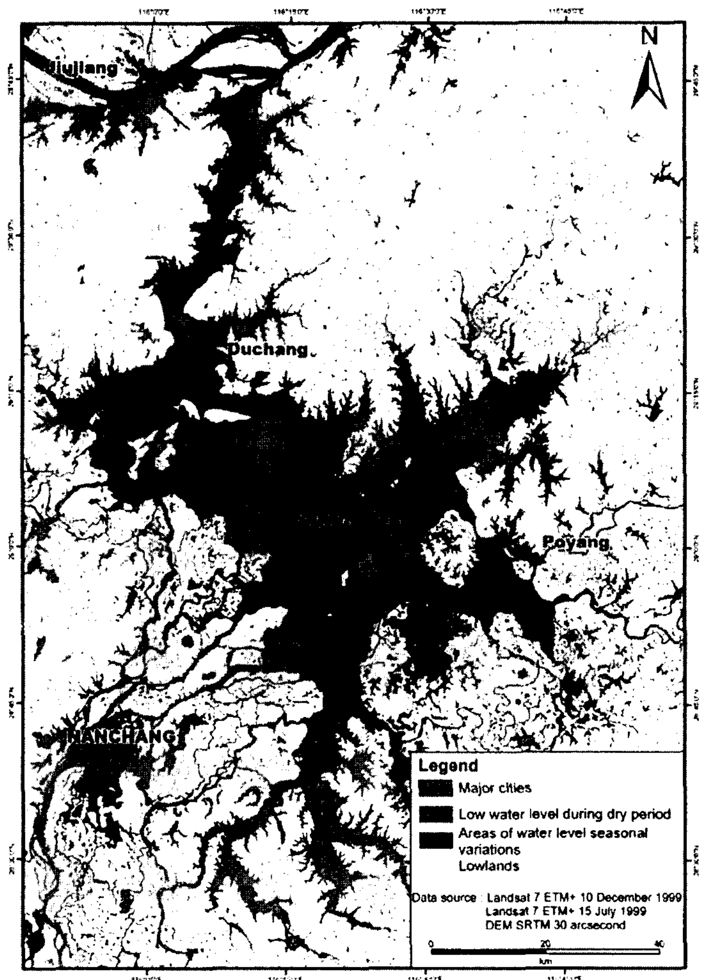

Fig. 4. Land cover of the Poyang lake area.

3.2. ENVISAT ASAR Global Monitoring Mode database

The *Global Monitoring Mode* (GMM), like the *Wide Swath Mode* (WSM), is based on the ScanSAR technique using five sub-swaths of ENVISAT either in HH or in VV polarization. This mode offers datasets with swath coverage up to 405 km and a spatial resolution of 1km for a pixel spacing of 500 m by 500 m with a theoretical ENL ranging from 7 to 9 [8]. It is a very power saving Mode, so it can gather data in permanent operation ENVISAT ASAR , having an operation capability up to 100 % of the orbit (strip of 40 000 Km). ASAR GMM data can provide a global coverage in 6 to 8 days and daily observations of the high latitude regions as the Labrador Sea, or Antarctica. Resolution of GMM products is coarse but efficient enough for large object detection; thus, GMM products are actually mainly exploited to monitor changes in sea ice extent, ice shelves and iceberg movement offerings very interesting possibilities for surveying large areas such as the Greenland region and the Northern Sea Route [9, 10].

Within the framework of the Flood DRAGN project, project 2551, a first selection of sixteen archived ENVISAT ASAR GMM images were ordered covering, on monthly basis, a period from the 20th February 2004 to the 9th April 2005. The five first images, acquired during the lake's infilling period, were in VV polarization whereas others were in HH polarization. Nevertheless, due

[2] Others sources, but not validated ones, said that water extent could varies from 500 km ^{2} up to 4600 km ^{2}. What is certain, it is that in the middle of the XX century, the Poyang lake area covered 5200 km ^{2}, therefore land reclamation and siltation due to sediment deposit in relation with erosion in the upper part of the catchment have reduced considerably its size accentuating height of the floods and their duration. [6]

Within the framework of the Flood DRAGN project, project 2551, a first selection of sixteen archived ENVISAT ASAR GMM images were ordered covering, on monthly basis, a period from the 20th February 2004 to the 9th April 2005. The five first images, acquired during the lake's infilling period, were in VV polarization whereas others were in HH polarization. Nevertheless, due to ambiguous backscattering of water body which could linked with the antenna pattern, relative position of the Poyang Lake within the images or associated with potentially bad weather conditions, the 15th June 2004 and the 08th March 2005 images have been assessed as not suitable for water extraction. Hence, it is a set of fourteen images which has been exploited; theirs characteristics are synthesised in the table 2. :

Table 2. ENVISAT ASAR Global Monitoring Mode images data set

A for Ascending; D for Descending

type	Pixel spacing	date	Hydrological period	mode[2]	polarization	orbit	track	remarks
ASAR_GM1	500	20/02/2004	Low water level	A	VV	10328	254	-
ASAR_GM1	500	26/03/2004	Infilling	A	VV	10829	254	-
ASAR_GM1	500	27/04/2004	Infilling	A	VV	11287	211	-
ASAR_GM1	500	16/05/2004	Infilling	A	VV	11559	483	-
ASAR_GM1	500	15/06/2004	Infilling	D	VV	11981	404	Not exploitable
ASAR_GM1	500	25/07/2004	High water level	A	HH	12561	483	-
ASAR_GM1	500	05/08/2004	High water level	D	HH	12711	132	-
ASAR_GM1	500	18/08/2004	High water level	D	HH	12897	318	-
ASAR_GM1	500	26/08/2004	High water level	A	HH	13019	440	-
ASAR_GM1	500	06/09/2004	High water level	D	HH	13169	89	-
ASAR_GM1	500	19/10/2004	Draw-off	A	HH	13792	211	-
ASAR_GM1	500	23/11/2004	Draw-off	A	HH	14293	211	-
ASAR_GM1	500	09/12/2004	Low water level	A	HH	14522	440	-
ASAR_GM1	500	31/12/2004	Low water level	A	HH	14837	254	-
ASAR_GM1	500	08/03/2005	Infilling	A	HH	15796	211	-
ASAR_GM1	500	09/04/2005	Infilling	A	HH	16254	168	Not exploitable

3.3. ENVISAT ASAR Global Monitoring Mode processing chain

An ENVISAT ASAR GMM images processing chain was designed and implanted. Meeting two distinct aims, water level monitoring and landscape analysis, this processing chain breaks up into three parts. First one corresponds to pre-processing steps. The second one is focussed on radiometry enhancement for landscape analysis. Finally, the third one corresponds to water bodies' extraction and water level monitoring (Fig. 5.).

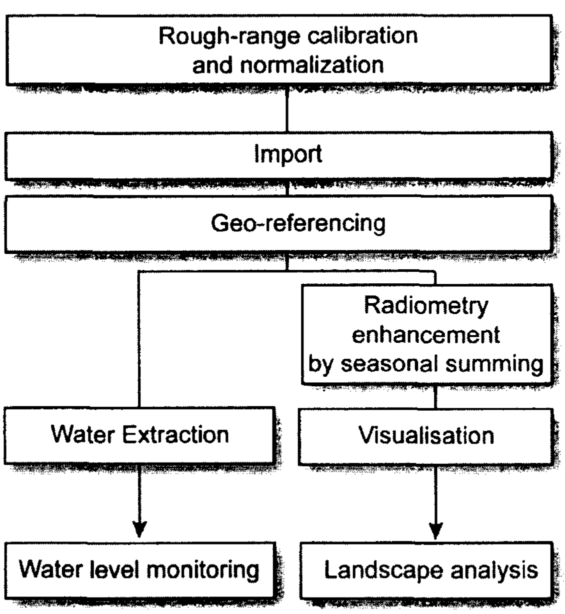

Fig. 5. ENVISAT ASAR Global Monitoring Mode processing chain

First steps consist in data calibration, data import, and geo-referencing. The antenna pattern was corrected using Rough-range calibration tool of the Basic Envisat SAR Toolbox (BEST) software. Data were standardized to make them comparable and geo-referencing on the reference dataset.

Landscape analysis required radiometric enhancement. Similar images, in terms of hydrological period at the acquisition time, polarization and mode (ascending or descending), have been summed to enhance radiometry according to the season (Table 3). It is noticeable that images in ascendant mode with polarization HH are well represented in the exploited dataset, whereas infilling period is only covered by VV data.

Table 3. Data used for radiometric enhancement by seasonal summing

Hydrological period	polarization	mode	date
Low water level	HH	A	09/12/2004
			31/12/2004
Infilling	VV	A	26/03/2004
			27/04/2004
			16/05/2004
High water level	HH	A	25/07/2004
			26/08/2004
			06/09/2004
Draw-off	HH	A	19/10/2004
			23/11/2004

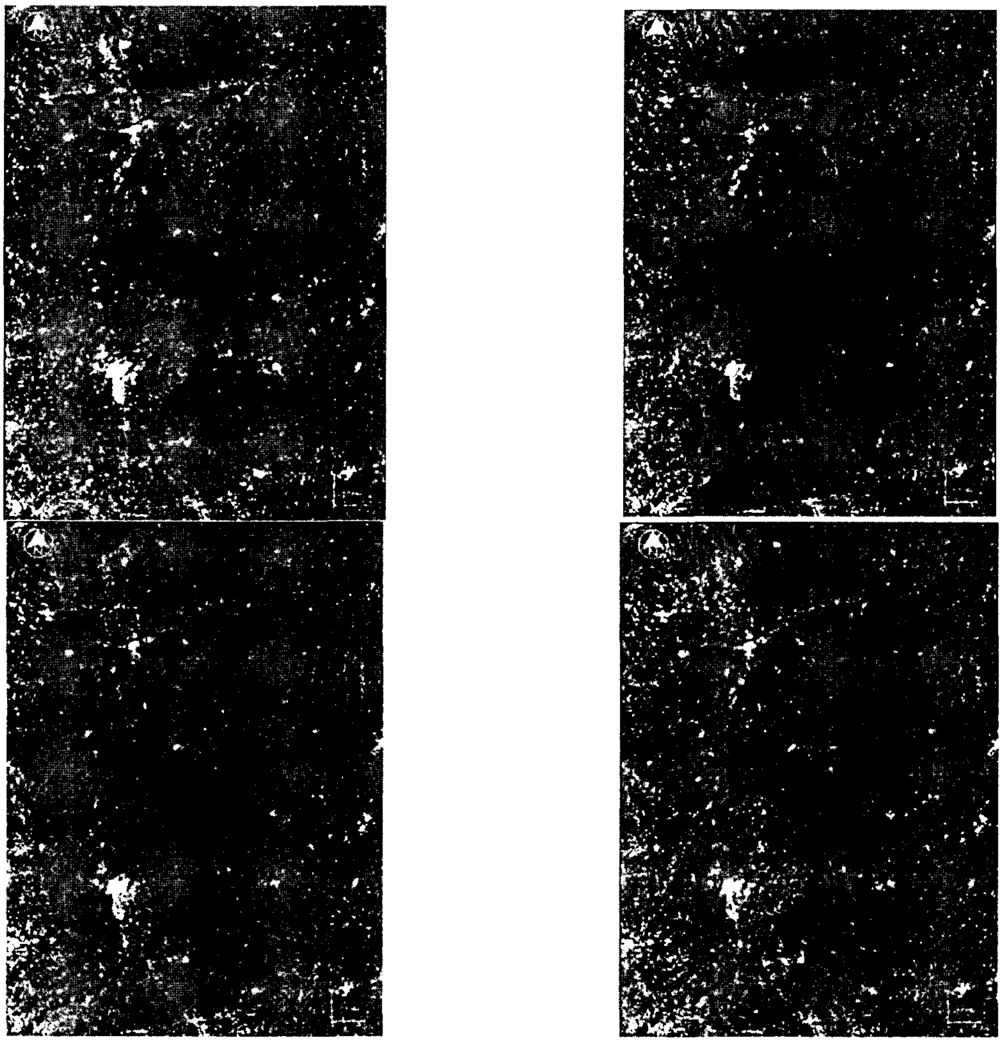

Fig. 6. Seasonal summing during; Top left: low water period; top right: infilling of the lake; bottom left: low water level period; bottom right: draw-off of the lake.

At the following step, the fourteen images were threshold in order to extract water bodies exploiting the low backscattering characteristic of water. Water level annual variations were obtained by summing the monthly averages extend of water extracted between February 2004 and April 2005.

4. RESULTS ANALYSIS

4.1. Landscape analysis

The multitemporal colour composite generated based on the seasonal summed products allowed distinguishing three major land cover types: the permanent water bodies between February 2004 and April 2005, the areas of seasonal water level variations, and the wet lowlands mostly consisting in marshes (Fig. 7. A.). From this colour composite, including information on urban area derived from reference data, a four classes land cover map has been dressed (Fig. 7. B).

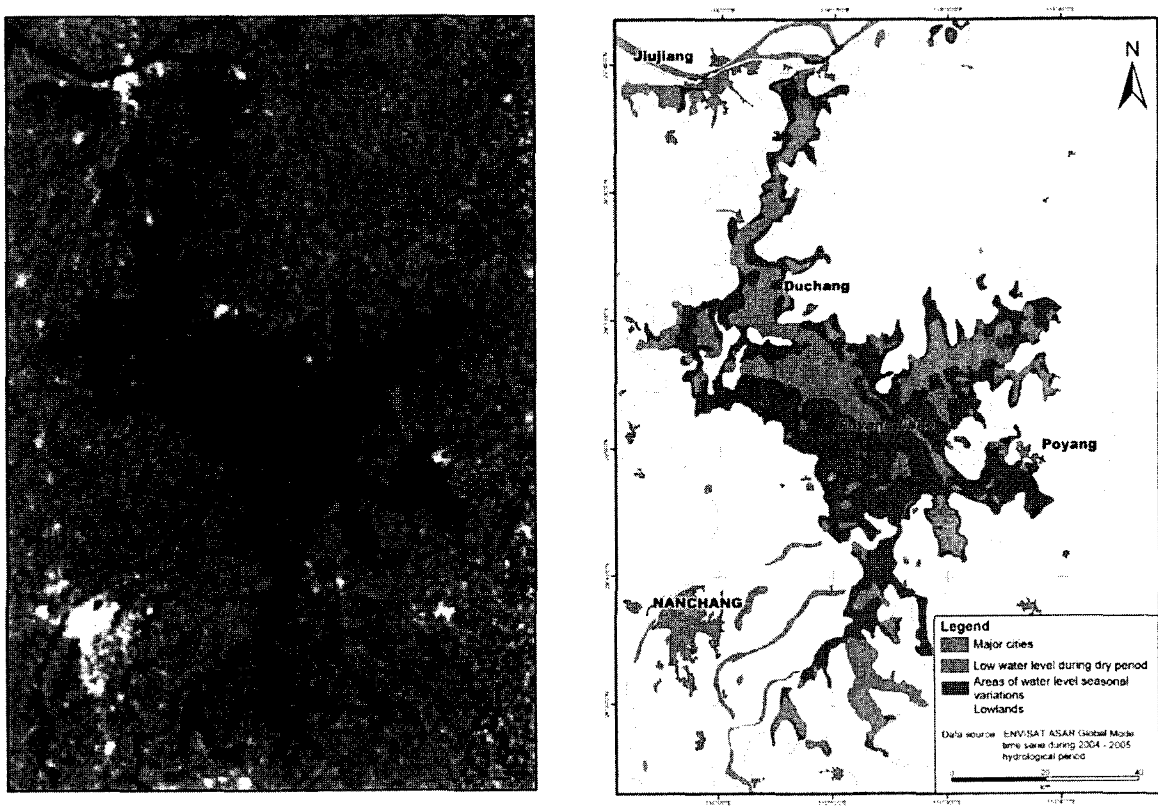

A B

Fig. 7.A. ASAR GMM colour composite with low water level (HH), high water level(HH), infilling period seasonal (VV) summings respectively in RGB; B. Land cover map derived from GMM colour composition.

Comparison of the GMM land cover map and the reference map derived from HR EO data shows that these first cartographic results are in a very good concordance (Fig. 4 and 7B). Shape of major perennial water bodies is well represented. The mapped depression of Gang and Fuhe rivers, from Nanshang to Poyang Lake, appears clearly in light green on the GMM colour composite are in a good concordance with the wet lowlands identified on the reference images. There are slight differences, for example, on the GMM derived document, the channel linking Poyang Lake to Changjiang seems to be larger than on the reference map. Therefore, there is a noticeable difference between the GMM and HR maps. From the HR EO derived map, lowlands and overbanks usually flooded, have been discriminated based on geomorphologic considerations exploiting topographic information. On the GMM derived document, these areas, appearing in green on the colour composite, have not been identified in the Changjiang valley (ie outside the area of interest on Northern part of the map) but well recognized in the depression on the Southern Poyang Lake banks (Fig.7). The following fact must be note; to dress the low resolution map, only ASAR data have been taken into account. Plus, the colour composite includes one VV seasonal summing controlling the blue layer which obviously due to a very low backscattering characterizing the Poyang lowland whereas the Changjiang banks present a middle value of backscattering. This difference in backscattering behaviour could be linked with a difference in vegetation composition and structure as lowland marshes are not the same as river banks riparian forest.

4.2. Monitoring the water level of the Poyang Lake

Water bodies' extraction had been made for the fourteen suitable GMM images. The first results consist in an estimation of Poyang Lake's area at the acquisition dates (Table 4.). If all values obtained appear concordant, the lake's surface estimated from the image of 20th February 2004 seems underestimated taking into consideration those obtained for December of the same year also acquired during a period of low water level.

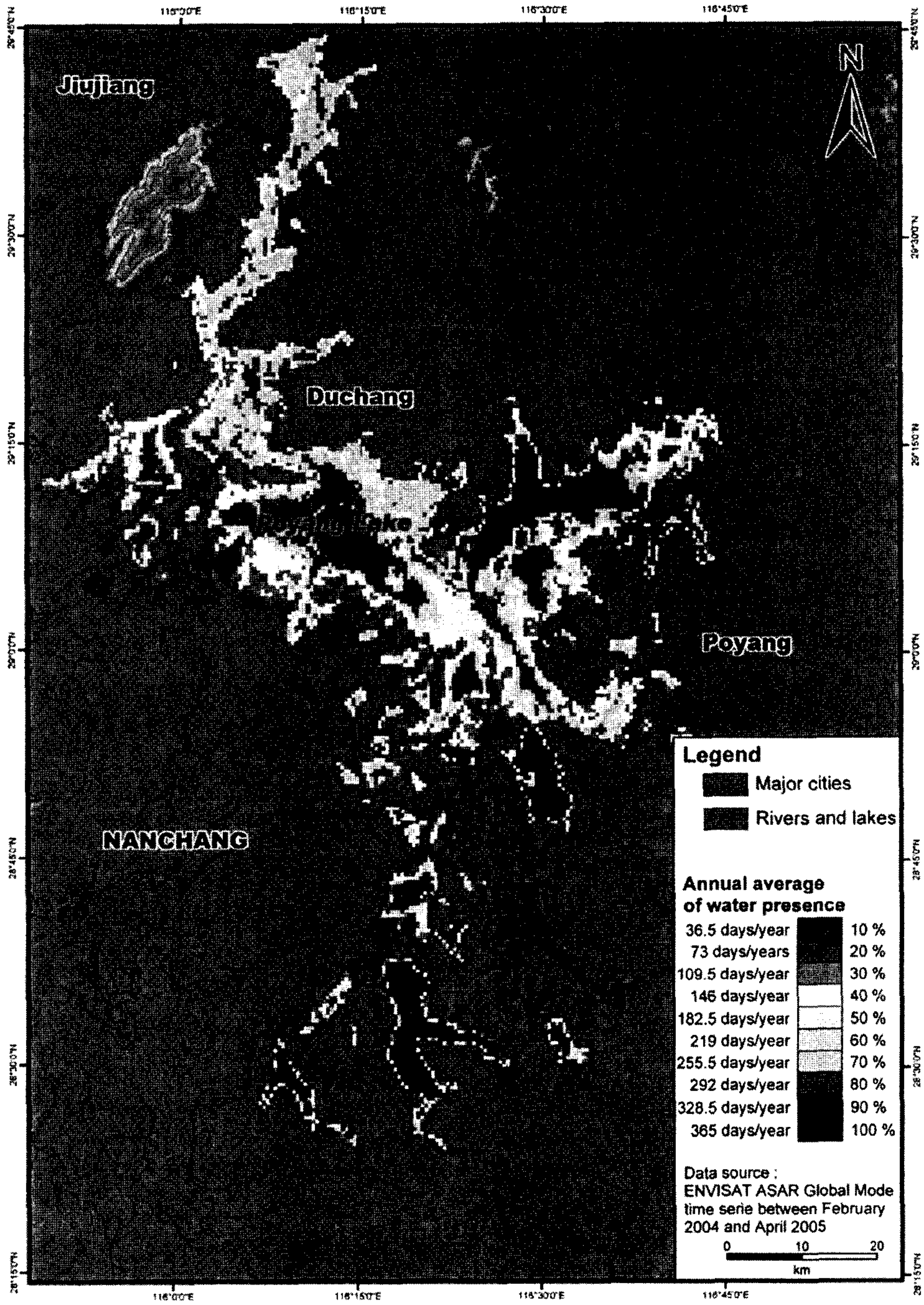

Fig.8 Poyang Lake's water level dynamic. Legend : perennial water bodies in dark blue; surfaces under water with a preliminary estimation of time of flooding (in lighter blue to red)

The results analysis indicates that during the year 2004, the surface of the Poyang Lake had not exceeded 3.000 km². Poyang Lake started to grow tardily from July to reach 2.939 km² at the end of August. This value is much lower than that of 3.583 km² found in literature [1]. These first results are in accordance with the fact that year 2004 in South-East of China was rather dry and the rain season remembered by some short but intense rainy events leading to some flooding and landslides [11, 12]. However, water's surfaces derived form EO data correspond to punctual measurement; it is also interesting to generate a map of maximal water extent. In this case the flood affected area for the year 2004 reach 3494,8 km² which is 1000 km² more than the instantaneous largest observed flood, on the 26th of August 2004 . This induce that flooding events induce not only a dilatation phenomena but also a translation of flooded area inside the depression (upstream to downstream of the bank's lake ?).

Table 4. Water surface of Poyang Lake between February 2004 and April 2005

GM	2004													2005
	20/02	26/03	27/04	16/05	25/07	05/08	18/08	26/08	06/09	19/10	23/11	09/12	31/12	08/03
Lake's area (km²)	376	1247	1567	2199	2327	2687	2377	2939	1988	1426	1175	873	992	1088

A surface average per month was calculated and added up in order to characterise the dynamics of the Poyang Lake for the period of interest, February 2004 to April 2005 (Fig. 8). This dressed map highlights perennial water bodies and surfaces under water with a preliminary estimation of time of flooding. Taking in account the largest inundated surface of the analysed times series, August 2004, as a reference surface, spatial analysis shows that

- Perennial water bodies represent less than 10% of maximal "lake" surface, more precisely 9,3 %
- 38 % of the surface is covered by water more than half a year.
- 52;7 % is covered by water less than 6 months in the year
- Areas under water less than 36,5 days/year cover 20,1 %.

These preliminary results will be validated exploiting exogeneous informations as well as EO data with finer resolution, ie ASAR Precision Image and MERIS Full Resolution Products.

5. CONCLUSION AND PROSPECTS

A consistent reference database has been set up using high resolution optical data acquired at different period of the hydrologic cycle allowing identifying 8 classes of land cover. This rich database was the key point for a rapid, fine and precise exploitation of the ASAR GMM time series.

This study consists in one of the first assessment of low resolution ASAR data, ENVISAT low rate mode, for land application, plus it is not one image but a time series of sixteen which have been exploited for inland water surface analysis. Indeed, over a complex hydrological system, ie the Poyang Lake (Jiangxi province, P.R. China),. this time series of sixteen ASAR GMM images, covering one hydrological year was analysed and assessed for flood mapping and monitoring. A complete processing chain has been set up including data calibration, import, geo-referencing, radiometric enhancement and water bodies extraction procedures.

The obtained results are very interesting and promising as well for landscape analysis as for water level variation monitoring. Firstly, over the Poyang lake area, GMM analysis allowed to distinguish three major land cover types: permanent water bodies between February 2004 and April 2005, areas of seasonal water level variations, and wet lowlands mostly consisting in marshes. These three classes are in very good concordance with those obtained from reference optical HR data. Water bodies' extraction had been made for the fourteen Envisat suitable GMM images and a map of an annual dynamic of the Poyang Lake has been generated.

The GMM exploited time series will be completed and updated in order to provide a higher temporal frequency, particularly at crucial period, such as the beginning of the flooding period, and to continue the analysis on a second or third continuous hydrologic year. Plus for validation as well as for assessment purposes, the ASAR database will be enriched, and this has already began with the integration of:

1) Envisat Wide ASAR Swath Mode, resolution 75 m, as well as high resolution radar data such as Envisat APP and/or IMP images
2) MERIS, Medium resolution optical data such as optical , FR product with a spatial resolution 300 m
3) Hydrological and meteorological data over Poyang Lake and Changjiang watershed

From a methodological point of view, further works will be carried on comparison of the mapping precision in regards to resolution and sensors type, plus a part will be focussed the extraction of secondary hydrological parameters, such as the mean height of water and its validation for which errors modelling must be considered.

These obtained results prove that application domain of GMM data could be extent for land monitoring. More generally, this approach could be renewed on other dynamic hydrological systems such as in Asia, Dongting Lake in P.R. China, Tonle Sap on the Mekong catchment in Cambodia, or in Africa, Niger delta or Chad lake. Those particular systems often correspond to densely populated areas where flood and epidemiologic risks are strong.

ACKNOWLEDGMENT:

This work have been carried out within the framework of the ESA DRAGON project 2551 and supported by ESA "Support Training of Young European Scientists Working "through a grant allocated for the project "Assessment of the synergistic exploitation of ENVISAT ASAR and MERIS data for Rapid Plain Flood Mapping". Authors are grateful for the ESA DRAGON staff, more particularly for Rita Malosti who very kindly and very professionally/efficiently provides lot of advice and help for data ordering. Thanks are also due to the EO Helpdesk for their quick and understandable help. Landsat mosaics have been obtained thank to the GLM facilities of the Maryland University, USA. Authors would finally associated SERTIT colleagues for all fruitful and animated discussions around a coffee mug or in front of a computer screen.

REFERENCES

[1] Laugier O., Fellah K., Tholey N., Meyer C., de Fraipont P., High Temporal Detection and Monitoring of Flood Zone Dynamic using ERS Data around Catastrophic Natural Events: the 1993 and 1994 Camargue Flood Events, *Proceedings of the third ERS Symposium*, ESA SP-414 1, 559-564, 1997

[2] Yésou H., Chastanet P., de Fraipont P., Dossmann P., Stock N, Béquignon J., Mapping Floods in France, *Backscatter*, 12 3, 23-26, 2001

[3] Pedersen L. T., Saldo R. Experience with the near real time distribution of Envisat ASAR data to end-users, *Proc. of the 2004 Envisat & ERS Symposium, Salzburg, Austria 6-10 September 2004,* ESA SP-572, 2005

[4] Yésou H., Li J., Li J., Wang X., Yida F., Wang Y., Huang S., Xin J., de Fraipont P. Assessment of the Synergistic Exploitation of ENVISAT ASAR and MERIS Data for Plain Flood Rapid Mapping: a Part of the Dragon Flood Project. *ENVISAT Symposium Salzburg 6-10 September 2004*, 2004

[5] Shankman D., and Liang, Q. Landscape Changes and Increasing Flood Frequency in China's Poyang Lake Region, *Professional Geographer*, Vol. 55(4), 434-446, 2003

[6] Yin H. and Li C., Human impact on floods and floods disasters on the Yangzte River, *Geomorphology*, vol. 14, 105-109, 2001

[7] Dartmouth Flood Observatory, Yangtze River in Central and Eastern China, *DFO-1999-043*; 1999

[8] ESA, *ASAR product Handbook*, 543 p, 2002

[9] Johannessen O., Sandven S., Kloster K., Bobylev L., Alexandrov V., Zaitsev A., Zaitsev L., Frolov I., Bessonov V., Shcherbakov Y., Babich N., Ninakova N. 2004 : Demonstration of ENVISAT data for sea Ice Monitoring in the Northern Sea Route, ENVISAT & ERS symposium, Salzburg, 6-10 September 2004.

[10] Andreassen T.S., ICEMON, Sea Ice monitoring in the Polar region. ENVISAT & ERS symposium, Salzburg, 6-10 September 2004

[11] Organisation Météorologique Mondiale, "Le climat de 2004", *Nouvelles du climat mondia,* n°27, 5, 2005

[12] Organisation Météorologique Mondiale, « Etat du climat mondial en 2004 », *Bulletin de l'OMM,* Vol 54(2), 87-91, 2005

APPLICATION OF ENVISAT ASAR IMAGE IN FLOOD MONITORING FOR WUZHOU CITY IN 2005

Xu Mei, Li Jiren, Huang Shifeng, Li Lin, Sun Tao, Li Xiaotao

Institute of Water Resource and Hydropower Research (IWHR), Ministry of Water Resources, P.R.China
Chegongzhuang West Road 20 , Beijing, China, 100044,
Email: xumei@iwhr.com

ABSTRACT

In 2005 summer, flood caused serious casualties and economic loss in many regions in the People's Republic of China (PRC). According to the Ministry of Civil Affairs, up to September, natural disasters across China had killed 1,630 people and caused economic losses of 163 billion yuan. Most of them is due to flood disaster or flood derived disaster, such as landslip, debris flow. According to the agreement between National Remote Sensing Center of China (NRSCC) and Europe Spatial Agency (ESA), we can get free Envisat data for flood monitoring. In 2005, we mainly depend on ESA's Envisat Advanced Synthetic Aperture Radar (ASAR) image for flood monitoring. In this paper, the advantages of Envisat ASAR image has been discussed, and a method of flood monitoring and assessment has been introduced. The application of Envisat ASAR image in flood monitoring and assessment of WuZhou city in the end of June has been carried out. The result shows that Envisat SAR is very useful data source for flood disaster monitoring.

1. ADVANTAGES OF ENVISAT ASAR IMAGE IN FLOOD MONITORING

Flood forecasting and monitoring is very important for flood control and mitigation. Remote sensing technology has particular advantages and potential in natural disaster monitoring. In China, remote sensing technology has been applied to flood monitoring and damage assessment from 1980's.

Many kinds of satellite image can be used for flood monitoring. The different image source may be chosen according to different requirement and different conditions, including flood range, time limited, precision, acquirability of data. In general, the following six kinds of remote sensing platform are most widely used in flood monitoring: meteorological satellite, land optical satellite, spaceborne SAR, airborne SAR, mid-resolution EOS/MODIS, and helicopter. Meteorological satellite image and MODIS have characteristics of wide cover range and low spatial resolution, which are fit for macroscopical, widely and dynamic flood monitoring. Both these two kinds and land optical satellite acquire image passively, data quality are importantly depend on weather condition. In this situation, radar, with capability of "all weather" monitoring and capability of penetration, become the best choice. Such as JERS SAR, Radarsat SAR, ESA's ERS and Envisat are commonly used to monitor flood.

In last several years, ESA's ERS and Canada's Radarsat-1 are the most ordinary used spaceborne SAR image source in summer flood monitoring in China. Radarsat image mainly used for flood monitoring widely happened on basin scale, ERS image mainly used for flood investigation of local regions. Flood Dragon project brings us much convenience to obtain appropriate radar image as Envisat. In this instance, we have more chance to monitor flood which occur possibly everywhere at any moment, especially in south China. The largest single instrument in Envisat satellite is the Advanced Synthetic Aperture Radar (ASAR), operating at C-band, it features enhanced capability in terms of coverage, range of incidence angles, polarisation, and modes of operation. The improvements allow radar beam elevation steerage and the selection of different swaths, 100 or 400m wide. Through the Dragon project titled 'Flood Plain Disaster Rapid

Proc. 2005 Dragon Symposium "Mid-Term Results", Santorini, Greece
27 June – 1 July 2005 (ESA SP-611, January 2006)

Mapping and Monitoring', Envisat ASAR image will be used freely for flood monitoring. In this summer, we used ASAR image in flood monitoring several times. Its capability of acquiring near real-time(NRT) image and "day and night" , "all weather" monitoring, are justly appropriate to flood monitoring.

2. METHOD DESCRIPTION

2.1. Data Preparation

Data preparation before flooding is the first step of flood monitoring. It includes real-time image ordering, background data collection and processing. Situation of rainfall and runoff are basic information for flood forecasting. Rainfall forecasting information in future days that mainly comes from weather forecast, together with real-time situation of hydrological engineering and water level of every river, lake and reservoir, help researchers making a primary estimation on where flood would occur and when it will happen. Based on the primary analysis, SAR image of the interested region can be ordered in advance more purposefully. Background data of monitoring area is important. Water body distribution at stage of normal water level will be used for making contrast with image of flood period so as to identify the area flooded or waterlogged, the social data such as population, build and economic data will be used for making damage assessment brought by flood.

2.2. Flood Rapid Mapping

Because the flood happened so urgently that the ordered image should and must be delivered to the researchers as soon as possible. The Chinese partners can acquire ASAR image from China Remote Sensing Satellite Ground Station (China RSGS) or ESA EOHelp Desk. If order success, the processed images are available to download from ESA servers within eight hours after acquisition.

After receiving ASAR raw image, first, we use EnviView software to read the data and export to geotiff format image, which can be read by ERDAS IMAGINE software; then we use ERDAS IMAGINE to project it to UTM or other kind of geographic coordination system for matching with background data; third, we compare ASAR image with image before flooding, the difference of water body distribution can be quickly identified, the region that flooded and waterlogged will be mapped rapidly.

In ordinarily, the method of automatic extraction for water area is more effective than digitalization manually. However, sometimes, it's difficult to distinguish water body with other body. For example, in mountainous area, mountain shadow is very familiar with water body in SAR image. The digital elevation model (DEM) is useful for judging which regions is flooded and waterlogged. Traditional visual interpretation can take the full advantage of human's transcendent knowledge and experience, the result is rather credible, however it is also time-consumed and strenuous. Automatic or semi automatic extracting water body is more efficient, but sometime the result is not very good. So it's better to integrate both of them.

On the thematic map of flood monitoring, the flooded area and waterlogged are respectively marked with red and orange or other color according to relative regulation, and the name of river, lake, reservoir, road, railway and important place, the important hydro-station and the water level should be mapped on as assistant information for identifying the flood situation.

Flood monitoring map is mainly used for peoples to know where flood occur and how about it, and very helpful for decision-maker to make decision for flood control and disaster mitigation.

2.3. DAMAGE ASSESSMENT

Flood mapping is the foundation for flood monitoring and assessment, but not all. It's more important to know how much loss caused by flood. That is damage assessment. The most important assessed items include casualties, ploughland, building and crucial project. It can be carried out under the function of spatial analysis in geographic information system (GIS). Coupled with land use map, building map, population density and economy gross, probable flood damage will be assessed on the basis of distribution of flooded and waterlogged area.

3. GENERAL FLOOD SITUATION OF WUZHOU IN SUMMER OF 2005

In the end of June, the water level of the branch of Guijiang River, Liujiang River, Yujiang River and main stream of Xijiang River rose badly because of strong and continuous rainfall. The regions along river suffered serious flood disaster. One of them is Wuzhou city of Guangxi provice. Wuzhou locates in downstream of Xijiang River, the flood occurred there this year was a-hundred-year return period flood. The Chendong dike of Wuzhou city was overflowed, and part of city zone was flooded, several ten thousands residents had to evacuate from their homes.

The change process of water level at Wuzhou station is described in Fig.1. The water level of the most high exceeded that of the assuring about 1.25 meters on 23 June. Until 28 June, the water level fell to that of warning about to 19.95 meters, flood control stress was catabatic but disaster had not been eliminated.

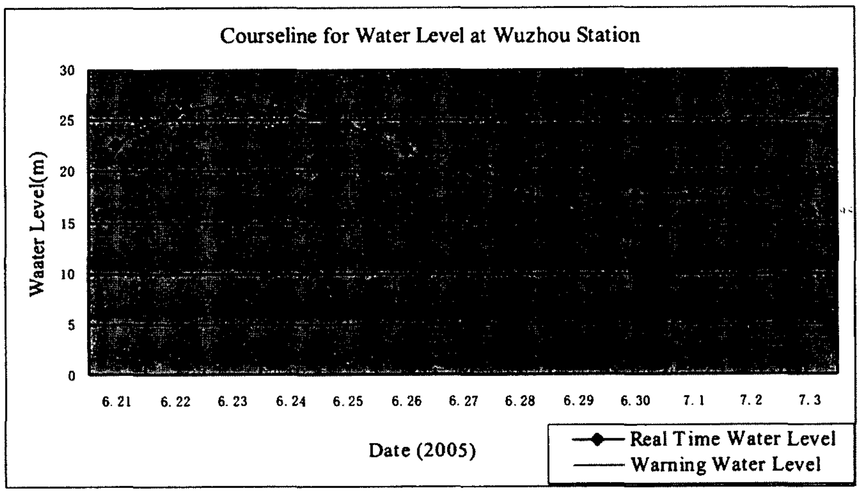

Fig.1. Process for Water Level Change at Wuzhou Station

4. FLOOD MONITORING TO WUZHOU BASED ON ENVISAT ASAR IMAGE

Flood monitoring based on Remote Sensing haS been carried out twice for Wuzhou in 2005. The Envisat ASAR image is the most important image source. The satellite overpass time for two periods of image acquired were Beijing June 25, 2005 10:38PM and July 3, 2005 10:35AM. The polarisation for first period of image is VV and for the second one is VV/HH. Due to lack of the last background vector data about water and dam, Landsat ETM+ acquired in 2003 have been used as main reference image for make comparison with Envisat image in flooding.

The monitored range is from Menxian city of Guangxi province to Yunan city of Guangdong province along the main stream of Xijiang River.

Fig.2 is the synthesized colorized image of Landsat ETM+, which shows the normal situation of monitored area. The water was not full of riverway and beach was discovered.

Fig.3 is the enhanced Envisat ASAR image and flood map of the first period, which shows that almost all the riverway were widen because of full of water and no beach was visible. Many regions along Xijiang River were flooded. The probable area of flooded is about 97km^2. In the urban zone of Wuzhou, local area of the east was flooded and the west was safe. In Guangxi province, great areas were flooded along the downstream of Guijiang River, downstream of Menjiang River, and main stream of Xijiang River. In Guangdong province, partial area in Fenkai city and Yunan city along river and downstream of Hejiang River were flooded, but the city zones were safe.

Fig.2. Image of Wuzhou before Flood (Landsat ETM+)

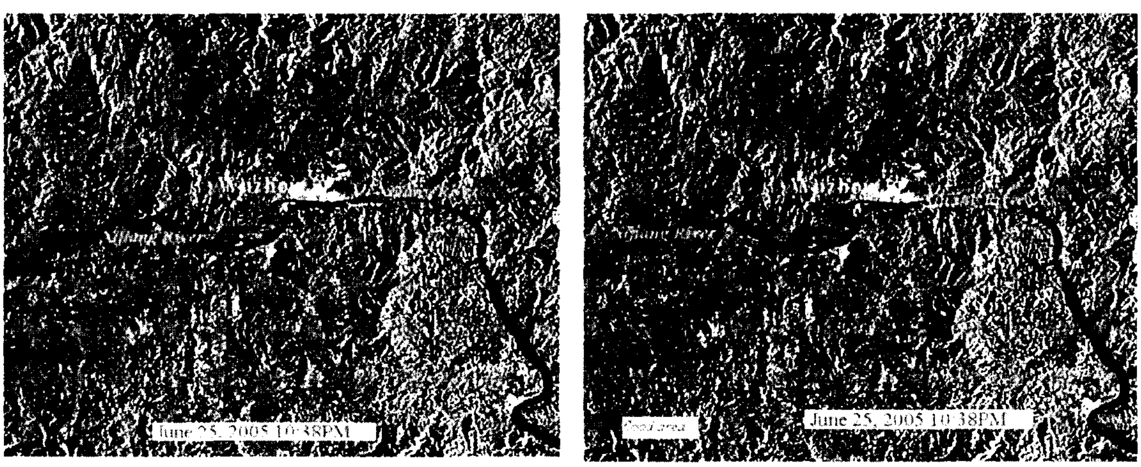

a. Envisat ASAR Image (VV) *b. Flood Map of June 25, 2005*

Fig.3. Flood Monitoring to Wuzhou on June 25, 2005

Fig.4 is the amplificatory Envisat ASAR image and flood change map between two periods. On the map, the green colored area means the flood there had disappeared and the red color means that still in flood, and the pink color means that flooded lastly after June 25. It shows that until July 4, the water level of Xijiang River had fall down on the whole, the flood had become weaken but not disappeared completely. The probable area of flooded is about 18km^2, it include the old and new flood area.

According to flood damage assessment result, a majority of flooded area of the first period is ploughland, about 64km^2, it means that agriculture there suffered calamity. The area of resident zone flooded and waterlogged is about 6.7km^2, many house were shattered. A majority of flooded area of the second period is grassland or woodland, the area of ploughland and resident zone flooded is little.

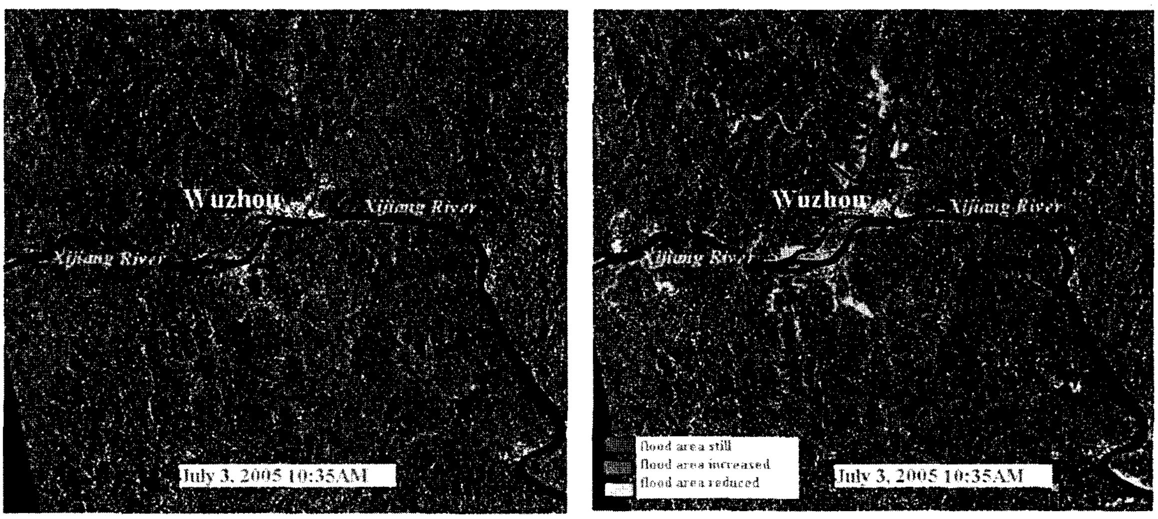

a. Envisat ASAR Image(HH)　　*b. Flood Change Map between June 25 and July 3*

Fig.4. Flood Monitoring to Wuzhou on July 3, 2005

5. PROBLEMS and CONSIDERATION

Two times of dynamic flood monitoring for Wuzhou provided direct basis for people to realize the flood happened to Wuzhou and clear about probable damage, and the most important is for correlative to make proper decision to mitigate loss. Include to Wuzhou, the researchers took advantage of Envisat ASAR image to monitor flood to many other regions of China, such as Huaihe River, Liaohe River and Fujian province and Zhejiang province where violent typhoon landed for several times and aroused local flood. It effectively supported the work of disaster mitigation.

Many problems or difficulties exit still. It mainly involved two aspects, one is limitative to data source, and the other is impercipient to flood. Because of wide range, it is possible especially in summer flood period that flood maybe happened to several province synchronously, but it's very difficult to get image of several flood risk regions at the nearly same time, in other words, the cover range of image is not wide enough to satisfied the request to monitor flood at the river scale. Another problem about image is that the special resolution is not high enough to monitor some local but pivotal damage such as to railway and dike and other important engineering. The geologic disaster caused by strong rainfall such as coast, collapse and debris flow and so on happen so frequently and are becoming the main factor that lead to calamity, but many of these scene can't been recognized expressly depending on image only. Of course the cover range and resolution are inconsistent for a long time. On the side, social and economic data of flood regions is too rough to make exact damage assessment. The other problem is the method for flood monitoring and control isn't perfect because of impercipient to flood itself. If flood monitoring depend on accurate flood forecast and integrate itself into flood forecast gradually then its significance will be more and more great, the first step for us to realize is that more and more flood disaster can be caught real-timely by image and more and more correct flood damage assessment be concluded.

6. REFERENCE

[1] Li Jiren, Huang Shifeng, *Guide for Application of "3S" in Water Resources*, China WaterPower Press, Beijing, 2003

[2] Wan Qin, et al. *Risk Analysis of Flood Disaster*, Science and Technology Press, Beijing, 2001

[3] Zhang Jincun, Wei Wenqiu, et al. Research about Monitoring to Flood by Remote Sensing, Disaster Transaction, Vol.16(1)

[4] Xu Mei, Li Jiren, et.al. Quickly Monitoring and Evaluation of Floodwater and Waterlogging Disaster in Huaihe River In 2003 Supported by Remote Sensing and GIS Technology, Water Resource and Hydropower Engineering, Vol.34(7).

Satellite Tools for Water Resources Assessment (id. 2584)

WATER RESOURCES ASSESSMENT IN THE HUAI RIVER BASIN: HYDROLOGICAL MODELLING AND REMOTE SENSING

Charles Baubion [1][2], Ghislain de Marsily [3], Li Jiren[4], Xin Jingfeng [4] , Huang Shifeng[4]

(1) *Center for Computing Geology, UMR Sisyphe, Paris School of Mines, 35 rue Ste-Honoré, 77305 Fontainebleau, France, E-mail:baubion@cig.ensmp.fr*
(2) *LIAMA, Sino-French joint laboratory in Informatics Automatics and Applied Mathematics, Chinese Academy of Sciences, Institute of Automation, PO Box 2728, 100080 Beijing, P.R. China, E-mail: baubion@liama.ia.ac.cn*
(3) *Laboratory of Applied Geology, University Paris VI, UMR Sisyphe, Case 105, 4, Place Jussieu, 75252 Paris cedex 05, France, E-mail : gdm@ccr.jussieu.fr*
(4) *Remote Sensing Technology Application Center, Institute of Water Resources and Hydropower Research, Ministry of Water Resources, No.20, West Road Chegongzhuang, 100044 Beijing, P.R. China, E-mail: lijiren@iwhr.com, xinjf@iwhr.com, huangsh@iwhr.com*

ABSTRACT/RESUME

The Huai River basin, in China is subjected to strong human pressure, and is geographically, meteorologically, and therefore hydrologically, very heterogeneous; it faces severe water management problems, concerning flooding and irrigation in particular. The Chinese local authorities are responsible for the management of the basin and the design of the infrastructure; a comprehensive water resources assessment using remote sensing technology and integrated hydrological modelling could be a great help to find long term solutions to the pending problems. In this paper, an attempt at developing such a complete water resources assessment is proposed, focusing first on a sub-catchment, the Shiguanhe watershed, which is well representative of the heterogeneity of the whole Huai river basin. The tools for this assessment are described here, both in hydrological modeling and in remote sensing. Meanwhile, a first attempt at modelling the Shiguanhe basin will help to define future developments that would allow these tools to be adapted to the Huai River basin and its complex hydraulic system, including many dams and irrigation channels. For this purpose, the MODCOU model was used; it is a distributed hydrological model using a conceptual reservoir-based approach. The processing of a digital elevation model first serves as a basis to build the structure that MODCOU needs; the model is then run with basic land-use and meteorological data, which might later be made more accurate through remote sensing data processing. A new function was developed within the MODCOU model to take the large artificial reservoirs into account. The first results provided a reasonable agreement between the measured and calculated flow at the outlet of the basin, and also showed the attention that has to be paid to the complex irrigation system, and to additional improvements that are required to accurately model such a complex system.

1. WATER MANAGEMENT IN THE HUAI RIVER BASIN

1.1 Brief description of the Huai river basin

In the great plain of east-central China, the Huai River basin (Fig. 1) is one of the seven major river basins in China and covers an area of 270,000 km². The major particularity of this basin is that the Huai River does not reach the sea directly. Its outlet is indeed a lake, the Hongze Lake. From there, a complex system of canals, connecting different lakes and river basins, finally reaches the Yellow Sea, with a yearly average discharge of 2,000-3,000 m^3/s, together with the Yangtse River, with a discharge of 12,000 m^3/s (Ref.[1]).

This part of China is located within the transitional area between the southern monsoon climate and the northern continental one. Furthermore, this meteorological duality is increased by the topography, with large plains to the north of the Huai River on one side, occupying two thirds of the basin, and a mountainous area in the southern

Proc. 2005 Dragon Symposium "Mid-Term Results", Santorini, Greece
27 June – 1 July 2005 (ESA SP-611, January 2006)

part. Thus with precipitation of 600 mm per year, the long northern tributaries run slowly toward the Huai River, where they meet the southern rivers, coming quickly from the mountains where the high precipitation (average of 1600 mm per year) occurs for 70 % from June to September, which is consequently called the flood season. From this brief introduction, we can understand that the Huai river basin shows great differences in natural geography, hydrology and meteorology.

1.2. Water management

Like all of eastern China, the Huai River basin is highly populated, its density reaches an average of 600 inh/km². In such conditions, the flood season requires appropriate measures to mitigate its impact, which can be very heavy. In 2003, for instance, with a 30-year return period flood, affecting 37 million people and killing 29 persons, the total damages were estimated at 3.5 billion US dollars (Ref. [2]). Infrastructure developments, such as dams, retentions areas, embankments may be one answer – there are now more than 5,000 dams in the basin, including 50 large ones. Reflecting on the water use in general, or on changing the way water is used, can also offer solutions. In addition to flooding, the other major water management issue is irrigation. Within the basin, the Pi Shi Hangs irrigation network is the second largest in China, provinding to the fields, between May and September, from 6 to 11 km^3 of water per year, mainly for rice production. But irrigation systems exist all over the catchment which makes the Huai River basin a complex hydraulic system, with many types of infrastructure diverting the water from one sub-basin to another. There are also two major Chinese projects in this area : the eastern and the central canals for water transfer from the south to the north, which will provide water from the Yangtse river to the arid north.

We have intentionally limited this presentation to quantitative issues, but, needless to say, the water quality is also an important issue in the Huai River basin, with many polluting sources : old industrial plants, especially in the Anhui and Henan Provinces, diffuse agricultural pollution, and a sanitation system for nearly 200 million inhabitants.

1.3. A necessary water management tool

With the flood and irrigation seasons occurring in the same period, both have a negative impact on each other. When the fields are already covered with water for the rice cultivation, they cannot absorb the heavy rains, a situation which increases the run-off and consequently the impact of the flood. Moreover, the majority of the dams are used for irrigation, and may therefore be full of water when heavy rainfall occurs, making them unable to store enough water to reduce the flooding. If we go further and consider climate change effects, which could increase the occurrence of extreme events, such as Chinese typhoons (Ref. [3]) and their effects on the borders of the Huai River basin, it becomes clear that a comprehensive water resource assessment is needed to obtain an overall image of these resources and their use, in order to evaluate long-term management options. This is a part of the complex study that we propose to conduct, focusing first on one sub-basin, the Shiguanhe basin. As tools to reach this objective, remote sensing will be widely used, together with hydrological modelling.

2. METHODS TO ASSESS WATER RESOURCES

2.1. The Shiguanhe basin

The first assessment will be made on the Shiguanhe basin using the hydrological model MODCOU. Why selecting the Shiguanhe basin ?

First, it is one of the mountainous sub-basin of the south, which receives the heaviest rainfalls, and the water from these parts of the Huai River basin is the major component of the discharge in the main river, particularly during the flood season. Second, half of the basin is in the flat valley, and the rice production is widely developed in this part with its specific hydrological behaviour, with a consistent irrigation system, composed of two large dams, several withdrawal stations and a dense irrigation network. These characteristics make the Shiguanhe basin a typical example of the Huai River basin, with an already significant area of 5,400 km², and a water resource assessment on this basin will consequently be very useful for the development of our tools, both in hydrology and remote sensing.

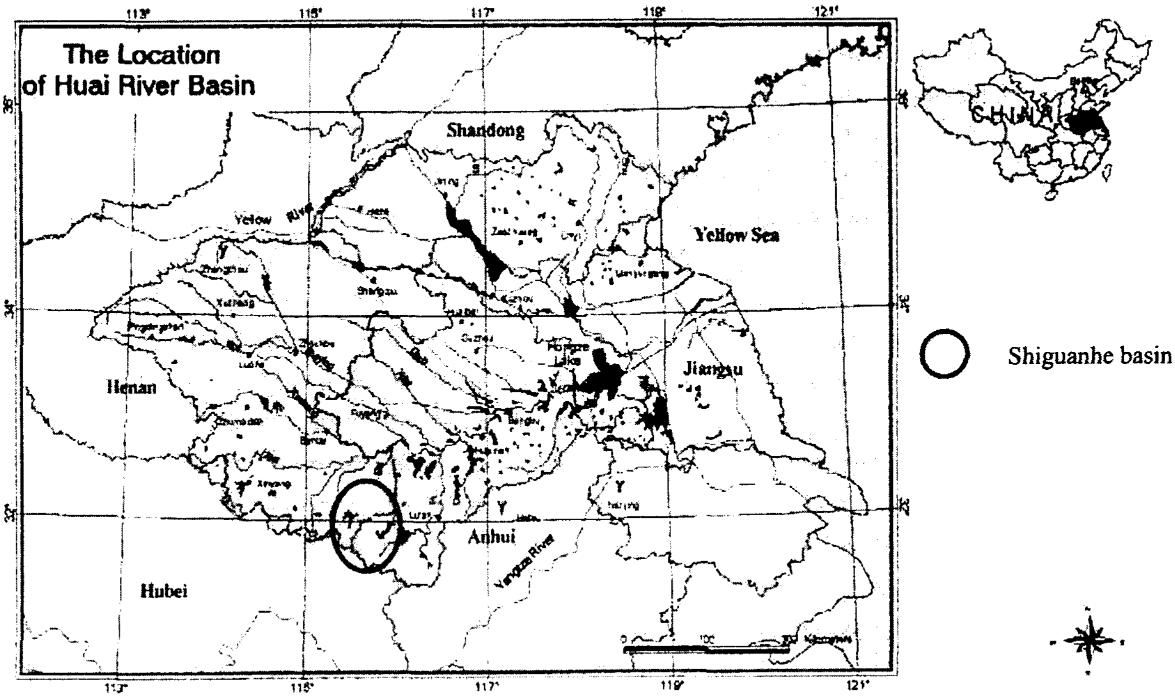

Fig. 1. Map of the Huai river basin

2.2. Description of the MODCOU model

MODCOU (Ref. [4]) is a regional spatially distributed model, which describes jointly surface and groundwater flow at a daily time step. At first, in every surface cell, surface runoff and infiltration are calculated from precipitation and potential evapotranspiration (PET) using a conceptual reservoir-based approach. Surface runoff is transferred through the drainage network with transfer times that depend on topography and a basin-wide parameter, the time of concentration. Infiltration, on the other hand, recharges the groundwater that can consist of a single or a multi-layered aquifer. A delay in the infiltration process can be imposed through the unsaturated zone between surface infiltration and aquifer recharge by means of a cascade of identical linear reservoirs. The recharge flow contributes to the dynamics of the groundwater, given in each aquifer layer by a finite-difference solution of the two-dimensional diffusivity equation. The resulting groundwater head is dynamically coupled to the water level in surface "river" cells. Depending on the hydraulic gradient between the river and the groundwater, the latter contributes to river flow or the river feeds the groundwater.

This model has successfully represented surface and groundwater flow in many basins of varying scales and hydrogeological settings. In particular, it was used to assess the hydrological impact of climate change on the Seine basin (79,000 km², Ref. [5]) or the Rhone basin. On the Shiguanhe basin, this model will calculate the discharge at the outlet, depending on the meteorological input, the management of the dams, of the irrigation channels and the irrigation practices, which will have to be taken into account as well as the land-use in the basin.

3. CLASSICAL APPLICATION TO THE SHIGUANHE BASIN

Because the Shiguanhe basin is mostly mountainous, and made of crystalline rocks, its geological structure does not favour groundwater flow. We will therefore focus on the surface hydrological part of the MODCOU model : MODSUR.

3.1. Structural building

As a distributed model such as MODSUR needs a specified geometry, we need to construct this geometry in a first step. First of all, the boundaries of the Shiguanhe watershed must be defined. To do this, we used a digital elevation model (DEM). The Shuttle Radio Topographic Mission (SRTM) DEM covers the whole world with a 3 arcsec resolution. Organised on binary rasters of one degree by one degree, the grids (Ref. [6]) are divided into 1200*1200 pixels, giving the elevation, based on the WGS 84 spheroid. The Shiguanhe basin is located between the latitudes of 31° 19' N and 32° 29' N and the longitudes of 115° 02' E and 115° 98' E. Two SRTM grids had thus to be joined : N31E115 and N32E115. To extract, join and project the DEM within the Chinese coordinates system, we used the SRTM extraction tool (Ref. [7]) under ArcView. Once projected, the pixels of the two grids do not have the same dimensions and do not cover a rectangular area. Moreover, some pixels do not have any information, on the large reservoirs for example, where the radar signal is not well received and sent back.

The question we have to answer here is : what do we need ? For the MODSUR model, we need a regular raster grid, where each cell is given an elevation. But in the first step, the elevation is needed only to determine the drainage direction required to build the structure of the watershed. The exact elevation and surface area of the reservoirs are not very important if care is taken to conserve the drainage direction. Because 3 arcsec equals around 80 m in the Shiguanhe region and because the size of the mesh must be 125 m, 250 m, 500 m or 1000 m - a divider of 1000 m, in fact, to fit well with other kinds of spatialized data that will be processed further -, we initially chose a 125 m resolution. A code was therefore built to calculate the elevation of each mesh, using an inverse distance averaging (power of two) between the points extracted from the SRTM grid and the center points of the MODSUR meshes, with a maximum distance of 125 m. For the missing data points, it allocates the smallest value between at least two adjacent meshes – the lowest value around the reservoirs represents their outlet. After several runs, we then obtained a complete regular grid, well adapted to the coordinate system.

At this stage, the DEM is sufficiently processed to serve as input to Hydrodem (Ref. [8]), the software that will define the river network and extract the watershed (Fig. 2). From the DEM, this model calculates the drainage direction of each mesh by comparison with the elevation of neighbouring meshes. Through a simple summing of the meshes along the slopes, this drainage direction map can then be used to obtain the drained surface reaching each mesh, which finally provides the river network after a threshold on this drained surface has been defined. We obtained good results with a threshold of 1000 meshes (around 15 km^2). Of course, this method does not automatically provide the correct shape of the network, and connection problems frequently occur, but could be handled with manual corrections and several attempts at defining the river threshold. Google-Earth maps were very useful in producing a good general idea of the shape which was defined by zooming either on the DEM, on the drained surface map, or on the drainage direction. Finally, we chose the outlet at Jianjiaji, the hydrological station of the Shiguanhe River, and the introduction of its coordinates into Hydrodem generated the catchment, composed of around 350,000 meshes for a total surface area of nearly 5,400 km^2. Subcatchments, drainage directions, drained surface areas and river networks are other data provided by Hydrodem for each mesh. We also used them in the next stages.

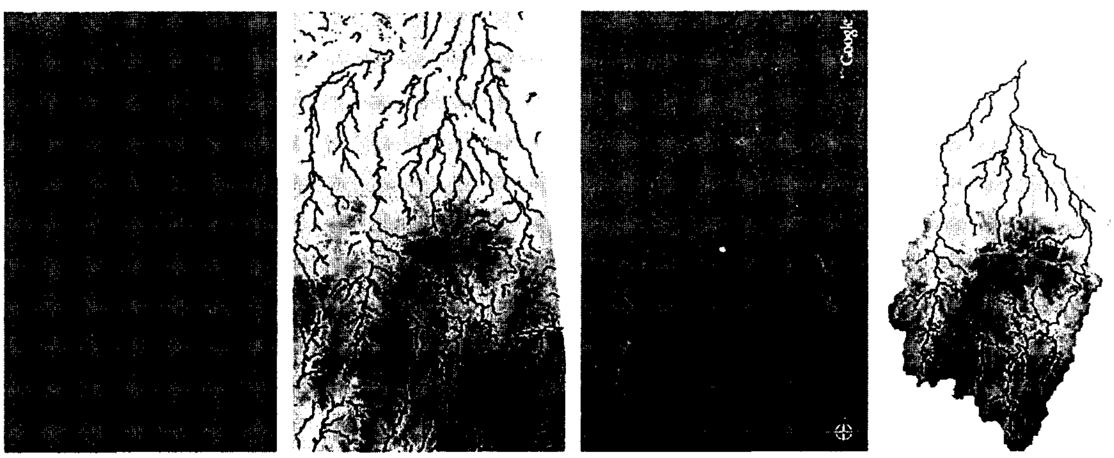

Fig. 2. Hydrodem process to obtain the DEM. Drained surface map (a) ; First river network with connecting problems (b) ; Google-Earth map of the basin (c) ; extracted watershed with corrected river network (d)

To conclude on this structural building, we have to consider the hydrologic model, making calculations on each mesh throughout the simulation period. As 350,000 meshes would need a lot of computation capacity, and as it is not necessary to have the same level of precision near the river and at the boundaries of the sub-basins as elsewhere in the basin, we used the SIGMOD model (Ref. [9]), to reduce this number by regrouping meshes. This software also calculates the attributes of the new meshes. Several levels of regrouping can be used. Here we chose four levels, so that the grid is composed of meshes with a 125 m, 250 m, 500 m or 1 000 m side. Two rules govern this regrouping. First, to be more precise near the hydrographic and the orographic networks, this means keeping the 125 m mesh size in those areas. Second, to use a size having only one level of difference with its neighbouring meshes. As a result, we obtained a grid of around 73,000 meshes, on which hydrological information can be introduced to run the flow model. This structural building as well as the subcatchments, drainage directions, drained surfaces and river network data set were obtained only through DEM processing.

3.2. Physiographical and meteorological input data

As mentioned earlier, the MODSUR model is based on a conceptual reservoir-based approach, called the production function. Therefore on each previously designed mesh, MODSUR calculates the hydrological balance between surface run-off and infiltration. Of course, this balance will not be the same in a rice-field as in a tropical forest. The soil type also has an important impact on this balance. This is why we crossed two data sets : a land-use map and a soil map (Fig. 3). We extracted these maps from the database of all of China. Hydrologically speaking, we found that we could in fact only refer to the land-use to define a typology of the production function on the basin. The two kinds of rocky soil in the south of the watershed have the same hydrological behaviour, with negligible infiltration; similarly, the eutric gley soils in the north also have a very low infiltration potential. Furthermore, this part of the basin is almost entirely occupied by rice-fields. We thus decided to limit the number of the production functions to four : rice-fields, other agricultural fields, forests, and hill grassland. Later on, we will also take into account two other specific landcovers, the urban areas and the free-water areas, such as the reservoir lakes. To do this, we will use a more accurate land-use map which will be obtained by remote sensing. For each of these production functions, we then have to calibrate a set of eight parameters which control the several conceptual reservoirs of this surface model, their filling-up and draining. Furthermore, because in winter, the farmers generally use their fields for a second crop (winter wheat for instance) after the rice harvest, the years are divided into two parts with a specific production function for each crop.

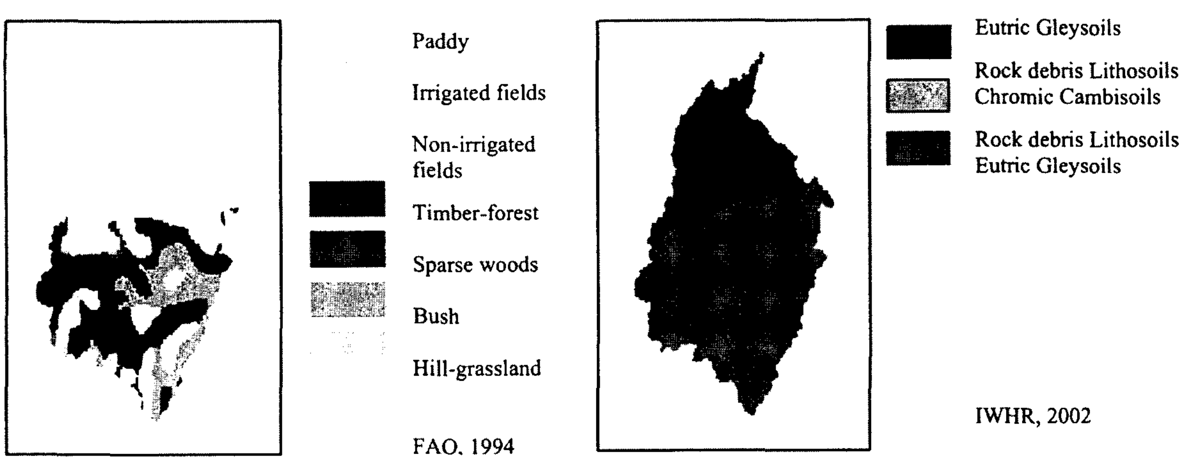

Fig. 3. Maps of the land-use and the soil types on the Shiguanhe basin

Once all the physiographical data have been processed, it is time to deal with the major input data of the MODSUR model, the meteorological data, i.e. daily rainfall and potential evapotranspiration (PET). Up to now, we have obtained three years (2001-2003) of records at five meteorological stations in the Shiguanhe basin. Unfortunately, all of them are located in the valley, and with a climate marked by orographic precipitation, the rainfall in the mountains must be heavier than in the valley. But in a first attempt, we used the traditional method of the area of influence for the distribution of these data over the whole area of the Shiguanhe basin (map of Fig.4). Remote sensing images of the clouds could also be useful for this distribution.

For the calculation of the PET, we used the Thornthwaite empirical formula based on temperature and latitude. With two meteorological stations, Huoshan (50 km to the east and in the mountainous area), and Xinyang (100 km to the west and in the valley), which are quite representative of the heterogeneity of the basin, we calculated monthly averages for the whole basin. This is quite aproximative, but nevertheless, it has been shown (Ref. [10]) that in hydrological modelling, errors on the evaluation of the PET can be balanced during the calibration of the model. Here again, remote sensing could provide a better data set, through satellite images that have the visible, near infrared and infrared bands information and by retrieving parameters such as surface temperature, surface albedo and surface emissivity.

4 INTEGRATING HUMAN-INDUCED FEATURES IN THE MODEL

4.1. The dams

As said earlier, the Shiguanhe basin represents well the Huai basin, with two major dams and a large irrigation network. Concerning the dams, since we obtained discharge data from these two dams, we decided to divide the Shiguanhe basin into three parts : the two sub-basins controlled by the dams, on one hand, and the northern sub-basin, on the other hand (Fig. 4). By adding the discharge from the dams to the meshes at their outlets through a newly built function connected to MODSUR, we can easily handle it and obtain the value of the discharge at the outlet of the Shiguanhe basin, controlled by the hydrological station of Jiangjiali. But in addition to the major dams, there are several small dams controlled by the farmers. We do not take them into account in this first attempt, but later on, the small dams should be represented either by altering the parameters of the Modcou surface storage reservoir in the production function, or by adding one special reservoir to this production function. In order to evaluate their density in the rice-field area, and the proportion of meshes affected by them, remote sensing data, such as Envisat Asar and Meris, could be used to locate and measure these water bodies. To understand how they are managed, for instance during large floods, water elevation information could be obtained from the ERS and Envisat altimeters. Furthermore, water elevation information could help to model the two southern sub-basins. Indeed, the discharge reaching the reservoirs could thus be estimated with the water level in the lakes, and provide a rule for simulating different dam management options.

4.2. First results

At this stage, several attempts with MODSUR showed that a concentration time of 4 days for the northern sub-basin was an appropriate choice. This parameter governs the whole timing process and is obtained by comparing the flood peaks as shown in Fig. 4. The available discharge measured in Jianjiali and from the dams is unfortunately incomplete.

These preliminary results show the two main components of this assessment, irrigation and floods, and their management on the Shiguanhe basin. In 2001 and 2002, the beginning of June is marked by an over-estimation of the flow by the model, which is due to the irrigation management not taken into account here. Some water is withdrawn from the river or stored in the small dams, so that the measured discharge in Jiangjiali is lower than the calculated one. Concerning floods, we have good results in 2002 (the year with the longest data record), but otherwise we underestimate the discharge, particularly in 2003, when a greater flooding occurred. Although the calibration has to be improved, this result has several potential causes : the overflowing of many reservoirs all over the basin, large and small, and thus the non-reliability of the measured discharge from the dams. There is also uncertainty about precipitation data during heavy rainfalls. In 2003, knowing that the floods all over the Huai River basin were centrally managed, we assume that the irrigation network was used in a manner very different from the usual : water could have been transferred to the Shiguanhe basin during this crisis.

4.3 Irrigation

These results also lead us to the irrigation issue. There are in fact two kinds of irrigation networks. First, those where the withdrawals in the river supply a canal which provides water to fields outside the Shiguanhe basin. In this case, we only have to withdraw water from those rivers, i.e. inverse the process used to take the dam discharge into account. We found that there was one irrigation station just north of the Meishan reservoir providing water to an irrigation zone external to the basin, the Pi Shi Hangs irrigation network (Fig. 5).

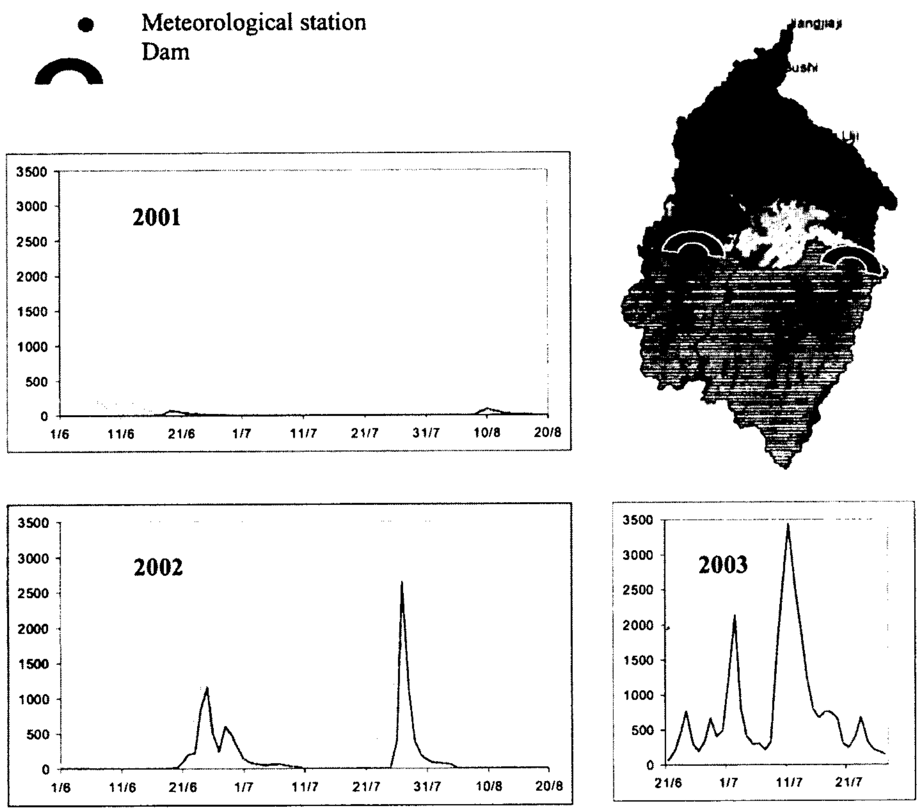

Fig. 4. Map of the Shiguanhe basin, with the 3 sub-basins and the 5 meteorological zones (upper left) and first results at the Jiangjiali stations for the period of 2001-2003. In blue, the discharge simulated by MODSUR and in red the measured one (daily average in m^3/s) during the flooding/irrigation season.

Second case, the network provides water for fields inside the basin. This water is also withdrawn from the river, but a part of it, which has to be quantified, should return to the river. Indeed, even though this water will in part be evapotranspirated by the crops, we have to take into consideration its infiltration and run-off. In fact, if the production function is well calibrated in the irrigated fields, we only need to know how much water we have to add daily to the rainfall in these fields. A first approach will be tested, knowing that an average of 500 m^3/mu (the mu is a Chinese surface unit equivalent to 0.06 ha) is needed for rice crops throughout the irrigation season (May to September), and knowing the rice growing process. But there is another important issue here : the impact of the irrigation network on the pathway of the water to the river. There is no doubt that the run-off which our model brings to the river can in fact reach a canal before the river or be stopped and diverted by the embankments of this canal.

So far, we lack irrigation data, and we do not have the irrigation network of the whole basin. Because the canals do not follow the natural topography, we cannot map them with a DEM; by using remote sensing images and then shape recognition, they might be distinguished from the natural rivers. Indeed, they are usually rectilinear, and this specific shape could be recognised by image processing.

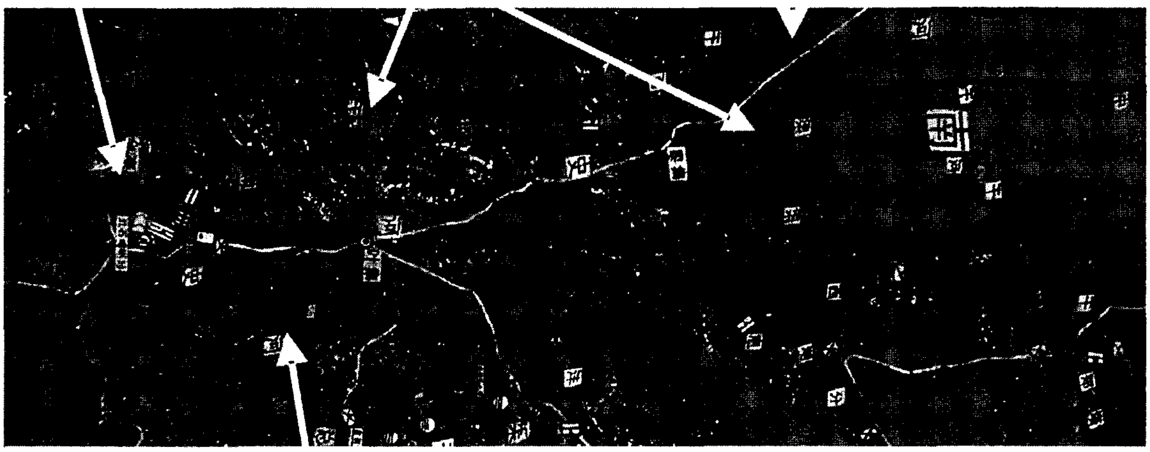

Fig. 5: Example of an irrigation network along the Shi river

CONCLUSION

At this stage of the programme, data have been assembled and processed on the selected basin, the Shiguanhe basin (5,400 km²) of the Huai River basin (270,000 km²). They consist of the geometry and elevation of the basin, its river network (from the Digital elevation Model), soil type and land use. From this data, a variable-size grid (from 125 m to 1000 m) has been built, with a total of 73,000 meshes, representing the surface hydrological system. Groundwater is not considered important in the basin. Three years of meteorological data and of discharge measurements at the outlet of two major dams and at the outlet of the Shiguanhe river have been obtained. The MODCOU model has been run and initially calibrated by comparing the measured discharge at the outlet with the calculated one, throughout the year, i.e. both in low flow and in flood situations. The first results show a reasonable agreement between the two discharges, indicating that the major hydrological processes are included and correctly represented in the model. But particular features of the Chinese landscape and water management system need to be better taken into account : water transfers between adjacent basins for irrigation or flood mitigation, and the presence and operation of a very large number of medium and small dams providing water for irrigation. A new data set with a 10 year record and 16 meteorological stations will soon be available, and will allow us to improve the calibration of the model. Remote sensing data will also be tested to improve the characterization of the land-use, to determine the position of the water transfer and irrigation channels, and to understand the operation rules of this very complex water management system. Once the model will satisfactorily represent the hydrological functioning of the basin, different management options will be tested, under present climate conditions or for future climate scenarios.

REFERENCES

1. Huai river Commission, Ministry of Water Resources, *Atlas of Huai river basin*, Science Press, Beijing PR China, 1999.

2. Liu, J., Wang, L., Wang, J., Huai river flood in 2003 and its forecasting, prediction and dispatching, 2nd Asia Pacific Association of Hydrology and Water Resources Conference, Singapore, 2004.

3. Knutson, T.R., Tuleya, R.E., Impact of CO_2-Induced Warming on Simulated Hurricane Intensity and Precipitation: Sensitivity to the Choice of Climate Model and Convective Parameterization, *J. Of Climate,* Vol. 17 : 3477-3495, 2004.

4. Ledoux, E., Girard, G., de Marsily, G., Villeneuve, J.P., Deschenes, J., Spatially distributed modeling: Conceptual approach, coupling surface water and groundwater. In: Morel-Seytoux H J, editor. *Unsaturated Flow in Hydrologic modeling - Theory and Practice.* NATO ASI Ser. C, volume 275. Kluwer Academic, Norwell, Massachussett, pp. 435-454, 1989.

5. Ducharne, A., Théry, S., Billen, G., Benoit, M., Brisson, N., Garnier, J., Kieken, H., Ledoux, E., Mary, M., Mignolet, C., Mermet, L., Poux, X., Sauboua, E., Schott, C., Viennot, P., Abu Alkhair, A., Baubion, C., Curie, F., Ducos, G., Gomez, E., Lebonvallet, S., Olive, G., Sicart, J.E., Influence du changement climatique sur le fonctionnement hydrologique et biogéochimique du bassin de la Seine. (*Influence of climate change on the hydrological and biochemical functioning of the Seine basin).* Rapport final du projet GICC-Seine, UMR Sisyphe, Paris, 60 pp., 2005.

6. Those data are available at this adress ftp://e0mss21u.ecs.nasa.gov/srtm/.

7. This tool was developed by the Remote Sensing and Land Management Laboratory of the ESA Purpan, Toulouse, France

8. Ducharne, A., Golaz, C., Leblois, E., Laval, K., Polcher, J., Ledoux, E., de Marsily, G., Development of a high resolution runoff routing model, calibration and application to assess runoff from the LMD GCM. *J. Hydrol*, 280: 207-228, 2003.

9. Etchevers, P., Golaz, C., Habets, F., Noilhan, J., Impact of a climate change on the Rhone river catchment hydrology. *J. of Geophys. Res.*, 107 (D16): ACL6 1-18, 2002

10. Andreassian, V., Perrin, C., Michel, C., Impact of imperfect potential evapotranspiration knowledge on the efficiency and parameters of watershed models. *J. Hydrol.,* 286: 19-35, 2004.

Forestry

Deriving Forest Information from PolInSAR Data (id. 2556)

CASE STUDY OF FACTORS AFFECTING TREE HEIGHT INVERSION PERFORMANCE USING SIR-C/X POLARIMETRIC INTERFEROMETRIC SAR DATA OF HETIAN TEST SITE IN CHINA

E.X. Chen[(1)], Z. Y. Li[(1)], K.P. Papathanassiou[(2)],T. Mette[(2)], S. R. Cloude[(3)]

[(1)]*Chinese Academy of Forestry, Beijing, 100091, PRC. China*

chenerx@forestry.ac.cn , zengyuan.li@forestry.ac.cn

[(2)]*DLR, Microwave and Radar Institute, D-82230, Wessling, Germany*

kostas.papathanassiou@dlr.de, tobias.mette@dlr.del

[(3)]*University of Adelaide, South Australia, 5005, Australia*

scloude@eleceng.adelaide.edu.au

ABSTRACT

In order to evaluate and study polarimetric SAR interferometry tree height inversion algorithm, three passes of SIR-C/X SAR L band full polarization SLC data were acquired for the same imaging area in the western region of *Hetian* district, *Xinjiang Vygur* Autonomous Region of PRC. China. The three images acquired in separate days of Oct. 7, Oct.8 and Oct. 9 of 1994 makes the study of the factors affecting performance of three-stage tree height inversion methodology possible. In addition to the SAR data, two scenes of Landsat TM/ETM+ data, one Land cover map and some sheets of 1:50000 topographic maps covering the test site were collected. Firstly, the INSAR preprocessing methods, such as sub-pixel accuracy co-registration, baseline estimation, flatten phase removal, effective wave number and incidence angel images generation, and the three-stage inversion method were outlined. Then data processing and tree height inversion results were analyzed. Some points established from physics theory and simulation POLInSAR data in some publications were confirmed by the primary results of the case study: It has been observed that the tree height image generated from full model inversion (FMI) is much noisy, and better inversion result was observed with vegetation bias removal (VBR) method; The maximum DEM difference (MDD) method can underestimate forest height. Some possible error sources that can lead to worse inversion result have been analyzed and the way to solve this problem has been suggested.

Keywords: POLinSAR, tree height, three-stage inversion, volumetric decorrelation

1. INTRODUCTION

As one of the approved DRAGON cooperation project between Chinese and European scientists, "Technique for deriving forest information from polarimetric SAR interferometry" aimed to study the potential impact of the POLinSAR technique on forestry application in China; to review the current status of POLinSAR research in China and Europe and enable technology transfer where required; to establish possibilities for future collaborative research aimed at development and validation of quantitative forestry remote sensing applications using POLInSAR techniques. The project has been formally started since the **DRAGON** programme kick off symposium hold from 27 to 30 April in Xia Men, Fujian Province, China. This project need POLinSAR data as inputs, but there is still no established test sites in China because of lacking of airborne full-polarization InSAR systems in China. But space-borne SIR-C multi-temporal InSAR images with full-polarization have been acquired from NASA to support this project by Chinese experts. This

Proc. 2005 Dragon Symposium "Mid-Term Results", Santorini, Greece
27 June – 1 July 2005 (ESA SP-611, January 2006)

paper summarized the primary achievements for the established SIR-C/X SAR POLinSAR Hetian test site in Xinjiang Autonomus Region of PRC. China.

Successfully tree height inversion result using SIR-C/X repeat pass POLinSAR dataset was published in 1998[1]. One generalized tree height inversion frame proposed for single baseline polarimetric interferometry was published in 2001[2]. A simplified three-stage inversion method for the estimation of underlying ground topography, vegetation height and mean extinction from single baseline polarimetric interferometric SAR data has been developed in 2003[3]. In this paper the tree high inversion methods developed in [3] were applied in order to evaluate their performance using the SIR-C/X POLinSAR datasets acquired in the Hetian test site. Some error sources were analyzed to explain the tree height estimate results obtained.

2. TEST SITE AND EO DATA

The test site is located in Hetian District of the Xinjiang Autonomus Region in the west of China. The geographical location of the test site is from 79°14′E~79°44′E and 36°48~37°14′. Fig.1 shows the location of Hetian in the County and city-boundary vector map of China. Totally 6 scenes of SIR-C/X SAR data have been acquired for this test site: three in L band and three in C band. All the images were covering almost the same region in the western part of Hetian district. Tab. 1 shows the two L band SLC images have been investigated and analyzed in this paper.

One scene of Landsat TM data and one scene of Landsat ETM+ data were collected. The Landsat TM data was acquired in Oct. 15, 1990; the Landsat ETM+ data was acquired in Oct. 24, 2000. Both of them were taken in the same month but with 4 years ahead and 6 years late to SIR-C/X SAR data respectively. Fig.2 shows the location of SIR-C/X SAR data coverage in the geo-referenced TM image (1990.10.15, R: band 5; G: band4; B: band3). Red box is the SIR-C/X SAR coverage, where the major land cover is agriculture filed, some forest stands (fruit orchard), grass land and farm houses.

One land cover map in vector format shown in Fig.3 has been collected for understanding of the ground cover in this region. The map was generated in 1996 through manual interpretation of Landsat TM data by trained and experienced local people under the supervision of remote sensing experts. Fig.4 shows the Landsat ETM+ image of this agricultural area. Topographic map sheets in the scale of 1:50000 and 1:100000 have been collected for the whole coverage of this test site.

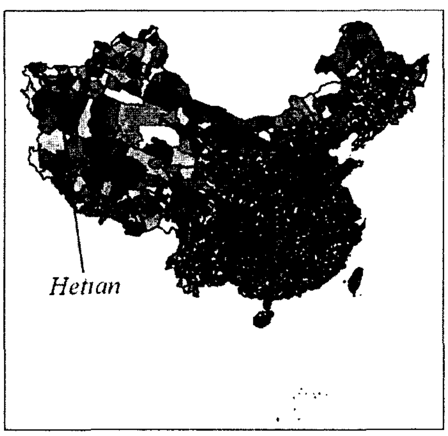

Fig. 1. The location of Hetian in China map

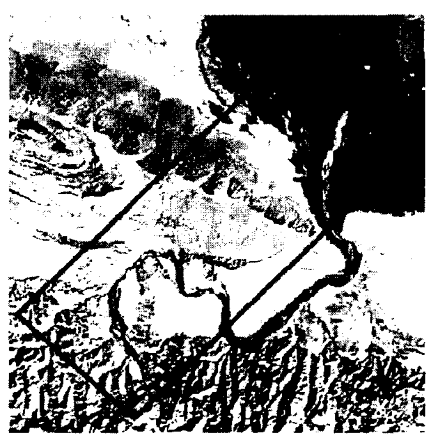

Fig. 2. SIR-C/X SAR coverage on TM image

Tab.1 *The SIR-C/X SAR dataset for Hetian of Xinjiang Autonomous Region, China*

Id number	Sensor imaging date	Band	Asc/Desending	INSAR definition
Pr42398	1994.10.07	L	Ascending	Master $[S]_1$
Pr42400	1994.10.08	L	Ascending	Slave $[S]_2$

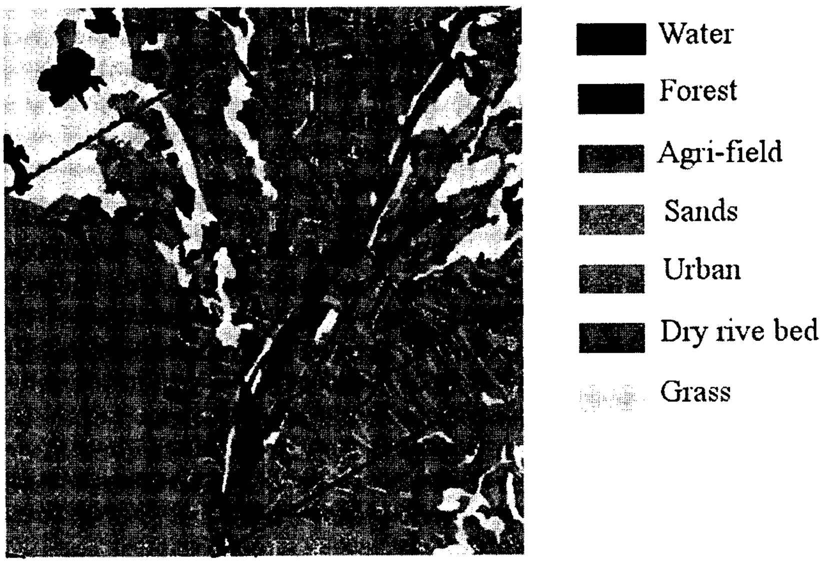

Fig.3. Land cover map of the test site: red box shows the SIR-C/X SAR covering region (only the up part agricultural region shown here. There is not much vegetation cover in other regions of the test site.

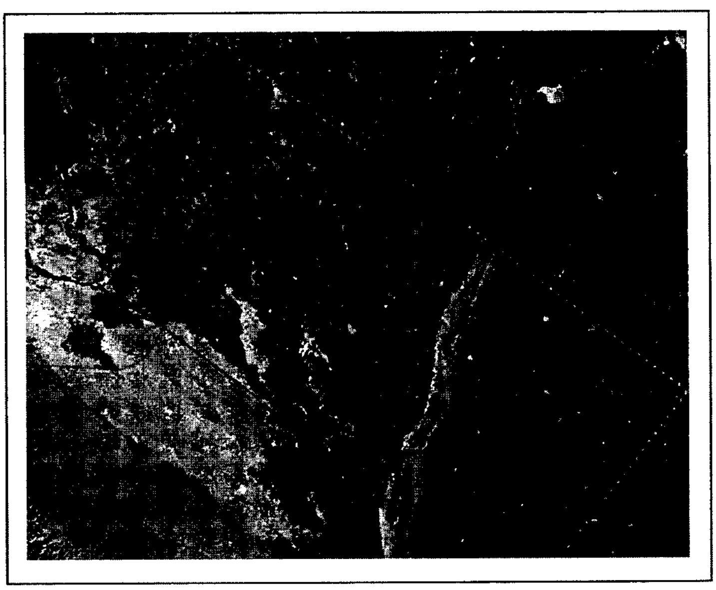

Fig. 4. Landsat ETM+ image of 2000.10.24 for the agricultural region of the test site. R: band 5; G: band4; B: band3

3. POLARIMETRIC & INTERFEROMETRIC DATA PROCESSING

3.1 Interferometric data processing

The general INSAR data processing routes have been adopted to carry out the data pre-processing procedures: (1) decompression of SIR-C/X SAR from its compressed scattering matrix; (2) master to slave image co-registration based on intensity image multi-resolution sub-pixel accuracy auto-registration algorithm; (3) Resample slave image to the master image space; (4) baseline parameters estimation using azimuth line and range pixel offset file generated from the auto-registration procedure; (5) computation of flat earth phase image, incidence angel image and effective wave number image. These steps can be introduced with the real datasets in more detail as follows:

(1)Extracting SLC data from compressed SIR-C quad Polarization-SLC data file

The extracted images from this step are: $[S]_1$ matrix for pr42398 and $[S]_2$ matrix for pr42400 in 4 data files denoted as
$[S]_1$: hh1_slc.data, hv1_slc.data, vh1_slc.data, vv1_slc.data
$[S]_2$: hh2_slc.data, hv2_slc.data, vh2_slc.data, vv2_slc.data

(2) Mater dataset to slave dataset co-registration. hh1_slc.data and hh2_slc.data were used for sub-pixel co-registration to get mater to slave range pixel and azimuth line offsets. The polynomial function used to resample the slave dataset to the image space of master dataset were computed with range and azimuth offsets as input. The results of this processing: range pixel and azimuth line offset file and the polynomial function for re-sampling.

(3) Re-sample $[S]_2$ to $[S]_1$ image space and multi-look both $[S]_1$ and $[S]_1$ with 2 looks in range and 4 looks in azimuth. The results are as follows:
$[S]_1$: hh1_mlc.data, hv1_mlc.data, vh1_mlc.data, vv1_mlc.data
$[S]_2$: hh2_mlc_registered.data, hv2_mlc_registered.data, vh2_mlc_registerd.data,
vv2_mlc_registered.data

(4)Baseline estimation using offset points generated from step 2 and other geometry parameters. From this function baseline geometry parameters were estimated: Horizontal baseline -200.88 m; Vertical baseline 54.18 m; Horizontal baseline rate -3.66E-005 m/m and Vertical baseline rate 2.18E-005 m/m.

(5) Flat earth phase image, incidence angle image and effective vertical wave number image computed with baseline and other imaging geometry parameters were demoted as: kz.data, earthph.data and theta.data respectively.

3.2 Polarimetric interferometric coherence and tree height inversion method

The hh1_mlc.data, hv1_mlc.data, vh1_mlc.data and vv1_mlc.data of $[S]_1$ and hh2_mlc_registered.data, hv2_mlc_registered.data, vh2_mlc_registered.data and vv2_mlc_registered.data from $[S]_2$, as well as the kz.data, earthph.data and theta.data were taken as inputs to the three-stage tree height inversion tool developed in [4]. Based on coherence images of HH-HH, HV-HV and VV-VV, the following three kinds of tree-height inversion routes have been investigated:
1) Maximum difference inversion (MDD);
2) Vegetation bias removal inversion (VBR);
3) Full model inversion (FMI).

4. RESULTS AND ANALYSIS

4.1 Polarimetric and interferometric data processing results

Fig.5 shows HV-HV coherence's phase images before (plate a.) and after (plate b.) earth phase flattening for the whole image. Please note that there is one red box on both images. Currently we only use the image shown in the box for tree height inversion. This small region is relatively flat, however, the low part of this image is in mountainous region and the interferometry fringes are not so clear, which was probably caused by topography decorrelation.

For all the images shown in this paper, the range direction is from left to right; and azimuth direction is from top to down. Fig. 6 shows some coherence phase images. The complex coherence images have been flatten using flat earth phase computed from co-registration offset points and imaging geometry. So Fig.6 shows the phase pattern caused by the real topography. These phase fringes were compared with the elevation contours of the 1:50 000 topographical map, their changing patterns are consistent with each other. So the baselines parameters estimated should not be so much deviated from their true values, which can never be found out for space-borne system without precise ground control points.

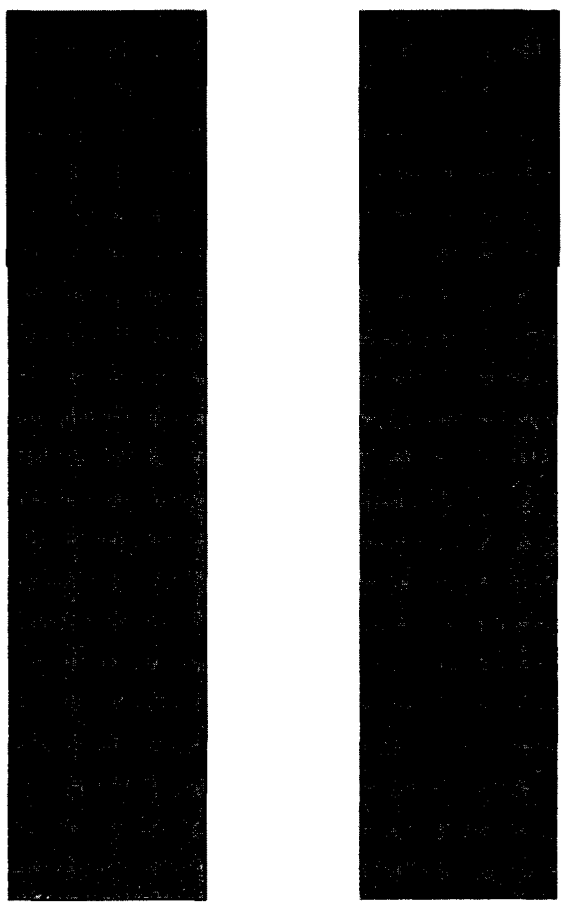

a. before flattening **b. after flattening**

Fig.5 HV-HV coherence's phase images before (plate a.) and after (plate b.) earth phase flattening for the whole image.

Fig. 7 shows absolute value of coherence images (coherence amplitude). Coherence smooth window size is 7*7 pixels for all the polarizations. Fig. 8 shows the histogram of HH-HH, VV-VV and VH-VH coherence. From Fig.7 and Fig.8, we know that most of the pixels' coherence is bigger than 0.5. The coherence distribution of HH-HH is almost the same as that of VV-VV. But the mean coherence of cross-polarization (VH-VH) is much lower than co-polarization coherence, specially in the Gobi area in the middle of the low part of Fig.7.

Fig. 9 is the incidence angle image corresponding to the master dataset $[S]_1$. According to the CEOS meta information records of the master SIR-C/X SAR dataset (pr2398), the near range incidence angle is 21.95 degree, the far range incidence angle is 26.43 and the middle incidence angle is 24.37. From Fig.9, the estimated incidence angle changes from 20.60 to 24.75 degree. The mean difference between the estimated and product provided incidence angle range is around 1.5 degree. So we think the accuracy of the estimated incidence angel image is good enough for inversion methodology validation. Fig. 10 is the effective wave number image, the range of the image value is also meaningful.

4.2 Comparison of tree height inversion results of three methods

Tree height inversion result by MDD method is shown in Fig.11- (a) for a selected window (see the red box shown in Fig.7-c) and that by VBR method is shown in Filg.11-(b). Fig.11-(c) is the inversion result using FMI method.

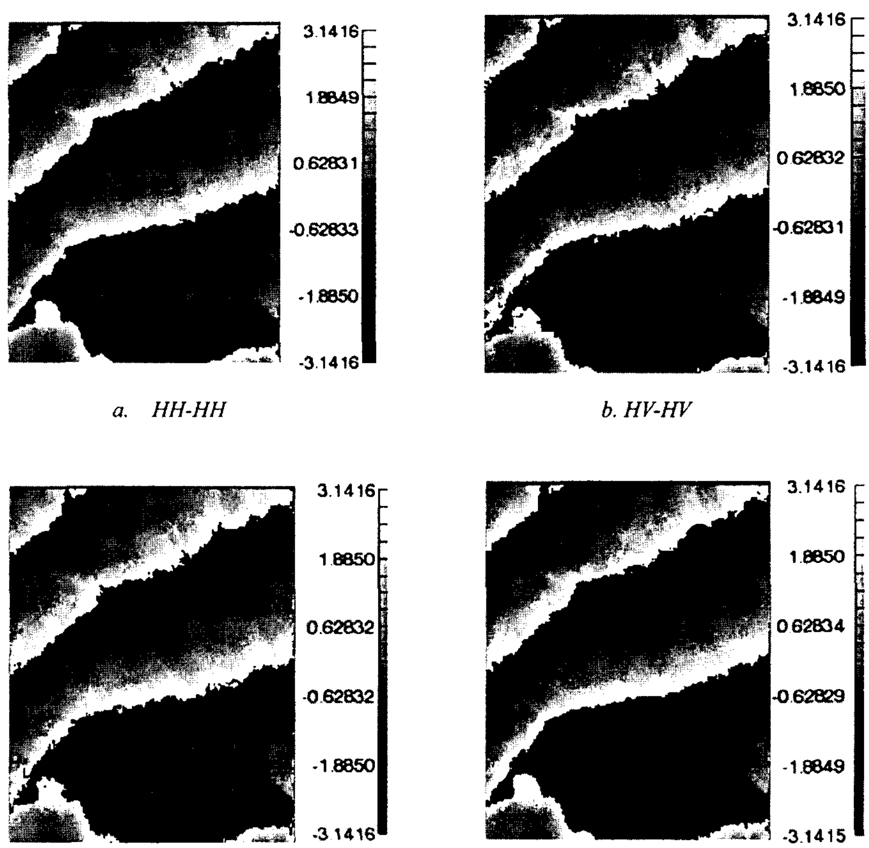

a. HH-HH *b. HV-HV*

c. VH-VH *d. VV-VV*

Fig.6 coherence phase image after earth phase flattening

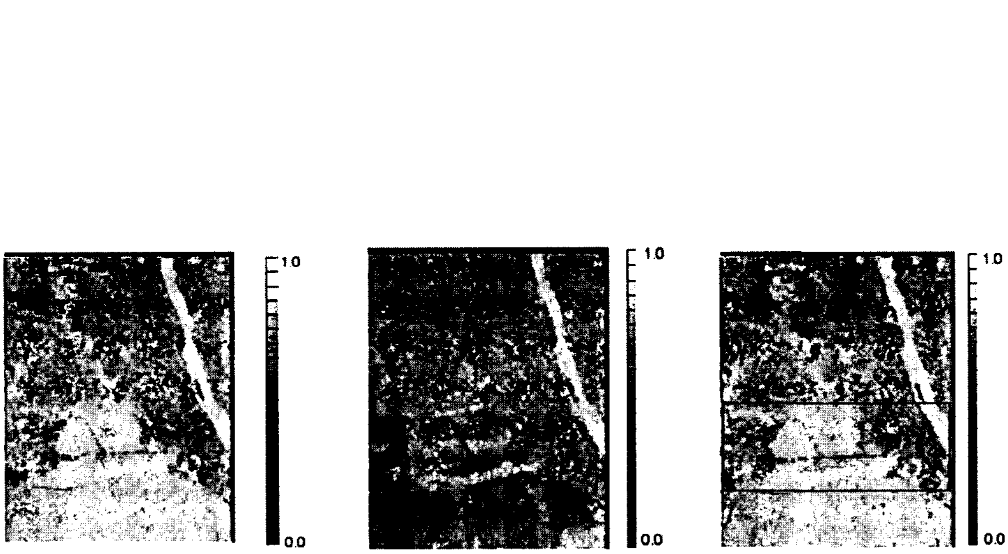

a. HH-HH coherence image *b. VH-VH coherence image* *c. VV-VV coherence image*

Fig.7 coherence coefficient images

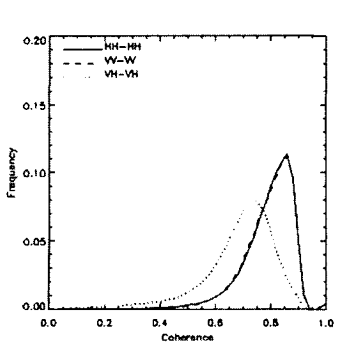

Fig.8 Coherence histogram

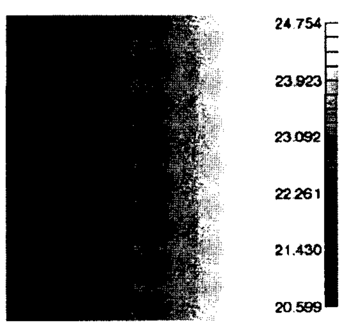

Fig.9 Incidence angle image in degree

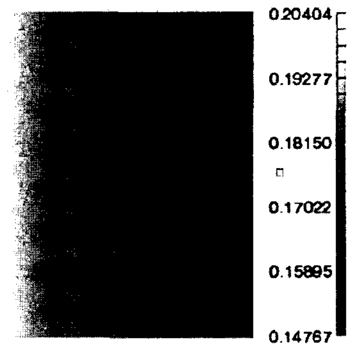

Fig.10 Effective wave number image

According to the Landsat ETM+ image shown in Fig.4 and the land use map shown in Fig.3, there existed forest stand and agriculture filed in the right and left region of this small area as shown in Fig.11, where the coherence is much lower than the inner part. But most of the inner part of them is Gobi area. Although it is difficult to know the ground true of this region in 1994, it is evident that there should not be many forest stand on the Gobi area. We also know that the tree height around this region was about 15 meters since that most of the forest stands in this region is fruit orchards.

Compared with MDD (Fig. 11-(a)) and VBR (Fig. 11-(b)), the tree height image generated with FMI (Fig. 11-(c)) appears much noisy and erroneous, especially in the bottom of this image, where the estimated tree high is large than 15 meters, but the terrain type of this area should be Gobi, where the tree height should be near zero. So, from Fig. 11 we can conclude that the tree height estimation results of MDD method and VBR method are relatively better than FMI.

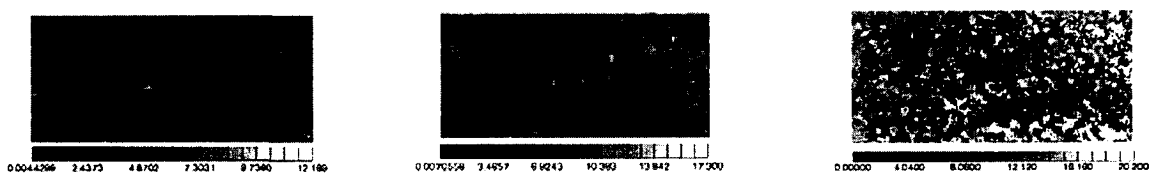

(a) Maximum DEM difference result *(b) Vegetation bias removal result* *(c) Full model inversion result*

Fig. 11 Tree height image generated from MDD (a), VBR (b) and FMI (c) using only HH-HH, VV-VV and VH-VH coherences.

Fig.12 is the histogram of tree height images generated from MDD and VBR methods. The mean tree height of MDD is 1.4m and that of VBR is 2.9m. Further more, Fig. 13 shows one horizontal tree height profile line comparing results from VBR and MDD. According to the ground true information, around the two end part of the horizontal profile line, there should be relative large forest stands, while the inner part of this line should be Gobi region without forest stands. Plate d. shows that the maximum tree height of MDD is below five meters, while the tree height of VBR varies from 5 to 12 meters. So it can be concluded that (1) MDD can underestimate tree height; (2) VBR can produce better tree height inversion result than MDD and FMI.

4.3 Tree height inversion error sources analysis

Although mean coherence amplitude of this area is high, temporal baseline de-correlation should be existed for this kind of repeat pass interferometric configuration. The problem is that we have no indication from the data itself how much temporal decorrelation has occurred [3]. As a comparison, using the same kind of SIR-C/X SAR polarimetic interferometry data acquired around Tianshan area, successful tree height inversion result has been produced [1]. It seems there should be other sources of error to lead to the bad performance of tree height inversion observed in the test site.

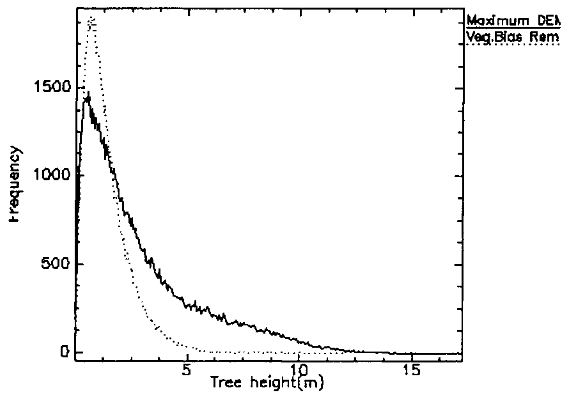

Fig. 12 Histogram comparison of tree height images generated by MDD method and VBR method.

a. Tree height image of VBR *b. Tree height image of MDD*

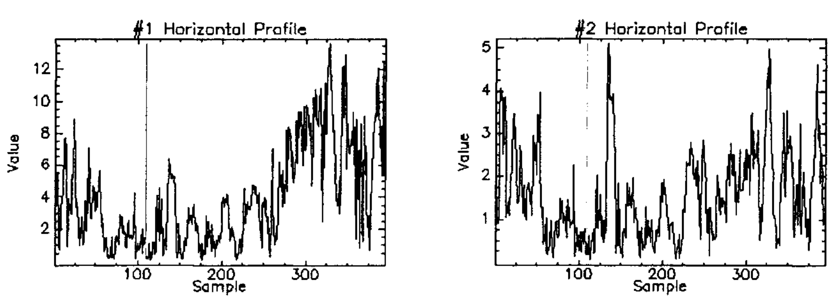

c. Profile of horizontal line show in plate a. *d. Horizontal profile for the line shown in plate b.*

Fig. 13. Comparison of tree height horizontal profile of the tree height image generated by VBR and MDD method.

As shown in equation (1), interferometric coherence can be written as the product of volume coherence and non-volumetric decorrelation caused by range, temporal, SNR, system and data processing.

$$\gamma_{total} = \gamma_{Volume} \cdot \gamma_{range} \cdot \gamma_{temporal} \cdot \gamma_{SNR} \cdot \gamma_{sytem/processing} \tag{1}$$

From the VH-VH and HV-HV coherence images shown in Fig. 7, we can see that the non-vegetation region (Gobi) has very low coherence leading to overestimated tree height in this smooth surface area. These areas may be seriously affected by SNR decorrelation, because smooth surfaces are susceptible of SNR decorrelation. Inversion processing can not distinguish these SNR decorrelation caused low coherence from volumetric coherence, so these non-volumetric coherence region should be masked out before model inversion. With inspection of the |HV| and |VH| images, it has been found that most of the smooth surface scatters can be masked out if the corresponding |HV|+|VH|<180. Fig. 14 shows the masked tree height image that was produced with FMI. The maximum tree height shown in Fig.14 is 21 meters. Fig.15 is the three dimension viewing of the FMI tree height image with non-volumetric decorrelation pixels being masked.

The boxcar filtering process for generating coherence images may be one possible error sources. With simulated SAR dataset, reference4 [3] has observed the effect of boxcar filter to tree height inversion: poor estimates happen at the edges of forest stands, because the boxcar filter can mix surface and volume scattering. In the flat crop filed area of this study site, there are pixels with low coherence. These pixels maybe small cluster of forest scattered in the crop filed. The boxcar filter applied can lead to noisy tree height estimate around these pixels [5]. Furthermore, the vertical tree structure is another possible cause for the poor estimates of FMI. From the ground true, we know that this area is not forestry region but agricultural region. The test site is one oasis with spatial extended large area of Gobi surrounding it. There exists forest stands on the left and right part of Fig.11 as shown by Fig.3 and Fig.4, but most of the forest stand here is fruit stand in orchards or around farm houses. So the forest stand has special vertical canopy structure which may not be modeled by the two-layer backscattering model [3]. This can also explain why VBR can achieve better tree height estimates than MDD and FMI. When temporal de-correlation and vertical structure exists, VBR is suggested as the best method for tree height inversion [3].

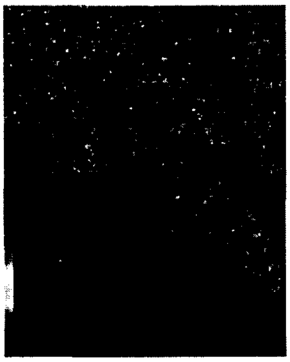

Fig. 14 FMR generated tree height image

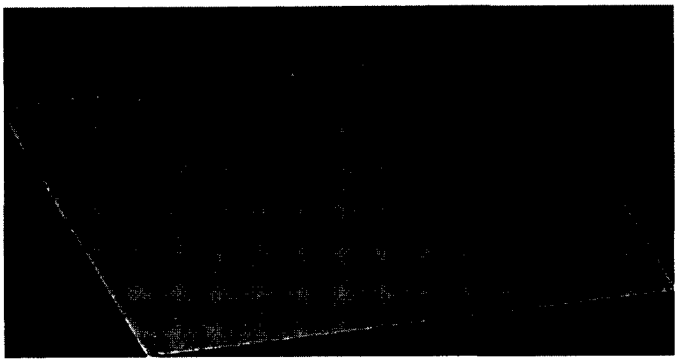

Fig.15 Three dimension representation of three height

5. CONCLUSIONS

The INSAR data pre-processing frame were adopted for SIR-C/X SAR POLinSAR tree height inversion application. With baseline parameters and co-registered scatter matrix [S] from INSAR data pre-processing as inputs, three-stage tree height inversion algorithm established by S. Cloude were evaluated taking some limited ground true information as reference. The results confirmed the issues concluded from theory analysis and simulated POLinSAR data study by S. Cloude, etal: (1) Longer temporal baseline and other factors makes the full model inversion method problematic; (2)

Better inversion result was observed using vegetation bias removal method; (3) The maximum DEM difference method can underestimate forest height. All these problems maybe existed for repeat pass POLinSAR have been observed in this case study.

Non-volumetric decorrelation in the smooth surface scatter region of the test site is observed and maybe caused by SNR decorrelation. These region should be masked out before applying full model inversion. In additional, temporal decorrelation, boxcar filtering and vertical canopy structure are some possible error sources.

ACKNOWLEDGEMENTS

Thanks a lot for ESA to provide the three-months-training program; Technique supports from Dr. Cloude, Dr. Konstans and Tobis to solve POLinSAR data processing problems are highly appreciated. Special thanks to Dr. Y.L. DESNOS for coordinating our study and help to solve problems relevant to software and data sources during our visiting time in ESA-ESRIN; Thanks Dr. Andy Zumda, Tim Pearson and Marcus Engdahl for their friendly help. The work was fund supported by the MOST project of contract no. 2005AA132030.

REFERENCES

[1] Cloude S. R., Papathanassiou K. P., Polarimetric SAR Interferomery, IEEE Trans. Geosci. Remote Sensing, vol. 36, pp. 1551~1565, Sept. 1998.

[2] Papathanassiou K. P., Cloude S. R., Single-Baseline Polarimetric SAR Interferometry, IEEE Trans. Geosci. Remote Sensing, vol. 39, pp. 2352~2363, Nov. 2001.

[3] Cloude S. R., Papathanassiou K. P., Three-stage inversion process for polarimetric SAR interferometry, IEE Proc. Radar Sonar Navig. Vol. 150, pp. 125~134, June 2003.

[4] Cloude S. R., Corr D., Tree-height retrieval using single baseline polarimetric interferometry, POLinSAR 2003 workshop on application of SAR polarimetry and polarimetric interferometry, ESA-ESRIN Frascati, Italy, 14-16 Jaunuary, 2003.

[5], Lee J. S., Cloude S. R., Papathanassiou K.P., Grunes M. R., Ainsworth T. L., Speckle filtering of POLINSAR data, Proceedings of IGARSS 2002, Toronto, Canada, pp.892-831.

Forest Map of China
(id. 2583)

MID-TERM STATUS OF THE FOREST DRAGON PROJECT

Christiane Schmullius [(1)], Zengyuan Li [(2)], Alexandre Bouvet [(3)], Oliver Cartus [(1)], Erxue Chen [(2)], Nicolas Jeannin [(3)], Thuy Le Toan [(3)], Julien L'Hermitte [(3)], Yong Pang [(2)], Maurizio Santoro [(1)], Xin Tian [(2)], Urs Wegmüller [(4)], Andreas Wiesmann [(4)], Charles Werner [(4)], Haizhen Zhu [(2)]

[(1)] Department of Geoinformatics and Earth Observation, Friedrich-Schiller University, Loebdergraben 32, D-07743 Jena, Germany, E-mail: c.schmullius@uni-jena.de
[(2)] Research Institute of Forest Resource and Information Techniques, Chinese Academy of Forestry, Beijing, 100091, China, E-mail: zengyuan.li@forestry.ac.cn
[(3)] Centre d'Etudes Spatiales de la Biosphére, Université Paul Sabatier, 18 Avenue Eduard Belin, bpi 2801, 31401 Toulouse, France, E-mail: letoan@cesbio.cnes.fr
[(4)] Gamma Remote Sensing Research and Consulting AG, Worbstrasse 225, 3074 Gümligen, Switzerland, E-mail: wegmuller@gamma-rs.ch

ABSTRACT

The objective of the Forest DRAGON Project is the development of algorithms for classification of synthetic aperture radar, SAR, data and interferometric SAR (InSAR) data, and the generation of forest maps at regional level for the main forested regions of China. For this purpose ERS-1/2 tandem coherence and ENVISAT ASAR data in Alternating Polarisation (AP) and Wide Swath (WS) mode are considered. ERS-1/2 tandem coherence has been chosen as primary candidate for the estimation of forest stem volume because of its strong sensitivity to forest biophysical parameters. Interferometric processing is carried out by means of a well-established chain at the end of which geocoded coherence, backscatter and local topography products are obtained. Forest base-maps are obtained for the mid-1990s making use of the SIBERIA Project algorithm. First investigations in Northeast China show the need of an improvement of the algorithm to take into account the availability of multi-seasonal data and misclassifications in areas with strong topography. To update the maps multi-temporal ENVISAT ASAR AP images in HH/HV mode are considered. A data processing chain, which includes data import, calibration, geocoding and mosaicing, has been set to process the ASAR data automatically. Preliminary results in Northeast China show that forest/non-forest types can be discriminated well using one date ASAR AP HH/HV images. ScanSAR or Wide Swath mode represent an important source of data for updating global and continental maps, yet to be explored. In this study, ENVISAT ASAR WS data over Northeast China are analysed for forest/non-forest mapping at regional scale. The results are compared with existing land cover maps, in particular the Vegetation Continuous Field (VCF) from MODIS.

1. INTRODUCTION

Forests in China have been undergoing dramatic changes during the last several decades due to forest fire, insect infestation, massive logging, agricultural conversion, and afforestation. The need to monitor forest is dramatically increasing in China, particularly after the introduction of new laws against deforestation. The well known potential of synthetic aperture radar, SAR, data to distinguish forest from non-forest areas and the interest of the Chinese authorities to perform forest monitoring based on remote sensing data have motivated the co-operation between the European Space Agency (ESA) and the Chinese Ministry of Science and Technology (MOST) for over a decade. For this purpose the Forest DRAGON project (Forest Related Development of Radar Applications for Geomatic Operational Networks, id 2583) in the framework of the DRAGON Project was initiated.

The main objective of Forest DRAGON is the development of methodologies aimed at the generation of forest maps for China using archived ERS-1/2 tandem coherence and currently acquired ENVISAT ASAR Alternating Polarisation (AP) data. Additionally JERS-1, Landsat, Shuttle Radar Topography Mission (SRTM) Digital Elevation Model (DEM) and low-resolution satellite data such as MODIS Vegetation Continuous Field (VCF) are considered. Final products will consist of forest biomass maps and forest/non-forest maps for the two most important forested regions in China, the Northeast and the Southeast, at high resolution. Additionally, ENVISAT ASAR Wide Swath (WS) is used for an assessment of large area forest non/forest mapping at regional scale.

ERS-1/2 tandem coherence, with the aid of JERS-1 intensity, is used to generate forest biomass maps of the type produced within the SIBERIA (SAR Imaging for Boreal Ecology and Radar Interferometry Applications) Project [1] for the mid-1990s. This activity is carried out at the University of Jena in cooperation with the Chinese Academy of

Proc. 2005 Dragon Symposium "Mid-Term Results", Santorini, Greece
27 June – 1 July 2005 (ESA SP-611, January 2006)

Forestry. The Chinese project partner is responsible for updating the maps using ENVISAT ASAR AP data acquired during 2004 and 2005. Finally the group at CESBIO investigates the potential of ENVISAT ASAR WS data for forest mapping purposes. Gamma Remote Sensing is the main provider of SAR processing software and guidance. In this paper we report on the mid-term results of the Project, which include the status of satellite data processing and a first evaluation of the data for forest mapping purposes in Northeast China.

2. STUDY AREA AND GROUND DATA

China can be divided into four forest regions: Northeast China (NE), Southeast China (SE), Centre-China (between Southeast and Northeast) and West-China. The NE and the SE are the two most important forest regions in China and represent the main mapping areas of the project, corresponding to the 1st and 2nd phase of the project respectively (see Fig. 1).

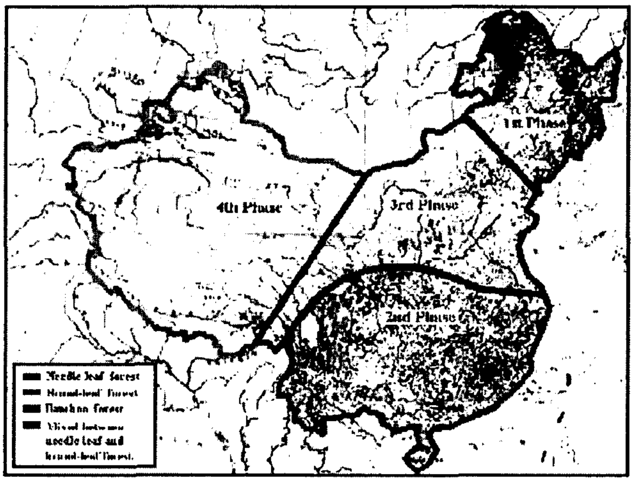

Fig. 1. Forest DRAGON project areas with respect to study phase.

2.1. Test sites

NE China, a region covering approximately 1.5 Million km^2, includes eastern Inner Mongolia and the Heilongjiang, Jilin and Liaoning provinces. The forests are mainly distributed over the mountains. As shown in Fig. 2, three test sites have been selected in this region: the Tuqiang Forest Bureau in Daxinganling, the Dailing Forest Bureau in Xiaoxinganling and the Lushuihe Forest Bureau on the Changbai Mountains. Cold-temperate needle-leaf forests, dominated by larch are distributed in the north part of Daxinganling (the Greater Xing'an Mountains), while the deciduous broad-leaf forests of the temperate zone, dominated by oak, aspen and birch, are distributed in the middle and southern parts of Daxinganling and the northern part of Xiaoxinganling. Broadleaved – Korean pine forests exist in the southern part of Xiaoxinganling and Changbai Mountains. There are also some white oak painted maple and ash trees in the southern part of Xiaoxinganling and Changbai Mountains.

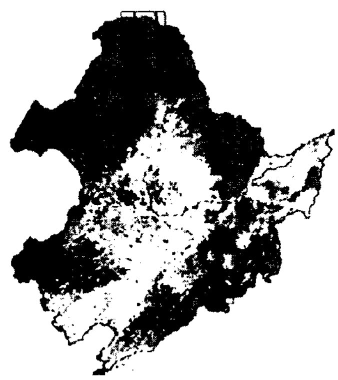

Fig. 2. Three test sites (up: Daxingaling, middle: Xiaoxinganling, low: Changbaishan) in NE China. The base map is an IGBP classification based on MODIS data from the year 2000.

2.2. Field data collection

Forest maps have been selected and digitised for all three test sites. In the forest map the smallest unit is the forest stand sub-compartment, which is also the smallest operational unit in China forest management planning. In a sub-compartment soil, relief and tree conditions are uniform; furthermore, each forest stand sub-compartment has uniform management plan and method. The attributes of each sub-compartment are described by field measurements. For each forest stand sub-compartment the information on soil, tree, understory vegetation, disturbance history, management methods etc. are contained in an inventory database. In the digital forest map, each polygon corresponds to a forest stand sub-compartment.

3. SATELLITE DATA

Since the Forest DRAGON project covers a very large area, a huge effort is dedicated to satellite data acquisition, archiving and processing. These activities have been the main concern throughout the first 18 months of the project.

3.1. ERS-1/2 tandem

The search for ERS tandem pairs with perpendicular component of the baseline shorter than 400 m resulted in 502 frames available, corresponding to 251 one-day interferometric image pairs. Almost 2/3 of the data have been acquired during the winter-spring seasons of 1995-1996; the additional dataset stems from the SIBERIA Project acquisition period during September-October 1997 and June 1998. Most of Northeast China is covered with at least one acquisition; multi-temporal datasets consisting of 2-3 frames (completely or partially overlapping) can be found locally. Acquisition gaps mostly occur in non-forested areas.

For the generation of the forest maps, SAR backscatter and interferometric SAR (InSAR) coherence are used. InSAR processing consists of co-registration of Single Look Complex (SLC) master and slave images at sub-pixel level, common range and azimuth band filtering, slope estimation followed by adaptive spectral filtering and computation of coherence using an adaptive window size [2].

For each processing step, indicators are used to assess the quality of the results (standard deviation of co-registration offsets, coherence dynamic range and bias, radiometric calibration). Standard deviation of the co-registration offsets is always below 0.2 pixels, which ensures that decorrelation due to processing is negligible Since the coherence of water bodies is always < 0.05, the coherence bias can be considered negligible. Finally forest/non-forest coherence contrast is mostly of the order of 0.3-0.4, thus representing the optimal condition for forestry applications using repeat-pass C-band InSAR.

The coherence and the corresponding calibrated intensity images are geocoded to 50x50 m pixel size using the Albers Conical Equal Area projection to adhere to the requirements of Chinese foresters. Geocoding is performed using an automatic procedure based on the offset estimation between image chips in the SAR and in the map geometry. The geolocational accuracy is assessed by means of the percentage of image chips with co-registration offsets having a SNR above a given threshold. Furthermore we check the overlap between consecutive frames. Typically areas with topography are well geocoded since the percentage of chips with SNR above the threshold is > 70%. Relative shifts of 1-2 pixels (i.e. <= 100 m) between consecutive frames occur in case of predominantly flat areas within the scene (e.g. agricultural fields, lakes or desert).

Besides the coherence and backscatter images, maps of local incidence angle, pixel area normalisation factor, local topography and layover/shadow are produced. Table 1 summarizes the state of processing at the date of submission of this mid-term report (September 2005). Fig. 3 includes two false colour composite mosaics for respectively the winter-spring 1995-1996 and the autumn 1997 data processed so far. The whole processing has been performed with Gamma RS software.

Table 1. Status of ERS-1/2 InSAR processing at the end of September 2005. Discarded images include frames with missing lines or not covering the study area.

SLCs ordered	502 (→ 251 InSAR pairs)
SLCs processed	368 (→ 184 InSAR pairs)
SLCs discarded	46 (→ 23 InSAR pairs)

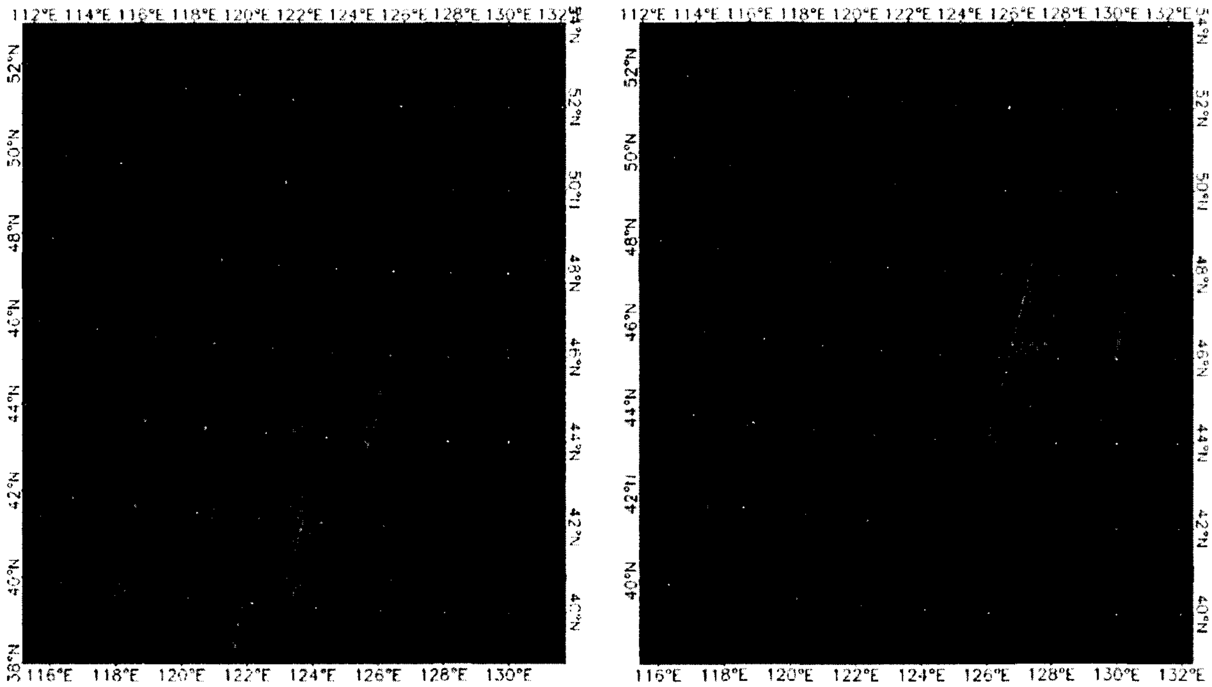

(a) (b)

Fig. 3. False colour composites of ERS coherence (Red), ERS backscatter (Green) and ERS backscatter difference (Blue) for the winter 1995-1996 (a) and the summer-autumn 1997-1998 (b) datasets.

3.2. ENVISAT ASAR Alternating Polarisation

Several cycles of ASAR AP data have been ordered and acquired between September 2004 and March 2005. The IS2 mode and HH/HV polarization was selected. More than one thousand scenes in Precision Image (PRI) and SLC format have been received. Gaps and data acquired in different modes because of conflicts with other orders did not allow a full coverage of the region of interest.

For data calibration a program has been developed according to the ASAR calibration document [3]. The calibrated ASAR images were geo-referenced with geo-location information in the data header using Range-Doppler geolocational model. As the orbit state vectors of ENVISAT ASAR data were provided with high accuracy in both between time interval and satellite position coordinates, the georeferencing accuracy is fine, especially for the data acquired along the same orbit. After geo-reference processing, the calibrated ASAR images have geographic coordinates and can be mosaiced together. The mosaic operation was performed with ERDAS Imagine software.

A data process chain, which includes ASAR data import, calibration, georeferencing, and mosaicing has been set to process the ASAR data automatically. As the ASAR data are provided in each scene, the software can be operated in batch mode, which can read in many ASAR AP scenes and perform PDS format read -> Calibration -> Georeferencing automatically. Fig. 4 shows the mosaiced image of cycle 35 ASAR data.

3.3. ENVISAT ASAR Wide Swath

Over NE China 62 archived ENVISAT ASAR WS images from 2003 and 2004 were available. The images were in HH or VV polarisation and on 22 different tracks. After slant to ground range correction and relative calibration the images are delivered with a resolution of 150 m by strips 400 km wide.

The forest mapping method is based on the temporal change of the backscatter, with forested area having smallest change, as compared to other natural land cover types [4]. The temporal change is quantified by the ratio of the backscatter intensity (or difference in dB), which has been proved to be resistant to multiplicative effects such as topography effects, and in many cases, to angular variation of the signal. The method is optimal using data acquired during summer for boreal forest because of the large contrast in temporal variation of forests relative to that of crops, soil, bogs and water. In other seasons (summer autumn, summer winter for example), the contrast could be reduced due to freezing conditions, but expected to be still exploitable. The method required multitemporal data acquired over the same track and at the same polarisation. Among the data provided, only two regions with multitemporal data taken in the same year are available, each covering 400 x 400 km.

An entirely automatised processing chain has been developed. This processing chain, including the basic steps needed to deal with multitemporal SAR data, is further adapted to better handle a large amount of data from different sources.

- Calibration
- Geocoding using SRTM 90m resolution DEM;
- Tiling (100x100km) and identification of available data by geographic localisation for an easier handling and an easier registration of images;
- Registration;
- Multi-channel filtering and an optional spatial filtering;
- Classification or parameter extraction.

Originally, geocoding is performed after filtering or after classification to avoid distortion in backscatter values. But in order to co-register a large amount of data, geocoding is done instead in a second step. The corresponding error has been assessed and found to be negligible for large-scale mapping. Gamma RS software is used for both calibration and geocoding.

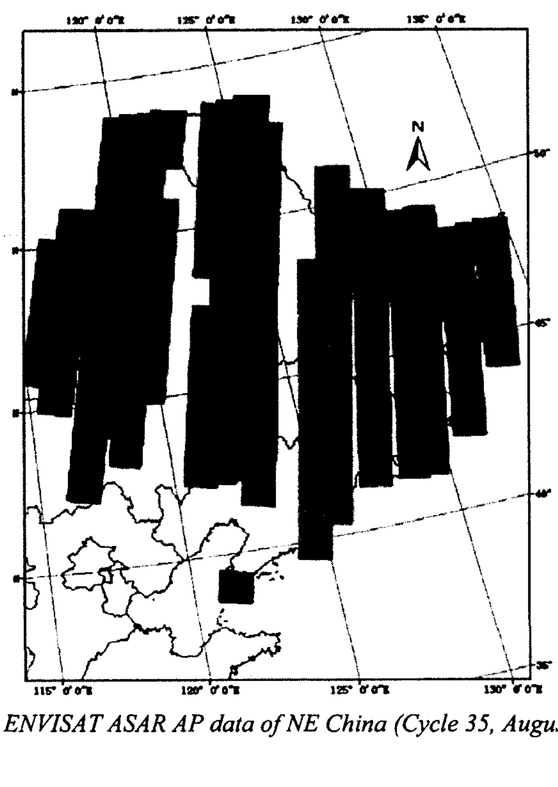

Fig. 4. Mosaiced ENVISAT ASAR AP data of NE China (Cycle 35, August-October 2004)

4. RESULTS

4.1 Retrieval of forest biomass using synergy of ERS-1/2 tandem coherence and JERS intensity

The creation of forest biomass maps from ERS-1/2 InSAR and JERS data is based on the SIBERIA-algorithm [1, 5]. Within SIBERIA a fully automatised classification procedure suitable for biomass retrieval in a 1 Mio km^2 large area in Siberia has been developed; the algorithm allows discriminating four forest stem volume classes (0-20, 20-50,50-80,>80 m^3/ha) and two non-forest classes (water, smooth open areas). The classification uses two simple exponential regression models: one for the ERS-1/2 coherence and one for the JERS intensity.

$$\gamma(v) = \gamma_{75} + (0.330 + 0.581 \cdot \gamma_{75}) \cdot e^{-\frac{v}{122.1}} \quad (1)$$

$$\sigma^0(v) = \sigma_{75} - 2.46 \cdot e^{-\frac{v}{107.34}} \quad (2)$$

For the model training only the image statistics of ERS-1/2 tandem coherence and JERS intensity images are needed. For Siberia it was found that the unknown γ_{75} in Eq. 1 and the unknown σ_{75} in Eq. 2 could be derived from histogram analysis since they were highly correlated to the coherence of the dense forest class (>80m^3/ha). The class centres for the four stem volume (v) classes were obtained using Eq. 1 for ERS-1/2 tandem coherence γ and Eq. 2 for JERS intensity σ^0. These class centres were then used as input to a Maximum Likelihood classifier. Although the algorithm should be adaptive to different imaging conditions, three main questions need to be addressed when considering NE China:

1) In the SIBERIA project only ERS-1/2 tandem coherence data acquired during fall was used. The ERS dataset used in Forest DRAGON contains multi-seasonal data. The behaviour of the algorithm needs therefore to be checked.
2) Topography strongly influences the classification accuracy. Since most of the forests in NE China are located on mountainous areas, masking out these areas (like it was done in SIBERIA project) is not appropriate.
3) Local weather effects need to be taken into account since the ERS-1/2 tandem coherence completely decorrelates when rainfall, thaw, etc. occurs.

As can be seen in Fig. 5 coherence of forested areas differ considerably for scenes acquired under frozen resp. unfrozen conditions. Under unfrozen conditions a peak around 0.2 related to forest can be observed. Under frozen conditions the coherence level shifts towards higher values. As the SIBERIA algorithm was developed for autumn coherence the complete image statistic needs to be checked. If necessary Eq. 1 has to be adapted to winter coherence images.

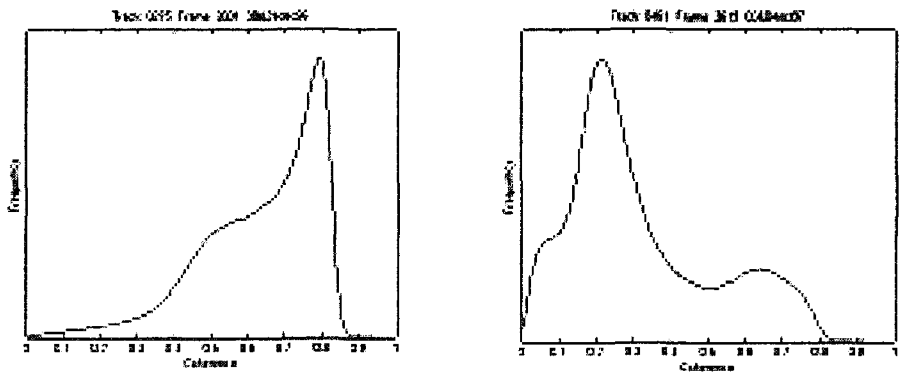

(a) (b)

Fig. 5. Histograms of coherence scenes over forested areas acquired in January (a) and October (b).

For both ERS-1/2 tandem coherence and JERS intensity measurements the clear dependency upon topography needs to be taken into account. ERS-1/2 tandem coherence suffers from strong decorrelation due to uncompensated wave-number shift on slopes facing the radar [6]. Since a correct compensation is not possible, misclassification of open areas and low volume classes can occur because the SIBERIA algorithm would classify these areas as water or dense forest. To overcome the problem, most of the wrong classified water areas can be masked out using a layover/shadow map. In order to obtain correct image statistics a coarse topographic mask of 1x1 km will be used to mask out mountainous areas. The mask will be applied using a threshold for standard deviation of slope within 1x1 km windows. The classification instead will be done for the complete scenes (merely layover/shadow areas will be masked out) as most forests are located in mountainous areas. A kind of quality flag layer may be produced indicating classified areas with significant topographic influence. JERS intensity can be compensated for local incidence angle using a simple cosine-equation according to [6]. The feasibility of the correction will be analysed when data, provided through the Global Boreal Forest Monitoring (GBFM) project initiated by the Japanese Aerospace Exploration Agency (JAXA) will be available.

As can be seen in Fig. 6 the dynamic range of ERS tandem coherence clearly suffers from decorrelation due to rainfall. Yet no statement can be given about the information content of coherence images suffering from decorrelation due to rainfall, thaw, etc. but a clear loss of dynamic range can be observed. If a coherence scene is decorrelated due to weather effects this can be integrated into the mentioned quality flag layer. For this, meteorological data are needed.

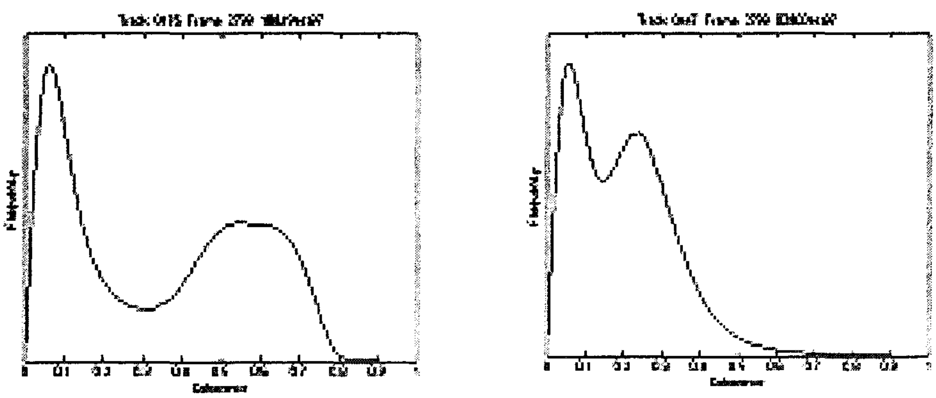

(a) (b)

Fig. 6. Histograms of coherence scenes over forested areas without (a) and with influence of local weather effects (b).

4.2. Forest map update using ENVISAT ASAR Alternating Polarisation data

Fig. 7 shows the comparison between an Interferometric Land Use (ILU) image from ERS-1/2 tandem data and the corresponding ENVISAT ASAR AP image. After image enhancement the two images show good accordance of forest distribution in most areas and some changes in clear-cut areas. Fig. 8 shows the corresponding forest maps obtained from the two data sources. It can be seen that forest/non-forest discrimination can be performed both using the ILU image and the ASAR AP image, hence forest change can be monitored from these two period SAR data. As only one-date ASAR data were used, the corresponding forest map shows misclassifications represented by the many small patches. This confusion is mainly because in early spring the backscatter coefficients from forest are very close to that from small towns and villages. These preliminary results show the high potential of HH/HV ASAR AP data for forest map update.

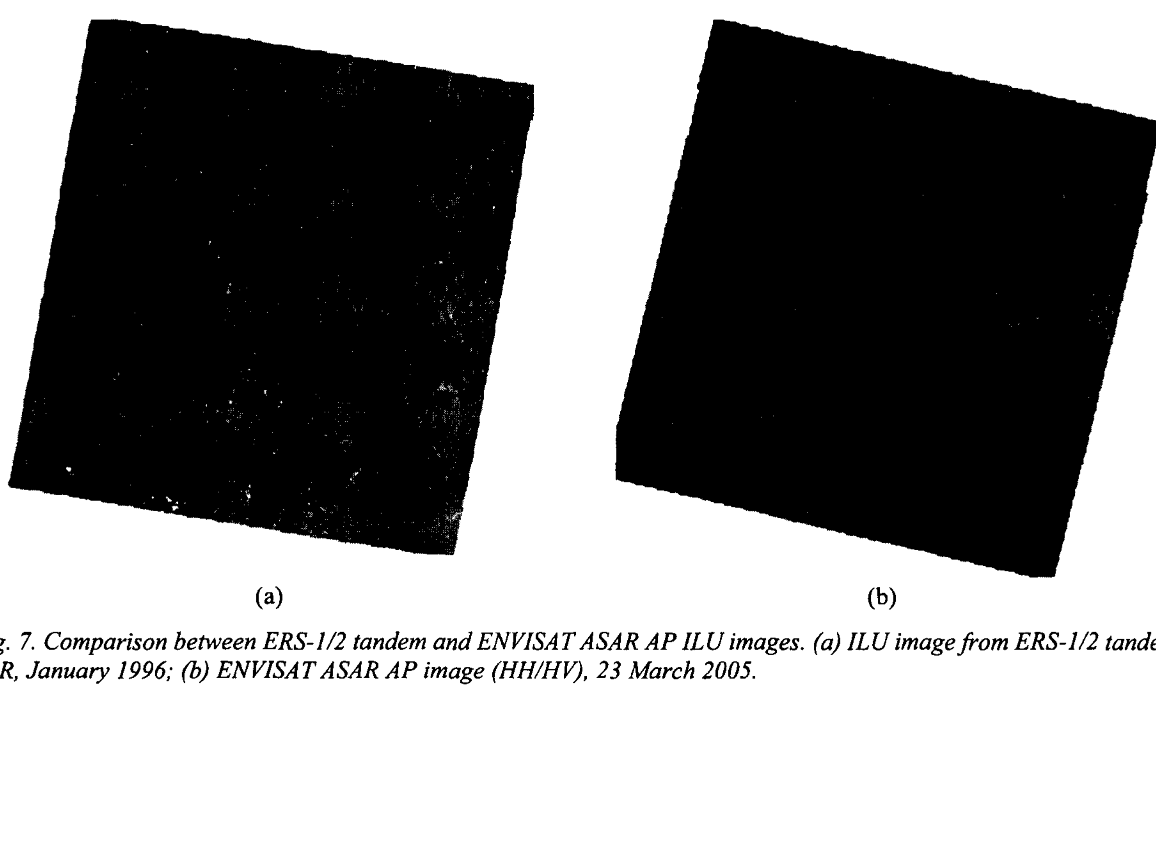

(a) (b)

Fig. 7. Comparison between ERS-1/2 tandem and ENVISAT ASAR AP ILU images. (a) ILU image from ERS-1/2 tandem SAR, January 1996; (b) ENVISAT ASAR AP image (HH/HV), 23 March 2005.

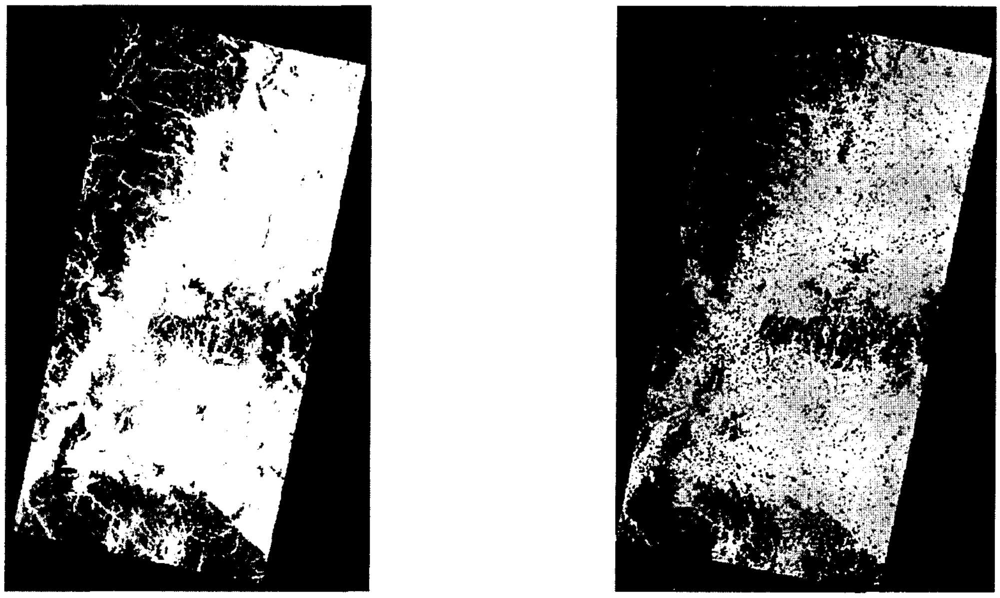

(a) (b)

Fig. 8. Comparison of forest/non-forest maps derived from ERS-1/2 tandem data acquired in January 1996 (a) and from ENVISAT ASAR AP data acquired on 20 March 2004 (b).

4.3. Forest mapping using ENVISAT ASAR Wide Swath data

Fig. 9a shows a composite image of 400x400 km^2 area between China, Russia and Mongolia centred on the city of Hailar in Inner Mongolia from 3 WS images in VV polarisation taken in August, October and November 2004 (no summer multi-date coverage available). Fig. 9b shows the forest/non forest map derived from the temporal change mapping method. The result is compared to the forest/non forest map derived from VCF product [7]. The comparison indicates that more than 90% of the VCF forest (tree cover higher than 10%) is classified as forest by ASAR WS. Figs. 10a and 10b show details of a 60 km x 60 km region. The SAR map shows a general agreement with the VCF map, however with a finer resolution.

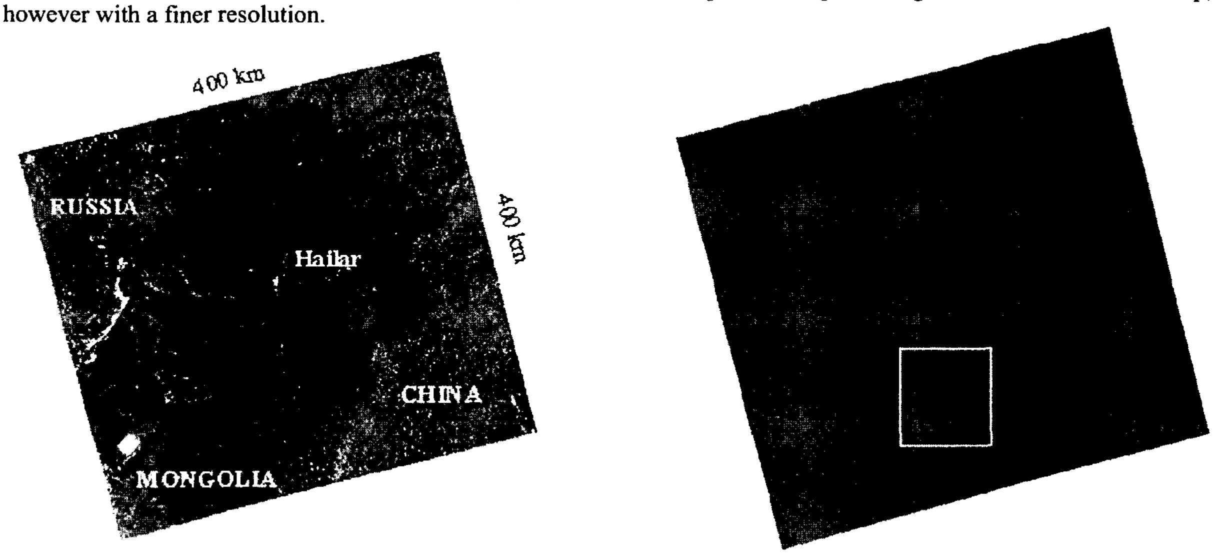

(a) (b)

Fig. 9. (a) Composite of calibrated, geocoded, co-registered and filtered WS VV images of 2004 August (Red), October (Green) and November (Blue) of the region between China, Mongolia and Russia. (b) Map of forest (Green) and non-forest (Yellow) derived from ASAR WS data in Fig. 10a using mapping algorithm based on the temporal change of backscattering coefficient. Coordinates of top left corner: 50,4N, 116,4E.

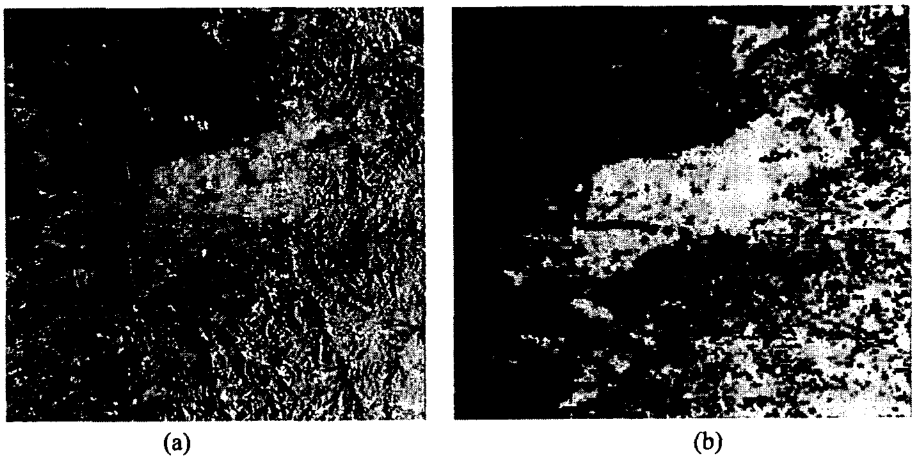

Fig. 10. (a) Map of forest (green) from ASAR WS superimposed on an intensity image. Region of about 80 km x80 km, spatial resolution 150 m. (b) VCF Map of forest (green) at 500 m resolution derived from MODIS data. The forest stand in the middle is a plantation of deciduous trees.

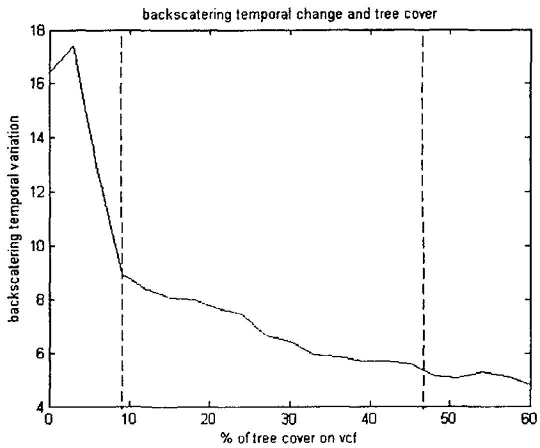

Fig. 11. Relation between the VCF percent tree cover and the mean backscatter temporal change.

The backscatter temporal change is in general related to forest biomass. In absence of in situ biomass data, the temporal change is analysed as a function of the VCF percent tree cover. Fig. 11 shows the relation between the VCF percent tree cover and the mean backscatter temporal change. VCF tree cover less than 10% corresponds to a very large dynamic range of the backscatter temporal change (8 dB in the data set under study). Between 10 and 50% tree cover, the backscatter temporal change decreases of about 4 dB and beyond 50%; the temporal change does not vary (the value of temporal change for dense forest is 5 dB for the data sets, from August to November, due to the decrease of the forest backscatter under frozen conditions). This result indicates that 1) ASAR WS cannot separate forest density beyond 50% of tree cover, 2) ASAR WS can map forest from 10 to 50%, possibly in 4 classes, 3) under 10% of tree cover, the large dynamic range of the backscatter in temporal change could be used for mapping different land cover and forest classes. The result also indicates that ASAR WS can be used to update maps derived from optical data (VCF or GLC), in particular after fires and forest logging.

4.4. Fire monitoring using ENVISAT ASAR Wide Swath images

The resolution of WS images combined with an all weather capability make the SAR images a useful data source for evaluating damages of large-scale forest fire. Fig. 12a shows an example of ASAR WS image of April and October 2003 of a region along the Heilongjiang river. The area with large temporal change shown in red corresponds to a fire that occurred in 2003 between April and October (http://www.nffc.aviales.ru). Fig. 12b shows the corresponding VCF from MODIS data (2000).

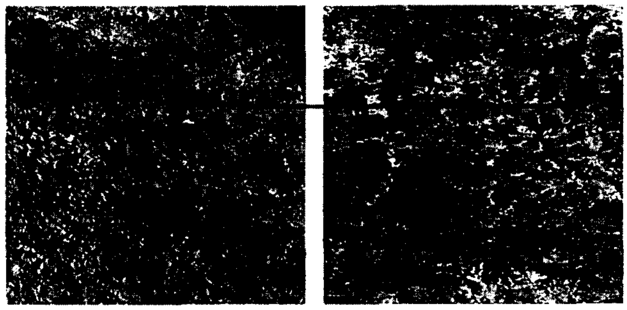

(a) (b)

Fig. 13. ASAR WS image of a region nearby the Heilongjiang river where fire occurred in 2003 (ligth red) (a), as compared to VCF (b). Note also the fire scar in dark red in the SAR image.

5. CONCLUSIONS AND FUTURE WORK

At mid-term the FOREST DRAGON is not only proceeding according to schedule but is also showing the potential of data sources, e.g. ENVISAT ASAR WS, initially regarded as less important for the aims of the project.

During the first phase of the project three typical test sites of NE China have been selected. The ground data and field data were collected and digitised. Most of ERS-1/2 tandem data needed for the generation of the forest biomass base map have been received and processed. The satellite image products are of high quality. Before the end of 2005 all remaining image pairs will be processed. The ASAR AP data processing chain was defined and developed. Efforts in future work will be devoted to improve the geocoding.

For the generation of the forest biomass map the SIBERIA Project algorithm has been tested for NE China. Current work concerns improvements to make the algorithm adaptive to the seasonal conditions of the ERS-1/2 coherence and to develop a quality flag for areas with strong topography. Preliminary classification results of the ENVISAT ASAR AP data showed a good agreement with previous results obtained from ERS-1/2 tandem data, thus making the HH/HV ASAR AP data suitable for forest map update. Summer season data are better suited for this purpose. The classification method for large regions is under development. ENVISAT ASAR WS data have been explored for large-area forest mapping using an algorithm based on the temporal change of the forest backscatter. The results show that it is possible to use WS data for mapping forest at regional scale and for monitoring forest change due to fires. Analysis of more ASAR WS data in 2005 will consolidate the findings, in particular together with the in situ biomass data.

6. ACKNOWLEDGMENTS

The authors would like to thank Y-L Desnos, A. Zmuda, B. Rosich, R. Malosti, V. Amans and ESA's EO-Helpdesk for their help for SAR data acquisition and processing.

7. REFERENCES

1. Schmullius C., et al., SIBERIA - SAR Imaging for Boreal Ecology and Radar Interferometry Applications, EC-Center for Earth Observation, Project Reports, Contract No. ENV4-CT97-0743-SIBERIA, Final Report, 2001.
2. Werner C., et al., GAMMA SAR and interferometric processing software, *Proc. ERS-Envisat Symposium*, Gothenburg, 16-20 October, CD-ROM, 2000.
3. Rosich B. and Meadows P., Absolute calibration of ASAR Level 1 products generated with PF-ASAR, Technical Note, ENVI-CLVL-EOPG-TN-03-0010, 2004.
4. Wiesmann A., et al., Mutli-temporal and multi-incidence angle ASAR Wide Swath data for land cover information, *Proc. 4th International Symposium on Retrieval of Bio- and Geophysical Parameters from SAR Data for Land Applications*, Innsbruck, 16-19 November, CD-ROM, 2004.
5. Wagner W., et al., Large-scale mapping of boreal forest in SIBERIA using ERS tandem coherence and JERS backscatter data, *Remote Sensing of Environment*, Vol. 85, 125-144, 2003.
6. Castel T., et al., Sensitivity of space-borne SAR data to forest parameters over sloping terrain. Theory and experiment., *International Journal of Remote Sensing*, Vol. 22, 2351-2376, 2001.
7. De Fries R. S., et al., A new global 1-km dataset of percentage tree cover derived from remote sensing, *Global Change Biology*, Vol. 6, 247-254, 2000.

Forest Fire Monitoring
(id. 2531)

DETECTION AND MONITORING OF FOREST FIRES IN CHINA THROUGH THE ENVISAT-AATSR SENSOR

A. Calle[(1)], J. Sanz[(1)], C. Moclán[(1)], J.L. Casanova[(1)], J. G. Goldammer[(2)] Li Zengyuan[(3)] & Quin Xianlin [(3)]

[(1)]Remote Sensing Laboratory. University of Valladolid. Faculty of Sciences. Spain. abel@latuv.uva.es
[(2)] GFMC. Max Planck Institute for Chemistry, Germany. johann.goldammer@fire.uni-freiburg.de
[(3)] Institute of Forest Resources Information Technique. The Chinese Academy of Forestry. noaags@caf.ac.cn

ABSTRACT/RESUME

Up until now, the polar satellites most widely used for detection tasks have been the NOAA-AVHRR, the EOS-MODIS and the European sensor ATSR-2. In March 2002, the ESA put into orbit the ENVISAT satellite allowing us to put the advanced sensor AATSR (Advanced Along Track Scanning Radiometer) into operation. It must be pointed out its characteristics for fire observation, detection and monitoring have already been made clear by its predecessors ATSR-1 and ATSR-2. The present work has a double aim. On the one hand, to carry out an exhaustive analysis of the AATSR sensor's response to the variation of different parameters which are difficult to quantify in real time and for each point in the territory according to the potential characteristics that the fire observed has. On the other hand, to apply the detection and monitoring techniques to fires that occurred in the northern regions of China, where the environmental conditions are different from the ones existing in Mediterranean Europe.

1. INTRODUCTION

The use of remote sensing techniques for the study of forest fires is a subject that started already several years ago and whose possibilities have been increasing as new sensors were incorporated into Earth Observation International Programmes and new goals were reached based on the improved techniques that have been introduced. In order to place this subject of study in its appropriate context, it must be pointed out that fire detection with an aim to create alarms that facilitate a rapid extinction is a necessity that hasn't been resolved yet. And it won't be solved until the geostationary satellites show their capacity to detect small fires and prove themselves useful to generate early alarm warnings, which seems pretty difficult given the difficulty in having high spatial resolution thermal sensors. In this sense, simulations have been carried out in order to establish the minimum detectable area according to the temperature on GOES and MSG (Prins and Schmetz, 1999), which are the most capable geostationary sensors to carry out this task. In the MSG's case, and on our latitudes, in order to detect a fire of 600 K a flame size larger than 1.5 ha is needed and this without including the effects of atmospheric attenuation. However, several research groups are already using MSG images to carry out the detection of high-temperature events (HTE) in real time and improve the detection algorithms as a larger number of cases are available. These improvements are aimed at the eradication of false alarms rather than at the perfection of the detection itself. On the other hand, the attempt to establish a system of early fire detection by means of polar satellites, which would solve the problem of spatial resolution, has already been considered in the well-known FUEGO project. that is currently being modified in its original definition through another initiative led by the ESA known as FUEGOSAT, which is being developed at this moment. The most relevant conclusion with respect to the current usefulness of fire detection through spatial sensors is that up until now, it has been useful mainly for the elaboration of fire occurrence maps and the obtaining of statistical results (Prins & Menzel, 1993).

Up until now, the polar satellites most widely used for detection tasks have been the NOAA-AVHRR (Li et al.,2001), the EOS-MODIS (Giglio et al., 2003) and the European sensor ATSR-2. In March 2002, the ESA put into orbit the ENVISAT satellite allowing us to put the advanced sensor AATSR (Advanced Along Track Scanning Radiometer) into operation. As is already known, this satellite has two different ways of observation: the nadir vision and the observation with a sloping angle of 55° in front of the sub-satellite point at a distance of approximately 1000 km above the ground. This observation is used for atmospheric correction processes taking into account that it is carried out at an interval of 150 seconds later than the former one. With respect to the spectral characteristics, AATSR has 7 bands centred in 0.56, 0.66, 0.87, 1.61, 3.70, 10.85 and 12µm respectively. The radiometric resolution these bands provide is quantified in 12 bits. Table 1 shows the radiometric characteristics of these bands. It must be pointed out that although this sensor's main goal is the study and establishment of the sea temperature, its characteristics for fire observation, detection and monitoring have already been made clear by its predecessors ATSR-1 and ATSR-2 (Arino and Mellinote, 1998).

Proc. 2005 Dragon Symposium "Mid-Term Results", Santorini, Greece
27 June – 1 July 2005 (ESA SP-611, January 2006)

The present work has a double aim. on the one hand, to carry out an exhaustive analysis of the AATSR sensor's response to the variation of different parameters which are difficult to quantify in real time and for each point in the territory according to the potential characteristics that the fire observed has. on the other hand, to apply the detection and monitoring techniques to fires that occurred in the northern regions of china, where the environmental conditions are different from the ones existing in Mediterranean Europe.

2. PHYSICS PRINCIPLES: DETECTION AND MONITORING

2.1. Detection of High-Temperature Events (HTE)

The detection has been developed through different algorithms that can be schematically classified into algorithms based on fixed thresholds (Kaufman et al.,1990) and contextual algorithms (Lee & Tag, 1990), whose parameters have been adapted to the different zones of study. Both types of algorithms have advantages and disadvantages and their application will depend on the type of sensors to which they are going to be applied. The detection algorithms based on fixed thresholds, also called multi-channel, are based on the establishment of minimum temperature values in different spectral bands from which the detection is established. The most common scheme is to consider that a pixel is affected by a fire when the following conditions are fulfilled simultaneously:

$$\begin{cases} T_{MIR} > V_{MIR} \\ T_{MIR} - T_{TIR} > V_{DIF} \\ T_{TIR} > V_{TIR} \\ R_{NIR} < V_{NIR} \end{cases}$$

where MIR and TIR refer to the spectral bands of the 3.7μm and 11μm regions respectively. In the former test, the first two conditions are the ones that carry out the detection of HTE strictly speaking according to the physic principles previously stated. The TMIR test is for fire detection and the TMIR-TTIR test is to carry out the differentiation between the fire, which has high values in the MIR, and the hot surfaces which have high values both in the MIR and TIR. The TTIR test is a cloud filter to apply the test to images in which the cloud cover has not been eradicated through other means. The RNIR test is to filter the reflectance in sun-glint situations that are responsible for the appearance of false alarms. The threshold values established are varied. They depend on the algorithm and, above all, on the geographic area due to the influence that the temperature can have on the environment. Thus, normally low surface temperature values use lower MIR threshold values without the appearance of false alarms. Concretely, to mention an American and a European algorithm both operating on NOAA-AVHRR, we will speak about the CCSR used by the Canadian Center of Remote Sensing (Li et al., 2000) and the ESA used by the European Space Agency (Arino et al., 2000) respectively. The CCSR is a valid algorithm on a regional scale and it uses the threshold values VMIR=315K, VDIF=14K, VTIR=260K and VNIR=22%, whereas the ESA algorithm is valid both on a global and on a regional scale and takes the values VMIR=320K, VDIF=15K, VTIR=245K and VNIR=25%. Both will be compared in the results section. To provide some quantitative values, the experience on the AVHRR has proved that a MIR temperature threshold of 320K is appropriate for the detection of fires in tropical forests, whereas in boreal forests a value of 310K would be better.

The disadvantage of the algorithms based on fixed thresholds is that the values established depend on the zone of study and their environmental temperatures. In order to avoid this dependence, contextual algorithms can be used. They are based on the obtaining of threshold values carrying out a statistical analysis of the environment, which is analyzed in a matrix with a size of NxN pixels, being N an odd value that depends on the sensor to which it is applied. Two representative examples are the IGBP algorithm (International Geosphere Biosphere Program) (Justice & Malingreau, 1993), and an adaptation of the current algorithm on MODIS (Kaufman et al., 1998). Contextual algorithms have the advantage of making the detection process independent from the season and the zone analyzed, since the thresholds are obtained by means of an statistical analysis of the environment. However, they have a serious drawback when they are applied to images in which the clouds have not been filtered since cloud edges cause false alarms.

Finally, the flowchart used to obtain fire detection is showed in the following outline. The algorithm is applied by means of a fusion between threshold and contextual analysis. After that, next step is to ask, if image is from day or night, and apply the test of saturation pixels. At the end, to consolidate detection results, a test based on sub-pixel analysis is applied. Figure 1 shows the flowchart used to apply detection and parameterization algorithms.

2.2. Fire monitoring

With respect to fire monitoring, a more realistic scheme derived from Dozier's methodology is the one suggested by Giglio & Kendall, 2001. This scheme modifies the former one by including terms of emissivity, atmospheric effects and sun reflection in the radiance equation of the MIR band. The following are the modified equations of Dozier:

$$\begin{cases} L_{MIR} = \tau_{MIR}\, p\, B(\lambda_{MIR}, T_f) + (1-p) L_{surf,MIR} + p L_{atm,MIR} \\ L_{TIR} = \tau_{TIR}\, p\, B(\lambda_{TIR}, T_f) + (1-p) L_{surf,TIR} + p L_{atm,TIR} \end{cases} \qquad 0 < p < 1$$

where $L_{atm,MIR}$ and $L_{atm,TIR}$ are the radiances emitted by the atmosphere to the sensor in the MIR and TIR bands respectively. These terms are worthless with respect to the radiances emitted by the surface, $L_{surf,MIR}$ and $L_{surf,TIR}$, and can be disregarded. τ is the atmosphere's spectral transmittance. The difference in these equations with respect to the original ones lies in the intervention of the radiances of the surrounding pixels instead of the temperature and finally, although they are taken into account, the surface's emissivity and temperature are not usually known explicitly. The techniques mentioned for the obtaining of fire parameters imply some difficulties related to the errors that are made. In the first place, they are not analytic equations so that their solution must be found by means of numerical calculation techniques. However, it must be said that their solution comes, in the end, from a convergent system. Other important sources of errors have their origin in different magnitudes that have been analyzed by Giglio & Kendall, 2001.

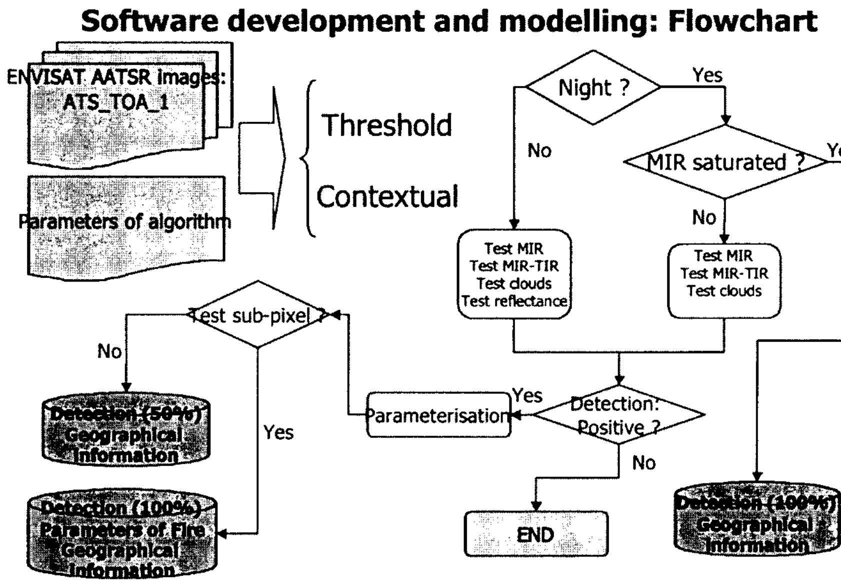

Figure 1: Flowchart used to fire detection and parameterization.

3. ANALYSIS OF AATSR SENSOR

The obtaining of results through the application of the bi-channel equations is a very delicate task since, as the solution is not obtained analytically, it is necessary to apply procedures of numerical calculation. On the other hand, the application of these equations requires the knowledge of both atmospheric and surface data, which are very difficult to quantify through remote sensing and in the real time in which these equations are carried out. This is the case of the atmospheric transmittance and earth parameters such as the surface emissivity and the surface temperature. It must be noticed that the fire has been considered as a blackbody, but not so the non-affected surface in the pixel, which contributes with the radiance term. On the other hand, the variation of all these parameters must be carried out for each sensor in particular since, in the end, and at the sensor's level, the apparent temperature provided will be filtered by the spectral response function.

In this section, we will tackle the analysis of the AATSR sensor according to the response obtained coming from pixels where there is a fire and quantifying the effects produced by the variation of the parameters mentioned in order to see whether taking approximations in the calculation method is justified or not.

3.1. Spectral response function of MIR AATSR

The main spectral band involved in fire detection and monitoring is the one centred in 3.75μm. This response function has a width equivalent to 0.35μm. In order to analyze the atmospheric and spectral effects to which it is subjected, figure 2 shows a comparison of the functions in the MIR bands of the AVHRR, MODIS, BIRD and AATSR sensors, as well as the spectral transmittance. As can be observed, the AATSR function is more similar to the AVHRR one, as much in width as in centre and form. It is narrower than BIRD's and this makes it possible to appear very well centered in the atmospheric

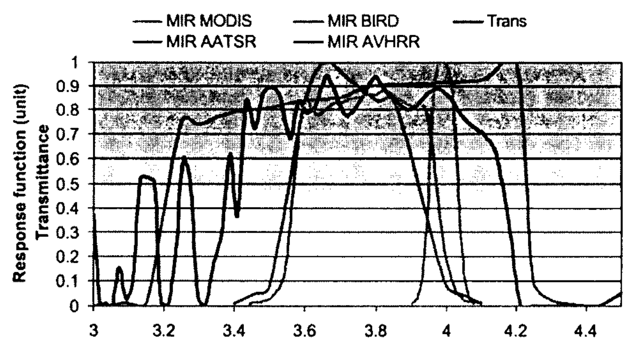

Figure 2. Comparison between different MIR spectral response functions: AVHRR, BIRD, MODIS & AATSR

window in this part of the spectrum. The largest difference is with respect to the MODIS function, which is much narrower. The MODIS function is displaced towards higher wavelengths, which implies a minor disturbance with respect to water vapor absorption and that it receives up to 40% less sun reflection. This is a very important datum in relation to the generation of false alarms and for a better accuracy in the calculation of fire parameters.

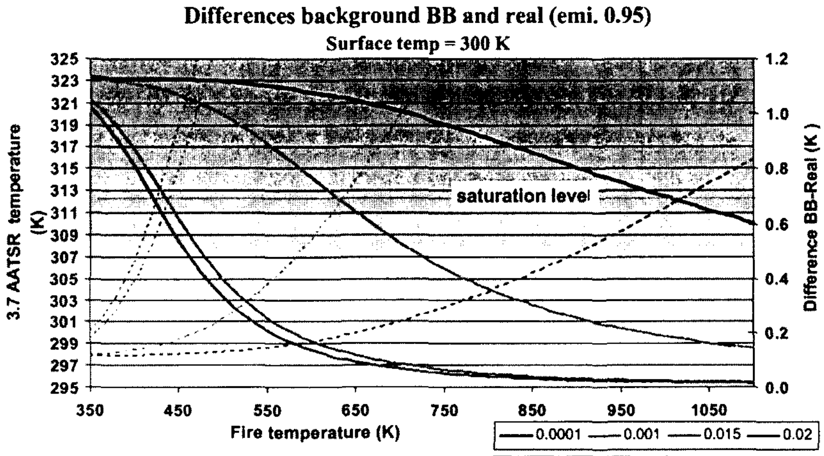

Figure 3. Effect of the considering different surface emissivity values over brightness temperature in AATSR-MIR channel. Different fire fraction of pixel are considered too.

3.2. Dependence on Surface Emissivity

The bi-spectral equations proposed by Giglio & Kendall, 2001, mentioned above, set out the radiance emission of a pixel divided, in a simplified way, into fire and background. In this last case, the radiance emitted depends on the surface emissivity, which moves further away from the behaviour of a blackbody than in the case of the fire. In order to know how the variation in the surface emissivity affects the brightness temperature provided by the final sensors for different temperatures and fire sizes, different simulations have been carried out through the MODTRAN code using, also, the spectral response function of the 3.75 and 11μm bands of the AATSR sensor.

In order to carry out this analysis, fire temperatures in the interval [350, 1100 K] were taken with an increase of 10 K and with fractions of pixel affected by the fire in the interval [0,1]. Special attention was paid to small values, where increases of 0.0001 were applied. With this scheme, the brightness temperatures that the AATSR sensor should provide in the bands involved in detection were established for standard atmospheric profiles. Figure 3 shows a representative result for the qualitative discussion. In it, a value of 300K has been used for the temperature of the surface non-affected by the fire. The figure 3 represents the potential fire temperature values on the abscissas , the brightness temperature of band 3.7 on the first ordinates axis and, on the second ordinates axis, the brightness temperature difference in that band from considering the surface as a black body and considering an emissivity body with a value of 0.95. Four different fractions of a pixel affected by the fire are represented: 0.0001, 0.001, 0.015, and 0,02. In the same figure, we can observe the sensor's saturation level, which means that only the detection could be carried out, but never the establishment of the fire parameters.

As was expected, different emissivity values affect more strongly the conditions in the pixels which are little affected by the fire, for which the ground contribution and lower fire temperature values are more important. Thus, a 100 m^2 fire at a temperature of 1000K surrounded by a surface at 300K is just in the saturation conditions and the difference from considering the emissivity value as 1 or 0.95 in that surface is little more than half a K in the brightness temperature. A fire of 8000 m^2 at a temperature of 450K would saturate the pixel.

Logically, this temperature difference is larger as surfaces with lower emissivity values are considered. These maximum differences correspond to the fires where the lowest temperatures were considered, 350 K in this case. On the other hand, this difference decreases as the surface taken by the fire increases so that this table is representative of the maximum errors committed. Let's also remember that forest fire observation is carried out on forested lands so that the most frequent real emissivity values will be superior to 0.95. Thus, maximum differences of 4.8 K have been found when considering the emissivity as 0.8 and for burning pixel fractions of 10^{-4}.

3.3. Source of error in the parameterization of fire

The errors corresponding to parameterization of fire area showed in the figure 4. There, its possible to find the behaviour of AATSR sensor to obtain fire temperature and flaming area. Of course, saturation situations are taken into account too. These results are been obtained by means of simulations of fires with MODTRAN code, and applying the inversion of Dozier equation after. All results are obtained by means of spectral response functions of AATSR sensor.

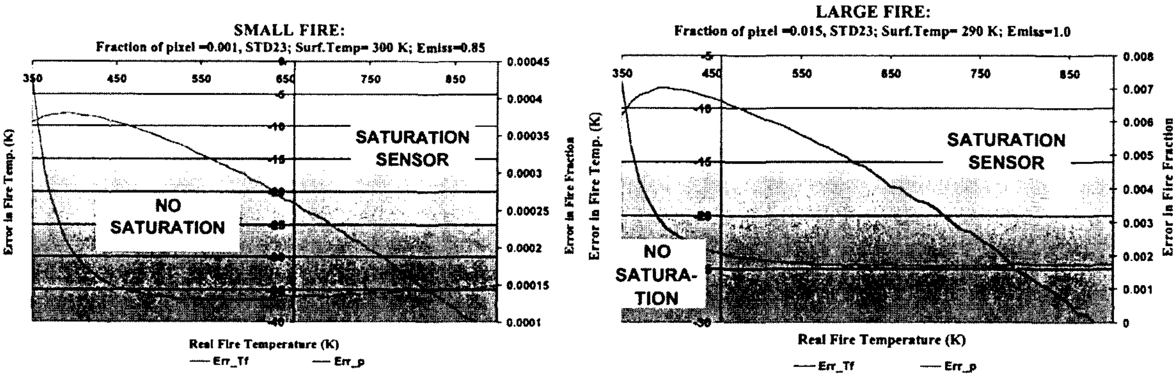

Figure 4: Analysis of small fire and large fire. Errors in the fire temperature and flaming fraction are showed.

The most important conclusion from this analysis is:

- For small fires: the maximun error in fire temperature is 20 K; the maximun error in fire size is400 m^2. From fire temp. of 400 K, error is practically constant to 150 m^2. Parameterisation is only available for fire temperature less than 680 K (saturation in other case)
- For large fires: the maximun error in fire temperature is 10 K; the maximun error in fire size is 7000 m^2. From fire temp. of 400 K, error is practically constant to 3000 m^2. Parameterisation is only available for fire temperature less than 460 K (saturation in other case).

4. FIRE DETECTION AND MONITORING IN CHINA

Next, we will present some results obtained in ENVISAT-AATSR images on Chinese territory. All the results presented have been provided by means of an interactive study of the cases that were more likely to be real fires. Thus, we have tried to obtain the representative characteristics so that automated analyses can be carried out later on.

4.1. Zone and period of study

The AATSR sensor images have been used for the analysis of forest fires in the northern and eastern regions of China. These regions are characterized by fire-prone forests, especially in the Heilongjiang Province, Jilin Province, Liaoning Province and Inner Mongolia autonomous region. Its natural environment is very complex (Shu Lifu et al., 2005). Plantation and secondary forest account for greater proportion of the total forest, and forest fire is severe. The forest fire occurrence is induced by many factors, as the forest fires are affected by inter-annual variability of weather and the regional distribution of fuel. Forest fires are characterized by distinct spatial and temporal distribution. The provinces that have more number of occurrences and burned area concentrate on the Northeast China, and impacted by atmosphere current and seasonal monsoon, the fire season of the two regions have distinct seasonal variation. Human caused fires dominate the most parts of all the fires. However, lightning fires are also common in the montane-boreal larch and pine forests along the border to Russia (Goldammer and Di, 1990). These regions are the ones framed in figure 5. The zone of study is delimited by the geographic co-ordinates of the interval: Longitude [120°-137°], Latitude [44°-53°N]. These coordinates correspond to China region and in several cases, the North-East Russia region too. The analysis was carried out during the months of April, May, June, July and August corresponding to the year 2002, 2003 and 2004 with a total of up to 49 scenes analyzed, although no fires were located in all of them. In total, 861 pixels affected by fire were analyzed.

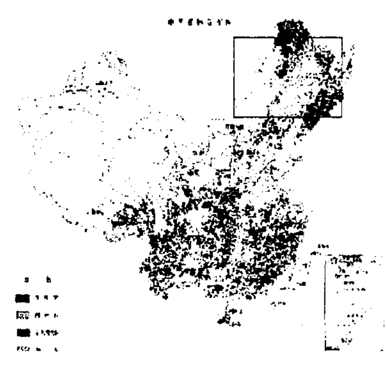

Figure 5: Forest cover analyzed in China

Before providing the numerical values relative to the detection and monitoring processes, it must be pointed out that the fires were not found uniformly spread out throughout this period of analysis, even if this was the most sensitive period for fires according to the country's authorities. Thus, a larger number of fires were found during the month of April, followed by May, whereas the number decreased for the rest of the months. Besides, most of the cases were found in night images, although this datum might be influenced by the fact that fires are much more reliable at night, when the sun's contribution does not exist.

4.2. Fire detection results

The goal in the detection phase was to search for the thermal conditions in which fires are found in this zone. As seen in the section of Physics Principles, the detection algorithms most successfully applied to the precedent sensor, ATSR-2, were the ones based on thresholds applied to the 3.7 and 11μm bands and their difference. However, the values suggested by Arino et al. (2000) of 308K for the MIR band (World Fire Atlas using AATSR-2), were not appropriate for this zone.

The statistics of the thermal values were analyzed according to the temperature in bands 3.7 and 11 and the difference between them, distinguishing between night images and diurnal images, always on non-saturated pixels, as is logical. Besides, for diurnal images, the reflectance in bands 0.87 and 0.67 were also analyzed with a view to using them for the filtering of false alarms in the automation of processes.

With respect to the band MIR, a threshold of 307.3K was found valid during the day and of 302.3K during the night. The difference between both values lies in the contribution of the sun's radiation in the former ones. The most relevant values correspond to the TIR band, whose representative values were 294K in diurnal situations, and 277K at night. It is very important to highlight the fact that the highest percentage of fires analyzed was concentrated in the month of April, which explains the low values detected in this zone of the spectrum and for these latitudes. On the other hand, and with respect to the characteristic values of the difference, the mean in pixels with fire was 14.12 K during the day, and 24.44K during the night, which was undoubtedly caused by the really low values of the surface temperature. Finally, the analysis of the reflectance in the diurnal images showed representative values of 18 % of pixels with fire in the 0.87μm region and of 8.8% in the 0.67μm region. These values were used to filter points that could present sun-glint situations and high signal values in the MIR; these values are more in accordance with the ones found in Mediterranean Europe.
It should be clear that the statistics have been obtained in an absolutely interactive way both visually and manually over a total of 861 pixels affected by the fire. Doubtful or confusing pixels have been discarded according to established criteria with the totality of AATSR bands in the nadir vision. This has allowed us to establish threshold values in the detection algorithms. Thus, this stage of obtaining information has been useful for the creation of an automated detection algorithm based on thresholds. The statistics presented have been divided into the different months of analysis due to the very different climate conditions found. This will allow us to use more accurate thresholds for each month.

One of the problems encountered has been the high percentage of saturated pixels found, which is due to the low saturation level of the AATSR sensor. The highest temperature found in the MIR band was 311.69 K, which agrees with the saturation level considered in the simulations presented at the beginning of this work, established in 312K. Thus, throughout the night images, groupings of affected pixels called clusters were analyzed. Within these groups, the percentage of affected and saturated pixels varied between 20 and 50% for large fires (and, consequently, hotter fires) and between 10 and 20% for small fires. Figure 6 shows some of the examples of clusters in fires analyzed and the occurrence of the situation of saturation.

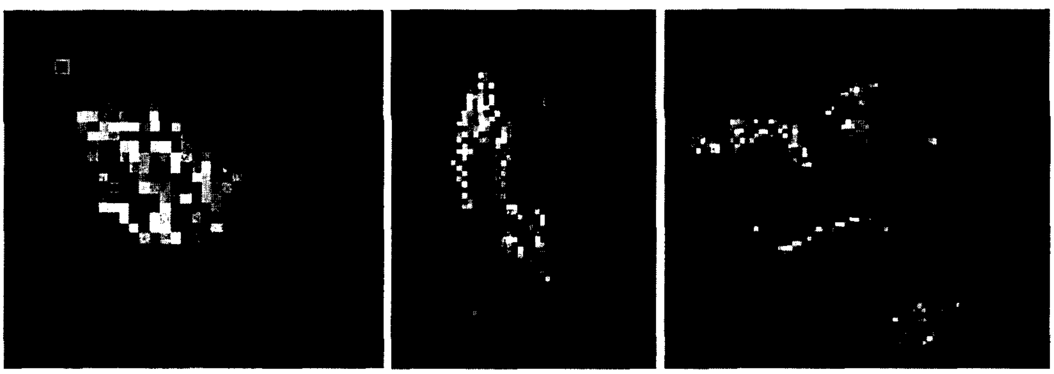

Figure 6. Several examples of forest fires clusters showing more typical saturation situations. Highest temperature founded is 311.7

4.3. Fire Monitoring results

Once the detection process has been carried out, the establishment of the fire parameters was done automatically on the pixels affected by applying the methodology described in section 2.2.

The monitoring phase was established through two processing levels: the pixel level and the cluster level. By cluster, it is understood a group of affected, neighbouring pixels. The first level consists of the establishment of the fire temperature and the fire's radiative energy. It must be taken into account that the power generated by the fire has three extinction processes: power transmitted by the heating-up of the ground, the power freed by convection processes and the radiated power. The latter one is the one calculated through the parameters accessible to the satellite. Figure 8 shows one of the examples analyzed, where the original scene processed, the fires detected and the analysis of the fire temperature and the fire radiated in MWatts can be observed.

With respect to the analysis at a cluster level, figure 8 shows a mask with the clusters detected in our process, enumerated for the obtaining of the cluster's parameters that will be explained below. The figure shows the average temperature values for each cluster. This temperature has been obtained through the mean of the temperature values in each pixel in the cluster, considered by the area occupied by the fire. Finally, the figure shows the power radiated for all clusters as the sum of the powers in each of the pixels that make up the cluster. This parameter is related to the fire's destructive power and, consequently, to the difficulty in the subsequent generation of the zone. The information obtained for each of the clusters is summarized in the table 1, for the ones enumerated as 27,28 and 29.

#Cluster	Avg fire Temp	Temp. (min,max)	Area of fire (ha)	Area (min,max) m^2	Intensity (Mwatts)	#pixels	Cluster Coordinates
Cluster 27	683.0 K	(683, 683)	0.1	(802, 802)	10	1	x=294 y=178
Cluster 28	641.7 K	(591,1038)	0.6	(60, 2160)	56	5	x=291 y= 176
Cluster 29	590.0 K	(590, 590)	0.2	(1602, 1602)	11	1	x=288 y= 176

Table 1. Example of parameters calculated for each cluster. Only 27,28 & 29 are showed.

The parameters listed are: number of the cluster corresponding to the mask code in order to be identified, fire temperature averaged and considered by the area occupied by the fire (in brackets, the minimum and maximum fire temperature found in the group of pixels), total area occupied by the fire in that cluster (in brackets, the minimum and maximum found in individual pixels in m2), the total power radiated by the cluster, the number of pixels affected in the cluster and, finally, the central co-ordinates of the cluster.

5. DISEMINATION OF RESULTS

All results are obtained in real time and disseminated via internet. Images are obtained from the ESA server and processed at LATUV. Detection and parameterization results are showed in the figure 7.

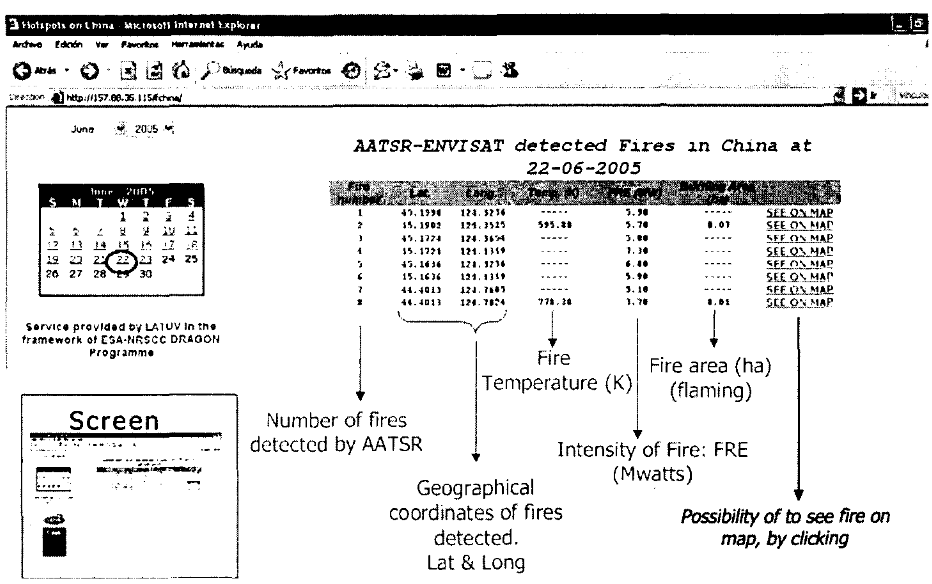

Figure 7. Web page to dissemination of results

6. CONCLUSIONS

Two outstanding parts have been differentiated in this work, both of them referring to the ENVISAT-AATSR sensor: First, an exhaustive analysis has been carried out on the dependence that certain magnitudes related with the pixels where there is fire present and the magnitudes that provide for the final sensor's measurement. The usefulness of this analysis is to show the sensor's characteristics to obtain fire parameters, as well as its limitations in respect with the saturation of the 3.7μm band. As has been seen, the fact that the atmospheric conditions are not known and are substituted by standard situations, or the fact that the emissivity and the ground temperature are not known either, does not imply strong variations in the brightness temperature measured by the sensor. However, the sensor's low saturation level makes the observation and analysis of fires with high-temperatures or with large fractions of the affected pixel tremendously difficult.

The second part of this work was the application of the methodology at a sub-pixel level to the AATSR sensor for Chinese scenarios. The values found in the temperatures of band 11μm differ notably from the conditions found in Mediterranean Europe. The difference between bands 3.7 and 11 is the first argument to be introduced in automated detection processes. So, Concerning Fire Detection with AATSR: Detection is possible. Best results over night images. False alarms detection must be improved, by means of mask: urban, river, etc

Concerning Fire Parameterisation AATSR: Errors in fire parameters are not big. Intensity of fire is the best magnitude to study the fire. The main restriction is low saturation level of MIR channel
The use of "forward vision" of AATSR will be used to calculate atmospheric conditions and will improve accuracy results.

Aknowledgements

This work has been carry out within the framework of the development of DRAGON research Project financed by European Space Agency. Authors want to thank to ESA for supplying ENVISAT-AATSR images and Chinese partners because forest and geographic information of China.

7. REFERENCES

Arino, O. & Mellinote, J.M. (1998). The 1993 Africa fire map. International Journal of Remote Sensing, 19, 2019-2023.

Arino 2000. Various Authors. ATSR World Fire Atlas validation. ESA-ESRIN, Italy.

Giglio, L & Kendall, J.D., (2001). Application of the Dozier retrieval to wildfire characterization. A sensitivity analysis. Remote Sensing of Environment, 77, 34-49.

Giglio, L. & Justice, C.O. (2003). Effect of wavelength selection on characterisation of fire size and temperature. Int. J. Remote Sensing, 24, 3515-3520.

Goldammer, J.G., and Xueying Di. 1990. The role of fire in the montane-boreal coniferous forest of Daxinganling, Northeast China: A preliminary model. In: Fire in ecosystem dynamics. Mediterranean and northern perspectives (J.G. Goldammer and M.J.Jenkins, eds.), 175-184. SPB Academic Publishing, The Hague.

Justice, C.O & Malingreau, J.P.(editors). (1993). The IGBP satellite fire detection algorithm workshop technical report, IGBP-DIS Working paper 9, NASA/GSFC, Greenbelt, Maryland, USA, February, 1993

Kaufman, Y.J., Tucker, C.J. & Fung, I. (1990). Remote sensing of biomass burning in the tropics. Journal Geophy. Res., 95:9927-9939.

Kaufman, Y.J., Justice, C., Flyn, L. Kendall, J. Prins, E., Ward, D.E., Menzel, P. & Setzer, A. (1998). Potencial global fire monitoring from EOS-MODIS. Journal of Geophy. Res., 103, 32215-32238.

Lee, T.M. &Tag, P.M. (1990). Improved detection of hotspots using the AVHRR 3.7 μm channel. Bull. Amer. Meteoro. Soc. 71:1722-1730

Li, Z., Nadon, S., Chilar, J. & Stocks, B. (2000). Satellite mapping of Canadian boreal forest fires: Avaluation and comparison of algorithms. International Journal of Remote Sensing, 21, 3071-3082.

Li, Z, Kaufman, Y.J., Ichoku, C, Fraser, R., Trishchenkp, A., Giglio, L. Jin, J and Yu, X. (2001). A review of AVHRR-based active fire detection algorithms: Principles, limitations and recommendations in Global and Regional vegetation fire monitoring from space: Planning a coordinated international effort, SPB Academic Publishing, The Haque, Netherlands, pp. 199-225.

Prins, E.M. and Menzel, W.P. (1993). Application of the GOES VAS Automated Biomass Burning Algorithm (ABBA) in South America: A trend analysis from 1983-1991.

Prins, E and Schmetz, J. (1999). Diurnal fire active detection using a suite of International geoestationary satellites. GOFC Forest Fire Monitoring and Mapping Workshop, JRC, Ispra.

Shu Lifu, Wang Mingyu and Tian Xiaorui. 2005. Forest fires Situation and Management in Northeast China. Analysis presented at the Regional Central Asia Wildland Fire Network Consultation, Irkutsk, Russian Federation, 8 September 2005. ECE/FAO International Forest Fire News (in press)

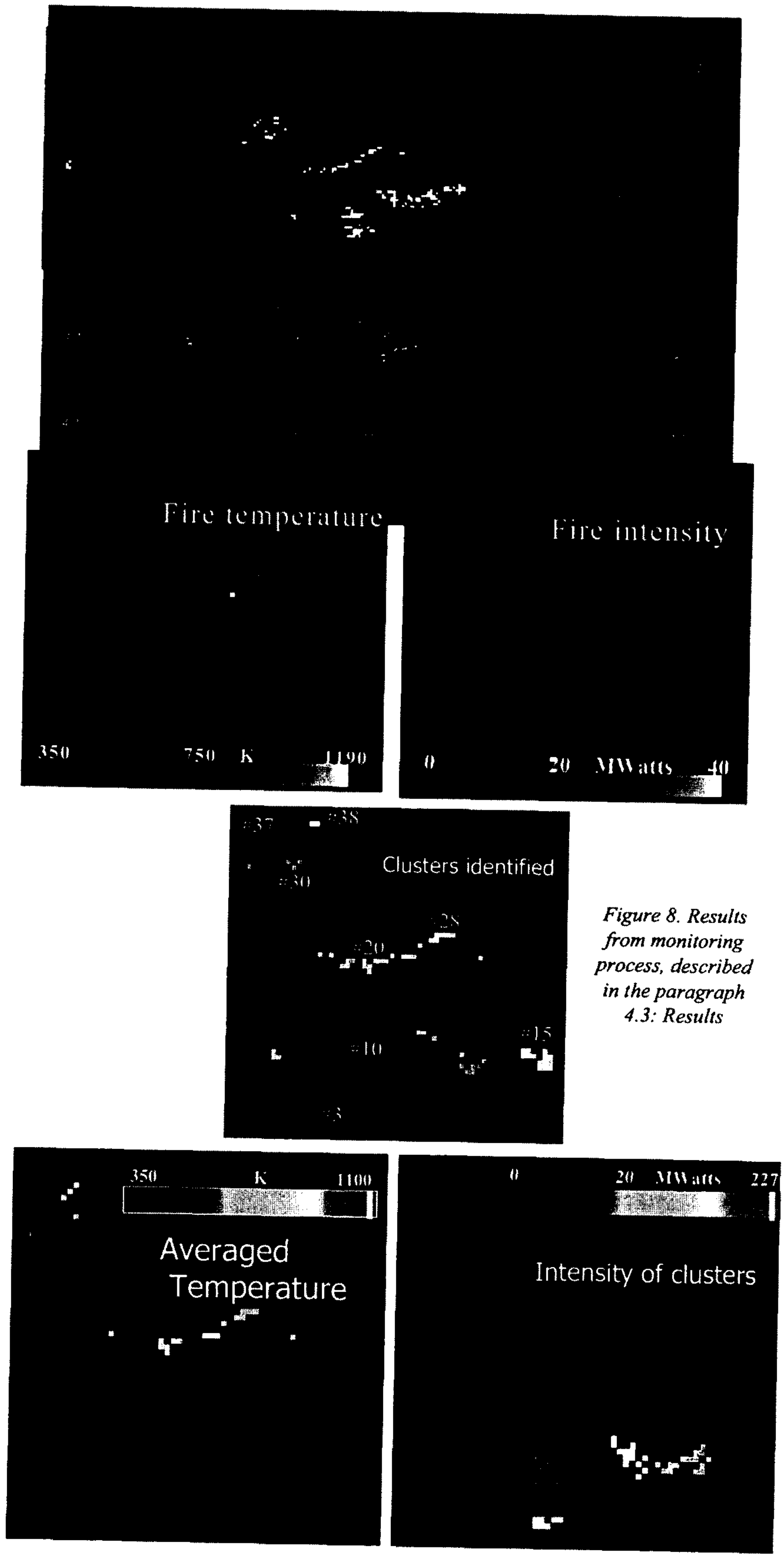

Figure 8. Results from monitoring process, described in the paragraph 4.3: Results

FOREST FIRES IDENTIFICATION USING AATSR AND MODIS DATA

Qin Xianlin[1], Li ZengYuan[1], Tian Xin[1], J.L. Casanova[2], A. Calle[2] and C. Moclán & J. Sanz[2]

(1) Institute of Forest Resources Information Techniques, CAF, Beijing, China, Email: noaags@forestry.ac.cn

(2) Remote Sensing Laboratory of University of Valladolid. Dept. Applied Physics Faculty of Sciences. 47071, Valladol, Spain, Email: Jios@latuv.uva.es

ABSTRACT

Forest fire is a kind of worldwide natural calamity. It is extensively distributed with high occurrence frequency and destroys forest resources thus disturbing normal living order of people and leading to environmental deterioration.

The appearance and development of modernistic new high technologies, such as Remote Sensing (RS), Geographic Information System (GIS) and Internet, have given more convenience for preventing and decreasing disaster than before. In this study, basing on analyzing the information of related bands of Advanced Along Track Scanning Radiometer (AATSR) and integration of background GIS data, a forest fire identification methodology has been developed. At the same times, the accuracy of the results by using AATSR and Moderate Resolution Image Spectroradiometer (MODIS) data has been tested in northeast of China.

1. INTRODUCTION

Forest fires are a prominent global phenomenon, which not only destroy natural vegetation, but also pose enormous danger to wildlife as well as to human life and property. In addition, biomass burning by fires has been identified as a significant source of aerosols, carbon fluxes, and trace gases, which pollute the atmosphere and contribute to radiative forcing responsible for global climate change[1]. Forest fire in Northeast of China region is especially severe and has aroused extensive attention by Chinese government.

Timely and accurate detection of fires has become an issue of considerable importance. Various international organizations, such as the International Geosphere and Biosphere Program (IGBP), have recognized the need for fire detection and monitoring [2]. Space-borne fire detection has been a topic of intensive research since the early 1980s [3, 4]. Much of the work has concentrated on fire monitoring methodology or estimation of atmospheric emissions from fires [5]. Until now, most fire detection activities have been based on the use of data from the Advanced Very High Resolution Radiometer (AVHRR) onboard the National Oceanic and Atmospheric Administration's (NOAA) polar orbiting satellites. The AVHRR series of sensors offer a spatial resolution of 1km and cover most of the Earth's surface every day, once in the daytime and once at night. AVHRR data have been widely used for fire detection because they have some unique radiometric advantages relative to other satellite data, and provide a good balance in spatial and temporal resolutions [6]. There are many algorithms by using AVHRR data to detect fires [3, 4, 7, 8, 9]. The Moderate Resolution Imaging Spectroradiometer (MODIS) which carried on both the Terra and Aqua satellites makes possible monitoring earth four times everyday. MODIS has the ability to observe fires, smoke, and burn scars globally. Its main fire detection channels saturate at high brightness temperatures: 500 k at 4 μm and 400 k at 11 μm which can only be obtained in rare circumstances at the 1 km fire detection spatial resolution [10]. Thus, MODIS is different from other polar orbiting satellite sensors with similar thermal and spatial resolutions (such as Advanced Very High Resolution Radiometer). In recently years, MODIS data has been broadly used for fire detection [11, 12, 13, 14, 15, 16, 17]. The Advanced Along Track Scanning Radiometer (AATSR) is the third in a series of instruments, continuing from ATSR-1 launched on ERS-1 in July 1991 and ATSR-2 launched on ERS-2 in April 1995. The instruments have a common heritage, although certain aspects of instrument design have evolved and improved. Data from the AATSR sensor have also been used for fire detection [18]. However, since the 3.7 band of ATSR-2 saturates at about 312 k, night-time data have been used in fire detection for global fire map [19, 20, 21, 22]. The 'Dragon Project' gives the opportunity to study the potential fire detection by using AATSR sensors in northeast of China.

Proc. 2005 Dragon Symposium "Mid-Term Results", Santorini, Greece
27 June – 1 July 2005 (ESA SP-611, January 2006)

2. STUDY AREA AND DATASET

2.1. Study Area

The northeast of China is the first of five important forest region of China. Its' climate belongs to temperate zone. The main vegetation is needleleaf forests in cold-temperate, needleleaf and broadleaf mixed forests in temperate zone and deciduous broadleaf forests in warm-temperate zone. At the same time, the northeast forest region is a region with high occurrence of large forest fires. Many large forest fires have been taken place in this region, such as the famous large forest fire which has taken place in 1987. The study site is located between 127°E to 136° E and 48.0° N to 56.0° N (Figure 1).

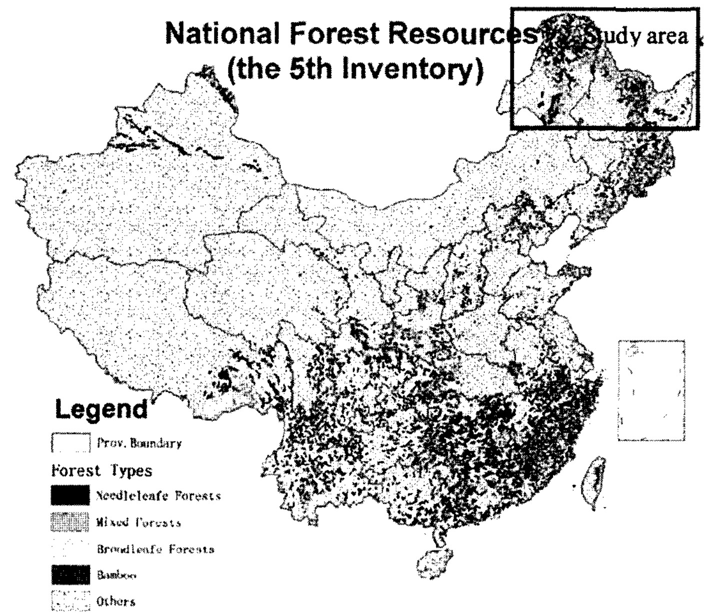

Fig. 1. National Forest Resources Map of China and the study area

2.2. Dataset

The AATSR_TOA images have been used for the analysis of forest fires in the northeast of China. The selected data with a total of 40 scenes have been supplied by our European partners. The analysis was carried out during the months of April, May, June and July corresponding to the year 2002, 2003 and 2004. At the same time, the fire points getting from Moderate Resolution Image Spectroradiometer (MODIS) and the large forest fire information, such as location, vegetation type and fire duration, have been collected.

3. METHODOLOGY

3.1 Samples Test

The AATSR-TOA production has seven bands at centre wavelength 0.55, 0.65, 0.87, 1.60, 3.7, 11 and 12μm. In order to get the fire detection model of northeast of China with AATSR data, the parameters of fire, vegetation, land, cloud, water and burnt scar have been sampled from the AATSR-TOA production image. We have sampled more than 100 pixels every classes. Here, The bright temperature of 3.7, 11, 12μm and the difference between 3.7μm and 11μm at the nadir direction has defined as T_4, T_{11}, T_{12} and DT_1. The bright temperature of 3.7, 11, 12μm and the difference between 3.7μm and 11μm at the fward direction has defined as TF_4, TF_{11}, TF_{12} and DT_2. The reflectance of 0.55, 0.65, 0.87 and 1.60μm at the nadir direction has defined as R_1, R_2, R_3 and R_4. The reflectance of 0.55, 0.65, 0.87 and 1.60μm at the fward direction has defined as RF_1, RF_2, RF_3 and RF_4.

The statistic analysis includes their average, maximum, minimum and standard deviation. The statistics of the thermal values were analyzed according to the bright temperature in the central wavelength bands 3.7, 11, 12μm and the difference between 3.7μm and 11μm, distinguishing between night images and diurnal images, always on non-saturated pixels. Besides, for diurnal images, the reflectance in bands 0.55, 0.67, 0.87 and 1.60μm were also analyzed with a view to using them for the filtering of false alarms. Part of analysis results have been listed in Fig. 2 and Fig. 3.

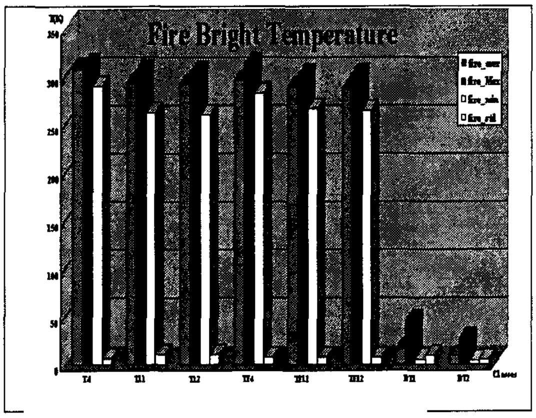

Fig. 2. Fire Bright Temperature in Different Bands in Diurnal Images

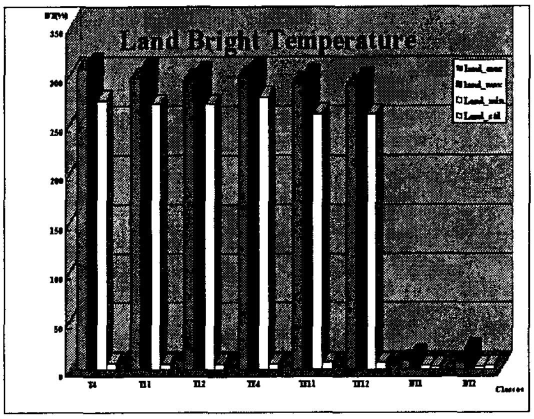

Fig. 3. Land Bright Temperature in Different Bands in Diurnal Images

3.2 Algorithm Description

According to the AATSR product Handbook [18, 22], the data just in nadir direction has been used for fire detection in this time.

3.2.1 Cloud Masking

Cloud detection was performed using a technique based on that used in the production of the International Geosphere Biosphere Program (IGBP) AVHRR derived Global Fire Product [23]. But we found sometimes the land's bright temperature in band 12 μm is lower than 265 k. So, heritage algorithms are developed in our cloud detection. We changed the bright temperature of band 12 μm from 265 k to 262 k. The Daytime pixels are considered to be cloud if one of Eqs.1-3 condition is satisfied.

$$R_2 + R_3 > 0.9 \tag{1}$$

$$T_{12} < 262\ \mathrm{K} \tag{2}$$

$$\begin{cases} R_2 + R_3 > 0.8 \\ T_{12} < 285k \end{cases} \tag{3}$$

Nighttime pixels are classed as cloud if the single condition Eq. 2 is satisfied.

These simple criteria were found to be adequate for identifying larger, cooler clouds but consistently missed out small clouds and cloud edges.

3.2.2 Water masking

Water pixels were identified if a pixel satisfied the condition of Eq. 4.

$$\begin{cases} R_3 < 0.03 \\ R_4 < 0.02 \\ NDVI < 0.0 \end{cases} \tag{4}$$

where: R_2 is the reflectance of band at 0.65μm;
R_3 is the reflectance of band at 0.87μm;
R_4 is the reflectance of band at 1.6 μm;
NDVI is the normal vegetation Index;

3.2.3 Potential Fire Pixels Identification

A preliminary classification is used to eliminate obvious non-fire pixels. Those pixels that remain are considered in subsequent tests (described in the next sections) to determine if they do in fact contain an active fire.

A daytime pixel is identified as a potential fire pixel if its' value satisfied Eq. 5.

$$\begin{cases} T_4 > 308K \\ DT_1 > 20K \\ 5\% < R_3 < 15\% \end{cases} \tag{5}$$

For nighttime image, the reflective test is omitted and the T_4 threshold reduced to 300 K. A Pixel will be identified as a potential fire pixel if its' value satisfied Eq. 6.

$$\begin{cases} T_4 > 300K \\ DT_1 > 20K \end{cases} \tag{6}$$

3.2.4 Background Characterization

In the next phase of the algorithm, an attempt is made to use the neighboring pixels to estimate the radiometric signal of the potential fire pixel in the absence of fire. Valid neighboring pixels in a window centered on the potential fire pixel are identified and are used to estimate a background value. Within this window, valid pixels are defined as those that (1) contain usable observations, (2) are located on land, (3) are not cloud-contaminated, and (4) are not potential fire pixels.

3.2.5 Fire Identification

A neighbour 'spilt windows' criterion identical method has been used for fire identification. The neighbour 'spilt windows' criterion identical method is widely used in fire detection of satellite image (e. g. NOAA-AVHRR). Here, a (5 × 5 pixels) 'spilt window' has been used to identify fire and a series of tests are used to perform fire detection. These look for the characteristic signature of an active fire in which both the 3.7 μm brightness temperature (T_4) and the 3.7 μm and 11 μm brightness temperature difference (DT_1) depart substantially from that of the non-fire background. Relative thresholds are adjusted based on the natural variability of the background. The conditional tests formula are listed from Eqs.7-11.

$$DT_1 > \overline{DT}b + 2.0\Delta DT_b \tag{7}$$

$$T_4 > \overline{T}_{4b} + 2.0\Delta T_{4b} \tag{8}$$

$$T_{11} > \overline{T}_{11b} + \Delta T_{11b} - 2k \tag{9}$$

$$R_3 < 10\% \tag{10}$$

$$R_4 < 15\% \tag{11}$$

where: DT_1 is bright temperature difference of 3.7 μm and 11 μm;
ΔDT_b is the standard deviation of background pixels of DT_1;
$\overline{DT}_b$ is the mean of background pixels of DT1;
$\overline{T}_{4b}$ is the mean of background pixels at 3.7 μm band;
ΔT_{4b} is the standard deviation of background pixels at 3.7 μm band;
$\overline{T}_{11b}$ is the mean of background pixels in 11 μm band;

ΔT_{11b} is the standard deviation of background pixels at 11 μm band;

A pixel in daytime will be flagged as fire point if it satisfies Eqs.7-11. However, a pixel in nighttime just need satisfy Eqs.7-9 and Eq.12.

$$R_4 < 10\% \tag{12}$$

3.2.6 False Alarm Rejection

To the diurnal image, false fire alarm can be caused by strong solar, desert boundary and coastal. The 1:1,000,000 scale map of vegetation has been used to identify the type of landcover in this experiment. So, we just consider the false fire caused by strong solar in this time. A pixel in daytime will be eliminated as sun false fire point from fire point if its' sun glint satisfies Eq.13.

$$\begin{cases} R_3 > 20\% \\ R_4 > 5\% \\ \theta < 40° \end{cases} \tag{13}$$

Here, θ is the sun glint. It is calculated by using Eq. 14 [10, 13].

$$\cos\theta = \cos\theta_v \cos\theta_s - \sin\theta_v \sin\theta_s \cos\Phi \tag{14}$$

Here, θ_v and θ_s are the view and solar zenith angles, respectively, and Φ is the relative azimuth angle.

4. Fire detection results

Six large forest fires have been selected to test the fire detection methodology in this time. Here, we use the hitting precision and missing precision to test the method. The hitting precision is calculated by using Eq. 15. The missing precision is calculated by using Eq. 16. At the same times, the fire results gotten from MODIS image have also been used. Part of results has been listed in Tab. 1 and Fig. 4.

$$\text{Hitting Precision} = \text{Hitting pixels numbers}*100\% / \text{Fire pixels numbers} \tag{15}$$

$$\text{Missing Precision} = 100\% - \text{Hitting precision} \tag{16}$$

Tab. 1. The fire detection results of AATSR-TOA and MODIS data

Date	Fire pixels' number	AATSR-TOA				MODIS			
		Hitting pixels' number	Missing Pixels' numbers	Hitting Precision (Unit: %)	Missing Precision (Unit: %)	Hitting pixels' numbers	Missing Pixels' numbers	Hitting Precision (Unit: %)	Missing Precision (Unit: %)
July 28, 2002	8	6	2	75.00	25.00	7	1	87.50	12.50
Apr.25, 2003	34	24	12	70.59	29.41	28	6	82.35	17.65
May 3, 2003	25	17	8	68.00	32.00	16	9	64.00	36.00
Oct. 2, 2005	16	12	4	75.00	25.00	14	2	87.50	12.50
Oct. 3, 2005	22	15	7	68.19	31.81	15	7	72.72	27.28

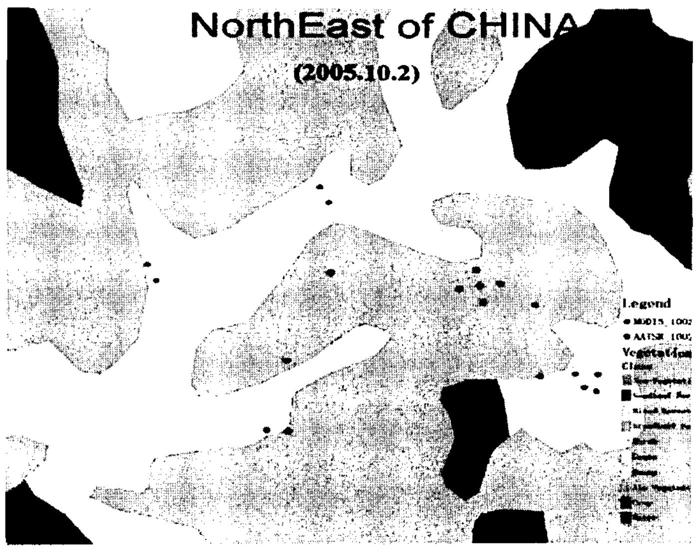

Fig. 4. Fire points overlay with Vegetation Map

5. Discussion and Conclusions

The relative threshold fire identification by using the bright temperature and reflectance of AATSR-TOA nadir image for the experiment area has been developed and validated in this time. From tab. 1, we can see all of the hitting precisions are more than 65%. It shows the methodology is viable. However, there are still missing some fire pixels in the experiment area. At the same time, this study just has been validated by using part of AATSR-TOA image. So, further study is needed to verify the algorithm of AATSR whether it can satisfy the condition of national of China. In the future, there might be some parameters that needed to be considered in the model, adjustment and modification.

By combining the hitting precision of AATSR and MODIS data from Tab.1, we can see the fire hitting precision by using MODIS data is relative higher than by using AATSR-TOA data. There are two reasons. One reason is the instrument. There are two satellite which carries MODIS sensor. So, the same place can be covered four times everyday. At the same time, its' main fire detection channels saturate at high brightness temperatures: 500k at 4 μm and 400 k at 11 μm [13]. However, there are just one ENVISAT which carries AATSR. It just can pass over the same place two times everyday and their bright temperature saturation is lower than 320k at 3.7 μm [22]. This will lose some fire information. The other is the methodology. The saturated pixels have been eliminated in the fire identification method. This will also miss some fire information. In fact, the forest fires often take place during 10:00 am to 15:00 pm in northeast of China. We can see there are spatial differences among the fire points by using AATSR and MODIS data from Fig. 4. It shows the fires' change with time. So, combining both AATSR and MODIS data, the Fire monitoring result will be more reliable.

6. References

1. ICHOKU C., KAUFMAN Y. J., and GIGLIO L. et al, Comparative analysis of daytime fire detection algorithms using AVHRR data for the 1995 fire season in Canada: perspective for MODIS, *International Journal of Remote Sensing*, Vol. 24(8), 1669–1690, 2003.
2. Giglio, L., Kendall, J. D., and Justice, C. O., Evaluation of global fire detection algorithms using simulated AVHRR infrared data, *International Journal of Remote Sensing*, Vol. 20, 1947–1985,1999.
3. Dozier, J., A method for satellite identification of surface temperature fields of subpixel resolution, *Remote Sensing of Environment*, Vol. 11, 221–229, 1981.
4. Matson, M., Dozier, J., Identification of subresolution high temperature sources using a thermal IR sensor, *Photogrammetric Engineering and Remote Sensing*, Vol. 47, 1311–1318, 1981.

5. Cahoon, D., Stocks, B., and Levine, J., et al, Satellite analysis of the severe 1987 forest fires in northern China and southeastern Siberia. *Journal of Geophysical Research*, Vol. 99, 18627-18638, 1994.
6. Li, Z., Kaufman, Y., and Ichoku, C., et al, *A review of AVHRR-based active fire detection algorithms: Principles, limitations, and recommendations, In Global and Regional Vegetation Fire Monitoring from Space: Planning and coordinated international effort,* edited by F. Ahern, J.G. Goldammer, and C. Justice (The Hague: SPB Academic Publishing), 199-225, 2001.
7. Flasse, S. P., Ceccato, P., A contextual algorithm for AVHRR fire detection, *International Journal of Remote Sensing*, Vol. 17, 419– 424, 1996.
8. Fang M. and Huang W., Tracking the Indonesian forest fire using NOAA/AVHRR images, *International Journal of Remote Sensing*, Vol. 19(3):387-390, 1998.
9. Pozo, D., Olmo, F.J., and Alados-Arboledas, L., Fire Detection and Monitoring Using a multitemporal Technique on AVHRR Mid-Infrared and Thermal Channels, *Remote Sensing of Environment*, Vol. 60,111-120. 1997.
10. Kaufman Y. J. et al, *ALGORITHM FOR REMOTE SENSING OF TROPOSPHERIC AEROSOL FROM MODIS.* Algorithm Technical Background Document, 10, 1998.
11. Kaufman, Y. J., Herring, D. D., Ranson, K. J., Collatz, G. J., Earth Observing System AM1 mission to Earth, *IEEE Transactions on Geoscience and Remote Sensing*, Vol. 36, 1045–1055, 1998.
12. Kaufman, Y. J., Justice, C. O., and Flynn, L. P., et al, Potential global fire monitoring from EOS-MODIS, *Journal of Geophysical Research*, Vol. 103, 32215–32238, 1998.
13. Kaufman, Y. J., ICHOKU, C., and KORONTZI, s., et al, Fire and smoke observed from the Earth Observing System MODIS instrument-production, and operational use, *International Journal of Remote Sensing*, Vol. 24(8), 1765–1781, 2003.
14. Louis Giglio et al, An Enhanced Contextual Fire Detection Algorithm for MODIS, *Remote Sensing of Environment*, Vol. 87: 273-282, 2003.
15. Justice, C. O., Giglio, L., and Korontzi, S., et al, The MODIS fire products, *Remote Sensing of Environment*, 83, 244– 262, 2002.
16. Justice, C. O., Kendall, J. D., and Dowty, P. R., et al, Satellite remote sensing of fires during the SAFARI campaign using NOAA AVHRR data, *Journal of Geophysical Research*, Vol. 101, 23851– 23863, 1996.
17. Justice, C. O., Townshend, J. R. G., and Vermote, E. F., et al, An overview of MODIS land data processing and product status, *Remote Sensing of Environment*, 83, 244–262, 2002.
18. Andrew Birks, *The AATSR Handbook*, Rutherford Appllet Laboratory, Chilton, 20 August 2002.
19. KELHÄ, V., RAUSTE, Y., and HÄME T., at al, Combining AVHRR and ATSR satellite sensor data for operational boreal forest fire detection, *International Journal of Remote Sensing*, Vol. 24(8), 1691–1708, 2003.
20. ARINO, O., and ROSAZ, J., *1999,1997 and 1998 world ATSR fire atlas using ERS-1 ATSR-2 data*, Proceedings of the Joint Fire Science Conference, Boise, 15-17 June 1999.
21. ARINO, O., and ROSAZ, J., *2000,1997 world ATSR fire atlas*, IUFRO, Conference on Remote Sensing and Forest Monitoring, 1-3 June 1999 (Luxembourg: European Commission), 606-615.
22. http://www.leos.le.ac.uk/aatsr.
23. Stroppiana, D., Pinnock, S., and Gregoire, J. M., The Global Fire Product: Daily fire occurrence from April 1992 to December 1993 derived from NOAA AVHRR data, *International Journal of Remote Sensing*, Vol. 21, 1279-1288, 2000.

Agriculture

Rice Monitoring
(id. 2562)

RICE MONITORING IN CHINA

MID-TERM REPORT

Thuy Le Toan (PI), Alexandre Bouvet
Centre d'Etudes Spatiales de la Biosphère, 18 Avenue Edouard Belin, 31401Toulouse Cedex 9, France,
Thuy.Letoan@cesbio.cnes.fr
Tan Bingxiang (PI), Li Zengyuan, He Wei
Institute on Forest Resources and Information Technique, Chinese Academy of Forestry, Beijing, P.R. China,
tan@mail.forestry.ac.cn
Li Bingbai, Zhang Pingping
Institute of Agricultural Resource and Environment, Jiangsu Academy of Agriculture Sciences, Nanjing, P.R. China
bbli88@sohu.com
Alberte Bondeau
Potsdam Institute for Climate Research (PIK), Potsdam, Germany
alberte@pik-potsdam.de

ABSTRACT

This paper summarises the objectives of the project, the works undertaken, the results obtained, and outlines the next steps of the project. The objective of the project is to develop methodology to use ENVISAT data for rice mapping and retrieving information characterising rice fields (biomass, photosynthetical activities, water management status) relevant to the modelling of rice growth. The overall goal is the estimation of rice production at local and regional scale and the estimation of the Carbon fluxes (CO_2, CH_4) at regional scale. In the first phase of the study, remote sensing methodology is developed at selected test areas for rice mapping and retrieving of rice parameters. The activities include ground data collection and analysis of remote sensing data. Meantime, preliminary works on large scale crop modelling in China have been undertaken. The results obtained using ENVISAT data in 2004 and 2005 at the test areas in Jiangsu province indicate that it is possible 1) to map rice fields at a single date using two polarisations of ASAR APP, 2) to retrieve rice biomass using the polarisation ratio, 3) to map the main rice varieties, 4) to achieve regional rice mapping using multidate ASAR WideSwath data, and 5) to detect intermittent drainage. These new findings, still to be validated and confirmed, show great potential for statistics of rice growth areas, and in providing the essential information for the modelling of rice growth. ENVISAT ASAR data are expected in 2006, for a demonstration of the methodology, at least at a regional scale, and for an integration of remote sensing in crop modelling.

1. INTRODUCTION

The United Nations declared the year 2004 the International Year of Rice, recognizing that rice is the primary food source for more than haft of the world's population and that it is essential to enhance the sustainability and productivity of rice production systems for global food security. Demand for rice in Asia is projected to increase by 70% over the next 30 years (IRRI 2002). At the same time, population increase and intensification of economic development will lead to decline of rice harvested area. Paddy rice cropland distributions and management intensity (fertilizer use, cultivars, water management, multi-cropping) will undergo changes over the coming decades.
Because of the importance of the world rice area (1.5 million km^2 in 1999), the changes in rice area and cultural practices can have a significant impact on the global climate change. Irrigated rice areas are the major sources of methane (CH_4) emissions from rice fields. The assured water supply and control, intensive soil preparation and resultant improved growth of rice favour production and emissions of methane (CH_4), the second in importance to CO_2 as a green house gas. Recent research indicated that methane emissions from rice paddies are 50-100 Tg CH_4/yr (Prather & Ehhalt, 2001), 10-20% of total global emissions.

China is the world's largest rice producer, accounting for 32-35% of total world production (190 million tons in 2000). This makes China the first continent where methodological studies on rice production systems and their impact on global change should be conducted. Area harvested to rice has declined during the past 25 years (37 million hectares in the mid-1970's to 30 million hectares today). At the same time, China's increased demand for grain has been met by raising yields and improved cultural practices. China has developed the most successful varieties of hybrid rice in the world, and more than one-third of total rice area is planted to hybrids. Chinese scientists have also developed irrigation techniques for rice that reduce water consumption by allowing intermittent drying of the paddy fields, without reducing grain yields. The shift from continuous flooding to midseason drainage water management resulted in a significant reduction of CH_4 emissions from China's paddy fields (Huang et al. 2004).

For both objectives, to monitor change in rice ecosystems in China and to study its impact on the global climate, satellite remote sensing data is an alternative that can be used to provide sufficient spatial and temporal details needed

Proc. 2005 Dragon Symposium "Mid-Term Results", Santorini, Greece
27 June – 1 July 2005 (ESA SP-611, January 2006)

for improved a) estimation of rice acreage and rice production and b) estimation of the impact of rice paddy agriculture on trace gas emissions. The overall objective will be to refine remote sensing methods and models to monitor changes in rice cultivation and their impacts on rice production and Green House Gases emissions. This constitutes the framework for the « Rice Monitoring in China », a Dragon project aiming at assessing the use of ENVISAT instruments for rice monitoring.

2. METHOD AND APPROACH

Remote sensing methods are combined to crop modelling to achieve the project objectives. ENVISAT ASAR and MERIS data, together with SPOT VGT data are used to derive rice mapping and rice biophysical parameters. The rice map and parameters, together with meteorological and ancillary data (soil, cultivation practices...) are used in crop models. The expected output will be the estimation of rice production and estimation of Carbon fluxes (CO_2, CH_4) from rice fields. Comparison with in-situ production estimates will be used to improve the rice models, whereas seasonal variation of the C fluxes will be compared to measurements from ENVISAT SCIAMACHY. The work flow of the project is depicted in Fig.1.

The methodology is developed during the first year based on data collected on the test area in Hongze county at the Jiangsu province (Fig.2). Jiangsu province is situated in the east of the People's Republic of China (116°22′- 121°55′E, 30°45′- 35°07′N), in the lower reaches of Yangtze and Huaihe rivers, in the agro-ecological zone of warm subhumid subtropics with summer rainfall. This is part of the largest grain production area in China, with rice, wheat and cotton being grown. The rice area is around 2.6 million hectares. The annual rice production is of 24 million tons (10% of China). ENVISAT data were ordered for 2004 and 2005 and ground data have been collected during satellite overpasses. In a next phase of the project, the methodology developed in Jiangsu will be tested on other Southern regions to account for multi cropping practices.

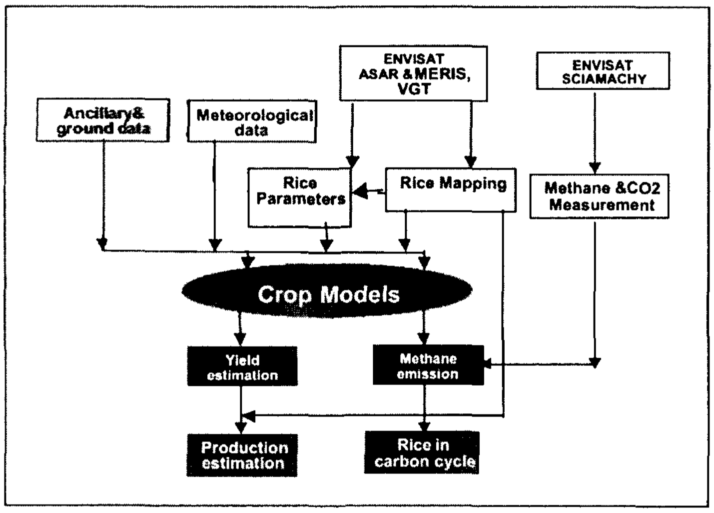

Fig.1. Rice monitoring project work flow

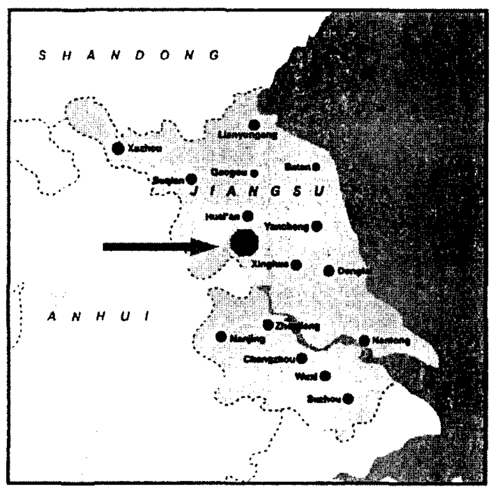

Fig.2. Test area in the Hongze county, Jiangsu

3. DEVELOPMENT OF RICE MAPPING AND RICE PARAMETER RETRIEVING METHODS

There are several factors that make synthetic aperture radar (SAR) data a logical choice for rice monitoring. First, the all weather capacity of the SAR is very important in tropical and sub-tropical areas where much of the world's rice is grown and the availability of optical satellite data is severely restrained by cloud cover. Radar backscatter has been found to be strongly correlated to several key growth parameters of the rice plant, including height, age, and biomass (Kurosu et al., 1995, Le Toan et al., 1997, Ribbes and Le Toan, 1999, Inoue et al., 2002). The backscatter of rice fields increases quickly during the vegetative stage of the rice crop and then reaches a saturation level. Second, the use of backscatter temporal change has proven to be effective in the mapping of paddy rice areas. Backscatter can increase by more than 10 dB from the beginning of the growth cycle (flooded fields) to the saturation level (Ribbes and Le Toan, 1999, Inoue et al., 2002). Because of this large backscatter variation, well-timed image acquisitions should be able to operationally identify paddy fields since other land covers do not experience such variation. Rice paddies have been mapped from multi-temporal SAR data using backscatter change thresholds in Indonesia (Ribbes and Le Toan, 1999) and Vietnam (Liew et al., 1998), and from land cover classifications in India and in Japan. Using ENVISAT ASAR data, there are two assets to be exploited: the first is the use of dual polarisation ASAR data, and the second is the use of ASAR WideSwath data for regional mapping. The methodology development, testing and validation constitute the major part of the first year activities of the project.

3.1 ASAR and ground data

ASAR data

2004: 33 APP frames (33% cancellation), 22 WS frames, and 39 MERIS images received.

2005: 2 APP (71% cancellation), 28 WSM (52% cancellation).

The ASAR data ordered suffered from frequent cancellation. Since rice mapping method requires multiple data acquired on the same frame, either for multi temporal method or for speckle filtering technique, the available data appeared insufficient. The limitation is more severe for the retrieving of rice parameters, which requires data acquired during the rice cycle.

Ground data

The objective of ground data collection is to provide a dataset that can be used to analyse the parameters of the plant growth, to analyse the radar data as a function of these parameters, to provide inputs in radar models for further understanding of the radar signal, and to validate the mapping and retrieving results. A guideline has been used to define the relevant parameters and procedures (Le Toan, 2004). In 2004, four sampling units in the middle of Jiangsu Province have been selected for ground data collection. The fields cover about 500m in length and 500m in width. They are located in Gaoyou county, Xinghua county, Funing county and Hongze county respectively (Table 1). In this sub tropical region, there is only one rice reason – from May to October. Generally rice is sown around May 15, transplanted around June 15, and harvested around October 15. The crop calendar may shift (within one-two weeks) according to local conditions (different varieties, labour availability, weather conditions). Other crops grown in this area are bean, cotton, mulberry, vegetables, which cover a smaller proportion of the area compared to rice.

Table 1. Location of sampling areas, paddy varieties and sowing transplanting dates in 2004

Location	Coordinates	Paddy varieties	Sowing	Transplanting
Gaoyou	32°53′00N 119°31′03E	zhendao88	May 10	June 15
Xinghua	32°55′51N 120°05′31E	wuyugeng-3	May 10	June 15
Funing	33°40′24N 119°42′52E	wuyugeng-3	May 7-8	June 14-15
Hongze	33°07′51N 118°48′33E	99-8	May 12-13	June 22

Ground data have been collected at the dates of satellite passes: July 15, July 20, August 2, August 18, September 10, September 25, October 11. They include ground condition (water layer or muddy, wet and dry soil), moist and dry biomass of paddy plants, and canopy and the following plant structural parameters:

a) Canopy structural parameters: planting distance, plant row direction, bunch distance, bunch diameter, plant height (above water layer), number of stems, stem diameter, stem inclination.

b) Leaf parameters: number of leaves per stem, leaf length, leaf width, leaf thickness, leaf insertion angle, bending angle of leaves.

c) Panicle parameters: number of panicles per bunch, panicle length, panicle angle, number of grains per panicle.

Table 2 lists the ground data collected at the Hongze test area in 2004.

Table 2. Ground data collected at the Hongze test field in 2004

Date of sampling	2004/07/20	2004/08/02	2004/08/18	2004/09/10	2004/09/25	2004/10/11
Plant phenological stage	tillering	jointing	heading	flowering	ripening	ready to harvest
Water layer height (cm)	9.56	7	3.75	0/muddy	0	0/ muddy
Bunch diameter (bottom) (cm)	6.05	6.725	7.5	5.25	5.75	5.5
Bunch diameter (middle) (cm)	13	12.375	15.25	13.75	17	12.5
Bunch diameter (top) (cm)	32.5	27.125	34.75	24	37	25.75
Plant height (cm)	65.625	68.125	82	97	100	112
Number of stems per bunch	12.8	17.5	14.02	10.05	11.9	11.325
Stem diameter (cm)		0.79	0.64	0.41	0.36	0.37
Stem inclination (°)	1.7	1.7	1.4	2.4	2.8	3.2
Wet weight per bunch (g)	80.005	115.35	173.39	110.225	161.66	144.2025
Dry weight per bunch (g)	12.87	19.99	44.98	29.425	48.36	55.99
Water content	83.91%	82.67%	74.02%	73.30%	70.09%	61.17%
Number of leaves per stem	4	3.9	5.8	5.7	4.6	3.5
Leaf length (cm)	30.71	38.66	40.82	37.95	36.5	39.45
Leaf width (cm)	1.03	1.3	1.31	1.26	1.24	1.37
Leaf thickness (cm)	0.14	0.2	0.2	0.15	0.2	0.2
Leaf insertion angle (°)	17	14.4	20.8	18.3	14.5	15.1
Number of panicles per bunch				4	11	10.5

Panicle length (cm)				13.71	15.35	15.35
Panicle width (cm)				0.98	1.59	1.78
Panicle angle (°)				4.8	13	15.6
Number of grains per panicle				10.3	11.9	12.4

In 2005, the ground data collection aimed at having a larger number of sampled fields, but restricted to major rice parameters. Measurements have been carried out at 11 test fields in the Hongze county (5 hybrid, 6 Japonica). Canopy parameters have been measured at the beginning of the season. On July 10, July 20, August 17, September 14, September 29, the following parameters have been measured: soil condition, plant height, number of stems per bunch, wet weight and dry weight per bunch, number of leaves per stem, leaf width.

3.2 Rice monitoring using ASAR APP

3.2.1. Rice/non rice mapping

Compared to the previously developed rice mapping method based on multitemporal data, the 2 polarisations of ASAR APP can bring an improvement in terms of the number of data necessary in an operational rice mapping programme. Previous experimental and theoretical studies suggested that HH backscatter is higher than VV backscatter at C band (Le Toan et al., 1997, Ribbes and Le Toan, 1999, Wang et al., 2004) and at X band (Le Toan et al., 1989). This is due to the strong attenuation of the VV waves by the paddy plants with vertical structure. ASAR provides the first satellite C-band data with both HH and VV.

Fig.3 shows an analysis of the temporal variation of the HH/VV ratio for different land covers in the Hongze area (cf. Li et al, 2005, this issue). HH/VV increases with the growth of the rice plant, up to 5-6 dB, whereas the ratio of the other main land covers in the area has small temporal change, with ratio values of the order of 0 to -2 dB. Water has ratio of -2,-3 dB, and urban areas can have temporally stable HH/VV with values up to 6, 7 dB. According to the analysis result, rice can be characterised using any single date ASAR during the period after end of tillering (August-September-October in Jiangsu province).

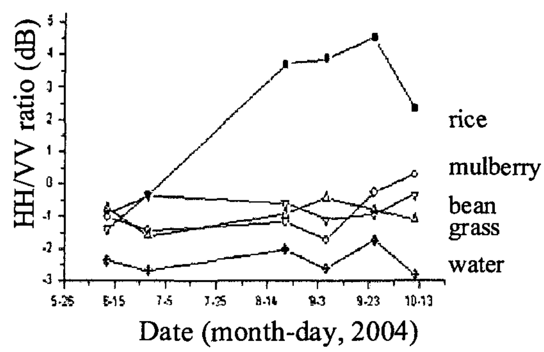

Fig.3. The ratio of HH/VV (or difference in dB) of different land cover types in the Hongze area

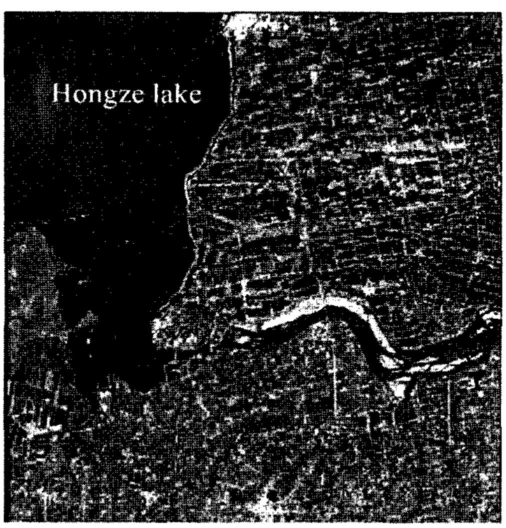

Fig.4a. ASAR image (magenta:HH, green:VV, 34 km x 38 km) of the Hongze area, Jiangsu province, 6-9-2004

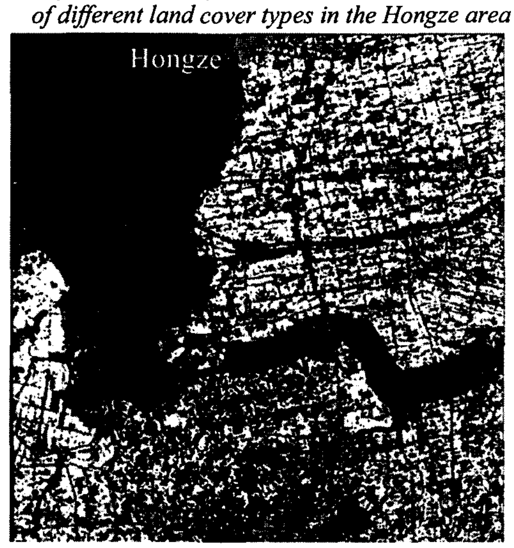

Fig.4b. Map of rice fields (yellow), urban areas (red) and other (black) from 4a.

Fig.4a shows the HH and VV colour composite image of the region of Hongze at the date of Sepember 6, 2004, where magenta colour depicts higher HH compared to VV, thus corresponding to rice fields. Rice/non rice mapping based on the relative HH and VV backscatter could be performed. An example of the 2004 results is shown in figure 4b. To map rice fields with small dimension, the mapping algorithm to be applied to single date ASAR data requires a high

Equivalent Number of Looks (ENL) of the images, i.e. achieved by efficient speckle filtering. The filter must also have preserved the fine structure of the images. Multi-temporal filtering method previously developed (Le Toan et al.,1997, Quegan et al., 2000) is applied to HH and VV images of the area, including archived past images. The mapping algorithm includes the following steps: calibration, co-registration of multi-images, multi-image filtering, optional spatial filtering, application of decision rules and geocoding. Different classification methods are developed and tested. One of the algorithms and results are described in details in Bouvet et al., this issue. The same algorithm, derived from 2004 data, is applied to 2005 data. The results are currently validated by comparison with reference maps of samples of about 1 km x 1 km, established using in situ DGPS measurements and Landsat ETM data. Preliminary results yield a percentage of good rice pixel classification > 87% (Bouvet et al., 2005).

3.2.2 Mapping of rice varieties

In Jiangsu province as in overall China, hybrid rice tends to replace the traditional varieties (18 million ha of a total 33 million ha in 1992). Rice hybrids yield about 20% higher than inbred rices, they are also more resistant to disease and have shorter growth cycle. In the future, the proportion of hybrid rice may have a significant increase. Detection of hybrid rice by remote sensing is thus an important objective. The difference in rice structure (more vertical structure of hybrid rice) can explain that HH/VV of hybrid rice in June-July-August is higher than that of Japonica rice (figure 5). It is then possible to map the two main rice varieties using multidate data (August for rice mapping and June for varieties mapping). Fig.6 shows a map of hybrid and Japonica rice that is in good agreement with the local observations (cf. Li et al. 2005, this issue).

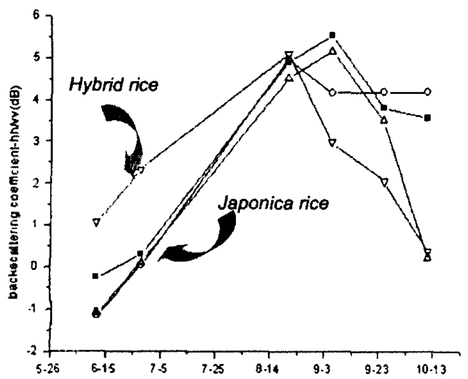

Fig.5. HH/VV ratio of two varieties of rice.

Fig.6. Map of hybrid rice (bright pink) and Japonica rice (black,blue and red, according to the crop calendar).

3.2.3 Map of midseason drainage

The possibility to detect midseason or intermittent drainage would have an important impact on the estimation of CH_4 emissions from rice fields. The main interaction mechanism between the radar waves and the flooded rice canopy is the vegetation-water interaction. When the water is drained, the dominant interaction mechanisms change (vegetation-wet soil interaction, attenuated ground interaction. etc.). Fig.7. shows the mean HH backscatter values of rice fields from two different areas having drainage in August and September. The decrease in HH backscatter could be related to the drainage (earlier drainage in Hongze compared to Gaoyou, two drainage periods in Hongze). However, more work needs to be done to confirm the analysis, i.e. by more observation on the water management. Radar backscatter modelling simulation can also be done to quantify the effect of drainage on the radar backscatter.

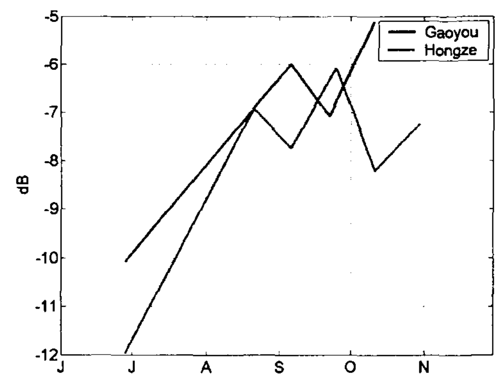

Fig.7. HH backscatter of rice at Hongze and Gaoyou

3.2.4 Retrieving of rice biomass

Fig.8. shows HH/VV of the test field in Gaoyou in 2004, as a function of rice wet biomass. The relationship differs according to the growth period, a linear increase from the beginning of tillering (first date, June 28) to flowering (September 8); after flowering, a decrease is observed. Fig. 9 shows the relationship between HH/VV ratio and wet biomass of all the fields where in situ biomass was measured: 1 field in Hongze and 1 in Gaoyou in 2004, and 7 fields in Hongze in 2005. The good correlation (R^2= 0.79, slope: 1.02) in Fig.9 suggests that rice biomass can be retrieved with small uncertainties until flowering (June to mid September in Jiangsu). When all the data of the whole cycle are put together, the relationship is slightly altered (R^2= 0.73, slope: 1.00). However, few data after flowering have been added due to lack of ASAR data in 2005.

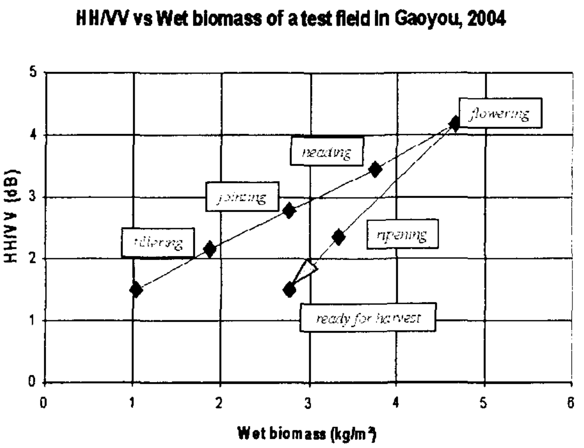

Fig.8. Temporal variation of HH/VV over a rice field as a function of rice wet biomass in Gaoyou, 2004.

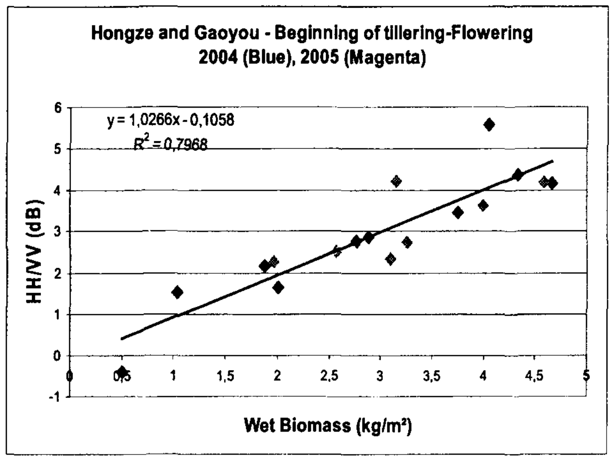

Fig.9. Relation between HH/VV and wet biomass of rice fields in Hongze(1 in 2004, 7 in 2005) and Gaoyou (1 in 2004).

3.3 Regional mapping with Wide Swath ASAR data

ASAR WideSwath data, at resolution of 150 m (and pixel size of 75 m), and swath width of 400 km, are more suitable to large scale rice mapping, for the provision of regional and continental statistics on rice grown areas and rice production. The data can also replace optical data at 1 km resolution, used in the modelling of carbon fluxes from rice fields. Since WS data have only one single polarisation, HH or VV, the mapping approach consists in using the backscatter temporal change. The processing steps are the same as for APP data, except that the speckle filtering requires a smaller number of multidate data, the initial WS images are of 15 looks (instead of 3 looks in APP).

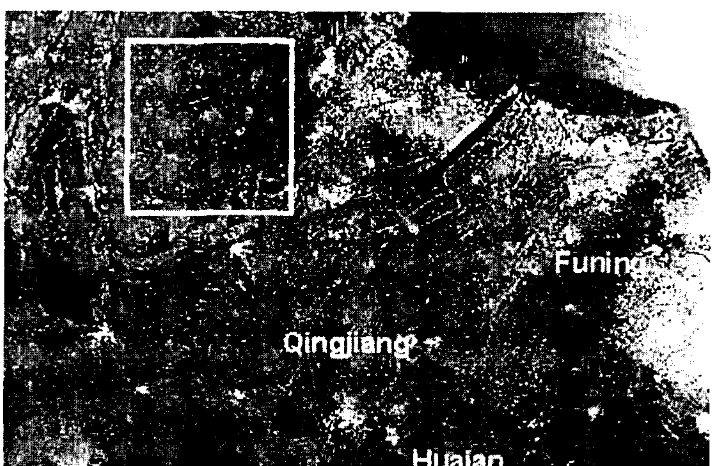

Fig.9a. Map of rice fields (blue) using ASAR WideSwath data (August and October). Region North of Qingjiang, Jiangsu (210 km x 127.5 km)

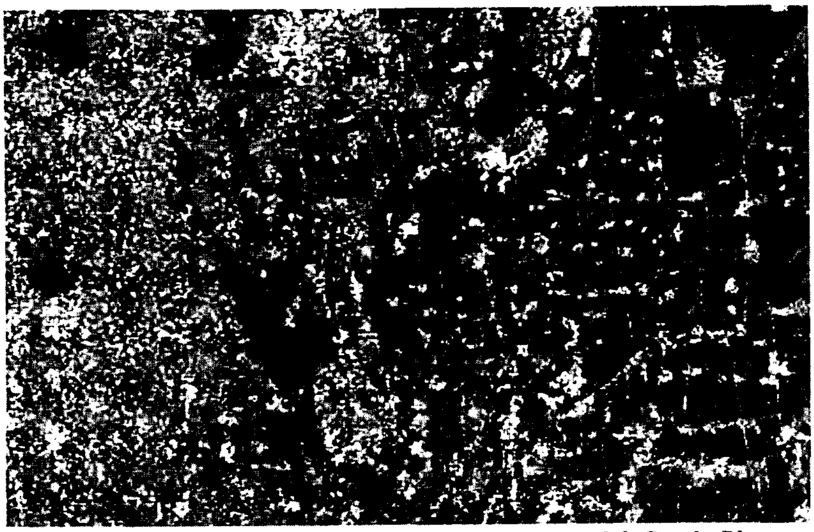

Fig.9b. Mapping of rice in the region of Qingjiangusing ASAR Wide Swath: Blow up of a region underligned in figure 9a

Figure 9a and 9b shows a part of a WS rice map using 2 dates, August and October 2004. Rice fields are identified as areas with strong decrease of the VV backscatter, from August to October.
The regional rice map, which appears promising, will be validated in the near future.

3.4 Monitoring of vegetation activities

MERIS data from ENVISAT were planned to derive the indicators of vegetation activities such as the Fraction of Photosynthetic Active Radiation (FPAR) and LAI, parameters which are to be used in crop modelling. The available MERIS data in 2004 were in most cases affected by cloud cover during the rice season. More frequent data acquisition would be needed in order to synthesise cloud free data for weekly or 10 day periods. For this reason, SPOT VEGETATION decadal data have been used instead of MERIS. Fig.10 shows the temporal variation of NDVI and NDWI over rice fields at Hongze area. NDVI (normalised combination of R and NIR) shows two cycles of vegetation activities (or greenness): the first, from March to June, corresponding to wheat, and the second, from June to October, corresponding to rice. NDWI (the Normalised Water Index) indicates the vegetation water content. Of importance is the minimum value in June that indicates the field flooding before transplantation (Xiao et al., 2002).On a continental scale, Figs.11 show selected maps of NDVI during the peak vegetation period, June-October 2004. Note that the vegetation activity (including rice) is well developed in the South thorough the period, whereas the maximum activity is found in the North only in the July-August period.

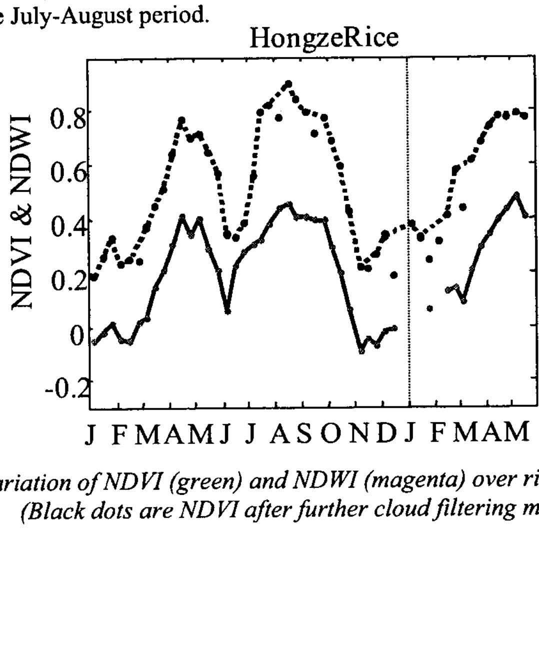

Fig.10. Temporal variation of NDVI (green) and NDWI (magenta) over rice fields at the Hongze area. (Black dots are NDVI after further cloud filtering method)

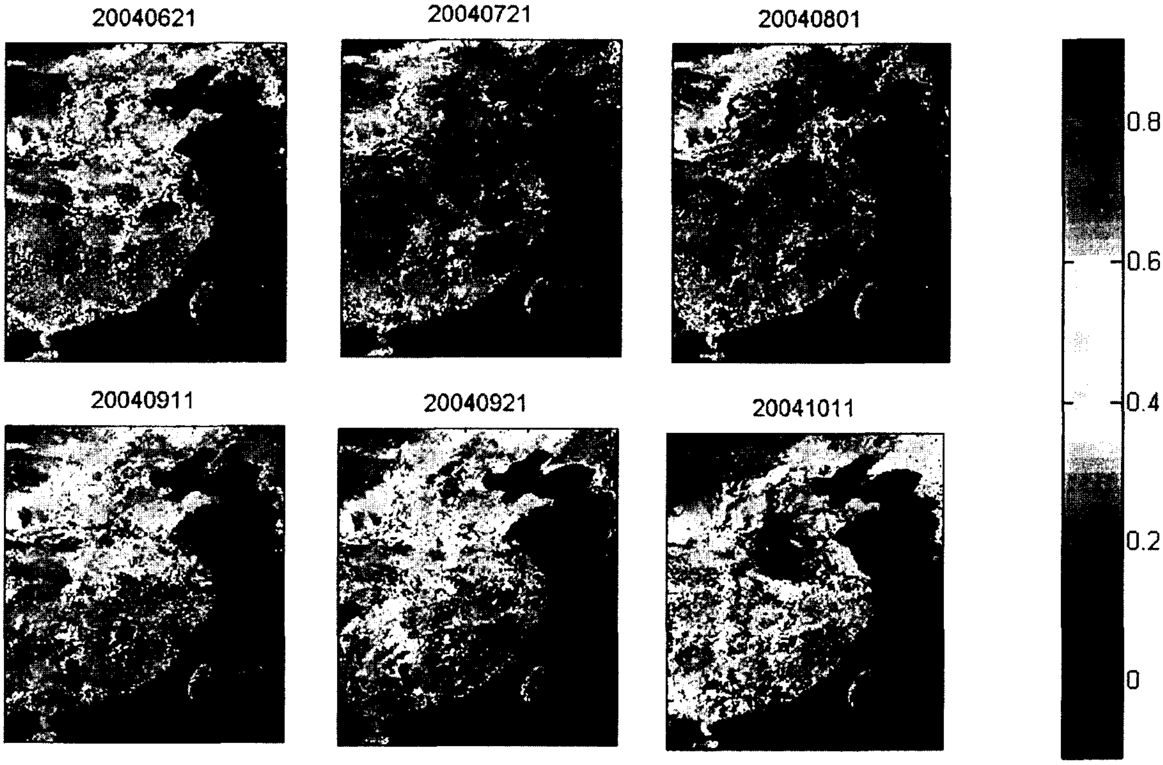

Fig.11. Selected maps of NDVI computed from SPOT VGT data during June-October 2004 period.

4. CROP MODELLING

Crop growth models generally simulate the daily growth and development rates of the crop, using as input meteorological parameters such as solar radiation, temperature, precipitation and humidity, together with ancillary data including plant species, soil type, fertilizer. The growth rate is calculated through the conversion of radiant energy to biomass. In general, remote sensing data are used to derive input parameters, usually FAPAR, percent vegetation cover or Leaf Area Index. Remote sensing data can also be used to reinitialise or reparameterise the model. ENVISAT will be an interesting data source, since biomass (and date of sowing) can be retrieved from ASAR data, and LAI or fAPAR from MERIS data. In this project, three crop models will be used and compared. The Rice growth model ORYZA-1 has been adapted to use "biomass" and "date of transplanting" retrieved from ERS (Ribbes and Le Toan, 1999). The model provided good prediction results on rice yield in Indonesia, Southern France and Vietnam. The rice model used by the Chinese team is the RCSODS (Rice Cultivational Simulation Optimization Decision Making System). These two models will be applied to rice in China, when the major remote sensing products will be available. The third model is the LPJ-C (Lund-Potsdam-Jena model for Crops), a dynamic vegetation model which can be used at regional or continental scales. Preliminary works consisted of adapting the LPJ-C model to multi-cropping system in China.

LPJ-C crop modelling

The fluxes of carbon (soil-vegetation-atmosphere) over rice areas can be simulated using the LPJ dynamic global vegetation model (Sitch et al. 2003). The original version of LPJ simulates the biogeochemical fluxes (carbon and water) for the potential natural vegetation. It is currently modified to account for agriculture and land use change (Scholze et al. 2005). The major crop types are implemented, such as rice, wheat, and soybean, the most common crops in China. The model is designed to run globally at the 0.5° spatial resolution, which is the resolution of the most commonly available global historical climate, soil, and land use/land cover dataset. For each crop type present within a 0.5° grid cell, it simulates according to the soil and climatic conditions the most appropriate sowing date, and the associated most productive variety. Multiple cropping is possible for rice if the seasonal temperatures allow it, but the model does not yet include the rice-wheat cropping system although this is common in many regions of Asia. Rice is always irrigated in the model. For the other crops the percentage of irrigated areas is estimated, according to a global dataset on areas equipped for irrigation. Photosynthesis and respiration are simulated at the daily or monthly time step, but the carbon fluxes to the atmosphere are restricted to the estimation of the CO_2 fluxes (autotrophic and heterotrophic respiration). The emission of CH_4 instead of CO_2 from flooded rice fields will be implemented in the near future. Phenology, assimilation, water status, and daily growth are coupled, which results in the simulation of the seasonal variations of the leaf area index (LAI) and the biomass of the different plant organs (roots, leaves, stems, grains). The simulated Fraction of Photosynthetic Active Radiation (FPAR) is derived from the LAI. To have a long time series of FPAR data, NOAA/AVHRR data have been used in the first test.

Fig.12 shows the seasonal variations over the period 1993-2003 of the FPAR and of the carbon fluxes (Net Ecosystem Exchange NEE) for one single grid cell in the Sichuan region. The simulated FPAR displays the same seasonal variations as the satellite FPAR, however it seems to be much too low. More information is needed about the area (real sowing dates, variety, multiple or single cropping, occurrence of wheat after rice, etc) to understand where the difference comes from. The simulated NEE displays the expected seasonal fluctuations between the growing season (CO_2 flux to the vegetation, negative NEE) and the non-growing season (CO_2 flux to the atmosphere, positive NEE). The balance depends to a great extent on the annual climatic conditions, leading to the occurrence of "carbon source" or "carbon sink" years. This figure will possibly change significantly with the implementation of methane emissions.

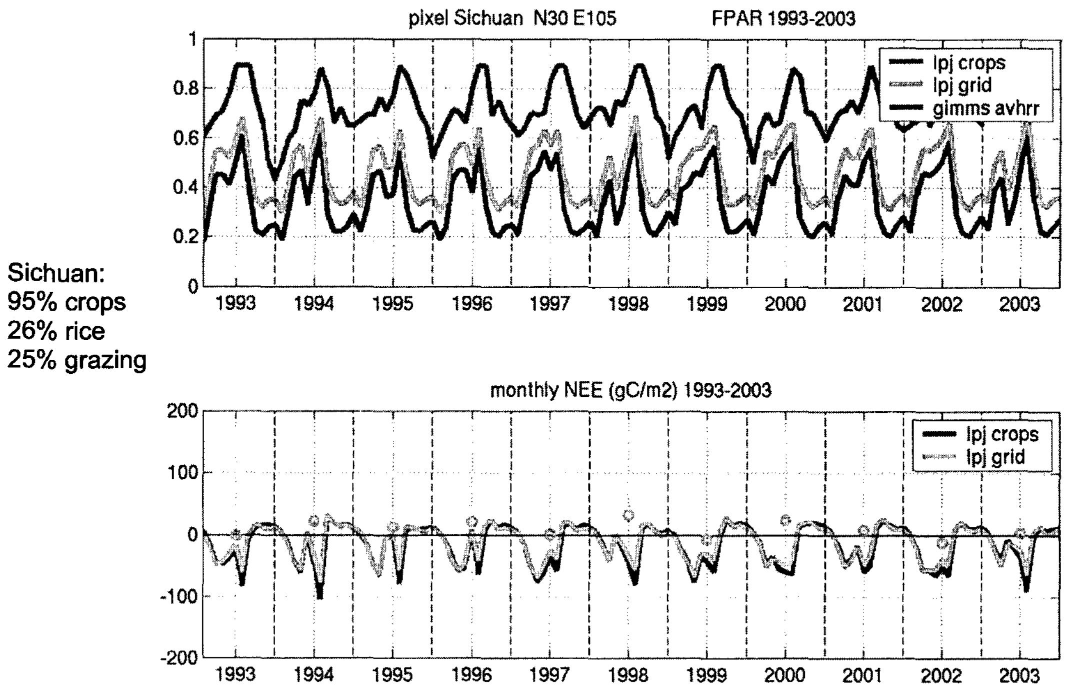

Fig.12. Seasonal simulations of FPAR (top) and NEE (bottom) for one grid cell in Sichuan for the period 1993-2003. The LPJ-C results are shown for the crops only (blue) and for the entire grid cell that includes natural vegetation as well (green). The satellite FPAR is shown in red.

Fig.13 shows the maps of the simulated monthly Net Primary Production (NPP), averaged over 10 years, for China. When all land covers are considered, i.e. natural vegetation and crops, the simulated pattern is smoother than when crops alone are simulated. This is due to the mixture of several vegetation types with different phenology in the case "all land covers" while "crops only" can display locally strong "monoculture" features leading to higher seasonal variations.

In the Dragon rice project, the use of better input data sets than the global data used up to now is planned. This includes data on exact rice coverage, sowing dates, variety, double/single cropping, and farming practices: these are input data and they will serve to better constrain the model. The data includes vegetation data as well such as yield, biomass, LAI, FPAR. These data allow a check of some model-simulated variables, and can be used to adjust/calibrate the model. The cooperation with the Chinese members of the Rice project will make this task possible. In parallel, the simulation of the methane emissions will be implemented in LPJ–C.

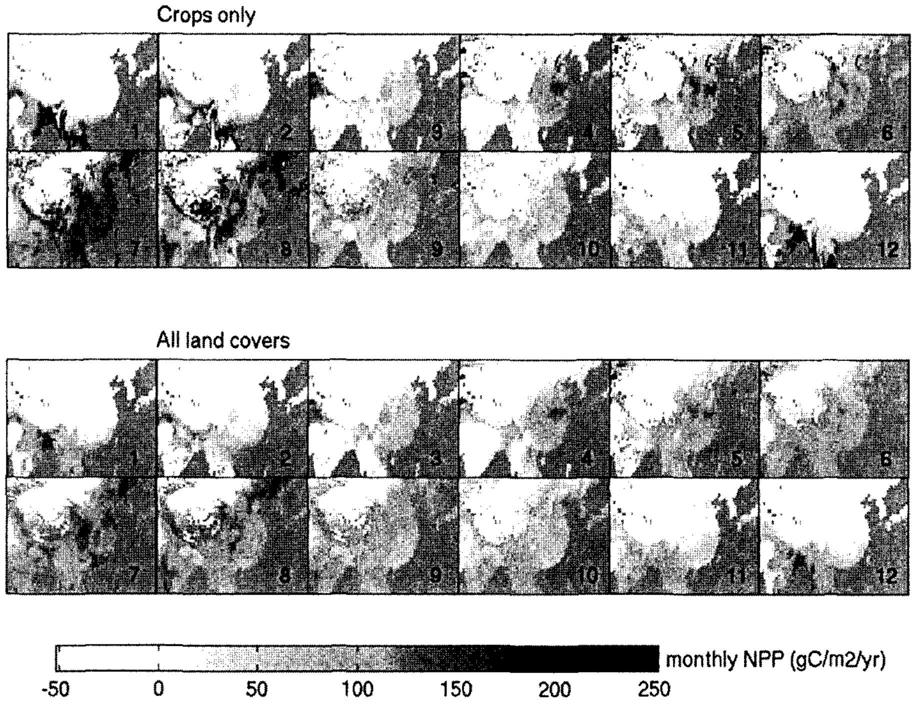

Fig.13. Maps of the monthly NPP as simulated by LPJ-C (10-year average). The top 12 plates show the NPP of the crops only; the bottom 12 plates show the NPP of the mixed grid cells (crops + natural vegetation).

5. METHANE EMISSION FROM RICE FIELDS

One of the objectives of the project is to relate the seasonal variation of atmospheric methane over China as measured by SCIAMACHY to the rice growth cycle and if possible, to relate variation of rice biomass or water management status to large scale spatial variation of methane emissions in China. SCIAMACHY already shows that China and other rice production countries correspond well to regions of high methane emissions. Monthly and seasonal methane concentrations show North South variation in China: high concentration over the whole China in June-July-August, whereas in September-October-November, only the Southern part has high methane concentration. However, comparison using SCIAMACHY is expected to be done with modelling results, in a further phase of the project.

6. SUMMARY AND FURTHER WORKS

In the first year of the project, works have been conducted to develop remote sensing methodology for rice mapping and monitoring of rice parameters. ENVISAT ASAR data are the main data source for a) rice mapping, b) mapping of rice varieties, c) detection of drainage, d) retrieving of rice biomass and e) regional rice mapping; whereas monitoring of vegetation photosynthetic activities has been done with SPOT VGT. Meantime, preliminary works have been carried out to adapt a Dynamic Vegetation Model to cropping system in China.

Current works consist in refining and validating the remote sensing results, at local and regional scale; and in improving the Dynamic Vegetation Model.

ENVISAT data are expected to cover an entire rice region (in Southern China) in 2006 for testing the methodology and for application of the crop models. The studies on methane emission will be initiated, in collaboration with a new team member (Prof. Huang Yao, Institute of Atmospheric Physics, CAS, Beijing). In particular, it is planned to study different methods to « upscale » the methane field measurements to a regional scale by using remote sensing and modelling. Links with the methane column measurements from SCIAMACHY will also be investigated.

REFERENCES

Bouvet A., Le Toan T., Tan B., Li B., He W., and Zhang P., "Assesment of ENVISAT ASAR alternating polarisation data for rice mapping in Jiangsu province, China", this issue

Huang Y., Zhang W., Zheng X., Li J. and Yu Y. (2004), "Modelling methane emission from rice paddies with various agricultural practices", *J. Geophys. Research*, Vol. 109, D08113, 12P, 2004.

Inoue Y., Kurosu T., Maeno H., Uratsuka S., Kozu T., Dabrowska-Zielinska K., and Qi J. (2002), "Season-long daily measurements of mulitifrequency (Ka, Ku, X, C, and L) and full-polarization backscatter signatures over paddy rice field and their relationship with biological variables", *Remote Sensing of Environment. 81*,194-204.

IRRI (2002) Riceweb, http://www.riceweb.org/, produced by International Rice Research Institute (IRRI), West Africa Rice Development Association (WARDA), and Centro Internacional de Agricultura Tropical (CIAT).

Kurosu T., Masaharu F., and Chiba K. (1995), "Monitoring of rice crop growth from space using the ERS-1 C-band SAR", *IEEE Transactions on Geoscience and Remote Sensing. 33*,1092-1096.

Le Toan T., Laur H., Mougin E. and Lopes A. (1989), "Multitemporal and dual polarisation observations of agricultural vegetation covers by X-band SAR images", *IEEE Transactions on Geoscience and Remote Sensing*, Vol GE-27, no 6, Nov 1989, pp709-717

Le Toan T., Ribbes F., Wang L., Floury N., Ding K., Kong J.A., Fujita M., and Kurosu T. (1997). "Rice crop mapping and monitoring using ERS-1 data based on experiment and modelling results", *IEEE Transactions on Geoscience and Remote Sensing. 35*,41-56.

Le Toan T., 2004, "Guidelines for ground data collection for rice monitoring experiments using radar data", CESBIO report, March 2004, 10 p.

Le Toan T. et al., 1999, RISAR Project Final Report, ESA / ESTEC-CESBIO-SCEOS-MS&I, n° 13201/98/NL/SB, Dec. 99

Li B., Zhang P., Le Toan T., Bouvet A., Bingxiang T., Li Z., He W., "Rice mapping and parameters retrieval using ASAR data in Jiangsu province, China", this issue

Li C., Qiu J., Frolking S., Xiao X., Salas W., Moore B., Boles S., Huang Y, and Sass R. (2002), "Reduced methane emissions from large-scale changes in water management of China's rice paddies during 1980-2000", *Geophysical Research Letters*, 29(20), doi:10.1029/2002GL015370.

Liew S.C., Kam S.-P., Tuong T.-P., Chen P., Minh V.Q., and Lim H., "Application of Multitemporal ERS-2 Synthetic Aperture Radar in Delineating Rice Cropping Systems in the Mekong River Delta, Vietnam", *IEEE Transactions on Geoscience and Remote Sensing*, vol. 36, pp. 1412-1420, Sept. 98.

Lu W.F., Chen W., Duan B.W., Guo W.M., Lu Y., Lantin R.S., Wassmann R., and Neue H.U. (2000), "Methane emissions and mitigation options in irrigated rice fields in southern China", *Nutr. Cycl. Agroecosystems* 58:65-73.

Prather M., Ehhalt D. (lead authors) et al. 2001. "Atmospheric chemistry and greenhouse gases". In *Climate Change 2001: The Scientific Basis.* IPCC Third Assessment Report. Cambridge U Press.

Ribbes F. and Le Toan T. (1999). "Rice field mapping and monitoring with RADARSAT data", *International Journal of Remote Sensing. 20*,745-765.

Ribbes F. and Le Toan T. (1999), "Coupling radar data and rice growth model for yield estimation", IGARSS'99 Proceedings

Scholze M., Bondeau A., Ewert F., Kucharik C., Priess J. and Smith P. (2005), "Advances in Large-Scale Crop Modeling" *Eos, Transactions, American Geophysical Union,* 186(26): 245, 247.

Sitch S., Smith B., Prentice I.C., Arneth A., Bondeau A., Cramer W., Kaplan J.O., Levis S., Lucht W., Sykes M.T., Thonicke K., Venevsky S. (2003), "Evaluation of ecosystem dynamics, plant geography and terrestrial carbon cycling in the LPJ Dynamic Global Vegetation Model", *Global Change Biology 9:* 161-185.

Xiao X., Boles S., Frolking S., Salas W., Moore B., Li C. et al., 2002, "Observation of flooding and rice transplantation of paddy rice fields at the site to landscape scalesin China using SPOT VGT", *Int J. of Remote Sensing*, 23, 3009-3022.

ASSESSMENT OF ENVISAT ASAR ALTERNATING POLARISATION DATA FOR RICE MAPPING IN JIANGSU PROVINCE, CHINA

Alexandre Bouvet (1), Thuy Le Toan (1), Tan Bingxiang (2), Li Bingbai (3), He Wei (2), Zhang Pingping (3)

(1) CESBIO, 18 Avenue Edouard Belin, 31401 Toulouse Cedex 9, France, Alexandre.Bouvet@cesbio.cnes.fr
(2) Institute on Forest Resources and Information Technique, Chinese Academy of Forestry, Wan Shou Shan Hou Haidian District, 100091, Beijing, China, tan@mail.forestry.ac.cn
(3) Institute of Agricultural Resource and Environment, Jiangsu Academy of Agricultural Sciences, Xiaolingwei, Nanjing, Jiangsu, 210014, China, bbli88@sohu.com

ABSTRACT/RESUME

The aim of this paper is to assess the use of ENVISAT ASAR alternating polarisation data for rice field mapping. The assessment is carried out using HH and VV data acquired in 2005 over the test area in Hongze county, Jiangsu province in China, where ground data have been collected for validation. As previously expected, polarisation ratio HH/VV during the second half of the rice season proves to be a very efficient rice classifier. A simple single-date mapping algorithm has been derived and the result has been compared with in-situ local mapping. The first results appear promising and algorithm refinements are planned in the near future.

1. INTRODUCTION

Rice is the main world staple food, and China is the first rice producer and consumer. As the Chinese rice production undergoes large interannual variability due to climatic and socio-economic factors, operational rice monitoring system is a necessity, at regional and national scales. Until now, rice statistics are based on ground collected information. Rice monitoring based on remote sensing, if possible, would be a relevant internative. Optical data are not well suited to rice monitoring, as they are hampered by clouds, which are very frequent in rice growing areas. Radar imaging systems have two assets: they can operate in all weather conditions, and the flooded ricefields have a very characteristic radar backscatter temporal behaviour. Past studies using SAR data from ERS-1 and 2 [1] and RADARSAT [2] focused on the use of the temporal variation of the C-band backscattering coefficient at either HH or VV polarisation for rice mapping and monitoring. Since the launch of ESA's ENVISAT in 2002, the use of dual-polarisation of the ASAR instrument for rice monitoring is expected to provide an interesting alternative to the use of the backscatter temporal change. The objective of this paper is to develop and assess a method using the polarisation ratio, HH/VV for rice mapping.

2. TEST SITE AND DATA DESCRIPTION

2.1. Test site description

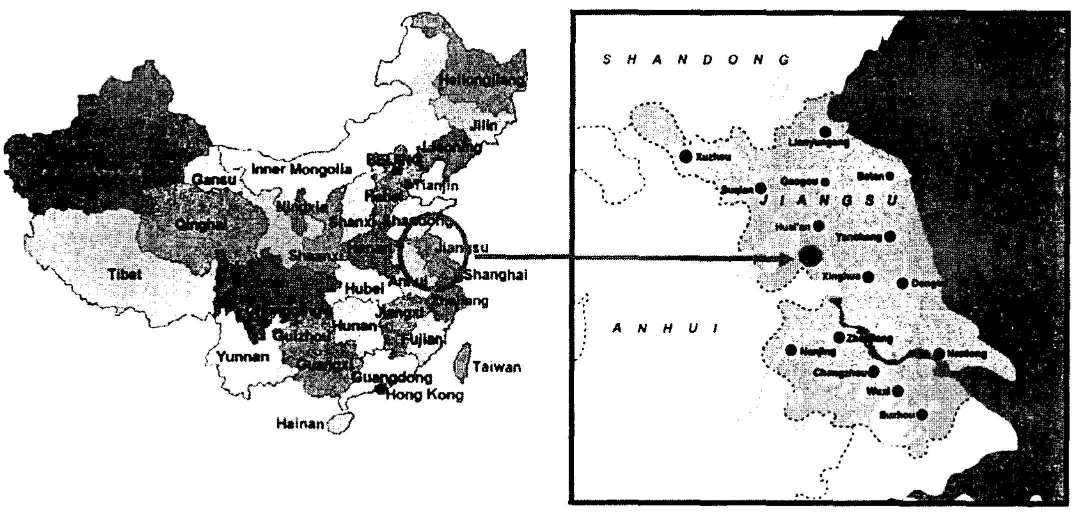

Fig.1. Study area at the Hongze county, Jiangsu province

Proc. 2005 Dragon Symposium "Mid-Term Results", Santorini, Greece
27 June – 1 July 2005 (ESA SP-611, January 2006)

The study area is located in the Hongze county (approximately 32°55'N–33°18'N and 118°37'E–119°00'E), Jiangsu province. The area is very flat (less than 30m above sea level), and the land use is dominated by cropland. Other cover types include trees, ponds, canals, roads and villages. The main cropping system is a two-crop rotation system, with wheat in winter and paddy rice in summer, but other plants are also grown locally, such as mulberry trees, soybeans, and various garden vegetables. The typical crop calendar is: wheat planted in November, harvested in late May or early June, and rice sown in early June, transplanted in late June in flooded fields and harvested in late October.

2.2. Available data

ASAR APP (Alternating Polarisation Precision image) images are used in this study. The ASAR instrument on board ENVISAT operates at C-band (λ=5.6cm) and the Alternating Polarisation mode provides two images of the same scene with different polarisations. There are three polarisation combinations available: HH&VV, HH&HV, VV&VH, and the incidence angle can be selected among 7 sub-swaths (IS1 to IS7). The data selection is based on previous studies which suggested that the most interesting combination for rice monitoring is HH&VV, with incidence IS2 (19.2°-26.7°)[1] [2]. APP images have a nominal resolution of 30m x 30m and pixel size of 12.5m x 12.5m, with a swath width of about 100km.
The images acquired during the 2004 rice season over the study area are at the following dates: June 28th, August 21st, September 6th, September 25th, October 11th, and October 30th. On October 30th, most rice fields may be harvested. In 2005, only two dates were successfully acquired during the rice season: July 2nd and August 6th.

3. DATA PROCESSING

In order to reduce the speckle noise, a pre-processing chain was designed. It comprises 4 steps: (a) calibration, (b) extraction of test area, (c) co-registration, (d) multi-image filtering. Steps (a), (b), (c) were implemented by the Gamma GEO software, from the Gamma Remote Sensing group, and a filter programmed in C was used for step (d).
This multi-image filter was developed and described by Bruniquel and Lopes [3], Le Toan et al. [1], Quegan et al., 2000 [4], and Quegan and Yu, [5]. It reduces speckle without damaging thin structures, by linearly combining M input images on a pixel-to-pixel basis, to create M output images with reduced speckle. For uncorrelated images with the same number of looks L, the linear combination is:

$$J_k(x,y) = \frac{\langle I_k(x,y)\rangle}{M}\sum_{i=1}^{M}\frac{I_i(x,y)}{\langle I_i(x,y)\rangle}$$

with

$J_k(x,y)$ = radar intensity of output image k at pixel (x,y)

$I_i(x,y)$ = radar intensity of input image i at pixel (x,y)

$\langle I_i(x,y)\rangle$ = local average intensity of input image I at pixel (x,y)

The local average intensity is calculated on a relatively homogeneous area around the pixel, which is determined by an adaptive window using edge, line and point detection algorithms.

Fig.2 shows the effect of this filter using 10 images (5 dates, 2 polarisations each). Fine structures, such as roads or fish ponds, which are not visible in the original images , are revealed after the multi-image filtering.
In general, for a backscatter ratio (HH/VV in this case) of about 3 dB, the ENL must be about 30 in order to classify rice with an error probability of 10%. The original number of looks for the APP data being 3, a large number of co-registered images should be used, including archived data. However, if not enough APP data are available, an additional spatial filtering can be applied, at the expense of a degradation of the geometric resolution

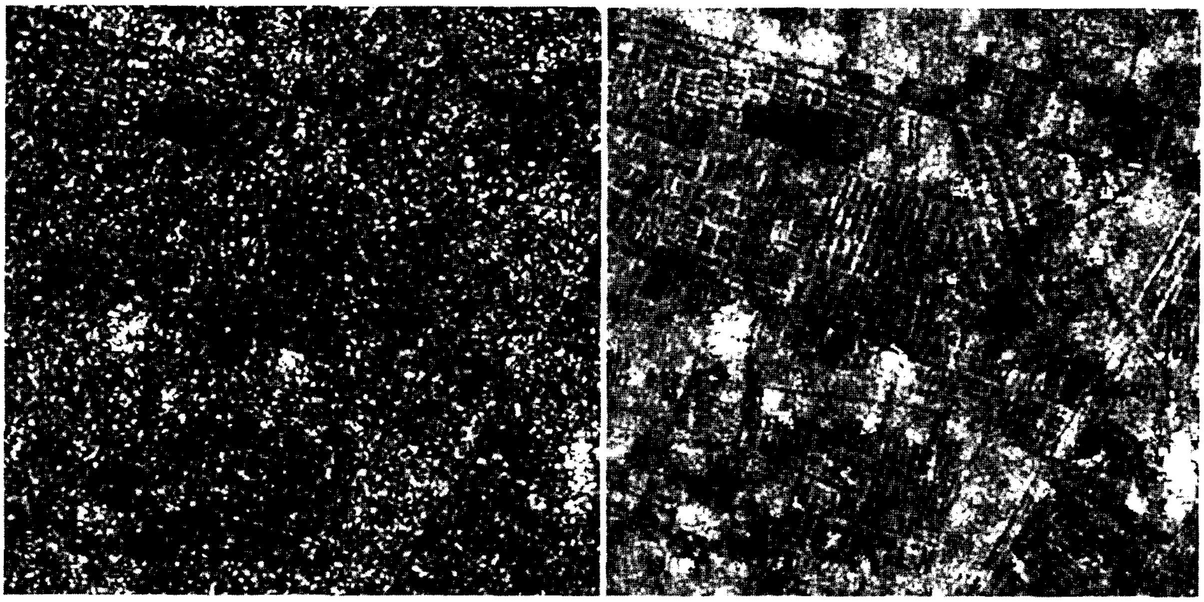

Fig.2. ASAR image before (left) and after (right) multi-temporal filtering

4. DATA ANALYSIS

NB. For simplification purposes, the backscattering coefficients in polarisation HH and VV, usually noted σ^0_{HH} and σ^0_{VV}, will be noted HH and VV respectively in this article. The polarisation ratio $\sigma^0_{HH} / \sigma^0_{VV}$ will thus be noted HH/VV.

The radar temporal behaviour of several land cover classes was studied. For each class, samples were visually selected on APP images and verified using a Landsat ETM image of the region.

Fig.3 presents the rice backscattering temporal evolution in 2004. The first available date is June 28th, one to two weeks after transplanting. At this stage, the plants are small and rice fields can be compared to water bodies, with a variable backscatter according to wind occurrence. With the growth of rice plants, the backscatter at both polarisation HH and VV increases. The HH and Vv figures indicate 2 groups of rice fields with shifted crop calendars. According to the ground observations, early rice corresponds to hybrid species and late rice to japonica species (Le Toan et al, [5]). In particular, the maximum backscatter values of VV was missing (no data in August). At the end of the season, HH and VV backscattering decreases slightly. The main scattering mechanism is the plant-water interaction.

The ratio HH/VV has an outstanding behaviour: no or little difference between the polarisations when the plants are small, but as soon as the plants grow, the rice plant vertical structure induces a strong attenuation of the vertically polarised electro-magnetic waves. Therefore, VV has smaller values than HH and the ratio HH/VV is significant. In the reproductive stage, starting around mid September, the plant structure gradually becomes less vertical and the difference between HH and VV decreases.

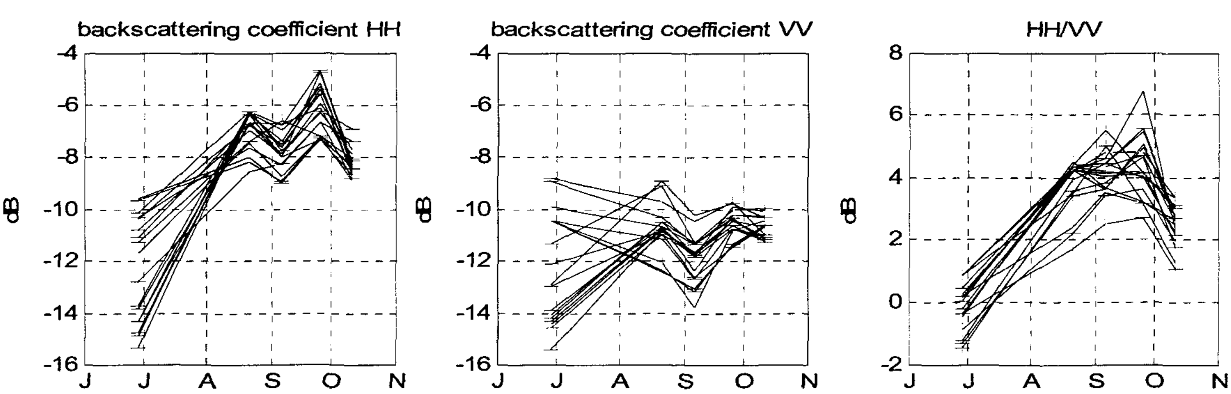

Fig.3. Rice backscattering behaviour

Other land use classes have been studied. Fig.4 shows the temporal evolution of the mean backscattering coefficients of a large number of samples of rice, lotus, water and urban areas. Urban areas have a high and stable backscattering coefficient for both polarisations, and a high HH/VV ratio. Water bodies have a spatially and temporally variable backscatter, but the HH/VV ratio is stable and close to -2 dB. Lotus ponds have a high VV backscatter compared to rice during the beginning of the rice season, and the HH/VV ratio increases as the lotus plant emerges vertically over the water.

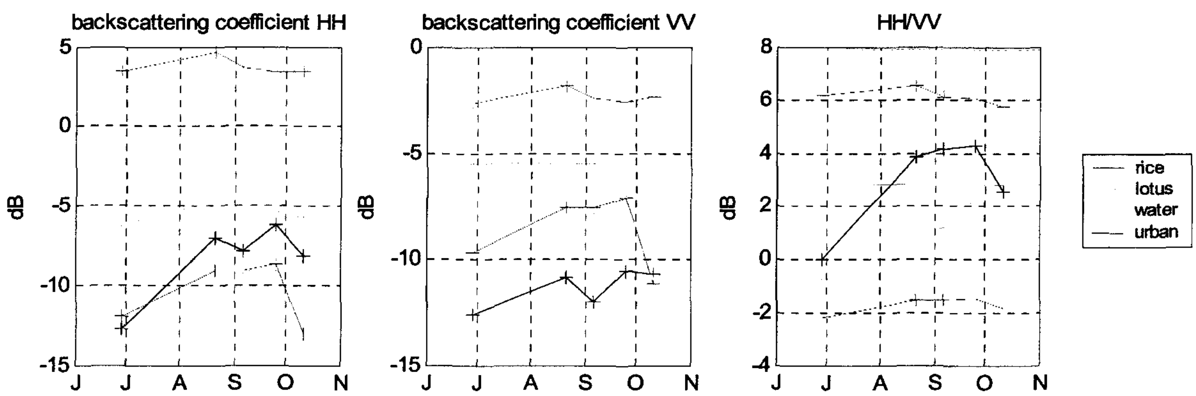

Fig.4. Backscattering behaviour of several land use classes

5. RICE MAPPING AND VALIDATION

5.1. Single-date mapping algorithm

From the previous analysis, HH/VV, HH and VV (at low incidence angle: IS2) appear to be good classifiers for rice mapping algorithm using APP data acquired at a single date, during the growth period when HH/VV of rice is higher than that of other land cover types present in the region. In Jiangsu, the optimum period is in August and September. Standard classification methods such as Maximum Likelihood supervised method.or unsupervised clustering method could be used for rice and other land use mapping. In this study, for rice/non rice mapping a simple physical based algorithm was developed, based on thresholding of HH, VV and HH/VV. Fig.5 summarises the mapping algorithm which assigns each pixel to one of the three classes: 'Rice', 'Urban', and 'Other'

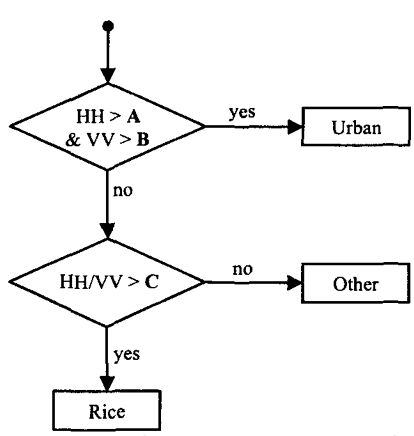

Fig.5. Single-date rice mapping algorithm

Parameters A and B were set respectively to -4 dB and -6 dB. Values of the HH/VV threshold – parameter C –, from 1 to 2.5 dB are tested. These values were based on results of analysis of 2004 data, however, the HH/VV threshold may vary as a function of the acquisition date. The test is applied on data of August 6th, 2005. Fig.6 shows a colour composite of an APP image of the Hongze area and the derived rice map with C = 1.5 dB. On the colour composite, rice fields appear in blue-pink (where HH and HH/VV are high), urban areas in bright colours (high backscatter) and other land cover classes in green-yellow (where VV is comparatively higher). In general, the results appear visually correct. A number of water pixels however are detected as urban areas of high backscatter, due to wind effects.

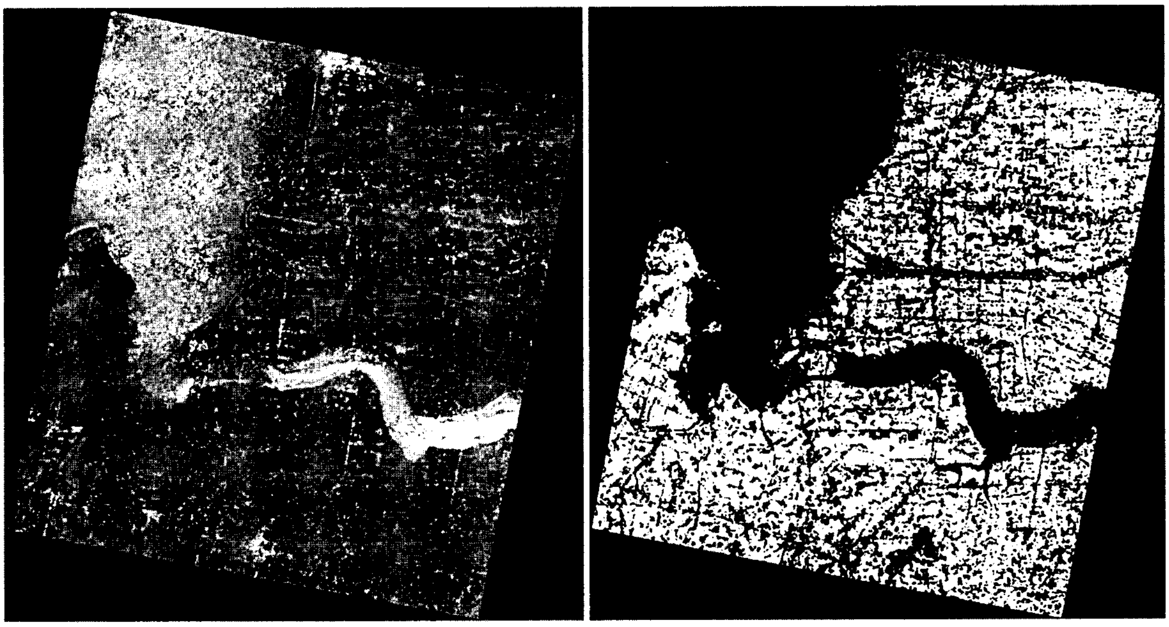

Fig.6. RGB colour composite (R = HH, G = VV, B = HH/VV) of ASAR APP image on August 6th, 2005 (left) and derived rice map (yellow = rice, red = urban area, black = not classified) (right)

5.2. Validation

During the 2005 field campaign, one sample of about one square kilometre was mapped with a DGPS in order to validate and improve the mapping algorithms.

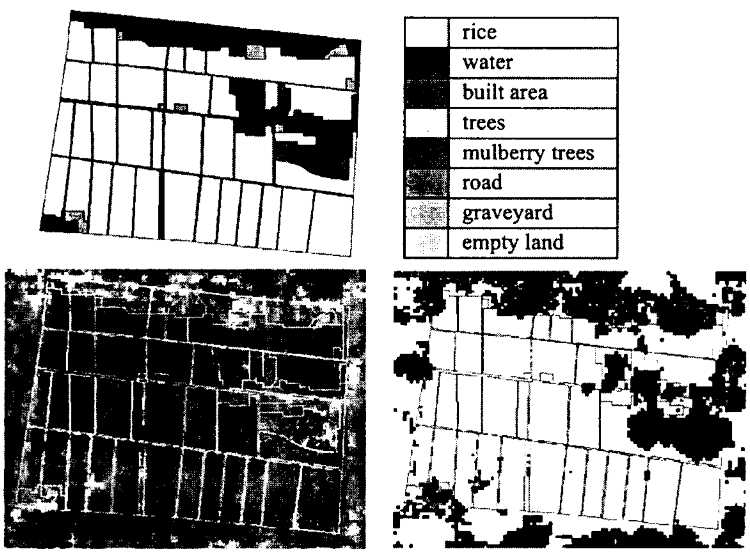

Fig.7. In-situ map (top), and corresponding RGB colour composite (R = HH, G = VV, B = HH/VV) of ASAR APP image on August 6th, 2005 (bottom left) and the derived rice map (yellow = rice, red = urban area, black = other) with parameter C equal to 1.5 dB (bottom right)

Fig.7 shows the mapping result, the colour composite image, as compared with the in-situ map. Visual interpretation of the colour composite image gives good detection of rice (magenta colour, due to high HH/VV and HH).The map also provides good detection of rice (yellow), and most habitat areas. However, some differences can be found , especially at field boundaries. To assess quantitatively the mapping algorithm, four values of the HH/VV threshold have been tested : 1 dB, 1.5 dB, 2 dB and 2.5 dB. For each value, the confusion matrix is calculated:

Table 1. Confusion matrices of the single-date mapping algorithm for 4 values of parameter C tested on one sample

C = 1 dB	Mapped rice	Mapped non rice	Total
In situ rice	**4486**	**268**	78.84%
In situ non rice	**489**	**787**	21.16%
Total	82.5%	17.5%	100%

C = 1.5 dB	Mapped rice	Mapped non rice	Total
In situ rice	**4360**	**394**	78.84%
In situ non rice	**343**	**933**	21.16%
Total	77.99%	22.01%	100%

C = 2 dB	Mapped rice	Mapped non rice	Total
In situ rice	**4110**	**644**	78.84%
In situ non rice	**232**	**1044**	21.16%
Total	72.00%	28.00%	100%

C = 2.5 dB	Mapped rice	Mapped non rice	Total
In situ rice	**3700**	**1054**	78.84%
In situ non rice	**142**	**1134**	21.16%
Total	63.72%	36.28%	100%

The values in bold font are the number of pixels. When the HH/VV threshold increases, the total number of pixels detected as rice decreases, and omission error increases while commission error decreases.

Table 2. Single-date mapping algorithm performances for 4 values of parameter C

C	1 dB	1.5 dB	2 dB	2.5 dB
Percentage of well classified pixels	87.44%	**87.77%**	85.47%	80.17%
Estimated rice area vs. real rice area	+4.6%	**-1.1%**	-9.5%	-23.7%

For the data acquired in August 6, 2005, 1.5 dB proves to be the best HH/VV threshold value among the four tested ones, with about 88% well classified pixels and a total rice area underestimated by 1.1% only. However, for this value of the HH/VV threshold, nearly one third of the non rice pixels according to the ground-truth data are detected as rice. This could seriously degrade the classification results in areas where the proportion of non rice areas is significant (in the Hongze area, rice covers about 80% of the land).

More generally, physical analysis of rice radar backscattering combined with knowledge of the crop calendar allows to define the optimum radar data sets (e.g. date, polarisation, and incidence) for rice mapping. Alternatively, a principal component analysis can be used to determine the optimum data, out of a larger number of data sets. Once the data sets with relevant information content are available, different methods can be used for classification, such as the Maximum Likelihood supervised classification. Figs.8 show scatterplots of VV vs. HH on August 6th 2005. The blue area (Fig.8a) covers all pixels that were classified as rice by the single-date mapping algorithm with C=1.5dB, and the yellow area (Fig.8b) covers the rice pixels obtained from a Maximum Likelihood supervised classification applied to 3 channels: HH, VV and HH/VV using rice and non rice training samples. The two areas are roughly the same.

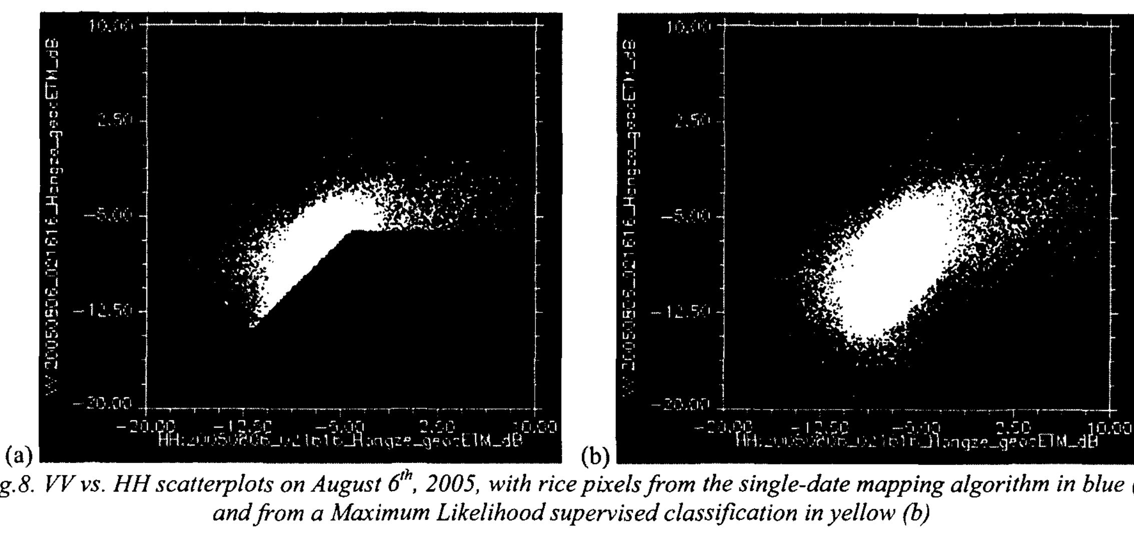

Fig.8. VV vs. HH scatterplots on August 6th, 2005, with rice pixels from the single-date mapping algorithm in blue (a), and from a Maximum Likelihood supervised classification in yellow (b)

6. CONCLUSIONS

ASAR APP data over rice area in the Hongze county, Jiangsu province have been analysed. Based on the particular polarisation behaviour of rice backscatter, a simple classification algorithm has been derived and applied to single date radar data. The algorithm, based on analysis of 2004 data, was applied to 2005 data. The results indicate about 88% of well classified rice and non rice pixels. The method will be further tested with more in situ sampled maps, and will be compared with other classification methods. The results already show the contribution of polarisation capability of ASAR APP as compared to single polarisation C-band SAR data.

7. REFERENCES

[1] T. Le Toan *et al.* , « Rice Crop Mapping and Monitoring Using ERS-1 Data Based on Experiment and Modeling Results », *IEEE Transactions on Geoscience and Remote Sensing*, vol 35, n°1, pp. 41-56, January 1997

[2] Y. Shao et al., « Rice monitoring and production estimation using multitemporal RADARSAT », *Remote Sensing of Environment*, vol. 76, pp.310-325, 2001

[3] J. Bruniquel and A. Lopes, « Multi-variate optimal speckle reduction in SAR imagery », *Inernational Journal of Remote Sensing*, vol. 18, pp. 603–627, 1997

[4] S. Quegan, T. Le Toan, J. J. Yu, F. Ribbes, and N. Floury, « Multitemporal ERS SAR Analysis Applied to Forest Mapping », *IEEE Transactions on Geoscience and Remote Sensing*, vol 38, n°2, pp. 741-753, March 2000

[5] S. Quegan and J. J. Yu, « Filtering of multichannel SAR images », *IEEE Transactions on Geoscience and Remote Sensing*, vol 39, n°11, pp. 2373-2379, November 2001

[6] T. Le Toan, A. Bouvet, B. Tan, Z. Li, W. He, B. Li, P. Zhang, A. Bondeau, « Rice monitoring in China – Mid-term report », this issue

RICE MAPPING AND PARAMETERS RETRIEVAL USING ASAR DATA IN JIANGSU PROVINCE, CHINA

Li Bingbai, Zhang Pingping
Jiangsu Academy of Agriculture Sciences, Nanjing, P.R. China
bbli88@sohu.com
Thuy Le Toan (PI), Alexandre Bouvet
Centre d'Etudes Spatiales de la Biosphère, 18 Avenue Edouard Belin, 31401 Toulouse Cedex 9, France,
Thuy.Letoan@cesbio.cnes.fr
Tan Bingxiang (PI), Li Zengyuan, He Wei
Institute on Forest Resources and Information Technique, Chinese Academy of Forestry, Beijing, P.R. China,
tan@mail.forestry.ac.cn

ABSTRACT
This paper presents a study of multi-temporal and dual-polarization (HH, VV) ASAR data, which aims to assess the use of ASAR data for rice field mapping and monitoring. Temporal variation of backscattering coefficients of 4 categories of rice fields were derived from 2004 ASAR images of the region of Jiangsu. Ground data were collected to calculate wet biomass and LAI of rice, NOAA images were utilized to derive NDVI, and the correlation between the backscattering coefficient and those rice parameters was analyzed. Based on the backscatter behaviors of rice, a method for rice fields mapping using image ratio techniques has been developed, with accuracy higher than 80%. Four classes of rice according to varieties (hybrid or Japonica) and crop calendar have been mapped, in addition to the other main land use classes in the region. The results appear promising for the use of ASAR data on rice monitoring and rice mapping.

1. INTRODUCTION
Rice monitoring and yield estimation have special significance in China, where rice is the major staple food. Because most of rice grows in rainy and cloudy regions, it is difficult to have optical images at the right time and place. Besides, traditional methods based on local statistics for rice monitoring are always inaccurate. Spaceborne SAR (Synthetic Aperture Radar) instruments, having all weather capability, present a good alternative to those traditional methods for rice monitoring and yield estimation.

The first investigation on rice monitoring have been carried out using X-band airborne synthetic aperture radar (SAR) in France [1], showing the possibility of rice monitoring and mapping based on the temporal change of the radar backscatter of rice, larger than that of other crops. In recent years, spaceborne SAR technologies have developed rapidly, and with the launch of the European ERS-1,2 and the Canadian RADARSAT, the use of radar data for rice monitoring and the detection of rice growing areas has been demonstrated [2-4]. Furthermore, the successful launch of the European ENVISAT satellite carrying the Advanced SAR (ASAR) instrument brings about more inspiring future for application of multi-polarization data. The objective of this paper is to assess the usefulness of ASAR data for rice area mapping and monitoring, and to develop an optimum method to achieve this purpose.

2. STUDY AREA AND DATA BASE
2.1 Study area
The study area is located in Hongze county, Jiangsu Province, where rice is the main crop. Due to the weather conditions, there is only one rice season, from May to October. Generally rice is sown around 15th May, transplanted around 15th June, and harvested around 15th October, but the dates can change with local conditions. Besides, some other vegetation types are

Proc. 2005 Dragon Symposium "Mid-Term Results", Santorini, Greece
27 June – 1 July 2005 (ESA SP-611, January 2006)

found in this area, such as beans, cotton, trees, vegetables, which cover a smaller area than rice.

2.2 Remote sensing data

ENVISAT ASAR data were available at 6 dates in 2004, namely 12th June, 28th June, 21st August, 6th September, 25th September, 11th October, which cover most areas of Hongze county and parts of Jinhu county and Xuyi county in Jiangsu province. In this paper, we use Alternating Polarization (AP) data containing HH and VV polarization. Besides, it has been possible to acquire NOAA/AVHRR data on 7 dates from May to October, which were used to derive Normalized Difference Vegetation Index (NDVI) that can reflect the growth of rice. Moreover, one ETM image on 21st August of 2002 was available.

2.3 Ground data

In order to investigate the relationship between rice growth and ASAR data, several parameters were measured in 4 rice fields under study during their growing cycle, such as plant height, number of stems, wet weight, dry weight, biomass, water content, Leaf Area Index, etc., and the irrigation status (water layer depth) was also recorded (Cf. Le Toan et al., 2005, this issue).

2.4 Validation

In order to have reference maps to assess the accuracy of mapping methods, Differential Global Positioning System (DGPS) has been used for accurate *in situ* mapping of several samples of about 1 km2, comprising rice fields and other land use classes..

3. DATA ANALYSIS

Prior to the data analysis, processing methods have been applied to the SAR images; those include image calibration and multi-image speckle reduction. This is described in Bouvet et al.2005, this issue [5].

3.1 Temporal variation of the backscatter

Backscatter coefficients (HH, VV) were then derived from selected rice fields on the preprocessed ASAR images, and the polarization ratio (HH/VV) was calculated. Figs. 1, 2 and 3 present the temporal behavior of HH, VV and HH/VV of the 4 fields. The backscatter of rice fields, named rice1, rice2, rice3, and rice4 show different temporal behaviors. Figs.1 and 2 show that rice1 and rice3 on June 28 have low backscatter at HH, and VV, indicating early stage after transplanting; whereas rice2 and rice4, transplanted earlier, have higher backscatter. On October 11, rice3 and rice4 are higher in VV than rice1 and rice2. In addition to the crop calendar, other factors may influence the backscatter temporal behavior such as paddy varieties and social-economical conditions and planting system. There are several rice varieties planted by farmers in Hongze county: they can be regrouped in hybrid, and japonica rice. Because each family in villages of China has its own planting system, it is common that the dates of transplanting and harvesting of rice shift from one field to the next. Fig.1 and Fig.2 show that it is possible to identify 4 types of rice field in Hongze county:

Rice1: transplanted later, harvested later, they are late maturing japonica rice, such as "zhendao 88"

Rice2: transplanted earlier, harvested later, they are late maturing japonica rice, such as "wuyujing"

Rice3: transplanted later, harvested earlier, they are mid maturing japonica rice, such as "xudao-6"

Rice4: transplanted earlier, harvested earlier, they are hybrid rice, such as "liangyoupeijiu"

Fig. 4 shows the false color image, where VV data on June 28 is in blue, August 21 in green and October 11 in red. The 4 categories of rice are well visible.

Fig.3 shows the polarization ratio HH/VV of the 4 classes of rice fields, where the temporal behavior appears to better reflect the ricegrowth. This temporal behavior and the very high values on August 21 (about 5dB) indicate that HH/VV has a strong potential for rice mapping.

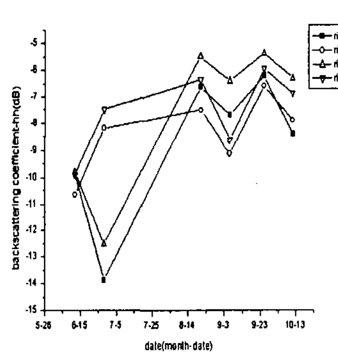

Fig.1 Temporal behavior of rice backscattering coefficients (HH)

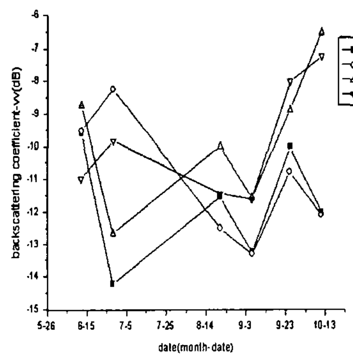

Fig.2. Temporal behavior of rice backscattering coefficients (VV)

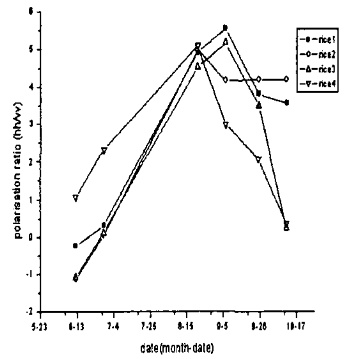

Fig.3 Temporal behavior of rice polarization ratio (HH/VV)

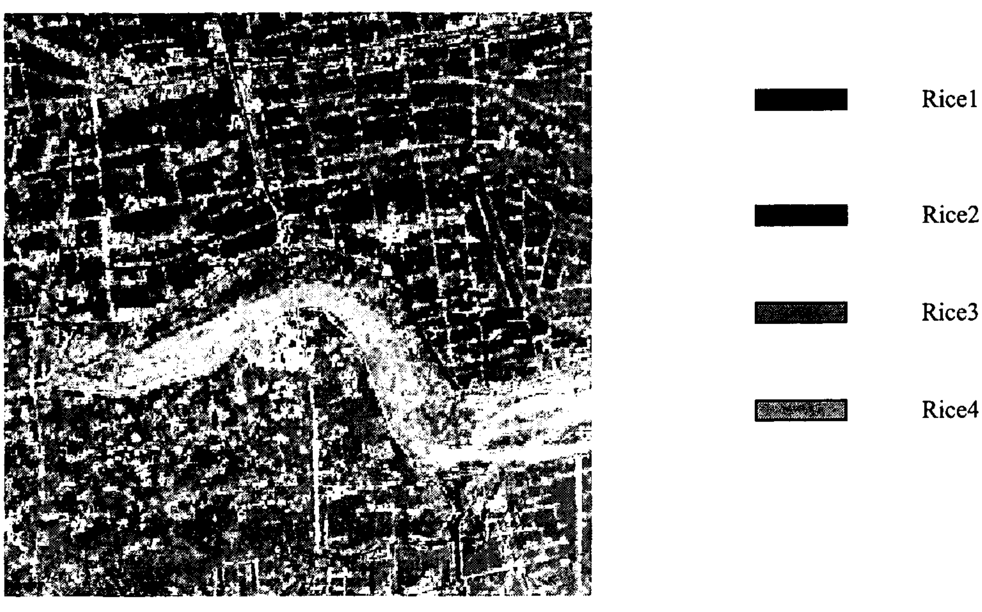

Fig.4. Composite map with 3 channels: VV data on 28th June (blue), VV data on 21st August (green), VV data on 11th October (red)

3.2 Correlation analysis between polarization ratio and rice parameters

From Fig. 3, it is found that the temporal variation of the polarization ratio has a closer correspondence with rice growing. It is interesting to study the relationship between polarization ratio and rice parameters. The ground data were collected in Hongze county, where rice belongs to rice1. Figs. 5,6 show the results of correlation between wet biomass, and LAI. Although some sample errors affect the accuracy of ground data, good correlations are found between polarization ratio of rice1 and wet biomass and LAI. Besides, it is interesting to analyze the polarization ratio as a function of NDVI, since both measures reflect the growing state of crops. NDVI, derived from 7 NOAA/AVHRR images we successfully acquired, shows also good correlation with the polarization ratio (Fig.7). The result indicates that rice monitoring can be done through polarization ratio.

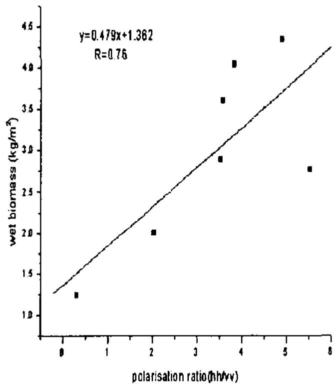

Fig. 5. Correlation analysis between polarization ratio and wet biomass

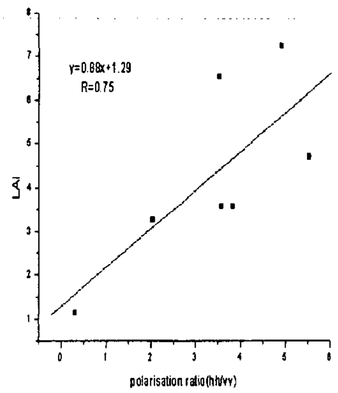

Fig. 6. Correlation analysis between polarization ratio and LAI

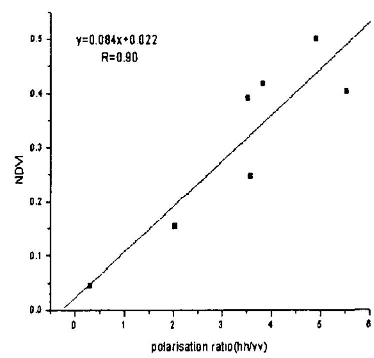

Fig. 7. Correlation analysis between polarization ratio and NDVI

3.3 Backscattering coefficient of different types of land

In order to do rice mapping in terms of its backscatter characteristic, it is necessary to study the backscatter behaviors of other lands. Figs. 8,9,10 display the polarization ratio, the HH backscattering coefficient and the VV backscattering coefficient of the main land use types in Hongze county, including rice, urban, water, bean, grass, tree. Urban has higher values in the ratio and in HH and VV. Rice has a particular behavior compared to other land use in polarization ratio, which appears to be a good rice classifier.

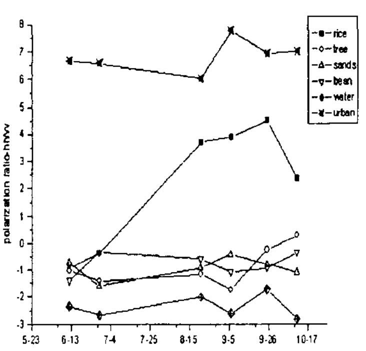

Fig.8. Polarization ratio(HH/VV) of different fields

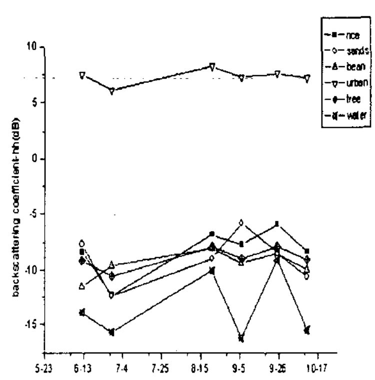

Fig.9. Backscatter behaviors for HH polarization of different fields

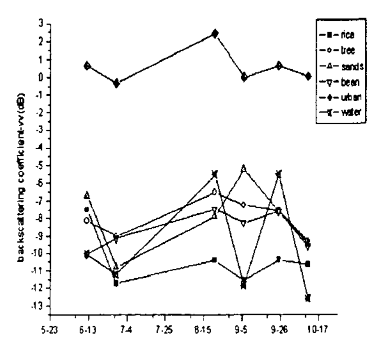

Fig.10. Backscatter behaviors for VV polarization of different fields

4. RICE MAPPING

4.1 Separate rice fields from other land use

The methodology is based on image ratio techniques developed by Le Toan et (1997)[8], the ratio here refers to the HH/VV of rice fields in the middle of the rice growing cycle. The method and results are presented in Bouvet et al., 2005, this issue [5]. The land use in Hongze county are classified using the polarization ratio and the backscattering coefficients into four types: rice, water, urban and other areas. The land cover along the bank of Sanhe river was classified into rice and urban wrongly; investigation to the region showed that these areas were covered with sand, hence this region must be reclassified using the radar images of 21st August.

Furthermore, large areas of trees are planted in Hongze county, including mulberry trees. To classify them, we use an ETM image in 2002 to derive tree areas. The classification in 6 classes is shown in Fig.12. Fig.11 displays a radar false color image for comparison to Fig.12. The classification accuracy was estimated using samples identified with Differential Global Positioning System (DGPS).The average accuracy of the rice classification is 82.68%, and the overall accuracy is 72.84%.

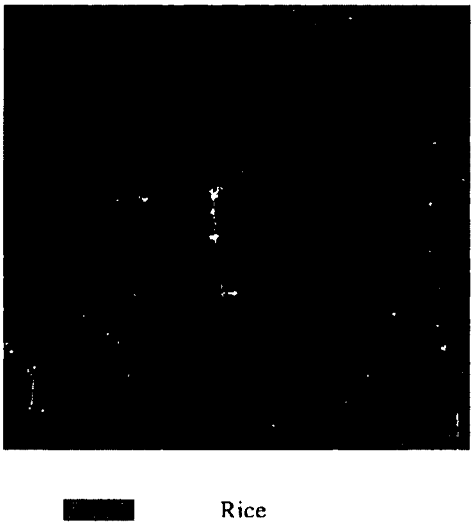

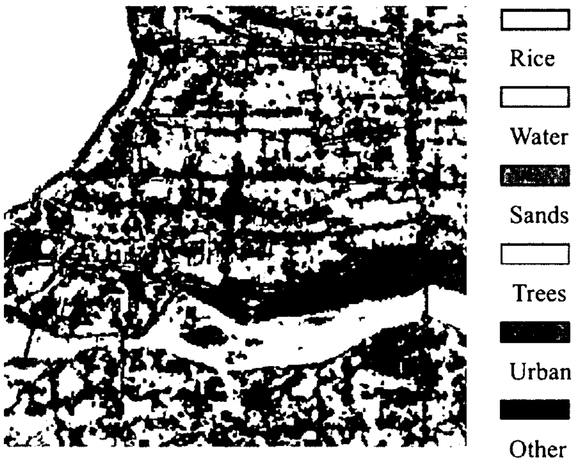

Fig. 11. Composite map with 3 channels: hh data on 28th Jun, hh/vv data on 21st Aug, hh data on 6th Sep

Fig.12. Rrice/non-rice segmentation

4.2 Separating different types of rice

The analysis result was used to develop mapping of different rice classes. It is interesting, besides the rice growth areas for rice statistics, to differentiate rice with different transplanting dates, and rice with different harvesting dates. First rice was derived by threshold of -2dB in the image of HH/VV on 21st August, then using the image of 28th June on HH polarization, rice1 and rice3 were separated from rice2 and rice4, and using the image of 11th October on VV polarization, rice1 and rice2 were differentiated from rice3 and rice4, both threshold values are -10dB.

Figs. 14 and 16 show the result of rice respectively with different transplanting and harvesting dates. Besides, two false color composite images were shown for comparison (Figs.13, 15).

Early-transplanted rice
Later-transplanted rice

Fig. 13. Composite image with 3 channels: HH data on 28th June, HH data on 6th Sep, VV data on 6th Sep

Early-transplanted rice
Later-transplanted rice

Fig. 14. Early-transplanted rice/later-transplanted rice segmentation

Early-harvested rice
Later-harvested rice

Fig.15. Composite map with 3 channels---VV data on 11thOct, HH data on 6th Sep, VV data on 6th Sep

Early-harvested rice
Later-harvested rice

Fig. 16. Early-harvested rice/later-harvested rice segmentation

5. DISCUSSION AND CONCLUSION

The major aim of this study was to assess the use of ASAR data for rice field mapping and rice growth monitoring. The approach includes the analysis of the temporal variation of the radar backscatter of 4 classes of rice fields, the analysis of correlation between the radar backscatter and rice parameters (wet biomass, LAI, NDVI), which was collected over a test site in Hongze county, and development of methodologies for rice field mapping. The results presented in this paper have provided confidence that multi-temporal and multi-polarization ASAR data are capable of rice mapping and monitoring. The mapping method presented here is developed based on the available ASAR data-sets on the Hongze county. To develop more general methodology, data acquired over more complex regions (multi rice cropping, small fields of more crop diversity, topography) should be analyzed. Moreover, the method of rice mapping offered by this paper is based on image ratio; some other methodology for classification can be attempted on rice mapping, such as supervised classification and neural network classification.

REFERENCES

1. Le Toan T., Laur H., Mougin E., Lopes A., "Multitemporal and Dual-polarization Observations of Agriculture Vegetation Covers by X-band SAR Images", *IEEE Transactions on Geoscience and Remote Sensing*, Vol.27, No.6, 709-717,1989.

2. Kurosu T., Fujita M., Chiba K., "Monitoring of Rice Crop Growth from Space Using the ERS-1 C-band SAR", *IEEE Transactions on Geoscience and Remote Sensing*, Vol.33, No.4, 1092-1096, 1995.

3. Liew S.C., Kam S.-P., Tuong T.-P., Chen P., Minh V.Q., and Lim H., "Application of Multitemporal ERS-2 Synthetic Aperture Radar in Delineating Rice Cropping Systems in the Mekong River Delta, Vietnam", *IEEE Transactions on Geoscience and Remote Sensing*, vol. 36, pp. 1412-1420, Sept. 98.

4. Liew S.C., Chen P. et al., "Rice Crops Monitoring in the Mekong River Delta Using Combined ERS and RADARSAT Synthetic Aperture Radar", IGARSS 1998 proceedings.

5. Bouvet A., Le Toan T., Tan B., Li B., He W., Zhang P., "Assessment of ENVISAT ASAR alternating polarisation data for rice mapping in Jiangsu province, China", this issue

6. Tan B., Li Z. et al., "Rapid Updating of Rice Map for Local Government Using SAR Data and GIS – In Zengcheng County, Guangdong Province, China", *Proceedings of the 20th Asian Conference on Remote Sensing, Hongkong China Vol.1,1-6 1999.*

7. Wooding M., Li Z., "Rice Mapping Using ERS SAR Data in Guangdong Province, China", ERS-ENVISAT Symposium, October 2000.

8. Le Toan T., Ribbes F., Wang L., Floury N., Ding K., Kong J.A., Fujita M., and Kurosu T. (1997). "Rice crop mapping and monitoring using ERS-1 data based on experiment and modelling results", *IEEE Transactions on Geoscience and Remote Sensing*. *35*,41-56.

Agricultural Monitoring in Fujian Province
(id. 2563)

ENVISAT ASAR DATA FOR AGRICULTURE MAPPING IN ZHANGZHOU, FUJIAN PROVINCE, CHINA

Xiaoqin Wang, Qinmin Wang, Feilong Ling, Xiaoming Shi, Yunzhi Chen, Xiaoling Zhu

Key Laboratory of Data Mining & Information Sharing of Ministry of Education, Spatial Information Research Center of Fujian Province, Fuzhou University, Fuzhou 350002, Fujian, China, E-mail:wangxq@fzu.edu.cn

ABSTRACT

This paper investigates the potential of ENVISAT ASAR data for agriculture crop mapping. The multi-temporal ASAR data with different polarization are used. The study area is located in Zhangzhou, Fujian province, China. Based on the analysis of radar signature of different land cover, crop types like rice, water bamboo and banana are classified using object oriented classifier. Compared to the field survey data, the accuracy of rice, banana and water bamboo in study area is more than 80%. The object oriented classifier is suitable for SAR data classification.

Keywords: ENVISAT ASAR, crop classification, multi-temporal, object oriented classifier

1. INTRODUCTION

Land cover mapping and the retrieval of bio- and geophysical information, including land use, soil, crop and forest parameters from space-borne SAR have become important applications over the last 10 years. The potential of Synthetic Aperture Radar (SAR) in discriminating among different agricultural crop types has been demonstrated in several studies [1-3], especially for rice mapping and monitoring [4-7]. The accuracy of classification depends on the sensitivity of the used backscattering coefficients to the differences of the biomorphological structures of the plants, hence to the different interaction behavior between the electromagnetic wave and the structure of the canopy [3]. One SAR image at given frequency, polarization and incidence angle, is often inadequate to attain the required accuracy of classification. Improvements are expected by multi-temporal and/or multi-polarization and/or multi-angle SAR images.

To successfully discriminate among different crop types, suitable classification algorithms should be used, which are capable of exploiting the information embedded in multi-temporal and multi-polarization SAR measurements. A variety of classification schemes have been proposed and used[2,3,8-10]. Object-oriented approach incorporates both spectral information (tone, color) as well as spatial arrangements (size, shape, texture, pattern, association with neighboring objects), which will increase classification accuracy. It's often used for high-resolution imagery with more spatial information and less spectral information. For SAR data, the spectral information is poor and spatial information is rich. So in this paper, we use object-oriented approach to classify the ASAR data.

The space-borne SAR data, like ERS1/2 SAR, JERS-1 SAR are single-polarization, single-angle. In 2002, ENVISAT with the advanced SAR (ASAR) as one important instrument was successfully launched. As compared to the preceding SARs on ERS-1 and ERS-2, ASAR can be operated in many different modes with relevant additional functionality including [11]: Beam steering capability; Large and multi-incidence angle data; multi-polarization capability; wide swath and global monitoring modes for large area coverage at reduced resolution spatial. ASAR works at C-band. Alternating Polarization Mode (AP Mode) product contains two co-registered images. In this paper, with object oriented classifier, we use multi-temporal AP products to identified crop types in Zhangzhou district, Fujian province, China.

Proc. 2005 Dragon Symposium "Mid-Term Results", Santorini, Greece
27 June – 1 July 2005 (ESA SP-611, January 2006)

2. STUDY AREA AND CROP CALENDAR

Our research was conducted in Zhangzhou District, the south of Fujian province in southeastern China. A 1230km^2 area was selected for our analysis (Fig.1). Zhangzhou District lies between 116°53'-118°09'E and 23°32'-25°13'N, belonging to the subtropical regions. The annual average temperature is 21°, non-frost period is more than 330 days, and the annual average sunshine-hour is more than 2000 hours. Mean annual precipitation is about 1500mm of which most occurs in May and June.

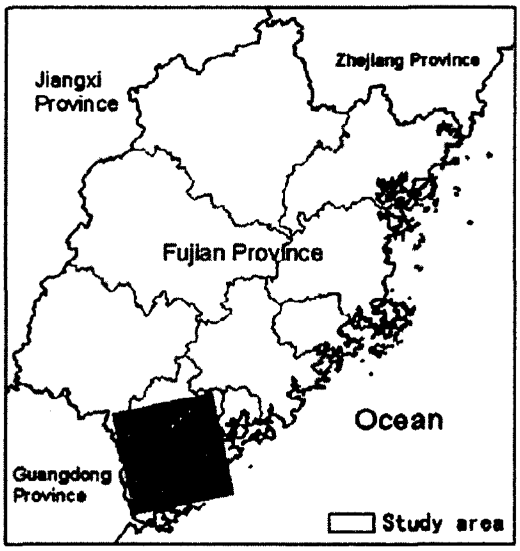

Fig.1 Location of study area

In Zhangzhou, the warm climate and the abundant precipitation are propitious to crop growth. So Zhangzhou is the main agriculture regions in Fujian province. The crop types are various and characteristic of warm and humid sub tropical regions. The main agriculture land use types are crops, vegetable garden, orchard and forest. The main crop types are rice, sweet potato, potato, banana, water bamboo, etc. Growth season of all crop types spreads all year round, from spring to winter. Rice, banana and water bamboo fields are classified in our study.

Table 1 Rice growth calendar in Zhangzhou

	transplanting period	seedling development period	ear differentiation period	heading period	Maturation period
Suitable Temperature	20—25℃	20—25℃	26—30℃	20—22℃	
Spring Rice	From the 3rd dekad of March to the 2nd dekad of April	From the 2nd dekad of April to the 2nd dekad of May	From the 2nd dekad of May to the 1st dekad of June	From the 1st dekad of June to the 2nd dekad of July	In the 2nd or 3rd dekad of July
Autumn Rice	From the 3rd dekad of June to the 3rd dekad of July	From the 3rd dekad of July to the 3rd dekad of August	From the 3rd dekad of August to the 3rd dekad of September	From the 3rd dekad of September to the 1st dekad of November	In the 1st or 2nd dekad of November

In Zhangzhou, there are two rice cycles per year: one is early season (spring) rice, from the third dekad of March to the second or third dekad of July; the other is late season (autumn) rice, from the third dekad of June to the first or second dekad of November. There are five major growth periods in the life cycle of rice: transplanting period, seedling development period, ear differentiation period, heading period and Maturation period [5]. The five periods for spring rice and autumn rice in Zhangzhou are listed in Table 1.

Water bamboo growth period is from the 2nd dekad of December to April of the 2nd year. Banana is a kind of herb throughout the year and changes little with season.

3. DATA BASIS

Because of its cloudy and rainy weather, SAR is anticipated to be the dominant high-resolution remote sensing data source for agriculture applications in tropical and subtropical regions. In our study, we use multi-temporal AP products with VV and VH data or VV and HH data obtained in 2004 and 2005. The orbit direction was ascending with an incidence angle of 19.2-26.7 degrees (IS2). The data used in this study are listed in Table 2.

Table 2 ASAR data overview

Acquisition Date	Dual- Polarization
May 29, 2004	VV & VH
August 7, 2004	VV & VH
September 11, 2004	VV & VH
October 16, 2004	VV & VH
November 20, 2004	VV & VH
December 25, 2004	VV & VH
March 5, 2005	VV & HH

According to the crop calendar, the ASAR data acquired on September 11, October 16 and November 20, 2004 are used for autumn rice mapping; the six pair of ASAR data acquired in 2004 are used for banana classification; ASAR data acquired on December 25, 2004 and March 5, 2005 are used for water bamboo classification. 1:50000 DEM data are also used for our analysis.

4. RADAR SIGNATURE OF CROP

Multi-temporal ASAR image preprocessing includes raw data input to image processing software, radiometric calibration, speckle suppression, ortho-rectification and conversion of data format from amplitude to dB [12]. The temporal behaviors of VV and VH backscatter for some typical land covers are shown in Fig.2 and Fig.3.

In VV polarization, residential area and banana have the high backscatter. Water bodies have low backscatter. But due to wind effect, ocean water has various backscatter coefficients. The backscatter of forest is temporally stable, while backscatter of rice is temporally variable. It has very low backscatter at the early growing season (September 11, 2004), but has higher backscatter at other growing periods. So whether the data during rice early growing season could be acquired is very important for rice mapping.

Compared with VV data, the backscatter behavior for both river and ocean water has no many variations, much lower value than other land covers. Residential area and banana still have very high backscatter as that of VV.

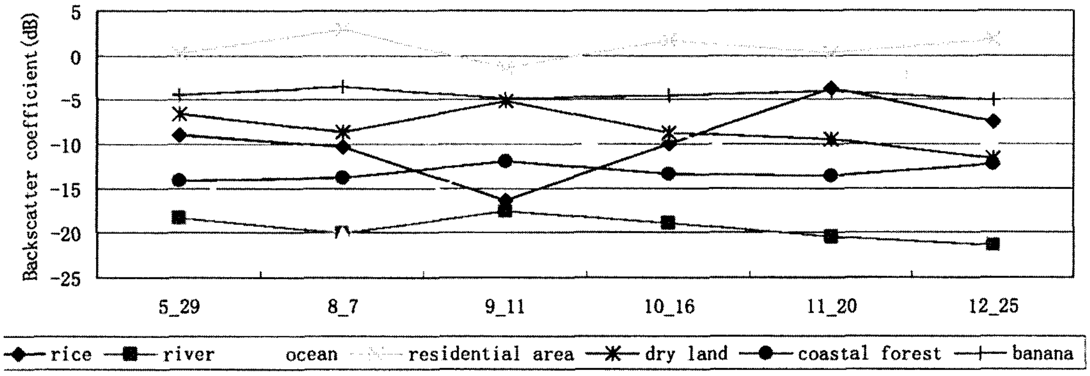

Fig.2 VV temporal behavior of some typical land covers in Zhangzhou

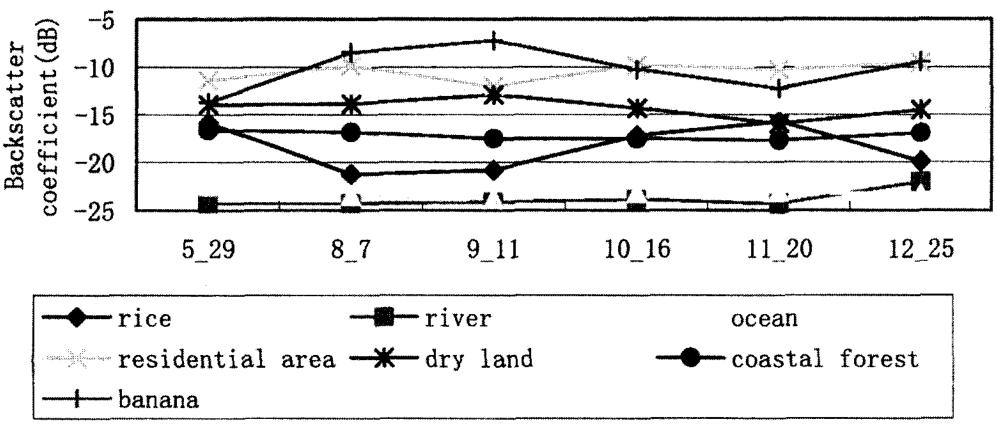

Fig.3 VH temporal behavior of some typical land covers in Zhangzhou

Principle component analysis is adopted for analysis. PC1 is the weighted sum of data, PC2 reflects the land cover changes. In our study, banana has the high backscatter and changes little, while the backscatter of rice changes sharply with season. So, in PC1, the banana fields are very bright; PC2 is mainly reflects the difference of early growing season and other growing seasons and the rice fields are very bright on PC2 image. These characters will improve the separability of different crop types.

5. OBJECT ORIENTED CLASSIFICATION AND RESULTS

We used the object-oriented multiscale image analysis method embedded in the software eCognition [13,14]. The relationships are represented with fuzzy rules, which are capable to deal with vague models and well suited to describe dependencies between different kinds of information. eCognition consists of two main steps, multi-resolution segmentation and objects based classification. The first step is a segmentation of the image based on three parameters: scale, color (spectral information), and shape (smoothness and compactness), where color and shape parameters can be weighted from 0 to 1. Within the shape setting, smoothness and compactness can also be weighted from 0 to 1. Scale is a unitless parameter related to the image resolution. The segmentation used in eCognition is bottom-up region merging technique [15].

Image objects are assigned to classes using a fuzzy rule base. The workflow of image analysis is described on Fig.4. The classification results are shown on Fig.5.

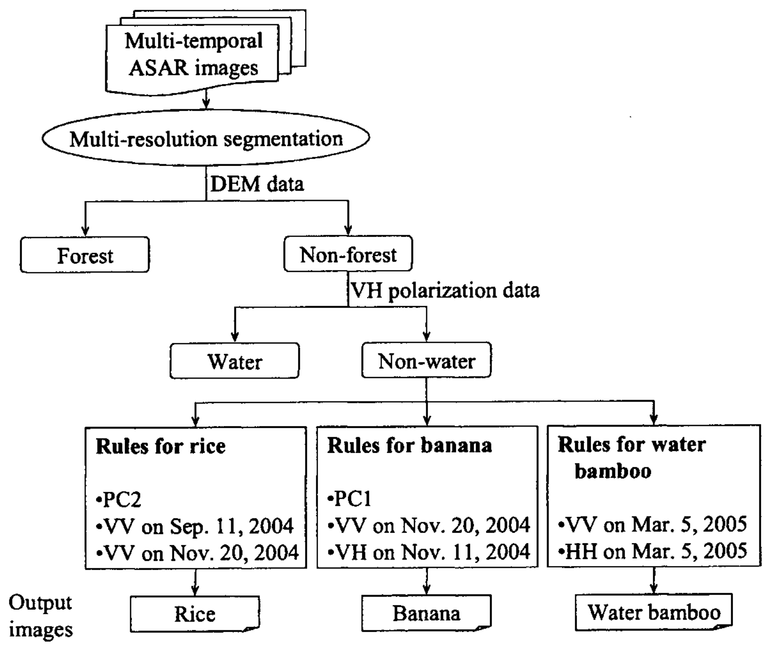

Fig.4 workflow of object-oriented image analysis

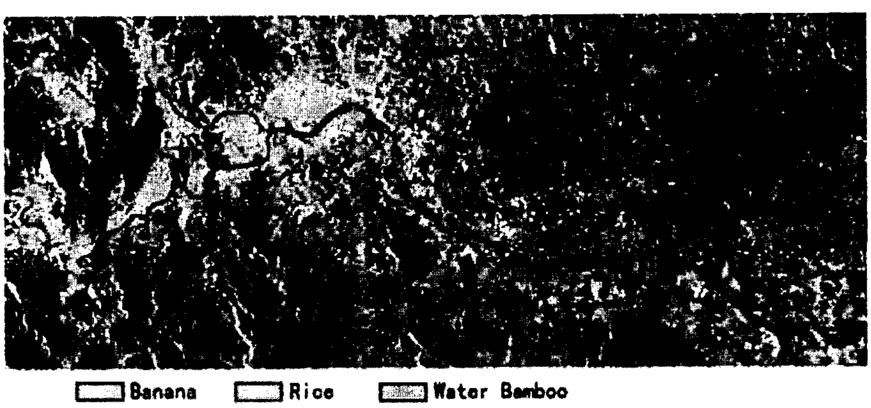

Fig.5 Crop map from ASAR data in study area

The classification assessment was carried out based on field survey data obtained in November, 2004 and April, 2005 (Fig. 6) and ASTER images acquired on April 5, 2004. The accuracy of rice, banana and water bamboo in study area is more than 80%. It means the object-oriented classifier is suitable for SAR data classification.

Fig.6 The distribution points of field survey

6. CONCLUSIONS

This paper investigates the potential of ENVISAT ASAR data for agriculture crop mapping. Based on the analysis the temporal behaviors of ASAR data, rice, banana and water bamboo fields are classified using objected-oriented classifier. The use of object-oriented classification has advantages over pixel based classification fro the extraction of different agriculture types from SAR data. With multi-temporal and dual polarization SAR data, it'll improve the accuracy of agriculture classification. The principle component analysis also provides the useful information in SAR images analysis.

REFERENCES

1. S. Henning, T. S. Morten, N. Flemming and T. Anton, Homsen crop classification by polarimetric SAR, IEEE 1999: 2333-2335.
2. H. Mcnairn, J. Ellis, J. J. Van Der Sanden, et al, Providing crop information using RADARSAT-1 and satellite optical imagery, Int. J. Remote Sensing, 23(5): 851-870, 2002.
3. Fabio Del Frate, Giovanni Schiavon, Crop Classification Using Multiconfiguration C-Band SAR Data, IEEE Trans. Geosci. Remote Sensing, *Vol.41*, 1611-1618, 2003.
4. J. Aschbacher, A. Pongsrihadulchai, S. Karnchanasutham, et al., Assessment of ERS-1 SAR data for rice crop mapping and monitoring, IEEE 1995: 2183-2185.
5. Yun Shao, Xiangtao Fan, Rice monitoring and production estimation using multitemporal RADARSAT, Remote Sensing of Environment, *76*,310–325, 2001.
6. T. Le Toan, F. Ribbes, Rice crop mapping and monitoring using ERS-1 data based on experiment and modeling results, IEEE Trans. Geosci. Remote Sensing, *vol. 35*, 41-56, 1997.
7. M. Chakraborty, S. Panigrahy, A processing and software system for rice crop inventory using multi-date RADARSAT ScanSAR data, ISPRS Journal of Photogrammetry & Remote Sensing, **55**,119–128,2000.
8. Y. Wong and E. C. Posner, A new clustering algorithm applicable to multispectral polarimetric SAR images, IEEE Trans. Geosci. Remote Sensing, vol. 31, 634-644, 1996.
9. J. S. Lee, M. R. Grunes And E. Pottier, Quantitative comparison of classification capability: sully polarimetric versus dual and single-polarization SAR, IEEE Trans. Geosci. Remote Sensing, vol. 39,2343-2351, 2001.
10. F. Zhu, H. Guo, Q. Dong and C. Wang, Multilayer perceptron classification for ENVISAT-ASAR imagery, IEEE 2004: 3077-3079.

11. U. Wegmuller, T. Strozzi, A. Wiesmann and C. Werner, ENVISAT ASAR for land cover information, IEEE 2003: 2996-2998.
12. F. Ling, Q. Wang, X. Wang, Identification of rice crop using ENVISAT ASAR in Fuzhou, Fujian Province, China (in this publication).
13. Definiens, Definies imaging, eCognition. Http://www.definiens-imaging.com, 2003.
14. Ursula C. Benz, Peter Hofmann, Multi-resolution, object-oriented fuzzy analysis of remote sensing data for GIS-ready information, ISPRS Journal of Photogrammetry & Remote Sensing, **58**,239–258, 2004.
15. A. S. Laliberte, A. Rango, K. M. Havstad, et al., Object-oriented image analysis for mapping shrub encroachment from 1937 to 2003 in southern New Mexico. Remote Sensing of Environ., 93: 198-210, 2004.

IDENTIFICATION OF RICE CROP USING ENVISAT ASAR IN FUZHOU, FUJIAN PROVINCE, CHINA

Ling Feilong, Wang Qinmin, Wang Xiaoqin

Key Laboratory of Data Mining & Information Sharing of Ministry of Education, Spatial Information Research Center of Fujian Province, Fuzhou University, Fuzhou 350002, Fujian, China, E-mail:lfl@fzu.edu.cn

ABSTRACT

Synthetic Aperture Radar (SAR) is anticipated to be the dominant high-resolution remote sensing data source for agricultural applications in tropical and subtropical regions due to its independent from cloud cover. ENVISAT-1 ASAR is the most advanced satellite radar-imaging instrument, its capabilities include beam steering for acquiring images with different incidence angles, duel polarization and wide swath coverage. Agricultural crop inventory based on remote sensed data will be improved greatly by ASAR's new capabilities. In this paper, multi-temporal ASAR alternative polarization data are used for the identification of rice crop in Fujian province. A procedure has been developed using multi-date ASAR data for rice crop identification. The procedure comprises two parts: data preprocessing and classification of multi-date data for rice field. Some novel methods are applied in image preprocessing such as correlation matching for image co-registration and multi-channel filtering for speckle suppression. Object-oriented classifier was used for classification. By adopting the procedure, classification accuracy of 90% was achieved in the test sites with multi-temporal Envisat ASAR data.

Keywords: ENVISAT, ASAR, rice crop identification, object oriented classifier

1. INTRODUCTION

Rice is one of the important crops in China. Therefore it is vital to estimate the area of paddy field as accurately as possible. Since most rice grows in monsoon area with heavy cloud cover and rainfall during the rice growing seasons, it is difficult to acquire optical remote sensed data with cloud free in the rice growing regions. Synthetic Aperture Radar (SAR) is anticipated to be the dominant high-resolution remote sensing data source for agricultural applications in tropical and subtropical regions due to its independent from cloud cover and rainfall. The rice crop mapping and monitoring was carried out using RDARSAT, ERS-1/2 and JERS-1 data and satisfied results were achieved[1-5]. ENVISAT-1 ASAR is the most advanced satellite radar-imaging instrument. Its new capabilities include beam steering for acquiring images with different incidence angles, duel polarization and wide swath coverage. Rice crop identification based on remote sensed data will be improved greatly by ASAR's new capabilities. Different from optical data, SAR data has its inherent geometric and radiometric distortion, more processing is needed than that for optical data. To best utilize the new features of ASAR data for rice crop identification, the classification method should be very robust. The preprocessing was discussed in detail and many novel techniques were introduced in this paper. Object oriented classifier was used for the identification of rice crop. Satisfied classification accuracy was achieved.

2. STUDY AREA AND DATA SET

The study area lies in the south-east of China near the city of Fuzhou. It locates approximately at the latitude of 25°53′ north, longitude of 119°30′ east(Fig.1). In the study area, there are two cycles of rice per year, early season (spring) rice and late season (autumn) rice. Seedlings are transplanted in rice fields filled with water in April. The crop is harvested during end of July to early of August.

Envisat alternating polarization SAR data were used for this study. Three pairs of ASAR images (VV and VH for each pair) were acquired during the growth period of spring rice in 2004(Table 1). The data are all C band, VV/VH polarization data from ascending orbit with 30 meter resolution. The imaging incident angle is from 19.2° to 26.7°. The first-date image used was acquired on May 7 when rice was in its early growth stage and the rice fields were flooded. The low backscatter makes rice fields covered by water easy to distinguish from other land cover types. Another two images were acquired on June 11 and July 16 respectively when rice was in its well developed and ripening stages and the backscatter coefficient is relatively high correspondingly.

Proc. 2005 Dragon Symposium "Mid-Term Results", Santorini, Greece
27 June – 1 July 2005 (ESA SP-611, January 2006)

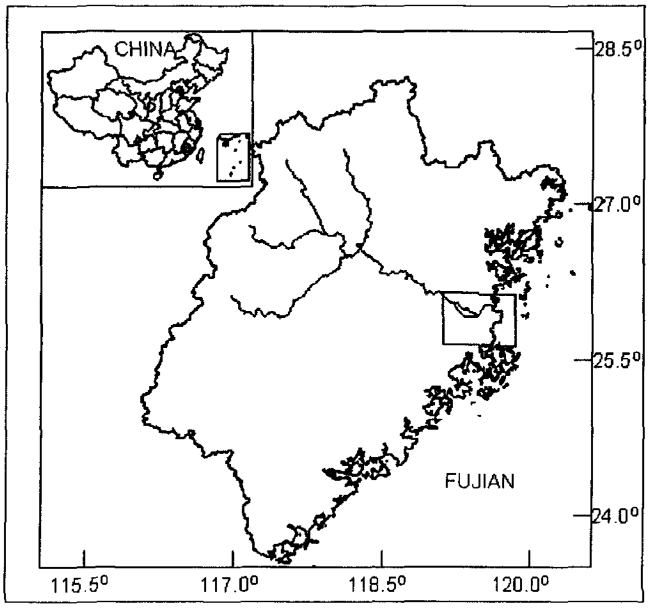

Fig.1. Study area

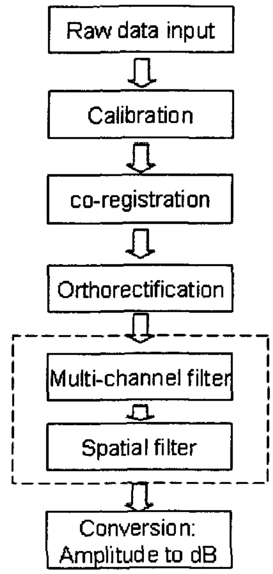

Fig.2. Image preprocessing flow

Table 1 Parameters of the Envisat ASAR data used for rice crop identification

Data characteristics	Parameters
SAR band and polarization	C band，VV/VH polarization
ASAR imaging mode	Alternating Polarization，IS2
Incidence angle(°)	19.2 - 26.7
Satellite orbit	Sun synchronous, ascending orbit
Ground coverage(km)	100
Repeat cycle	35 days
Resolution(m)	30
Pixel spacing(m)	12.5
Data acquisition date(dd/mm/yy)	07/05/2004, 11/06/2004, 16/07/2004

3. DATA PREPROCESSING

Multi-date Envisat ASAR data were used as dataset to extract information on rice fields. PCI software (PCI Geomatics, 2003) was used for most of the image processing. eCognition software(DEFiNiENS, 2004) was used for objected-oriented classification. SAR image preprocessing includes raw data input to image processing software, radiometric calibration, speckle suppression, orthorectification and conversion of data format from amplitude to dB. Fig.2 shows the flow diagram of the procedure for image preprocessing. The following subsections describe the steps.

3.1. Data input

All required geometric and radiometric metadata information was transferred to the same image file when importing the raw data to PCIDSK file. A 16-bit unsigned integer file is created which includes all of the requested imagery channels from the raw data, and saves the satellite path information and other required information in several segments.

3.2. Calibration

In order to be able to compare images from different dates and for quantitative measurement, radiometric calibration should be applied. For ASAR APP format data, the radar backscatter is calculated as Eq.1 and Eq.2:

If the output is in decibels:

$$SIGMA_{ij} = 10.0 \times \log_{10}((DN_{ij}^{2} + A_0) / A_j) + \log_{10}(\sin(I_j)) \tag{1}$$

If the output is in amplitude values:

$$SIGMA_{ij} = \sqrt{(DN_{ij}^{2} + A_0) / A_j \times \sin(I_j)} \tag{2}$$

Where, $SIGMA_{ij}$ is the output backscatter coefficient for scan line i, pixel j, DN is the input image value for scan line i, pixel j, A_0 is the fixed gain offset, Aj is the scaling gain value, Ij is the incidence angle at the jth range pixel.

If quantitative measurement of radar brightness over point and distributed targets is the objective, the calibrated result should be given in decibels. It is important to note that decibel values are on a logarithmic scale. As a result, certain mathematical operations applied to the dB output channel may not be valid. Any such operations should be done on either amplitude or power values and the result then converted to dB. If the imagery is to be further processed with filtering or classification, the calibrated result should be set to amplitude values. For this study, speckle suppression, orthorectification and classification will be carried out, therefore, the output calibrated multi-date data are all given in amplitude values.

3.3. Image co-registration

Correlation matching technique was used for image co-registration. As mentioned above, three pairs of ASAR images were used for this study. For further process and analysis purposes, these data should be co-registered to the same coordinates. In this case, the degree of accuracy in registration needs to be very high, even to the sub-pixel level. There are two common methods for co-registration: the use of ground control points (GCPs) and image correlation matching. The GCP method is more flexible than correlation matching, but the correlation matching is more powerful when dealing with translation. All images were acquired from ascending orbit from the 35-day repeat cycle, with no rotation, skewing, etc. involved. Hence registration between the images can be achieved simply by shifting the image frame along the azimuth and range direction. Image co-registration was done by GCPs and by correlation matching separately. Registered results have shown that these two approaches both work very well, but the accuracy from correlation matching seems much higher. The first-date image acquired on May 7 was treated as the master image, the subsequent date images acquired on June 11 and July 16 were registered to the master in correlation matching process. Then the co-registered images were used as one combined dataset similar to multispectral optical data for further processing and analysis.

3.4. Orthorectification

Orthorectification is the process of using a rigorous math model and a digital elevation model (DEM) to correct distortions in raw images. At the step of raw data input, make sure all required orbit header be transferred to the same image file, because they are essential to build the math model. The collection of ground control points (GCPs) is a time consuming task in orthorectification. Most of the GCPs are obtained from a 1:50000 topographic map, some GCPs in mountainous area are obtained from simulated SAR image derived by orbit parameters and DEM. For the data in Fuzhou area, the data acquired on June 11 and July 16 were registered to the data on May 7 and put together into one image file as different channels at the step of image co-registration. At this step, the orbit information segment in the data acquired on May 7 was transferred to the composite 6-channel image file, all the images were orthorectified once with 1:50000 DEM and the math model derived from the orbit information of data acquired on May 7, which made the job simplified to a great extent.

3.5. Speckle suppression

Fields are in small size in the study areas, it is essential to have very efficient speckle suppression methods. For handling the multi-date ASAR data, a multi-channel filtering[6] has been used. The idea behind multi-channel filtering is to linearly combine N images from the same scene to produce N speckle reduced images. Multi-channel filtering allows significant speckle reduction without degrading the image resolution. After the multi-date images were co-registered, multi-channel filtering was carried out. Multi-channel filter has not been encoded in commercial image processing software such as PCI and ERDAS. In this study, a model has been built in PCI Modeler module to realize multi-channel filter with three pairs of ASAR images. Multi-channel filtering shows a better preservation of edge and texture features than other filters, but seems to need more processing to reduce speckles. To further smooth the data, a 3*3 Enhanced Lee filter was next applied.

3.6. Amplitude to dB Conversion

At the calibration step, the calibrated data were given in amplitude values for further processing. If quantitative measurement of radar brightness over point and distributed targets is the objective, the output of calibrated result should be given in decibels. The data can be converted from amplitude to decibels by the following formula:

$$SIGMA = 10.0 \times \log_{10}(A^2) \quad (3)$$

Where, $SIGMA$ is backscatter coefficient (dB), A is the input amplitude value.

4. DATA ANALYSIS

In order to examine the backscatter behavior of different land-cover types, the data were converted from amplitude to backscatter coefficient (dB) to facilitate making absolute comparisons of the backscatter behavior of land-cover types. Fig.3 shows the backscatter coefficients of five land-cover types from calibrated ASAR images used in this study.

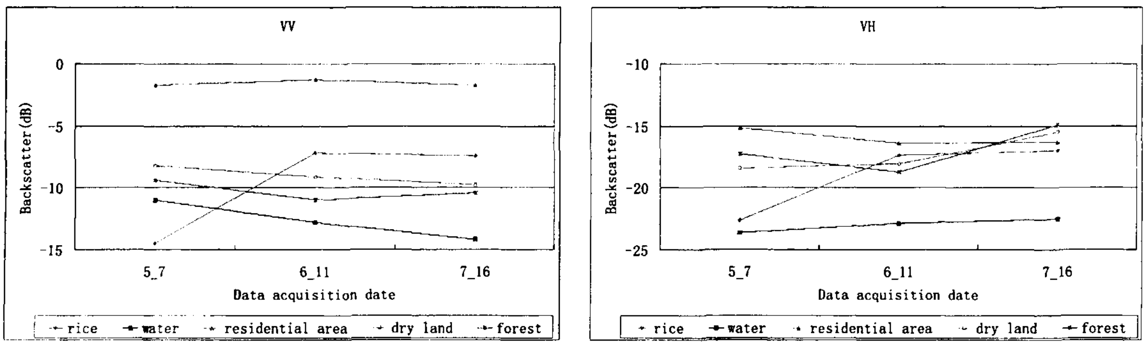

(a)VV polarization images (b)VH polarization images

Fig.3. backscatter coefficients as a function of time (2004)

There are five land cover types: rice, water, residential area, dry land and forest. Rice represents a special curve in the figure, the first date data was acquired on May 7 when the rice was shortly after transplanted, the backscatter is low(~ -14dB in VV and ~ -23dB in VH). As the rice grew, the backscatter increased, reaching a maximum of ~ -7dB in VV and ~ -17dB in VH, which is shown on the data acquired on June 11. Any other land cover type doesn't show as many variations as rice on backscatter coefficient, which is the primary characteristic for rice discrimination. Especially when rice is at its early growth stage, the rice field is flooded, the backscatter coefficient of rice is much lower than those of other land cover types except water. Because of the wind effect, the roughness of water surface changes with time, then water shows some variations on backscatter coefficient, which makes water to be mixed with rice field during the process of classification. Figure 1 shows that the variations on backscatter coefficient of water are obvious in VV polarization ASAR image but not so in VH polarization image. Water has the lowest backscatter coefficient. On July 16 the backscatter coefficient difference between water and other land cover types is the greatest in VH polarization image. This image is suitable most to separate water from non-water.

5. CLASSIFICATION

The multi-date data were classified using an objects based classifier, which was developed by DEFiNiENS and implemented in a powerful software, eCognition[7]. Here, analysis of images mainly bases on features, spatial and hierarchical relationships of objects instead of single pixels. The relationships are represented with fuzzy rules, which are capable to deal with vague models and well suited to describe dependencies between different kinds of information . eCognition consists of two main steps, multi-resolution segmentation and objects based classification. Multiresolution segmentation is the first step in eCognition. It creates image objects on several scales: Similar pixels in each level are aggregated to segments, whereby the increasing heterogeneity over the whole image is minimized. There are two major strategies for classification: a) Nearest neighbour classification and b) rule base development using fuzzy sets and fuzzy logic. The latter was used in this project. The amplitude values from each image were used as elements to classify multi-date data.

5.1. Multi-resolution segmentation

The distortions in the mountainous area, e.g. foreshortening, layover and shadow, will result in a lot of misclassification. DEM data was used to reduce the effect of those distortions. The continuous raster DEM data was first recoded to a thematic raster with only two values. The pixel value was set to 1 if the original value is equal to or larger than 45, otherwise the pixel value was set to 2. The thematic raster was then converted to vector layer in Arcview shapefile format to be used for the segmentation.

The ratio of spectral homogeneity to spatial homogeneity was set to 0.8. Three scale levels have been created with scale parameters 30, 20 and 10 respectively. Only the thematic DEM layer was used for the first time segmentation, the 3 pairs of images in Fuzhou area were used for the other 2 segmentations. For each object meaningful features can be evaluated, e.g. the average value of each image. However, most important are the hierarchical and neighbor relations: Each object knows its relations not only to its neighbors within one scale but also to its super-objects and sub-objects.

5.2. Hierarchical fuzzy classification rule base

Image objects are assigned to classes using a fuzzy rule base, which has a three-level hierarchy according to the three-scale-level segmentation. The mask-out strategy was used in the classification to exclude the forest and water's interferences to rice class. The rule base's approach is to classify forest and non-forest based on the thematic attribute DEM characteristic on level 3 consisting of large basic image objects. The rule base's approach on level 2 is to classify water and non-water within the area of non-forest on level 3. Firstly, the rule base of forest on level 2 is defined by its super objects' class attribute. The feature is called "Existence of forest super-objects". The rule base of non-forest on level 2 is defined in the same way. Secondly, 2 new classes water and non-water were inserted to the class hierarchy as the sub-classes of non-forest. The rule base of water is defined by objects' mean layer values of the 16/7/2004 VH polarization image. Non-water is defined by the inverted expression of water. The rule base's approach on level 1 is to classify rice and non-rice within the area of non-water on level 2. The super classes non-forest, non-water are inherited from level 2. The rule base of rice is defined by objects' mean layer values of May 7 VV image and June 11 VV image. Rice has low backscatter on May 7 VV image and high backscatter on June 11 VV image. The 2 features are combined to describe the rice class by "and(min)" logical operator. The inverted expression is used for non-rice. The final rice map is generated on level 1. Fig.4 shows a subset of the data set and its classification results, which illustrates how the classification was carried out step by step.

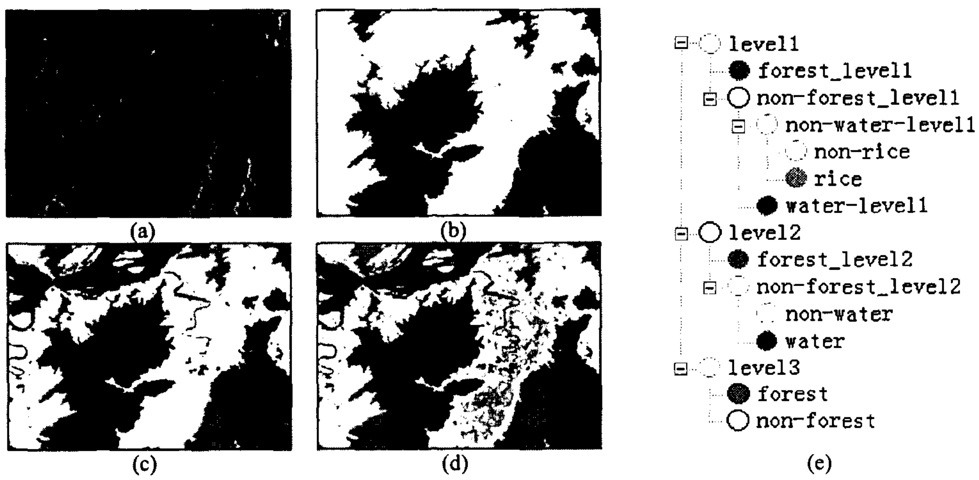

Fig.4. Classification map at different class hierarchy level
((a)ASAR images; (b)level 3; (c)level 2; (d)level 1;(e) class hierarchy)

5.3. Classification accuracy

For comparison, unsupervised classification and supervised classification were carried out with the same data. The classification accuracy referred to land-use map was calculated through the PCI software. The classification results were aggregated into 2 classes rice and non-rice to simplify the accuracy assessment. The classification assessment was then carried out based on the 2 classes. The classification accuracy at confidence level of 95% and kappa coefficients of the class rice were listed in Table 2. The object oriented classifier represents the highest accuracy, which means it is best suited for the classification of multi-date ASAR data for rice.

Table 2 Accuracy of the classification for rice

classifier	Producer's accuracy	User's accuracy	Kappa coefficient
Unsupervised classifier	70	60	0.6444
Supervised classifier	85	75	0.8024
Object oriented classifier	92	91	0.9430

6. DISCUSSION AND CONCLUSION

The investigation using ENVISAT-1 ASAR APP data have shown promising results for rice crop classification.

A number of processing steps are to be carried out before the data can be used for classification. The header of Envisat ASAR raw data is necessary for data calibration and orthorectification, which must be imported correctly along with image data. Data calibration is essential to compare images from different dates and for quantitative measurement. Calibrated data is given in dB for image analysis and quantitative measurement. If the imagery is to be further processed with filtering or classification, the output calibrated result should be set to amplitude values. The data format can be converted between amplitude and dB. Much higher accuracy is required for image-to-image registration than for image-to-map registration. It is extremely difficult to identify and locate good quality GCPs in SAR images and therefore the high accuracy can not be achieved by using GCPs. Correlation matching technique is adopted for image co-registration in this procedure and the accuracy is at sub-pixel level. Effective speckle filter is needed for the images with small size rice fields in the study area. Multi-channel filtering followed by spatial filtering is the best and adopted for this kind of situation. The co-registered images are used as one combined dataset for orthorectification, the images are orthorectified once, which makes the job simplified to a great extent.

Rice crop is separable from most other land-cover types in two or three ASAR data when data acquired at early growth stage of rice is included.

Object oriented classifier was used for rice crop classification. Classification accuracy of greater than 90% was achieved, which proves that the classifier is well suited for the classification of multi-temporal ASAR data.

ACKNOWLEDGEMENTS

The authors are grateful to ESA for the support of ASAR data. We are thankful to CTCD(Centre for Terrestrial Carbon Dynamics, University of Sheffield) and CAF(The Chinese Academy of Forestry) for the technical supports for image processing.

REFERENCES

1. Yun Shao, Xiangtao Fan, "Rice monitoring and production estimation using multitemporal RADARSAT", Remote Sensing of Environment, *76*,310–325, 2001.
2. T. Le Toan, F. Ribbes, "Rice crop mapping and monitoring using ERS-1 data based on experiment and modeling results," IEEE Trans. Geosci. Remote Sensing, *vol. 35*, 41-56, 1997.
3. M. Chakraborty, S. Panigrahy, "A processing and software system for rice crop inventory using multi-date RADARSAT ScanSAR data", ISPRS Journal of Photogrammetry & Remote Sensing, **55**,119–128,2000.
4. M. Chakraborty, S. Panigrahy, "Discrimination of rice crop grown under different cultural practices using temporal ERS-1 synthetic aperture radar data", ISPRS Journal of Photogrammetry & Remote Sensing, **52**,183–191, 1997.
5. Fabio Del Frate, Giovanni Schiavon, "Crop Classification Using Multiconfiguration C-Band SAR Data", IEEE Trans. Geosci. Remote Sensing, *Vol.41*, 1611-1618, 2003.
6. S. Quegan, J.J. Yu, "Filtering of Multichannel SAR Images," IEEE Trans. Geosci. Remote Sensing, *Vol.39*, 2373-2379.November, 2001.
7. Ursula C. Benz, Peter Hofmann, "Multi-resolution, object-oriented fuzzy analysis of remote sensing data for GIS-ready information", ISPRS Journal of Photogrammetry & Remote Sensing, **58**,239–258, 2004.

LAND USE/COVER CLASSIFICATION AND RICE MAPPING BASED ON ENVISAT ASAR DATA

Shaun Quegan[1] Guojin He[2,1] Mirko Santuari[3,1] Xiaoqin Wang[4] Qinmin Wang[4]

[1] Centre for Terrestrial Carbon Dynamics, Sheffield Centre for Earth Observation Science, University of Sheffield, Hicks Building, Hounsfield Road, Sheffield S3 7RH, UK, E-mail: S.quegan@sheffield.ac.uk
[2] China Remote Sensing Satellite Ground Station, Chinese Academy of Sciences, P. O. Box 2434, Beijing 100086, P. R. China, E-mail: gjhe@ne.rsgs.ac.cn
[3] Department of Information and Communication Technology, University of Trento, 38050, Povo, Trento, Italy
[4] Key Laboratory of Data Mining & Information Sharing of Ministry of Education, Spatial Information Research Center, Fuzhou University, Fuzhou 350002, Fujian, P. R. China

ABSTRACT

The main objective of this project is to develop and test methodology using ENVISAT ASAR data for agricultural applications, with an emphasis on land use, land cover classification and rice mapping. An optimal pre-processing chain for ASAR data is first constructed to provide input data to the classification steps. Experiments at the Zhangzhou test site, Fujian province, southern China, indicate that rice mapping based on Principal Components Analysis is effective at packing multi-temporal information on rice fields into a dominant component and gives results similar to a rule-based approach. A radial basis function neural network approach provides reasonable accuracies for broad land cover classification, with clear gains in statistical accuracy as more data are added, but without major impacts on the visual quality of the classified images

Key word: ENVISAT ASAR data, Agriculture, Land use and land cover classification, Rice mapping, Zhangzhou region, Fujian Province

1. INTRODUCTION

Land use/land cover and crop classification are usually performed using high resolution optical data, such as Landsat TM or SPOT HRV data. For many regions in China with very diverse land use and crop types, and particularly in the southern China, the main limitation of optical data is cloud cover, which prevents multi-date acquisition during the growing season. Hence, the potential of multi-temporal SAR data for producing land-cover maps has become of increasing interest, both in China and elsewhere. A further stimulus to the use of SAR is its special properties for identifying different land cover types, including: 1) the backscattering coefficient is sensitive to target geometry and dielectric; 2) radar signals are coherent, allowing their use for interferometry. Furthermore, recently developed information processing technologies for SAR data [1, 2] allow multi-channel (different polarizations, frequencies and times) SAR data to be used for dealing with real problems in many application domains.

The ENVISAT satellite, launched by ESA in 2002, carries 10 instruments and serves many applications, including agriculture, forestry, oil and gas exploration and ice mapping. The Advanced Synthetic Aperture Radar (ASAR) instrument on ENVISAT operates at C-band, like the ERS SARs, but has important new capabilities: beam steering for acquiring images with different incidence angles, dual polarization and wide swath coverage. Users have access to a variety of modes that can provide swaths from 56 to 405 km in width, with resolutions from 30 to 150 m and incidence angles from 15 to 45 degrees. With ASAR dual polarization and multi-incidence angle data, the backscattering behaviour of land cover as a function of polarization and incidence angle can be used to enhance the information content and aid speckle reduction.

A main objective of this research (Dragon project 2563) is to develop and validate methodology using the new features of ENVISAT ASAR data for land use and land cover classification, with an emphasis on agriculture and forestry. This application relies on exploiting multi-channel intensity data, with multi-temporal data being particularly important.

The paper is organized as five sections. Section II describes the characteristics of the Zhangzhou test site in Fujian province, southern China. Section III gives a brief description of the remote sensing datasets. In section IV, the methodology is addressed, focusing on ASAR preprocessing methods and feature extraction approaches, followed by reporting of the experimental results, while Section V presents a discussion and conclusions.

2. TEST SITE CHARACTERISTICS

Zhangzhou and Fuzhou are the main test sites used in this project, but the aim is to develop approaches applicable to the whole flat coastal zone in Fujian. Here we focus on Zhangzhou District in the south of Fujian Province, between

Proc. 2005 Dragon Symposium "Mid-Term Results", Santorini, Greece
27 June – 1 July 2005 (ESA SP-611, January 2006)

116°53'-118°09' E and 23°32'-25°13'N, with an area of 12897 km^2, of which about 77% is below 500 m in altitude. The main land use types are arable land (12.91%), garden plots (13.45%) and forest (52.49%). Longhai County in Zhangzhou is the primary test site. The warm climate (the average annual temperature is 21°) and abundant precipitation are propitious to various crop types characteristic of warm and humid sub-tropical regions. The growth season of all crop types runs throughout the year, from spring to winter. Normally, three crop cycles can be produced, and the main cycles are as follows:

1). Narcissus (haricot bean, peas /water bamboo) + rice + narcissus (haricot bean, peas /water bamboo)
2). Potato + rice + rice
3). Potato + soybean (peanut) + soybean (peanut)

There are early and late rice crops, whose growth calendars (shown in table 1) are approximately from April to October.

Table 1 Rice growing calendars

	Vegetative Stage (Tiller, elongation, and booting)	**Reproductive stage** (heading, panicle initiation and flowering)	**Ripening stage** (grain filling, milk and dough stages)	**Harvesting**
Suitable temperature	20-25	26-30	20-22	
Seasons for early rice in Zhangzhou	The last ten days of March to the middle ten days of May	The middle ten days of May to the first ten days of June	The first ten days of June to the middle ten days of July	The last ten days of July
Seasons for late rice in Zhangzhou	The last ten days of June to the last ten days of August	The last ten days of August to the last ten days of September	The last ten days of September to the first ten days of November	The first or middle ten days of November

Sheffield was supplied with a section of a coarse land use map for Longhai county produced in 2000, and a field survey was performed in early April 2005.

3. REMOTE SENSING DATASETS

The ENVISAT ASAR is the main satellite data resource used in this project. The initial intention was to obtain complete sequences of 35-day repeat ENVISAT ASAR data from the test sites, especially during the rice growing seasons, as well as investigating the use of images with different polarization and different incidence angles. Unfortunately, the data sets were often not sequential due to conflicts with other Dragon projects or commercial orders. For example, up to October 2004 only three pairs of ASAR data sets for the Zhangzhou target test site were received, on 29 May, 7 August and 16 October, all in the same polarisation mode (VV-VH) and with the same incidence angle (23^0). This affected the data analysis for crop identification purposes.

The situation has improved in 2005, but data conflicts still exist, particularly from May to October. Up to July, six pairs of ASAR data sets from Zhangzhou city were acquired, on 29 January, 5 March, 9 April, 25 April, 30 May and 4 July; all have 23^0 incidence angle and all are in HH-VV mode except the first, which is a VV-VH pair. The first three are from one repeat cycle, the second three from a different repeat cycle. The latter are particularly significant in terms of repeat coverage during the early rice season in the Zhangzhou region. In addition, several scenes of ASAR data with VV-VH polarisation and 37^0 incidence angle are available.

Preprocessing techniques were developed based on 2004 data, followed by validation with the 2005 data sets. The feature extraction studies used the sequential HH-VV data from 25 April, 30 May and 4 July. In addition, Landsat TM data from 28 September 2004 and IRS-P6 LISS III from 1 March 2005 were used to assist land cover analysis. Note that Sheffield did not have access to a high resolution DEM of the region, so the technical development is based on ASAR data in APG format.

4. METHODOLOGY

The processing chain developed for this study is shown as Fig. 1 and includes two main steps, preprocessing and feature extraction. Given a set of M multi-channel ASAR images from the same geographic area at different dates (and with different polarizations), the preprocessing stage implements calibration, co-registration and multi-channel filtering, and forms a set of speckle-reduced images, while the main purpose of feature extraction is to extract thematic information, such as land cover type or rice maps, from the preprocessed images.

4.1. Preprocessing methods

4.1.1. Data calibration

Given an ASAR image, the relationship between the digital number of the image pixel, the uncalibrated intensity and the radar backscattering coefficient is given by Eqs. 1 and 2:

$$I_{i,j}=DN_{i,j}^{2} \tag{1}$$

$$\sigma_{i,j}^{0} = (DN_{i,j}^{2} * \sin(\alpha_{i,j})) / K \tag{2}$$

Where, at position (i, j), $DN_{i,j}$ is the digital number ,$I_{i,j}$ is the pixel intensity, $\sigma_{i,j}^{0}$ is the backscattering coefficient, $\alpha_{i,j}$ is the incidence angle and K is the absolute calibration constant. Since detailed slope information is normally not available at the processing time, a "flat terrain" (based on the ellipsoid WSG84) is assumed during processing and the final intensity image is therefore proportional to the radar brightness of the illuminated scene [3].

4.1.2. Image co-registration based on correlation matching

For analysis purposes, the multi-temporal ASAR images should be co-registered with high accuracy, even to sub-pixel level. There are two common methods for co-registration: the use of ground control points (GCPs) and image correlation matching. The GCP method is more flexible and widely available in commercial remote sensing software like ENVI, ERDAS and PCI. It deals with simple translation, but is also capable of handling more complicated operations, such as scaling and rotation. Correlation matching is much more powerful when dealing purely with translation. A problem often associated with correlation matching is that its success depends on a sensible choice of the chip. A technique using a large number of automatically selected chips has been developed and is available in a commercial package from GAMMA software.

In the following analysis, the APG_1P ASAR images used are from the same 35-day repeat cycle, with no rotation, skewing, etc. involved. Hence image registration can be achieved simply by translation in the azimuth and range directions. Image co-registration was carried out using both GCPs and correlation matching. Both approaches worked well, but correlation gave much higher accuracy and could be performed automatically.

4. 1.3. Multi-channel filtering

Image filtering is necessary to reduce the effects of speckle is a key step in land cover classification with ASAR data. It improves visual interpretation, but more importantly increases the accuracy of the estimate of backscatter at each pixel, with direct impact on classification.

The usual approach to filtering is in the spatial domain; numerous spatial filters are described in the literature and some of them are encoded in commercial image processing software. The best known are the Frost, Lee and Kuan linear filters, as well as Gamma filters [4]. They are designed to process SAR images on an individual basis, and do not take advantage of the multiple images in this project. Instead, we use a multi-channel filter [1] whose basic concept is to linearly combine M registered intensity images from the same scene to produce M speckle-reduced, unbiased images. It has the form:

$$J_i = \frac{\sigma_i}{M}\sum_{j=1}^{M}\frac{I_j}{\sigma_j}, \quad i = 1,\ldots,M \tag{3}$$

Here the I_i are the M original intensity images, J_i is the filtered output for the ith input image, and σ_i is the estimate of the local mean backscattering coefficient in image i, estimated by averaging intensity values in a local window around each pixel in each image. This filter minimizes speckle while in principle preserving the radiometry and spatial resolution of the individual channels. Reasonable results are achieved in tests with the ASAR images described in Section III. Fig. 2-a shows a colour overlay of filtered VV images for the three ASAR image pairs acquired on 29 May, 7 August and 16 October 2004 (note that all six images were used in the filtering); Fig. 2-b is the TM image received on 28 September 2004. Fig. 2-c and 2-d are respectively the original and filtered HH colour overlay images from 29 January, 4 March and 9 April 2005. Comparison with the TM image indicates that the ASAR images allow most of the vegetated areas in the TM image to be identified, but agriculture is distinguished from forest by its temporal variability. The high resolution of the ASAR images also allows many of the details of the field and dyke structure to be picked out.

4.2. Feature extraction and rice mapping

4.2.1. Signatures of ASAR Backscatter

To assess whether the temporal behaviour of land cover and crop types could be exploited in classification, ASAR backscatter signatures were studied, taking published results into account. ASAR returns from different land cover types (urban, forest/orchard, bare land, agriculture areas and water surfaces) were measured on the three pairs of ASAR images from 29 January (VV-VH), 5 March (HH-VV) and 9 April (HH-VV) in 2005. Features to note include: 1) the urban and forest classes exhibit lower temporal variability than most other cover types; 2) there is large variation in agricultural areas due to different planting structures, cultural practices and vegetation growth; 3) large variations also occur for water surfaces, due to wind effects on surface roughness. These findings agree with previous results [1, 5, 6].

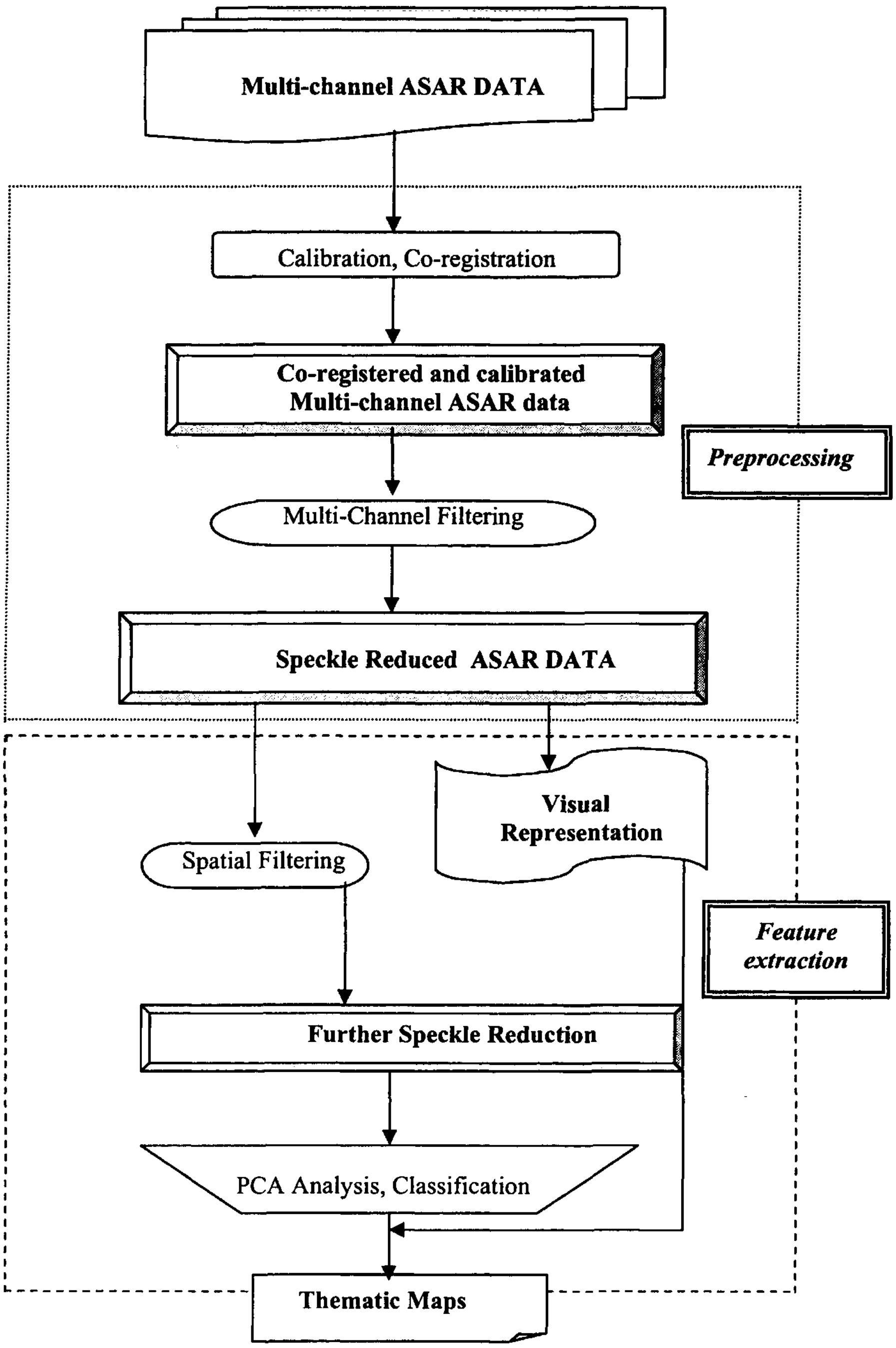

Fig. 1 Optimal processing chain

In addition, the backscattering coefficients corresponding to riparian grasses and different rice growing stages were measured on ASAR HH-VV data from 25 April, 30 May and 4 July 2005. Both rice and grass show the same increasing trends in HH backscatter from April to July, but riparian grass gives much lower backscatter than rice. The VV backscatter of rice decreases from May to July, unlike riparian grass (see table 2 and Fig. 3). This peculiarity aids feature extraction and rice mapping.

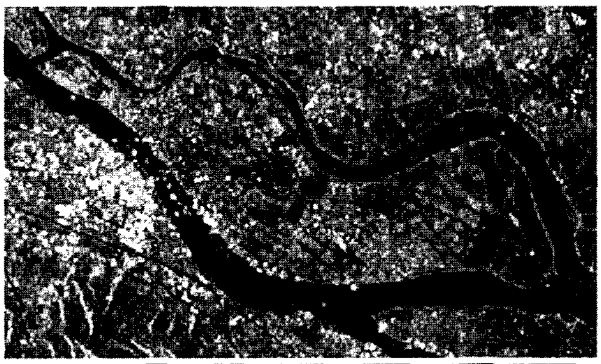

Fig. 2-a Filtered ASAR VV data, Longhai County: 2004 May (R), August (G) and October (B)

Fig. 2-b TM image acquired on 28/09/04: band 5 (R), band 4 (G), band 3 (B)

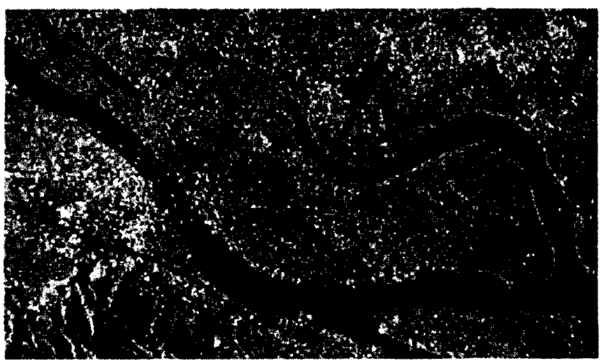

Fig. 2-c Original image overlay, 2005: HH Jan (R), Mar (G), Apr (B)

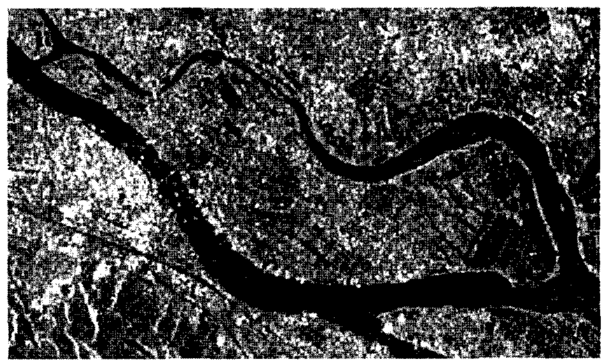

Fig. 2-d Filtered ASAR overlay, 2005: HH Jan (R), Mar (G), Apr (B)

Table 2 Measured backscattering coefficients for rice and riparian grass sample regions

Dates and ROI Samples	2005/07/04		2005/05/30		2005/04/25	
	HH	VV	HH	VV	HH	VV
Rice1	-5.657306	-9.923680	-5.311021	-9.041216	-12.032277	-16.927347
Rice2	-4.103302	-9.187402	-4.413841	-7.817688	-11.656147	-15.282614
Rice3	-3.613911	-11.383503	-4.330298	-9.006979	-14.786694	-13.532021
Rice4	-5.989599	-7.797697	-5.683509	-8.216740	-14.968815	-15.803038
Rice5	-2.638320	-6.616221	-6.611218	-6.073481	-15.452489	-16.684048
Mean rice	**-4.400488**	**-8.981701**	**-5.269977**	**-8.031221**	**-13.779284**	**15.6458118**
River1	-9.284453	-9.021207	-11.534198	-9.792250	-19.386765	-19.067399
River2	-10.059182	-9.707229	-9.164981	-5.326047	-17.867124	-17.088364
Mean river	**-9.6718175**	**-9.364218**	**-10.349590**	**-7.559149**	**-18.626945**	**-18.077882**

4.2.2. Rice mapping

Previous studies and the above measurements show that rice fields normally exhibit large variation in their temporal radar responses. This is the basis of the approach to rice field mapping relying on temporal change measurement in [5]. Here, instead, a Principal Components Analysis (PCA) based method is used to enhance the rice distribution information. PCA is a well-known tool for image information compression and enhancement of multi-spectral data. It can compress information and reduce noise, thus enabling efficient automated image segmentation and /or better human interpretation.

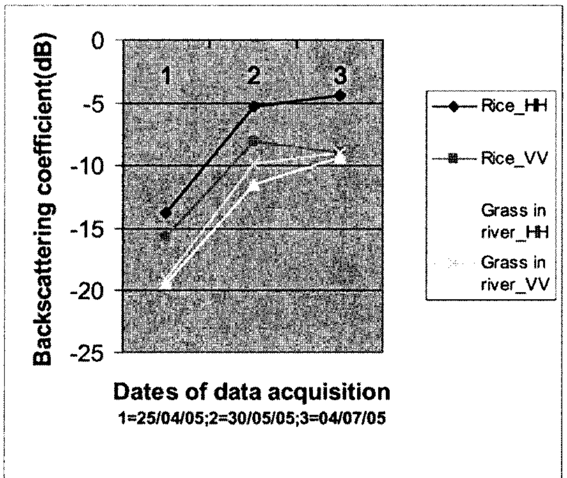

Fig. 3 Comparison of temporal development of σ^0 for rice and riparian grass

Given a set of co-registered and filtered multi-channel ASAR images, the rice mapping process consists of the following steps: PCA transform, rice/non-rice segmentation on the rice dominated component, and map production. An experiment was implemented with the HH-VV data acquired on 25 April, 30 May and 4 July 2005 by selecting two different areas, including and excluding the river. Similar results were obtained, both showing strong brightness of rice fields in PC2. One of the PC2 component images is shown in fig. 4. The eigenvectors associated with the PCA analysis are listed in table 3. The PC2 vector is not quite as expected from a rule-based approach [5] or Fig.3. In effect it subtracts the April and the May VV values from the HH values in May and July. The reason for the polarization difference in May is not at all clear from the signature analysis. However, a direct rule-based treatment (subtracting the April HH value from the average of the May and July HH values) gave very similar results. Note that the riparian grass has the same appearance as rice in PC2, probably due to their similar backscatter trends as shown in Fig. 3. However, so do large sections of the open water in the river, due to the particularities of wind conditions during the acquisitions. Fig.5 is the rice distribution map from Fig.4.

Table 3 Eigenvectors of the PCA transform

Image	PC1	PC2	PC3	PC4	PC5	PC6
July HH	0.435561	0.392792	0.437340	0.400420	0.405980	0.373603
July VV	0.457149	0.048127	0.379396	0.108115	-0.446010	-0.658896
May HH	-0.145446	**0.660258**	-0.378265	0.326347	0.523810	0.137626
May VV	-0.520426	-0.367255	0.352994	0.668171	-0.150059	0.026566
April HH	0.295265	-0.329214	0.171284	-0.196019	-0.575459	0.636806
April VV	0.471299	-0.405216	-0.606436	0.486412	0.090593	-0.033305

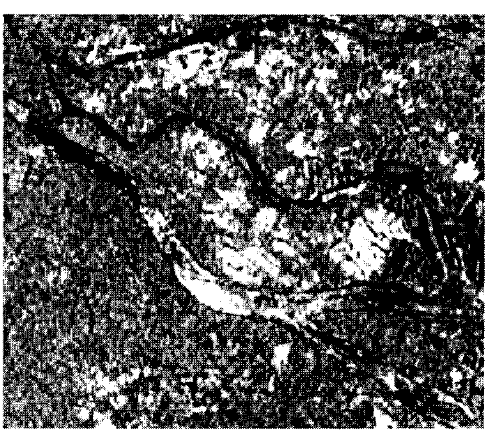

Fig. 4. PC2 from multi-channel filtered images

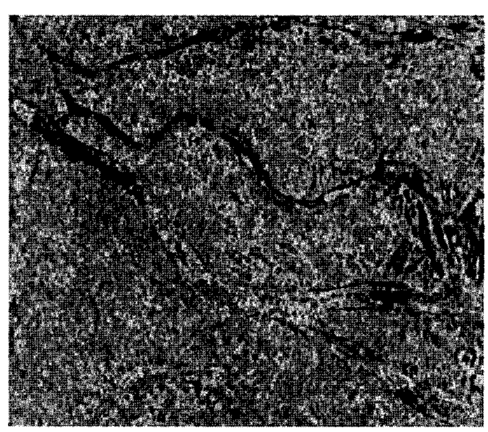

Fig.5 Rice distribution map – rice shown in red (including some riparian grass)

4.2.3. Land use/cover classification

The general problem faced in this work is whether the new features of ASAR support improved classification algorithms. Some general principles can be stated. For instance, forests can be distinguished from other types of vegetation using their temporal stability in the radar images [1], while fields exhibit great temporal variability due to the soil moisture changes, crop growth and cultivation practices. The urban class also has high temporal stability compared to most natural targets, but with a very wide range of backscattering values that overlaps significantly with other land cover types. Urban areas may be separated from other land cover types using long-term coherence measured on interferometric pairs, but no suitable pairs exist for the Zhangzhou area. Urban areas are likely to exhibit texture, and ratios of images with different polarisations should be able to distinguish oriented vegetation (such as cereals and rice) from more random cover types, such as forest.

These principles can be used in rule-based classification schemes, or more statistical data-driven methods based on training datasets may be used, of which Maximum Likelihood is the most robust pixel-based classifier. However, in their basic forms, these kinds of classifiers are not well-adapted to SAR images. This is not only because SAR data are noisier and texture abundant but also because nonlinear features are often valuable. Thus it is important to adopt new, more suitable algorithms.

Rule-based schemes are still being developed, so the results described below are based on a RBF Neural Network-based approach.

4. 2.3.1. Rationale of RBF neural networks

Many features of value in classifying SAR images have irregular and complex joint probability distributions, mainly because they are obtained by applying nonlinear operators to SAR images. Hence parametric classification approaches like Gaussian or Gamma distributed maximum likelihood algorithms are inappropriate, as it is impossible to formulate a reasonable model of class distributions in the feature space. As an alternative, a radial basis functions (RBF) neural network classifier has been adopted. Fig. 6 shows the architecture of an RBF neural network classifier.

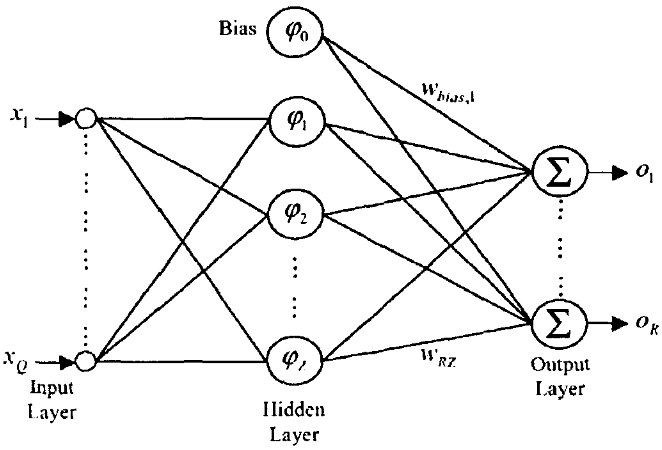

Fig. 6 Architecture of an RBF neural network classifier

RBF neural networks are embedded in an architecture with an input layer, a single hidden layer characterized by units with radial symmetric activation functions $\varphi_z()$ (here they are Gaussian functions), and an output layer characterized by neurons with linear activation functions. The input layer is made up of as many units as the number of input features (i.e., Q) whereas the output layer contains as many neurons as the number of classes to be recognized (i.e., $\boldsymbol{R}$). Each activation function associated with each unit of the hidden layer is characterized by a centre vector $\overline{u}_z$ and a width h_z. Each output neuron computes a weighted summation over the responses of the hidden neurons of the network for a given pattern $\overline{x}_p$, i.e.,

$$o_l(\overline{x}_p) = \sum_{z=1}^{Z} w_{lz} \cdot \varphi_z(\overline{x}_p) + w_{bias,l} \tag{4}$$

where Z is the number of hidden neurons, w_{lz} represents the weight associated with the connection between the kernel function $\varphi_z()$ and the output neuron o_l, and $w_{bias,l}$ is the bias of the output neuron o_l. Training of the RBF classifier is carried out in two steps: 1) training of the hidden layer (i.e., selection of both the centres $\overline{u}_z$ and the width h_z of the kernel functions associated with the hidden units); 2) training of the output layer (i.e., the weights w_{lz} associated with the connections between the hidden and the output units are computed).

In training the hidden layer, in order to avoid the typical problems of standard learning procedures, the algorithm proposed in [7] was chosen. Such an algorithm considers the class membership of training samples to select the centres and widths of the kernel functions. In particular, it avoids the generation of mixed kernel functions and tunes the kernel widths to limit the overlap in boundary regions between different classes.

4. 2.3.2. Experimental classification results with RBF

For validation purposes, the 28 September 2004 Landsat ETM+ image was used. By analyzing this image, a set of regions of interest (ROIs) was defined from which training and test sets were generated (the training and test sets were extracted from different ROIs) (Table 4).

Table 4. Number of training and test samples used in the experiments

Land-Cover Class	Training Set	Test set
Urban area	5246	9487
Water	3732	9615
Fields	2755	4102
Forest	1487	3036
Total pixels	**13220**	**26240**

The classification experiments were performed on the three HH-VV ASAR image pairs from 25 April, 30 May and 4 July 2005, as well as a set of 12 ASAR images from 2004 (VV-VH) and 2005 (HH-VV). Before classification, all the data sets were pre-processed as described in Section 4, but in order to increase the ENL, a Frost spatial filter with a 5x5 moving window was applied to the pre-processed images, followed by conversion to log data. Some texture features were computed from the original images using the co-occurrence and occurrence matrices using a 5x5 moving window. For each texture feature we computed a mean value on all the images used.

The input layer in the RBF network has the same number of neurons as the features used in the dataset. For the output layer we defined as many units as the number of classes (water, forest, urban, field). In order to evaluate the effectiveness of the RBF network several experiments were carried out, changing the type and the number of the features used. A list of the datasets used is shown in table 5.

Table 5. List of the datasets used in the experiments

Dataset	Features used in the dataset
1	Original images
2	Original images + variance
3	Original images + all textures

For each dataset, with increasing number of hidden neurons (8, 20, 40, 60, 100 and 160 hidden neurons), three different trials were carried out and a confusion matrix and Kappa coefficient of accuracy was computed for each trial. For comparison, a classification focusing on some data sets was also carried out using the well known ML classifier. Figs. 7 and 8 present the Kappa coefficient of accuracy for the data sets shown in table 5 on the basis of 6 images and 12 images respectively.

From Fig. 7, we can see that the overall classification accuracy increases when texture features are added to the RBF classifier, especially when the number of neurons is high, while the accuracy decreases in the ML classifier due to the non-Gaussian distribution of the texture features. The overall accuracies are similar if no extra texture features are used. In this case, a Kappa coefficient of about 81% was achieved by classifying on 6 images from 2005 plus all the texture features (data set 3 in table 5). The classified image is shown in Fig. 9. The main errors are between the URBAN and FIELD classes, and the mountainous region is sometimes confused with the URBAN class in the lower-left corner of the map.

Comparing Fig. 8 with Fig. 7 shows that classification with 12 images gives much higher overall accuracies than with 6 images. In this case, the Kappa coefficient reaches 88% when classifying on 12 images plus all the texture features (data set 3 in table 5). The resulting image is shown in Fig. 10. Although the main classification errors are still between the URBAN and FIELD classes, and the mountainous region is still confused with the URBAN class in the lower-left corner of the map, the distinction between the URBAN and FIELD class is much better than in Fig. 9. This results from combining multi-polarisation ASAR images (HH-VV and VV-VH) but at the price of using much more data and processing time.

For each different dataset used in the experiments, we computed for each different architecture (8, 20, 40, 60, 100, 160 hidden neurons) the mean standard deviation versus the number of datasets used for the 3 different trials for each architecture (Fig. 11). As expected, the standard deviation decreases as the number of neurons increases and the results are more reliable for each dataset used in the experiments.

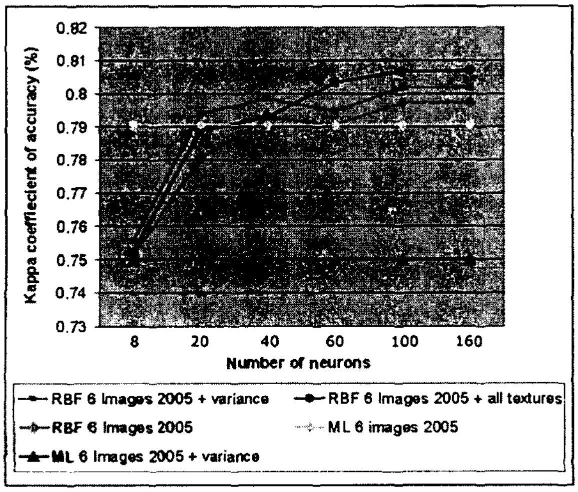

Fig. 7. Behaviour of the Kappa coefficient of accuracy(mean on 3 different trials) versus number of hidden neurons for different datasets generated using the 6 single-polarization images from 2005.

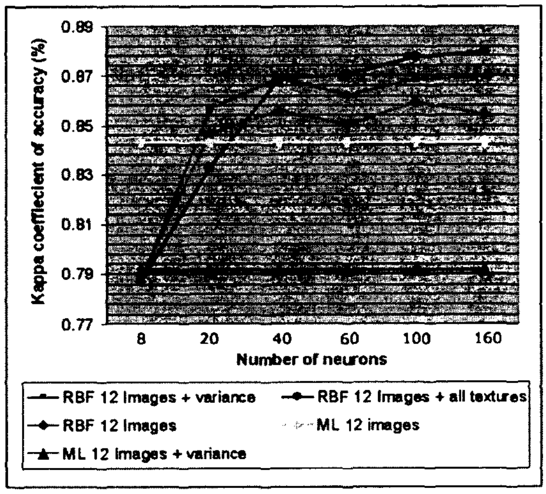

Fig. 8. Behaviour of the Kappa coefficient of accuracy (mean on 3 different trials) versus number of hidden neurons for different datasets generated using the 12 single-polarization images from 2004

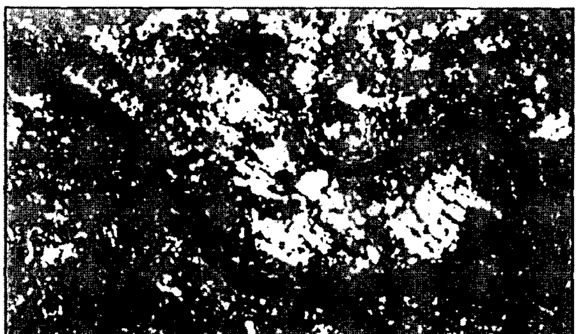

Fig. 9. Classified test area obtained from an RBF network classifier using the dataset made up of the 6 single-polarization original images from 2005 and all the texture features

Fig. 10. Classified map of the test area obtained from an RBF network classifier using the dataset made up of the 12 single-polarization original images from 2004 and 2005 and all the texture features

5. CONCLUDING REMARKS

The main objective of this research is to develop and validate methodology using ASAR data for land use and land cover classification. Although we are interested in rule-based approaches to classification, this paper mainly reports results from data-based methods. A rice field mapping approach relying on Principal Components Analysis (PCA) seems to be effective in packing rice information from multi-temporal data sets into a dominant component, and gives similar results to a rule-based approach, but the interpretation of the projection vector is unclear. A distribution-free classification strategy based on a RBF-based neural net, with features based on expected properties of SAR images, gives reasonably accurate land cover classification into water, forest, agriculture and urban classes. The use of more images and multiple polarisations improves classification accuracy, but at the cost of much more data resource and processing time.

A key issue to be addressed is whether the results obtainable from ASAR add significantly to what can be obtained from optical data, either by giving reliable coverage or by providing information not available in the optical data (such as separation of forest from other vegetation covers). This is still being assessed.

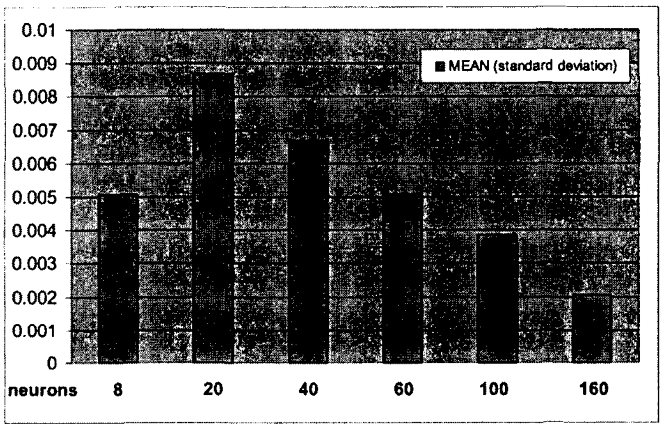

Fig.11. Mean standard deviation versus number of datasets used for the 3 different trials for each architecture (8, 20, 40, 60, 100 and 160 hidden neurons).

REFERENCES:

1. S. Quegan and J.J. Yu, "Filtering of Multichannel SAR Images," *IEEE Trans. Geosci. Remote Sensing,* Vol.39, pp 2373-2379.November, 2001

2. C. J. Oliver and S. Quegan, Understanding synthetic aperture radar images. Boston, MA: Artech House, 1998.

3. http://envisat.esa.int/instruments/asar/data-app/dataprod.html

4. http://www.ResearchSystm.com

5. T. Le Toan, F. Ribbes, L.-F. Wang, N. Floury, K.-H. Ding, J. A. Kong, M. Fujita, and T. Kurosu, "Rice crop mapping and monitoring using ERS-1 data based on experiment and modeling results," *IEEE Trans. Geosci. Remote Sensing,* Vol.35, pp. 41-56, Jan, 1997.

6. L. Bruzzone, M. Marconcini, U. Wegmuller and A. Wiesmann, "An advanced system for the automatic classification of multitemporal SAR images," *IEEE Trans. Geosci. Remote Sensing,* Vol.42, pp 1321-1334, June, 2004.

7. L. Bruzzone and D. F. Prieto, "A technique for the selection of kernel function parameters in RBF neural networks for classification of remote-sensing images", *IEEE Trans. Geosci. Remote Sensing*, vol. 37, pp. 1179–1184, Mar, 1999.

8. J. J. Yu, "Analysis and classification methods for synthetic aperture radar data applied to forest monitoring," Ph. D. dissertation, University of Sheffield, Sheffield, U. K. 2000.

Elevation Models and Terrain Motion

Landslides
(id. 2558)

INTERFEROMETRIC PHASE NOISE FILTERING BASED ON ADAPTIVE OPTIMIZED WAVELET PACKETS TRANSFORM

Qiming Zeng[1,2], Liang Gao[1,2], Ruihong Liu[1]

[1] *Institute of Remote Sensing and GIS, Peking University, Beijing, 100871, P.R.China, E-mail: qmzeng@pku.edu.cn*

[2] *Key Lab of Spatial Information Integration and Engineering Application of Beijing, Beijing, 100871, P.R.China, E-mail: qmzeng@pku.edu.cn*

Abstract—

Interferometric synthetic aperture radar (InSAR) has been used widely in investigation of surface deformation, such as earthquake, volcano, ground subsistence and landslides. But there are still some obstacles standing in the stage of the application. One of those is the phase noise in the interferogra. In particular, there are much noise in the inteferograms derived in steep topographic area with dense vegetation cover, such as the Three Gorges Area in China. This paper addresses the problem of phase noise filtering in InSAR. One difficulty of phase noise filtering of SAR interferometry is to reduce phase noise as much as possible while maintaining the phase information at the same time. The use of wavelet transform filtering is easy to ignore the high-frequency information, and make the image detail slur. One of the merits of wavelet packets transform is that most detail information in each frequency band will be analyzed. But over subtle decomposition in the high frequency bands, where noise is dominant, is apt to treat phase noise in those bands as signal. This would lead to erroneous result. In this paper, a phase noise filtering method based on adaptive optimized wavelet packets transform, or optimized tree-structured wavelet transform, is given out. By checking the correlation of wavelet coefficients in each wavelet scale, we decide whether each wavelet component in this scale should be decomposed further or not. According to such an adaptively constructed wavelet packets tree, complex phase image is decomposed. For the purpose of keeping the phase information, wavelet transform is executed in complex domain, and different threshold values are computed at each wavelet scale by using the intensity of their wavelet coefficients. Moreover, we have used an improved thresholding process method to try to overcome the disadvantages by both hard-thresholding and soft-thresholding methods.

Keywords- Phase noise filtering, SAR interferometry, Wavelet packets transform

I. INTRODUCTION

The technique of interferometric SAR has been a feasible means of deriving high-resolution DEM and surface deformation caused by earthquake, volcano, subsistence and landslide. However, the InSAR process is often interdicted by the interferometric phase noise. Because the information of the interferometric phase is the key factor for the whole process of InSAR, the phase noise suppression or filtering must be executed before phase unwrapping. There are mainly four sources of noise in SAR interferometry: (1) Thermal noise caused by radar system, (2) Decorrelation noise of InSAR due to spatial and temporal baseline, (3) Processing noise introduced in the processing chain, and (4) Noise due to atmosphere propagation delay which is mainly contributed by stochastic water vapor. Among them, the deterministic noise, such as spatial baseline decorrelation, could be reduced by spectrum pre-filter in range and azimuth direction. The noise introduced by other unknown or stochastic sources are the main sources that affect the accuracy of the interferometric phase. In this paper, attention is concentrated on introducing a novel method of using adaptive optimized wavelet packets transform in complex domain to decrease phase noise in interferogram.

This new technique is based on the Wavelet Packets Transform. The algorithm adapts to the quantity of noise, executing filtering process in higher coherence areas, and basically avoiding the introducing artifacts or false information in low coherence areas.

2. NOISE MODLE

As mentioned in [3], the interferometric phase follows an additive noise model, which can be expressed as:

$$\phi_z = \phi_x + \upsilon \qquad (1)$$

where ϕ_z represents the result of measured phase, ϕ_x is the 'true' phase without noise, and υ is the noise. According to trigonometric relations and Fourier transform, the real and imaginary parts of the measured phase ϕ_z are encoded in the unit circle:

Proc. 2005 Dragon Symposium "Mid-Term Results", Santorini, Greece
27 June – 1 July 2005 (ESA SP-611, January 2006)

$$e^{j\phi_z} = \cos(\phi_z) + j\sin(\phi_z) \tag{2}$$

C. Lopez et al. [1] proved that the noise models for the complex phase signals can be expressed as:

$$\cos(\phi_z) = N_c \cos(\phi_x) + \upsilon_c \tag{3}$$

$$\sin(\phi_z) = N_c \sin(\phi_x) + \upsilon_s \tag{4}$$

The merits of reducing the interferometric phase noise in complex domain is both decreasing random noise and keeping the phase jumps that represent useful information. For the purpose of keeping the phase information, wavelet transform is executed in complex domain. The reason is that the energy of the useful signals appears concentrated in the wavelet domain, whereas the random noise is not affected during the course of wavelet transform. The noise model in wavelet domain can be written as: [1]

$$C_w = DWT\{\cos(\phi_z)\} + j \cdot DWT\{\sin(\phi_z)\} \tag{5}$$

$$DWT_{2D}\{\cos(\phi_z)\} = 2^i N_c^w \cos(\phi_x^\omega) + \upsilon_c^\omega \tag{6}$$

$$DWT_{2D}\{\sin(\phi_z)\} = 2^i N_c^w \sin(\phi_x^\omega) + \upsilon_s^\omega \tag{7}$$

The complex wavelet coefficients C_w is divided into the real and imaginary parts and decomposed in different scales. It can be proved that the amplitude of C_w is an important reference to separate signal and noise. That is, the characteristics of a coefficient, signal or noise, can be decided by checking the amplitude of C_w.

3. NOISE FILTERING

The noise filtering is carried out within the wavelet domain. The phase information is contained in the relation between the real and the imaginary parts of the signal. In order to maintain this phase information, both the real and the imaginary parts have to be processed for the same times in the transformed domain. It is known that wavelets transform is a special case of wavelet packets transform. The former only execute decomposing in low frequency bands. Thus using wavelet transform can not avoid losing some high frequency information during the transforming. Wavelet packets transform behaves better in analyzing and detecting detail information within high-frequency bands. But complete wavelet packets transform is unfeasible in filtering interferometric noise. In fact, not every wavelet decomposition band contains useful phase signals. There generally exist some bands where noise information is dominant. Detecting detail information in these bands can only obtain false information. So it is necessary to analyze the information in these bands, and to establish a wavelet packets decomposition scheme.

So, we put forward a new method of phase noise filtering based on adaptive optimized wavelet packets transform. It primarily includes three steps: (1) Generating the optimized wavelet packets tree. (2) Filtering by using thresholding processing of the complex wavelet coefficients generated by the wavelet packets decomposition. (3) Reconstructing the filtered phase image.

Firstly, we use Lp-norm to generate wavelet packets tree. After each step of wavelet decomposition, four sub-bands are generated. The formula (8) can be used to compute E values of the amplitude of C_w for each of four sub-bands.

$$E(X) = \frac{1}{MN}\sum_{i=1}^{M}\sum_{j=1}^{N}|x_{ij}| \tag{8}$$

Then compare each E value with the maximum among them. If the ratio is larger than C_L, decomposition would be executed further in the corresponding sub-band. Otherwise, decomposition stops there. The value C_L is a parameter related to the average coherence of phase images. The maximal depth of decomposition is limited to 3. Following this scheme, a wavelet packets tree is generated from an interferogram.

Secondly, we choose value λ as filter threshold and t as filter threshold buffer to execute thresholding process on complex wavelet coefficients. The formula can be expressed as:

$$TH\left(R_w + iI_w\right) = \begin{cases} R_w + iI_w & E \geq \lambda \\ \sqrt{\frac{E-t}{\lambda - t}}R_w + i\sqrt{\frac{E-t}{\lambda - t}}I_w & t \leq E < \lambda \\ 0 & E < t \end{cases} \tag{9}$$

Where $\lambda > t > 0$, $E = \sqrt{(R_w)^2 + (I_w)^2}$ R_w represents the real part of the complex wavelet coefficients, and I_w represents the imaginary part. The method does not change the coefficients above threshold λ, and sets the coefficients below threshold buffer t zeroes. The coefficients values between λ and t are decreased smoothly to zero. Its purpose is to keep signal phase unvariable, to decrease noise phase, and to avoid producing fake stripes artificially.

Finally, the coefficients after filter thresholding process have been used to reconstruct the phase image back to original resolution and dimension, and the filtering result has been obtained.

4. RESULTS

We applied the proposed algorithm to simulated and real interferograms to test its performance.

First, we use a simulated pyramid interferograms fully covered with controlled noise under different coherence level from 0.1 to 0.9 respectively. Figure1 is the quantitative comparing result, from which, one can find that, after filtering, SNR (Signal Noise Ratio) is improved evidently and MSE (Mean Square-root of Error) is reduced clearly when noise coherence is larger than 0.3. That means the quality of filtered result is affected obviously by the inteferogram coherence.

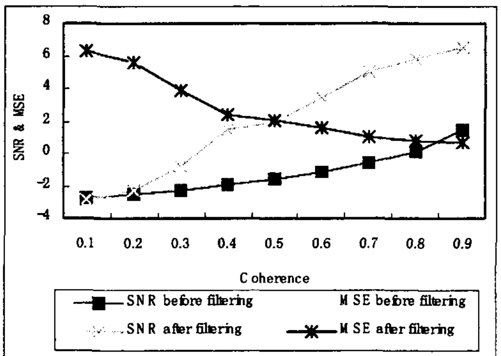

Fig.1. SNR and MSE with coherence before and after filtering

Second, a simulated pyramid phase image, adding 9 blocks of phase noise with different coherence, from 0.1 on the top left to 0.9 on the bottom right, has been used. In Fig.2, phase jump and filtered interferogram images with different filtering methods have been presented. One can notice that hard-thresholding filtering which abruptly set all coefficients below the threshold to zero that a sharp discontinuity will occur in filtered wavelet domain, obviously it could not take balance between filtering and keep information; soft-thresholding filtering improved hard-thresholding by subtracting the threshold from the coefficients that could reduce discontinuity in phase jump images, however, for different noisy level, a uniform threshold could not effectively remove noise. Adaptive wavelet packets filtering by taking transit interval, in which the coefficient is gradually decreased to zero, and integrate the merits of hard-thresholding and soft-thresholding, could effectively reduce noise while keeping normal phase jumps.

Finally, a real ERS interferometric phase has been filtered with different types of filtering methods, including multilook filtering (Fig.3), wavelet soft-thresholding filtering (Fig.4), pivot median filtering (Fig.5), adaptive power spectrum filtering (Fig.6), and adaptive wavelet packets filtering (Fig.7). As a result, the last one has the best filtering effect. By direct visual checking, the result from adpative power spectrum filtering seems the clearest one. But some important topographic detail information has been changed after frequency domain filtering, such as the area framed by red rectangle. In contrast, adaptive wavelet packets filtering method maintains the detail phase information very well.

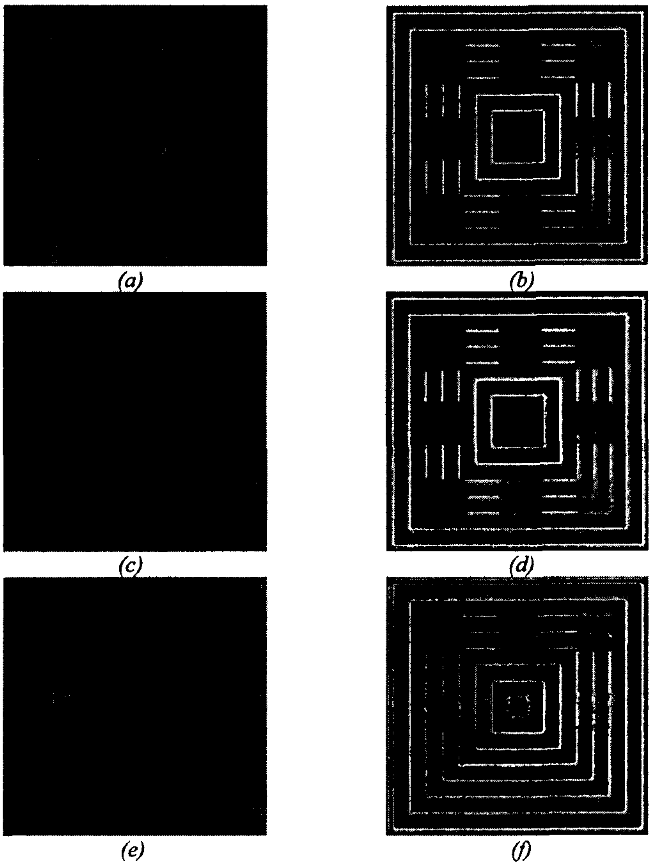

Fig. 2. Comparison of phase jump images and interferograms by different wavelet filtering methods,
(a), (c), (e) are phase jump images; (b), (d), (f) are interferograms
(a), (b) by hard-thresholding wavelet filtering;
(c), (d) by soft-thresholding wavelet filtering
(e), (f) by adaptive wavelet packets filtering

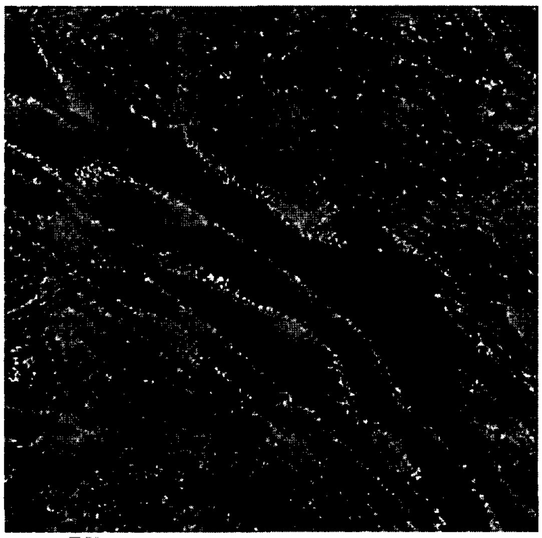

Fig.3. Multilooked noisy interferogram

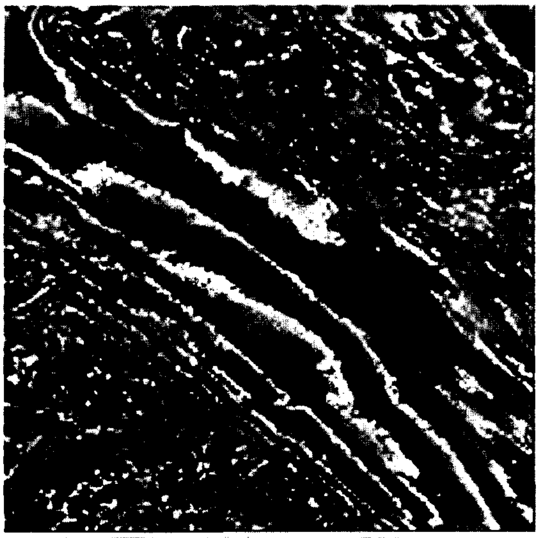

Fig.4. Soft-thresholding wavelet filtering

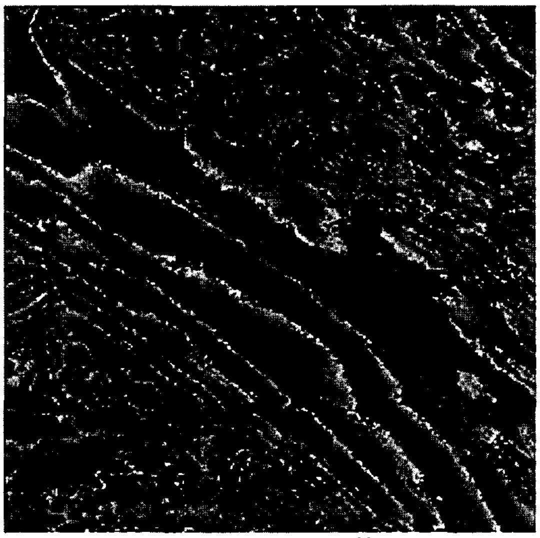

Fig.5. Pivoting median filtering

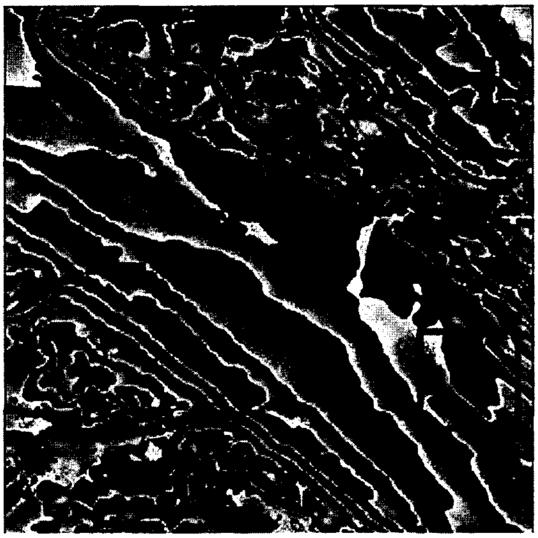

Fig.6. Adaptive power spectrum filtering

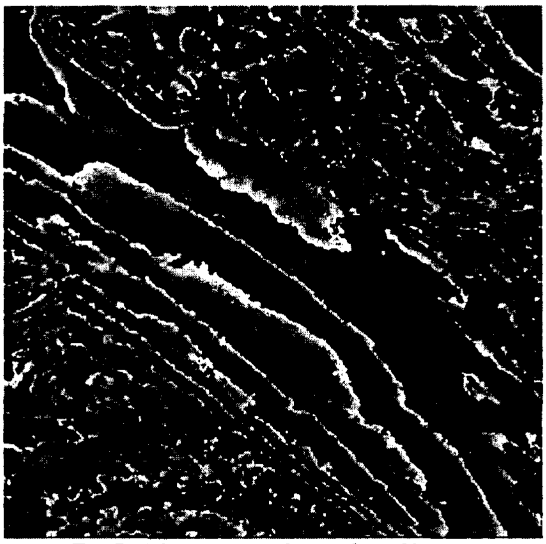

Fig.7. Adaptive wavelet packets filtering

5. CONCLUSIONS

A novel method to filter noise in SAR interferograms has been presented. Reported results show the effectiveness of this approach in both sides of noise reduction and keeping detail information. This method could almost fully remove phase noise in high coherence area and partially in moderate coherence area without introducing artifacts or false fringe, but for low coherence area, has no effect.

6. ACKNOWLEDGEMENT

The authors are grateful to National Remote Sensing Center of China and ESA for their support via Dragon Project 2558. This work is sponsored by 863 high technology program of China (2005AA132030XZ05).

REFERENCES

1.Carlos Lopez-Martinez, Xavier Fabregas. Modeling and Reduction of SAR Interferometric Phase Noise in the Wavelet Domain, *IEEE Trans. Geoscience and Remote Sensing*, VOL.40, No.12, pp. 2553-2566, Dec 2002.

2.Yuan Yunneng, Hu Qingdong, Mao Shiyi. Denoising Methods In Interferometric SAR Images Processing Chinese Journal of Aeronautics, VOL. 12, No.2, pp. 87-92, May 1999.

3. Lee, J. S., K. P. Papathanassiou, T. L. Ainsworth, M. H. Grunes, and A. Reigber, A New Technique for Noise Filtering of SAR Interferometric Phase Images, IEEE Trans. Geosci. Remote Sensing, vol. 36, pp. 1456–1465, Sept. 1998.

The work of this paper has been sponsored by the 863 high technology program of China (2005AA132030XZ05) and ESA-NRSCC Dragon Project 2558.

Monitoring Seismic Activity
(id. 2577)

MODELING CO-SEISMIC DEFORMATION OF THE MANI (NOV 8, 1997) EARTHQUAKE (TIBET) BY INSAR DATA AND LINEAR ELASTIC MODEL

Jianbao Sun[(1)], Fang Liang[(2)], Xiwei Xu[(3)], Zhengkang Shen[(3)]

[(1)] *Beijing Normal University, Beijing 9803#, 100029 Beijing, China, suninsar@yahoo.com*
[(2)] *Beijing Earthquake Administration, 100081 Beijing, China*
[(3)] *Institute of Geology, China Earthquake Administration, Beijing 9803#, 100029 Beijing, China*

ABSTRACT

The Mani Earthquake happened on Nov 8,1997. Peltzer et.al(Science, 1999) inferred the non-linear elastic deformation mechanism of the event by ERS radar interferometry. We revisited this event by radar interferometry and linear elastic modeling. By analyzing radar interferogram and field observation we give the segment characteristics of the seismic fault. By using linear elastic model and INSAR data, we use a Sequential Quadratic optimization (SQP) method to inverse the source parameters of the earthquake. The inversion gives possible explanation of the earthquake with linear elastic model and more complicated fault geometry.

INTRODUCTION

The Mani earthquake (Mw7.6) happened on Nov 8,1997 in North Tibet. Another large earthquake, the Kokoxili event (Nov14, 2001, Mw7.8) also happened on the same fault. Because of the hard natural conditions of the area, there are no detailed field investigations for the Mani earthquake before. Peltzer et.al [1] utilized ERS radar interferometry to infer the non-linear elastic deformation mechanism of the earth crust. In his model, the fault was simplified as trapezoidal shape in geometry with pure strike-slip motion and the dip angle was fixed to 90°.

But non-linear elastic is not a usual case for co-seismic deformation of earthquakes. In this event we try to retrieve the fault parameters with more general elastic models. Besides ERS INSAR data for the event we also constrain the fault model with field investigation. According to our fieldwork, the fault is not a pure vertical system, its dip angle vary along the fault slightly. By analyzing correlation map of co-seismic deformation, a clear curve show rupture zone of the earthquake where strong ground motion lead to de-correlation in the map. In all, the fault is not a straight line and it should be composed of a few short segments. In addition, the fault called East Kunlun fault is almost a pure strike-slip fault. But even in this kind of fault, there also exists possible dip slip in some segment because of the interaction between neighbor fault segments.

INSAR data provide an effective way to constrain this complicated system because of its very dense spatial sampling on the ground. Even if only descending pass data available we still can retrieve the fault parameters effectively due to very high correlation in the whole interferogram in the arid and no vegetation covered area.

INSAR DATA AND PROCESSING

The ERS2 radar data is used in the processing. The data is from Track 305, Frame 2889 and Frame 2907. We have processed 2 pairs INSAR data that have different time interval. The first pair is the same as in [1]. This pair has good temporal baseline (105 days) and spatial baseline (105m). The time interval of the other pair is from April 16, 1996 to Dec 2, 1997. This pair has longer temporal baseline (595 days) and **normal baseline**. But even in this less hopefully pair it almost gives the same processing result without too much loss of correlation. The ideal natural conditions and stable attitude of ERS2 satellite in this period made these measurements possible.

Level 0 SAR data were used to process into interferograms using the JPL/Caltech INSAR package ROI_ PAC [2] with SRTM 90m DEM data [3] to remove topographic phase and DELFT precise orbit data [4] to replace the orbit data in the RAW data header.

The most important and most difficult step in interferometry is the phase unwrapping. The traditional branch cut method leave too many holes, which is not unwrapped because of low correlation, also some phase jump in some area. In our

Proc. 2005 Dragon Symposium "Mid-Term Results", Santorini, Greece
27 June – 1 July 2005 (ESA SP-611, January 2006)

processing, we use the SNAPHU software as a global optimization method to minimize the phase discontinuity and interpolate the gaps in the interferogram. Because of high correlation, this interpolation should be very reliable because only small gaps exist in the interferogram. An obvious problem is the abrupt phase jump across the fault rupture. The global optimization code will automatically minimize the phase jump and make the phase continuous across the fault. This leads to big problem in phase unwrapping. Out solution is separating the interferogram along the fault rupture into 2 parts and unwrapping the complex data separately. After phase unwrapping, the quadratic baseline correction is applied to remove residue orbit phase. We show here the results of the longer temporal baseline pair.

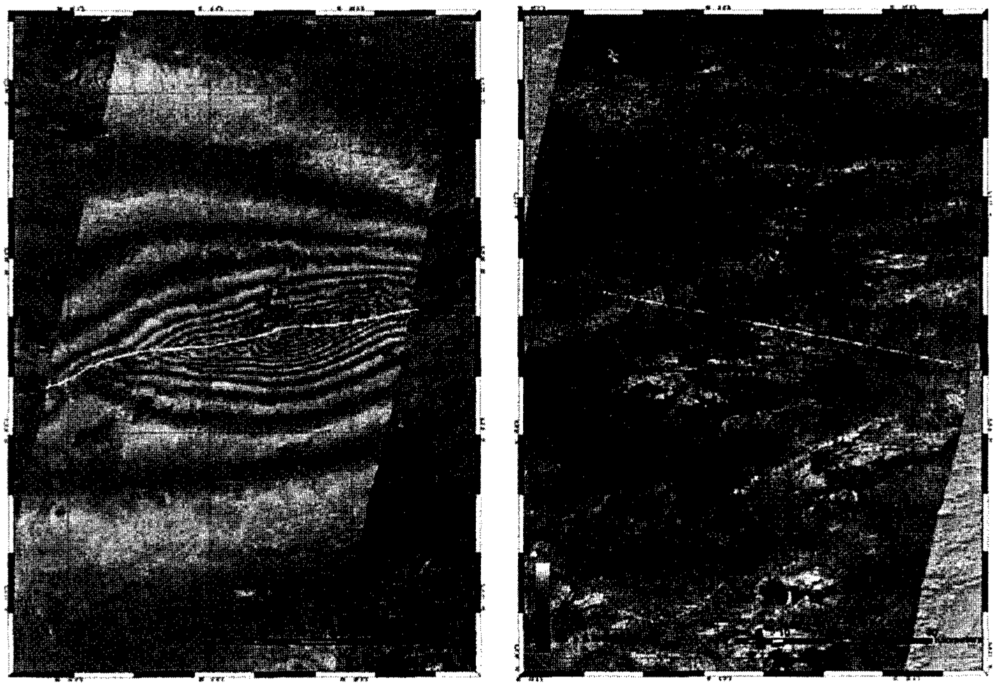

Fig.1. co-seismic interferogram in 10 cm cycles and the correlation map

The 10cm interferogram show continuous fringes in the 2 sides of the fault zone, but phase jump across the yellow fault line. South of the fault moves to the east and north of the fault moves to the west. This is consistent with the left-lateral strike-slip fault activity. In the middle of correlation map there exists a clear black line, which has low correlation because strong fault motion lead to de-correlation. In one pair of pre-seismic interferogram we can't see this clear line. This line gives us the information of the location of the seismic fault. At the same time, we can infer that the fault ruptured the whole upper crust.

INSAR DATA INVERSION

From field investigation we can separate the long fault at least into 3 parts, which is consistent with the interferogram fringe-varying pattern. Because the fieldwork did not cover the whole fault zone, we can't give the details at this time, but in all its geometry is complicated and can't be described as a vertical straight plane.

In the correlation map we can identify the exact fault location, but in the inversion we allow it to vary in some range so that we can evaluate the resolution of our inversion.

Before inversion the continuous deformation map have to be sampled with some strategy to reduce the size of the matrix in the inversion and avoid oscillation of the parameters. In this work we use the quad-tree decomposition method [5] to average the non-zero deformation area into points. After this operation only 566 points left for inversion. It works as a mean filter to suppress noises in the data.

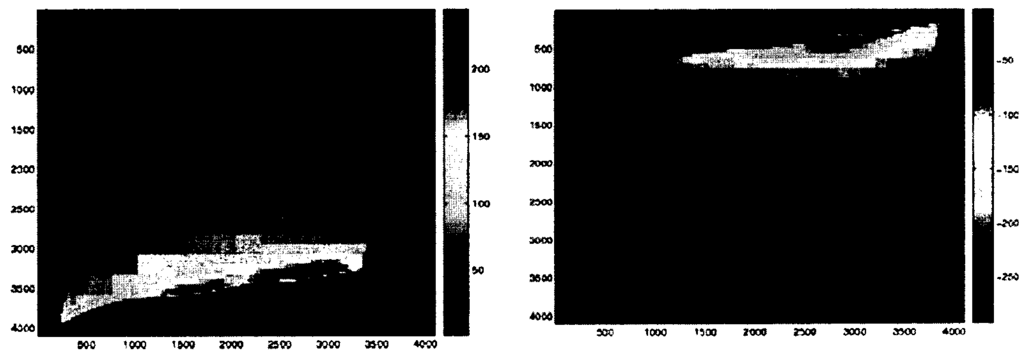

Fig.2. Quad-tree decomposition of the deformation data

We can see there are enough points near the fault zone and there are also some points in the far field.
In the modeling we use widely used Okada linear elastic model [6] to compute the predicated deformation or Greens' function.
In order to find the most suitable source parameters we minimize the WRSS (weighted residue sum of squares) value (Eq.1) between the INSAR range change d and the predicated deformation in LOS direction $\overline{d}$.

$$WRSS = (d - \overline{d})^T Cov^{-1}(d - \overline{d}) \tag{1}$$

The difference is weighted with the covariance of INSAR data that consider the general noise level of it, 1 or 2 cm in most cases. Only diagonal element is used because it's difficult to predicate the atmospheric noises of the data.

$$\overline{d} = G \bullet m \tag{2}$$

In Eq.2 we rewrite the predicated deformation as the point product of linear elastic Green's function and the fault model. In the Green's function we considered a phase constant and 2 gradients along the azimuth and range direction.
This inverse problem is actually a quadratic optimization problem. We use the so-called Sequential Quadratic optimization (SQP) method to search the best parameters of this problem as a constrained optimization process in an iterated way.

INVERSION RESULTS

After many times inversion starting with different initial faults model and 1cm noises level, we got 2 kinds of results. One is the 3-segment inversion; the other is 4-segment inversion. In all of the inversion, the fault location can vary in some degree to test its consistency with real fault location from INSAR correlation map.
In Tab.1, we can see that the WRSS for 4-segment inversion is decreased effectively to a reasonable value. The WRSS/N is slightly bigger than one.
In the 3-segment inversion (Fig.3) the residue can be as large as ± 0.2 m in some area, especially near the western part of the 3rd segment. This big error let us to consider the segmentation scheme of the fault. So we separated the 3rd segment into 2 parts to inverse. Now we can see very small residue left in the near field and also in the far field. The error can be as small as ± 0.08 m. This is a reasonable value for this big earthquake because its maximum ground motion as large as 7.4m. In addition, we can see the very good consistency between the inverted fault location and the real fault location from INSAR observation.

Table.1. Linear elastic inversion results using 3 and 4 segments

LENGTH (km)	WIDTH (km)	DIP ANGLE (deg)	STRIK (deg)	STRIKE SLIP (km)	DIP SLIP (km)
27.78	10.92	-98.3	75.04	5.27±0.068	0.75±0.031
31.94	18.33	-97.15	79.30	6.32±0.057	0.45±0.025
36.35	18.63	-88.17	79.75	3.34±0.075	-0.99±0.031
WRSS=4234.73 WRSS/(N-P)=7.60 WRSS/N=7.48 (3 segments inversion)					
27.88	9.81	-94.00	72.20	5.26±0.064	0.06±0.028
28.00	15.57	-96.46	81.83	5.39±0.063	0.10±0.027
18.35	21.08	-96.84	76.61	3.23±0.051	-1.23±0.018
21.98	15.77	-84.17	83.39	5.60±0.083	0.061±0.034
WRSS= 2522.07 WRSS/(N-P)= 4.54 WRSS/N= 4.46 (4 segments inversion)					

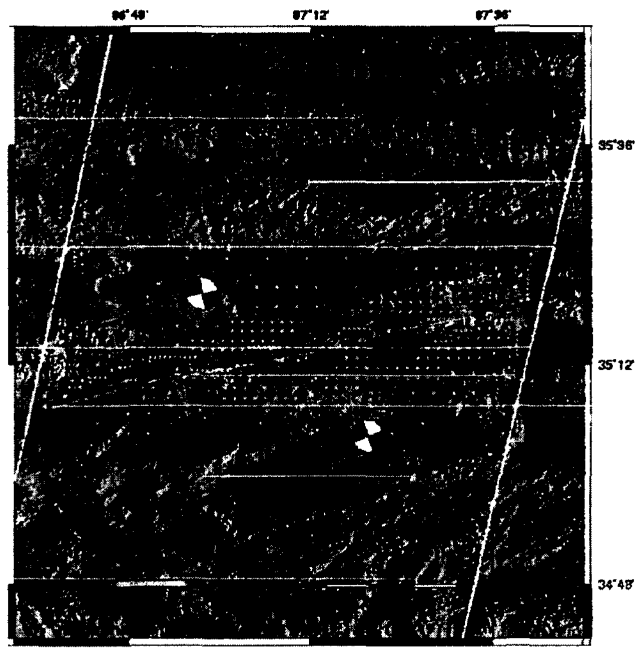

Fig.3. Three segment inversion result

DISCUSSION

From the linear elastic model and complicated fault geometry we used the SQP method to invert the INSAR deformation data. The inversion result show that the linear elastic model can be used to interpret the INSAR observation quite well because this inversion use more actual fault model which is consistent with our field observation and INSAR correlation map. The residue is small as in general case for INSAR inversion.

One more interesting thing is the big vertical motion of segment 3 from our inversion. In [1], Peltzer use a pure strike-slip model and there is no vertical motion in his non-linear model. This seems reasonable because of this big fault's long-term behavior, but we have another explanation. We argue that this should be a local vertical motion due to the interaction between segment 2 and segment 4 when their dip angles vary dramatically, also due to their special strike angels and geometry characteristics. This segment is important because it's just near the two maximum deformation point of the whole fault. The asymmetric deformation may be one of the initial thinking to infer the non-linear elastic deformation.
This vertical deformation could also be inferred from the profile of [1]. In Peltzer's profile the difference of 2 neighbor tracks (track 305 and track 33) could not be removed completely by normalizing the deformation data to ALD direction. The location of the non-zero deformation difference area is almost the same location of our segment 3 of the four-segment inversion. According to our preliminary evaluation from imaging geometry of the 2 tracks the vertical motion could be as large as 1.5 meter at least.

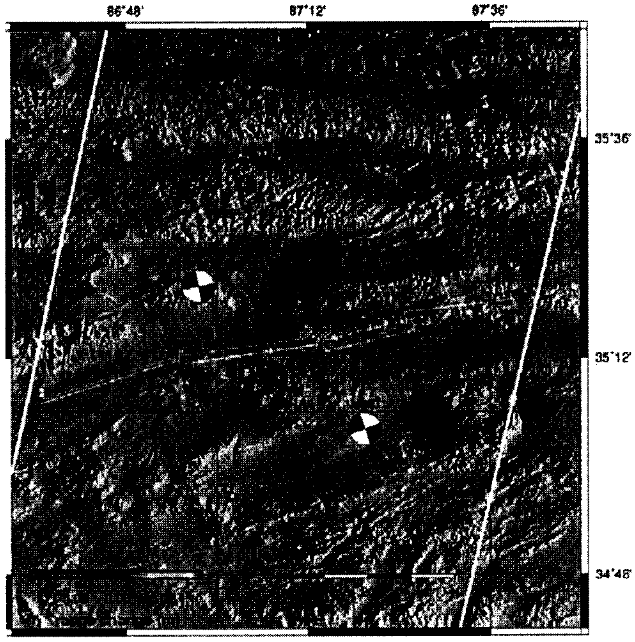

Fig.4. Four segment inversion result

REFERENCES

[1] Peltzer G., Frederic Crampe and Geoffrey King, Evidence of Nonlinear Elasticity of the Crust from the Mw7.6 Manyi(Tibet) Earthquake, *Science*, Vol. 286, October 1999, pp272-276
[2] Rosen, P., S. Hensley, and G. Peltzer, Updated Repeat Orbit Interferometry Package Released, *EOS Trans*. AGU, 85 (5), 2004.
[3] Farr, T. G., and M. Kobrick, Shuttle Radar Topography Mission produces a wealth of data, *EOS Trans*. AGU, 81 (48), 583–585, 2000.
[4] Scharroo, R., & Visser, P. 1998. Precise orbit determination and gravity field improvement for the ERS satellites. *J. Geophys. Res.*, 103(C4), 8,113–8,127.
[5] Sigurjon J., Modelling volcano and earthquake deformation from satellite radar interferomety observations. *PhD Thesis*. Stanford University.2002
[6]Okada Y, Surface deformation due to shear and tensile faults in a half-space, *Bull. Seismological Society of America*, 1985, 75: 1135-1154

ACKNOWLEDGEMENTS

This work supported by NSFC (No. 40474037) and National High Technology Research and Development Program of China (863 Program) (No.2005AA132031XZ06). Prof. Roland Burgmann at UC Berkeley gave help for the data inversion. All of the data used in this work is copyright of ESA provided to the PI of Dragon Project 2577. The GMT software was used to produce Fig3 and Fig4.

Terrain Measurement
(id. 2567)

VALIDATION OF THE RESULT FROM PERMANENT SCATTERER INSAR IN SHANGHAI

Deren Li, Mingsheng Liao, Yan Wang , Lijun Lu
State Key Laboratory for Information Engineering in Surveying, Mapping and Remote Sensing, Wuhan University Luoyu Road 129, Wuhan, P.R.China, 430079, E-mail: liao@whu.edu.cn
Zheng Fang, Zixin We, Hanmei Wang, Lijun Yang, Ying Liu
Shanghai Institude of Geological Survey, Shanghai, China, 200072
Fabio Rocca
Dipartimento di Elettronica e Informazione Politecnico di Milano, Milano, Italy
Alessandro Ferretti
Tele-Rilevamento Europa, Italy.

Abstract: This paper discusses the validation of the data sets of Permanent Scatterer (PS) technique. The test area is chosen in the main town of Shanghai. Using 26 scenes of ERS-1/2 images within 1993 to 2000, more than 22,000 Permanent Scatterers (PSs), data sets of PS technique, are derived. Because of the linear model of them in time series, the main points of this validation is their spatial distribution and accuracy of subsidence, which include both the quantifiable velocity field and the surface characters of some typical PSs on the earth. Field survey presents the location and surface characters of PSs. The comparison between PSs and optical leveling is made by two interpolation methods, nearest neighbor and kriging interpolation. High accuracy of PS's land subsidence of about 2mm is obtained in this experiment.

Key words: Permanent Scatterers, Validation, InSAR, Optical Leveling, Nearest Neighbor, Kriging interpolation

1 INTRODUCTION

Long term monitoring is very important to resist the geological disasters. Permanent Scatterer(PS)[1, 2], the extended technique of Differential InSAR (D-InSAR), initiated by A. Ferretti *et al*, Dipartimento di Elettronica e Informazione Politecnico di Milano (POLIMI), Italy, could overcome both temporal decorrelation and atmospheric heterogeneities, which limited the application of tranditional Differential In-SAR in monitoring long-term deformation. The extended technique may improve the accuracy in subsidence monitoring from centimeter to millimeter.

Table 1 Land subsidence History of Shanghai.[3]

Period	Stage	Average subsidence quantity (mm/y)	Main causes
1921-1965 The land subsidence	1921-1948 development	-24	Underground water pumped
	1949-1956 acceleration	-40	Underground water over-pumped
	1957-1965 serious	-87 (max.: 110)	
1966 – 2000 Control subsidence	1966-1971 rebound	+3	Reduced pumping and artificial intake of water
	1972-1989 slightly subsidence	-3.5	Reasonable adjusted the quality of water pump
	1990- 2000 accretion	-16	Increase the quantity of water pump & municipal engineering constructions

*with the quality of subsidence , "+" means uplift and "–" means subsidence.

Proc. 2005 Dragon Symposium "Mid-Term Results", Santorini, Greece
27 June – 1 July 2005 (ESA SP-611, January 2006)

Shanghai, as one of the important city of China, suffering land subsidence can back to 1921, and it has a successful history to research and control of this disaster. The simple history of subsidence in Shanghai has been show in the Table 1. "Up to now the land subsidence discovered by level measure in 1921 is 80mm. the average accumulative land subsidence of the central town is 1.9m. The loss of ground elevation in urban area is nearly 2m on average; the biggest loss reached to 3.0m."[3]

From 1990 to 2000, the subsidence is with the average velocity of 16mm/y and has a wild range of the whole city in Shanghai, as fig. 1 shows.

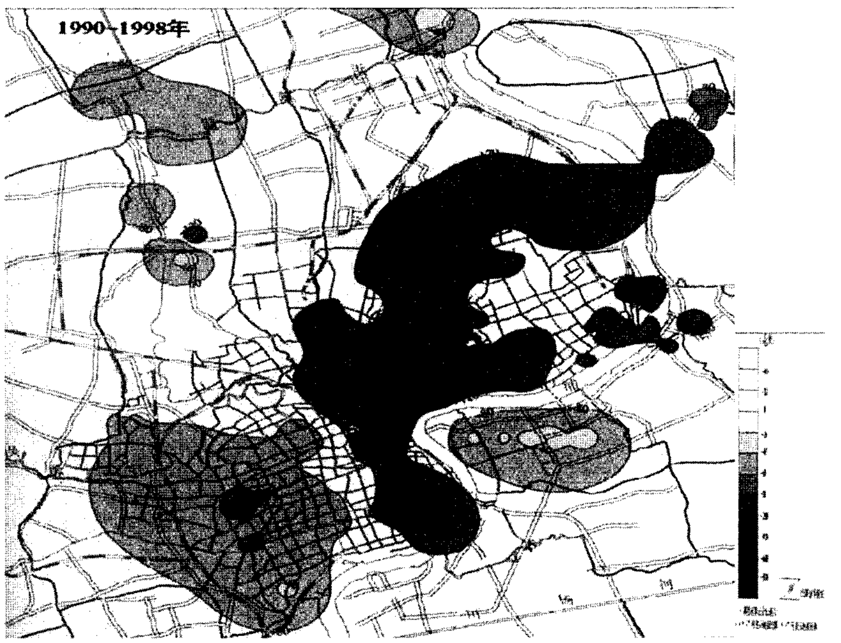

Fig.1. Land Subsidence in Shanghai from 1990 to 1998[3]

ERS-1 and ERS-2 have created historic archive since 1991 and Envisat/ASAR has acquired images since 2003. As the accumulation of SAR images, it is possible to use PS to monitoring long-term deformation with higher spatial and temporal resolution than those of traditional techniques, such as GPS and Optical Leveling etc. It is perspective of the potential application of PS InSAR technique in detection of deformation. But more experiment in different test areas and various fields should be carried out and its data sets should be validated.

This paper presents the validation of the data sets of permanent scatterers(PSs) in Shanghai test site. Because of the linear model in time series, the main point is the spatial distribution and accuracy of subsidence of PSs. The evaluation includes field survey and comparison between the PSs and optical leveling in the accuracy. Field survey validated the locations and the natural characteristics of PSs. The comparison between the subsidence distributions from PSs and optical leveling is made by two interpolation methods, nearest neighbor and kriging interpolation. It not only assesses the accuracy of the PSs in the value of the velocity field but also provides the quantity of some typical PSs on the earth.

The DRAGON Programme, a co-operational framework between China and ESA, prompts this research. The State Key

Lab. for Info. Eng. in Surveying, Mapping and Remote Sensing (LIESMARS), Wuhan University, organizes the field survey and the validation. Dipartimento di Elettronica e Informazione Politecnico di Milano (POLIMI) / Tele-Rilevamento Europa, Italy completed the data processing with PS InSAR technique. The Shanghai Institute of Geological Survey (SIGS) provided the geological interpretation and local logistics for field survey. Data analysis and evaluation of the results of PSs was made by LIESMARS.

The paper has 6 sections. Section 1 describes the background of the project. Section 2 showes the SAR data and the PS points derived from them. Section 3 shows the data sets of field survey, which presents the location and surface characters of PSs. Section 4 uses two methods to validate the value of the subsidence from PSs. Section 5 and 6 are conclusion and acknowledgement.

2 Data Description

The PS analysis shows areas of strong subsidence in Shanghai as clearly visible in the average velocity map of Fig. 2 [4]. The basic information of 26 ERS 1/2 images of Shanghai is shown in the table 2. The image with red color is the master image.

There are 22,139 PSs distributing on the about 1,000km^2 area. The density of derived PSs is about 22 points/ km^2. Fig. 2 shows the subsidence distribution. The small pink circle is the reference point. The pink rectangle is the test site chosen for the filed of survey, which includes Yanpu block and part of the Huangpu districts of Shanghai.

Table 2 Basic description of SAR images[4]

Sensor	Date	Bn	Bt
ERS1	19930417	474.92	-2439.0
ERS1	19930731	377.29	-2334.0
ERS1	19950619	-235.69	-1646.0
ERS1	19951002	430.82	-1541.0
ERS1	19951211	559.97	-1471.0
ERS1	19960115	-428.12	-1436.0
ERS2	19960116	-919.52	-1435.0
ERS2	19960220	781.46	-1400.0
ERS1	19960325	-829.64	-1366.0
ERS2	19960326	-928.87	-1365.0
ERS1	19960603	-600.72	-1296.0
ERS2	19960604	-682.94	-1295.0
ERS2	19971111	-353.96	-770.0
ERS2	19980224	-689.71	-665.0
ERS2	19980331	-120.41	-630.0
ERS2	19980505	387.19	-595.0
ERS2	19990420	504.88	-245.0
ERS2	19990525	245.13	-210.0
ERS2	19990629	290.08	-175.0
ERS2	19991116	46.72	-35.0
ERS2	19991221	0.00	0.0
ERS2	20000125	61.68	35.0
ERS2	20000229	-430.69	70.0
ERS2	20000509	738.58	140.0
ERS2	20000613	-75.89	175.0
ERS2	20000926	503.11	280.0

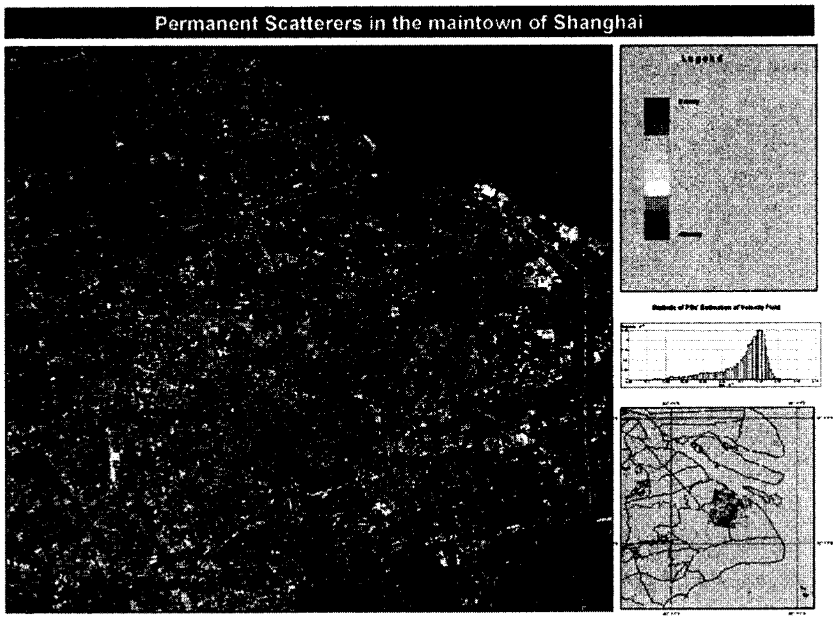

Fig. 2 Distribution map of subsidence velocity with PSs[4].

3 Field Survey

Two goals of field survey are considered, and they are (1) the accuracy of the location of the PSs, (2) the natural characteristics of them.

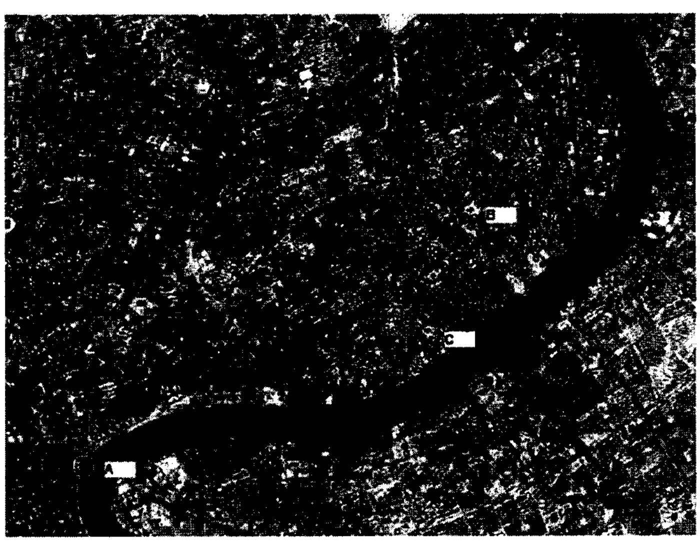

Fig.3. Test Area for Validation of PSs

Field survey collected data in ten benchmarks and their surrounding. We selected the benchmarks around which there are many PSs, i.e., within 100 meters. There is an obvious PS point located on the southwestern bank of the conjunction of Huangpu river and Wusong river, Hero's Monument (PS No. AU085, A area in figure 3). PSs may locate both on the surface or the side surface of building or structure as shown in B & C in fig. 3.

There are three points are shown as Table 3 this paper to show the surface characteristics of PSs. They are respectively, Hero's Monument, mental object on the roof and building. All of them have been built between 1990 and 2000.

Table 3 Three areas of survey field

Area	PS No.	Character of the Surface	Picture 1	Picture 2
A	AU085	Concrete		
B	AO579 AO583 AO584 AO589 AO592 AO596 AO605 AO611	Concrete and mental		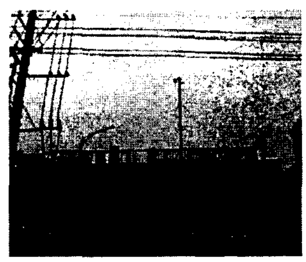
C	AQ909	Concrete and mental		

4 Data Comparison

Two interpolation methods are used to validate the accuracy of the deformation value of PSs, Nearest Neighbor and Kriging Interpolation as show in Table4. This table shows that the accuracy of PS InSAR is with small standard deviations less than 2mm. It should be satisfied for monitoring long term deformation.

Table 4 Subsidence velocity in benchmarks (optical leveling and PSs by NN and KI methods)

Benchmark No.	Optical Leveling(OL) (mm/y)	Nearest Neighbor(NN) (mm/y)	Difference between OL&NN (mm/y)	Kriging Interpolation(KI) (mm/y)	Difference between OL & KI (mm/y)
0-225	-11.63	-7.85	-3.78	-8.03083	-3.59917
0-193	-8.25	-5.36	-2.89	-5.8725	-2.3775
0-192	-13.38	-12.48	-0.9	-14.9567	1.5767
0-195	-11.63	-9.39	-2.24	-9.655	-1.975
0-240	-7.25	-5.62	-1.63	-5.925	-1.325
0-236A	-10.38	-7.61	-2.77	-7.26167	-3.11833
0-221	-14.75	-11.15	-3.6	-10.395	-4.355
0-222	-11.13	-5.82	-5.31	-10.3208	-0.8092
0-223	-11.38	-13.16	1.78	-11.0875	-0.2925
0-212A	-11	-9.02	-1.98	-7.89083	-3.10917
AVERAGE		-2.332		-1.938417	
STANDARD DEVIATION		1.904980606		1.772363931	

The tendency of the distribution of velocity values is shown in Fig. 4. There seems a systematic error between the different data sets. The value of PSs appears lower than that of optical leveling. This may be the error relatied with the selection of reference point. More detailed investigation should be conducted in the future.

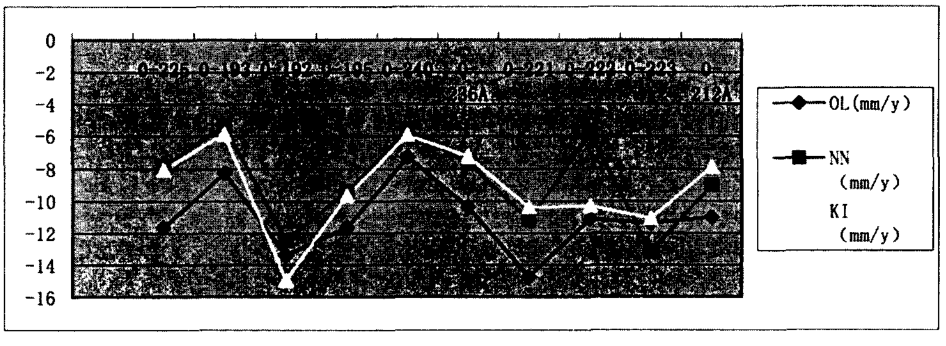

Fig.4. Map of Velocity Field in benchmarks between optical leveling and PSs by NN and KI methods

5 Discussions and Conclusions

The limitations of conventional InSAR could bereduced with PS technology if we can stack a number of SAR images. While it is applied in Shanghai test site, its capability is assessed in two main aspects. Most of the PSs are the reflectors with high backscatter, for example, concreted or mental objects. On the other hand, the stability of the backscateer should also be considered while apply the PS technology. In Shanghai area, the *dense* PSs are distributed in central urban area, but slight sparse in new developing area, such as Pudong district, where obvious change appeared from 1990s. In this case the SAR data collection is the key point for monitoring long-term deformation. It is important to collect more ASAR data in the next step of DRAGON Programme.

In this investigation on the validation of PS InSAR in Shanghai, comparison between PS distribution and subsidence map shows that the results from InSAR and leveling are quite consistent. And the comparison between velocity values of PSs and benchmarks shows that the errors from InSAR and leveling are quite small.

6 Acknowledgement

The work was supported by Nature Science Foundation of China (Contract No. 60472039) and the 863 High Technology Programme (Contract No. 2005AA132030XZ04). The authors wish to thank ESA for providing the SAR data through ESA-NRSCC Dragon Cooperation Programme (id:2567).

References

1. Alessandro Ferretti, Claudio Prati , Fabio Rocca, " Permanent scatterers in SAR interferometry," *IEEE Transactions on Geoscience and Remote Sensing*, vol. 39, pp. 8 - 20, 2001.
2. Carlo Colesanti , Alessandro Ferretti, F. Novali ,Claudio Prati , Fabio Rocca, "SAR monitoring of progressive and seasonal ground deformation using the permanent scatterers technique," *Geoscience and Remote Sensing, IEEE Transactions on*, vol. 41, pp. 1685 - 1701, 2003.
3. Zhang Agen, Luo Dingyi, Shen Xinguo, Lv Lianan, Chen Huawen, Wei Zixin, Yan Xuexin, Fang Zheng, Shi Yuqi, *Shanghai Geological Environment Atlas*, 1 ed. Beijing: Geological PUblishing House, 2002.
4. Fabiao Rocca, Using Permanent Scatterers to Measure Subsidence in Shanghai, the presentation on The Kick-off Symp. of Dragon Programme, Xiamen, 2004.

DEM RECONSTRUCTION USING SHORT BASELINE ERS-1/2 TANDEM DATA AND SRTM DEM

Mingsheng LIAO, Teng WANG, Lijun LU, Deren LI

State Key Laboratory for Information Engineering in Surveying, Mapping and Remote Sensing, Wuhan University, Luoyu Road 129, Wuhan, P.R.China, 430079, E-mail: liao@whu.edu.cn

ABSTRACT

Considering the geometry formula of synthetic aperture radar interferometry (InSAR), interferogram with short baseline is rarely used for Digital Elevation Model (DEM) generation. However, in some areas, high fringe frequency and geometry decorrelation caused by long baseline make phase unwrapping difficult. A new approach is presented in this paper to produce DEM in mountainous areas with a steep slope using interferogram with short baseline. Instead of ground control points (GCPs), an external DEM such as that from Shuttle Radar Topography Mission (SRTM) is used in this approach. Facilitated by SRTM DEM, systematic phase errors and unreliable height points are removed respectively. The application of this approach to an ERS Tandem interferogram with baseline of 16 m over the Three Gorges region in China shows that the resultant DEM agrees to a 1:50,000 DEM from National Center for Geomatics of China within about 50m.

INTRODUCTION

It is well known that the quality of InSAR DEM is affected by geometrical and temporal decorrelation especially for repeat-pass satellite mode [1]. Although the height errors caused by interferometric phase errors can be reduced when perpendicular baseline is long [2], the signal-to-noise ratio (SNR) of interferogram decreases along with the baseline increases. Moreover, the height change that leads to a 2π change in interferometric phase (height ambiguity) is inversely proportional to the length of perpendicular baseline. Therefore, in mountainous areas, steep terrain often causes phase aliasing in interferogram with long baseline, and the performance of phase unwrapping is very difficult.

Although short baseline can reduce the difficulties described above, phase errors would lead to huge errors in height and make the DEM unusable due to large inaccuracy. Furthermore, the distribution of phase errors may not be normal and it can be influenced by the uncertainty of orbital parameters and atmospheric phase screen (APS) difference of the master and slave images [3]. The systematic phase errors cause height trend in the generation of DEM from the InSAR data. In the case of short baseline, this height trend may be up to hundreds of meters. These shortcomings make interferogram with high coherence and short baseline be scarcely used for the DEM generation.

In this paper, a novel method is presented to produce DEM from unwrapped interferogram with short baseline. SRTM DEM facilitates the procedure because of its easy access. The usage of SRTM DEM in this method is for two purposes. One is to model the linear part of phase errors (trends) in radar's slant range space by linear regression analysis, and the other is to remove the unreliable height points before DEM reconstruction. An interferogram with short baseline (16 m) in mountainous areas is used to show the method's effectiveness to reduce phase errors. Finally, comparison of DEMs created by this method and obtained from the national geomatics center of China is given over the Three Gorges region of Yangtze River, China. The region is famous for steep slopes and rough terrain.

INTERFEROGRAMS WITH LONG AND SHORT BASELINE

The Three Gorges region of Yangtze River in China is chosen as our test area. Its mountains with steep slopes and vegetation-covered surface cause strongly geometry and temporal decorrelation. The following Fig.1 (a) – (d) represent

Proc. 2005 Dragon Symposium "Mid-Term Results", Santorini, Greece
27 June – 1 July 2005 (ESA SP-611, January 2006)

two pairs of ERS-1/2 tandem interferograms and coherence maps with different baselines. From the interferogram with long baseline (195m), the fringe frequency is higher and the coherence is lower, so it is very difficult to unwrap. On the other hand, a 1/4 scene of the interferogram with short baseline (16m) is successfully unwrapped using Flynn's minimum discontinuity method [4] for the DEM reconstruction. The 1345 x 1283 interferogram with 20 multi-looks (10 looks in azimuth and 2 looks in range) is shown in Fig. 2 (a). The unwrapped phase is shown in Fig 2(b).

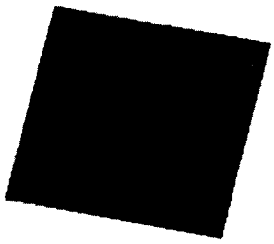

Fig. 1 (a) Interferogram with long baseline

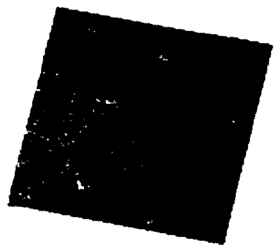

Fig. 1 (b) Coherence map of (a)

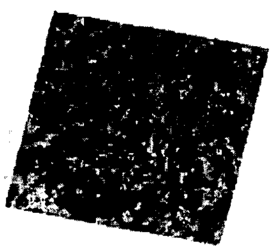

Fig. 1 (c) Interferogram with short baseline

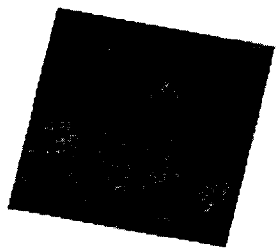

Fig. 1 (d) Coherence map of (c)

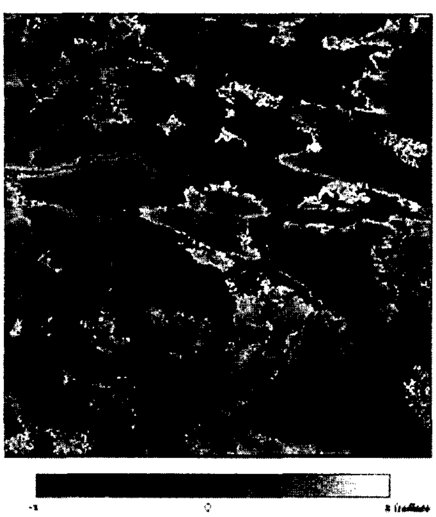

Fig. 2(a) 1/4 scene of Interferogram with short baseline

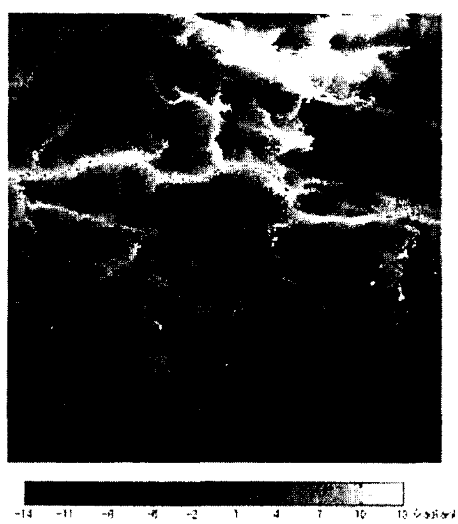

Fig. 2(b) Unwrapped phase map of (a) using Flynn's minimum discontinuity method

SRTM DEM data in test site

SRTM obtained elevation data on a near-global scale to generate the most complete high-resolution digital topographic database of Earth [5]. The expected horizontal and vertical accuracy are approximate 20m and 16m (linear error at 90%

confidence) for the final 1 arc-second data release of the U.S. [6]. In areas outside the U.S., only 3 arc-seconds data are available and the quality is poorer. Because of its single-pass dual-antenna radar system, we then assume that the errors of SRTM DEM fit a normal distribution of zero mean and constant standard deviation in our test area. Then the systemic errors of ERS-1/2 interferogram can be modeled from the phase difference between interferogram and SRTM DEM.

The SRTM DEM over the Three Gorges region is shown in Fig 3. The void pixels (i.e. having invalid elevations) are removed by a 3x3-moving window via (1), the removal procedure has been applied to the entire study area.

$$\frac{1}{\text{Number of positive height points}} \sum (\text{positive height points}) \tag{1}$$

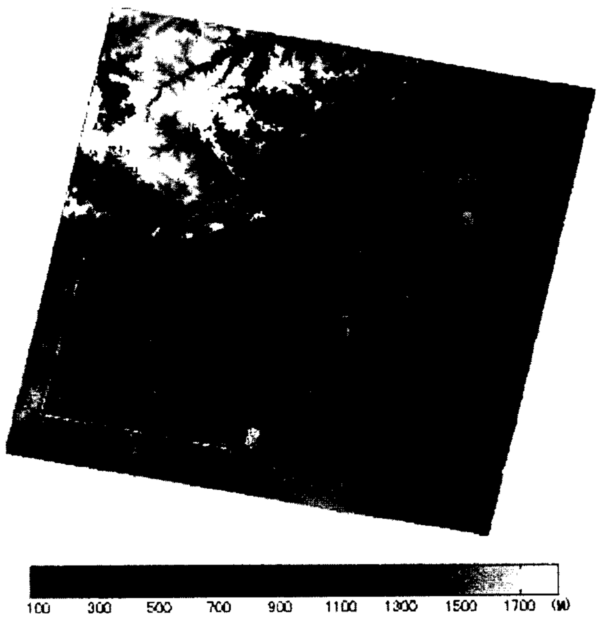

Fig. 3 SRTM DEM of the whole scene radar image. The white frame indicates the experiment region.

Phase trends removal

The unwrapped interferometric phase can be modeled after flatten earth step as:

$$\phi = c + l_1 \text{line} + l_2 \text{pixel} + \phi_z + E \tag{2}$$

Where c is a constant, l_1 and l_2 are slope of phase trends along the line (azimuth) and pixel (slant range) directions, ϕ_z is the phase difference between two sensors caused by height of target on ground, and E is the residue due to atmospheric effect and other phase errors caused by decorrelation and thermal noise. The purpose is to estimate the linear coefficients c, l_1 and l_2 by regression method. Phase derived from SRTM DEM is used for calculating ϕ_z.

Once the phase differences between interferogram and SRTM DEM are determined, the linear regression equations can be written as

$$\begin{bmatrix} line_1 & pixel_1 & 1 \\ \dots & \dots & \dots \\ line_n & pixel_n & 1 \end{bmatrix} \begin{bmatrix} l_1 \\ l_2 \\ c \end{bmatrix} = \begin{bmatrix} \Delta\phi_1 \\ \dots \\ \Delta\phi_n \end{bmatrix} \tag{3}$$

Where n is the number of pixels. c, l_1 and l_2 can be solved from (3) by least-square regression method.

Because the phase difference derived from pixels with low coherence may be far off from our model (2), only the pixels with coherence larger than 0.2 are selected for this calculation. The simulated phase trends are shown in Fig. 4. Because the range is about 8 radians, such a large range can potentially lead to heights with uncertainties of up to hundreds of meters in the case of such baseline.

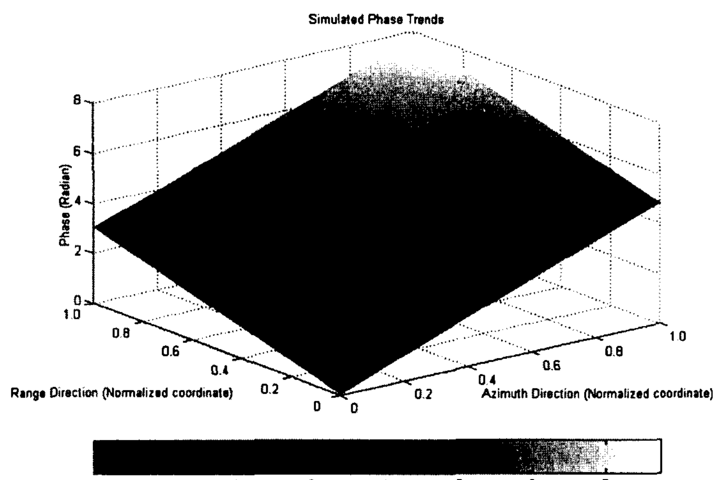

Fig. 4 Simulated phase trends

Unreliable height points filtering

After removing the phase trends, the unwrapped interferogram can be converted to height map. In the case of short baseline, there may be large uncertainties for some pixels due to phase noise and/or phase unwrapping, which will have a strongly impact on the quality of the final DEM product. Therefore, the pixels with uncertain height should be removed before converting the height map to final DEM.

Based on Chebyshev theorem, no matter what distribution of the errors fits, the probability that any error is within the interval of $\mu \pm 4\delta$ is at least 94%. (μ and δ are mean and standard deviation here.) Therefore, we set 4 times the SRTM height error as our threshold to remove unreliable pixels. The absolute height difference between InSAR height points and corresponding SRTM height is considered, only the points with smaller height difference than threshold are used to reconstruct DEM. The threshold for identifying unreliable height value is estimated from each pixel's location in SRTM DEM grid and error of grid node. The final DEM production is shown in Fig. 5.

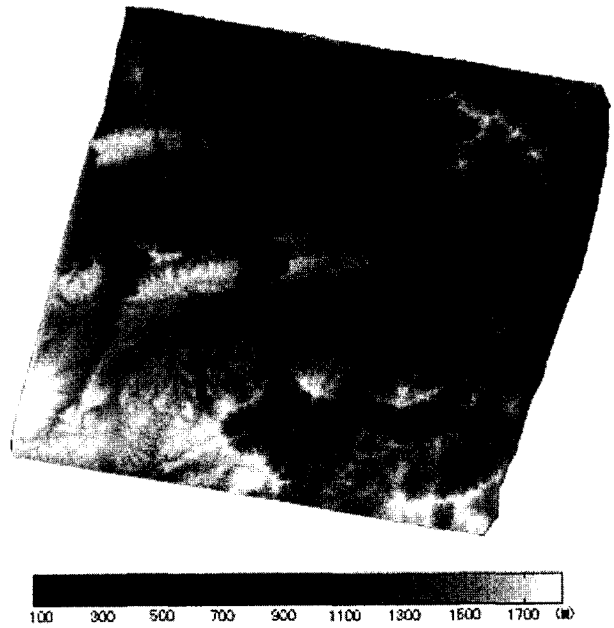

Fig. 5 DEM derived from InSAR height map after removing unreliable points.

Discussion

In order to assess the quality of the DEM derived using our approach, a 1:50,000 DEM over the Three Gorges (Fig 6) was used for inter-comparison. The 1:50,000 DEM was created by digitizing map in National Center for Geomatics of China, and the accuracy of grid nodes is claimed to be 11m in mountainous region.

Fig.7 is the difference map between InSAR DEM derived using our approach and the 1:50,000 DEM. The standard deviation is 56.6 m for the whole test area. It is clear that the errors mainly occur in the steep valley or radar shadow areas. Also, certain low frequency errors can be observed in the difference map. For example, the negative errors are apparent in the top and bottom, positive errors are along the Yangtze River in the middle. These phenomena may be caused by APS differences between master and slave images.

Conclusions

In this paper, an approach to generate DEM from short baseline ERS-1/2 data is presented. SRTM DEM is used for removing systematic phase errors and filtering unreliable height points. Considering the steep slopes and the short baseline, the standard deviation of errors is acceptable. Also, the model of phase trends can be used in D-InSAR processing.

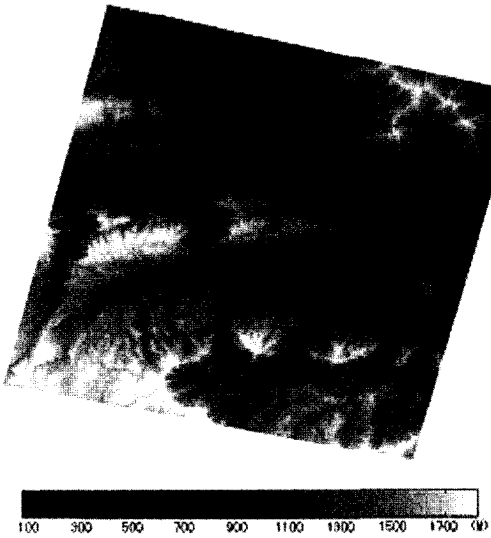

Fig.6 1:50,000 DEM over test area

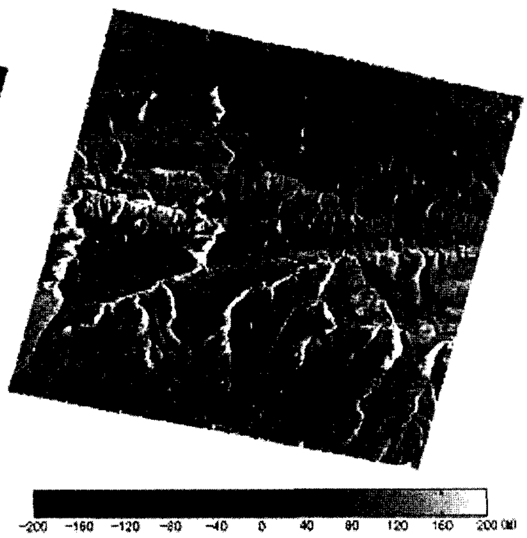

Fig. 7. The difference map of InSAR derived DEM and 1:50000 DEM

Acknowledgment

The work was supported by Nature Science Foundation of China (Contract No. 60472039) and the 863 High Technology Programme of China (Contract No. 2005AA132030XZ04). The authors wish to thank ESA for providing the SAR data through ESA-NRSCC Dragon Cooperation Programme (id2567) and Dr. Jie YANG for geo-processing the 1:50000DEM data.

References

1. Zebker, H.A., and Villasenor, J. Decorrelation in interferometric radar echoes. *IEEE Transactions on Geoscience and Remote Sensing*, Vol. 30, 950-959 1992.

2. Madsen, S.N., H.A. Zebker, and J.M. Martin, "Topographic Mapping Using Radar Interferometry: Processing Techniques", *IEEE Transactions on Geoscience and Remote Sensing*, Vol.31, No.1: 246-256 1993.

3. Goldstein, R. Atmospheric limitations to repeat-pass interferometry, *Geophys. Res. Lett.*, vol. 22, pp. 2517–2520 1995.

4. T. J. Flynn. "Two-dimension phase unwrapping with minimum weighted discontinuity," *Journal of the Optical Society of America A*, Vol. 14, No. 10. 10, pp. 2692-2701, October 1997.

5. Ramirez E. Shuttle Radar Topography Mission. The Mission to Map the World JPL website URL: http://www2.jpl.nasa.gov/srtm/ Jet Propulsion Laboratory California Institute of Technology, California (Site Last Updated: August 28, 2005).

6. Bridget Smith and David Sandwell. "Accuracy and resolution of shuttle radar topography mission data," *Geophysical Research Letters*, Vol. 30, No. 9, 1467, 2003.

MONITORING TIANJIN SUBSIDENCE WITH THE PERMANENT SCATTERERS TECHNIQUE

Dr. Daniele Perissin[1], Dr. Alessandro Parizzi[1], Prof. Claudio Prati[1] and Prof. Fabio Rocca[1]

[1] Politecnico di Milano, Via Ponzio 34/5, 20133 Milano, Italy

1. ABSTRACT

Many urban areas in China are affected by land subsidence. The Permanent Scatterers (PS) technique [1], [2] is a powerful tool for monitoring terrain motions by means of space-born radar data on a large number of coherent targets. Core idea of the PS technique is the exploitation of a high density of measure points (usually but not necessarily corresponding to man-made objects) in order to estimate and remove atmospheric artifacts that normally prevent a correct displacement analysis. Aim of this paper is the description of the results obtained by means of the PS technique over the area around Tianjin city in the Popular Republic of China, where a subsidence at the present time is active. Furthermore, the dispersion of acquisition parameters like normal baseline and Doppler centroid (DC) frequency has been used for characterizing the physical nature of PS's, thus providing the first basis for the identification of targets visible by different satellites [4], [5], [6].

2. INTRODUCTION

The area of P.R. of China situated between the capital Beijing and the Yellow Sea is known being affected by geological instability. The Tangshan earthquake of July 28, 1976 is one of the largest earthquakes in loss of life to hit the modern world. The epicenter of the earthquake was near the industrial city of Tangshan in Hebei, which housed around one million inhabitants. Seismic events are not the only problems affecting the ground stability of this area. With the rapid growth of the local economy, the ground subsidence caused by water withdrawal has begun to concern a lot of towns [3]. Tianjin City is one of the four greatest municipalities in China, with a very large population and an old history. In the 1960s due to the development of local industry and the consequent increase of inhabitants, water supply became a major issue. Under such conditions, the ground water was over-withdrawn causing a progressive subsidence that till now has reached up to 3 meters of displacement. According to local surveys, in the recent years the subsidence rate in Tianjin downtown is decreased to 10mm/year.

The present work has been carried out within the Dragon Project by Politecnico di Milano in order to evaluate the possibility of a ground subsidence control by means of space-born radar data over the area of Tianjin. To this aim, the recently developed PS technique [1], [2] has been adopted for processing the data. Main advantage of such a study is supplying a high density of measure points at very low costs exploiting archived SAR data.

3. PS ANALYSIS

The data available for monitoring the Tianjin subsidence have been acquired by the satellites ERS1 and ERS2 of the European Space Agency (ESA) in an 8 years time span, from 18/06/1992 to 25/06/2000. The data-set is formed by 23 images with normal baseline ranging from −1500 to 1000 m and Doppler centroid (DC) variations limited between −0.4 and 0.4 PRF (pulse repetition frequency) replicas with respect to the master acquisition acquired on 19/10/1997. The processed area is 3200x5000 pixels (range interpolation factor 4), equivalent to about 16x20 km^2. In Figure 1 the main parameters of the dataset are shown. In the lower part of the figure on the left, dots are plotted in correspondence of the acquisition date, highlighting lack of data in years 1994 and 1999. Moreover, only about between 1995 and 1996 images have been acquired regularly. As further shown, such a lack of data prevents from observing fast and non-linear motions.

Proc. 2005 Dragon Symposium "Mid-Term Results", Santorini, Greece
27 June – 1 July 2005 (ESA SP-611, January 2006)

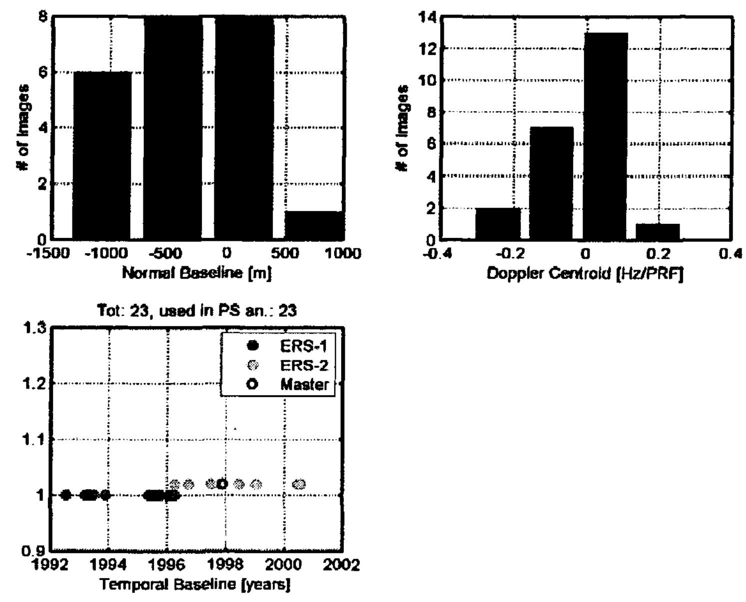

Fig. 1. Data-set parameters: normal baseline, Doppler centroid and acquisition date.

First step of the PS analysis is the selection of PS candidates (PSC) [1], [2]. To this aim the reflectivity map of the analyzed area, visible in Figure 2, is obtained as the incoherent time-average of the amplitudes of the radar images. Then local maxima are extracted and side lobes eliminated. For the selected points birth and death dates are estimated analyzing the amplitudes as a function of the acquisition time. Exploiting the acquisitions in the lifetime the amplitudes stability index is calculated and

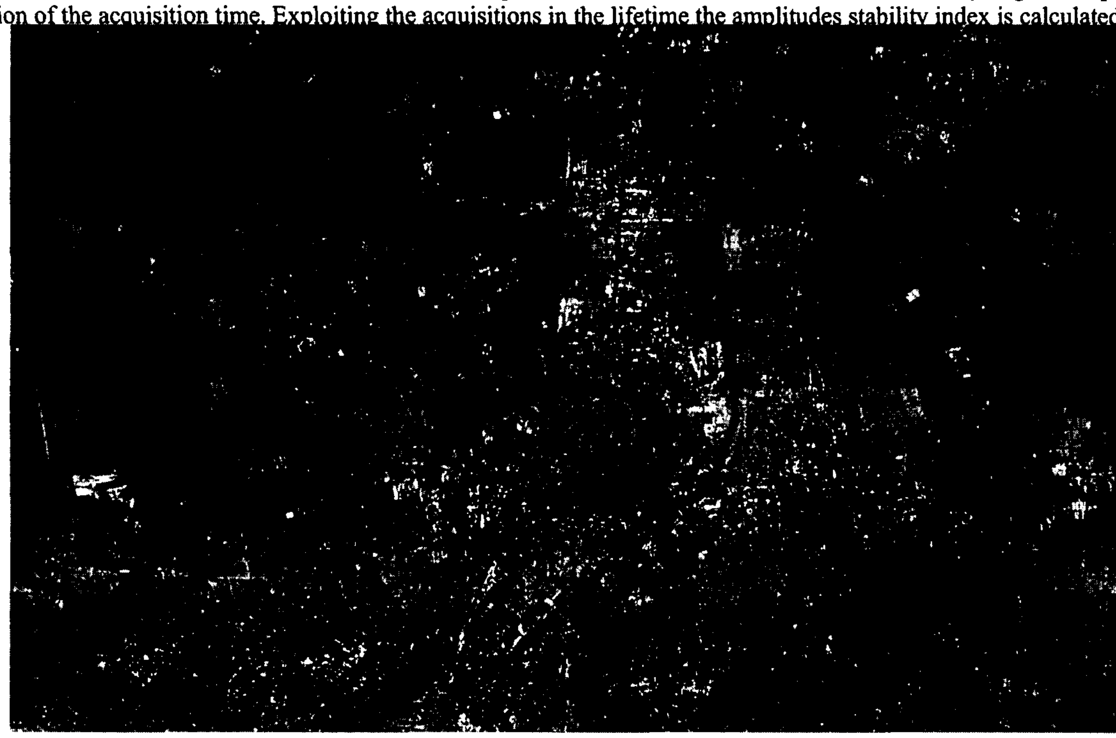

Fig. 2. Reflectivity map of the processed area.

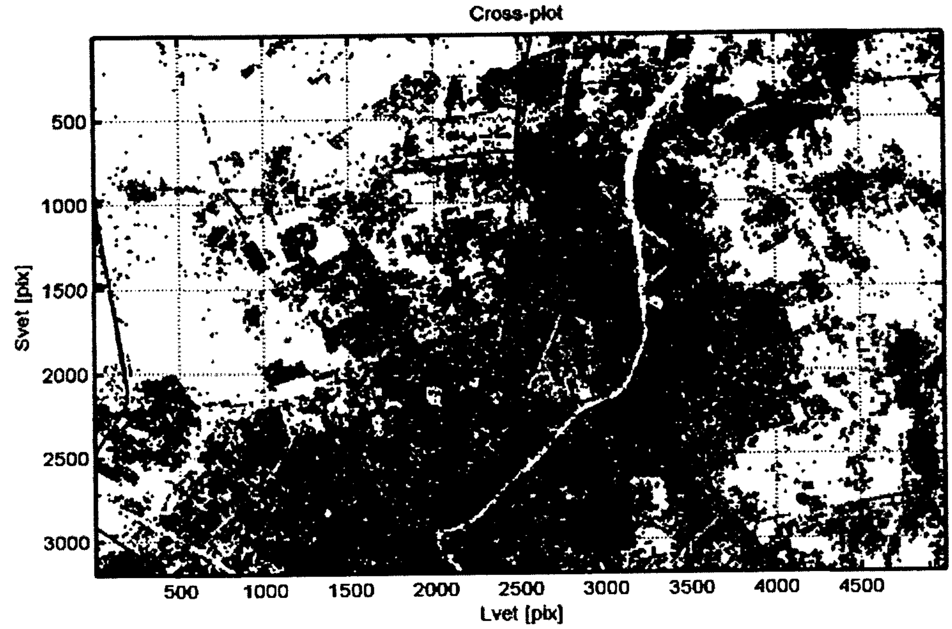

Fig. 3. 100,000 PSC selected in the area of interest.

PSC are individuated posing a threshold on its value. In Figure 3 the ensemble of the obtained PSC (more than 100,000 points) is plotted as a function of their SAR coordinates (samples and lines). From Figures 2 and 3 the city profile and the surrounding rural areas can be easily recognized. The Hai He River crosses the radar image in the middle from the top to the bottom, many streets are visible and on the left a railway appears evident. In Figure 4 on the left the birth dates are shown for a subset of PSC with a colored scale. As clear from Figure 4, the city is increasing its size as years go. On the right of the image the histogram of birth dates is reported.

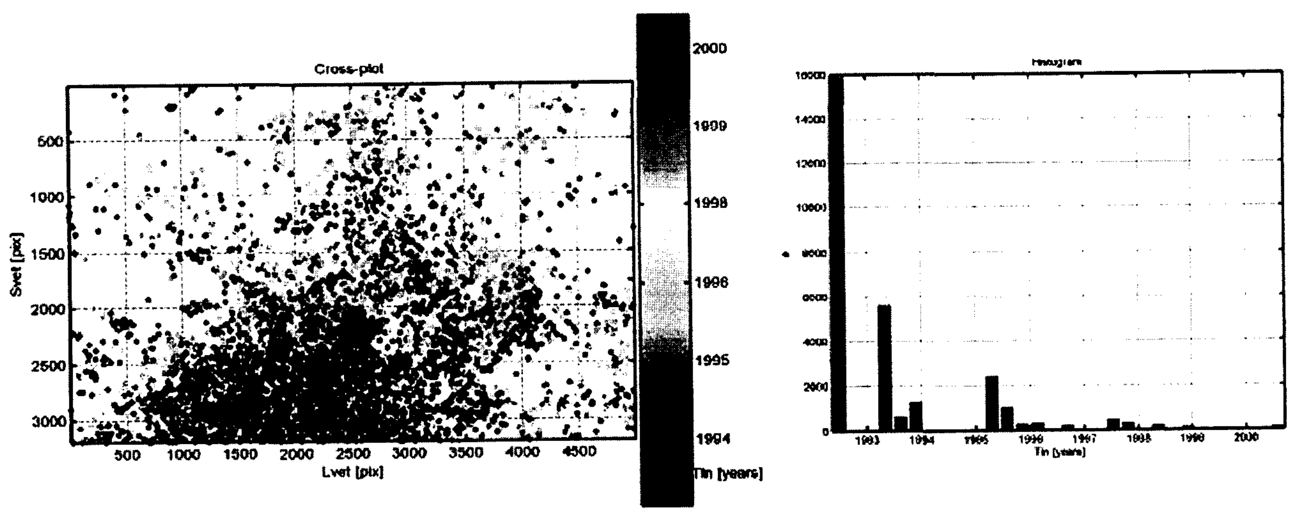

Fig. 4. Birth dates for a subset of PSC (left) and birth dates histogram (right).

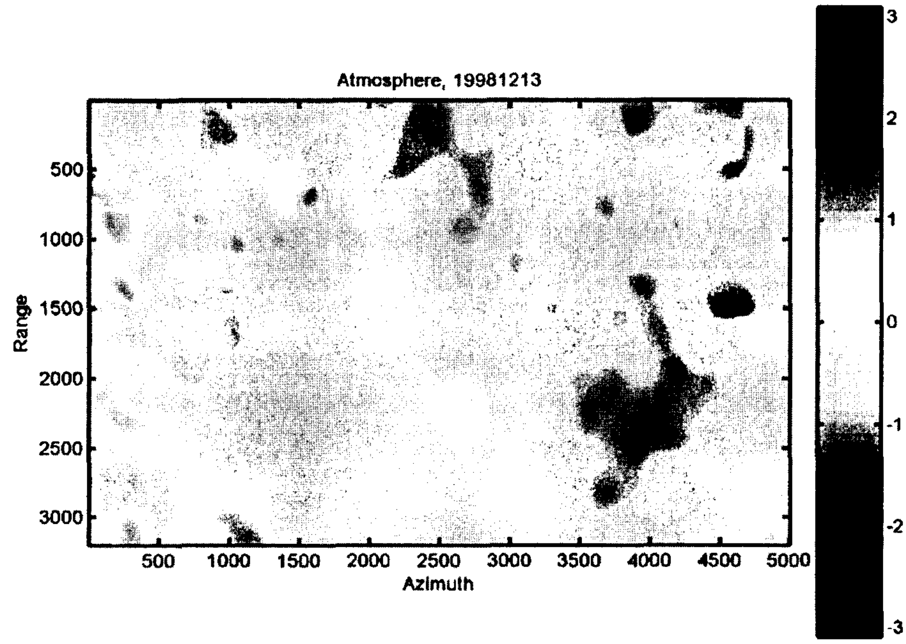

Fig. 5. APS of acquisition 19981213 in radians.

Once PSC are identified, a subset of them equally distributed in space is exploited to retrieve the atmospheric phase screen (APS) through the interferometric phase processing [1], [2]. In Figure 5 an example of APS is reported. Note that far away from the city center the APS is estimated with less accuracy due to the lack of PS's. After removal of the APS for each image, height and average deformation trend are estimated with respect to a reference point. At the end of the processing chain about 10,000 PS's are detected with multi-interferogram coherence $\gamma \geq 0.8$.

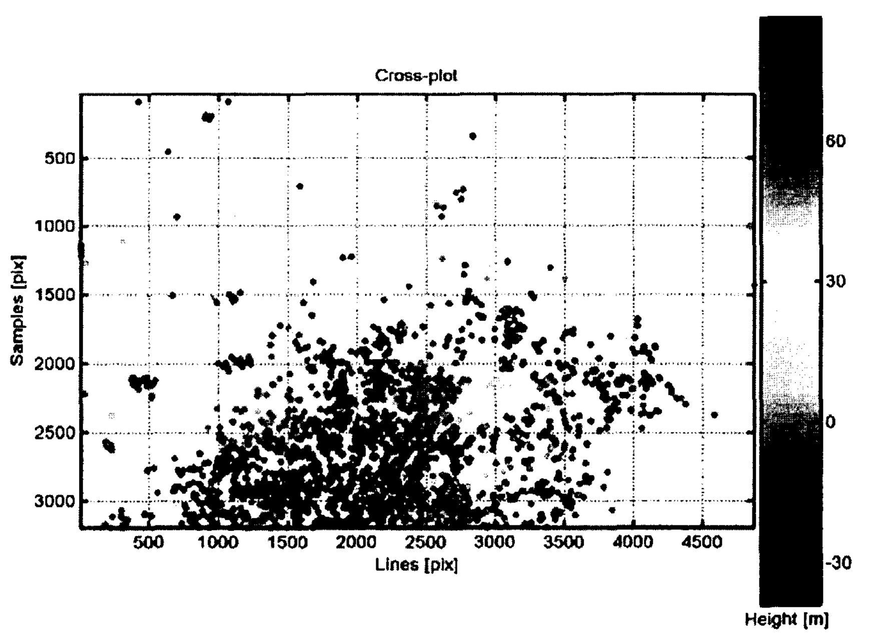

Fig. 6. PS's estimated height.

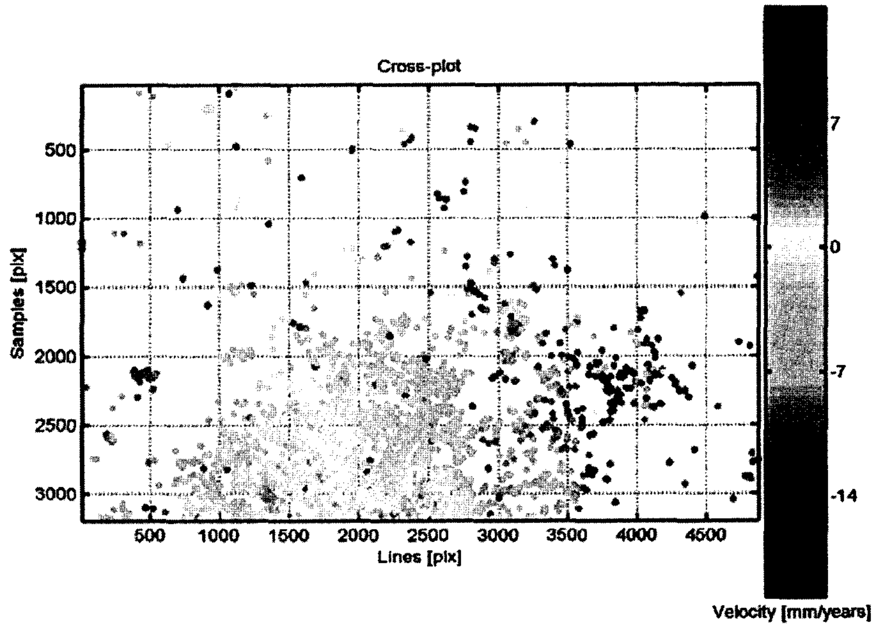

Fig. 7. PS's average deformation trend.

In Figure 6 and 7 the estimated height and average deformation trend are plotted as a function of SAR coordinates. As visible from Figure 7, the city center is almost unaffected by terrain motion, whereas the surrounding areas, in particular on the right of the Hai He River, show an active subsidence with a rate up to about –15mm/year, in good agreement with the local surveys conclusions. In Figure 8 an example of displacement time series is reported for a PS with coherence γ=0.91 and subsiding rate –11mm/year. The lack of data in years 1994 and 1999 in Figure 8 makes evident the impossibility in this case to reconstruct a possible non-linear motion.

The last result we show is a preliminary study on the physical nature of PS's in Tianjin, aimed to the identification of targets visible by other satellites. In this way, possible further work can foresee the exploitation of more satellites or more acquisition geometries for the subsidence monitoring [4], [5], [6]. The adopted strategy is based on the analysis of the amplitudes of each PS as a function of the acquisition geometry, characterized by different values of normal baseline and DC frequency [6]. The variation of the amplitudes is connected to the PS dimensions and orientation in range and azimuth, thus identifying the point-wise targets not affected by geometrical decorrelation. In Figure 9 and 10 the histograms of the obtained parameters are reported respectively for the range and azimuth dimensions.

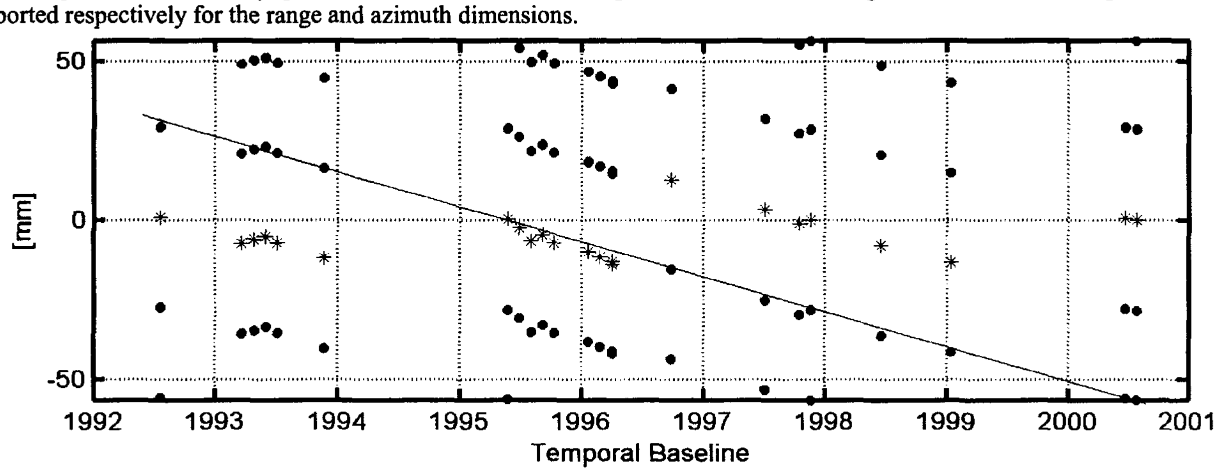

Fig. 8. Example of displacement time series of a PS with coherence γ=0.91 and subsiding rate –11mm/year.

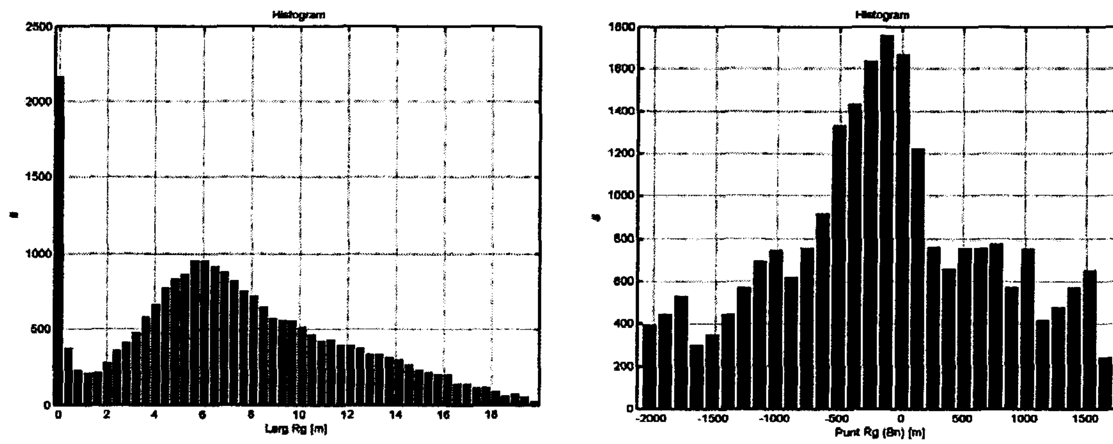

Fig. 9. Histograms of PS's width (left) and orientation (right) in cross-slant range. The peak on zero width identifies possible point-wise targets in cross-slant range (like dihedrals).

References

1. Ferretti A., Prati C., Rocca F., *Permanent Scatterers in SAR Interferometry*, IEEE TGARS, Vol. 39, no. 1, 2001.
2. Ferretti A., Prati C., Rocca F., *Non-linear subsidence rate estimation using permanent scatterers in Differential SAR Interferometry*, IEEE TGARS, Vol. 38, no. 5, 2000.
3. Li T., Liu J., Liao M., *Monitoring City Subsidence by D-InSAR in Tianjin Area* Geoscience and Remote Sensing Symposium IGARSS '04. Proceedings. 2004 IEEE International Volume 5, Page(s): 3333 - 3336 vol.5, 2004
4. Colesanti C., Ferretti A., Perissin D., Prati C., Rocca F., *ERS-ENVISAT permanent scatterers interferometry*, Geoscience and Remote Sensing Symposium, Proceedings. 2003 IEEE International , Volume: 2 , Pages:1130 - 1132 vol.2, 2003.
5. Ferretti A., Perissin D., Prati C., Rocca F., *ERS-ENVISAT Permanent Scatterers* Geoscience and Remote Sensing Symposium IGARSS 2004, Proceedings Anchorage (Alaska), 2004.
6. Ferretti A., Perissin D., Prati C., Rocca F., *On the physical nature of SAR Permanent Scatterers*, URSI Commission F Symposium, http://ursi-f-2005.jrc.it/fullpapers/URSI-F-2005-Art_1.2.pdf, 2005.

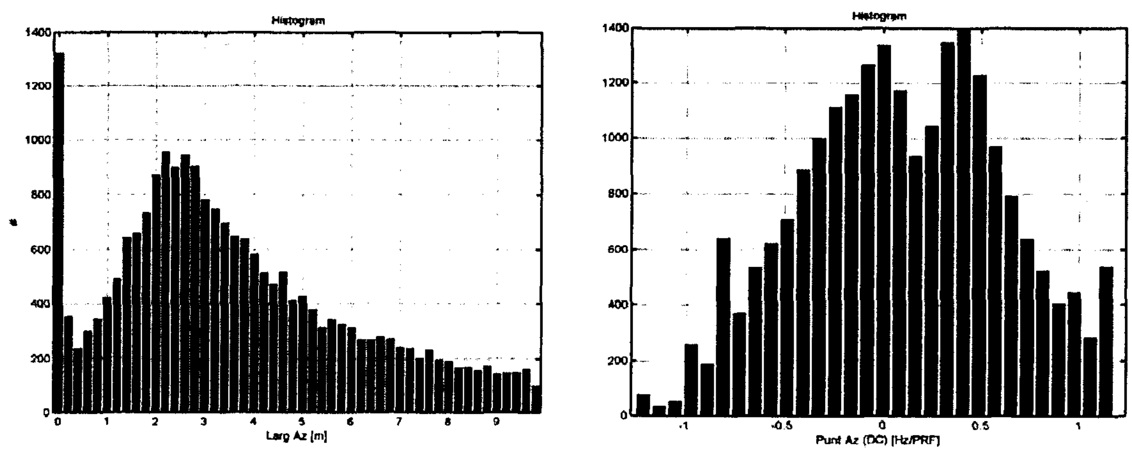

Fig. 10. Histograms of PS's width (left) and orientation (right) in azimuth. The peak on zero width identifies possible point-wise targets in azimuth (like dihedrals and trihedrals).

ARTIFICIAL SCATTERERS FOR S.A.R. INTERFEROMETRY

Parizzi A. (1) , Perissin D. (1), Prati C. (1), Rocca F. (1)

(1) Politecnico di Milano, Via Ponzio 34/5, 20133 Milano, Italy

ABSTRACT.

The evaluation of land displacement using SAR interferometry becomes often very difficult if we consider areas characterized by limited coherence. In this cases it is necessary the use of artificial scatterers. Presently, it is possible to utilize different kinds of reflectors: mirrors, dihedrals, and trihedrals, i.e. corner reflectors. We try to develop new generations of artificial scatterers with better properties. The possibility to use the same reflector for ascending and descending orbits would be a very powerful instrument to better characterize landslides, subsidence or other displacements. Exploiting the experience achieved with Corner Reflectors a new object is proposed to pursue this objective.

1. INTRODUCTION.

SAR interferometry is a good tool to measure topography or crustal deformations; however, changes in reflectivity properties of the area of interest can compromise its utility. If we consider urban areas concrete structures work as good scatterers, but if we have to analyze areas characterized by fields or vegetation it could be impossible to find good scatterers to estimate ground motion. In these cases it is necessary to use artificial scatterers. There are several types of artificial scatterers, the mirror, the diherdral reflector and the corner reflector, plus poles, etc. Each of them has its own characteristics to exploit in different situations. The main object of our studies has been the Corner Reflector. This object is composed by three metal plates (usually of triangular shape), joint together using their sides in order to build a corner. Its main advantages are the high Radar Cross Section granted and the installation that results to be easier than the other artificial reflectors.

2. CORNER CUBES.

The typical Corner Reflector utilized for calibration or as permanent scatterer, is made of triangular plates. However it has been shown that, to optimize the scattering surface, other shapes could be used to build this object [1]. If we consider a Corner Reflector built with squared plates and simulating its behavior using geometrical optics, it's easy to notice that all the surface of the object is exploited (Fig.1, Fig.2), if properly pointed.

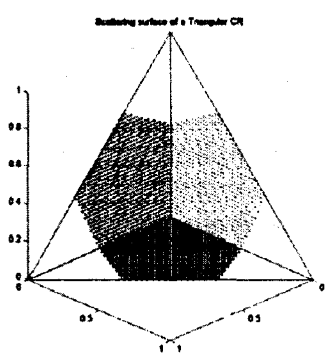

Fig. 1

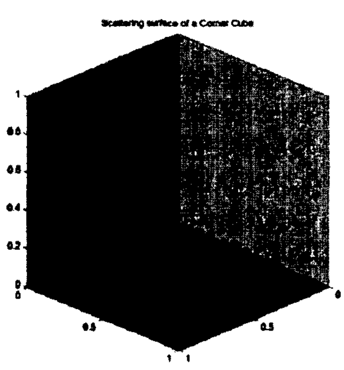

Fig. 2

This explains the different Radar Cross Section formulas (1), (2).

Proc. 2005 Dragon Symposium "Mid-Term Results", Santorini, Greece
27 June – 1 July 2005 (ESA SP-611, January 2006)

$$R.C.S._{tria} = \frac{4\pi l^4}{3\lambda^2} \tag{1}$$

$$R.C.S._{cube} = \frac{12\pi l^4}{\lambda^2} \tag{2}$$

3. ASYMMETRICAL CORNER CUBES.

The aim of the work was the project of new corners that could be as much as possible independent from the pointing, in order realize a multi-platform reflector. A square based corner cube with a longer vertical side has been designed. In this way it is possible to avoid the elevation pointing without loosing too much RCS. A Corner Cube with 1m x 1m base plate and two 1m x 1.5 m lateral plates can be placed sitting on the ground and giving to it only an approximate azimuth orientation. The RCS that can be obtained from this object depends from the platform's look angle (Fig. 3, Fig.4). The Corner could then be seen from different platforms but with different RCS.

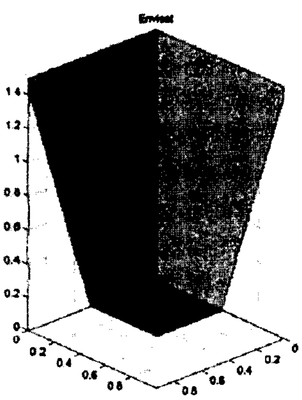

Fig. 3

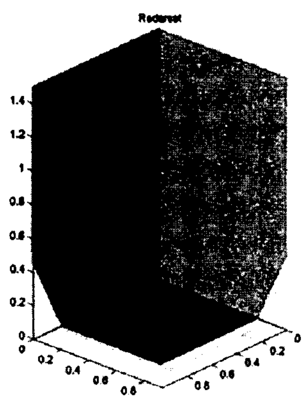

Fig. 4

4. THE HOLED PLATES.

The corner reflectors are objects that must be exposed to atmospheric phenomena at times for many years. The impact of wind and water should be then taken into account. The simplest way to solve this problem is the use of holed plates: wind forces are lower and water can filter through the base avoiding problems due to the accumulation of rain.

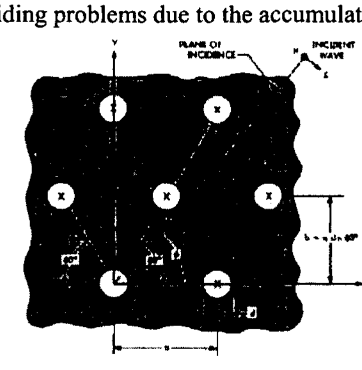

Fig. 5

Moreover, the weight of the object can be reduced. Now the only parameter to define is the holes' dimension: typically the dimension of the hole should be less than $\lambda/8$. However, considering that incidence on the plates it is never 0° and the different scattering properties at different frequencies, it can be shown that in the case of C-band but also of X-band the holes in the plates can reach a diameter of 1 cm, with a respective filled/vacuum ratio of the plates of 60%, preserving a good RCS. It has been shown in [2] that the trasmittivity through holes is given by the following formula:

$$T_{db} = 20Log_{10}\left(\frac{3ab\lambda_0}{2\pi d^3 \cos(\theta_{inc})}\right) + \frac{32t}{d} \tag{3}$$

Where the dimensions a, b, d are shown in the above figure (Fig. 5). (F/V) is the filled/vacuum ratio and t is the thickness of the plates. Considering the dimensions of the object, it is necessary to reinforce the rigidity of the structure with one or more rods between faces. Geometrical optics simulation of the scatterer showed that a rod between the two corners of lateral faces does not create significant RCS losses, because of the small incident angle: however with increasing off-nadir angle some losses may occur but at the same time RCS increases very fast and so their effect can be considered negligible. Two prototypes of this artificial scatterer, with holes in the plates respectively of the diameter of 0.5 cm and 1 cm, has been tested in Milan firstly (Fig. 6, Fig. 7) and then the design has been used in other test sites.

Fig. 6

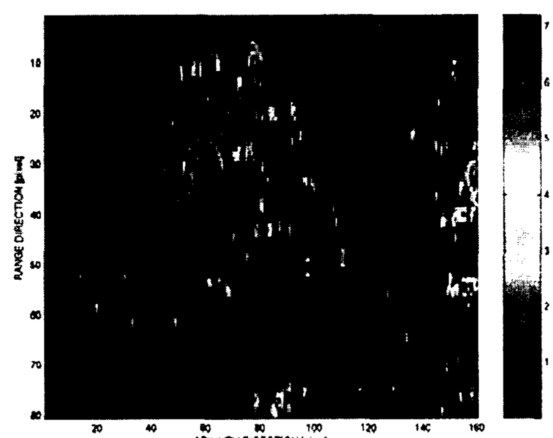

Fig. 7

5. A PROPOSED ASCE/DESCE CORNER REFLECTOR.

The next step in developing artificial scatterers is to design an object that could be seen from both ascendant and descendant orbits. Knowing displacements in different directions permits to understand not only one but two motion components helping the interpretation of data. The solution proposed here exploits the experience achieved from the Corner Reflector proposed before. The idea is to merge two of the corners to create an object that works in two different directions as a corner reflector but with just one scattering center. The main problem to face is related with orbits directions. Ascendant and descendant directions cannot be considered parallel and the angle between them varies changing the latitude of the test site. In Milan, for instance, angles are 26^0 for ENVISAT and 16^0 for RADARSAT. According with this observation it is necessary to optimize the reflector's geometry in order to maximize the RCS in both directions. This can be obtained modifying the ratio between lateral plates (Fig. 8, Fig.9).

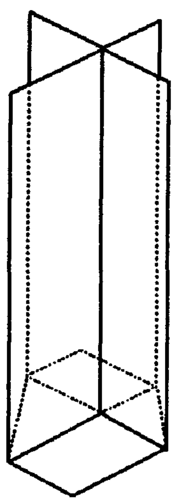

Fig. 8

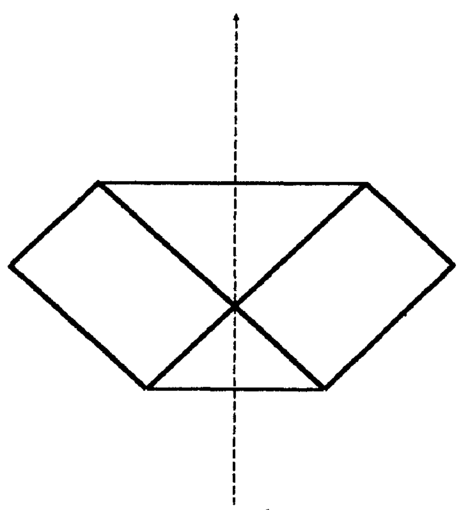

Fig. 9

Some simulations have been done to evaluate this design, plotting the RCS as a function of the difference (X) between the dimension of the two lateral plates. In the figure below we show an example of a simulation using Milan dataset acquisition geometry. It is possible to observe that optimizing sides' proportion the object could be seen by four different orbits each with RCS greater than 2500 m^2 (Fig. 10, Fig.11).

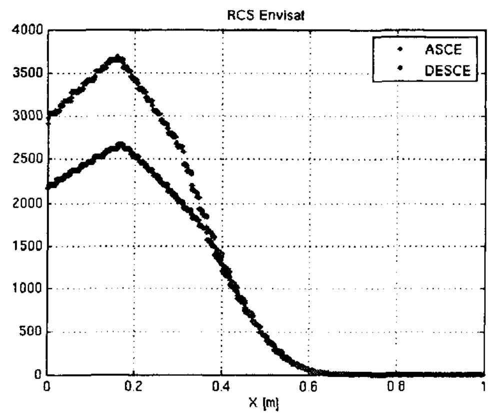

Fig. 10

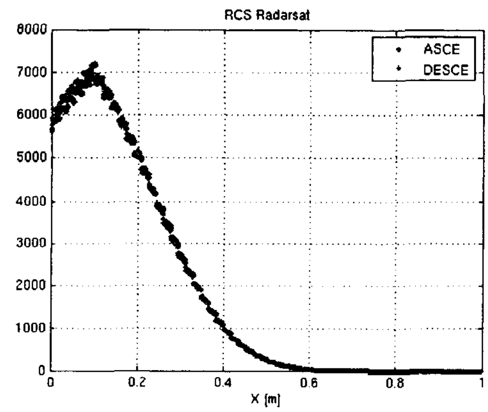

Fig. 11

REFERENCE:

[1] Sarabandi, K., and T. C. Chiu, An optimum corner reflector for calibration of imaging radars, *IEEE Trans. Antennas Propagation,* submitted for publication (Feb. 1995).

[2] T.Y .Otoshi. A Study of Microwave Leakage Through Perforated Flat Plates. *IEEE Trans. Microwave Theory and Techniques,* v. 20, pp. 235-236, March 1972.

New Project

EO and Sport Events
(id 3362)

USE OF EARTH OBSERVATION AND GEOGRAPHIC INFORMATION SYSTEMS IN SUPPORT OF THE OLYMPIC GAMES OF ATHENS 2004

Costas Cartalis

Assistant Professor – University of Athens
former Secretary General for the Olympic Games at the Ministry of Culture

1. INTRODUCTION

The use of earth observation data and Geographic Information Systems was proven supportive for the preparation as well as for the organization of the Olympic Games of Athens 2004. The preparation of the event expanded in a time span of seven years whereas the location of the venues used for the event covered an extended part of the overall Athens area. Earth observation data were used for a number of diverse applications such as land cover/use, urban planning and regeneration, mapping of the thermal environment, air pollution prediction, forecasting meteorology and development of digital elevation models. Geographic Information Systems were used for a variety of applications such as transportation, city operation, telecommunications, etc. Taken the improvement of the technical capacities of satellite missions (with respect to temporal, spatial and spectral resolutions), the potential of earth observation to support the needs of major sport events is growing rapidly.

2. APPLICATION AREAS

Earth Observation was not used on a systematic basis in the Olympic Games of 2004, but rather on a case by case basis and supportively – directly or indirectly - of the following: a) the operational needs of the Olympic Games,
b) the planning of the host city so as to accommodate the requirements of the Olympic Games and
c) the planning interventions for the host city as related to legacy issues.

In particular a number of applications were supported in the pre-Games period (PreG) and the Games period (G) with the use of data from such satellites as NOAA/AVHRR, Meteosat, Landsat, SPOT, IKONOS, etc. The applications included:

1. Land use/cover (PreG)
2. Urban and spatial planning (PreG)
3. Thermal environment of Athens (PreG)
4. Forecasting meteorology (G)
5. Marine meteorology (G)
6. Air pollution (G)
7. Digital Elevation Models (G)

For example, Figure 1 shows the land cover map and the thermal environment of the overall Athens area as depicted with the use of Landsat satellite images in the visible and thermal infrared channels.

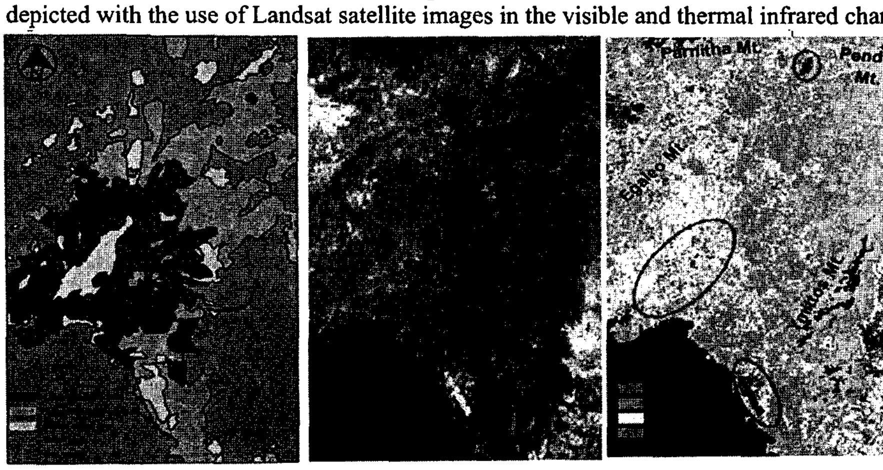

Land cover map Raw thermal image Spatial SUHI mapping

Figure 1. Land cover map and spatial surface urban heat island distribution for the overall Athens area as depicted from the use of Landsat satellite images (20/5/2000).

A number of other needs of the Olympic Games were indirectly supported from earth observation data or satellite services. Such needs refer to telecommunications, transportation, security, mapping, city operations, etc. The exploitation of the EO data was supported with the use of Geographic Information Systems especially designed for the needs of the Olympic Games.

CONCLUSIONS

Taken the experience of the Athens Games, the assessment is that the potential of EO to support the overall (planning and organisational) needs and legacy priorities of an event of the size and characteristics of the Olympic Games is high. It should be mentioned that the level of support varies, depending the application and its specific requirements. Difficulties stem from the limited penetration of EO in the public administration as well as from the limitations of the data in terms of their temporal or spatial resolutions. Table 1 provides the potential of Earth Observation in supporting needs related to the Olympic Games.

Table 1. *Potential of Earth Observation to support needs of the Athens 2004 Olympic Games*

Environmental needs for the Olympic Games	Potential of Earth Observation to support needs
Assessment of land use/cover	High
Spatial planning support	High
Spatial definition of air pollution (suspended particles)	Moderate
Microclimatic assessment of the area (thermal environment and thermal comfort indices)	High
Support of environmental impact assessments	High
Forecasting meteorology	High
Decision making tools (GIS) regarding the city area	High

Demonstration of successful case studies needs to be promoted so as interested parties (e.g. those involved or having the responsibility of the Olympic Games of 2008 and 2012) to be convinced on the potential of EO to support planning and organisational needs of events of the scale and the complexity of the Olympic Games.

**This extended abstract is based on a presentation made by the author during the DRAGON Symposium, Santorini, June 2005. In addition, a specific project has been promoted within DRAGON so as to explore the use of earth observation in support of sport events.*

List of Participants

Constantinos Cartalis
University of Athens
Department of Applied Physics (Remote Sensing)
Building Phys-V,
Panepistimiopolis
106 80 Athens
Greece
ckartali@cc.uoa.gr

Irene Renis
Serco S.P.A C/O ESA/ESRIN
Via Galileo Galilei
00044 Frascati
Italy
irene.renis@esa.int

Andrew Zmuda
Serco S.P.A C/O ESA/ESRIN
Via Galileo Galilei
00044 Frascati
Italy
andy.Zmuda@esa.int

Cecile Lasserre
ENS-Paris
Laboratire De Geologie
24 Me Lhomond Cedex 15
75231 Paris
France
Lasserre@Geologie.Ens.Fr

Seppo Hassinen
Finnish Meteorological Institute
Earth Observation
503, 00101
Finland
Seppo.Hassinen@Fmi.Fi

Oliver Cartus
Friedrich - Schiller University
Dept of Geoinformatics and Remote Sensing
Loebdergraben 32
D-07743 Jena
Germany
Oliver@Cartus.Com

Yves-Louis Desnos
European Space Agency (ESA/ESRIN)
Research & Development Section
Via Galileo Galilei
00044 Frascati
Italy
yves-louis.desnos@esa.int

Rita Malosti
Serco S.P.A C/O ESA/ESRIN
Via Galileo Galilei
00044 Frascati
Italy
rita.malosti@esa.int

Karl Bergquist
European Space Agency (ESA/ESRIN)
8-10 Rue Mario Nikis Paris Cedex 15
75738 Paris
France
Karl.Bergquist@esa.int

Erkki Kyrola
Finnish Meteorological Institute
Earth Observation
503, 00101
Finland
Erkki.Kyrola@Fmi.Fi

Maurizio Santoro
Friedrich - Schiller University
Department of Geoinformatics and Remote Sensing
Loebdergraben 32
D-07743 Jena
Germany
Maurizio.Santoro@Uni-Jena.De

Herve Yesou
SERTIT
Ensps, Parc D'innovation
Bouvelard Sebastien Brant
Bp 10413
F-67412 Illkirch Graffestaden
France
Herve@Sertit.U-Strasbg.Fr

Remi andreoli
SERTIT
9 Bld Sebastien Brandt
BP 10413
67412 Illkirch
France
Remi@Sertit.U-Strasbg.Fr

Tobias Mette
DLR
1116
82234 Wessling
Germany
tobias.mette@dlr.de

Zhongbo (Bob) Su
ITC
7500 AA Enschede
Netherlands
B_Su@Itc.nl

Johnny Johannessen
Nansen Environmental and Remote Sensing Center
Thormøhlensgt. 47
N-5006 Bergen
Norway
Admin@Nersc.No

Knut-Frode Dagestad
Nansen Environmental and Remote Sensing Center,
Thormøhlensgt. 47
N-5006 Bergen,
Norway
Admin@Nersc.No

Ghislain De Marsily
Universite Paris Iv
Umr Sisyphe Case 105, 4 Place Jussiev
75252 Paris Cedex 05
France
Gdm@Ccr.Jussieu.Fr

Danielle Altlmeyer-Bertuca
ESA
International Relations
8-10, Rue Mario-Nikis
75015 Paris
France
Danielle.Bertuca@esa.int

Danielle Altlmeyer-Bertuca
ESA
International Relations
8-10, Rue Mario-Nikis
75015 Paris
France
Danielle.Bertuca@esa.int

Rogier V.D. Velde
ITC
N. 6
7500 AA Enschede
Netherlands
Rogier.Vandervelde@Wur.Nl

Hui Li Gong
Capital Normal University
No 105 At West 3rd-Ring
North Road
Beijing
China
Gonghl@263.Net

Xiaojuan Li
Capital Normal University
No 105 Xisanhuanbei Road
100037 Beijing
China
Gonghl@263.Net

Shaun Quegan
University of Sheffield
Sceos/Ctcd, Hicks Building,
Hounsfield Road
Sheffield
UK
M.Bullock@Shef.Ac.Uk

Xiufen Li
Heilongjiang Province Institute of
Meteorological Sciences
No 71 Diantan Street Xiangfang
Dist. Harbin
China
China_Licn@Yahoo.Com

Bingxiang Tan
Institute of forest Resources
Information Techniques of Chinese Academy of forestry
Wan Shou Shan Hou, Haidian District
100091 Beijing
China
Tan@forestry.Ac.Cn

Jiren Li
China Institute of Water Resources and
Hydropower Research
Dept of International Cooperation & Scientific Research
20 West Chegongzhuang Road
100044 Beijing
China
Lijiren@Iwhr.Com

Jingfeng Xin
China Institute of Water Resources and
Hydropower Research
Remote Sensing Technology Application Centre
20 West Chegongzhuang Road
Beijing
China
Xinjf@Iwhr.Com

Shifeng Huang
China Institute of Water Resources and
Hydropower Research
Remote Sensing Technology Application Centre
20 West Chegongzhuang Road
Beijing
China
Huangsf@Iwhr.Com

Thuy Le Toan
CESBIO
18 Avenue E. Belin
31401 Toulouse Cedex 4
France
Thuy.Letoan@Cesbio.Cnes.Fr

Guocheng Zhang
Ministry of Science and Technology
NRSC - Science and Technology of
People's Republic of China
15b Fuxing Road
100862 Beijing
China
Zhsongmei@Nrscc.Gov.Cn

Ling Shi
Ministry of Science and Technology
Dept. of High and New Technology and
Industrialization of Ministry of Science and
Technology of People's Republic of China
15b Fuxing Road
100862 Beijing
China
Zhsongmei@Nrscc.Gov.Cn

Songmei Zhang
Ministry of Science and Technology
National Remote Sensing Centre of China of Science
and Technology of People's Republic of China
15b Fuxing Road
100862 Beijing
China
Zhsongmei@Nrscc.Gov.Cn

Xiao Han Liao
Ministry of Science and Technology
Department of High and New Technology
15b Fuxing Road
100862 Beijing
China
Zhsongmei@Nrscc.Gov.Cn

Xin Tian
Chinese Academy of forestry
Research Institute of Forest Resources
Information Techniques
Haidian District
100091 Beijing
China
Tianxin@Nrscc.Gov.Cn

Zhihai Gao
Chinese Academy of forestry
Research Institute of forest Resources
Information Techniques
Haidian District
100091 Beijing
China
Zhihai.Gao@Nrscc.Gov.Cn

Zhihai Gao
Chinese Academy of forestry
Research Institute of forest Resources
Information Techniques
Haidian District
100091 Beijing
China
Zhihai.Gao@Nrscc.Gov.Cn

Pang Yong
Chinese Academy of forestry
Research Institute of forest Resources
Information Techniques
Haidian District
100091 Beijing
China
Pangy@forestry.Ac.Cn

Xianlin Qin
Chinese Academy of Forestry
Research Institute of forest Resources
Information Techniques
Haidian District
100091 Beijing
China
Noaags@forestry.Ac.Cn

Qin Min Wang
Spatial Information Research Centre
Fujian Province
Level 13, Science Building
Fuzhou Universit
No 523, Gongye Road
Fuzhou
China
Qmwang@Fzu.Edu.Cn

Hong Qiu
National Satellite Meteorological Centre
China Meteorological Administration
No 46 of South Avenue of Zhong Guan Cun
Beijing
China
Qiuh@Nsmc.Cma.Gov.Cn

Tom Rientjes
ITC
N.6
7500 AA Enschede
Netherlands
Rientjes@Itc.Nl

Erxue Chen
Chinese Academy of forestry
Research Institute of forest Resources
Information Techniques
Haidian District
100091 Beijing
China
Chenerx@forestry.Ac.Cn

Zengyuan Li
Chinese Academy of forestry
Research Institute of forest Resources
Information Techniques
Haidian District
100091 Beijing
China
Zengyuan.Li@forestry.Ac.Cn

Liao Mingsheng
Wuhan University
State Key Laboratory for Information Eng. In
Surveying, Mapping and Remote Sensing
Luoyu Road 129
C310 - 430079 Wuhan
China
Liao@Whu.Edu.Cn

Xiaoqin Wang
Spatial Information Research Centre
Fujian Province
Level 13, Science Building
Fuzhou University
No 523, Gongye Road
Fuzhou
China
Wangxq@Fzu.Edu.Cn

Ruyun Tan
Missions of the Ministry of Science and
Technology of the People's Republic of Chine
15b Fuxing Road
100862 Beijing
China
Tanruyun@Htrdc.Com

Kan Zeng
Ocean Remote Sensing Institute
Yu Shan Road
Ocean University of China
266003
China
Zengkan@Orsi.Ouc.Edu.Cn

Keping Du
Research Centre of Remote Sensing & Gis
Beijing Normal University
China
Kpdu@Bnu.Edu.Cn

Lei Guan
Ocean Remote Sensing Institute
Yu Shan Road 5
Ocean University of China
266003
China
Leiguan@Orsi.Ouc.Edu.Cn

Mingqiang Fang
Ocean Remote Sensing Institute
Yu Shan Road
Ocean University of China
266003
China
Fmq@Orsi.Ouc.Edu.Cn

Tinglu Zhang
Ocean Remote Sensing Institute
Yu Shan Road 5
Ocean University of China
266003
China
Zhangtl@Orsi.Ouc.Edu.Cn

Hongping Li
Ocean Remote Sensing Institute
Yu Shan Road 5
Ocean University of China
266003
China
Lihp@Orsi.Ouc.Edu.Cn

Mingxia He
Ocean Remote Sensing Institute
Yu Shan Road 5
Ocean University of China
266003
China
Mxhe@Orsi.Ouc.Edu.Cn

Zhishen Liu
Ocean Remote Sensing Institute
Yu Shan Road 5, Ocean University of China
266003
China
Zsliu@Orsi.Ouc.Edu.Cn

Werner Alpers
University of Hamburg
Institute of Oceanography
Bundesstr. 53
20146
Germany
Alpers@Ifm.Uni-Hamburg.De

Xueen Chen
Ocean Remote Sensing Institute
Bundesstr. 53
D-20146 Hamburg
Germany
Chen@Ifm.Uni-Hamburg.De

Jin Song Chong
Chinese Academy of Sciences
Instutute of Electronics
2702
100080 Beijing
China
Lily@Mail.Ie.Ac.Cn

Huai Zu Liu
China Centre of Adeviced Science and Technology
8730
100080 Beijing
China

Min Hui Zhu
Chinese Academy of Sciences
Institute of Electronics
2702
100080 Beijing
China
Mihzhu@Mail.Ie.Ac.Cn

Xiwei Xu
China Earthquake Administration
Dewai Qijiahuozi
Beijing
China
Xiweixu@Vip.Sina.Com

Fang Liang
Beijing Earthquake Administration
No 28, Suzhou Street
Beijing
China
Liang.F@Mail.China.Com

Jianbao Sun
China Earthquake Administration
Dewai Qijiahuozi
Beijing
China
Suninsar@Yahoo.Com

Deren Li
Wuhan University
State Key Laboratory for Information Eng. In
Surveying, Mapping and Remote Sensing
Luoyu Road 129 - C310
430079 Wuhan
China
Drli@Whu.Edu.Cn

Bingbai Li
Jiangsu Academy of Agricultural Sciences
Institute of Agricultural Resource and Environment
Xiaolingwei
210014 Jiangsu
China
Bbli88@Sohu.Com

Youqi Chen
Jiangsu Academy of Agricultural Sciences
Inst. of Agricultural Resource and Environment
100081 Beijing
China
Chenyqi@Mail.Caas.Net.Cn

Fei Li
Ministry of Science and Technology of the People's
Republic of China
Department of Personnel
15b Fuxing Road
100862 Beijing
China
Lif@Mail.Most.Gov.Cn

Lin Shi
Ministry of Science and Technology of the People's
Republic of China
Department of High and New Technology
Development and Industrialization
15b Fuxing Road
100862 Beijing
China
Zhsongmei@Nrscc.Gov.Cn

Jingmei Yang
Institute of Atmospheric Physics
Deshengmenwai
100029 Beijing
China
Pcwang@Mail.Iap.Ac.Cn

Jinhuan Qiu
Institute of Atmospheric Physics
Deshengmenwai
100029 Beijing
China
Pcwang@Mail.Iap.Ac.Cn

Pucai Wang
Institute of Atmospheric Physics
Deshengmenwai
100029 Beijing
China
Pcwang@Mail.Iap.Ac.Cn

Yi Liu
Institute of Atmospheric Physics
Deshengmenwai
100029 Beijing
China
Pcwang@Mail.Iap.Ac.Cn

Xiaojing Li
National Satellite Meteorological Centre
China Meteorological Administration
No 46 of South Avenue of Zhong Guan Cun
Beijing
China
Lixjing@Nsmc.Cma.Gov.Cn

Muriel Simon
Serco S.P.A C/O ESA/ESRIN
Via Galileo Galilei
00044 Frascati
Italy
Muriel.Simon@esa.int

Eric Pottier
IETR
Umr Cnrs 6164
University of Renes 1
Campus De Beaulieu, Bat 11d
263 Avenue Gal Leclerc
35042 Rennes
France
Eric.Pottier@Univ-Rennes1.Fr

Laurent Ferro-Famil
IETR
Umr Cnrs 6164
University of Renes 1
Campus De Beaulieu, Bat 11d
263 Avenue Gal Leclerc
35042 Rennes
France
Laurent.Ferro-Famil@Univ-Rennes1.Fr

Issaak Parcharidis
Harokopio University of Athens
Department of Geography
El. Venizelou 70
176 71 Athens
Greece
Parchar@Hua.Gr

Fabio Rocca
Politecnlco
Piazza Lonardo Da Vonci 32
Italy
Rocca@Elet.Polimi.It

Alexandre Bouvet
Cesbio
Bpi 2801 - 18 Avenue Edouard Belin
31401 Toulouse Cedex 9
France
Alexandre.Bouvet@Cesbio.Cnes.Fr

George Technitis
Harokopio University of Athens
Department of Geography
El. Venizelou 70
17671 Athens
Greece
George.Technitis@Gmail.Com

Michael Foumelis
University of Athens
El. Venizelou 33
15773 Athens
Greece
Mfoum@Geol.Uoa.Gr

Qinghua Yang
China Aero Geophysical Survey & Remote
Sensing Center for Land Resources
29 Xueyuan Road
100083 Beijing
China
Yangqh9090@Sina.Com; Crsgagrs@163bj.Com

Shengqing Xiong
China Aero Geophysical Survey & Remote
Sensing Center for Land Resources
29 Xueyuan Road
100083 Beijing
China
Yangqh9090@Sina.Com; Crsgagrs@163bj.Com

Xiao Guiyi
China Geology Survey
29 Xueyuan Road
100083 Beijing
China
Yangqh9090@Sina.Com; Crsgagrs@163bj.Com

Xuwen Qin
China Geology Survey
29 Xueyuan Road
100083 Beijing
China
Yangqh9090@Sina.Com; Crsgagrs@163bj.Com

Nie Hongfeng
China Aero Geophysical Survey & Remote
Sensing Center for Land Resources
29 Xueyuan Road
100083 Beijing
China
Yangqh9090@Sina.Com; Crsgagrs@163bj.Com

Zhenhong Li
University College of London
Department of Geomatic Engineering
Gower Street
WC1E 6BT London
United Kingdom
Zhli@Ge.Ucl.Ac.Uk

Qiming Zeng
Perking University
Institute of Remote Sensing & Gis
100871 Beijing
China
Qmzeng@Pku.Edu.Cn

Jingfa Zhang
Chinese Seismological Bureau
Institute of Crustal Dynamics
2855# Beijing
China
Zhangjingfa@263.Net

Hennie Kelder
KNMI
Postbus 201
3730AE De Bilt
Netherlands
Kelder@Knmi.Nl

Charles Baubion
CIG Paris School of Mines
Chinese Academy of Sciences
Sino-French Joint Laboratory In Informatics
Autom.& Applied Mathematics
Inst. of Automation 2728
100080 Beijing
China
Baubion@Liama.Ia.Ac.Cn

Jan-Peter Muller
University College of London
Department of Geomatic Engineering
Gower Street
London
United Kingdom
Jpmuller@Ge.Ucl.Ac.Uk

Konstantinos Kourtidis
Demokritus University of Thrace
Department of Environmental Engineering
12 Vasilisis Sofias Street
67100 Xanthi
Greece
Kourtidi@Env.Duth.Gr

Xue Jun Cao
Ministry of Science and Technology
Department of High and New Technology
Development and Industrialization of Ministry of
Science and Technology of People's Republic of China
15b Fuxing Road
100862 Beijing - China
Zhsongmei@Nrscc.Gov.Cn

Guy Vasseur
CNRS
SDU/INSU
3 Rue Michel Ange
75016 Paris
France
Guy.Vasseur@Cnrs-Dir.Fr

Stephen Briggs
ESA
ESRIN
Via Galileo Galilei 44
I-00044 Frascati
Italy
Stephen.Briggs@esa.int

Abel Calle
University of Valladolid
Latuv
Paseo De Belen 1
47005 Valladolid
Spain
Abel@Latuv.Uva.Es

Jose-Luis Casanova
University of Valladolid
Latuv
Paseo De Belen 1
47005 Valladolid
Spain
Jois@Latuv.Uva.Es

Cristina Moclan
University of Valladolid
Latuv
Paseo De Belen 1
47005 Valladolid
Spain
Christina@Latuv.Uva.Es

Vassilis Anastasopoulos
University of Patras
Department of Physics
Electronic Laboratory
26500 Rio
Greece
Vassilis@Physics.Upatras.Gr

Vassilis Tsagaris
University of Patras
Department of Physics
Electronic Laboratory
26500 Rio
Greece
Vassilis@Physics.Upatras.Gr

George Cristoulas
University of Patras
Department of Physics
Electronic Laboratory
26500 Rio
Greece
Vassilis@Physics.Upatras.Gr

Guojin He
University of Sheffield - Inf. Processing Dept.
China Remote Sensing Satellite
Visiting Scholar at CTCD
702 Attercliffe Road
S9 3RP Sheffield
United Kingdom
He.Guojin@Shef.Ac.Uk

Ronald van der A
KNMI
201
3730AE De Bilt
Netherlands
Avander@Knmi.Nl

Christiane Schmullius
Friedrich Schiller University Jenna
Loebdergraben 32
D-07743 Jena
Germany
C.Schmullius@Uni-Jena.De

Christine King
BRGM
B.P. 6009
45060 Orleans
France
C.King@Brgm.Fr

Nicolas Baghdadi
BRGM
B.P. 6009
45060 Orleans
France
N.Baghdadi@Brgm.Fr

Roland Doerffer
Gkss Research Centre Geesthacht
Max Planck Street 1
21502 Geesthacht
Germany
Doerffer@Gkss.De

Alessandro Parizzi
Politecnico Di Milano
Via Giuseppe Ponzio 34/5
20133 Milano
Italy
Parizzi@Elet.Polimi.It

Daniele Perissin
Politecnico Di Milano
Via Giuseppe Ponzio 34/5
20133 Milano
Italy
Perissin@Elet.Polimi.It

Claudia Kunzer
German Remote Sensing Data Center
DFD, DLR
Postfach 1116
82230 Wessling
Germany
Claudia.Kuenzer@DLR.De

Athanassios Ganas
National Observatory of Athens
Institute of Geodynamics
Lofos Nymfon - Thission
118 10 Athens
Greece
Aganas@Gein.Noa.Gr

Isabelle De Smedt
BIRA
IASB
3 Avenue Circulaire
01180 Brussels
Belgium
Isabelle.Desmedt@Aeronomie.Be

Jeroen Kuenen
KNMI
TUE - 201
3730AE De Bilt
Netherlands
Kuenenj@Knmi.Nl

David Peters
KNMI
TUE - 201
3730AE De Bilt
Netherlands
Peters@Knmi.Nl

Sean-Francois Piolle
IFREMER
Cersat
Technopole Brest-Iroiso
29280 Plouzane
France
Jfpiolle@Ifremer.Fr

Paul Simon
Institute D'aeronomie Spatiale De Belgique
IASB
3, Eaunue Cuculaire
B-1180 Brussels
Belgium
Paul.Simon@Aeronomic.Be

Pierre Potin
ESA
Via Galileo Galilei, Casella Postale 64
00044 Frascati
Italy
Pierre.Potin@esa.int

Alberte Bondeau
Potsdam Institute for Climate Impact Research (PIK)
601203
D-14412
Germany
Alberte.Bondeau@Pik-Potsdam.De

Veronique Amans
ESA
ESRIN
Via Galileo Galilei
00044 Frascati
Italy
Veronique.Amans@esa.int

Lars Freden
ESA
8-1-Rue Mario Nikls
F-75738 Paris
France
Lars.Freden@esa.int

Christos Zerefos
University of Athens
National Observatory at Athens
Laboratory of Climatology and Atmospheric
Environment, Faculty of Geology
15784 Athens
Greece
Zerefos@Geol.Uoa.Gr

Jing Li
Beijing Normal University (BNU)
Beijing 100875
China

Group Photos

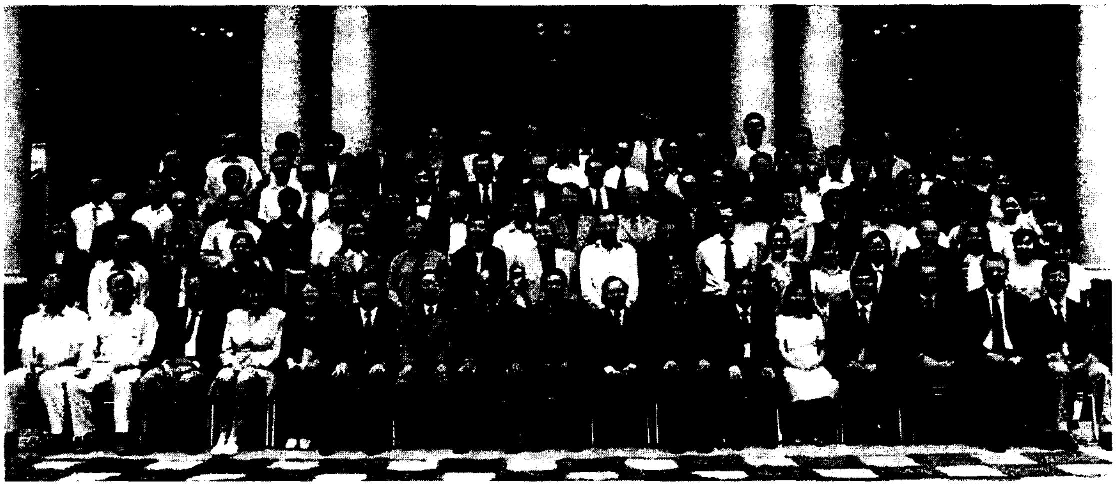

Dragon Programme, Xiamen Symposium, P.R. China, 27-30 April 2004

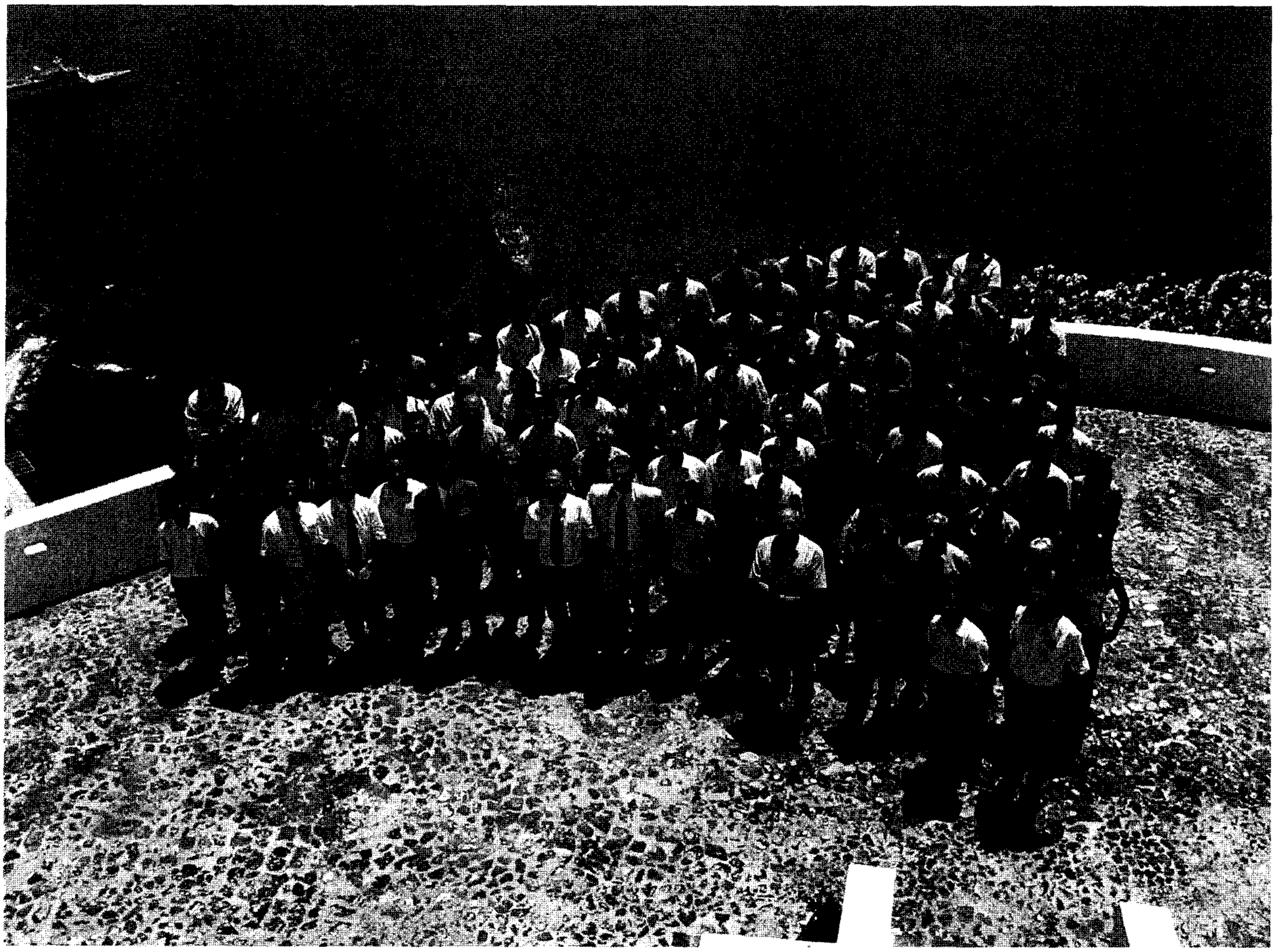

Proc. 2005 Dragon Symposium "Mid-Term Results", Santorini, Greece
27 June – 1 July 2005 (ESA SP-611, January 2006)